MAGNETIC NEUTRON SCATTERING FROM TRANSITION METAL ALLOYS

by

Stephen Keast Burke

Submitted for the degree of
Doctor of Philosophy

Imperial College of Science and Technology, London

September 1980

ABSTRACT

The magnetic properties of b.c.c. Cr Fe alloys with concentrations between 5% and 25% Fe were studied by neutron scattering, low field magnetization and resistivity measurements. The magnetic order evolved from antiferromagnetism (C < 16% Fe) to ferromagnetism (C > 19% Fe) with increasing concentration. Spin glass type behaviour was found in the narrow concentration range between the two critical concentrations.

The Néel temperature and ordered antiferromagnetic moment decreased with increasing Fe concentration. This is contrary to the rigid band model for Cr alloys and was explained by the pair breaking effect of localized Fe moments.

The magnetization distribution in antiferromagnetic Cr Fe alloys is spatially inhomogeneous. Large, slowly relaxing clusters of ferromagnetically coupled Fe moments were found to coexist with the antiferromagnetic spin density wave (SDW) for concentrations above 10%. The spin glass phenomena observed in the low field magnetization of these antiferromagnetic alloys was attributed to such clusters. A neutron polarization-analysis study of a Cr Fe 5% alloy suggested a long range magnetic disturbance of the SDW in the vicinity of isolated Fe moments.

The spin correlations in the neighbourhood of the critical concentration for ferromagnetism (C_F) were studied using neutron small-angle scattering. The concentration and temperature dependence of the inverse correlation range for $C < C_F$ was in semi-quantitative agreement with models for the percolation multicritical point, indicating a geometrical element in the development of ferromagnetic order. Ferromagnetic alloys close to C_F showed complex behaviour and significant spatial magnetic inhomogeneity.

The spin glass behaviour observed between the two critical concentrations could be well described by a phenomenological fine particle model.

The magnetization density in Pt_3Cr was determined by polarized neutron diffraction. A large moment of $2.88 \pm 0.06\ \mu_B$ was found on Cr sites. The moment on Pt sites was best described by a combination of an antiferromagnetic Cr moment and a ferromagnetic Pt moment.

CONTENTS PAGE

ABSTRACT i
ACKNOWLEDGEMENTS viii

CHAPTER 1
INTRODUCTION 1

CHAPTER 2
MAGNETIC NEUTRON SCATTERING 5
2.1 Introduction
1 The scattering cross section 5
2 The nuclear interaction 9
3 The magnetic interaction 13
4 Summary 16
2.2 Magnetic scattering with unpolarized beams 17
1 Correlation functions 17
2 Bragg scattering 22
3 Elastic magnetic diffuse scattering 25
4 The quasistatic approximation 28
5 The orientational average 35
2.3 Magnetic scattering with polarized beams 39
1 Introduction 39
2 Bragg scattering 41
2.4 Polarization - analysis 43
1 Introduction 43
2 Spin flip and non spin flip scattering 45
2.5 Small angle scattering 48
1 Introduction 48
2 Scattering from superparamagnetic particles 50

PAGE

CHAPTER 3 53

EXPERIMENTAL

3.1 Sample preparation 53

3.2 Neutron scattering instruments and experimental procedure 57

1 General remarks 57

2 Absolute Intensity measurements 57

3.3 Small angle scattering 61

1 Introduction 61

2 The small angle scattering camera: D11A 61

1 Description 61

2 Sample environment 63

3 Experimental procedure 63

3 The high κ resolution spectrometer: D17 64

1 Description 64

2 Sample environment 65

3 Experimental procedure 65

4 Time of flight measurements 66

4 Data analysis 67

3.4 Powder diffraction 69

1 Introduction 69

2 CURRAN 70

1 Description 70

2 Sample environment 70

3 Experimental procedure 71

3 PANDA 71

3.5 Diffuse scattering - time of flight 72

1 Introduction 72

2 Diffuse scattering instrument: D7 74

1 Description 74

2 Sample environment 74

3 Sample geometry 75

4 Experimental procedure 75

PAGE

3.6 Polarized beam diffraction 77
1 Introduction 77
2 Polarized beam diffractometer: D3 77
1 Description 77
2 Sample environment 78
3 Experimental procedure 78
3 Unpolarized single crystal diffractometer: MKV1 79
3.7 Polarization - Analysis 81
1 Introduction 81
2 Polarization - analysis instrument: D5 82
1 Description 82
2 Sample environment 83
3 Experimental procedure 84
3.8 Bulk Magnetic measurements 86
1 Introduction 86
2 Low field magnetization 86
3 AC susceptibility 88
3.9 Resistivity measurements. 89

CHAPTER 4
ANTIFERROMAGNETISM IN CR-FE ALLOYS 90
4.1 The itinerant antiferromagnetism of Cr 91
1 Introduction 91
2 The itinerancy of antiferromagnetism in Cr 91
3 The SDW and Fermi surface nesting 94
4 Two band models for Cr 97
5 Alloying behaviour 103
6 Discussion 107
4.2 Previous work on Cr Fe antiferromagnetic alloys 110
1 Metallurgy of the Cr Fe alloy system 110
2 Dilute Cr Fe alloys (C < 5%) 111
1 Magnetic transitions in dilute Cr Fe alloys 111
2 The nature of the Fe moment in dilute Cr Fe alloys 112
3 Theory 116

PAGE

3 Concentrated antiferromagnetic alloys (5% < c < 20%) 121
1 The critical concentration for antiferromagnetism 122
2 Bulk magnetization 122
4.3 Determination of the commensurate antiferromagnetic phase boundary 124
1 Introduction 124
2 Results of Bragg scattering measurements 124
3 Determination of T_N from resistivity measurements 126
4 Analysis and Discussion 126
4.4 The nature of the Fe moment in antiferromagnetic Cr Fe alloys 131
1 Introduction 131
2 Coexistence of SDW and spin glass states in Chromium alloys containing Fe 132
1 Spin glass behaviour in (Cr Mo 2%) Fe 14% and CrFe 14% alloys 132
2 Results of low field static susceptibility measurements 133
3 Discussion 134
3 Spin dynamics in Cr Fe 10% 135
1 Results 135
2 Discussion 138
4 Polarization - analysis study of Cr Fe 5% 138
1 Introduction 138
2 Results and Analysis 142
3 Discussion 145

CHAPTER 5

THE ONSET OF FERROMAGNETISM IN CR FE ALLOYS 149
5.1 The evolution of magnetic order in binary alloys 149
1 Introduction 149
2 The percolation description 150

		PAGE
	1 Introduction	150
	2 The pure percolation problem	151
	3 Magnetic percolation at finite temperatures	156
3	Spin glasses and superparamagnets	165
	1 Spin glasses	165
	2 Theory	167
	3 Ferromagnetic fine particles	169
4	Some systems with a critical concentration	174
	1 Dilute insulating antiferromagnets	174
	2 Au-Fe	177
5.2	Previous work on Cr Fe ferromagnetic alloys	180
1	Pure Fe	180
2	Cr Fe ferromagnetic alloys	182
5.3	Determination of the ferromagnetic phase boundary	186
1	Introduction	186
2	Results of neutron small angle scattering measurements	186
	1 Zero field data: D17	186
	2 Zero field data: D11	187
3	Determination of T_c from low field susceptibility measurements	188
4	Discussion	189
5.4	Magnetization between the critical concentrations	192
.1	Results of low field magnetization measurements	192
2	Discussion	193
3	The magnetic phase diagram	196
5.5	Spin correlations in the vicinity of the critical concentration	198
1	Introduction: general trends	198
2	The small angle scattering law	200
	1 The κ dependence of the small angle scattering	200
	2 Results and analysis	201
	3 Discussion	204
3	Test of the quasistatic approximation	206
	1 Results	206
	2 Comparison with bulk susceptibility	209
	3 Discussion	210

PAGE

4 Magnetic correlations below C_F 211
1 Introduction 211
2 Results 212
3 Analysis and discussion 213
5 Magnetic correlations above C_F 218
1 Results 218
2 Analysis and Discussion 219
5.6 Small angle scattering in an applied field 223
1 Results 223
2 Analysis and Discussion 224

CHAPTER 6

MAGNETIZATION DENSITY IN PT_3CR 227
6.1 Introduction 227
6.2 Previous work 228
1 Metallurgy of the Pt-Cr system 228
2 Magnetic properties of Pt_3Cr 228
3 Magnetic properties of related Pt_3-3d compounds 229
6.3 Magnetization density in Pt_3Cr 231
1 Introduction 231
2 Nuclear structure factor determination 231
3 Measurement of magnetization density 236
1 Introduction 236
2 Results 236
3 Analysis 238
4 Discussion 242

APPENDICES

Appendix A:
Effect of shape anisotropy on small angle scattering 244

Appendix B:
A polymer model for the small angle scattering law 246

REFERENCES 250

PUBLICATIONS

ACKNOWLEDGEMENTS

I am indebted to my supervisor, Dr. B.D. Rainford, for his untiring and inspiration help, encouragement and guidance during the course of this work.

I wish to thank the Rutherford Memorial Committee of the Royal Society for the award of the Rutherford Scholarship and the administrative staff of the Royal Society, in particular Mr. W.M. Malcolm, for their support.

I would also like to extend my sincere thanks to the following: Professor B.R. Coles and the members of the Metal Physics group for providing experimental facilities and many hours of assistance, discussion and argument.

Dr. J.R. Davis for his continued interest and assistance, and for setting an example of meticulous experimentation with neutron beams.

Dr. R. Cywinski for his lively support and assistance in the D17 measurements.

Dr. H.E.N. Stone for advice on sample preparation.

The technical and scientific staff of AERE, Harwell and ILL, Grenoble; in particular Dr. W. Just, Dr. M. Roth, Dr. P.J. Brown and Dr. R.E. Ghosh for their invaluable assistance with the neutron scattering experiments.

Dr. R.B. Stinchcombe, Dr. J. Strom-Olsen and Dr. A.P. Murani for many fruitful discussions.

SRC for the provision of neutron scattering facilities.

Mrs. N. Gibbons and Mrs. L. Birch for their expertise in typing of this thesis.

Finally, I wish to express my gratitude to my wife, Andrea, for her unfailing support and good humour during this time.

This thesis is respectfully dedicated to
the memory of Lord Rutherford of Nelson.

CHAPTER 1

INTRODUCTION

By analysing the change in energy, momentum and spin component of neutrons scattered by interactions with magnetic materials it is possible to deduce the spatial and temporal variation of magnetization on a microscopic level. The use of neutron scattering techniques over the past twenty-five years has led to a deeper understanding of a wide range of magnetic phenomena. In this present work, the application of these techniques to certain problems in the study of magnetic transition metal alloys is reported.

The major part of this work is concerned with the evolution of magnetic order from itinerant antiferromagnetism to ferromagnetism in Chromium-Iron alloys containing between 5 and 25% Fe. Here, neutron diffraction is the sole experimental means of determining the antiferromagnetic order parameter and the techniques of neutron diffuse scattering provide the sole experimental means of investigating the real space variation of spin correlations and magnetic defects. In the second part of this work, the microscopic distribution of magnetization in Pt_3Cr is determined by polarized neutron diffraction. Where appropriate, the neutron scattering measurements are complemented by low field magnetization and resistivity data.

The disappearance of long range itinerant antiferromagnetism and the onset of ferromagnetism in Cr Fe alloys was reported to occur in the concentration range 10-20% Fe, but the precise critical concentrations were not known. Previous work, based on bulk magnetization and resistivity measurements, gave conflicting results for the critical concentrations. Furthermore, the published magnetic phase diagrams showed a region of concentration which

supported both antiferromagnetism and ferromagnetism. In order to clarify the features of the magnetic phase diagram a series of neutron diffraction and small angle scattering experiments was initiated to determine both the antiferromagnetic and ferromagnetic phase boundaries. These experimental methods do not suffer from the difficulties encountered in previous phase boundary determinations which relied on bulk measurements.

Once the details of the magnetic phase diagram were established, attention was turned to questions of wider significance. The first of these was to describe the evolution of ferromagnetic order with concentration and temperature in the vicinity of the critical concentration for ferromagnetism. Much experimental and theoretical effort has been directed to the study of systems with a critical concentration for long range order. Despite this work, there is very little experimental information concerning the spatial variation of magnetic correlations as a function of both temperature and concentration in metallic systems close to a critical concentration. Neutron small angle scattering was used to determine the range of magnetic correlations in Cr Fe alloys both above and below the critical concentration for ferromagnetism. This information could then be compared with theoretical models for the simplest type of critical concentration, the percolation multicritical point.

The percolation description has been frequently invoked to account for the magnetic properties of metallic alloys close to a critical concentration. In view of the complexity of metallic magnetism it is not clear whether this simple description is valid. The small angle scattering data provides an important test of the applicability of these concepts.

The distribution of magnetic moment in antiferromagnetic Cr Fe alloys was also investigated. This work is an extension of the now classical studies of the distribution of magnetization in disordered

Nickel and Iron alloys to Cr based antiferromagnetic alloys. Cr alloys are of general interest because of their predominantly itinerant nature and the rapid changes in magnetic properties brought about by alloying. Antiferromagnetic Cr Fe alloys are of particular interest as they do not follow the well established alloying trends of other Cr based alloys and are 'anomalous' in this respect. This anomalous behaviour has been attributed to the existence of localized Fe moments in antiferromagnetic Cr Fe alloys. The precise nature of the Fe moment and its relation to the antiferromagnetic spin density wave (SDW) are unknown. Descriptions vary; from a 'good' local moment of $1.8\mu_B$ to a spin compensated 'Kondo' moment of $0.5\mu_B$. The coupling between the Fe moment and the SDW has been variously described as weak ($\sim$ 4K) and strong ($\sim T_N$). In an attempt to resolve these conflicting descriptions, a series of neutron polarization-analysis and time of flight experiments were performed to determine the Fe moment, its dynamical response and the disturbance it produces on neighbouring Cr moments.

In addition to antiferromagnetism and ferromagnetism, 'mictomagnetism' and 'superparamagnetism' have also been reported for Cr Fe alloys in the concentration range under investigation. These phenomena, under the all-embracing title of 'spin glass behaviour', are currently amongst the most intensively studied and controversial aspects of magnetism and the physics of disorder in general. Low field magnetization measurements were performed on a range of Cr Fe alloys to define the occurrence of spin glass behaviour. These data, together with the complementary neutron small angle scattering measurements, may be compared with the results of the phenomenological fine particle models for spin glasses.

The second part of this work was concerned with an atomically ordered compound, Pt_3Cr. Pt_3Cr is one member of a class of 5d-3d compounds which have been extensively studied in recent years, both through inelastic neutron scattering and polarized neutron diffraction. Interest in this class of materials lies partly in the observation of a Pt magnetic moment. For Pt_3Cr, in contrast to the other compounds, the Pt moment was reported to be aligned antiparallel

to the Cr moment: Pt_3Cr is ferrimagnetic. A polarized neutron diffraction study was initiated to study in more detail the distribution of magnetic moment around Pt and Cr atoms in this interesting compound.

The theory of neutron scattering from magnetic materials is presented in the following chapter. Experimental apparatus and procedures are discussed in Chapter 3. The experimental results, analysis and discussion are presented in Chapters 4, 5 and 6. Chapter 4 is devoted to antiferromagnetic Cr Fe alloys. Chapter 5 deals with spin glass and ferromagnetic Cr Fe alloys. Chapter 6 is concerned with Pt_3Cr. In the interest of clarity, the relevent theory and previous work for these disparate topics are presented at the beginning of each chapter. Thus, as far as possible, each chapter is self-contained.

CHAPTER 2

MAGNETIC NEUTRON SCATTERING

The purpose of this chapter is to relate the neutron scattering cross section to the magnetic properties of condensed matter. The formalism and terminology introduced here will be used in subsequent chapters as a basis for calculation and discussion. This treatment concentrates on elastic and quasielastic scattering of thermal neutrons as experimentally this was our main concern. The approach presented here is largely based on the monograph by Marshall and Lovesey (1971) and a full account may be found in this work.

2.1.1 The scattering cross section

The neutron is scattered by two main interactions with matter: the strong nuclear force between neutron and nucleus and the electromagnetic interaction between the neutron dipole moment and electronic magnetic moments. There are further residual electromagnetic interactions with electric field gradients and charge distributions. In this section the scattering cross section is related to a general potential $\hat{V}$. The form of this potential for nuclear and magnetic interactions is then examined.

Consider the scattering of a neutron with mass m and wavevector $\underset{\sim}{k}$ by a central potential $\hat{V}(r)$. The solution of the appropriate Schrödinger equation has the asymptotic form

$$\psi_{k}(r) \underset{r\to\infty}{\sim} e^{i\underset{\sim}{k}.\underset{\sim}{r}} + f(\Omega)\,\frac{e^{ik'r}}{r} \qquad (2.1a)$$

where the first term may be identified with the incident beam and the latter term represents the outgoing scattered beam with wavevector k' along the direction of the solid angle Ω. Following this interpretation the number of neutrons scattered into an element of solid angle $d\Omega$ centred on Ω per unit time is just $\frac{\hbar k'}{m}\,|f(\Omega)|^2 d\Omega$. Dividing by the

incident flux $\frac{\hbar k}{m}$ one obtains the differential scattering cross section

$$\left(\frac{d\sigma}{d\Omega}\right)_{k\to k'} = \frac{k'}{k} |f(\Omega)|^2 \qquad (2.2a)$$

The scattering amplitude $f(\Omega)$ is given by

$$f(\Omega) = -\frac{m}{2\pi\hbar^2} \langle \underset{\sim}{k} | \hat{V}(r) | \underset{\sim}{k'} \rangle$$

For weak potentials the solution of the Schrödinger equation $\psi_k(r)$ is not expected to differ greatly from a plane wave $e^{i\underset{\sim}{k}.\underset{\sim}{r}}$ and the exact expression for the scattering amplitude may be approximated by

$$f(\Omega) \simeq -\frac{m}{2\pi\hbar^2} \int d^3\underset{\sim}{r}\, e^{-i\underset{\sim}{k'}.\underset{\sim}{r}}\, \hat{V}(r)\, e^{i\underset{\sim}{k}.\underset{\sim}{r}} \qquad (2.3a)$$

This is the first Born approximation: the cross section is proportional to $V(\underset{\sim}{\kappa})^2$, the square of the Fourier component of the interaction potential corresponding to the neutron scattering vector $\underset{\sim}{\kappa} = \underset{\sim}{k'} - \underset{\sim}{k}$. As the substitution of the unperturbed wavefunction is equivalent to first order perturbation theory this same result may be derived via the Fermi 'golden rule' as in Marshall and Lovesey (1971).

As the neutron has an intrinsic spin $\hat{\underset{\sim}{s}}$ the results of the Born approximation must include the spin dependence of the cross section. So, rather than the spatial wavefunction $\psi_K(r)$ in (2.1a), one should use the two component spinor wavefunction $|K, \sigma\rangle$ which may be written as a linear combination,

$$|K, \sigma\rangle = \psi_K^{(+)}(r)|+\rangle + \psi_K^{(-)}(r)|-\rangle \qquad (2.1b)$$

where $|+\rangle$ and $|-\rangle$ are eigenfunctions of the z component of spin. The manipulations associated with spin $\frac{1}{2}$ particles can be performed using the matrix representation in which the spin operator $\hat{\underset{\sim}{s}}$ is expressed in terms of the Pauli matrices $\hat{\underset{\sim}{\sigma}}$ via $\hat{\underset{\sim}{s}} = \hbar/2\, \hat{\underset{\sim}{\sigma}}$. Expressed as components with respect to some arbitrary cartesian axes

$$\hat{\sigma}^z = \begin{pmatrix} 1 & 0 \\ 0 & -1 \end{pmatrix} \hat{\sigma}^y = \begin{pmatrix} 0 & -i \\ i & 0 \end{pmatrix} \quad \hat{\sigma}^x = \begin{pmatrix} 0 & 1 \\ 1 & 0 \end{pmatrix}$$

and the eigenvectors $|+>$ and $|->$ are simply $\begin{pmatrix} 1 \\ 0 \end{pmatrix}$ and $\begin{pmatrix} 0 \\ 1 \end{pmatrix}$. To describe the spin dependence of the scattering it is necessary to replace (2.3a) by the spin dependent scattering amplitudes

$$f_{\sigma\sigma'}(\Omega) \simeq - \frac{m}{2\pi\hbar^2} <\sigma|\hat{V}(\underset{\sim}{\kappa})|\sigma'> \tag{2.3b}$$

which correspond to scattering from an initial spin state $|\sigma>$ to a final state $|\sigma'>$ due to the spin dependent potential $\hat{V}$. In a conventional experiment the final spin state is not measured so the cross section is obtained by summing the squared scattering amplitudes over all final states σ'. Furthermore, as any real neutron beam is a mixture of spin states the cross section must be averaged over the initial spin spin states σ in the beam. The cross section (2.2a) then becomes

$$\frac{d\sigma}{d\Omega}_{K\to K'} = \frac{k'}{k} \sum_{\sigma,\sigma'} p_\sigma f^+_{\sigma\sigma'} f_{\sigma'\sigma} \tag{2.2b}$$

where p_σ is the probability distribution of initial spin states.

It is important to make some formal remarks about the spin state of the neutron beam. The average spin state of the beam can be described by the polarization,

$$\underset{\sim}{P} = < \underset{\sim}{\hat{\sigma}} >$$

defined as the expectation value of the Pauli spin operator. If the beam is a pure ensemble, that is all neutrons are in the same spin state, the polarization is complete and $|\underset{\sim}{P}| = 1$. The polarization will be incomplete for a mixed ensemble, that is if the beam is an incoherent mixture of spin states, and $|\underset{\sim}{P}| \neq 1$. Consider how the polarization may be measured. Any measurement of the spin component of a single neutron (S^α) automatically defines the z component of spin

and the values + $\hbar/2$ or $-\hbar/2$ will be returned. If this measurement is repeated and the number of neutrons with spin parallel (n^+_α) or antiparallel (n^-_α) to the particular coordinate direction in question are counted the polarization component is simply

$$p^\alpha = \frac{n^+_\alpha - n^-_\alpha}{n^+_\alpha + n^-_\alpha} \qquad \alpha = x, y, z$$

This may be repeated for the remaining two cartesian components in subsequent measurements and the polarization vector completely determined.

According to quantum statistical mechanics the expectation value of any operator $\hat{\underset{\sim}{G}}$ acting on a mixed state can be found by taking the sum of the diagonal elements i.e. taking the trace Tr of the product of the density matrix operator $\hat{\rho}$ and the operator $\hat{\underset{\sim}{G}}$ in any convenient representation $|\chi>$,

$$<\hat{\underset{\sim}{G}}> = \sum_\chi <\chi|\hat{\underset{\sim}{G}}\hat{\rho}|\chi> = \mathrm{Tr}\ \hat{\underset{\sim}{G}}\hat{\rho} \tag{2.4a}$$

In the case of non interacting spin $\frac{1}{2}$ states the density matrix can be represented by the 2 × 2 matrix as shown for example by Kessler (1976)

$$\hat{\rho} = \hat{I} + \tfrac{1}{2}\underset{\sim}{P}.\hat{\underset{\sim}{\sigma}} \tag{2.4b}$$

which is consistent with the definition of polarization $\underset{\sim}{P} = \mathrm{Tr}\hat{\rho}\hat{\underset{\sim}{\sigma}}$. (Here $\hat{I}$ is the unit matrix). With this notation the cross section (2.2b) can be written in the alternative form

$$\frac{d\sigma}{d\Omega} = \left(\frac{m}{2\pi\hbar^2}\right)^2 \frac{k'}{k}\ \mathrm{Tr}\hat{\rho}\hat{V}^+(\kappa)V(\kappa) \tag{2.2c}$$

where the trace is understood to be with respect to neutron spin coordinates.

These results may be generalized now to include scattering from a macroscopic target with internal structure. In this case there is the possibility of energy transfer between the neutron and target.

The partial differential cross section for the process in which the neutron induces a transition from a target state $|\ \lambda >$ with energy E_λ to a state $|\ \lambda' >$ with energy $E_{\lambda'}$ is

$$\frac{d^2\sigma}{d\Omega dE'}_{\substack{k\to k' \\ \lambda\to\lambda'}} = \left(\frac{m}{2\pi\hbar^2}\right)^2 \frac{k'}{k}\ Tr\ \hat{\rho}<\lambda|\hat{\underset{\sim}{V}}^{+}(\underset{\sim}{\kappa})|\lambda'><\lambda'|\hat{\underset{\sim}{V}}(\underset{\sim}{\kappa})|\lambda>\delta(\hbar\omega+E_\lambda-E_{\lambda'})$$

with energy conservation ensured by the delta function and the sum over incident and final spin states has been performed using the density matrix. If there is no energy transfer $\hbar\omega$ between neutron and target the scattering is elastic, otherwise the scattering is inelastic. This partial differential cross section must be summed over the unobserved final target states $|\ \lambda' >$ and averaged over initial states $|\ \lambda >$ to give the master formula

$$\frac{d^2}{d\Omega d(\hbar\omega)} = \left(\frac{m}{2\pi\hbar^2}\right)^2 \frac{k'}{k} \sum_{\lambda\lambda'} p_\lambda\ Tr\ \hat{\rho}<\lambda|\hat{\underset{\sim}{V}}^{+}(\underset{\sim}{\kappa})|\lambda'><\lambda'|\hat{\underset{\sim}{V}}(\underset{\sim}{\kappa})|\lambda>\delta(\hbar\omega+E_\lambda-E_{\lambda'}) \qquad (2.5)$$

The initial target states are distributed according to the probabilities p_λ. Here $|\ \lambda >$ is understood to include all eigenvariables associated with the target, in particular the spatial distribution of scattering centres as well the energy E_λ. Thus the average is both a thermal and configurational average over initial states of the system.

2.1.2 The nuclear interaction

The interaction between the neutron and the nucleus is strong and short ranged and hence cannot be treated in the Born approximation. The scattering cross section for such a potential may be calculated by decomposing ψ_k into a series of partial waves with angular momenta ℓ. For thermal neutrons the range of the nuclear potential is much less than the neutron wavelength and only the $\ell = 0$ component need be considered. In this limit the cross section is isotropic and the scattering amplitude $f \simeq f_{\ell=0} = -b$ where b is termed the scattering length. We shall treat b as a phenomenological parameter which is in general complex, the real part may be positive or negative depending

on the energy and the isotope involved and the imaginary part, which is generally small, represents absorption.

The neutron nuclear interaction is spin dependent. The simplest form of rotationally invariant potential which can describe the interaction between neutron with spin $\hat{s}$ and nucleus with angular momentum $\hat{I}$ is of the form $V_1(r) + V_2(r)\hat{\sigma}.\hat{I}$ which has two eigenvalues depending upon whether the nuclear and neutron angular momenta are coupled parallel (+) or antiparallel (-). Corresponding to these two eigenvalues are the two scattering lengths $b^{(+)}$ and $b^{(-)}$.

It is possible to construct a pseudo potential which can give the correct form of the scattering when substituted in the expression for the cross section derived using the Born approximation. This is convenient as it puts magnetic and nuclear scattering on the same formal footing. Such a pseudo potential has the form

$$\hat{V}_N(r) = \frac{2\pi\hbar^2}{m}\ \hat{b}\ \delta(r)$$

with the delta function ensuring an isotropic cross section on Fourier inversion and the scattering length operator $\hat{b}$ includes the spin dependence of the interaction,

$$\hat{b} = A + \tfrac{1}{2}B\hat{\sigma}.\hat{I} \qquad (2.6a)$$

The constants A and B are determined by the requirement that $\hat{b}$ has eigenvalues $b^{(+)}$ and $b^{(-)}$ and are treated as parameters to be determined by experiment. For a collection of N nuclei situated at positions R_i the individual pseudo potentials may be superimposed to form the total potential $\hat{V}_N$ with the Fourier transform

$$\hat{V}_N(\kappa) = \frac{2\pi\hbar^2}{m}\ \sum_i \hat{b}_i\ \exp(i\kappa.R_i) \qquad (2.6b)$$

The elastic scattering which arises from this potential can be calculated using (5),

$$\frac{d\sigma}{d\Omega} = \Sigma p_\lambda \sum_{i,j} \exp(i\kappa.R_{ij})\langle\lambda|\ \mathrm{Tr}\ \hat{\rho}(A_i+\tfrac{1}{2}B_i\hat{\sigma}.\hat{I}_i)(A_j+\tfrac{1}{2}B_j\hat{\sigma}.\hat{I}_j)|\lambda\rangle$$

The average over initial target states λ in this case simply involves a configurational average over all distributions of nuclear species and a thermal average ($< >$) over nuclear spin orientations. At all but milli Kelvin temperatures the nuclear spin orientations are random so that any terms linear in nuclear spin cannot survive the thermal average. The cross term involving nuclear spin which survives the thermal average is the self correlation term $\hat{\underset{\sim}{I}}_i . \hat{\underset{\sim}{I}}_i$. The trace over neutron spin components can be trivially evaluated using the fact that Tr $\hat{p} = 1$ to give the cross section,

$$\frac{d\sigma}{d\Omega} = \sum_{i,j} \exp(i\underset{\sim}{K}.\underset{\sim}{R}_{ij}) (\overline{A_i A_j} + \frac{1}{4} \delta_{ij} \overline{B_i B_j \hat{\underset{\sim}{I}}_i . \hat{\underset{\sim}{I}}_j})$$

where the configurational average is denoted by the bar. The result is independent of incident polarization as may be expected for a system with no preferred orientation.

It is useful to identify the various contributions to this cross section in the specific case of a random binary alloy composed of a concentration C_A of type 'A' atoms dissolved in a matrix of 'B' type atoms. The coherent scattering, which depends on the square of the average scattering length, is to be distinguished from the incoherent scattering which is due to the mean squared deviation of the average scattering length.

The coherent scattering cross section in this case is of the form

$$\frac{d\sigma}{d\Omega} = \bar{b}^2 (\sum_i \exp(i\underset{\sim}{K}.\underset{\sim}{R}_i))^2$$

which gives rise to Bragg scattering at scattering vectors defined by the geometrical factor in brackets. The average scattering length for the alloy is $\bar{A}$ which is usually written simply as $\bar{b}$,

$$\bar{b} = C_A \bar{b}_A + (1 - C_A) \bar{b}_B \qquad (2.7a)$$

where $\bar{b}_A$ and $\bar{b}_B$ are the average scattering lengths for the atomic

'A' and 'B'. The average scattering length for a particular atomic species is

$$\bar{b}_A = \sum_\xi C_\xi \bar{b}_\xi \tag{2.7b}$$

where C_ξ is the abundance of the isotope ξ with average isot opic scattering length $\bar{b}_\xi$. This in turn is the scattering amplitude of the isotope ξ in question averaged over all random nuclear spin orientations, in full $< \bar{b}_\xi > = \bar{b}_\xi$

$$\bar{b}_\xi = \bar{A}_\xi = (2I_\xi + 1)^{-1}(I_\xi b_\xi^{(-)} + (I_\xi + 1)b^{(+)}) \tag{2.7c}$$

where the probability of interaction with neutron spin parallel (+) or antiparallel (-) to the nuclear angular momentum is weighted according to the number of available states with total angular momentum $\hat{\underset{\sim}{I}} \pm \hat{\underset{\sim}{\sigma}}$.

It is possible to identify three sources of incoherent scattering:

(i) the 'Laue' or crystal disorder incoherent scattering arises from the fluctuations about average scattering length of the alloy due to the presence of different scattering lengths for the two atomic species,

$$\frac{d\sigma}{d\Omega}_{Laue} = N\, C_A(1 - C_A)(\bar{b}_A - \bar{b}_B)^2 \tag{2.8a}$$

(ii) the 'isotopic' incoherent scattering is due to fluctuations about the average scattering length of a particular atomic species due to the presence of different scattering lengths for the constituent isotopes,

$$\frac{d\sigma}{d\Omega}_{iso} = N\left[C_A \sum_\xi C_\xi \overline{(A_\xi - \bar{b}_A)^2} + (1-C_A)\sum_\phi C_\phi \overline{(A_\phi - \bar{b}_B)^2}\right] \tag{2.8b}$$

(iii) the 'nuclear spin' incoherent scattering is due to fluctuations about the average scattering amplitudes for nuclear spin states,

$$\frac{d\sigma}{d\Omega}_{nsi} = \frac{1}{4} N[C_A \Sigma C_\xi B_\xi^2 \, I_\xi(I_\xi+1) + (1-C_A)\Sigma C_\phi B_\phi^2 \, I_\phi(I_\phi+1)] \qquad (2.8c)$$

or in terms of $b_\xi^{(+)}$ and $b_\xi^{(-)}$,

$$\frac{d\sigma}{d\Omega}_{nsi} = N[C_A \Sigma C_\xi \frac{I_\xi(I_\xi+1)}{(2I_\xi+1)^2} (b_\xi^{(+)} - b_\xi^{(-)})^2 +$$

$$(1-C_A)\Sigma C_\phi \frac{I_\phi(I_\phi+1)}{(2I_\phi+1)^2} (b_\phi^{(+)} - b_\phi^{(-)})^2]$$

The incoherent scattering is isotropic in the case of randomly distributed fluctuations.

In order to parameterize the nuclear interaction it is usually sufficient to know the average scattering length $\bar{b}$, the isotopic incoherence and the nuclear spin incoherence for each atomic species, a detailed knowledge of $b^{(+)}$ and $b^{(-)}$ is not necessary.

2.1.3 The magnetic interaction

The neutron may interact with magnetic and electric fields via the neutron magnetic dipole moment $\underset{\sim}{\mu}_n$. These electromagnetic interactions are weak and the cross section may be treated in the Born approximation. The interaction potential for a neutron in a magnetic field $\underset{\sim}{H}$ and an electric field $\underset{\sim}{E}$ is

$$\hat{V}_M(r) = - \gamma \, \mu_N \underset{\sim}{\hat{\sigma}} . \underset{\sim}{H} + \text{terms of order } \frac{1}{m^2}$$

where μ_N is the nuclear magneton and $\gamma = - 1.91$ is the gyromagnetic ratio. We shall be concerned only with the dipolar magnetic interaction, the residual interactions are weak and unrelated to the magnetic properties.

Consider the interaction between the neutron and a magnetic field $\underset{\sim}{H}(\underset{\sim}{r})$ produced by an electron with momentum $\underset{\sim}{p}_e$ mass m_e and spin $\underset{\sim}{s}$ situated at a distance $\underset{\sim}{r}$ from the neutron. Here,

$$\underset{\sim}{H}(r) = \text{curl}\left(\frac{-2\mu_B \hat{\underset{\sim}{s}} \times \underset{\sim}{r}}{r^3}\right) + \frac{-e}{m_e c}\frac{\hat{\underset{\sim}{p}}_e \times \underset{\sim}{r}}{r^3}$$

and the interaction potential is

$$V_M(\underset{\sim}{r}) = \gamma\mu_N\left[2\mu_B \underset{\sim}{\sigma}.\text{curl}\left(\frac{\hat{\underset{\sim}{s}} \times \underset{\sim}{r}}{r^3}\right) - \frac{e}{2m_e c}\left(\hat{\underset{\sim}{p}}_e \cdot \frac{\underset{\sim}{\sigma} \times \underset{\sim}{r}}{r^3} - \frac{\underset{\sim}{\sigma} \times \underset{\sim}{r}}{r^3} \cdot \hat{\underset{\sim}{p}}_e\right)\right]$$

where the momentum term has been symmetrized according to the correspondance principle. The fourier transform of $\hat{V}_M(\underset{\sim}{r})$ is

$$V_M(\underset{\sim}{\kappa}) = \frac{2\pi\hbar^2}{m}\left(\frac{\gamma e^2}{m_e c^2}\right)\underset{\sim}{\sigma}.\hat{\underset{\sim}{Q}}_{\perp} \qquad (2.9a)$$

where the operator $\hat{\underset{\sim}{Q}}_{\perp}$ is

$$\hat{\underset{\sim}{Q}}_{\perp} = \left(\bar{\underset{\sim}{\kappa}} \times \left(\hat{\underset{\sim}{s}} \times \bar{\underset{\sim}{\kappa}}\right) - \frac{i}{\hbar|\underset{\sim}{\kappa}|}\underset{\sim}{\kappa} \times \hat{\underset{\sim}{p}}_e\right)\exp(i\underset{\sim}{\kappa}.\underset{\sim}{R}) \qquad (2.10a)$$

Here $\bar{\underset{\sim}{\kappa}}$ is a unit vector in the direction of the scattering vector and $\underset{\sim}{R}$ is the position vector of the electron. The electron spin and momentum may be considered as two contributions to a magnetization $\hat{\underset{\sim}{M}}(\underset{\sim}{r})$ so that we may generalize this result to any system of electrons generating a magnetization. The form of the interaction potential is then exactly as in (eq.2·9a) but with

$$\hat{\underset{\sim}{Q}}_{\perp} = -\frac{1}{2\mu_B}\int d^3r \exp(i\underset{\sim}{\kappa}.\underset{\sim}{r})\left|\bar{\underset{\sim}{\kappa}} \times \left(\hat{\underset{\sim}{M}}(r) \times \bar{\underset{\sim}{\kappa}}\right)\right| \qquad (2.10b)$$

There is a coupling between the neutron spin and the component of magnetization which is perpendicular to the neutron scattering vector, hence the subscript "$\perp$". This is a central result.

The average of the interaction $\hat{V}_M(\kappa)$ over target states which occurs in the expression for the cross section involves the evaluation of both thermodynamic and quantum mechanical expectation values. It is convenient to treat the spatial averages $\langle\phi_\lambda|\hat{\underset{\sim}{Q}}_{\perp}|\phi_\lambda\rangle$ (where ϕ_λ is the electronic wavefunction) separately and introduce the concept

of a magnetic form factor. Take for example the case where the magnetization is generated by electron spins localized in the vicinity of a lattice site $\underset{\sim}{R}_i$, as is the case for a 3d transition ion with orbital angular momentum quenched by the crystal field. Under these conditions

$$\hat{\underset{\sim}{Q}}_\perp = \sum_i \exp(i\underset{\sim}{\kappa}.\underset{\sim}{R}_i) f_i(\underset{\sim}{\kappa}) \tilde{\underset{\sim}{\kappa}} \times (\hat{\underset{\sim}{S}}_i \times \tilde{\underset{\sim}{\kappa}}) \qquad (2.9b)$$

where the magnetic form factor $f_i(\underset{\sim}{\kappa})$, being the normalized fourier transform of the spin density associated with the site $\underset{\sim}{R}_i$, has been introduced. The form factor is normalized so that $f_i(0) = 1$. The individual electronic spins couple to form the total spin $\hat{\underset{\sim}{S}}_i$ of the ion situated at $\underset{\sim}{R}_i$.

In general, both the orbital and spin components of the electronic magnetic moment are present and the calculation of the matrix elements of $\hat{\underset{\sim}{Q}}_\perp$ with respect to the electronic wave function is complex. For small scattering vectors, however, the term involving the electron momentum in the expression for $\hat{\underset{\sim}{Q}}$ has the same form as that for the spin, namely (compare with (2.10d))

$$\exp(i\underset{\sim}{\kappa}.\underset{\sim}{R})\hat{\underset{\sim}{p}}_e + \hat{\underset{\sim}{p}}_e \exp(i\underset{\sim}{\kappa}.\underset{\sim}{R}) \simeq i\hbar \underset{\sim}{\ell}_e \times \underset{\sim}{\kappa}$$

where $\underset{\sim}{\ell}_e$ in the orbital angular momentum of the electron. If then the individual electronic spin and orbital angular momenta couple to give a total spin $\hat{\underset{\sim}{S}}_i$ and orbital angular momentum $\hat{\underset{\sim}{L}}_i$ at a given site $\underset{\sim}{R}_i$ then $\hat{\underset{\sim}{Q}}_\perp$ has the form.

$$\hat{\underset{\sim}{Q}}_\perp = \sum_i \exp(i\underset{\sim}{\kappa}.\underset{\sim}{R}_i) \bar{\underset{\sim}{\kappa}} \times (\bar{j}0_i \hat{\underset{\sim}{S}}_i + \tfrac{1}{2}(\bar{j}0_i + \bar{j}2_i)\hat{\underset{\sim}{L}}_i) \times \bar{\underset{\sim}{\kappa}} \qquad (2.10c)$$

where the coefficients $\bar{j}_{n_i}$ are the radial integrals

$$\bar{j}_{n_i} = \int dr\, r^2\, j_n(\kappa r) |f_i(r)|^2$$

in which $j_n(\kappa r)$ is the nth order spherical Bessel function and $f_i(r)$ is the radial part of the electronic wavefunction for electrons in an

unfilled shell of orbital angular momentum $\underset{\sim}{\ell}_e$ situated at a lattice site $\underset{\sim}{R}_i$. Now, for 3d ions in which a relatively small orbital contribution to the magnetization exists via $\underset{\sim}{L} = (g-2)\underset{\sim}{S}$ this allows us to write

$$\hat{\underset{\sim}{Q}}_\perp = \sum_i \tfrac{1}{2} g_i f_i(\kappa) \exp(i\underset{\sim}{\kappa}.\underset{\sim}{R}_i) \bar{\underset{\sim}{\kappa}} \times (\underset{\sim}{S}_i \times \bar{\underset{\sim}{\kappa}}) \qquad (2.10d)$$

where $f_i(\kappa) = \bar{j}0_i + (g_i - 2/g_i)\bar{j}2_i$ is the magnetic form factor for the ion at $\underset{\sim}{R}_i$. This approximation is known as the 'dipole' approximation and will be used almost entirely in the sections which follow. For generality $fg\underset{\sim}{S}$ can be replaced by the Fourier transform of the magnetization if necessary.

2.1.4 Summary

The neutron scattering cross section in the Born approximation is proportional to the square of the Fourier transform of the interaction potential between neutron and target. This potential is the sum of nuclear (N) and magnetic (M) terms both of which have the general form

$$\hat{V}(\underset{\sim}{\kappa}) = \hat{\beta} + \hat{\underset{\sim}{\sigma}}.\hat{\underset{\sim}{\alpha}}$$

where $\hat{\beta}$ and $\hat{\underset{\sim}{\alpha}}$ are operators obtainable from (2.6), (2.9) and (2.10) Substituting these potentials into the master formula (2.5) for the cross section gives contributions which are purely magnetic, purely nuclear and a nuclear-magnetic interference term. In the following section 2.2 the purely magnetic scattering will be examined under the condition of an unpolarized beam. The polarized case is treated in section 2.3. The circumstances in which the polarization of the scattered beam is analysed are considered in section 2.4.

2.2 Magnetic scattering with unpolarized neutrons

2.2.1 Correlation functions

The magnetic cross section for scattering with an unpolarized incident beam can be calculated by substituting the form of the magnetic interaction (2.9) and (2.10) into the master formula (2.5)

$$\frac{d^2\sigma}{d\Omega dE'} = \left(\frac{\gamma e^2}{m_e c^2}\right)^2 \frac{k'}{k} \sum_{\lambda\lambda'} p_\lambda \, \mathrm{Tr}\, \hat{\rho} \langle\lambda| (\hat{\underset{\sim}{\sigma}}.\hat{\underset{\sim}{Q}}_\perp)^+ |\lambda'\rangle\langle\lambda'| (\hat{\underset{\sim}{\sigma}}.\hat{\underset{\sim}{Q}}_\perp) |\lambda\rangle \delta(\hbar\omega - E_\lambda, + E_\lambda)$$

The average over neutron spin components for an unpolarized beam can be performed by noting that in this case the density matrix is the unit matrix,

$$\mathrm{Tr}\, \hat{\rho} (\hat{\underset{\sim}{\sigma}}.\hat{\underset{\sim}{Q}}_\perp)^+ (\hat{\underset{\sim}{\sigma}}.\hat{\underset{\sim}{Q}}_\perp) = \hat{\underset{\sim}{Q}}_\perp^+ . \hat{\underset{\sim}{Q}}_\perp$$

Using the definition of the operator $\hat{\underset{\sim}{Q}}$ via $\hat{\underset{\sim}{Q}}_\perp = \bar{\underset{\sim}{\kappa}} \times (\hat{\underset{\sim}{Q}} \times \bar{\underset{\sim}{\kappa}})$ the scalar product can be written longhand in Cartesian component form,

$$\hat{\underset{\sim}{Q}}_\perp . \hat{\underset{\sim}{Q}}_\perp = \sum_{\alpha,\beta} (\delta_{\alpha\beta} - \bar{\kappa}^\alpha \bar{\kappa}^\beta) \hat{Q}^{+\alpha} \hat{Q}^\beta$$

where α, β are x, y, z components. If the integral representation of the delta function

$$\delta(\hbar\omega - E_\lambda + E_\lambda') = \frac{1}{2\pi\hbar} \int_{-\infty}^{\infty} dt \, \exp(-i/\hbar(\hbar\omega - E_\lambda + E_\lambda'))$$

is used as an ad hoc device to introduce time dependence (following Van Hove (1954a)) and with $\hat{\underset{\sim}{Q}}$ in the dipole approximation the cross section may be written,

$$\frac{d^2\sigma}{d\Omega dE'} = \left(\frac{e^2\gamma}{2m_e c^2}\right)^2 \frac{k'}{k} \sum_{\alpha,\beta} (\delta_{\alpha\beta} - \bar{\kappa}^\alpha \bar{\kappa}^\beta) \times \frac{1}{2\pi\hbar}$$

$$\sum_{i,j} \int dt \, e^{-i\omega t} \langle e^{i\kappa . \hat{\underset{\sim}{R}}_i(0)} g_i f_i(\kappa) \hat{S}_i^\alpha(0) e^{i\kappa . \hat{\underset{\sim}{R}}_j(t)} g_j f_j(\kappa) \hat{S}_j^\beta(t) \rangle \qquad (2.11)$$

where $\hat{\underset{\sim}{R}}(t)$ and $\hat{\underset{\sim}{S}}(t)$ are position and spin operators in the Heisenberg picture and the sum over initial target states is performed by the configuration and thermal average. Only those terms which are elastic in the position coordinates are of interest so the average above may be written

$$\overline{\langle\ \rangle} = \exp i\underset{\sim}{\kappa}.\underset{\sim}{R}_{ij}\ \exp(-2W(\underset{\sim}{\kappa}))\ \overline{\langle \hat{S}_i^{\alpha}(0)\hat{S}_j^{\beta}(t)\ g_i g_j f_i(\kappa) f_j(\kappa)\rangle}$$

in which $W(\underset{\sim}{\kappa})$, the Debye Waller factor, takes account of the motion of $\hat{\underset{\sim}{R}}_i(t)$ about the mean time averaged position $\underset{\sim}{R}_i$. For simplicity it will be assumed that the g factors, form factors and Debye Waller factors are site independent. This assumption is valid for identical magnetic ions and is good approximation for binary 3d alloys. Furthermore a Bravais lattice structure will be assumed. With these simplifications the cross section becomes,

$$\frac{d^2\sigma}{d\Omega dE} = \left(\frac{\gamma e^2}{2m_e c^2}\right)^2 \frac{k'}{k}\, g^2 f^2(\kappa) e^{-2W(\kappa)} \sum_{\alpha,\beta} (\delta_{\alpha\beta} - \kappa^{\alpha}\kappa^{\beta}) \mathcal{S}^{\alpha\beta}(\underset{\sim}{\kappa}, \omega) \qquad (2.12a)$$

where $\mathcal{S}^{\alpha\beta}(\underset{\sim}{\kappa}, \omega)$ contains the essential material parameters,

$$\mathcal{S}^{\alpha\beta}(\underset{\sim}{\kappa}, \omega) = \frac{1}{2\pi\hbar} \int_{-\infty}^{\infty} dt\ e^{-i\omega t} \overline{\langle \hat{S}^{\alpha}(-\underset{\sim}{\kappa}, 0)\hat{S}^{\beta}(\underset{\sim}{\kappa}, t)\rangle} \qquad (2.12b)$$

where

$$\hat{S}^{\beta}(\underset{\sim}{\kappa}, t) = \sum_i \exp(i\underset{\sim}{\kappa}.\underset{\sim}{R}_i)\hat{S}_i^{\beta}(t) \qquad (2.12c)$$

This is an important result, a neutron measurement gives directly the function $\mathcal{S}^{\alpha\beta}(\underset{\sim}{\kappa}, \omega)$ which describes the correlations between the spins in both space and time.

It is possible to relate $\mathcal{S}^{\alpha\beta}(\kappa, \omega)$ to the fundamental response functions of the spin system. Firstly, the part of the correlation function which is due to correlation between time independent quantities must be isolated. This will be the part of the correlation function which survives as $t \to \infty$,

$$\overline{\langle \hat{S}^{\alpha}(-\underset{\sim}{\kappa}, 0)\hat{S}^{\beta}(\underset{\sim}{\kappa}, \infty)\rangle} = \overline{\langle \hat{S}^{\alpha}(-\underset{\sim}{\kappa})\rangle\langle \hat{S}^{\beta}(\underset{\sim}{\kappa})\rangle}$$

and may be identified with the elastic scattering. In an ordered magnet, for example, $\langle \hat{S}^{\alpha}(-\kappa) \rangle$ is proportional to a Fourier component of the spontaneous magnetization (which is presumably a time independent quantity). Thus for correlations between time independent quantities,

$$\mathcal{S}^{\alpha\beta}_{\text{elastic}}(\underset{\sim}{\kappa}, \omega) = \overline{\langle \hat{S}^{\alpha}(-\underset{\sim}{\kappa}) \rangle \langle \hat{S}^{\beta}(\underset{\sim}{\kappa}) \rangle} \, \delta(\omega) \tag{2.13}$$

The elastic scattering will be considered in the sections 2.2.2 and 2.2.3. The remaining part of the spin correlation function is the power spectrum of the spontaneous fluctuations in the magnetization and gives rise to inelastic scattering. The fluctuation-dissipation theorem relates $\mathcal{S}^{\alpha\beta}_{\text{inelastic}}(\kappa, \omega)$ to the imaginary (dissipative) part of the generalized susceptibility $\chi^{\alpha\beta}_{\underset{\sim}{\kappa}}[\omega]$,

$$\mathcal{S}^{\alpha\beta}(\underset{\sim}{\kappa}, \omega) - \mathcal{S}^{\alpha\beta}_{\text{elastic}}(\underset{\sim}{\kappa}, \omega) = (1-\exp(-\hbar\omega\beta))^{-1} \operatorname{Im} \chi^{\alpha\beta}_{\underset{\sim}{\kappa}}[\omega] \tag{2.14a}$$

The physical significance of this expression is succinctly explained by Marshall and Lowde (1968). As with any phasor, the imaginary part of the response function governs the out of phase or dissipative response of the system to a perturbation. In this case the neutron beam provides a magnetic perturbation $\underset{\sim}{H}(\underset{\sim}{\kappa}, \omega)$ and the energy of this source "can only be dissipated in the Born approximation, by processes which remove the neutrons physically from the scene." Furthermore, as $\chi^{\alpha\beta}_{\underset{\sim}{\kappa}}[\omega]$ measures the response of the spin system to a general component of magnetic field, the inelastic scattering cross section provides a very complete set of microscopic information about the target. This is the great power of the technique.

In practice, there are several response functions related to $\chi^{\alpha\beta}_{\underset{\sim}{\kappa}}[\omega]$ which are more commonly used. To explain the relationship between these quantities consider the definition of a response function; the magnetization $M^{\alpha}_{\underset{\sim}{q}}(t)$ arising from a magnetic field with spatial dependence $H_{\underset{\sim}{q}}(t')\exp(i\underset{\sim}{q}.\underset{\sim}{R}_i)$ is the linear response

$$M^{\alpha}_{\underset{\sim}{q}}(t) = -g\mu_B \langle S^{\alpha}(q) \rangle + \int_{-\infty}^{t} dt' \sum_{\beta} \phi^{\alpha\beta}(\underset{\sim}{q}, t-t') H^{\beta}_{\underset{\sim}{q}}(t')$$

where

$$\phi^{\alpha\beta}(\underset{\sim}{q}, t) = \frac{i}{\hbar} \langle [\hat{S}^{\alpha}(\underset{\sim}{q}, t), \hat{S}^{\beta}(-\underset{\sim}{q}, 0)] \rangle \frac{(g\mu_B)^2}{N}$$

and

$$\chi_{\underset{\sim}{q}}^{\alpha\beta}[\omega] = \int_0^\infty dt\, \exp(i\omega t)\phi^{\alpha\beta}(\underset{\sim}{q},\, t)$$

The relaxation function $R^{\alpha\beta}(\underset{\sim}{q},\, t)$ is defined as the antiderivative of $\phi^{\alpha\beta}(\underset{\sim}{q},\, t)$ according to

$$\frac{\partial}{\partial t} R^{\alpha\beta}(\underset{\sim}{q},\, t) = \frac{-N}{(g\mu_B)^2} \phi^{\alpha\beta}(\underset{\sim}{q},\, t)$$

and describes the evolution of magnetization in time ($t > 0$) after a steady field $H^{\alpha}_{\underset{\sim}{q}}$ has been turned off at $t = 0$,

$$M^{\alpha}_{q}(t) = - g\mu_B \langle \hat{S}^{\alpha}(\underset{\sim}{q}) \rangle + H^{\alpha}_{\underset{\sim}{q}} R^{\alpha\beta}(\underset{\sim}{q},\, t)$$

hence the name. The inelastic cross section may thus be expressed in terms of the Fourier transform of the relaxation function $R^{\alpha\beta}(\underset{\sim}{\kappa},\, \omega)$

$$\mathcal{S}^{\alpha\beta}(\underset{\sim}{\kappa},\, \omega) - \mathcal{S}^{\alpha\beta}_{\text{elastic}}(\underset{\sim}{\kappa},\, \omega) = \frac{\omega}{(1-\exp(-\hbar\omega\beta))} R^{\alpha\beta}(\underset{\sim}{\kappa},\, \omega) \qquad (2.14b)$$

Alternatively, if $\chi_{\underset{\sim}{q}}^{\alpha\beta}[0]$ is identified with the isothermal wavevector dependent susceptibility $\chi_{\underset{\sim}{q}}^{\alpha\beta}$ then

$$R^{\alpha\beta}(\underset{\sim}{q},\, \omega) = \chi_{\underset{\sim}{q}}^{\alpha\beta} F_{\underset{\sim}{q}}^{\alpha\beta}(\omega)$$

where the dynamics of the system are embodied in the spectral weight function

$$F_{\underset{\sim}{q}}^{\alpha\beta}(\omega) = \frac{1}{2\pi} \int_{-\infty}^{\infty} dt\, \exp(i\omega t) R^{\alpha\beta}(\underset{\sim}{q},\, t)/R^{\alpha\beta}(\underset{\sim}{q},\, 0)$$

which is normalized so that $\int_{-\infty}^{\infty} d\omega F_{\underset{\sim}{\kappa}}^{\alpha\beta}(\omega) = 1$. The inelastic scattering cross section can then be conveniently written as

$$\frac{d^2\sigma}{d\Omega dE'}_{\text{inelastic}} = \left(\frac{\gamma e^2}{2m_e c^2}\right)^2 g^2 f^2(\kappa)\, \frac{k'}{k} \exp(-2W(\underset{\sim}{\kappa})) \frac{N}{(g\mu_B)^2} \frac{\omega}{(1-\exp(-\hbar\omega\beta))}$$

$$\times \sum_{\alpha,\beta} (\delta_{\alpha\beta} - \bar{\kappa}_\alpha \bar{\kappa}_\beta) \chi_{\underset{\sim}{\kappa}}^{\alpha\beta} F_{\underset{\sim}{\kappa}}^{\alpha\beta}(\omega) \qquad (2.15a)$$

which is the central result of this section for our purposes.

These expressions for the cross section can be considerably simplified if the total z component of the spin is a constant of motion. In such a case only the operators $S_i^z S_j^z$ and $S_i^x S_j^x$, $S_i^y S_j^y$ survive the thermal average and the cross section can be divided into transverse and longitudinal parts,

$$\frac{d^2\sigma}{d\Omega dE'}_{\substack{\text{long.}\\ \text{inelastic}}} = \left(\frac{\gamma e^2}{2m_e c^2}\right)^2 g^2 f^2(\kappa)\frac{k'}{k} \exp(-2W(\kappa)) \frac{N}{(g\mu_B)^2}$$

$$\times \frac{\omega}{1-\exp(-\beta\hbar\omega)} (1-\kappa_z^{-2}) \chi_{\underset{\sim}{\kappa}}^{zz} F_{\underset{\sim}{\kappa}}^{zz}(\omega) \qquad (2.15b)$$

and

$$\frac{d^2\sigma}{d\Omega dE'}_{\substack{\text{trans.}\\ \text{inelastic}}} = \left(\frac{\gamma e^2}{(2m_e c^2}\right) g^2 f^2(\kappa)\frac{k'}{k} \exp(-2W(\kappa)) \frac{N}{(2g\mu_B)^2}$$

$$\frac{\omega}{1-\exp(-\beta\hbar\omega)} (1+\kappa_z^2) \chi_{\underset{\sim}{\kappa}}^{xx} F_{\underset{\sim}{\kappa}}^{xx}(\omega) \qquad (2.15c)$$

In the case of a Heisenberg ferromagnet it is the transverse cross section which is related to creation and annihilation of spin waves via the spin raising and lowering operators implicit in $\chi_\kappa^{xx} F_\kappa^{xx}(\omega)$. The longitudinal part is related to the quasielastic scattering involving $\chi_\kappa^{zz} F_\kappa^{zz}(\omega)$.

It should be noted that all forms of the scattering cross section must satisfy the detailed balance condition,

$$\frac{d^2\sigma}{d\Omega dE'}_{\underset{\sim}{\kappa},\ \omega} = \exp(\hbar\omega\beta) \frac{d^2\sigma}{d\Omega dE}_{-\underset{\sim}{\kappa},\ -\omega} \qquad (2.16)$$

2.2.2 Bragg scattering

The elastic scattering cross section is, from (2.12) and (2.13),

$$\left(\frac{d\sigma}{d\Omega}\right)_{\text{elastic}} = \left(\frac{\gamma e^2}{2m_e c^2}\right)^2 \sum_{\alpha,\beta} \left(\delta_{\alpha\beta} - \bar{\kappa}_\alpha \bar{\kappa}_\beta\right) \sum_{i,j} \overline{g_j g_i f_i(\kappa) \langle S_i^\alpha \rangle f_j(\kappa) \langle S_j^\beta \rangle e^{-2W(\kappa)}} \tag{2.17}$$

If in this expression the mean and fluctuating parts of the configurational average are separated, assuming $g_i = g_j = g$ and $f_i = f_j = f(\kappa)$,

$$\overline{\langle \hat{S}_i^\alpha \rangle \langle \hat{S}_j^\beta \rangle} = \langle \bar{S}_i^\alpha \rangle \langle \bar{S}_j^\beta \rangle + \left(\overline{\langle \hat{S}_i^\alpha \rangle \langle \hat{S}_j^\beta \rangle} - \langle \bar{\hat{S}}_i^\alpha \rangle \langle \bar{\hat{S}}_j^\beta \rangle\right) \tag{2.18}$$

the cross section can be separated into two terms. The first is the scattering arising from the periodic static spin structure. In this case the phases of the scattered neutrons add together coherently by virtue of the phase relationships set up by the periodic average magnetic potential and the cross section is a series of delta functions centred at the magnetic reciprocal lattice positions $\underset{\sim}{G}_M$. This is the magnetic Bragg scattering. The second term, which represents deviations from the mean is related to static magnetic inhomogeneties and gives the weakly κ dependent magnetic diffuse elastic cross section which is treated in the next section.

The Bragg scattering from a periodic magnetic structure is, from (2.17) and (2.18), with N_M unit cells within the system,

$$\left(\frac{d\sigma}{d\Omega}\right)_{\text{Bragg}} = N_M \left(\frac{\gamma e^2}{m_e c^2}\right)^2 \frac{(2\pi)^3}{v_M} \sum_{G} \delta(\underset{\sim}{\kappa} - \underset{\sim}{G}) \left[\bar{\underset{\sim}{\kappa}} \times \bar{\underset{\sim}{\mathcal{F}}}(G) \times \bar{\underset{\sim}{\kappa}}\right]^2 \tag{2.19a}$$

in which the problem has been reduced to that of describing the interference phenomena within the magnetic unit cell. The unit cell is assumed to have a volume v_M and a magnetic vector structure factor

$$\bar{\underset{\sim}{\mathcal{F}}}(\underset{\sim}{G}) = \sum_{d} \exp(i\underset{\sim}{\kappa}.\underset{\sim}{d}) \left[\tfrac{1}{2} g_d f_d(\underset{\sim}{\kappa}) \langle \hat{S}_d \rangle \exp(-W_d(\kappa)) \bar{\underset{\sim}{\eta}}_d(\underset{\sim}{G})\right] \tag{2.19b}$$

where $\underset{\sim}{d}$ defines the spin positions within the unit cell and $\bar{\underset{\sim}{\eta}}_d(\underset{\sim}{G})$ defines the spin direction. In a non-collinear spin structure $\bar{\underset{\sim}{\eta}}$ is a function of the reciprocal lattice vector $\underset{\sim}{G}$, and describes the screw direction and pitch of helical order for example. In a collinear spin structure all spins are either parallel or anti-parallel to a given direction $\bar{\underset{\sim}{\eta}}$ so that $\bar{\underset{\sim}{\eta}}_d(G) = \bar{\underset{\sim}{\eta}}\sigma_d$ where $\sigma_d = \pm 1$ depending upon the relative orientation. For such a collinear structure the Bragg scattering cross section is

$$\frac{d\sigma}{d\Omega}_{Bragg} = N_M\left(\frac{\gamma e^2}{m_e c^2}\right)^2 \frac{(2\pi)^3}{v_m} \left(1-(\underset{\sim}{G}.\bar{\underset{\sim}{\eta}})^2\right)_{av} \sum_{G} \delta(\underset{\sim}{\kappa}-\underset{\sim}{G})\bar{F}_M^{+}(\underset{\sim}{G})\bar{F}_M(\underset{\sim}{G}) \qquad (2.20a)$$

with the cross section averaged over domain orientations via subscript 'av." and the magnetic structure factor now a scalar $\bar{F}_M(\underset{\sim}{G})$,

$$\bar{F}_M(\underset{\sim}{G}) = \sum_d \exp(i\underset{\sim}{\kappa}.\underset{\sim}{d})\overline{\left[\tfrac{1}{2}g_d f_d(\kappa)\langle S_d\rangle \exp(-W_d(\kappa))\right](\sigma_d)} \qquad (2.20b)$$

These expressions have been derived using the dipole approximation for the cross section but serve to illustrate the general point that the Bragg scattering occurs at magnetic reciprocal lattice positions and with an intensity which is proportional to $|M_\perp(\kappa)|^2$, the square of the fourier component of the average static magnetization which is perpendicular to the scattering vector.

In the case of many Chromium alloys, the spins are arranged in a simple antiferromagnetic structure consisting of two simple cubic sublattices. The magnetic unit cell is simple cubic and has the reciprocal lattice $\underset{\sim}{G} = 2\pi/a\ (h, k, \ell)$ with lattice parameter a and the structure factor $F_M(\underset{\sim}{G}) = 0$ for $h + k + \ell$ even and $F_M(\underset{\sim}{G}) = \bar{\mu}f(\underset{\sim}{G})e^{-W(\underset{\sim}{G})}$ for $h + k + \ell$ odd. In calculating the structure factor according to (2.20b) the average sublattice moment $\bar{\mu}$ has been used to replace $g\langle S\rangle$ and $f(\kappa)$ is a 3d type form factor which is assumed to be appropriate to the problem. The magnetic Bragg scattering cross section is then,

$$\frac{d\sigma}{d\Omega}_{Bragg} = \frac{2}{3} N_M\left(\frac{\gamma e^2}{m_e c^2}\right)^2 \left(\frac{2\pi}{v_m}\right)^3 \sum_{\underset{\sim}{G}_{odd}} \delta(\underset{\sim}{\kappa}-\underset{\sim}{G}_{odd})|\bar{\mu}|^2 f^2(\underset{\sim}{\kappa})e^{-2W(\underset{\sim}{\kappa})} \qquad (2.21)$$

where $\underset{\sim}{G}_{odd}$ in a reciprocal lattice vector for which h + k + ℓ is an odd integer and the cross section has been averaged over random domain directions. This is to be contrasted with the nuclear scattering cross section. The nuclear Bragg scattering is, by analogy with (2.20),

$$\frac{d\sigma}{d\Omega}_{Bragg} = N_N \frac{(2\pi)^3}{v_N} \sum_{\underset{\sim}{G}} \delta(\underset{\sim}{\kappa}-\underset{\sim}{G}) \; \bar{F}_N^{+}(\underset{\sim}{G}) \bar{F}_N(\underset{\sim}{G}) \tag{2.22a}$$

where the nuclear structure factor is

$$\bar{F}_N(\underset{\sim}{G}) = \sum_d \exp(i\underset{\sim}{\kappa}.\underset{\sim}{d}) \; \overline{b_d \exp(-W_d(\kappa))} \tag{2.22b}$$

For bcc Chromium alloys the Bragg scattering cross section becomes,

$$\frac{d\sigma}{d\Omega}_{Bragg} = 4 N_N \frac{(2\pi)^3}{v_N} \sum_{\underset{\sim}{G}_{even}} \delta(\underset{\sim}{\kappa}-\underset{\sim}{G}_{even}) |\bar{b}|^2 \exp(-2W(\kappa)) \tag{2.23}$$

where $\underset{\sim}{G}_{even}$ is a reciprocal lattice vector for which h + k + ℓ is an even integer. By virtue of the different periodicities of the magnetic and nuclear potentials the corresponding Bragg reflections occur at mutually exclusive scattering vectors $\underset{\sim}{G}_{odd}$ and $\underset{\sim}{G}_{even}$.

The magnetic order in pure Chromium is based on the simple antiferromagnetic structure which has just been discussed. However, in this case, the collinear magnetization has a periodicity which is incommensurate with the lattice; that is, the magnetic repeat distance is not an integral number of nuclear lattice spacings. In this structure the collinear magnetization lies along one of the <100> directions ($\underset{\sim}{e}$) with a magnitude which varies from site to site in an oscillatory manner,

$$\underset{\sim}{\mu}(\underset{\sim}{R}_i) = \mu_{max} \underset{\sim}{\bar{e}} \exp(i \underset{\sim}{G}_{100}.\underset{\sim}{R}_i) \cos \underset{\sim}{Q}.\underset{\sim}{R}_i \tag{2.24}$$

corresponding to a sinusoidal modulation of the moment along another <100> direction with a wavevector $\underset{\sim}{Q}$ which is incommensurate with the lattice. The factor $\exp(i \underset{\sim}{G}_{100}.\underset{\sim}{R}_i)$ simply selects one of the

two simple cubic sublattices of the underlying antiferromagnetic structure, the moment modulation changes sign from one sublattice to the other. The moment propagation can be transverse, in which case $\underset{\sim}{e}$ and $\underset{\sim}{Q}$ are perpendicular or longitudinal for the case when $\underset{\sim}{e}$ and $\underset{\sim}{Q}$ are parallel. The concept of a magnetic unit cell is not useful in this case and direct substituion of the moment (2.24) into the expression for the cross section (2.17) gives the Bragg scattering

$$\left(\frac{d\sigma}{d\Omega}\right)_{\text{Bragg}} = \frac{N}{4}\frac{(2\pi)^3}{v_N}\left(\frac{\gamma e^2}{m_e c^2}\right)^2 \bar{\mu}^2_{max}(1-(\bar{\underset{\sim}{\kappa}}.\bar{\underset{\sim}{e}})^2)\sum_{G_{even}} \delta(\underset{\sim}{\kappa}-\underset{\sim}{G}\pm\underset{\sim}{Q}) f^2(\underline{\kappa}) e^{-2W(\underline{\kappa})} \tag{2.25}$$

at scattering vectors $\underset{\sim}{G}_{even} \pm \underset{\sim}{Q}$. As $\underset{\sim}{Q}$ deviates only slightly from $\underset{\sim}{G}_{100}$ type reciprocal lattice vectors i.e. $\underset{\sim}{Q} = (1 \pm \delta)G_{\{100\}}$ the magnetic Bragg peaks appear as equally spaced satellites clustered around the simple antiferromagnetic reciprocal lattice positions G_{odd}. In fact the structure of Cr is more complex than this, the nuclear positions are modulated with a wavevector $2\underset{\sim}{Q}$ and a further component of magnetization at $3\underset{\sim}{Q}$ also exists, Pynn et al.(1976).

2.2.3 Elastic magnetic diffuse scattering

Having dealt with the coherent Bragg scattering which comes from the average periodic component of magnetization, we now turn to the second part of the magnetic elastic cross section, the magnetic diffuse scattering. Measurement of this diffuse scattering can provide valuable information concerning the magnitude and spatial extent of defects in magnetically disordered systems. The classic application of the technique has been in the study of disordered binary ferromagnets by Low (1969) but has been extended recently by Davis and Hicks (1977) to the study of antiferromagnets.

Consider a binary disordered collinear ferromagnetic alloy with moments $\underset{\sim}{\mu}_R = g\langle\hat{S}^z_R\rangle\underset{\sim}{\hat{z}}$ aligned along the z direction. The diffuse scattering cross section is, from (2.17) and the fluctuating part of (2.18)

$$\left(\frac{d\sigma}{d\Omega}\right)_{el} = N\left(\frac{\gamma e^2}{2m_e c^2}\right)^2 (1-\bar{\kappa}_z^2) f^2(\underset{\sim}{\kappa}) T(\underset{\sim}{\kappa}) \exp(-2W) \qquad (2.26a)$$

where

$$T(\underset{\sim}{\kappa}) = \frac{1}{N} \sum_{i,j} \exp(i\underset{\sim}{\kappa}.\underset{\sim}{R}_{ij}) (\overline{\mu_i \mu_j} - \bar{\mu}^2) \qquad (2.26b)$$

This diffuse scattering is distinguished by the orientation factor $(1-\bar{\kappa}_z^2)$ which is zero if the scattering vector is along the direction of ferromagnetic saturation. Of particular note is the scattering in the forward direction which is a direct measure of the mean squared spatial fluctuations in magnetic moment, viz,

$$T(\underset{\sim}{0}) \sim \overline{(\mu - \bar{\mu})^2} \qquad (2.27)$$

Making sense of the general information contained in $T(\underset{\sim}{\kappa})$, however, requires a specific model for the moment distribution.

The simplest model is that for which all A atoms and all B atoms have constant moments $\bar{\mu}_A$, $\bar{\mu}_B$, irrespective of their environment. In this case, the only $\underset{\sim}{\kappa}$ dependence comes from the 3d type form factor and the Debye-Waller factor, and

$$T(\underset{\sim}{\kappa}) = C_A(1 - C_A)(\bar{\mu}_A - \bar{\mu}_B)^2 \qquad (2.28a)$$

which is entirely analogous to the 'Laue' incoherent scattering observed in the purely nuclear scattering (2.8a). The mean moments on each species can be extracted by combining the mean magnetization $\bar{\mu} = C_A \bar{\mu}_A + (1 - C_A)\bar{\mu}_B$ with this result. Such a model is not satisfactory in detail because it is clear that the magnetic moment will depend in some complex way on the atomic and magnetic environment.

The simplest way to include such effects is to consider dilute alloys. In this limit it is reasonable to assume that the impurity atoms have the same moment but that the impurity perturbs the host moments in their vicinity. If the host moment is modified by an amount $\phi(\underset{\sim}{R})$ due to an impurity at $\underset{\sim}{R}$ and assuming that the disturbances simply add together one finds

$$T(\underset{\sim}{\kappa}) = C_A(1-C_A)(\bar{\mu}_A-\mu_B+\Phi(\underset{\sim}{\kappa}))^2 \qquad (2.28b)$$

where $\Phi(\underset{\sim}{\kappa})$ is the Fourier transform of the magnetic disturbance, giving a $\underset{\sim}{\kappa}$ dependence above and beyond that of the form factor and Debye-Waller factor.

These results are valid in the case when there are, on average, no preferred atomic correlations; that is, the alloy is atomically random. For any real alloy there is a tendency toward atomic correlation, the expressions above must be multiplied by the atomic modulation factor $S(\underset{\sim}{\kappa})$ which is the Fourier transform of the static atomic spatial correlations,

$$S(\underset{\sim}{\kappa}) = \frac{1}{N}\sum_{i,j} \exp(i\underset{\sim}{\kappa}.\underset{\sim}{R}_{ij})\alpha(\underset{\sim}{R}_{ij}) \qquad (2.28c)$$

where $\alpha(\underset{\sim}{R}_{ij})$ is the short range order parameter introduced by Cowley (1950). The parameter α is defined to be positive if there is a more than statistical preference for like atoms to be separated by a vector $\underset{\sim}{R}_{ij}$ and are zero for a random alloy. In the presence of nuclear short range order the Laue incoherent cross section is modulated by the factor $S(\underset{\sim}{\kappa})$ so that the α parameters are accessible to experiment.

The generalization of these results to concentrated alloys is difficult: the assumption of linear superposition of defects is invalid and there are a large number of possible environments to contend with. There is also the possibility that the moment variation is driven by short range order. In most cases the analysis is performed using the assumption of superimposed linear defects $H(\underset{\sim}{\kappa})$ and $G(\underset{\sim}{\kappa})$ defined as the Fourier transforms of the disturbances due to a type B atom on type A and vice versa, and

$$T(\underset{\sim}{\kappa}) = (\bar{\mu}_A-\bar{\mu}_B+(1-C_A)G(\underset{\sim}{\kappa})+C_AH(\underset{\sim}{\kappa}))^2 S(\underset{\sim}{\kappa})\, C_A(1-C_A) \qquad (2.28d)$$

In the limit of large $\underset{\sim}{\kappa}$, any $\underset{\sim}{\kappa}$ dependence due to the disturbances $G(\underset{\sim}{\kappa})$ and $H(\underset{\sim}{\kappa})$ have subsided and in general $T(\underset{\sim}{\kappa})$ will tend to the limit $(\bar{\mu}_A-\bar{\mu}_B)^2 S(\underset{\sim}{\kappa})$ and the mean moments may be extracted independently of any model. A cross check on the analysis is provided from the

limiting behaviour of the cross section as $\kappa \to 0$, if the fluctuations in magnetization are driven by concentration fluctuations (eq. 27a) becomes

$$T(0) = C_A(1-C_A)\left(\frac{d\bar{\mu}}{dC_A}\right)^2 \tag{2.27b}$$

In the case of antiferromagnetic binary alloys these results may be generalized to give the magnetic elastic diffuse scattering from a two sublattice antiferromagnet. For random domain distributions Cywinski and Hicks (1980) find,

$$\frac{d\sigma}{d\Omega}_{el} = \frac{2}{3}\left(\frac{\gamma e^2}{m_e c^2}\right)^2 \times \quad f^2(\kappa) T(\underset{\sim}{\kappa}) S(\underset{\sim}{\kappa}-\underset{\sim}{G}_m) \tag{2.29a}$$

The factor $S(\underset{\sim}{\kappa}-\underset{\sim}{G}_m)$ is included to account for the presence of atomic short range order and $\underset{\sim}{G}_m$ is the smallest magnetic reciprocal lattice vector. The function $T(\underset{\sim}{\kappa})$ depends on the fourier transform of the spatial distribution of the magnetic defect and may be written following (2.28b) to give for a dilute alloy

$$T(\underset{\sim}{\kappa}) = (\bar{\mu}_A - \bar{\mu}_B + \Phi(\underset{\sim}{\kappa}-\underset{\sim}{G}_m))^2 C_A(1-C_A) \tag{2.29b}$$

The disturbances are assumed to superimpose in a linear fashion so that

$$\Phi(\underset{\sim}{\kappa}-\underset{\sim}{G}_m) = \sum_i \phi(\underset{\sim}{R}_i) e^{-i\underset{\sim}{G}_m \cdot \underset{\sim}{R}_i} e^{i\underset{\sim}{\kappa}\cdot\underset{\sim}{R}_i} \tag{2.29c}$$

where $\phi(R_i)$ represents the magnitude of the disturbance on the host atom B by the impurity at site R_i. In this case the cross section at $\underset{\sim}{G}_m$ is related to the concentration derivative of the sublattice magnetization.

2.2.4 The quasi static approximation

There is an important sum rule on the magnetic scattering which may be derived from (2.12), namely

$$\int_{-\infty}^{\infty} d\omega \mathcal{S}^{\alpha\beta}(\underset{\sim}{\kappa}, \omega) = \frac{1}{N} \overline{\langle \hat{S}^{\alpha}(-\underset{\sim}{\kappa}, 0) \hat{S}^{\beta}(\underset{\sim}{\kappa}, 0)\rangle} \tag{2.30a}$$

The value of this expression lies in the fact that, if the inelasticity of the scattering is small in comparison to the incident neutron energy, the integral may be approximately represented by the total scattering cross section at a given scattering vector $(\frac{d\sigma}{d\Omega})$, which is precisely what is measured with a fixed detector angle and without energy analysis in a conventional 2 axis experiment. Under these conditions the integrated cross section may be directly related to the instantaneous spin pair correlation function. From (2.30a),

$$\frac{d\sigma}{d\Omega} = \left(\frac{\gamma e^2}{2m_e c^2}\right)^2 e^{-2W(\underset{\sim}{\kappa})} g^2 f^2(\kappa) \sum_{\alpha,\beta} (\delta_{\alpha\beta} - \bar{\kappa}_\alpha \bar{\kappa}_\beta) \sum_{i,j} \exp(i\underset{\sim}{\kappa}.\underset{\sim}{R}_{ij}) \overline{\langle \hat{S}_i^\alpha(0) \hat{S}^\beta(0) \rangle} \tag{2.30b}$$

This is a significant result as it implies that the instantaneous spatial correlations can be determined in a straightforward way without any detailed knowledge of the dynamical properties of the system.

The instantaneous spin pair correlation function is made up of two parts. The first is simply the product of the thermal average of the spin components on each site, this is essentially the square of the order parameter and results in elastic scattering as detailed in 2.2.2. The remaining part is the average of the fluctuations of the spin components about the static values and is related to the isothermal wavevector dependent susceptibility. Making this separation (2.30b) becomes,

$$\frac{d\sigma}{d\Omega} - \frac{d\sigma}{d\Omega}_{\text{elastic}} = \left(\frac{\gamma e^2}{2m_e c^2}\right)^2 \frac{N f^2(\kappa)}{\mu_B^2} \sum_{\alpha,\beta} (\delta_{\alpha\beta} - \bar{\kappa}_\alpha \bar{\kappa}_\beta) kT \, e^{-2W(\underset{\sim}{\kappa})} \chi^{\alpha\beta}(\underset{\sim}{\kappa}) \tag{2.31a}$$

with

$$(kT)\chi^{\alpha\beta}(\underset{\sim}{\kappa}) = \sum_{i,j} e^{i\underset{\sim}{\kappa}.\underset{\sim}{R}_{ij}} \overline{\langle (\hat{S}_i(0) - \langle \hat{S}_i^\alpha \rangle)(\hat{S}_j^\beta(0) - \langle \hat{S}_j^\beta \rangle) \rangle} \tag{2.31b}$$

This expression could have been derived from (2.15a). Thus the wavevector dependent susceptibility can also be extracted from the

total cross section without any detailed knowledge of the behaviour of $F_{\underset{\sim}{\kappa}}^{\alpha\beta}(\omega)$ provided the elastic scattering is known and can be subtracted from the total. The expressions (2.30) and (2.31) are approximate, valid in the limit of high incident neutron energies. This approximation is known as the 'quasistatic' (or quasielastic or static) approximation. If the conditions of quasistatic approximation hold true, it is possible to measure the spatial dependence of the spin-spin correlation function independently of its temporal variation. This amounts to a consideration of the equilibrium thermodynamic properties of the system.

The spin-spin correlation function has two familiar limits; that for a pure paramagnet where correlations are confined to the same site and that for a system close to a critical point where the correlations are very long ranged. Between these two limits analysis of the correlations is more complex and depends strongly on the particular crystal structure etc. under consideration. In this case the system may be characterized by the average correlations between coordination shells, allowing the local couplings between spins in a disordered system to be determined. We shall treat these cases in more detail.

Consider the scattering from a binary alloy in the quasistatic approximation. If the spins are free from all interactions only the correlation of the spin with itself can survive the thermal average giving a cross section which is linear in the concentration C_A of magnetic species, quadratic in the spin S and has no $\underset{\sim}{\kappa}$ dependence apart from the form factor.

The cross section simply amounts to a statement of the Curie law,

$$\frac{d\sigma}{d\Omega} = \left(\frac{\gamma e^2}{2m_e c^2}\right)^2 g^2 f^2(\underset{\sim}{\kappa}) \frac{2}{3} N \cdot C_A \cdot S(S+1) e^{-2W(\underset{\sim}{\kappa})} \qquad (2.32a)$$

or alternatively

$$\chi_0^{\alpha\beta}(\underset{\sim}{\kappa}) = \delta_{\alpha\beta}(g\mu_B)^2 S(S+1)/3kT \qquad (2.32b)$$

For a non interacting spin system the wave vector dependent susceptibility has no κ dependence.

In the vicinity of a critical point, the κ dependence of the susceptibility is marked. Intuitively one may expect the system to be most susceptible to perturbations with a wavevector $\underset{\sim}{G}_0$ corresponding to the periodicity of the incipient long range order: hence $\chi(\underset{\sim}{\kappa})$ would be peaked at $\underset{\sim}{\kappa} = 0$ and at other nuclear reciprocal lattice vectors $\underset{\sim}{G}_n$ for a system close to its ferromagnetic Curie temperature (T_c) or at appropriate reciprocal lattice vectors $\underset{\sim}{G}_M$ for more complex structures close to the Néel temperature (T_N). At the ordering temperature the susceptibility diverges at $\underset{\sim}{\kappa} = \underset{\sim}{G}_0$ so just above the critical temperature the susceptibility may be expanded as a power series in the small deviations $\underset{\sim}{q} = \underset{\sim}{\kappa} - \underset{\sim}{G}_0$ about the peak value, to give for an isotropic system

$$\chi^{-1}(\underset{\sim}{q}) = \chi^{-1}(\underset{\sim}{G}_0)\left[1 + q^2/\kappa_1^{\,2} + \ldots\right] \tag{2.33}$$

where the expansion coefficient κ_1 has the dimensions of inverse length and must tend to zero as $T \to T_c$.

This form for the susceptibility is found in the mean field approximation for a three dimensional Heisenberg ferromagnet. It was shown by Van Hove (1954b) that for small k,

$$\chi^{\alpha\beta}(\underset{\sim}{\kappa}) = \frac{\chi_0^c}{v_1^{\,2}(\kappa^2 + \kappa_1^{\,2})} \tag{2.34a}$$

where the parameters v_1 and κ_1 are found to be

$$v_1^{\,2} = \frac{1}{6} J^{(2)}/J^{(0)} \qquad \kappa_1 = \left(\frac{T-T_c}{T_c}\right)^{\frac{1}{2}} \frac{1}{v_1} \tag{2.34b}$$

with $J^{(n)}$ the n^{th} moment of the exchange interaction and χ_0^c the Curie susceptibility (2.32) at $T = T_c$. For nearest neighbour interactions $v_1 \tilde{\propto} a$ and varies slowly with temperature. This form for the susceptibility implies that the instantaneous spin correlation function has the asymptotic form,

$$\langle S_i S_j \rangle_{R_{ij}\to\infty} \sim \frac{1}{R_{ij}} \exp(-R_{ij}\kappa_1) \tag{2.34c}$$

It is this expression which epitomises critical phenomena. As the temperature is lowered towards the critical point the range of correlations $\xi = 1/\kappa_1$ tends to diverge and the correlation function ultimately falls off as $1/R$ at T_c and is no longer integrable. This leads to a divergence in the susceptibility at $\kappa = G_0$ and $T = T_c$ and gives rise to the singularities in thermodynamic variables. These results were first obtained by Ornstein and Zernicke for the density-density correlations in a fluid close to the critical point and the expressions above are associated with these names. The analogy with a fluid is particularly apt: in a fluid the density correlations couple with light via the refractive index to give critical opalescence, in a spin system the spin fluctuations couple to the neutron via the susceptibility to give critical magnetic scattering which is singular in q and T at T_c.

At temperatures very close to T_c the expansion (2.33) for the wavevector dependent susceptibility is no longer valid and the Ornstein-Zernicke theory breaks down. Fisher and Burford (1967) suggest that the susceptibility should be of the general form

$$\chi^{-1}(\kappa) = \chi^{-1}(0)\left[1 + \psi \frac{\kappa^2}{\kappa_1^2}\right]\left[1 + \phi \frac{\kappa^2}{\kappa_1^2}\right]^{-\eta/2} \quad T \to T_c^{+} \tag{2.35a}$$

The parameter $\psi = 1 + \eta\phi^2/2$ and ϕ vary smoothly with temperature and both η and ϕ are small, of the order 0.1 or smaller in the vicinity of T_c. For small κ this expansion reduces to a quasi-Lorentzian shape,

$$\chi^{-1}(\kappa) = \chi^{-1}(0)\left[1 + \kappa^2/\kappa_1^2 (1-\eta/2)^{-1}\right]^{1-\eta/2} \tag{2.35b}$$

so that at T_c the spin correlations fall off rather more slowly than $1/R$, the asymptotic form being

$$\langle \underset{\sim}{S}_i \cdot \underset{\sim}{S}_j \rangle \sim \frac{1}{R^{2-d+\eta}} \qquad T = T_c,\ R \to \infty \tag{2.35c}$$

in d dimensions. The inverse range parameter κ_1 approaches zero as T approaches T_c (from above) as in Ornstein-Zernicke theory but with an exponent $\nu > 0$ which may be different from $\frac{1}{2}$,

$$\kappa_1 \sim \left(\frac{T-T_c}{T_c}\right)^{\nu} \qquad T > T_c \tag{2.35d}$$

In this way the bulk susceptibility $\chi(0)$ diverges at T_c according to

$$\frac{\chi(0)}{\chi_0} \sim \left(\frac{T-T_c}{T_c}\right)^{-\gamma} \qquad T > T_c \tag{2.35e}$$

where the exponent γ is 1 in mean field theory. For equations (2.35) to be self consistent the exponents γ, η and ν must satisfy the equality $(2 - \eta)\nu = \gamma$. It is possible in principle to determine these critical exponents and the important quantities $\chi(0)$ and κ_1 directly from critical scattering measurements.

The elastic component of the scattering which appears below the critical temperature must be subtracted in order to determine the susceptibility according to (2.31). Furthermore, as the system shows long range order, it is necessary to take due account of this symmetry breaking by distinguishing between the correlations between spin components parallel and perpendicular to the local axis of the order parameter (z). The cross section in this case may be written, (compare with (2.15b) and (2.15c)),

$$\frac{d\sigma}{d\Omega} - \frac{d\sigma}{d\Omega}_{\text{elastic}} = N\left(\frac{\gamma e^2}{2m_e c^2}\right)^2 \frac{f^2(\kappa)}{\mu_B^2} e^{-2W(\kappa)} kT\left[(1-\bar{\kappa}_z^{-2})\chi^{zz}(\kappa)+(1+\bar{\kappa}_z^{-2})\chi^{xx}(\kappa)\right] \tag{2.36}$$

where χ^{zz} and χ^{xx} are the longitudinal and transverse susceptibilities. The Ornstein-Zernicke result for $T < T_c$ is

$$\chi^{zz} = \frac{\chi_0^c}{\nu_1^2(\kappa^2+(\kappa_1^z)^2)} \tag{2.37a}$$

where the longitudinal inverse correlation length ,

$$\kappa_1^z = \frac{1}{2r_1} \frac{J(2)}{J(0)} \left(\frac{T-T_c}{T_c}\right)^{\frac{1}{2}} \qquad (2.37b)$$

is numerically twice as large as κ_1 for the same reduced temperature. The transverse susceptibility is not in any sense critical,

$$\chi^{xx}(\kappa) = \frac{\chi_\sigma^c}{r_1 \kappa^2} \qquad (2.37c)$$

and κ_1^x is zero below T_c. More sophisticated theories propose that κ_1^z diverges with an exponent ν' which is identical to ν and the bulk longitudinal susceptibility $\chi^{zz}(0)$ diverges with an exponent γ' which is identical to γ. The longitudinal susceptibility $\chi^{zz}_{(\kappa)}$ assumes the quasi Lorentzian form given in (2.35b) with an exponent η' which is equal to η. Further aspects of neutron critical scattering are reviewed by Als-Nielsen (1976).

The intermediate case, that of a correlated system which is not close to criticality, is more difficult to deal with. It is possible to parameterize the problem in a phenomenological way by defining correlation coefficients between spins, atomic planes or coordination shells depending on the symmetry of the system involved. For example, consider a random binary alloy comprising C_A of magnetic species dissolved in a non magnetic host. In this case the cross section (2.30) may be expressed as a fourier series

$$\frac{d\sigma}{d\Omega} = N\left(\frac{\gamma e^2}{2m_e c^2}\right)^2 g^2 f^2(\kappa) \sum_{\alpha,\beta} (\delta_{\alpha\beta} - \bar{\kappa}_\alpha \bar{\kappa}_\beta) e^{-2W(\kappa)} \left[C_A \overline{\langle S_0^\alpha S_0^\beta \rangle} + \sum_{\underset{\sim}{m}\neq 0} \overline{\langle S_0^\alpha S_{\underset{\sim}{m}}^\beta \rangle} e^{i\underset{\sim}{\kappa}\cdot\underset{\sim}{m}}\right] \qquad (2.38)$$

By fitting the data to this series it is possible to determine the effective spin from the self correlation term $\overline{\langle S_0^\alpha S_0^\beta \rangle}$ and the nearest neighbour (m=1) or higher order correlations $\overline{\langle S_0^\alpha S_m^\beta \rangle}$ from the fourier components. Such a procedure has been performed by Davis and Hicks (1979) for CuMn alloys. From the temperature dependence of the correlation coefficients it is possible to estimate the magnitude of the exchange interactions. Stanley (1967) has illustrated the reverse procedure by applying the results of high temperature series expansions for the nearest neighbour Heisenberg model to the case of paramagnetic cubic spinels.

2.2.5 The orientational average

The cross section must be averaged over all orientations of crystallites in a polycrystal or random defect orientations in single crystals. Even for materials with cubic crystal structure this average is non trivial as it is necessary to allow for the vector nature of the neutron-electronic moment interaction. This problem has been treated by Blech and Averbech (1964) and as the original paper contains a number of misprints, the major steps in the derivation are presented here.

Consider the scattering in the quasi static approximation (2.30). In a polycrystal it is not possible to distinguish between relative orientations of the scattering vector $\underset{\sim}{\kappa}$ and the vector $\underset{\sim}{r}_n = \underset{\sim}{R}_i - \underset{\sim}{R}_j$ separating spins. The measurement returns the average scattering arising from all pairs of spins separated by a distance r_n irrespective of direction, thus

$$\left(\sum_{\alpha,\beta} (\delta_{\alpha\beta} - \bar{\kappa}_\alpha \bar{\kappa}_\beta) \exp i\underset{\sim}{\kappa}.\underset{\sim}{r}_n \overline{\langle \hat{S}_i^\alpha \hat{S}_{i+n}^\beta \rangle} \right)_{av.} = \frac{1}{4\pi} \int\int d\Omega \left\{ \sum_{\alpha,\beta} (\delta_{\alpha\beta} - \bar{\kappa}_\alpha \bar{\kappa}_\beta) \overline{\langle S_i^\alpha S_{i+n}^\beta \rangle} \cos(\kappa r_n \cos\phi) \right\}_n \qquad (2.39a)$$

where $d\Omega$ is an element of solid angle $\sin\phi d\phi d\omega$ centred on a particular orientation (ϕ, ω) of $\underset{\sim}{r}_n$ with respect to $\underset{\sim}{\kappa}$ and the average over all pairs separated by a distance $\underset{\sim}{r}_n$ has been denoted $\{\}_n$. In order to evaluate this average it is convenient to resolve the spins and the scattering vector into components along the radius vector (R) and in a direction perpendicular to it (T) as shown in Fig. 2.1.,

$$\left\{ \sum_{\alpha,\beta} \delta_{\alpha\beta} - \bar{\kappa}_\alpha \bar{\kappa}_\beta \overline{\langle S_i^\alpha S_{i+n}^\beta \rangle} \right\}_n = \left\{ (1-\bar{\kappa}_R^2) \overline{\langle S_i^R S_{i+n}^R \rangle} + (1-\bar{\kappa}_T^2) \overline{\langle S_i^T S_{i+n}^T \rangle} \right\}_n$$

and with the definition of the angles ϕ, ω in Fig. 2.2 $\bar{\kappa}_R = \cos\phi$ and $\bar{\kappa}_T = \sin\phi \cos\omega$ the integration over Ω in (2.39) may be readily performed to yield the orientational average

Fig.2.1 Spin vectors S_i and S_j and their projections along the radius vector. (Blech and Averbech (1964))

Fig.2.2 Geometrical relation between spin directions, radius vector and scattering vector. (Blech and Averbech (1964)).

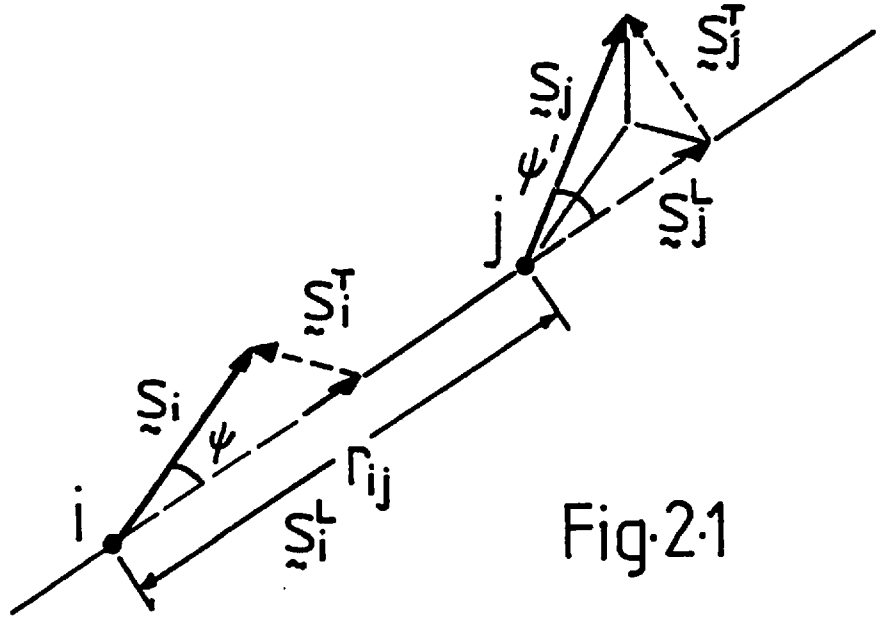
S_j^T
S_j
ψ'
j
S_j^L
S_i^T
S_i
ψ
r_{ij}
i
S_i^L

Fig·2·1

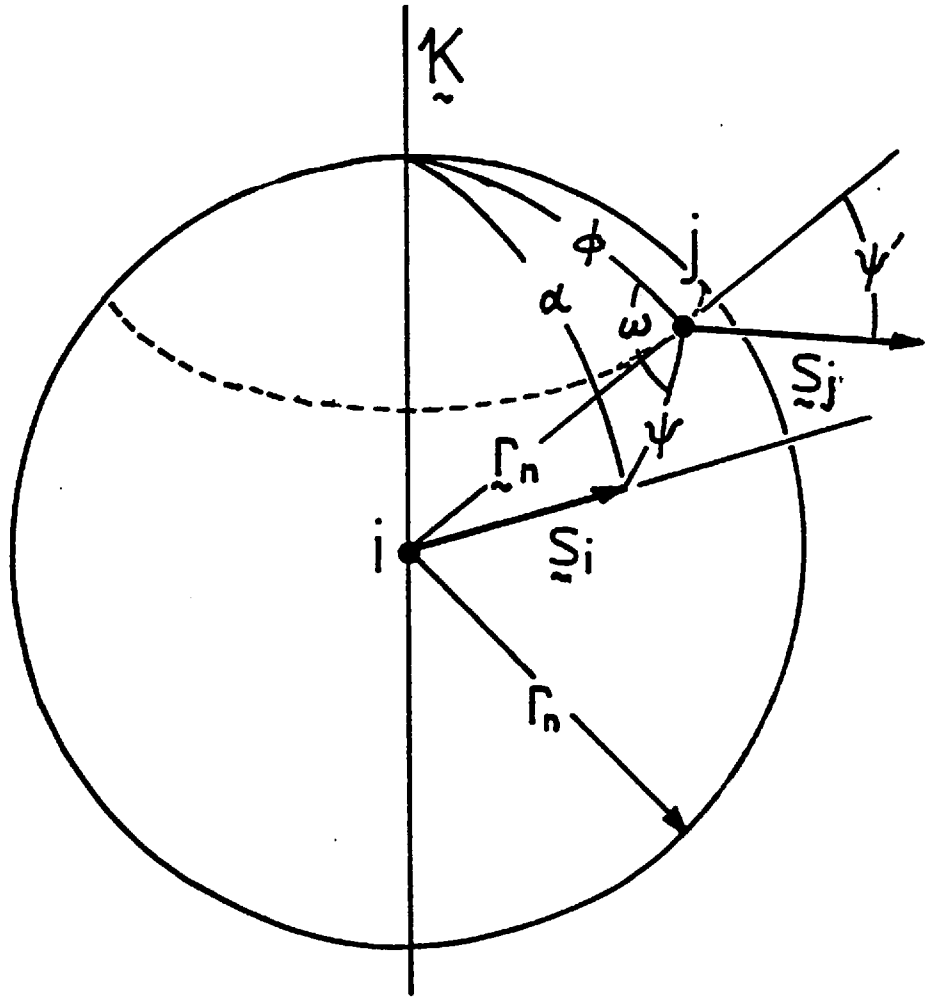
K
ϕ
j
ψ'
α
ω
S_j
ψ
r_n
i
S_i
r_n

Fig·2·2

$$\left(\sum_{\alpha,\beta} \delta_{\alpha\beta} - \bar{\kappa}_\alpha \bar{\kappa}_\beta \overline{\langle S_i^\alpha S_{i+n}^\beta \rangle} \exp(i\underset{\sim}{\kappa}\cdot\underset{\sim}{r}_n) \right)_{av} = a_n \frac{\sin \kappa r_n}{\kappa r_n} + b_n \left(\frac{\sin \kappa r_n}{(\kappa r_n)^3} - \frac{\cos \kappa r_n}{(\kappa r_n)^2} \right) \tag{2.39b}$$

with the average correlation coefficients a_n, b_n defined as

$$a_n = \{\overline{\langle S_i^T S_{i+n}^T \rangle}\}_n \tag{2.39c}$$

$$b_n = \{\overline{2\langle S_i^R S_{i+n}^R \rangle} - \overline{\langle S_i^T S_{i+n}^T \rangle}\}_n \tag{2.39d}$$

In performing this decomposition the spin has been treated as a classical vector quantity.

If, after averaging over all orientations, the spin correlations are independent of the radius vector direction (such as the case when local correlations or defects have cubic symmetry) the average correlation coefficients are

$$a_n = \frac{2}{3} \{\overline{\langle \underset{\sim}{S}_i \cdot \underset{\sim}{S}_{i+n} \rangle}\}_n \tag{2.40a}$$

$$b_n = 0 \tag{2.40b}$$

and the cross section is

$$\frac{d\sigma}{d\Omega} = \frac{2}{3} \left(\frac{\gamma e^2}{2m_e c^2} \right)^2 g^2 f^2(\kappa) \sum_{i,n} \{\overline{\langle \underset{\sim}{S}_i \cdot \underset{\sim}{S}_{i+n} \rangle}\}_n \frac{\sin \kappa r_n}{\kappa r_n} \tag{2.40c}$$

This is exactly the same form as the expression for the nuclear scattering averaged over all orientations. In the nuclear case the cross section averaged over random orientations is

$$\frac{d\sigma}{d\Omega_N} = \exp(-2W(\kappa)) \sum_{i,j} \bar{b}_i \bar{b}_j \frac{\sin \kappa r_{ij}}{\kappa r_{ij}} \tag{2.41a}$$

For Laue scattering (2.8a) and (2.28) this cross section has the dependence

$$\frac{d\sigma}{d\Omega}_N = N C_A (1-C_A) (b_A - b_B)^2 \exp(-2W(\kappa)) \sum_n \alpha_n \frac{\sin \kappa r_n}{\kappa r_n} \tag{2.41b}$$

where α_n is the Cowley parameter $\alpha(\underset{\sim}{R}_{i\ i+n})$ averaged over all directions. The orientational average (2.40) is commonly used but is strictly only valid in the situation where the vector nature of the magnetic interaction between neutron and magnetic moment is unimportant as the close analogy with the nuclear cross section (2.41) demonstrates.

In general the averaged correlations are different for components parallel and perpendicular to the radius vector $\underset{\sim}{r}_n$. This occurs in MnO where the local symmetry is not cubic, as treated by Blech and Averbach (1964). The presence of magnetic dipolar forces which depend on the relative orientation of the spins and radius vector via the term $(\underset{\sim}{r}_n.\underset{\sim}{S}_i)(\underset{\sim}{r}_n.\underset{\sim}{S}_{i+n})$ in the Hamiltonian may lead to different correlations parallel and perpendicular to the radius vector. This has been demonstrated by Nagele et al. (1978) for manganese aluminosilicate glasses and in the case of shape anisotropy within small particles in Appendix A.

2.3 Magnetic scattering with polarized beams

2.3.1 Introduction

The cross section for scattering of polarized neutrons by combined nuclear and magnetic interactions can be divided into purely magnetic scattering, purely nuclear scattering and nuclear magnetic interference scattering terms, each of which has the overall form

$$\frac{d^2\sigma}{d\Omega dE} = \left(\frac{m}{2\pi\hbar^2}\right)^2 \frac{k'}{k} \sum_{\lambda\lambda'} p_\lambda \, \mathrm{Tr}\, \hat{\rho} \langle\lambda|\hat{V}_1^+|\lambda'\rangle\langle\lambda'|\hat{V}_2|\lambda\rangle \delta(\hbar\omega - E_{\lambda'} + E_\lambda)$$

The average over neutron spin components can be performed using the properties of the Pauli matrices,

$$\mathrm{Tr}\, \hat{\rho}\hat{V}_1^+\hat{V}_2 = \hat{\underset{\sim}{\alpha}}_1 \cdot \hat{\underset{\sim}{\alpha}}_2 + \hat{\beta}_1\hat{\beta}_2 + \hat{\beta}_1^+(\hat{\underset{\sim}{\alpha}}_2 \cdot \underset{\sim}{P}) + (\hat{\underset{\sim}{\alpha}}_1 \cdot \underset{\sim}{P})\hat{\beta}_2 + i\underset{\sim}{P} \cdot (\hat{\underset{\sim}{\alpha}}_1^+ \times \hat{\underset{\sim}{\alpha}})$$

where the general form of the interaction potential $\hat{V} = \hat{\beta} + \hat{\underset{\sim}{\alpha}} \cdot \hat{\underset{\sim}{\sigma}}$ has been used. From section 2.1 the spin dependent and spin independent parts of the scattering potentials are

$$\hat{\beta}_N = \frac{2\pi\hbar^2}{m} \sum_i \exp(i\underset{\sim}{\kappa} \cdot \underset{\sim}{R}_i) \exp(-W_i(\kappa)) A_i \qquad (2.42a)$$

$$\hat{\underset{\sim}{\alpha}}_N = \frac{2\pi\hbar^2}{m} \sum_i \exp(i\underset{\sim}{\kappa} \cdot \underset{\sim}{R}_i) \exp(-W_i(\kappa)) \frac{1}{2} B_i \hat{\underset{\sim}{I}}_i \qquad (2.42b)$$

$$\hat{\beta}_M = 0 \qquad (2.42c)$$

$$\hat{\underset{\sim}{\alpha}}_m = \frac{2\pi\hbar^2}{m} \left(\frac{\gamma_e}{m_e c^2}\right)^2 \hat{\underset{\sim}{Q}}_\perp \qquad (2.42d)$$

At all but the lowest temperatures the nuclear spins are randomly oriented so any terms which are linear in the nuclear spin $\hat{\underset{\sim}{I}}$ average to zero. With this assumption the nuclear, magnetic and nuclear magnetic terms are then

$$\mathrm{Tr}\, \hat{\rho}\hat{V}_m^+\hat{V}_m = \hat{\underset{\sim}{\alpha}}_m^+ \cdot \hat{\underset{\sim}{\alpha}}_m + i\underset{\sim}{P} \cdot (\hat{\underset{\sim}{\alpha}}_m^+ \times \hat{\underset{\sim}{\alpha}}_m) \qquad (2.43a)$$

$$\mathrm{Tr}\ \hat{\rho}\hat{V}_N^{+}\hat{V}_N = \hat{\underset{\sim}{\alpha}}_N^{+}\cdot\hat{\underset{\sim}{\alpha}}_N + \hat{\beta}_N^{+}\hat{\beta}_N \tag{2.43b}$$

$$\mathrm{Tr}\ \hat{\rho}\hat{V}_m\hat{V}_N = (\hat{\underset{\sim}{\alpha}}_m^{+}\cdot\underset{\sim}{P})\hat{\beta}_N \tag{2.43c}$$

The purely nuclear cross section is independent of polarization as the nuclei have no preferred axis. The purely magnetic cross section consists of a polarization independent term $\hat{\underset{\sim}{\alpha}}_m^{+}\cdot\hat{\underset{\sim}{\alpha}}_m^{+}$ which was dealt with in section 2.2 plus an additional polarization dependent term $i\underset{\sim}{P}\cdot(\hat{\underset{\sim}{\alpha}}_m^{+}\times\hat{\underset{\sim}{\alpha}}_m)$ which is zero for a collinear spin system but may contribute to the scattering in more complex structures. For our present purposes it is the polarization dependent nuclear magnetic interference term $(\hat{\underset{\sim}{\alpha}}_m^{+}\cdot\underset{\sim}{P})\hat{\beta}_N$ which is most important. This term is linear in the magnetic scattering amplitude so that the absolute sign may be determined unambiguously. Furthermore this term may represent a potential amplification of the weak magnetic amplitude by the stronger nuclear amplitude and hence may be employed to determine very small magnetic cross sections with great accuracy.

Such a polarization dependent term may be separated from the polarization independent terms in the cross section simply by observing the change in scattering on reversing the incident polarization. (Further information may be gained by analysing the scattered polarization and this extension will be treated in section 2.4). Consider the change in scattering cross section observed on reversing the polarization from $\underset{\sim}{P}$ to $-\underset{\sim}{P}$ for a collinear system in the dipole approximation

$$\frac{d\sigma}{d\Omega}_{\underset{\sim}{P}} - \frac{d\sigma}{d\Omega}_{-\underset{\sim}{P}} = 4\left(\frac{\gamma e^2}{m_e c^2}\right)\exp(-2W(\underset{\sim}{\kappa}))\sum_{i,j}\exp(i\underset{\sim}{\kappa}\cdot\underset{\sim}{R}_{ij})\overline{(A_i\tfrac{1}{2}g_j f_j(\kappa)\ S_j>)}\ \underset{\sim}{\bar{\eta}}\cdot\underset{\sim}{P}_{\perp}$$

The cross section appears with a contrast factor $\underset{\sim}{\bar{\eta}}\cdot\underset{\sim}{P}_{\perp}$ which depends on the orientation of the collinear spin axis $\underset{\sim}{\bar{\eta}}$ with respect to $\underset{\sim}{P}_{\perp}$, and $\underset{\sim}{P}_{\perp} = \underset{\sim}{\bar{\kappa}}\times(\underset{\sim}{P}\times\underset{\sim}{\bar{\kappa}})$ is the component of polarization perpendicular to the scattering vector. This cross section is linear in <S> and depends on the correlation between magnetic moment and site occupation.

2.3.2 Bragg scattering

The coherent interference of nuclear and magnetic Bragg scattering amplitudes can only occur at scattering vectors where the purely nuclear and purely magnetic Bragg reflections coincide. In a simple ferromagnet all nuclear and magnetic nuclear reciprocal lattice positions coincide so the Bragg scattering contains all three contributions, using (2.42) and (2.43),

$$\frac{d\sigma}{d\Omega} = N_c \frac{(2\pi)^3}{v_0} \sum_{\underset{\sim}{G}} \delta(\underset{\sim}{\kappa} - \underset{\sim}{G}) \left[F_N^2 + \left(\frac{\gamma e^2}{m_e c^2}\right)^2 (1-(\underset{\sim}{G}.\bar{\underset{\sim}{\eta}})^2) F_M^2 \right.$$

$$\left. + \frac{2\gamma e^2}{m_e c^2} F_N F_M \bar{\underset{\sim}{\eta}}.\underset{\sim}{P}_\perp \right] \qquad (2.44a)$$

where again $\bar{\underset{\sim}{\eta}}$ is the unit magnetization direction and F_N and F_M are the nuclear and magnetic structure factors introduced in (2.20) and (2.22) of section 2.2.2. The extra contribution to the Bragg intensity occurs with the contrast factor $\bar{\underset{\sim}{\eta}}.\underset{\sim}{P}_\perp$ so that if the ferromagnet is saturated with $\bar{\underset{\sim}{\eta}}$ perpendicular to the scattering plane and the incident polarization is arranged to be either parallel (+) or antiparallel (-) to $\bar{\underset{\sim}{\eta}}$ the contrast factor becomes simply $\pm|\underset{\sim}{P}|$ and the cross section becomes

$$\frac{d\sigma^{(\pm)}}{d\Omega} = N_c \frac{(2\pi)^3}{v_0} \sum_{\underset{\sim}{G}} \delta(\underset{\sim}{\kappa} - \underset{\sim}{G}) \left[F_N \pm \frac{\gamma e^2}{m_e c^2} F_M\right]^2 \qquad (2.44b)$$

where ± correspond to perfect parallel or antiparallel polarization. For a given Bragg position the ratio of these two intensities, the 'flipping ratio' R is given by

$$R = \frac{(1+\gamma)^2}{(1-\gamma)^2} \quad \text{and} \quad \gamma = \left(\frac{\gamma e^2}{m_e c^2}\right)\frac{F_M}{F_N} \qquad (2.44c)$$

If the nuclear structure factors are known it is possible to accurately determine the magnetic structure factors by measuring the flipping ratio. By Fourier inversion of the magnetic structure factor data it is possible to measure the real space collinear (z)

component of the magnetization density. This is a model independent result.

The polarized technique is well suited to the determination of magnetization density because of its potentially high sensitivity and also due to the fact that the sign of the magnetic structure factor may be deduced, resolving the ambiguity in the unpolarized case.

It is important to note that although the determination of magnetization density is model independent it is not possible to allocate the spin, orbital and delocalized components of the density without model assumptions and further information. In particular it may be necessary to know the bulk magnetization in order to specify the delocalized component of the magnetization density or the g factor to assign the orbital component of the total moment according to (2.10d). The techniques of data treatment and schemes to separate the constituent parts of the magnetization are analysed by Moon (1971) for example and will be considered in more detail in chapter six.

2.4 Polarization analysis

2.4.1 The polarization of the scattered beam

The polarization state of the scattered beam contains additional information about the target system. In particular, by analysing the final polarization in the direction of the incident polarization it is possible to affect a complete separation of the purely magnetic and purely nuclear scattering from paramagnets and antiferromagnets.

The change in polarization on scattering may be found by considering the transformation of the density matrix of the incident beam $\hat{\rho}$ into the density matrix of the scattered beam $\hat{\rho}'$ by the spin dependent scattering potential $\hat{V}$. From Kessler (1976), for example,

$$\hat{\rho}' = \frac{\hat{V}^{+}\hat{\rho}\hat{V}}{\mathrm{Tr}(\hat{V}^{+}\hat{\rho}\hat{V})}$$

and the polarization of the scattered beam is formed from (2.4) and above,

$$\underset{\sim}{P}' \equiv \mathrm{Tr}\hat{\rho}'\underset{\sim}{\sigma} = \frac{\langle \mathrm{Tr}(\hat{V}^{+}\hat{\rho}\hat{V}\underset{\sim}{\sigma})\rangle}{\langle \mathrm{Tr}(\hat{V}^{+}\hat{\rho}\hat{V})\rangle} \tag{2.45}$$

The denominator is simply proportional to the cross section. Using the explicit form for the scattering potential and the properties of the Pauli matrices the trace may be evaluated to give

$$\mathrm{Tr}\ \hat{\rho}\hat{V}_1^{+}\underset{\sim}{\sigma}\hat{V}_2 = \hat{\beta}_1^{+}\hat{\beta}_2 + \hat{\underset{\sim}{\alpha}}_1\hat{\beta}_2 + \hat{\beta}_1\hat{\beta}_2\underset{\sim}{P} + \hat{\underset{\sim}{\alpha}}_1^{+}(\hat{\underset{\sim}{\alpha}}_2.\underset{\sim}{P}) + (\hat{\underset{\sim}{\alpha}}_1^{+}.\underset{\sim}{P})\hat{\underset{\sim}{\alpha}}_2 - \underset{\sim}{P}(\hat{\underset{\sim}{\alpha}}_1^{+}.\hat{\underset{\sim}{\alpha}}_2) - i\hat{\underset{\sim}{\alpha}}_1^{+}.\hat{\underset{\sim}{\alpha}}_2$$

$$+ i\hat{\beta}_1^{+}(\hat{\underset{\sim}{\alpha}}_2 \times \underset{\sim}{P}) + i(\underset{\sim}{P} \times \hat{\underset{\sim}{\alpha}}_1^{+})\hat{\beta}_2$$

For randomly oriented nuclear spins the purely magnetic, purely nuclear and magnetic nuclear interference contributions may be separated

$$\mathrm{Tr}\ \hat{\rho}\hat{V}_M^{+}\underset{\sim}{\sigma}\hat{V}_M = \hat{\underset{\sim}{\alpha}}_M^{+}(\hat{\underset{\sim}{\alpha}}_M.\underset{\sim}{P}) + (\hat{\underset{\sim}{\alpha}}_M^{+}.\underset{\sim}{P})\hat{\underset{\sim}{\alpha}}_M - \underset{\sim}{P}(\hat{\underset{\sim}{\alpha}}_M^{+}.\hat{\underset{\sim}{\alpha}}_M) - i\hat{\underset{\sim}{\alpha}}_M^{+} \times \hat{\underset{\sim}{\alpha}}_M \tag{2.46a}$$

$$\mathrm{Tr}\ \hat{\rho}\hat{V}_{N\sim}\hat{\sigma}\hat{V}_{N} = \hat{\beta}^{+}_{N}\hat{\beta}_{N}\underset{\sim}{P} - \frac{1}{3}(\hat{\underset{\sim}{\alpha}}_{N}\cdot\hat{\underset{\sim}{\alpha}}_{N})\underset{\sim}{P} \tag{2.46b}$$

$$\mathrm{Tr}\ \hat{\rho}\hat{V}^{+}_{N\sim}\hat{\sigma}\hat{V}_{M} = \hat{\beta}^{+}_{N}\hat{\alpha}_{N\sim M} + i\hat{\beta}^{+}_{N}(\hat{\underset{\sim}{\alpha}}_{M}\times\underset{\sim}{P}) \tag{2.46c}$$

These results taken with the results for the cross section in the previous section 2.3.1 are sufficient to completely describe the general scattering problem for polarized neutrons.

Two of these terms can produce polarization from an initially unpolarized beam. The first term is the purely magnetic term $i\hat{\underset{\sim}{\alpha}}_{M}\times\hat{\underset{\sim}{\alpha}}_{M}$ in (2.46a) which is zero for all but complex spin structures. The second term is the interference term $\hat{\beta}^{+}_{N}\hat{\alpha}_{N\sim M}$ which, for example, can give rise to a polarized beam on Bragg reflection from a ferromagnet. In this case, the created polarization is perpendicular to the scattering vector,

$$\underset{\sim}{P} = 2\,\frac{F_M F_N}{F_N^2 + (1 - (\underset{\sim}{\eta}\cdot\underset{\sim}{G})^2)F_M^2}\,(\underset{\sim}{\bar{G}}\times(\underset{\sim}{\bar{\eta}}\times\underset{\sim}{\bar{G}})) \tag{2.47}$$

If the magnetization is aligned perpendicular to the scattering vector perfect polarization can be achieved if a reflection exists for which the magnitude of the nuclear and magnetic structure factors are equal. In such a case the cross section for scattering with incident polarization antiparallel to the magnetization direction is zero (compare (2.44b)) and because an unpolarized beam may be regarded as a superposition of two beams with equal and opposite perfect polarizations only the parallel part is selected by reflection and a fully polarized beam results. Such reflections exist in many crystals.

The purely nuclear terms which involve the average scattering length $\bar{b} \equiv \bar{A}$ cannot alter the polarization. This includes coherent elastic scattering, multiple nuclear coherent scattering, nuclear isotopic incoherent scattering, nuclear Laue incoherent scattering and thermal diffuse (phonon) scattering, all of which depend on $\bar{b}$. These terms only involve $\hat{\beta}^{+}_{N}\hat{\beta}_{N}$ in (2.43) and $\hat{\beta}^{+}_{N}\hat{\beta}_{N\sim}\underset{\sim}{P}$ in (2.46) so that on substitution into (2.45)

$$\underset{\sim}{P}' = \underset{\sim}{P} \tag{2.48a}$$

The only nuclear scattering process which can change the polarization of the beam is the nuclear spin incoherent scattering which depends, not surprisingly, on the spin dependent part of the scattering amplitude. Substituting the terms $\hat{\alpha}_N \cdot \hat{\alpha}_N$ from (2.43) and $-\frac{1}{3}\hat{\alpha}_N \cdot \hat{\alpha}_N P$ from (2.46) into (2.45) gives

$$P' = -1/3\ P. \tag{2.49a}$$

The purely magnetic scattering can give rise to complex polarization dependent phenomena, particularly in the case of inelastic scattering. The general case is discussed by Marshall and Lovesey (1971). We shall consider elastic and quasielastic scattering from systems which do not create polarization. This essentially restricts the discussion to paramagnets and collinear antiferromagnets. In this case the scattered polarization is from (2.43) and (2.45)

$$P' = 2\overline{\langle (P \cdot \hat{Q}_\perp)\hat{Q}_\perp \rangle} \,/\, \overline{\langle \hat{Q}_\perp \cdot \hat{Q}_\perp \rangle} - P \tag{2.50}$$

so that the components of $\hat{Q}_\perp$ which are perpendicular to P reverse the incident polarization whereas the components of $\hat{Q}_\perp$ which are parallel to P do not change the polarization. One notes that if P is parallel to the scattering vector the polarization of the incident beam is reversed. For a paramagnet the first term in (2.50) is $\bar{\kappa} \times (P \times \bar{\kappa})$ so that the scattered polarization is along the scattering vector,

$$P' = -\bar{\kappa}(\bar{\kappa} \cdot P) \tag{2.51a}$$

The polarization depends upon the direction of the scattering vector for magnetic scattering but not for nuclear scattering. This difference, together with the fact that only nuclear spin incoherent scattering and magnetic scattering can reverse the incident polarization may be exploited to separate the magnetic and nuclear scattering from paramagnets and antiferromagnets.

2.4.2 Spin flip and non spin flip scattering

This separation was first performed by Moon, Riste and Koehler (1969). In this experiment the final polarization was measured only along the

direction of the incident polarization and hence is a polarization analysis experiment only in a restricted sense. The vector equation (2.45) may be alternatively written in terms of the partial cross sections connecting neutron spin up (+) and spin down (-) states

$$\frac{d^2\sigma}{d\Omega dE}\,\underset{\sim}{P}' = n^+ \frac{d^2\sigma^{++}}{d\Omega dE} + n^- \frac{d^2\sigma^{-+}}{d\Omega dE} - n^- \frac{d^2\sigma^{--}}{d\Omega dE} - n^+ \frac{d^2\sigma^{+-}}{d\Omega dE}$$

where $n^{\pm}$ are the initial spin populations and are related to the incident polarization via $n^{\pm} = \frac{1}{2}(1 \pm P)$. The four partial scattering cross sections can be divided into processes which do not change the beam polarization (++)(--), the so called 'non spin flip' scattering and the processes which reverse the beam polarization (+-) (-+) the 'spin flip' scattering. Experimentally these partial cross sections can be determined by performing a series of of measurements with 'crossed' and 'uncrossed' polarizer and analyser as described in chapter 3.

Following Moon et al.(1969) the polarization equations found in the previous section may be more conveniently expressed in terms of these partial cross sections. In summary, the coherent nuclear, Laue incoherent, isot opic incoherent and thermal diffuse scattering is entirely non spin flip, thus ensuring that the initial polarization is left unchanged (compare (2.48a)). Two thirds of the nuclear spin incoherent scattering occurs with spin flip and one third with non spin flip,

$$\frac{d\sigma}{d\Omega}^{+-}_{-+} = \frac{2}{3}\frac{d\sigma}{d\Omega}_{nsi} \qquad \frac{d\sigma}{d\Omega}^{++}_{--} = \frac{1}{3}\frac{d\sigma}{d\Omega}_{nsi} \tag{2.49b}$$

which ensures that the final polarization is $-\frac{1}{3}\underset{\sim}{P}$ (compare (2.49)). If the polarization is parallel to the scattering vector all magnetic scattering must occur with spin flip. So, for example, the quasi elastic spin flip scattering from a paramagnet is

$$\frac{d\sigma}{d\Omega}^{+-}_{-+} = \frac{1}{2}\left(\frac{d\sigma}{d\Omega}\right)_{para.} (1 - (\underline{P}.\underline{\bar{\kappa}})^2) \tag{2.51b}$$

and the non spin flip scattering is

$$\frac{d\sigma}{d\Omega}^{(++)} = \frac{1}{2}\left(\frac{d\sigma}{d\Omega}\right)_{para}(1 + (\underset{\sim}{P}.\bar{\kappa})^2) \qquad (2.51c)$$

giving the correct final polarization (2.51a) if $\underset{\sim}{P}'$ is resolved along $\underset{\sim}{P}$. The fact that only the magnetic and 2/3 of the nuclear spin incoherent scattering occurs with spin flip may be used to separate these two contributions from the remaining nuclear scattering processes which occur with non spin flip. If the nuclear spin incoherence is known, the separation is complete. Otherwise it may be necessary to perform two experiments, with the polarization parallel and subsequently perpendicular to the scattering vector to separate out the nuclear spin incoherence.

By measuring the spin flip and non spin flip scattering it is possible to separate the magnetic and nuclear defect scattering in antiferromagnets (Davis and Hicks 1977) as well as the nuclear and magnetic Bragg scattering from antiferromagnets (Moon et al. 1969). The technique has also been applied successfully to the problem of separation of magnetic disorder scattering from correlated paramagnets in the presence of nuclear disorder (Davis et al. 1980). Such measurements could not be attempted without spin analysis.

2.5 Small Angle Scattering

2.5.1 Introduction

The diffuse scattering in the vicinity of the (000) reciprocal lattice position is sensitive to long range fluctuations in magnetic and nuclear correlations and thus provides a link between the macroscopic world at $\underset{\sim}{\kappa} = 0$ and the microscopic world at higher $\underset{\sim}{\kappa}$. In this section some rather general statements about the scattering cross section for unpolarized neutrons as $\underset{\sim}{\kappa}$ approaches (000) will be made.

The (000) position has a special importance in scattering experiments since classical laboratory measurements of bulk properties all take place at $\underset{\sim}{\kappa} = 0$. For consistency the scattering cross section must extrapolate to the correct bulk values at $\underset{\sim}{\kappa} = 0$. Thus, the forward scattering in the quasi static approximation for a system with no elastic scattering must approach $kT\chi$ and for a ferromagnetic alloy with concentration driven fluctuations in moment the forward scattering must approach $C_A(1-C_A)(\frac{d\mu}{dC_A})^2$. Furthermore, for a ferromagnet, the (000) position is an allowed Bragg position having an intensity which must equal $\frac{2}{3}\bar{\mu}^2$ for a random domain distribution. In the general case all of these contributions are present and after averaging over all orientations according to section 2.2.5 the forward scattering must approach the limit (for purely magnetic terms)

$$\frac{d\sigma}{d\Omega} = \left(\frac{\gamma e^2}{2m_e c^2}\right) g^2 \sum_{i,n} \left(a_n + \frac{1}{3} b_n\right) f^2(0) \exp(-2W(0))$$

where for convenience the validity of the quasi static approximation has been assumed. A predominance of ferromagnetic correlations will lead to enhanced forward scattering. Similar limits also exist for purely nuclear scattering.

The small $\underset{\sim}{\kappa}$ limit is obtained by expanding the cross section as a power series about $\underset{\sim}{\kappa} = 0$, with $f(0) = 1$ and $e^{-2W(0)} = 1$,

$$\frac{d\sigma}{d\Omega} = \left(\frac{\gamma e^2}{2m_e c^2}\right) g^2 \sum_{i,n} a_n \left(1 - \frac{1}{3!}(\kappa r_n)^2 + .. + \frac{1}{3} b_n \left(1 - \frac{1}{10}(\kappa r_n)^2 + \ldots\right.\right.$$

where the cross section in the quasi static approximation has been assumed and averaged over all random orientations. This may be equivalently written

$$\frac{d\sigma}{d\Omega} = \frac{d\sigma}{d\Omega}_{\kappa=0} (1 - \frac{1}{3}\kappa^2\overline{R^2} + \ldots) \tag{2.52a}$$

where the coefficient of κ^2 has the dimensions of length squared,

$$\overline{R^2} = \frac{1}{2} \sum_n \frac{(a_n + \frac{1}{5} b_n) r_n^2}{\sum_n (a_n + \frac{1}{3} b_n)} \tag{2.52b}$$

and characterises the size of magnetic inhomogeneities within the system. These inhomogeneities may be static magnetic defects such as domain walls or groups of static impurity moments, or they may be dynamic fluctuations in the magnetization. If the correlations are independent of the direction of the radius vector connecting the two spins, as for example, with a Heisenberg interaction the term b_n disappears (compare with (2.40)) and

$$\overline{R^2} = \frac{1}{2} \frac{\sum_n r_n^2 \overline{\langle \underset{\sim}{S}_i \cdot \underset{\sim}{S}_{i+n} \rangle}}{\sum_n \overline{\langle \underset{\sim}{S}_i \cdot \underset{\sim}{S}_{i+n} \rangle}} \tag{2.52c}$$

which is essentially the second spherical moment of the spin distribution. If, for example, the fluctuations are dynamic fluctuations described within the Ornstein Zernicke theory the range parameter $\xi = \frac{1}{\kappa_1}$ is simply $\frac{1}{\sqrt{3}} (\overline{R^2})^{\frac{1}{2}}$.

The quadratic expansion of the cross section (2.52) is valid in some κ range such that $\kappa R << 1$ known as the "Guinier region". This expansion was originally derived by Guinier in the case of small angle X Ray scattering and is usually written as an exponential which is equivalent, up to second order in κ_1^2 to the series (2.52). One notes in passing that if the system is exceedingly close to a critical point this form of the cross section (2.35) is inappropriate. Similar results can be derived in the case of nuclear small angle scattering as shown in the monograph by Guinier and Fournet (1955).

2.5.2 Scattering from superparamagnetic particles

Consider the scattering produced by a single superparamagnetic particle. Within the particle the individual atomic moments are coupled ferromagnetically to every other moment to form the nett moment $\underset{\sim}{S}_{tot}$ which is allowed to rotate freely. In this case the spin correlations are not coupled to the particle shape so that one may expect $b_n = 0$. Averaging over all particle orientations of $\underset{\sim}{S}_{tot}$ with respect to particle orientation the cross section may be written according to the Guinier law (2.52). In the case of a superparamagnetic particle the spin correlation function $\overline{\langle \underset{\sim}{S}_i . \underset{\sim}{S}_{i+n} \rangle}$ may be replaced by the site occupation function $\overline{p_i p_{i+n}}$ where the operators p_j are 0 or 1 depending upon the site R_j being outside or inside the particle. With this definition,

$$\overline{R^2} = \frac{1}{2} \frac{\sum_n r_n^2 \overline{p_i p_{i+n}}}{\sum_n \overline{p_i p_{i+n}}} = R_G^2 \qquad (2.53a)$$

which is simply the square of the radius of gyration of the particle, R_G^2. The radius of gyration may thus be determined without any assumption as to particle shape. For a collection of randomly oriented superparamagnetic particles of differing size and shape the cross section can again be written in the Guinier form but with

$$\overline{R^2} = \frac{\sum_s n_s S_{tot}^2(s) \overline{R_G^2(s)}}{\sum_s n_s S_{tot}^2(s)} \qquad (2.53b)$$

if the particles are not correlated with one another. Here n_s is the number of particles with s spins, $S_{tot}^2(s) = (sS)^2$ is the total spin of the particle and $R_G(s)$ is the mean squared radius of gyration for all particles with s spins (irrespective of shape). This expression is analogous to the Z average used to describe the small angle scattering from polymer chains.

The concept of a particle structure factor $P(\kappa)$ is useful in the description of X ray small angle scattering (Guinier and Fournet 1955). It is also useful in the case when the neutron small angle scattering does not involve the magnetic term b_n. For instance the

cross section for a superparamagnetic particle containing S spins, averaged over all orientations is

$$\frac{d\sigma}{d\Omega} = \left(\frac{\gamma e^2}{2m_e c^2}\right)^2 \frac{2}{3} g^2 S_{tot}^2 \left[\frac{1}{s^2} \sum_{i,n} \overline{\langle p_i p_{i+n} \rangle} \frac{\sin \kappa r_n}{\kappa r_n}\right] \qquad (2.54)$$

where the function in square brackets may be alternatively written as the average of the square of the structure factor of the particle $\overline{f(\kappa)^2}$. The structure factor $f(\kappa)$ is obviously related to the structure factor of Bragg scattering $F(\kappa)$: indeed, small angle scattering from fine particles may be viewed as the mosaic broadening of the (000) ferromagnetic Bragg peak. One may write,

$$f(\kappa) = \frac{1}{s} \sum_i p_i \exp(i\underset{\sim}{\kappa}.\underset{\sim}{R}_i) \qquad (2.55a)$$

The structure factor concept is most useful if the particle is spherically symmetric as $f(\kappa)$ is real and independent of particle orientation, allowing (2.54) to be written in the alternative form $\overline{f(\kappa)^2} = \overline{f(\kappa)}^2$

$$\frac{d\sigma}{d\Omega} \sim \left(\frac{\gamma e^2}{2m_e c^2}\right)^2 \frac{2}{3} g^2 S_{tot}^2 \overline{f(\kappa)}^2 \qquad (2.55b)$$

The analogy with purely paramagnetic scattering is obvious (2.32). This analogy has been exploited by Cywinski et al. (1977) to explain the small angle scattering from an array of superparamagnetic particles under an applied field by expressing the results of the calculation for a paramagnet (Marshall and Lovesey (1971)) in terms of $f(\kappa)$ and S_{tot}.

In the case of nuclear scattering it is possible to show that for uncorrelated particles the higher κ behaviour of the small angle scattering follows the 'Porod' law (Guinier and Fournet 1955)

$$\frac{d\sigma}{d\Omega} \sim \frac{A}{\kappa^4} \qquad (2.56)$$

where A is the surface area of the particle. The same limit exists for the magnetic small angle scattering from a superparamagnet.

The results in this section have been limited to the specific case where the magnetic and nuclear radii of gyration are equal, in the more general situation of nonuniform magnetization the nuclear and magnetic R^2 are not equal. It is important to note that if the motion of the nett particle moment is correlated with the particle shape due to dipolar anisotropy the b_n term must be included in the analysis and $\overline{R^2}$ is found to be smaller than R_g^2. This problem is treated in appendix A for the simple case of a rodlike particle.

CHAPTER 3

EXPERIMENTAL

3.1 Sample preparation

The series of CrFe alloys used in this work were prepared by Argon arc melting. The starting materials were pure Cr and Fe provided by Johnson Matthey Chemicals Ltd. in the form of electrolytic Cr beads (JMC 703) and iron rod (JMC 848). Levels of metallic impurity in these 'Specpure' materials were below 3 p.p.m. in both cases. Electrolytic Cr from this source is reported to contain approximately 1 a/0 dissolved oxygen (H.E.N. Stone, private communication). Some alloys were prepared using low oxygen content Cr from the iodide process and supplied by Koch Light Industries (8181 h).

The weights of starting materials used to make up an alloy of C atomic percent Fe were calculated according to the ratio

$$\frac{m_{Fe}}{m_{Cr}} = 1.0741(100/C(\%) - 1.0)^{-1}$$

where m_{Fe}, m_{Cr} are the weights of Fe and Cr. These weights of Cr and Fe were placed on the water cooled copper hearth of the arc furnace and the furnace was flushed several times with industrial argon. A Ti 'getter' button was then melted thoroughly using an arc current of 100 A under a partial pressure of Argon of 150 mm Hg. The absence of residual reactive gases was indicated by the bright and untarnished surface of the Ti getter after melting. The constituent metals were then melted several times using an arc current of 100-150 A. The resulting button was then turned over and remelted. This melting cycle was repeated at least six times to ensure bulk homogeneity. Weight losses were small, of the order of 0.5%, and could be attributed to the evaporation of Cr which has a high vapour pressure. Great care was taken to ensure that all

material was melted and any samples with large weight loss were discarded.

Cr rich CrFe alloys are hard and brittle. This makes alloy fabrication difficult as the slab and cylindrical specimen geometry used in neutron scattering experiments cannot be achieved by cold work. To overcome this problem the homogeneous alloy buttons were remelted using a low arc current (70A) and encouraged to flow into slots cut into the copper hearth. After sufficient practice this rough casting procedure could be used to produce approximately cylindrical ingots with a diameter of some 1 cm and length of about 4 cm which were used for Bragg scattering measurements. A similar procedure was followed to produce flat coin shaped buttons of 2 cm diameter which could be spark machined with parallel sides for use in small angle scattering measurements. The specimen thickness was calculated to give an attenuation α_s of 1/e. Magnetization and resistance samples were spark machined from the neutron samples.

Samples fabricated in this way were encapsulated in a length of quartz tube which was evacuated to below 10^{-5} mm Hg and sealed. The alloys were then given a homogenizing anneal at 1050°C in the α phase field for a period of between 4 and 7 days and then quenched directly into water. Often a small weight gain ($\lesssim$ .05%) was found after heat treatment and attributed to reaction between the hot alloy surface and water during the quenching process. This tarnished surface layer also suffered thermal etching due to preferential evaporation of Cr. This surface damage was removed by spark machining and light mechanical polishing followed by etching in H_2O_2 and HCl/HNO_3.

Microscopic examination of the samples by optical microscope and electron microscope showed the alloys to be single phase and homogeneous. (P.R.Monk, private communication). Typical electron microprobe traces are reproduced in Fig. 3.1. The iron concentration is homogeneous to within ± 5% and shows no systematic drift. Non metallic inclusions several μm in size were found distributed at random in most samples. These inclusions were low in Fe content

Fig. 3.1 Electron microprobe traces for a Cr Fe 10% alloy. Upper and lower traces represent Cr and Fe concentrations respectively. A non metallic inclusion is shown by an arrow.

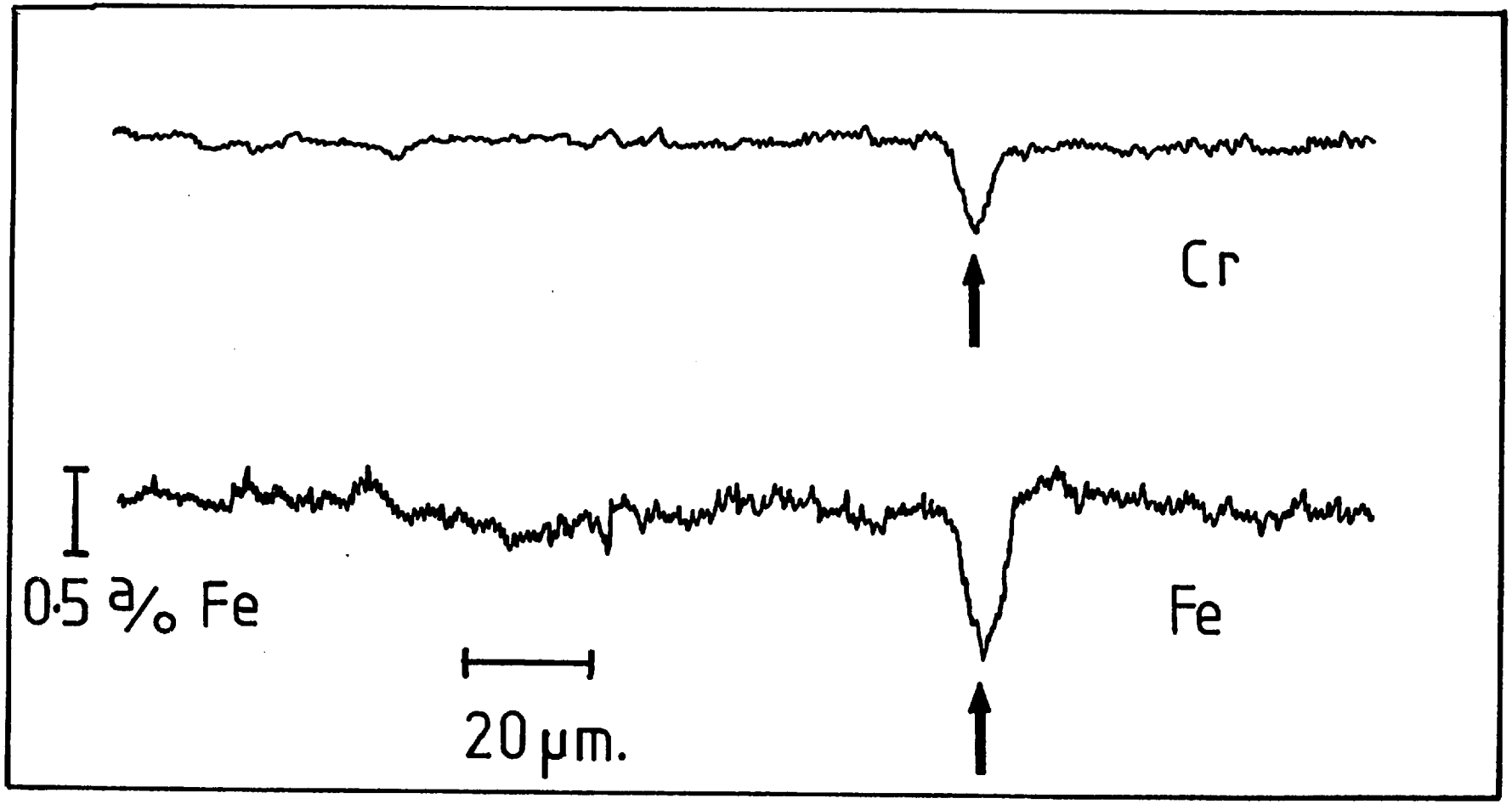

Fig. 3·1

as shown in the lower part of Fig. 3.1 and were tentatively identified with CrN and Cr_2O_3 arising from the dissolved gases in electrolytic Cr. The samples used in polarization-analysis experiments were made from iodide Cr and fewer inclusions were found in this alloy because of the low concentration of dissolved gases in iodide Cr.

The concentrations of each alloy were established by electron microprobe analysis and corroborated by wet analysis of Cr content. The results of this analysis are presented in Table 3.1. A slight drift in Fe content is noted here due to evaporation of Cr and presence of Cr_2O_3. The preferred concentrations were taken to be the nominal concentrations unless indicated.

Table 3.1

Analysis and description of Cr Fe alloys used in this work

Nominal concentration a/o Fe	Analysed concentration a/o Fe		Preferred concentration a/o Fe	Description
	Microprobe	Wet chemical		
5.0	-	-	NOMINAL	PA
4.5	-	4.1	"	BD
7.0	-	7.5	"	BD
9.3	-	10.0	"	BD
10.2	-	11.4	"	BD,M,R
11.2	-	11.9	"	BD
12.3	-	13.0	"	BD
13.3	-	14.6	"	BD,M
13.6	-	15.5	"	BD
14.2	14.2	15.4	"	BD,M
15.4	-	17.6	"	BD,M
10.0	13.5	-	"	TOF
15.5	15.5	17.0	"	SAS,M
16.0	16.7	17.0	16.7	SAS
18.0	16.8	18.4	16.8	SAS
17.5	18.0	19.1	NOMINAL	SAS,M
18.5	17.5	20.0	"	SAS,M
19.5	20.6	20.9	"	SAS,M
23.0	19.9	20.5	19.9	SAS,M
20.8	19.9	22.7	NOMINAL	SAS,M
20.0	21.7	21.4	21.7	SAS
21.7	24.0	23.4	24.0	SAS
25.0	28.3	25.4	NOMINAL	SAS,M

Legend: PA - Polarization-Analysis
BD - Bragg Diffraction
M - Magnetization
R - Resistivity
TOF - Time of flight
SAS - Small angle scattering

3.2 Neutron scattering instruments and experimental procedure

3.2.1 General remarks

The neutron scattering measurements were performed using the facilities provided by the Institut Laue-Langevin, Grenoble and AERE, Harwell. The instruments used in the course of this investigation were designed and built by the technical and scientific staff of these establishments and were used without modification.

With this in mind, the purpose of this experimental chapter is three fold:

(i) to explain the basic measurement principles behind each of the instruments

(ii) to describe briefly the instrument set up, including sufficient detail to assist with the understanding of the experiment and future planning of experiments

(iii) to document the experimental procedures in sufficient detail that the important experimental steps can be followed and part of the unwritten "folklore" of the instrument is available for future users.

Emphasis is placed on the experimental decisions and compromises which were made in order to optimize the measurements. It was not considered appropriate to record the full details of instrument construction, operation and performance; this information may be found in the technical reports quoted in the individual sections. Unless otherwise indicated the information on ILL instruments has been taken from Maier (1977).

3.2.2 Absolute intensity measurements

The number of neutrons counted by the detector can be converted to an absolute scattering cross section in barn per steradian by carrying out a series of calibrations, applying various corrections to the data and then normalizing the results of those of a standard scatterer, usually Vanadium.

A typical scattering experiment is shown in Fig. 3.2. The first task is to isolate those counts entering the detector due solely to scattering from the sample (I_S). Some of the many sources of background have been illustrated. Here I_A are 'air' scattering events which come from scattering of the incident beam by air paths etc. before the sample (I_{A1}) or after the sample (I_{A2}). A proportion of the scattered neutrons I_{A1} will be attenuated by passage through the sample and it is convenient to break up I_{A1} into the the fractions f_A which will pass through the sample and $(1 - f_A)$ which will not. The fraction which passes through the sample will be attenuated by a factor α_A. I_R is the background due to 'residual' sources of neutrons (for example, from other instruments or through the shielding). Again it is useful to subdivide this scattering into the fraction f_R which passes through the sample and is attenuated by a factor α_R and the fraction $(1 - f_R)$ which does not. Finally I_B represents electronic noise. It is assumed that the incident beam is attenuated by a factor α_S on passing through the sample.

It is possible to isolate I_S by performing the following six experiments:

1. Sample in place, beam open. This will give a count rate proportional to

$$I_1 = I_S+(f_A\alpha_A+(1-f_A))I_{A1}+(f_R\alpha_R+(1-f_R))I_R+I_{A2}+I_B$$

2. Sample in place, beam off

$$I_2 = (f_R\alpha_R+(1-f_R))I_R+I_B$$

3. Sample removed, beam open

$$I_3 = I_{A1}+I_R+I_B+\frac{1}{\alpha_S}I_{A2}$$

4. Sample removed, beam off

$$I_A = I_R+I_B$$

Fig.3.2 Schematic diagram of a typical neutron scattering experiment.

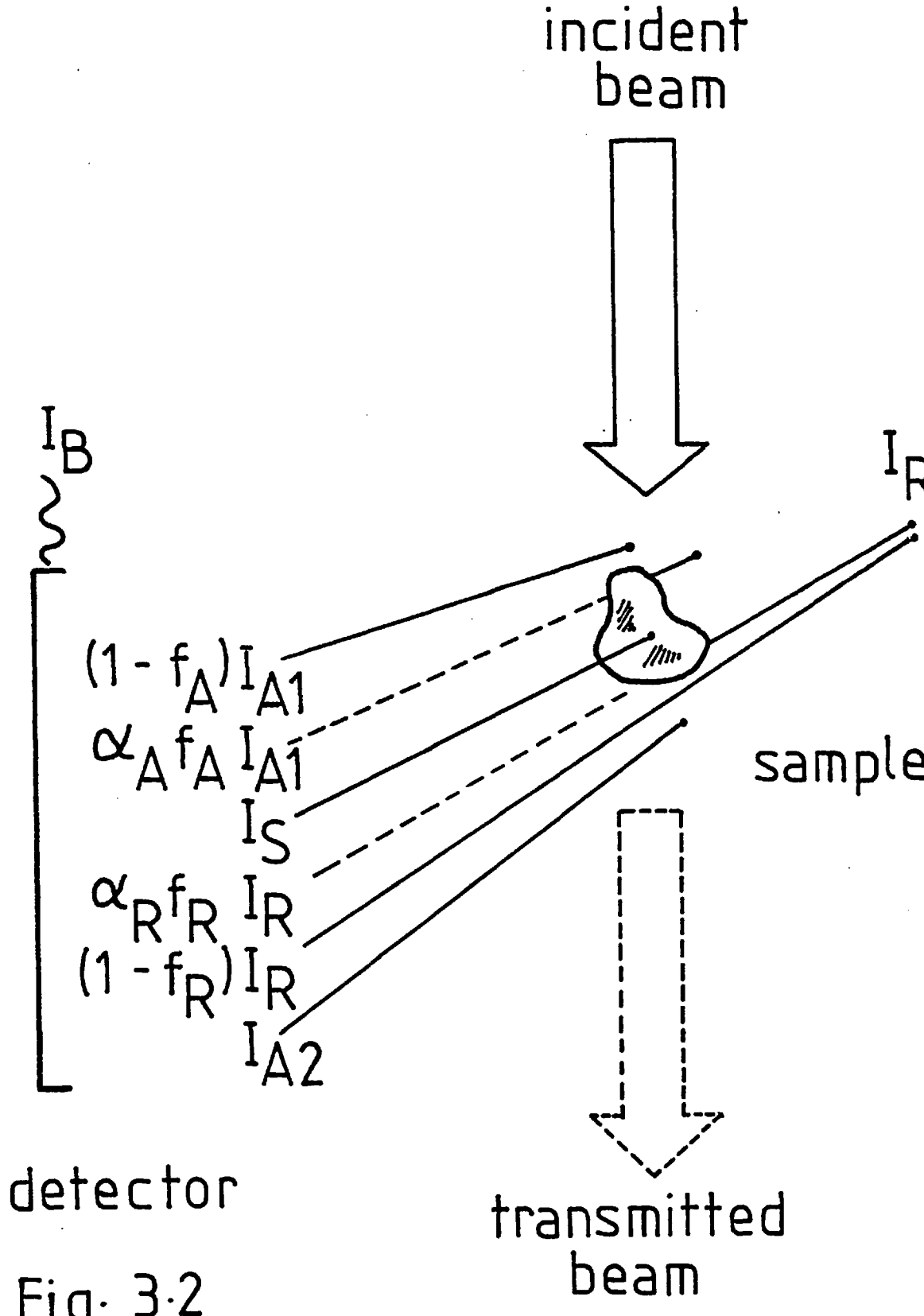
incident
beam
I_B
I_R
$(1 - f_A) I_{A1}$
$\alpha_A f_A I_{A1}$
I_S
$\alpha_R f_R I_R$
$(1 - f_R) I_R$
I_{A2}
sample
detector
transmitted
beam

Fig. 3.2

5. Neutron opaque material of identical dimensions as the sample, beam open.

$$I_5 = (1-f_A)I_{Al} + (1-f_R)I_R + I_B$$

6. Neutron opaque sample, beam off

$$I_6 = (1-f_R)I_R + I_B$$

Combining these expressions one finds the sample counts to be

$$I_S = I_1 - I_2 - I_5 + I_6 - \alpha_S[I_3 - I_4 - I_5 + I_6] + \frac{f_A}{1-f_A}(\alpha_S - \alpha_A)(I_5 - I_6) \qquad (3.1)$$

The latter term may be neglected as $\alpha_S \simeq \alpha_A$ and $I_5 \simeq I_6$ under most experimental conditions. In practice only the calibrations with the beam on are performed so that

$$I_S = I_1 - I_5 - \alpha_S(I_3 - I_5) \qquad (3.2)$$

The attenuation factor α_S may be directly determined by measuring the intensity of the straight through beam for cases 1, 3 and 5.

Having isolated the specimen counts it is necessary to correct for the finite dimensions of the sample. It is convenient to divide this procedure into two parts; firstly, to correct for the attenuation of the incident beam as it passes through the sample and also for the attenuation of the scattered beam as it passes out of the sample, and secondly to correct for all higher order multiple processes. The first corrections, the attenuation corrections, have a simple analytical form for most scattering geometries. For example, if the beam is incident on a plane slab which is characterized by an attenuation factor α_S when normal to the beam, the absorption corrections are of the form

$$I'_S = I_S / C(2\theta) \qquad (3.3a)$$

where I's are the corrected counts and

$$C(2\theta) = \alpha_S(\alpha_S^{\sec 2\theta - 1} - 1)/(\ell n \alpha_S)(\sec 2\theta - 1) \qquad (3.3b)$$

for the plate in normal geometry and

$$C(2\theta) = \cos\theta(\alpha_S)^{\sec\theta} \qquad (3.3c)$$

for θ-2θ geometry. More general cases are treated by Sears (1975). The corrections for multiple scattering are in general non-analytic and the treatment of multiple processes is not a routine matter. For small samples it is possible to use an analytic approximation to the multiple scattering as discussed by Sears (1975) and this approximate treatment is often sufficient for samples having small (< 10%) multiple scattering. For convenience, the counts corrected for absorption and multiple scattering will be denoted I_S''.

It is possible to put the counts on an absolute scale by performing the experiments with a standard scatterer at the sample position. Vanadium, which has a small coherent cross section $\sigma^V_{coh} = 0.03$ b and a large bound incoherent nuclear cross section $\sigma^V_{MC} = 4.93$ b (Dilg 1974) is used for this purpose. The corrected sample counts may be normalized to the corrected V data to give the sample scattering cross section (per atom),

$$\frac{d\sigma}{d\Omega} = \frac{m_v}{m_S}\frac{\sigma^V_{inc}}{4\pi}\frac{I_S''}{I_v''} \qquad (3.4)$$

where m_v and m_S are the number of scattering centres in the beam for V and sample respectively and the data has been corrected for multiple scattering.

The correction of data for time of flight experiments and polarized beam experiments is entirely analogous. In the case of inelastic measurements the energy dependence of absorption, detector efficiency and so forth must be taken into account (see for example Poncet (1977)) and in polarized measurements the spin dependence needs to be considered. The corrections for polarized beam experiments are discussed by Brown and Forsyth (1964) and including multiple scattering by Freeman, Meardon and Williams (1978).

3.3 Small angle scattering

3.3.1 Introduction

The small angle scattering experiments were carried out at ILL using the small angle scattering camera D11A and the high κ resolution spectrometer D17. These instruments are based around a two dimensional LETI detector and both instruments operate beyond the Bragg cut off of most materials using long wavelength neutrons. In the case of D11A the high resolution at low angles is due to the length of the instrument whereas in the case of D17 a very long incident wavelength in conjunction with moderate length is used. Both instruments employ two dimensional 'pin hole' geometry which requires minimal κ resolution corrections.

3.3.2. The small angle scattering camera: D11A

3.3.2.1 Description

D11A lies at the end of the H15 cold neutron guide, a schematic diagram of the instrument is shown in Fig. 3.3. The machine consists of a helical slot velocity selector which allows incident neutron wavelengths from 4.5 to 20 Å to be employed. Two such monochromators are available: the drum 'Brunhilde' gives 9% FWHM wavelength spread and the drum 'Adele' gives a relaxed wavelength spread of 50% FWHM. 'Brunhilde' was used in all the present experiments. After monochromation the beam passes through a series of neutron guides which may be translated sideways out of the beam to allow the incident collimation length to be matched to the sample-detector distance. There is a variable iris before the sample which defines the beam size and divergence. Three sample positions are available at the D11 sample station. In all measurements the 'cloche' position was used. After passing through an evacuable flight tube the scattered neutrons are detected by the 64 × 64 element BF_3 LETI multidetector

Fig.3.3 Schematic diagram of the small angle scattering camera D11A. Legend. M:Monochromator, C20, C10, C5 and C2.5: 20m, 10m, 5m and 2.5m collimation, T:time of flight chopper, B:background shutter, I:sample iris, S1-S3: sample positions 1,2,3,A:attenuator, BS:beam stop and D: detector.

Fig.3.4 Collimating system used for D11A.

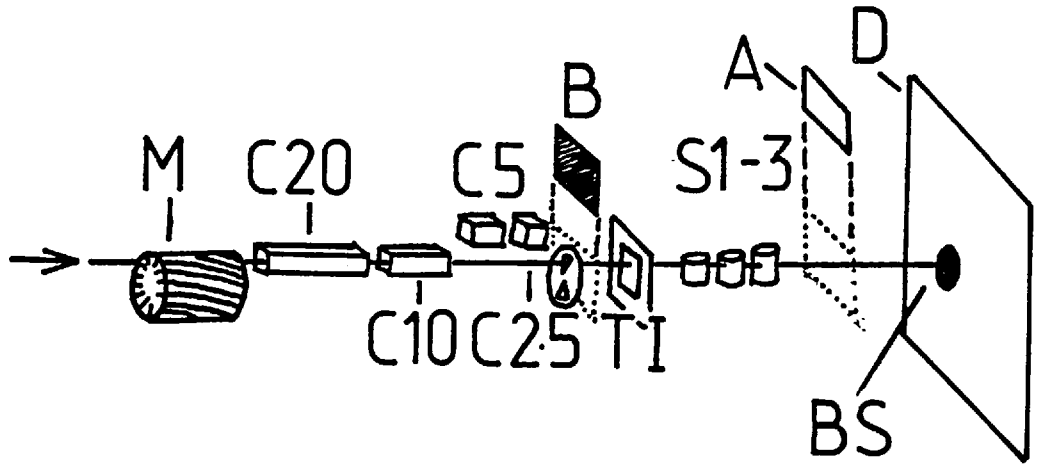

Fig. 3·3

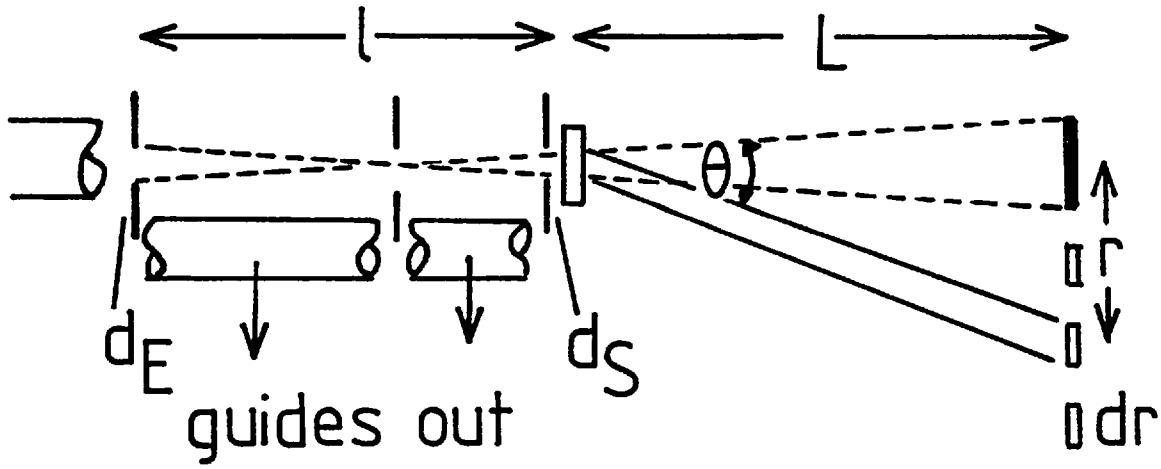

Fig. 3·4

which is centred in the beam and may be placed at sample to detector distances of 2.5, 5, 10, 20 and 40 m. In our experiments all but the 40 m position were used. The full length of the instrument is evacuated to minimize air scattering. A time of flight facility is available but was not used in D11A experiments. The detector is protected from saturation by an adjustable Cd beam stop. A beam attenuator may be put in position after the sample to allow transmission measurements to be carried out. The sample may be shielded from the incident beam by using the background shutter. Further details are described by Ibel (1976).

The conditions under which the wavelength resolution and intensity can be optimized are discussed by Schmatz et al (1974). The resolution is given by

$$\frac{\Delta\kappa^2}{k^2} \doteq \frac{1}{12}\left[\left(\frac{d_r}{L}\right)^2 + \left(\frac{d_E}{\ell}\right)^2 + d_S\left(\frac{1}{L} + \frac{1}{\ell}\right) + \left(\frac{\Delta\lambda}{\lambda}\right)^2\theta^2\right] \qquad (3.5)$$

where d_r, d_E and d_S are the detector grid spacing, entrance pupil diameter and sample pupil diameter respectively. The sample to detector distance is L and a length of guide ℓ has been removed so that the effective source lies at this distance from the sample, as shown in Fig. 3.4. The resolution can be increased for a given sample to detector distance by increasing ℓ, this also leads to a decrease in intensity via the inverse square law. The resolution and intensity together can be optimized if all contributions to (3.5) are more or less equal. This can be achieved if $L = \ell$ and $d_E = d_r = 2d_S$. The first condition was satisfied in all D11A experiments by removing a length of guide equal to the sample to detector distance ('symmetric' configuration) and the second condition was roughly satisfied by using a sample pupil of 1 cm diameter which is equal to the 1 cm grid separation of the LETI multidetector.

The κ range accessible using D11A is variable between 3×10^{-4} Å^{-1} and 1 Å^{-1}, and is determined by the incident wavelength (λ_0) and the sample to detector distance (L). The κ ranges covered by various λ_0 and L configurations are shown in Fig. 3.5. The choice of λ_0 and L for a given experiment must be made carefully as

Fig.3.5 κ range accessible using D11A (solid curves) and D17 (dashed curves) for various sample to detector distances and incident wavelengths. The κ range used in the experiments described in Chapter 5 are indicated.

Fig.3.6 Intensity optimization chart for scattering from objects of size R_G for D11A in symmetric configuration with velocity selector Brunhilde. Operating points used in the experiments described in Chapter 5 are indicated. (Haas (1978))

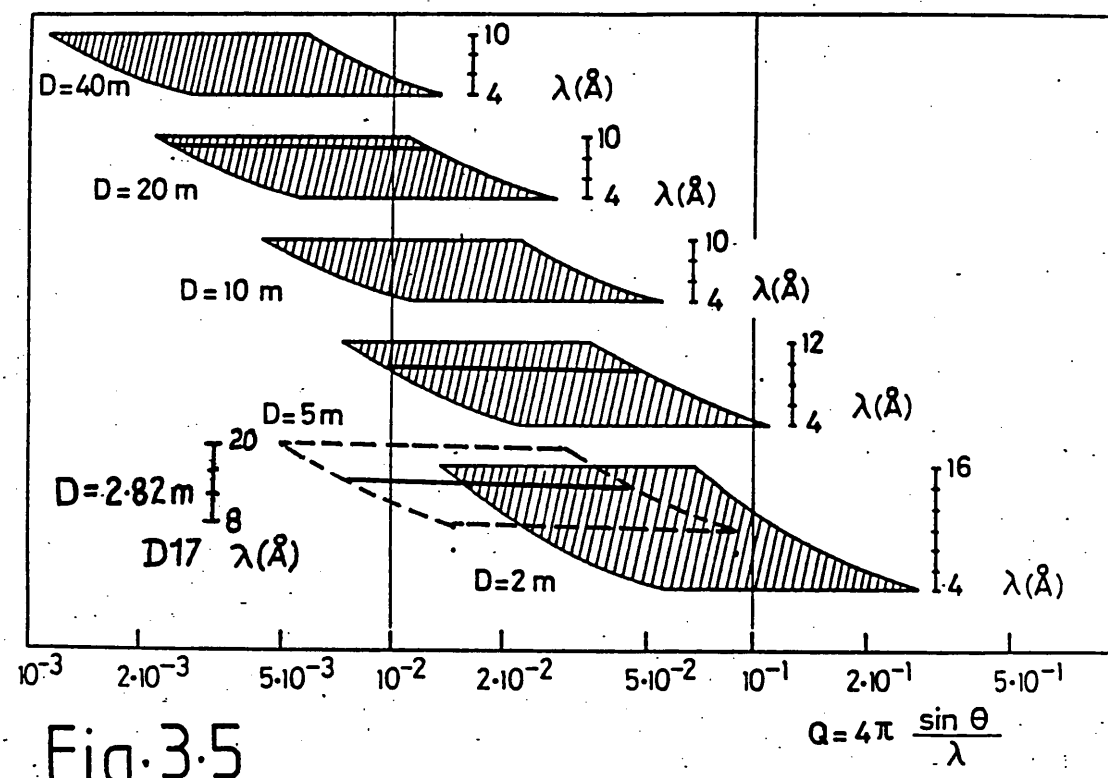
D=40m
10
4
λ(Å)
D = 20 m
10
4
λ(Å)
D = 10 m
10
4
λ(Å)
12
4
λ(Å)
D=5m
20
D=2·82m
8
D17 λ(Å)
D=2 m
16
4
λ(Å)
10⁻³
2·10⁻³
5·10⁻³
10⁻²
2·10⁻²
5·10⁻²
10⁻¹
2·10⁻¹
5·10⁻¹
Q = 4π sin θ / λ

Fig·3·5

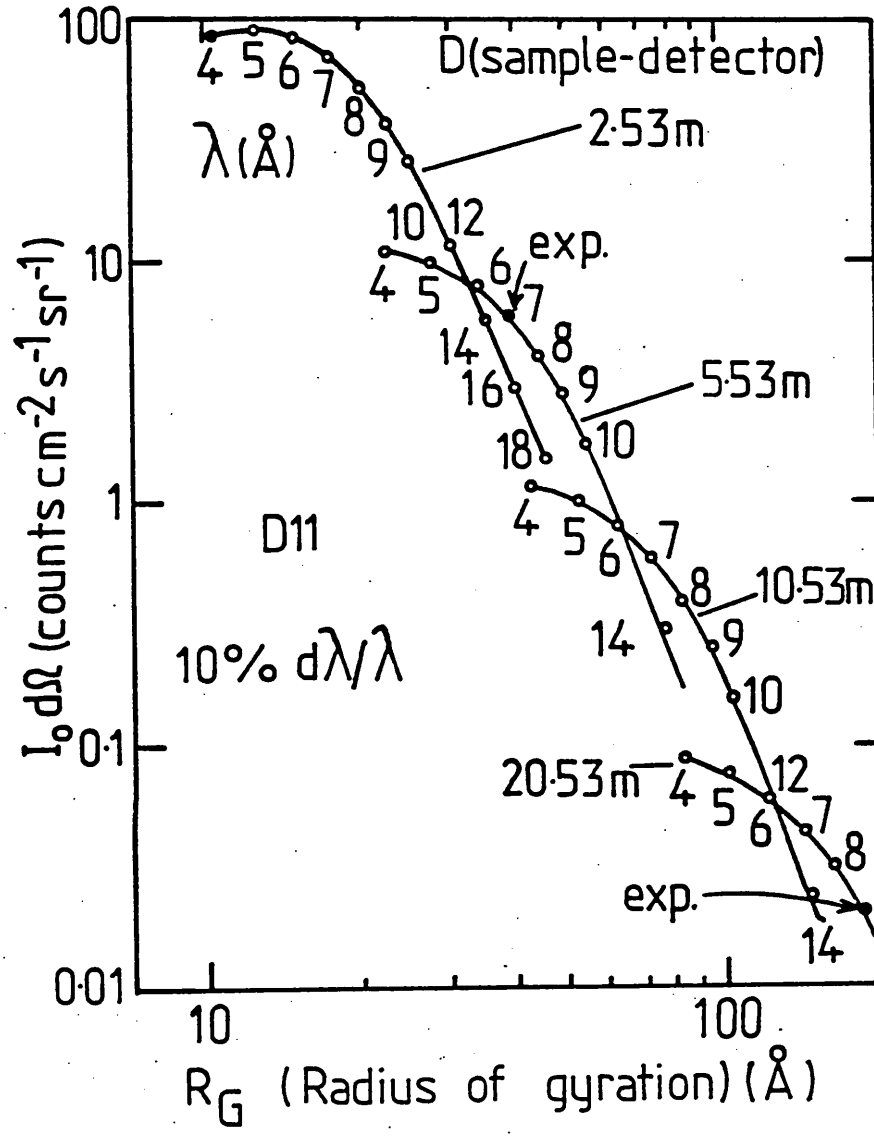
D(sample-detector)
λ(Å)
2·53m
5·53m
10·53m
20·53m
exp.
D11
10% dλ/λ
I₀dΩ (counts cm⁻²s⁻¹sr⁻¹)
100
10
1
0·1
0·01
10
100
R_G (Radius of gyration) (Å)

Fig·3·6

the κ ranges for a given λ_0 and L are quite restricted and much beam time is lost in changing detector positions. The choice of λ_0 and L may be optimized by reference to Fig. 3.6 which gives the incident flux at the sample position (I_0) multiplied by the solid angle corresponding to one detector cell (1 cm^2) as seen from the sample position as a function of $\lambda_0 L$. Individual λ_0 values are marked on the curve. (Haas (1978)). Here $\lambda_0 L$ is simply the $1/\kappa$ value which corresponds to setting the edge of the Guinier region ($\kappa R_G = 1$) at the mean radius of the detector. So if one knows the size of the scattering object (R_G) or one wishes to make observations over this scale of distance the detected intensity (which varies as $I_0 \delta\Omega$) will be optimized by choosing the maximum $I_0 \delta\Omega$ value for a given $R_G = \lambda_0 L$. The operating points used in the experiments described in Chapter 5 are shown on the diagram.

3.3.2.2 Sample environment

Two top loading cryostats were used in the course of D11A experiments: 47 OX HV 40 and 55 IL HV 49. The former is a convenentional He flow cryostat with quartz windows and could be operated in the range 1.5 to 300 K. This cryostat could be placed between the pole pieces of an electromagnet at the cloche position, unfortunately a section of the flight path vacuum must be broken to do this, giving increased air scattering. This problem did not arise with the latter cryostat which simply located within the cloche vacuum vessel. The cryostat was provided with single crystal sapphire windows. Temperature measurement in both cases was via a calibrated Si diode and the temperature could be stabilized to within $\pm \cdot 1$ K.

3.3.2.3 Experimental procedure

The optimum sample to detector distance was chosen by reference to Fig. 3.6 and an equivalent section of guide removed. A wavelength corresponding to maximum intensity was chosen: in all cases the wavelength was beyond the Bragg cut off so that multiple Bragg

scattering did not pose a problem. The sample was placed in position and the area of sample exposed to the incident beam was defined by a ϕ 1.0 cm Cd entrance pupil and ϕ 1.1 cm exit pupil. The optimum sample height was found using a He-Ne laser or by neutron photographs. The sample rotation was adjusted so that the slab was normal to beam by maximizing the transmission: this procedure was reproducible to $\pm 2^{\circ}$, which was sufficient for our purposes. The sample transmission α_S and the beam centre could be determined by placing the attenuator in the beam and counting the straight through intensity without a beam stop for some 30 s. With the sample correctly aligned, the beam stop (a rectangular Cd place 6 × 8 cm^2) was centred on the straight through beam.

Small angle scattering spectra were then taken at various temperatures. A measurement time of 10 minutes was enough to give excellent statistics and the temperature could be stabilized to within ± .1 K during this time. Empty cell, Vanadium and Cadmium spectra were also taken. To correct for detector efficiency it was necessary to use a perspex sample as the V showed some residual small angle scattering.

3.3.3 The high κ resolution spectrometer: D17

3.3.3.1 Description

D17 is situated at the end of the H17 cold neutron guide. The incident neutron spectrum peaks at 12 Å as opposed to 4.8 Å for the H15 guide which serves D11A. The mechanical velocity selector allows monochromation with wavelength resolution of 10% FWHM or 4% FWHM with a range of useable wavelengths from 8 to 20 Å. The 10% selector was used for total scattering measurements and the 4% selector for time of flight. Unlike D11A, the D17 multidetector may be rotated out of the forward beam and the instrument becomes a hybrid 2 axis diffractometer as shown in Fig. 3.7. The LETI multi-detector is made up of 128 × 128 cells of size .5 cm × .5 cm and can be placed at sample to detector distances of 1.4 to 2.8 m. A

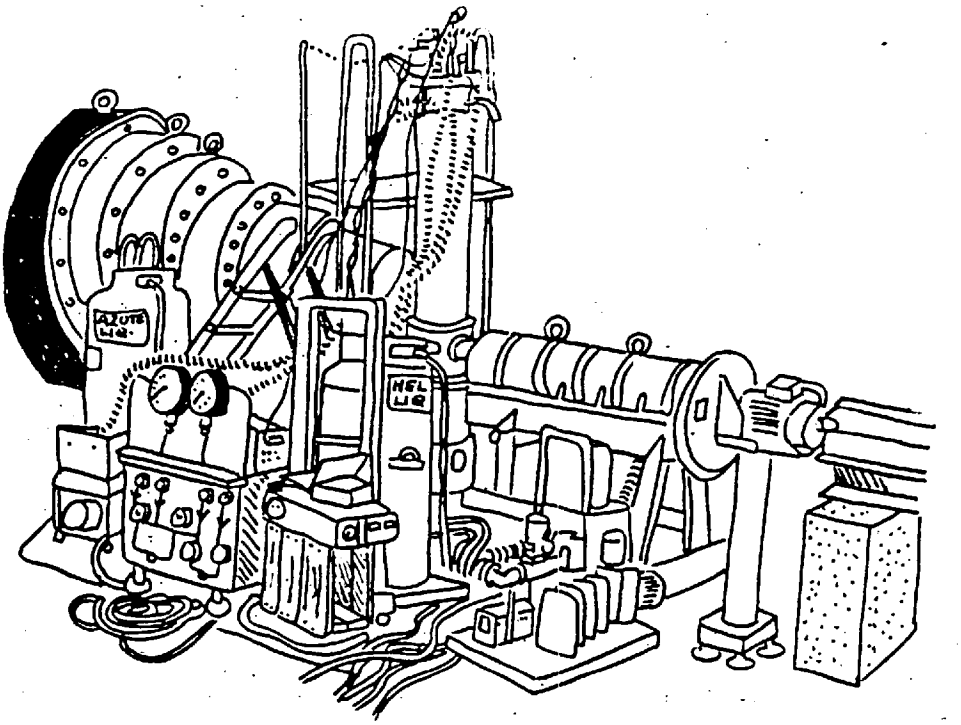

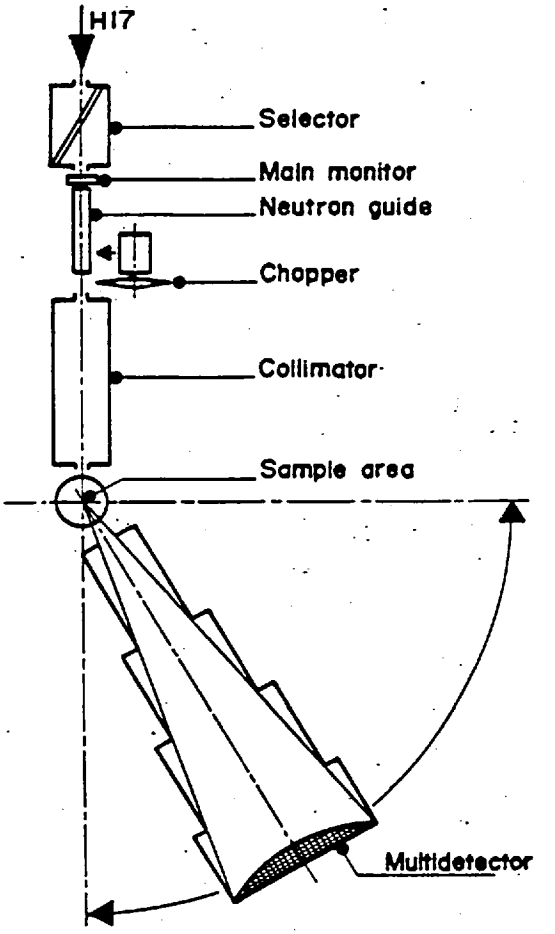
H17
Selector
Main monitor
Neutron guide
Chopper
Collimator
Sample area
Multidetector

Fig. 3-7

distance of 2.85 m was used throughout. This allows a range of scattering vectors from 1Å^{-1} to 5×10^{-3} Å^{-1} to be covered. This region overlaps with D11A as shown in Fig. 3.5.

The collimation on D17 is fixed. It is possible to relax the κ resolution by grouping together sets of detector cells if increased intensity is desired: usually four cells were added to give one cell of 1 cm × 1 cm. The sample diameter of 1 cm was chosen to match this regrouped cell size. The instrument characteristics $I_0\delta\Omega$ as a function of $R_G = \lambda_0 L$ for D17 is shown in Fig. 3.8 (Haas (1978)), here $\delta\Omega$ is chosen to correspond to a regrouped cell of 1 cm × 1 cm. The operating point used in the experiments of chapter 5 are indicated. The instrument can be modified for time of flight measurements and this aspect is considered in section 3.3.3.4.

3.3.3.2 Sample environment

For total scattering measurements the cryostat 34 AL HV 30M was used. This is a conventional He gas flow cryostat equipped with a superconducting magnet which provides a vertical field of up to 2T and can be operated over a temperature range 1.5 to 300 K. In practice an upper limit of some 200 K was achieved. Temperature measurement is via a calibrated Si diode, the diode is unfortunately field dependent in behaviour. This cryostat is equipped with quartz windows. In the case of time of flight measurements the D11A cryostat 55 IL HV 49 was used.

3.3.3.3 Experimental procedure

The same experimental procedure as described for the D11A experiments was followed. Here the sample height could be optimized by rotating the detector out of the forward direction and using a theodolite to view the sample along the incident beam direction.

Fig.3.8 Optimization chart for scattering from objects of size R_G for D17 in standard configuration with 5% and 10% velocity selectors. The operating points used in the experiments described in Chapter 5 are indicated.

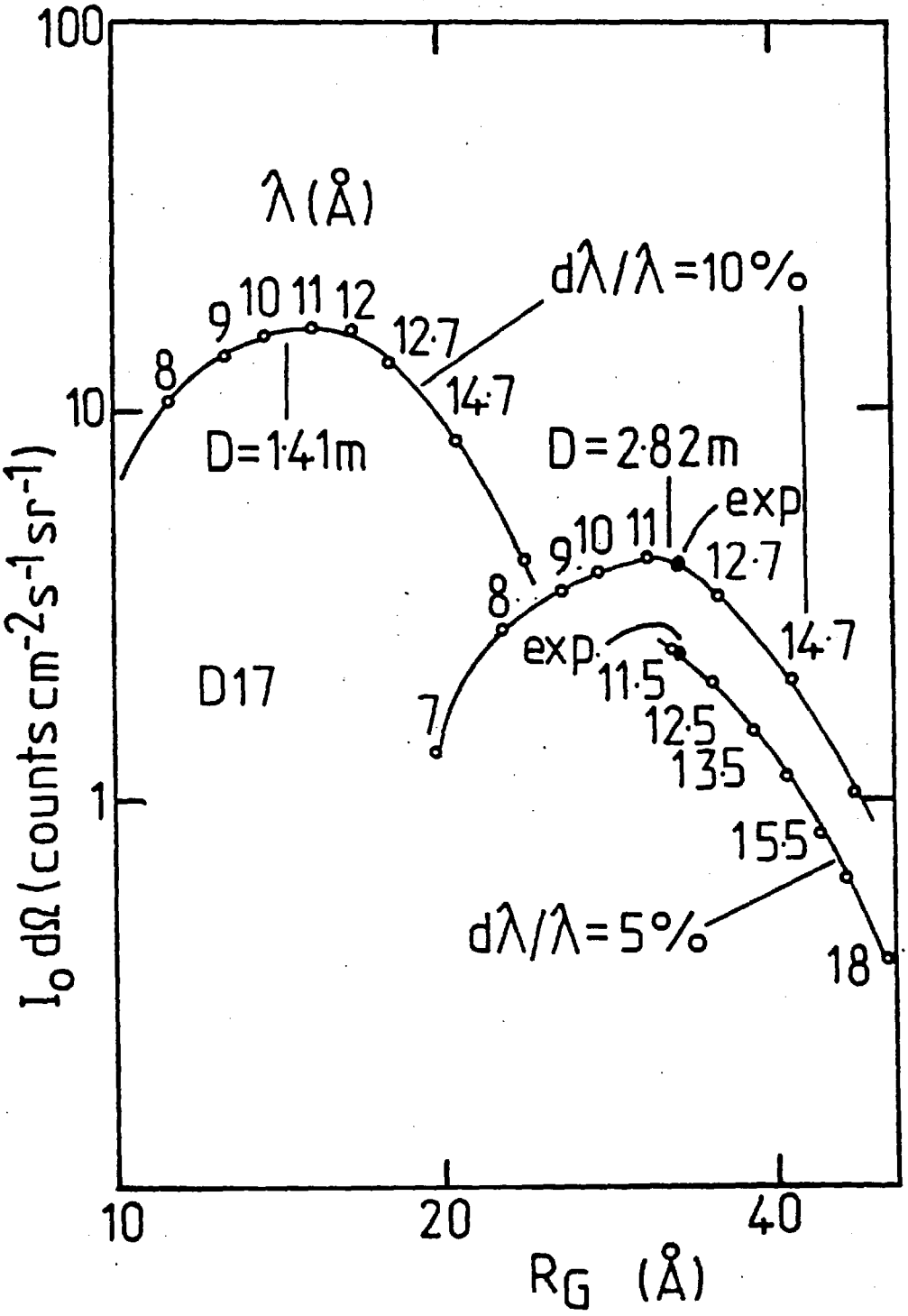
100
10
1
λ (Å)
dλ/λ = 10%
8
9
10
11
12
12·7
14·7
D = 1·41m
D = 2·82m
exp
D17
7
exp.
11·5
12·5
13·5
15·5
18
dλ/λ = 5%
10
20
40
$I_o\,d\Omega$ (counts $cm^{-2}s^{-1}sr^{-1}$)
R_G (Å)

Fig. 3·8

3.3.3.4 Time of flight measurements

The spectrometer configuration used for time of flight measurements is slightly different from that illustrated in Fig. 3.7 in that the chopper was placed at the other end of the collimator. The time of flight chopper itself consists of 4 slots of 1 cm width and can be operated at speeds up to 6000 rpm. The chopper radius was 20 cm, the sample to detector distance 2.85 m and sample to chopper distance was 25 cm. Two monitors were used.

The 16 K memory capacity of D17 limits the amount of time of flight data which can be taken. If the instrument is operating without the time of flight option each one of the 128 × 128 memory locatations is used to register counts coming from the individual cells of the multidetector. Each memory location is specified by a 14 bit number: the first seven bits are used to specify the X coordinate and the remaining seven the Y coordinate. If a time of flight measurement is to be made this 14 bit number must also specify a time of flight channel so that some of the bits used to describe the cell position must be used to provide room for time of flight (tof) coordinates: tof information can only be recorded at the expense of κ resolution. In practice what happens is that groups of cells can be ganged together to form a larger cell. In the case of our experiment 64 0.5 × 0.5 cm^2 cells were added together to form one cell 4 × 4 cm^2. In this way the detector effectively consists of 16 × 16 cells, requiring one four bit number to specify the X coordinate and one four bit number to specify the Y coordinate , the remaining six bits of the 14 bit memory address can be used to specify 64 time of flight channels. An attempt to increase the number of tof channels to 256 would require the detector to be regrouped into an 8 × 8 array of cells 8 × 8 cm^2 which would lead to unacceptably large κ resolution.

The prime consideration in designing this particular tof measurement was good energy resolution, even at the expense of intensity. With this in mind the 4% FWHM selector was used and the tof chopper was moved as close as possible to the sample. In this way

the largest contribution to the energy resolution is set by the wavelength spread. A low incident energy of 0.62 meV ensures that the absolute energy width arising from the wavelength spread is small, approximately 50 μeV. This amounts to an uncertainty in tof of some 380 μsec in an elastic time of flight of 8192 μsec.

The channel width is determined strictly by the relatively small number of tof channels. The low incident energy implies that neutron energy loss events are highly restricted. With this in mind the elastic energy channel was placed at channel 9 allowing 55 channels for neutron energy gain, adequately covering the resolution broadened elastic peak. If the channel width is chosen to be 80 μsec this essentially covers energy transfer from between + 0.2 meV to -1.0 meV. The chopper speed was chosen as 2786 rpm giving a burst time of 80 μsec and a period between bursts of 5.4 ms. This minimizes problems with frame overlap. Combining these various contributions one finds an energy resolution of 75 μeV which compares well with the experimentally determined 80 μeV.

With this choice of parameters a typical spectrum could be collected in 2 hours with adequate statistics. The data was averaged using the program INLD17 which simply adds cells together. These data were radially averaged by hand. Further discussion of the tof technique may be found in section 3.5.1.

3.3.4 Data analysis

Data reduction and data analysis for small angle scattering experiments (total scattering) were carried out using a suite of programs compatible with both D11A and D17. This group of programs is described by Ghosh (1978).

Isotropic data were treated using the data reduction programme RNILS which converts the counts over the multidetector into a radial average I(R) using a previously determined beam centre. The radially averaged spectra can then be manipulated using the programme SPOLLY to allow correction for absorption, air scattering

instrumental background and variation of detection efficiency as outlined in section 3.2.2. For small θ the normal beam absorption correction is simply $C(2\theta) = \alpha_S$ and so the cross section is

$$\frac{d\sigma}{d\Omega} = \frac{\left[(I_{sample}-I_{cd})-\alpha_S(I_{air}-I_{cd})\right]}{\left[(I_v-I_{cd})-\alpha_v(I_{air}-I_{cd})\right]} \frac{m_v}{m_S} \frac{\sigma^v_{inc}}{4\pi} \frac{\alpha_v}{\alpha_S} \qquad (3.6)$$

As both the V and perspex calibrations showed forward peaking the division in (3.6) was not performed. The perspex calibration was used to show up regions of abnormal detector efficiency which were deleted using a GRUND file. In this way relative cross sections were determined via

$$\frac{d\sigma}{d\Omega}_{rel} = \frac{1}{m_S\alpha_S}\left[(\bar{I}_{sample}-\bar{I}_{cd})-\alpha_S(\bar{I}_{air}-\bar{I}_{cd})\right] \qquad (3.7)$$

using the edited counts $\bar{I}_{sample}$, $\bar{I}_{air}$ and $\bar{I}_{cd}$.

Data taken with an applied field were reduced using the anisotropic data reduction routine ANDATA. The beam stop area and cells which showed abnormal efficiency were deleted from the analysis using a GRUND file. The corrected relative cross section was then fitted to the functional form,

$$\frac{d\sigma}{d\Omega}_{rel} = A(\kappa) + B(\kappa)\cos^2\alpha \qquad (3.8)$$

using ANCOS2. Here α is the angle between the magnetic field and the scattering vector in the plane of the detector. The relative cross sections were also listed in 15^o sectors using ANSECT.

3.4 Powder diffraction

3.4.1 Introduction

Diffraction measurements on polycrystalline CrFe alloys were performed at AERE, Harwell using the 2 axis powder diffractometers CURRAN and PANDA. Measurements at 4.2 K were carried out using PANDA and the temperature variation carried out using CURRAN.

A description of the technique of powder diffraction is given in the monograph by Bacon (1962). If the sample is uniformly bathed in the incident beam the number of neutrons reaching the detector per unit time for a particular (hkℓ) reflection is given by

$$I_{hk\ell} = I_0 \frac{\lambda_0^3 \ell_S}{8\pi L} V u_c^2 \frac{j_{hk\ell} F_{hk\ell}^2}{\sin\theta_{hk\ell} \sin 2\theta_{hk\ell}} e^{-2W(2\theta_{hk\ell})} A_{hk\ell} \qquad (3.9)$$

where I_0 is the incident flux, λ_0 is the incident wavelength, ℓ_S-the height of the counter slit, L-the sample-detector distance, V-the volume of sample in the beam, U_c the number of unit cells per unit volume, $j_{hk\ell}$ is the number of equivalent planes contributing to the reflection {hkℓ} and $A_{hk\ell}$ is an attenuation correction. Here $F_{hk\ell}$ is the unit cell structure factor and $W(2\theta_{hk\ell})$ is the Debye-Waller factor for the reflection occuring at a scattering angle of $2\theta_{hk\ell}$. In writing (3.9) it has been assumed that there is no preferred orientation.

In principle it is possible to deduce the average sublattice moment for the sample by measurement of the integrated intensity using (3.9) and applying the appropriate corrections. In practice this method is unsatisfactory and it proves easier to normalize the integrated intensity of one peak to another. For CrFe alloys which have the simple antiferromagnetic structure described in section 2.2.2 it is convenient to normalize the {100} purely magnetic reflection to one of the adjacent nuclear reflections such as {110} or {200} using the known scattering lengths of Cr and Fe. The average sublattic magnetization is then,

$$\bar{\mu}(\mu_B \text{at}^{-1}) = \frac{\sqrt{3/2}\,\bar{b}}{0.269\, f_{100}} \frac{j_{hk\ell}}{j_{100}} \frac{\sin\theta_{hk\ell} \sin 2\theta_{hk\ell} \sqrt{I}_{100}}{\sin\theta_{100} \sin 2\theta_{100} \sqrt{I}_{hk\ell}} \qquad (3.10)$$

which can be derived using (3.9), (2.21) and (2.23). It has been assumed that the absorption correction $A_{hk\ell}$ and the Debye-Waller factor do not vary greatly over the angular range between the magnetic peak {100} and the nuclear peak {hkℓ}. These are reasonable assumptions if the reflections {110} and {200} are used for normalization. In this expression f_{100} is the form factor of Cr for the {100} reflection and assumed to be 0.68, a value taken from the work of Moon et al. (1966) on CrMn. The multiplicity factors $j_{100} = j_{200} = 6$ and $j_{110} = 12$.

3.4.2 CURRAN

3.4.2.1 Description

The 2 axis diffractometer CURRAN is situated at the 4H2 hole of the DIDO reactor at AERE, Harwell. A schematic diagram is presented in Fig. 3.9. A squashed Ge crystal with [110] vertical acts as a monochromator and allows wavelengths in the range 0.9 to 2.6 Å to be selected. For the series of experiments described in Chapter 4 the (311) reflection was selected. This reflection gives a wavelength of 1.37 Å with reportedly 'undetectable' second order contamination. The measured $\lambda/2$ contamination was in fact less than .1%. The instrument is equipped with five BF_3 detectors arranged at 10° intervals in the horizontal plane and allows an angular range of $-10 \leq 2\theta \leq 169^\circ$ to be covered in steps as small as 0.01°. This was particularly convenient as it allows the {100} and {200} reflections to be scanned simultaneously. Full details of the instrument may be found in the report by Hance (1973).

3.4.2.2 Sample environment

In an initial series of experiments an Oxford Instruments top loading cryostat with V tail was used allowing the sample to be continuously rotated to offset any preferred orientation. For later experiments two CT14 cryostats were used in parallel; as preferred

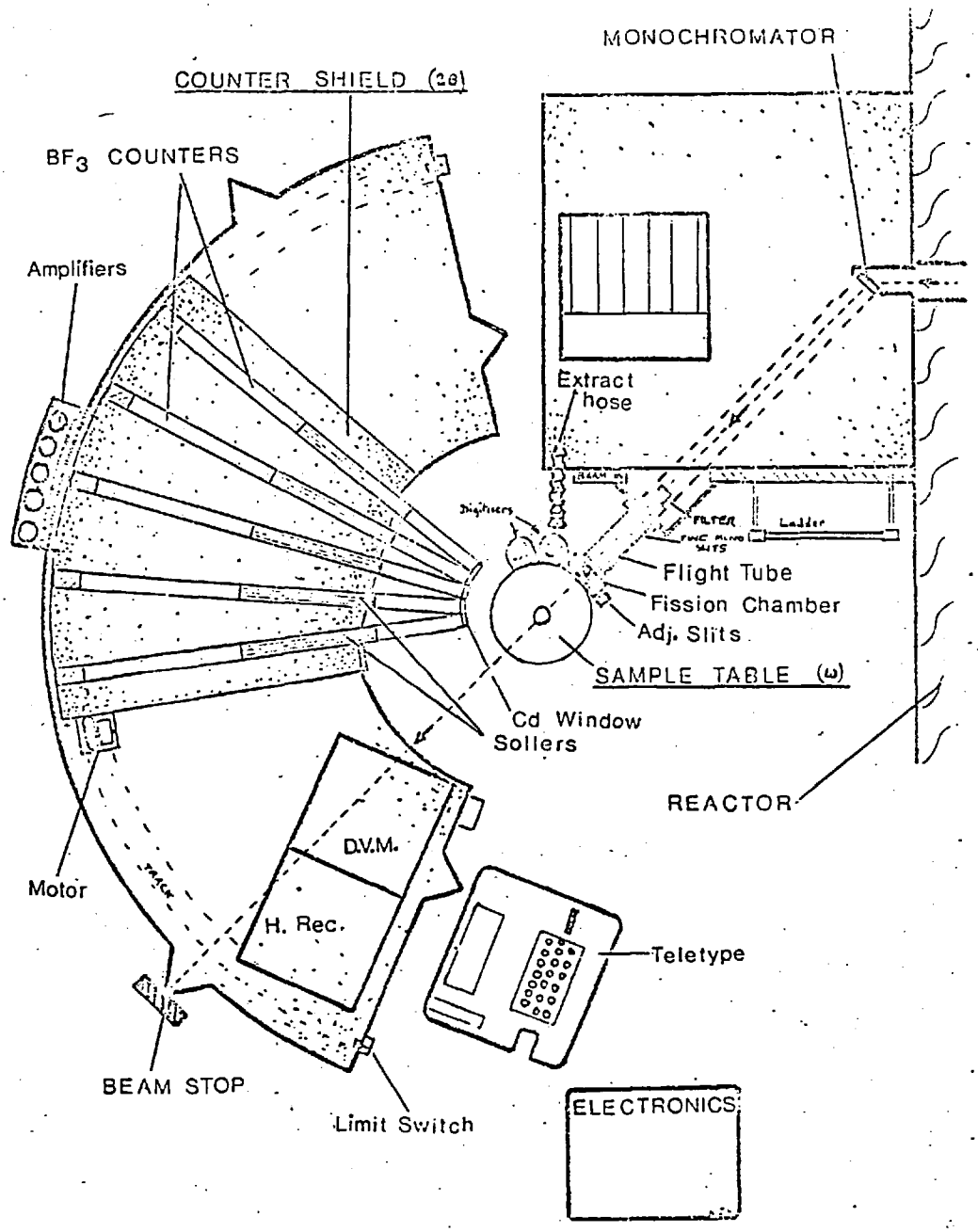
MONOCHROMATOR
COUNTER SHIELD (2θ)
BF3 COUNTERS
Amplifiers
Extract hose
Flight Tube
Fission Chamber
Adj. Slits
SAMPLE TABLE (ω)
Cd Window
Sollers
REACTOR
D.V.M.
H. Rec.
Motor
Teletype
BEAM STOP
Limit Switch
ELECTRONICS

Fig. 3.9

orientation in the {100} is the same as {200}, the {200} was used for normalization in these experiments as the sample could not be rotated.

3.4.2.3 Experimental procedure

The samples used were the roughly cylindrical ingots described in section 3.1. A shallow hole was drilled in one end, and a M4 stud was fastened in place using a small amount of 'Kwikfill'. A thin Cd collar was wrapped around the base of the stud to prevent background scattering and mark the sample height. Once in the cryostat the sample height and alignment was adjusted using a neutron camera, great care was taken to ensure that the sample was centred and evenly illuminated. The large nuclear incoherent scattering of Cr and the small {100} peak intensity made long counting times necessary. A typical scan across the {100} peak required 5 hrs for a 15 gm sample.

3.4.3 PANDA

The PANDA diffractometer is similar to CURRAN except with the provision of 9 counters arranged in 3 banks of 3 vertical detectors. The instrument is situated at the 7H4R hole in the PLUTO reactor at AERE, Harwell. The Ge(511) was used with $\lambda_0 = 1.547$ and 90^o take off. A small $\lambda/2$ component of 0.2% was observed.

Measurements were performed at a fixed temperature of 4.2 K using the 'PANDA' liquid He cryostat. The sample was maintained at a fixed temperature of 4.2 K by direct contact with liquid He. The sample was rotated and the same experimental procedure was followed as for the CURRAN outlined in section 3.4.2.3. The counts from each of the three detectors in the bank were added to form the total counts.

3.5 Diffuse scattering - time of flight

3.5.1 Introduction

The time of flight measurements to investigate the dynamics of antiferromagnetic CrFe alloys were undertaken using the diffuse scattering spectrometer D7 at ILL, Grenoble. A preliminary experiment attempted using the 4H5 instrument at AERE, Harwell did not prove successful because of large background signal .

In a tof experiment the energy and momentum dependence of the partial scattering cross section $d^2\sigma/d\Omega dE'$ is determined by measuring the flight time of a neutron as it travels from a gating chopper to the detector via the sample. The energy transferred to the sample by a neutron which arrives at the detector at a time t is given by

$$\hbar\omega = E_0\left(1 - \left(\frac{t_{e\ell}-t_\infty}{t-t_\infty}\right)^2\right) \qquad (3.11a)$$

where the neutron is assumed to leave the chopper at a time t_∞ and an elastically scattered neutron is assumed to arrive at the detector at a time $t_{e\ell}$. Here E_0 is the incident energy. Similarly the momentum change is of magnitude

$$|\underset{\sim}{\kappa}| = k_0\left(1 + \frac{(t_{e\ell}-t_\infty)}{(t-t_\infty)}\left[\frac{(t_{e\ell}-t_\infty)}{(t-t_\infty)} - 2\cos 2\theta\right]\right)^{\frac{1}{2}} \qquad (3.11b)$$

where 2θ is the scattering angle. These two relations (3.11a) and (3.11b) define trajectories in (κ, ω) space which are accessible to a single detector sited at an angle 2θ. These trajectories are illustrated schematically in Fig. 3.10.

It is usual to deal with the 'time of flight' τ, defined as the inverse neutron speed, rather than the time t. The number of neutrons which arrive at the detector in a given time interval is proportional to $d^2\sigma/d\Omega d\tau$ where τ is the scattered neutron time of flight. This partial differential cross section is related to the more usual cross section $d^2\sigma/d\Omega dE'$ via

$$\frac{d^2\sigma}{d\Omega dE'} = 2\,\frac{5.223\times10^6}{\tau^3}\,\frac{d^2\sigma}{d\Omega d\tau} \qquad (3.12)$$

where τ is in units μsec/m and E' is in meV. The $1/\tau^3$ factor ensures that the cross section at large negative energy transfers is amplified at the expense of cross sections at small negative and positive energy transfer. The time of flight scale is non linear in energy as indicated by (3.11a).

The energy resolution in a time of flight experiment depends upon all the time uncertainties in the system. There will be contributions arising from the uncertainty in defining the neutron start time t_∞ due to the finite open time of the chopper (Δt_β) and uncertainty in defining the neutron arrival time because of the subdivision of time of flight into discrete time channels of width Δt_G by the counter electronics. In addition there will be uncertainties in the system due to the finite sample size, detector volume and beam divergence so that not all neutrons travel the same sample-detector or chopper-sample distance. In the present case the most important contribution comes from the spread in incident velocity of the beam due to incomplete monochromation. The optimization of energy resolution with respect to intensity for a give experiment depends on the energy scale of the scattering and for the D7 experiments involved a choice of incident wavelength, chopper speed, sample size, chopper slot size and finally gate width Δt_G. It is important to note that the $1/\tau^3$ focussing effect leads to relaxed energy resolution at large energy transfers, this can be an intrinsically favourable feature of the tof method provided the incident energy is of the same order as the processes of interest within the specimen.

For the optimum use of counting time the time interval between neutron bursts from the chopper must be matched to the time interval over which neutron arrival times are measured. It is important that these counting intervals are separated sufficiently in time that straggling neutrons from one 'frame' do not appear in the following frame. Here the $1/\tau^3$ factor is effective in suppressing unwanted background structure from frame overlap. This places

Fig.3.10 The (κ,ω) trajectories covered by a single fixed detector at 2θ in a neutron time of flight experiment.

Fig.3.11 Schematic diagram of the diffuse scattering spectrometer D7 operating in unpolarized time-of-flight mode.

Fig.3.12 Composite Cr and Cr Fe 10% sample assembly.

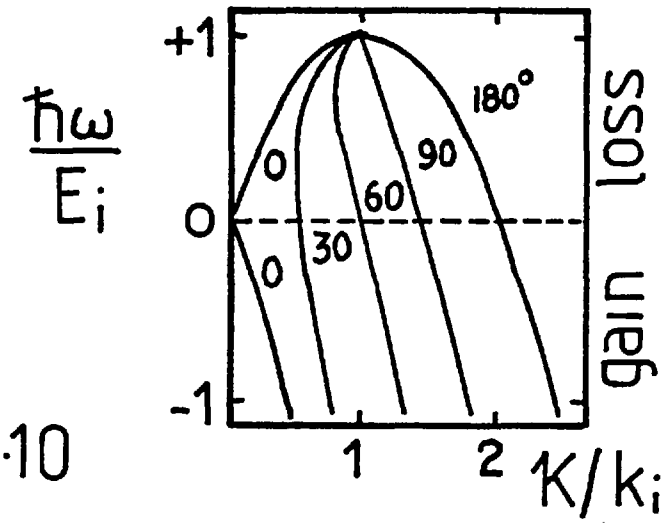

Fig·3·10

Fig·3·11

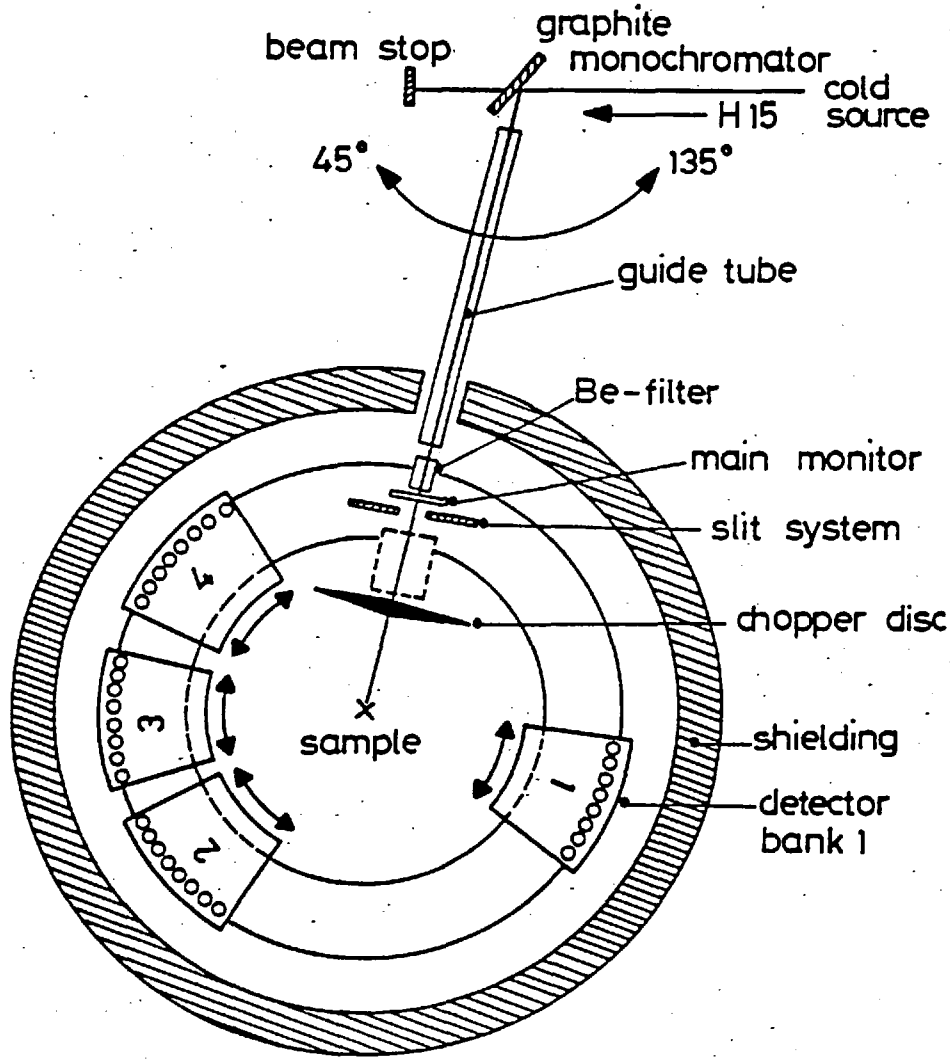

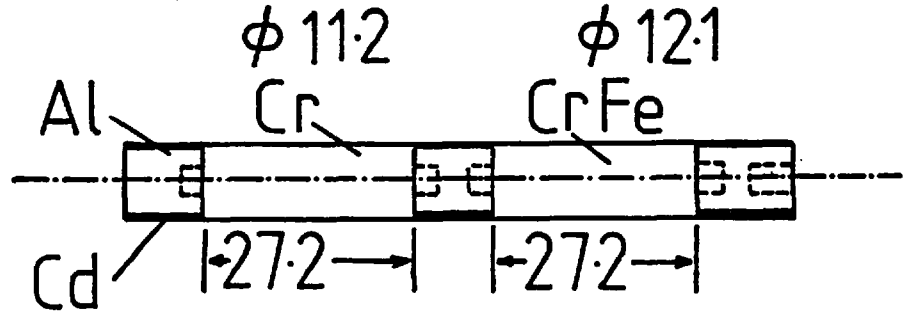

Fig·3·12

severe limitations on the application of the time of flight method to neutron energy loss processes. A more quantitative discussion of the tof technique is given by A.H.Baston (1972).

3.5.2 The diffuse scattering instrument: D7

3.5.2.1 Description

The diffuse scattering instrument D7 at ILL, Grenoble is served by the H15 cold neutron guide. The apparatus may be operated in either polarized or unpolarized mode. In our case the unpolarized mode was used, a schematic diagram may be found in Fig.3.11.. An incident wavelength from 3$\mathring{A}$ to 6$\mathring{A}$ is selected using a graphite monochromator which gives a wavelength resolution of 3% FWHM at 4.73$\mathring{A}$ which corresponds to peak flux. Higher order contamination of the beam is removed by a Be filter and the incident beam is chopped by a disc chopper after passing through a collimating slit system. The chopper has a diameter of 50 cm and consists of 4 slots of width 0.3cm and may be operated routinely at speeds of up to 10, 000 rpm. The detection system consists of 32 He 3 detectors arranged in four horizontal banks of eight detectors. Each bank is made up of two sets of four detectors separated by 5^{o}. The banks may be independently positioned over a range of $\pm 175^{o}$ so that an elastic κ range of between 0.1 $\mathring{A}^{-1}$ and 4 $\mathring{A}^{-1}$ may be covered. The time of flight information is encoded in 127 channels. Further details of the instrument and its performance are summarized by Just (1978).

3.5.2.2 Sample environment

The top loading flow He cryostat 20 ST HV 48 was used for the Cr/CrFe experiments. This cryostat could be connected to a sample changer so that the pure Cr and CrFe samples could be cycled in an out of the beam. To decrease the amount of air scattering the external diameter of the cryostat was made quite large. Temperature measurement was via a Calibrated Si diode and the temperature could

be stablilized to within ± .1 K for a period of 24 hours.

3.5.2.3. Sample geometry

In order to make an ideal difference measurement the sample (Cr 10% Fe) and the blank (pure Cr) must be of identical geometry, scattering power and absorption. This was not possible. However, if the sample geometry is well known, any variation between the two samples may be corrected in a straight forward way.

Large cylindrical Cr and CrFe 10% samples were fabricated by spark trepanning an as-cast ingot using $\frac{3}{8}$" Cu tube as a tool. The starting ingot was prepared using a large slot on the hearth. Off-cuts arising from the trepanning operation were argon arc melted onto the butt ends of the specimen. The irregularities and taper in the roughly cylindrical samples were removed by turning in a spark lathe. The ends of the cylinders were turned down to a smaller diameter to fit into the Cd covered aluminium spacers which held the composite sample together. The final sample assembly is illustrated in Fig. 3.12.

3.5.2.4 Experimental procedure

The detectors were disposed symmetrically about the incident beam; counters 16 and 17 being at the lowest angles + 11.25° and - 11.25° and counters 1 and 32 being at the highest angles + 89.9° and - 89.9°. A monitor was placed after the sample in the straight through beam and counter 1 masked off. A wavelength of 4.73 Å corresponding to peak flux was chosen and the two sample positions (height and rotation) were optimized by taking neutron photographs. The chopper slit was set at the sample diameter of 12 mm and the cryostat tail masked down with Cd to give an entrance window slightly larger than the sample. The chopper was placed as close as possible to the sample (∿ 30 cm) and the sample to detector distance was fixed at 130 cm for all detectors.

A chopper speed of 9017 rpm and gate width of 12 μ sec was

chosen and the elastic peak placed at channel 95. In this way energy transfers from + 1.5 meV to - 35 meV could be covered in one frame. This configuration gave an energy resolution measured with a V sample of 0.2 meV FWHM, which was adequate for measurements of relaxation processes with a half width of some 1-2 meV.

Spectra were collected at various temperatures above and below the Neél temperature. Counting times of 24 hours (12 hours sample and 12 hours blank)were adequate and the counts from corresponding banks of detectors were added to improve statistics. Vanadium and empty cell calibrations were also performed.

3.6 Polarized neutron diffraction

3.6.1 Introduction

As described in section 2.3.2 the measurement of the flipping ratio R for Bragg reflections allows a very sensitive determination of the magnetic structure factors and magnetization density in ferromagnets. The measurement of the flipping ratio can be made by switching the incident polarization parallel and antiparallel to the sample magnetization using a spin flipping device and counting the scattered neutrons for the two polarized directions. In designing a polarized beam experiment it is necessary to provide a small magnetic field along the neutron flight path to prevent beam depolarization and to define the quantization axis, this is known as the 'guide' field.

3.6.2 Polarized neutron diffractometer: D3

3.6.2.1 Description

The diffractometer D3 at ILL, Grenoble is a polarized beam 2 axis instrument with a single tilting He3 detector. A schematic diagram of the instrument is shown in Fig. 3.13.

The machine is situated at the thermal beam hole H5 and may be operated at wavelengths between 0.7 and 1.0 Å. A Co 8% Fe crystal is used as a polarizing monochromator and the optimum polarization of 98% is obtained at a wavelength of 0.9 Å using the (200) reflection. The monochromator is saturated magnetically by a permanent magnet and is used in transmission. The vertical guide field at the polarizer is turned into the horizontal plane at the cryoflipper. The sample is maintained in a large vertical magnetic field of up to 4.6 T (superconducting magnet) or 1.7 T (conventional electromagnet). The cryoflipper enables the beam polarization to be reversed so that the polarization at the sample may be either parallel or antiparallel to the magnetic field. The cryoflipper

works by setting up a reversal in the guide fields across a sheet of superconducting Nb or Pb. The neutron polarization cannot follow such a rapid change and the incident polarization direction is maintained on leaving the sheet, thus the beam polarization may be flipped by reversing the guide field in front of the Nb foil. The cryoflipper has almost 100% efficiency and is insensitive to stray fields. The guide fields at the flipper are generated by Helmholtz coils and can be flipped at a maximum frequency of 100 Hz. This is a white beam flipper.

The tilting detector can cover an angular range of - 135° to 5° in 2θ, - 190° to 190° in sample rotation and - 5° to 32° in tilt.

3.6.2.2. Sample environment

The sample, sample holder, cryostat and electromagnet used in the D3 experiment form part of a composite magnetic circuit designed to allow a strong homogeneous magnetic field at the sample. This is essential if beam depolarization is to be avoided. A fixed temperature liquid He cryostat 35 TH HF 18 was used in conjunction with the 1.7 T electromagnet. The narrow tail of the cryostat fits down inside a hole through one of the pole pieces and the sample is held between two Fe slugs so that the effective pole gap is 1.2 cm,

3.6.2.3 Experimental procedure

The crystal was in the form of a parallelipiped 1 × 1 × 10 mm^3 with the <1$\bar{1}$0> axis 10° off the sample axis. This sample was carefully mounted on a Cd alloy spigot and fixed in place using 'Kwikfill'. The sample dimensions are limited by the sample holder and must fit into a cylindrical volume 1.2 cm by 0.6 diameter. The crystal orientation was checked by taking a neutron Weissenberg photograph with the instrument D12. It is sufficient to have the crystal aligned to within ± 2°.

The polarization and flipping efficiency were determined by measuring the flipping ratio for standard Heusler and CoFe reflections.

The polarization was 0.9718 and the flipping efficiency 1.027.

The UB matrix which relates the crystallographic axes of the sample to the diffractometer axes (Busing and Levy, 1963) can be generated by accurately measuring the position of two non equivalent crystal reflections. This was done using the standard iterative procedure with half shutters to define θ and tilt angles and correcting the sample height. With the UB matrix determined the flipping ratio s could be collected automatically.

The measurement routine involved a peak search, followed by a background-peak-background flipping ratio scan with statistics automatically optimized. A standard (210) reflection was taken after every 10 reflections. Flipping ratios were collected for all accessible reflections out to sin θ/λ of 0.85 $\mathring{A}^{-1}$. The flipping ratios were corrected for dead time, imperfect polarization and flipping efficiency and for the contrast factor which arises from the angle between incident polarization and the scattering vector as shown in section 2.3.2. The resulting flipping ratios were averaged over all equivalent reflections and converted in γ values with the assumption $|\gamma|<1$.

A further series of experiments using D5 in the polarized 2 axis mode at three separate wavelengths were carried out to check for multiple reflection and to determine the importance of extinction in the crystal. Measurable extinction was present and the extinction correction routine is described in chapter 6.

3.6.3 Unpolarized single crystal diffractometer: MKVI

The γ values found by the polarized neutron measurements can only be converted into magnetic structure factor data with a knowledge of the nuclear structure factors. The nuclear structure factors were collected using the MKVI two circle diffractometer at AERE, Harwell. All reflections in the zeroth layer out to a sin θ/λ of 0.65 $\mathring{A}^{-1}$ were collected at 77 K. The integrated intensity was determined using the 'Andromache' system and converted to structure factor data in arbitrary units via

$$F_{hk\ell} = (I_{hk\ell} \sin 2\theta)^{\frac{1}{2}} \qquad (3.13)$$

The lattice parameter was also determined.. Insufficient data were collected for the Debye-Waller factor to be calculated. The wavelength was 1.0928 Å.

Fig.3.13 Schematic diagram of the polarized neutron diffractometer D3.

Fig.3.14 Schematic diagram of the polarization-analysis instrument D5.

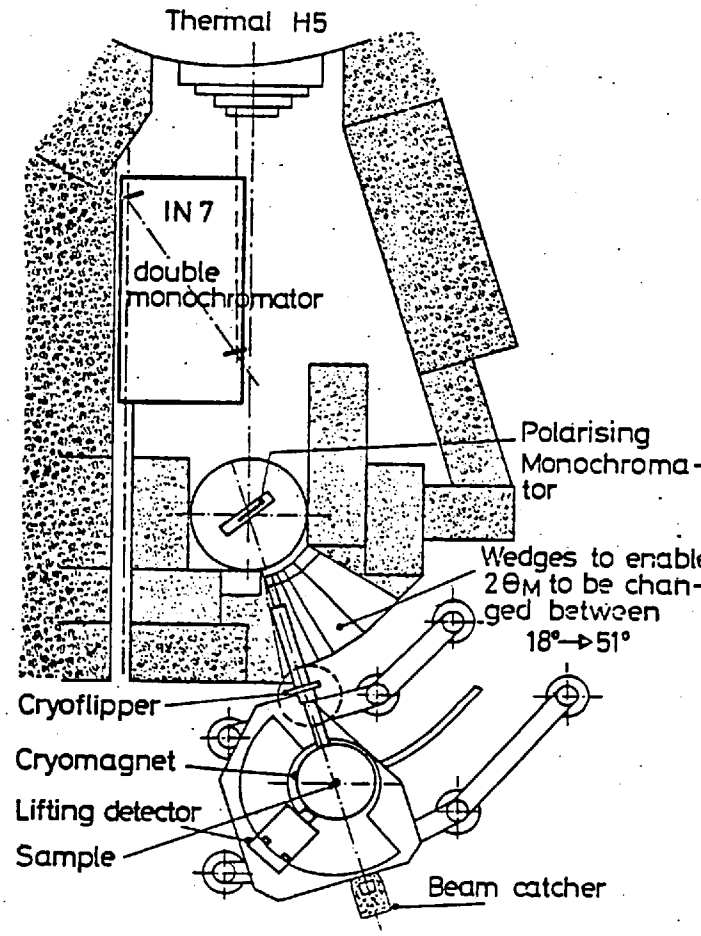

Fig. 3.13

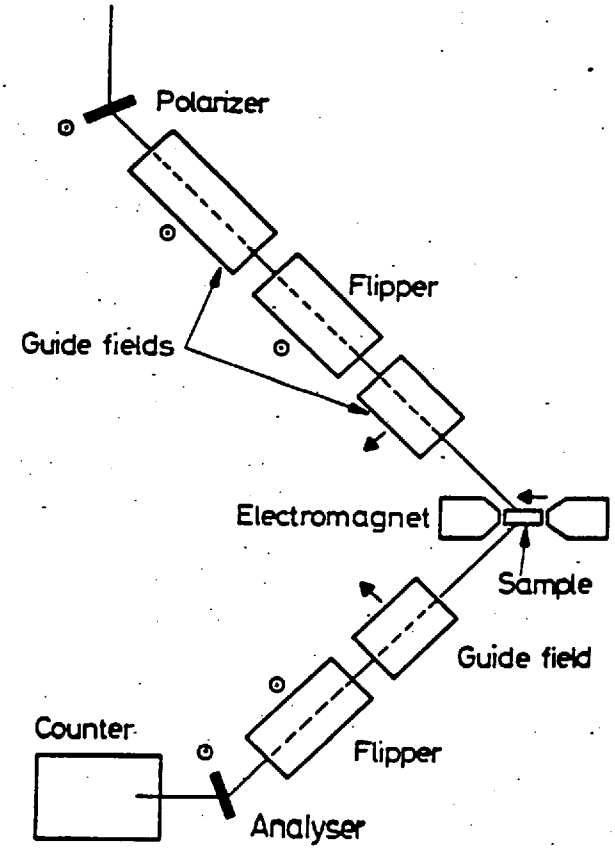

Fig. 3.14

3.7 Polarization-analysis

3.7.1 Introduction

The polarization-analysis technique allows an unambiguous isothermal separation of the nuclear and magnetic scattering from paramagnets and antiferromagnets as described in section 2.5.

The instrument D5 may be used to determine the spin flip and non spin flip cross sections in exactly the same manner as described by Moon, Riste and Koehler (1969). The sample is placed between a polarizer and analyser which transmit only (+) neutrons, a radio frequency spin flipper is placed in front of the sample. If the flipper is off only the non spin flip cross section (++) is measured. If the flipper is on, the spin flip (+-) cross section is measured. For a sample which has a paramagnetic cross section M, a nuclear spin incoherent cross section NS and other non spin dependent nuclear cross sections N the spin flip and non spin flip cross sections are

$$\frac{d\sigma^{\parallel}}{d\Omega}_{SF} = \frac{2}{3} NS + M$$
$$\frac{d\sigma^{\parallel}}{d\Omega}_{NSF} = \frac{1}{3} NS + N \qquad (3.14a)$$

if the polarization is parallel to the scattering vector and

$$\frac{d\sigma^{\perp}}{d\Omega}_{SF} = \frac{2}{3} NS + \frac{1}{2} M$$
$$\frac{d\sigma^{\perp}}{d\Omega}_{NSF} = \frac{1}{3} NS + N + \frac{1}{2} M \qquad (3.14b)$$

if the polarization is perpendicular to the scattering vector. A measurement of these partial cross sections is sufficient to isolate the magnetic scattering even in the presence of an unknown nuclear-spin incoherence.

3.7.2 Polarization-analysis instrument: D5

3.7.2.1 Description

The instrument D5 is a triple axis spectrometer which has been modified by the inclusion of a polarizing monochromator and polarizing analyser along the lines of the polarization-analysis instrument described by Moon, Riste and Koehler (1969). It is possible to operate D5 as a conventional 2 axis polarized neutron diffractometer or as a triple axis spectrometer with polarization-analysis.

A schematic diagram of the instrument operating in polarization-analysis mode is presented in Fig. 3.14. The instrument is situated at the H4 hot neutron beam hole at ILL, Grenoble. A range of incident wavelength from 0.4 Å to 1.1 Å can be selected using either Co 8% Fe or Cu_2MnAl polarizing monochromators. The Heusler alloy(Cu_2MnAl) monochromator was used throughout. The polarized beam produced by the monochromator can be reversed by the RF spin flipper which is located between monochromator and sample. The RF frequency must be tuned to the Larmor precession frequency of the neutron in the guide field and the amplitude adjusted to suit the neutron transit time through the coil. The flipper must be optimized for each wavelength. After passing through the flipper the beam polarization is adiabatically rotated out of the vertical plane into the horizontal plane by rotation of the guide field. The polarization is maintained parallel to the scattering vector at the sample position by the use of a horizontal 1T electromagnet. For the study of antiferromagnetic CrFe alloys this magnet provided a guide field of 250 Oe, which was sufficient to define the polarization direction and prevent any depolarization but was not high enough to perturb the sample magnetization greatly. The scattered polarization is then adiabatically rotated back into the vertical plane to undergo analysis by reflection from a Cu_2MnAl analysing crystal mounted on the analysing arm of the triple axis spectrometer. The analysed beam is then detected by a single He3 detector which is usually set for elastic scattering from the Heusler (111). The second spin flipper was not

used. All spectrometer movements are controlled by computer sub-routines and no manual option is available.

The energy resolution of the instrument operating at 0.84 Å with the Heusler (111) monochromator is typically of the order 15 meV FWHM. The wavelength spread is of the order 7% and the incident divergence some 0.5°. This rather poor figure for energy resolution is the result of the short incident wavelengths available at H4. To avoid serious $\lambda/2$ and $\lambda/3$ contamination short wavelengths must be used, which dictates the low take off angles from monochromator and analyser in order to use polarizing reflections. The Q resolution is also relatively coarse for the same reasons.

The guide fields both immediately before and after the sample, together with the guide field at the sample position can be rotated by 90° to allow the polarization to be disposed perpendicular to the scattering plane. This is made possible by the use of a vertical Helmholtz pair which is added to the horizontal electromagnet assembly. The guide fields are produced by permanent magnets arranged in removable box like sections and it is possible to rotate the guide field by simply rotating the box. These boxes are lined with boron plastic and are fitted with B_4C apertures so that they serve an additional role as collimators.

The machine may be operated in a two axis mode by removing the analyser, analyser shield and appropriate sections of guide; the detector can then be translated forward into the analyser position. For conventional 2 axis measurements it is necessary to replace the existing magnet assembly by a single crystal cradle with a vertical 2T electromagnet. This procedure was adopted to study the extinction in the Pt_3Cr crystal.

3.7.2.2 Sample environment

Diffuse scattering measurements in the PA mode were made using a conventional He flow cryostat 12 ST HV 48 which fitted conveniently between the vertical Helmholtz coils and the pole pieces of the horizontal electromagnet. The electromagnet pole gap is 15 cm.

With the instrument in 2 axis mode, the narrow tail cryostat 15 CR HF 11 was used. This cryostat fits into the small hole in the vertical pole pieces of the 2T magnet and can be used only over the restricted temperature range 1.3 to 30 K. In the case of both cryostats, temperature measurement was made using a calibrated diode.

3.7.2.3 Experimental procedure

The peak flux from the hot neutron beam hole H4 occurs at 0.840 Å. This wavelength was selected using the Heusler (111). The RF frequency and amplitude was automatically trimmed to give optimum flipping efficiency for this wavelength. The sample $2\theta_S$ and analyser $2\theta_A$ zero angles were then determined and the Heusler (111) analyser was set for elastic scattering. Several thin sheets of Erbium were placed in front of the collimating guide after the sample to filter out the $\lambda/2$ contribution.

The Cr 5% Fe sample used in this series of experiments was a slab of 0.6 cm thickness which was mounted behind a 1.65 cm × 2.2 cm Cd slot using 'Kwikfill'. The sample position was checked using a neutron camera. The sample transmission was measured with the sample normal to the beam with a sheet of perspex attenuating the beam to prevent saturation of the detector. The flipping ratio was found to be approximately 20.

Data were then collected at various sample temperatures with the machine operating in θ-2θ mode. A range of 2θ from 3° to 40° was covered in steps of $\frac{1}{2}^\circ$. Counting time was divided in the ratio 1:1 initially but subsequently changed to 1:4 nonspin flip to spin flip in order to obtain equal statistics for each partial cross section. Data were also taken with the analyser offset by 3° from the elastic position and also with the guide field at the sample vertical. Counting time was typically 15 m per point. Empty cell and Vanadium calibrations were made in the same way.

The data were analysed by hand following a standard procedure (J.Davis, Private communication, Freeman et al. (1978)). The raw counts C_{SF}, C_{NSF} were normalized to the same counting time and the

offset background subtracted to give C'_{SF}, C'_{NSF}. The air scattering was similarly corrected and after adjustment for the sample transmission α_S (assumed to be spin independent) was subtracted from the offset corrected counts to give the counts coming from the specimen I_{SF}, I_{NSF}. These counts were then corrected for imperfect flipping efficiency and polarization using the values of 0.983 for flipping efficiency (f) and 0.96 for polarization, and were then corrected for slab absorption in θ-2θ geometry using (3.3) to give I'_{SF} and I'_{NSF}. This procedure was also followed for the V calibration.

The V calibration was corrected for the Debye-Waller factor and multiple scattering following the procedure of Freeman et al. (1978). The ratio of second to first scattering was found to be approximately 10%. This procedure gave an isotropic V spectrum with the ratio of spin flip to non spin flip of 2:1 as expected and provides a stringent cross check on the experimental technique. The sample counts could then be normalized to this value. In short, the data analysis may be summarized by the expressions

$$\frac{d\sigma}{d\Omega}_{SF} = \frac{m_V}{m_S}\frac{2}{3}\frac{\sigma^V_{inc}}{4\pi}[2f \sec\theta(\alpha_S)^{\sec\theta} I''_{SFV}]^{-1}[I'_{SF}(1+p^{-2})+I'_{NSF}(2f-1-p^{-2})]$$

$$\frac{d\sigma}{d\Omega}_{NSF} = \frac{m_V}{m_S}\frac{1}{3}\frac{\sigma^V_{inc}}{4\pi}[2f \sec\theta(\alpha_S)^{\sec\theta} I''_{NSFV}]^{-1}[I'_{NSF}(2f+p^{-2}-1)+I'_{SF}(1-p^{-2})] \qquad (3.15)$$

where I''_{SFV} and I''_{NSFV} are the Vanadium spin flip and non spin counts corrected for multiple scattering and I'_{SF}, I'_{NSF} are sample spin flip and non spin flip counts corrected for absorption but not multiple scattering.

3.8 Bulk magnetic measurements

3.8.1 Introduction

Bulk magnetic measurements were made on offcuts from the neutron scattering samples to complement the neutron scattering measurements. The two sets of apparatus described here rely on the measurement of an induced EMF for their operation. In the case of the vibrating sample magnetometer the EMF induced in the pick up coils is due to the oscillation of the sample in a homogeneous, static magnetic field. This EMF is proportional to the magnetization of the sample and the technique is well suited to the study of remanent or slowly relaxing magnetization. The measurement of AC susceptibility, on the other hand, is based on the measurement of the EMF induced in a pick up coil by the action of an alternating magnetic field on a stationary sample. The EMF is proportional to the frequency dependent permeability of the sample.

The two sets of apparatus were constructed by C.N.Guy and W.Howarth, and C.N.Guy and B.V.B.Sarkissian and described in great detail by Howarth (1978) and Sharif (1979). These instruments were used without modification and only a brief description of the measurement principle and the basic experimental set up is appropriate here. In making bulk magnetic measurements on highly susceptible samples it is important to keep the demagnetizing field as small as possible, this was achieved by machining the samples with the spark machine into long needles ($c/a > 5$) or thin disks ($c/a < 10$).

3.8.2 Low field vibrating sample magnetometer

In this particular vibrating sample magnetometer (VSM) the sample is vibrated up and down between two pick up coils. The coils are arranged as a Helmholtz pair connected in opposition and the vibration direction is along and on the axis joining the two coils. A static magnetic field is applied along the axis using a larger set of Helmholtz coils. This geometry is illustrated inset in

Fig.3.15 Schematic diagram of the measuring circuit for the low field vibrating sample magnetometer. Coil geometry is shown inset.

Fig 3.15

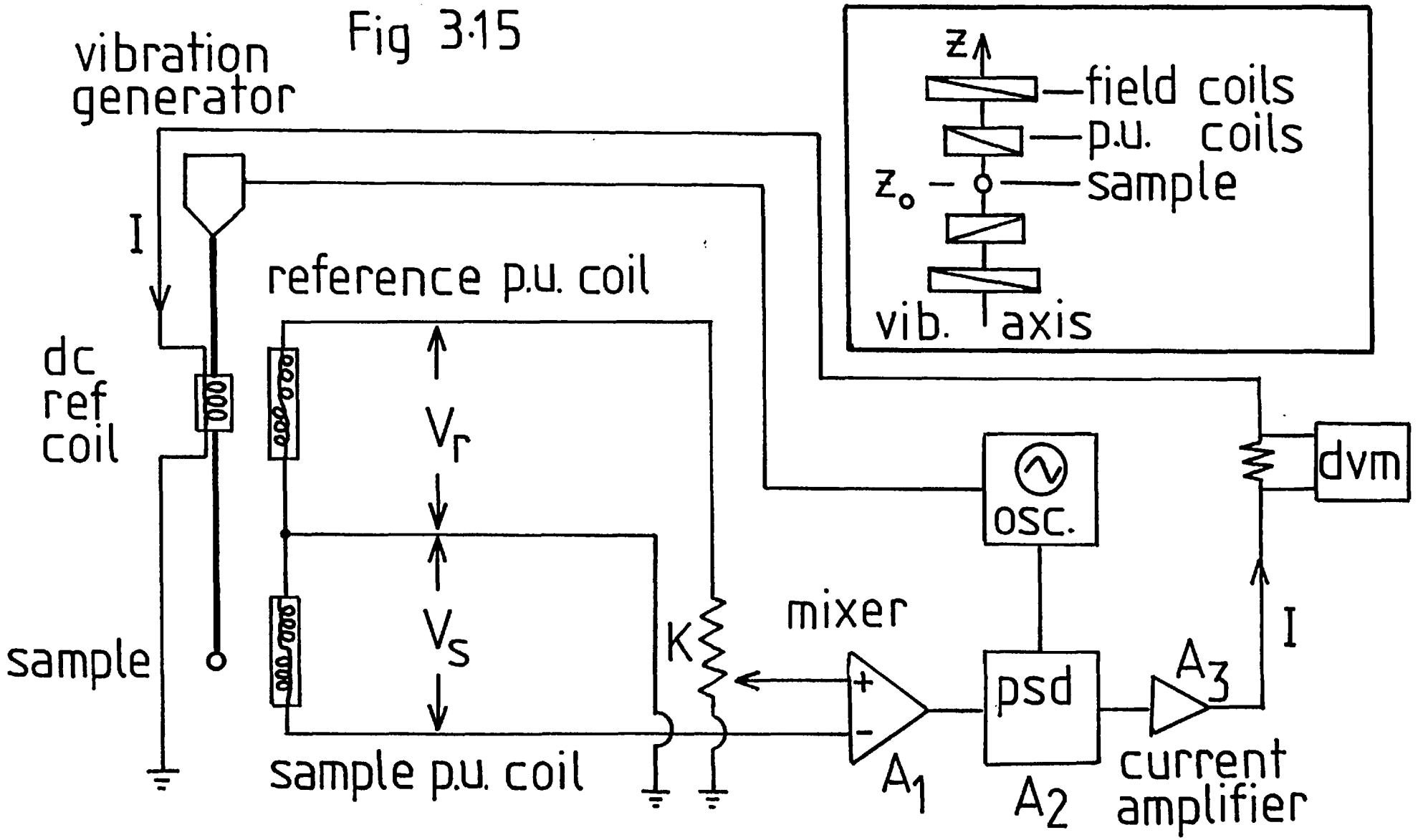
vibration generator
z
field coils
p.u. coils
z_o
sample
vib. axis
I
reference p.u. coil
dc ref coil
V_r
V_s
sample
K
mixer
osc.
dvm
psd
A_3
I
A_1
A_2
current amplifier
sample p.u. coil

Fig. 3.15. Guy (1976) has presented a complete analysis of the signal produced in the pick up coils for this geometry. Using the reciprocity theorem and a Taylor expansion it can be shown that the EMF is given by

$$\varepsilon = -\mu_0 M_Z \{ i\omega_0 \alpha_0 h'(Z)\big|_{Z=Z_0} e^{i\omega_0 t} + i\omega_0 \alpha_0^2 h''(Z)\big|_{Z=Z_0} e^{i2\omega_0 t} + \ldots \} \qquad (3.16)$$

where ω_0 is the vibration frequency, α_0 the vibration amplitude, M_Z is the magnetic dipole moment along the vibration (Z) axis and μ_0 is the SI permeability of free space. Here $h'(Z)$, $h''(Z)$ are derivatives of the Z component of the ficticious magnetic field $\underset{\sim}{h}$ which would be produced at a point Z along the axis if unit current were flowing in the coils. If the sample is vibrated about a mean position Z_0 which is midway between the coils all higher order harmonics disappear and the EMF has the vibration frequency only and is proportional to the magnetic moment. It is important to stress that the measurement is made in a static field and it is only by virtue of the vibration that a signal is generated.

A schematic diagram of the measuring circuit is shown in Fig. 3.15. The induced EMF is detected by balancing the signal against a standard current dipole. To do this a reference signal is produced in a second set ofpick up coils by allowing a dc current to flow through a small coil wound on the same vibrating rod as the sample, a fraction of this signal is taken to balance out the sample signal. The current flowing through the current dipole to achieve balance is then proportional to the sample magnetization. Such a null technique is not sensitive to small variation in vibration amplitude or frequency. A phase sensitive detector is used to detect the balance condition; this may be sought manually as described by Howarth (1978) or using a feed back loop as shown in Fig. 3.15. Temperature measurement is achieved using a calibrated Si diode and He vapour pressure and the sample temperature may be varied from 1.6 K to room temperature. Magnetic fields as low as 20e may be used and a magnetization of 10^{-6} emu can be detected using this arrangement. Full details are given by Howarth (1978).

3.8.3. AC susceptibility

The measurement of AC susceptibility was performed using the apparatus designed and built by Guy and Sarkissian and described by Sharif (1979). The apparatus is simply a mutual inductance bridge with the mutual inductance of one arm varied by a ratio transformer to balance the mutual inductance of the arm containing the sample. The balance condition is indicated by a zero in phase component at the PSD, the quadrature signal being negligible. A schematic diagram of the apparatus is shown in Fig. 3.16.

In this set up, the mutual inductance of the sample arm of the bridge is in principle entirely due to the susceptibility of the sample; as it is located inside one of a pair of compensated coils. In practice the compensation is not perfect and the residual inductance of the coil system can be measured by withdrawing the sample and finding the new balance condition. The difference between these two mutual inductances - with the sample inside one coil and withdrawn - is proportional to the magnetic susceptibility of the sample.

The AC magnetic induction applied to the sample via the primary circuit can be varied over a frequency range 10Hz- 20 kHz. For the CrFe measurements a frequency of 80 Hz was used and an rms field of 0.3 Oe was applied. Measurements could be made over a temperature range 1.6 to 300 K and a calibrated Si diode was used for thermometry. A DC bias field can be simultaneously applied to the sample. Further experimental details are described by Sharif (1979).

Fig. 3·16

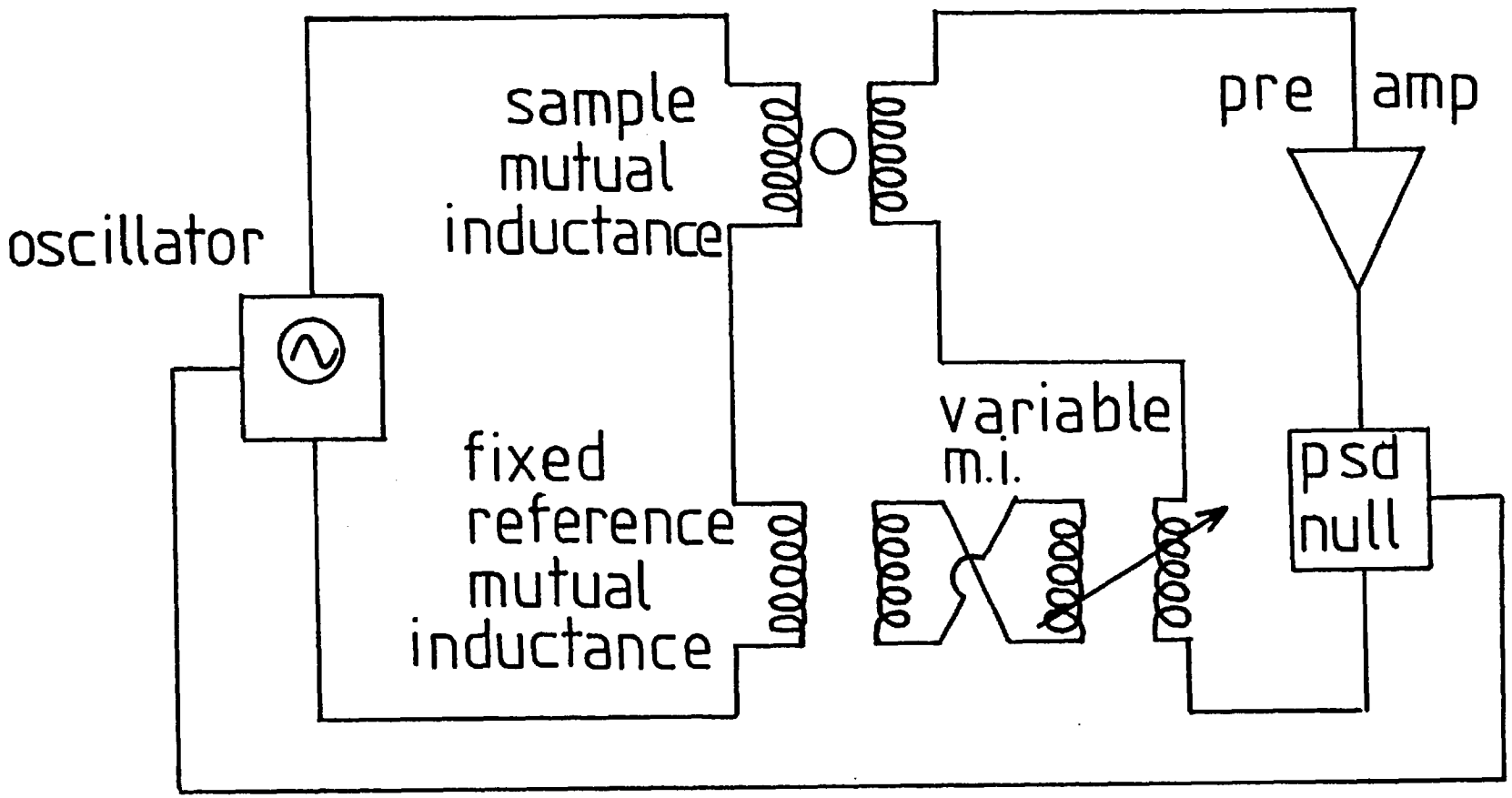
sample
sample
mutual
inductance
pre
amp
oscillator
variable
m.i.
fixed
reference
mutual
inductance
psd
null

3.9 Resistivity measurements

The resistivity of an antiferromagnetic CrFe 10% alloy was measured so that the resistivity anomaly at the Neél temperature could be correctly identified.

This experiment was carried out using the apparatus described by Barber (1974) based on the standard four terminal DC technique for resistance measurement. The sample current is supplied by a high stability ($1 : 10^6$) Tinsley current supply and the potential developed across the sample is found potentiometrically with a Tinsley stabaumatic potentiometer together with a standard cell. The balance condition could be determined to great accuracy using a galvanometer amplifier and photocell arrangement, the accuracy was of the order ± 1 nV. The temperature could be varied over a range 1.6 to 300 K and thermometry performed via a Ge resistance or Cu-constantan thermocouple. The apparatus was modified by the inclusion of a Si diode for temperature measurement. The linear characteristics of the diode are particularly useful for the direct determination of the temperature derivative of resistivity.

The sample itself was in the shape of a long needle. Two sets of Pt leads were spot welded in place, one at either end to act as current leads and two more closely spaced to act as voltage leads. Leads were soldered in place using low thermal EMF solder. Data were taken with the current flowing both forward and reverse in order to cancel any stray EMF. Full details of the experimental procedure may be found in Barber's thesis (1974).

CHAPTER 4

ANTIFERROMAGNETISM IN CR-FE ALLOYS

For convenience, the work on the Cr Fe alloy system has been divided into two parts. In this chapter the properties of antiferromagnetic Cr Fe alloys are presented. Ferromagnetic and spin-glass Cr Fe alloys are treated in Chapter 5.

The itinerant antiferromagnetism of Cr and its alloys is discussed in section 4.1. Previous work on Cr Fe antiferromagnetic alloys is reviewed in section 4.2. Experimental results and discussion are presented in sections 4.3 and 4.4. Section 4.3 is devoted to the determination of the antiferromagnetic phase boundary and ordered moment. Section 4.4 is concerned with the nature of the Fe moment in antiferromagnetic Cr Fe alloys.

4.1 The itinerant antiferromagnetism of Chromium and its alloys

4.1.1 Introduction

The unusual magnetic properties of Chromium and its alloys have been the subject of an intensive experimental and theoretical effort dating back to the original suggestion of antiferromagnetism in Chromium metal by Néel (1932). Since that time, a very convincing case for the itinerancy of antiferromagnetism in Cr has been put together and there is mounting evidence to show that the antiferromagnetic state is specifically related to the Fermi surface geometry of paramagnetic Cr. The most successful current theoretical descriptions of Cr and its alloys are based on these concepts.

Despite these achievements, there is still no wholly satisfactory theory for the antiferromagnetism of Cr. To a certain extent this reflects the fact that there is no wholly satisfactory theory for metallic 3d magnetism as such (Hubbard, 1979, Gunnarsson, 1976) although Cr does pose its own problems: notably, the order of the magnetic transition and the role of higher order harmonics, the pressure dependence of the Néel temperature and the nature of the magnetic excitations have yet to be adequately understood.

4.1.2 The itinerancy of antiferromagnetism in Cr

The itinerant nature of antiferromagnetism in pure Cr is clearly demonstrated by three observations:

(a) Sinusoidal spin modulation

As a result of careful neutron diffraction studies by Corliss, Hastings and Weiss (1959), Shirane and Takei (1962) and Brown, Wilkinson, Forsyth and Nathans (1965) among others, it is possible to conclude that the state of magnetic order in pure Cr below its Néel temperature of 311K is based on the sinusoidal spin polarization of the d like electrons on the two simple cubic sublattices which make up the bcc lattice of Cr. This modulation of the

antiferromagnetic moment is long ranged, incommensurate with the lattice periodicity and has a small amplitude. (Typically the modulation period is between 20-22 unit cells along a <100> direction and the maximum moment per Cr site in 0.59 μ_B at 4.2 K.) Such a structure, in which the total moment varies from site to site in this way, is incompatible with conventional models for antiferromagnetism in insulators, for example, where localized, constant, atomic moments are coupled by effective antiferromagnetic forces.

In fact, this sinusoidal modulation is termed a linear spin density wave (SDW) in recognition of the essential itinerancy of antiferromagnetism in Cr. The term SDW, first coined by Overhauser (1959) has come to be used as a generic name for states of non uniform spin polarization in itinerant systems. For example, a spiral SDW in a conduction electron gas would be described by a fractional spin polarization $\underset{\sim}{\rho}(\underset{\sim}{r})$ which varied continuously in magnitude and direction according to,

$$\underset{\sim}{\rho}(\underset{\sim}{r}) = \rho(\hat{\underset{\sim}{x}} \cos Qz + \hat{\underset{\sim}{y}} \sin Qz) \qquad (4.1a)$$

which corresponds to a spiral of moment ρ propagating with a wave-vector $\underset{\sim}{Q}$ along the z direction. Overhauser (1962) makes the distinction between 'flexible' and 'rigid' spin systems. In a 'flexible' spin system, such as the conduction electron gas (4.1a) the spin polarization density follows the phase of the SDW smoothly throughout the unit cell. However, in a 'rigid' spin system the amplitude and direction of the spin polarization within the unit cell is determined by the phase of the SDW at the lattice position at the centre of the cell. The rigid spin model is found to be more appropriate to the case of Cr, as it is evident that the d electron charge distribution about the lattice site is polarized as a whole. This point is discussed further by Overhauser (1962).

The (primary) SDW in Cr can thus be described according to the rigid spin model as the moment variation,

$$\underset{\sim}{\mu}(\underset{\sim}{R}_{\ell d}) = \mu_{max}\,\hat{\underset{\sim}{e}}\,\exp(i\underset{\sim}{w}.\underset{\sim}{d})\cos(\underset{\sim}{Q}.\underset{\sim}{R}_{\ell d}) \qquad (4.1b)$$

where $\underset{\sim}{\mu}(\underset{\sim}{R}_{\ell d})$ is the moment at a site $\underset{\sim}{R}_{\ell d}$ having lattice vector $\underset{\sim}{\ell}$ and basis vector $\underset{\sim}{d}$. The factor $\exp(i\underset{\sim}{w}.\underset{\sim}{d})$, where w is any convenient (100) reciprocal lattice vector, has values ±1 depending on the sublattice selected by the choice of $\underset{\sim}{d}$ and thus generates the underlying two sublattice AF_0 structure. Here μ_{max} is the maximum amplitude of the SDW and $\hat{\underset{\sim}{e}}$, the moment direction, is a <100> type direction. At low temperature $\underset{\sim}{Q}$, the wavevector of the SDW, is parallel to $\hat{\underset{\sim}{e}}$ and the spin configuration is a longitudinal linear SDW. Above the 'spin flip' temperature of 121 K the moment direction changes so that whilst $\hat{\underset{\sim}{e}}$ is still a <100> type direction it is now perpendicular to $\underset{\sim}{Q}$. $\underset{\sim}{Q}$ always remains along the same <100> type direction. Thus above the spin flip temperature the spin configuration is a transverse linear SDW. As mentioned previously $\underset{\sim}{Q}$ is incommensurate with the lattice and is slightly less than a (100) reciprocal lattice vector; typically $\underset{\sim}{Q} \simeq 0.95\,\frac{2\pi}{a}$ (100). These relationships are illustrated in Figure 4.1.

(b) Paramagnetic neutron scattering

The diffuse neutron scattering measurements of Wilkinson et al. (1962) did not detect any paramagnetic scattering from Cr to within the experimental error of ± 1 mb $sr^{-1}at^{-1}$. This lack of a low frequency magnetic response above T_N indicates that localized atomic moments do not exist above the Néel temperature and suggests that the antiferromagnetic moment is induced on ordering.

It is worthwhile remarking that according to an itinerant electron model one may expect the high frequency response to persist above T_N. Such a response, highly localized in q about the (100) position, has been observed in Cr above T_N in the hot source triple axis measurements of Booth and Ziebeck (private communication).

(c) Entropy of transition

Specific heat measurements reveal a very small, first order, anomaly at T_N for pure Cr. (Williams, Gopal and Street, 1979). The entropy change on ordering ($\tilde{\sim}$ 35 $mJmol^{-1}K^{-1}$) deduced from these specific heat data represents only 1% of the value expected for a

system with localized spins ($S = \frac{1}{2}$) which are involved in the transition.

In addition, the marked difference between the induced ferromagnetic form factor of Cr above T_N (Stassis et al., 1975) and the form factor of the antiferromagnetic state argues against a local moment picture and suggests that the Néel temperature of Cr corresponds to the temperature at which a moment is created as well as ordered. Further evidence for the itinerancy of Cr can be drawn from the weak temperature dependence of the bulk susceptibility. Rather more indirect support for the itinerancy hypothesis can be found in a host of other physical properties, these are reviewed by Arrott (1966).

4.1.3 The SDW and Fermi surface 'nesting'

Overhauser (1962) succeeding in proving that a free electron gas, interacting via Coulomb interactions, was unstable with respect to the formation of a SDW state in the Hartree Fock approximation. It was suggested that the SDW state in Cr reflected just such an instability. Later, it became apparent that if the effect of electron correlation was taken into account via a screened Coulomb interaction this instability disappeared for the free electron case, but could still be realized if the band structure of a 'real' solid was particularly favourable (Fedders and Martin, 1966). In the case of Cr the SDW is believed to be the result of just such a fortuitous band structure, or more precisely, the presence of two matching sheets of the paramagnetic Fermi surface as first suggested by Lomer (1962).

Lomer's argument was as follows. In an itinerant electron system the Coulomb repulsion is smaller for electrons with parallel spin as opposed to antiparallel spin by virtue of the exchange symmetry of the Fermion wavefunctions; this favours the formation of a magnetic state. On the other hand, if one spin state is to be preferentially occupied to create a ferromagnetic polarization the Fermi energy must be increased in order to accommodate these extra

states, this increase in kinetic energy tends to favour a non-magnetic state. This compromise is well illustrated by the Stoner criterion for ferromagnetism $IN(E_F) > 1$. Now, consider the effect of a sinusoidal (rather than uniform) spin density; in this case the sinusoidal exchange perturbation does not shift the unperturbed one electron energies to first order. Rather, the exchange potential mixes one electron states with crystal momentum $|\underset{\sim}{k}>$ and $|\underset{\sim}{k}'>$ which differ by the wavevector $\underset{\sim}{Q}$ of the modulation. This mixing is greatest when the unperturbed electron energies E_k and E_{k+Q} are equal and the sinusoidal exchange potential creates a gap at this energy. The origin of the gap is simply that the unpeturbed wavefunctions are mixed by the sinusoidal spin density in such a way that up spin parts of the unpeturbed wavefunctions reinforce in regions where the up spin density of the peturbing modulation is large for the states at the bottom of the gap, and the up spin parts of the unpeturbed wavefunctions are mixed in such a way that they cancel in the same regions for states at the top of the gap. This process may lead to a self consistent lowering of the total energy if the mixing occurs between states close to the Fermi energy. The energy lowering is simply achieved by removing occupied states near the Fermi energy by the introduction of a SDW energy gap. As the amplitude of the SDW increases, the gap increases and the total energy is lowered until states above the gap became occupied and reduce the SDW amplitude. The optimum situation is therefore, one is which E_F lies within the gap. Using the Fermi surface deduced from earlier band structure calculations for Fe, Lomer (1962) suggested that in Cr two branches of the Fermi surface - the hole octahedron at the H point ($\frac{\pi}{a}(100)$) and the electron 'jack' at $\Gamma(000)$ - were self consistently coupled by such an exchange field. The fact that these surfaces showed matching flat and parallel sides implied that the Q of a single perturbation would couple them very efficiently, leading to a SDW state with wavevector equal to the vector connecting these two branches.

This rather qualitative argument can be made more formal by considering the static susceptibility $\chi(q)$ of paramagnetic Cr. The

paramagnetic state becomes unstable with respect to a magnetically ordered state when the response of the system to an infinitesimal magnetic perturbation of wavevector q becomes infinite. In the present case $\chi(q)$ must show a divergence at the Néel temperature and for a wavevector $\underset{\sim}{q} = \underset{\sim}{Q}$, the wavevector of the SDW.

The calculation of $\chi(q)$ for an interacting many electron system is not trivial. Recent calculations by Windsor (1972) and Gupta and Sinha (1971) were based on the RPA expression for the exchange enhanced susceptibility

$$\chi(\underset{\sim}{q}) = \frac{\chi^0(\underset{\sim}{q})}{1 - I\chi^0(\underset{\sim}{q})} \tag{4.2a}$$

where $\chi^0(\underset{\sim}{q})$ in the susceptibility of the unenhanced system and I is an (effective) Hubbard type enhancement factor. The susceptibility of the unenhanced system may be calculated via the standard Lindhard expression,

$$\chi^0(q) = \frac{1}{2} \sum_{\underset{\sim}{k}} \sum_{\mu,\nu} \frac{f^{\nu}_{\underset{\sim}{k}+\underset{\sim}{q}} - f^{\mu}_{\underset{\sim}{k}}}{E^{\nu}_{\underset{\sim}{k}+\underset{\sim}{q}} - E^{\mu}_{\underset{\sim}{k}}} \left[M^{\mu\nu}_{\underset{\sim}{k},\underset{\sim}{k}+\underset{\sim}{q}}\right]^2 \tag{4.2b}$$

where the summation is taken over all $\underset{\sim}{k}$ within the Brillouin zone and μ and ν are band indices. Here E^{ν}, E^{μ} are the one electron energies calculated for the bands μ, ν according to some self consistent Hartree Fock type scheme and $f^{\mu}_{\underset{\sim}{k}} = (1+\exp \beta(E_F - E^{\mu}_{\underset{\sim}{k}}))^{-1}$ is the Fermi function. The matrix elements $M^{\mu\nu}_{\underset{\sim}{k},\underset{\sim}{k}+\underset{\sim}{q}}$ are frequently taken as constants, although Winsor (1972) expresses them in terms of tight binding orbitals $|\psi^{\nu}_{\underset{\sim}{k}+\underset{\sim}{q}}\rangle$, $|\psi^{\mu}_{\underset{\sim}{k}}\rangle$,

$$M^{\mu\nu}_{\underset{\sim}{k},\underset{\sim}{k}+\underset{\sim}{q}} = \langle\psi^{\nu}_{\underset{\sim}{k}+\underset{\sim}{q}}|\psi^{\mu}_{\underset{\sim}{k}}\rangle \tag{4.2c}$$

According to these expressions, the susceptibility $\chi(q)$ will diverge when $\chi^0(q)$ becomes equal to I^{-1} and the wavevector of the ordered structure will be the q for which $\chi^0(q)$ shows its maximum value at T_N. If the matrix elements $M^{\mu\nu}$ are neglected, this peak in $\chi^0(q)$ will be pronounced if there are flat and parallel portions of the Fermi surface which can be translated onto one another by a single

wavevector q. This 'nesting' feature of the Fermi surface will give rise to a small energy denominator for the nesting wavevector $\underset{\sim}{q}$ and hence to a peak in $\chi^0(q)$. This reproduces Lomers argument.

The energy bands, density of states and the (100) section of the Fermi surface for paramagnetic Cr are shown in Fig. 4.2. These data are taken from the self consistent tight binding calculation of Rath and Callaway (1973). This calculation amounts to an approximate solution of the Hartree-Fock equations with the non local exchange potential replaced by the local statistical expression of Slater (1974). The 'nesting' property of the electron and hole octahedra is immediately obvious and the nesting wavevector $\underset{\sim}{Q}$ ranges from 0.955 to 0.976 $2\pi/a$ (100) in excellent agreement with the observed wavevector of the SDW in Cr. Similar results were also obtained in other band structure calculations, using the KKR method (Asano and Yamashita, 1967) and the APW method (G upta and Sinha (1971), Loucks (1965)).

4.1.4 Two band models for the SDW

Following Lomer's suggestion, a number of simplified models were proposed which treat only the exchange coupling between the two nesting portions of the Fermi surface and neglect all other interband contributions. These models vary in sophistication and complexity but all treat essentially the same Hamiltonian, within the Hartree-Fock approximation, for a given simplified band structure.

The two band Hamiltonian is of the form,

$$\hat{H} = \hat{H}_0 + \hat{H}_1 \tag{4.3a}$$

where $\hat{H}_0$ is the sum of one electron energies for all bands and $\hat{H}_1$ represents the screened Coulomb interaction $V(\underset{\sim}{r} - \underset{\sim}{r}')$ between the electrons in band 'a' centred at Γ and the electrons in band 'b', the hole band centred at H. That is,

$$\hat{H}_0 = \sum_{\nu} \sum_{\underset{\sim}{k}\sigma} E^{\nu}_{\underset{\sim}{k}\sigma} \hat{n}^{\nu}_{\underset{\sim}{k}\sigma} \tag{4.3b}$$

Fig.4.1 The primary SDW in pure Cr.

Fig.4.2 Energy bands, density of states and (100) section of the Fermi surface of paramagnetic Cr. (Rath and Callaway (1973)). The main Fermi surface features are:

(a) a large closed hole octahedron at H = $\frac{2\pi}{a}$ (100)

(b) a smaller closed electron octohedron at Γ = (000)

(c) six electron balls situated along the ΓH axis, which together with the surface (b) make up the electron 'jack'

(d) six ellipsoidal hole surfaces at the N points, π/a ($\frac{1}{2}$,$\frac{1}{2}$,0)

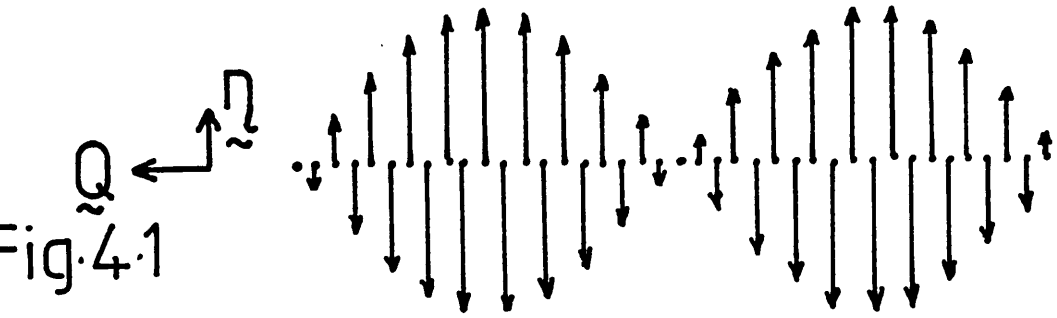
Q
Ω
body corner
body centre

Fig·4·1

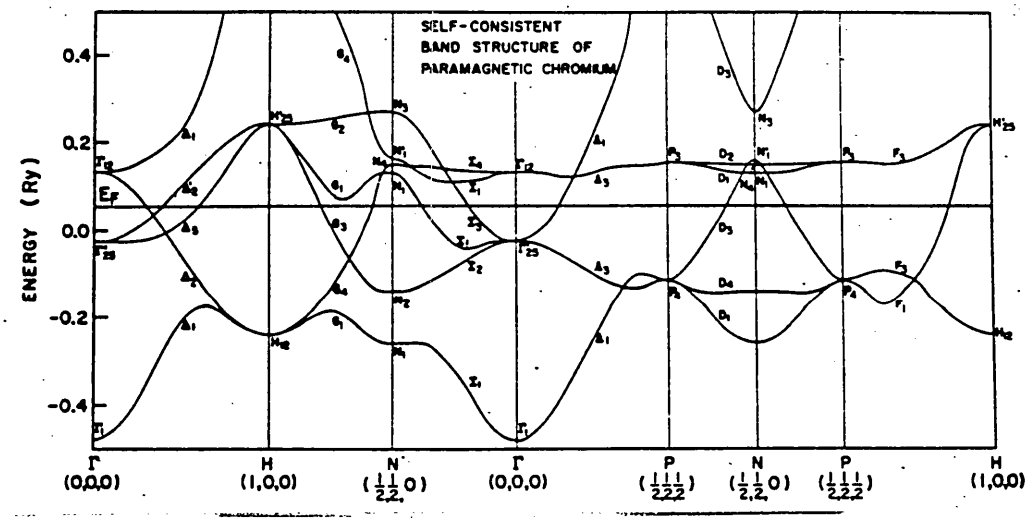
SELF-CONSISTENT
BAND STRUCTURE OF
PARAMAGNETIC CHROMIUM
ENERGY (Ry)
0.4
0.2
0.0
-0.2
-0.4
Γ (0,0,0)
H (1,0,0)
N (1/2,1/2,0)
Γ (0,0,0)
P (1/2,1/2,1/2)
N (1/2,1/2,0)
P (1/2,1/2,1/2)
H (1,0,0)

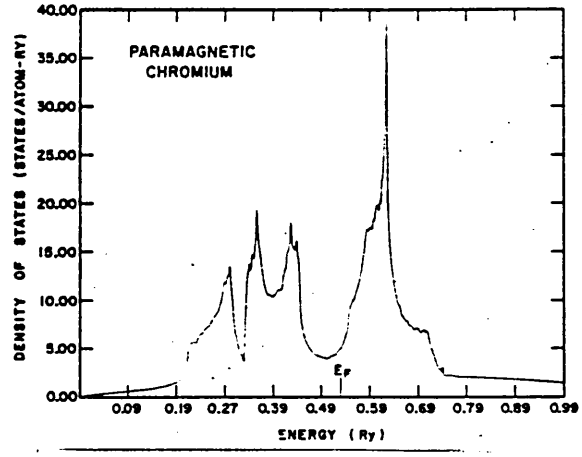
PARAMAGNETIC
CHROMIUM
DENSITY OF STATES (STATES/ATOM-RY)
40.00
35.00
30.00
25.00
20.00
15.00
10.00
5.00
0.00
0.09 0.19 0.27 0.39 0.49 0.59 0.69 0.79 0.89 0.99
ENERGY (Ry)

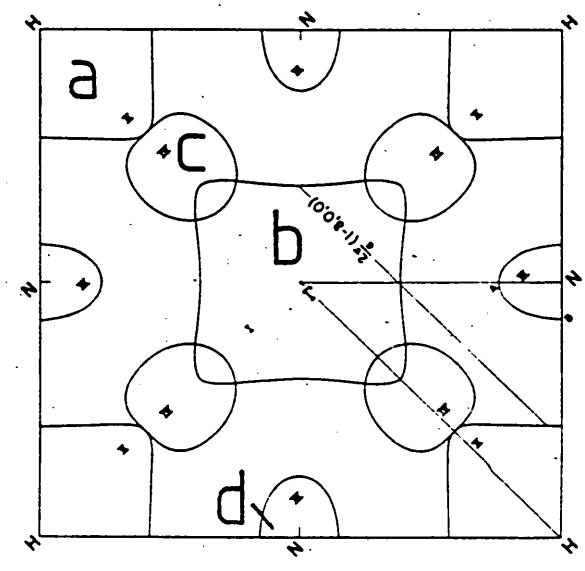
a
c
b
d
H
N
(100)-(1-10)

Fig·4·2

and

$$\hat{H}_1 = \sum_{\underset{\sim}{k}\underset{\sim}{k}'\underset{\sim}{q}} \sum_{\sigma\sigma'} V_{\underset{\sim}{k}\underset{\sim}{k}'} \hat{a}^{+}_{\underset{\sim}{k}+\underset{\sim}{q}\sigma} \hat{a}_{\underset{\sim}{k}\sigma} \hat{b}^{+}_{\underset{\sim}{k}'-\underset{\sim}{q}\sigma'} \hat{b}_{\underset{\sim}{k}'\sigma'} \qquad (4.3c)$$

where $E^{\nu}_{\underset{\sim}{k}\sigma}$ are the one electron energies for wavevector $\underset{\sim}{k}$, spin σ and band index ν, $n^{\nu}_{\underset{\sim}{k}\sigma}$ is the appropriate number operator and the operators $\hat{a}^{+}$, $\hat{a}$ and $\hat{b}^{+}$, $\hat{b}$ are creation and annihilation operators for electrons in bands a and b. The matrix element of the screened Coulomb interaction between the electrons ($V_{\underset{\sim}{k}\underset{\sim}{k}'}$) is usually replaced by a constant, effective value I (as in equation 4.2a) which may be written $I = \gamma^2 J$ where γ is an average overlap integral and J reflects the strength of the interaction.

The properties of this Hamiltonian have been almost exclusively been studied in the Hartree Fock approximation. According to this scheme $\hat{H}_1$ is written in the form,

$$\hat{H}_1 = \hat{\underset{\sim}{V}}.\hat{\underset{\sim}{\sigma}} \quad \text{with} \quad \hat{\underset{\sim}{V}}(\underset{\sim}{r}) = -J\,\hat{\underset{\sim}{s}}(\underset{\sim}{r})$$

which represents the interaction of a particular electron with spin $\hat{\underset{\sim}{\sigma}}$ with the average exchange field $\hat{\underset{\sim}{V}}(\underset{\sim}{r})$ produced by the electrons in bands a and b. This exchange field is simply proportional to the nett spin density $\underset{\sim}{s}(\underset{\sim}{r})$ and must be determined self consistently. Within the Hartree Fock (HF) approximation $\hat{H}_1$ may be written, Nakanishi and Kasuya (1977),

$$\hat{H}_1 = -\sum_{\underset{\sim}{k}\underset{\sim}{q}} \sum_{\sigma\sigma'} \Delta_{\underset{\sim}{q}} \hat{b}^{+}_{\underset{\sim}{k}+\underset{\sim}{q}\sigma} (\hat{\underset{\sim}{\sigma}})_{\sigma\sigma'} \hat{a}_{\underset{\sim}{k}\sigma'} + \text{H.C.} + \frac{1}{I} \sum_{\underset{\sim}{q}} |\Delta_{\underset{\sim}{q}}|^2 \qquad (4.4a)$$

where $\Delta_{\underset{\sim}{q}}$ is to be determined self consistently via

$$\bar{\underset{\sim}{n}}\,\Delta_q = I \sum_{\underset{\sim}{k}} \sum_{\sigma\sigma'} \langle \hat{a}^{+}_{\underset{\sim}{k}\sigma} (\hat{\sigma})_{\sigma\sigma'} b_{\underset{\sim}{k}+\underset{\sim}{q}\,\sigma'} \rangle \qquad (4.4b)$$

where $\bar{\underset{\sim}{n}}$ is a unit vector along the direction defined by this average. In writing this expression the original Hamiltonian has been re-arranged to make use of the Pauli matrices $\hat{\underset{\sim}{\sigma}}$, to emphasise the form $\underset{\sim}{V}.\underset{\sim}{\sigma}$ of the interaction between a given spin and the average self

sistent exchange field. Now, in a normal paramagnetic system the expectation value $\Delta_{\underset{\sim}{q}}$ is clearly zero as the motion of electrons in band a and b are on average uncorrelated. However, it is precisely the coherent motion of such electrons which gives rise to the long range magnetic order in the SDW state. In fact, $\bar{\underset{\sim}{n}}\Delta_{\underset{\sim}{q}}$ can ultimately be related to the SDW vector amplitude and plays the role of an order parameter. (Writing the Hamiltonian in this form amounts to expressing the product of pairs of operators $\hat{a}^{+}\hat{b}$ in terms of their mean and fluctuating parts and subsequently expanding up to terms which are bilinear in the fluctuations.)

The first of these two band models was proposed by Fedders and Martin (1966). In this model the electron surface at Γ and the hole surface at H were approximated by two spheres of equal radius which nest perfectly into each other under a translation of $\frac{1}{2}\underset{\sim}{G} = \underset{\sim}{Q}_0$. No other sections of the Fermi surface were considered. The electron and hole dispersion relations were assumed to be linear and isotropic about Γ and H,

$$\begin{aligned} E^{a}_{\underset{\sim}{k}} &= E_F + \hbar v_a(|\underset{\sim}{k}| - k_F) \\ E^{b}_{\underset{\sim}{k}+\underset{\sim}{Q}_0} &= E_F - \hbar v_b(|\underset{\sim}{k}| - k_F) \end{aligned} \tag{4.5a}$$

where a and b are band indices (cf. 4.4) and v_a, v_b are Fermi velocities. The radius of the sphere is k_F. In this treatment, Fedders and Martin (FM) consider only pairing between electron states in band a and hole states in band b whose momenta differ by $\hbar Q_0$ and which have opposite spin. This amounts to considering only those terms which contribute to a commensurate linear SDW polarized in the x direction, that is,

$$\bar{\underset{\sim}{n}}\Delta_{\underset{\sim}{q}} = \Delta\ \delta_{\underset{\sim}{q}\underset{\sim}{Q}}\bar{\underset{\sim}{x}} \tag{4.5b}$$

with

$$\Delta = I \sum_{\underset{\sim}{k}} \langle b^{+}_{\underset{\sim}{k}\uparrow} a_{\underset{\sim}{k}\downarrow}\rangle + \text{H.C.} \tag{4.5c}$$

Assuming Δ to be non zero, the Hamiltonian (eq. 4.4) may be

diagonalized to give the eigenvalues

$$E_{\underset{\sim}{k}}^{\pm} = \frac{1}{2}\left[E_{\underset{\sim}{k}}^{a} + E_{\underset{\sim}{k}}^{b}\right] \pm \left[\frac{1}{4}(E_{\underset{\sim}{k}}^{a} - E_{\underset{\sim}{k}}^{b})^2 + \Delta^2\right]^{\frac{1}{2}} \tag{4.6a}$$

which opens an energy gap of magnitude $g = 2\Delta$ at the Fermi surface. The mixing of states in bands a and b in turn must modify the value Δ and for self consistency

$$\Delta = -I \sum_{(\text{occ } k)} \frac{\Delta}{2E_{\underset{\sim}{k}}^{\pm}} \tag{4.6b}$$

At $T = 0$, in the limit of weak exchange coupling $N(E_F)I \ll 1$, this may be solved to give the zero temperature order parameter

$$\Delta(0) = 2D \exp(-1/2N(E_F)I) \tag{4.7a}$$

where D is the band width and $N(E_F)$ the average density of states of the bands a and b at the Fermi surface. Having shown that a self consistent solution with $\Delta \neq 0$ exists, Fedders and Martin proceed to demonstrate that it has a lower energy than the paramagnetic state ($\Delta = 0$) below the Néel temperature

$$k_B T_N = 2 \frac{\gamma_e}{\pi} D \exp(-1/2N(E_F)I) \tag{4.7b}$$

$-\ln(\gamma_e)$ is the Euler constant 0·57 . The $T = 0$ order parameter and T_N are proportional, for example if $v_a = v_b$,

$$\Delta(0) = \frac{\pi}{\gamma_e} k_B T_N \tag{4.7c}$$

The temperature dependence of the order parameter follows the BCS relationship found in the theory of superconductivity,

$$1 = N(E_F)I \int_0^D dE(E^2+\Delta^2)^{-\frac{1}{2}}(1-2f(\sqrt{E^2+\Delta^2}))$$

where f(x) is the Fermi function. This implicit equation may be

approximated by the explicit expression

$$\Delta(T)/\Delta(0) \simeq B_{\frac{1}{2}}(T/T_N) \qquad (4.7d)$$

where $B_{\frac{1}{2}}(x)$ is the Brillouin function for $J = \frac{1}{2}$. The FM theory is, incidently, mathematically identical to the BCS theory of superconductivity.

This simple model was extended by Shibatani, Motizuki and Nagamiya (1969) using a more realistic model for the Fermi surface. The electron and hole nesting surfaces were approximated by perfect octahedra of different size: the hole octahedron was assumed to be slightly larger than the electron surface in accordance with the band structure calculations (section 4.1.2).This imperfect nesting model allows the formation of an incommensurate SDW with $\underset{\sim}{Q} \neq \frac{1}{2}\underset{\sim}{G}$ as well as a commensurate SDW, $\underset{\sim}{Q} = \underset{\sim}{Q}_0 = \frac{1}{2}\underset{\sim}{G}$ discussed by FM. A third portion of Fermi surface, an electron reservoir, termed band 'r' was also added. This band, which can be identified with the electron balls at N, allows a flow of electrons to enlarge or diminish the nesting octahedra during the formation of the SDW. Shibatani et. al. (SMN) find that if the reservoir is neglected, the incommensurate SDW (ISDW) state with wavevector $\underset{\sim}{Q}$ equal to the nesting wavevector always has lower energy than the equivalent helical or commensurate SDW. If the reservoir is taken into account the wavevector may be shifted from the nesting value. The magnitude of this shift was found to depend on the size of the reservoir and the degree of nesting. A sudden shift in $\underset{\sim}{Q}$ from one incommensurate value to another is observed as the degree of nesting is changed. The reservoir is also found to be necessary in order to obtain a reasonable value for the antiferromagnetic moment.

Rice (1970) also considers imperfect nesting using a model bandstructure with spherical electron and hole pockets of unequal radii as well as a nonmagnetic reservoir. The dispersion relations for the electron and hole pockets, measured relative to the Fermi energy were taken as, $\hbar = 1$,

$$E^{a}_{\underset{\sim}{k}} = v_F(k-k_{Fa}) = v_F(k-k_F)+h$$

$$E^{b}_{\underset{\sim}{k}+\underset{\sim}{Q}_0} = -\, v_F(k-k_{Fb}) = -\, v_F(-k_F)+h \qquad (4.8a)$$

where k_F is defined as the average Fermi radius of the two spheres and $h = v_F(k_{Fa}-k_{Fb})$ is the amount by which the Fermi level would need to be altered in order to achieve perfect nesting (Fig. 4.3). Rice considers a linear SDW with wavevector $\underset{\sim}{Q}$ which is incommensurate with the lattice, $\underset{\sim}{Q} - \underset{\sim}{Q}_0 = \delta$, so the order parameter is (cf.eq.4.4)

$$\bar{n}\,\Delta_{\underset{\sim}{q}} = \frac{1}{\sqrt{2}}(\delta_{\underset{\sim}{q}-\underset{\sim}{\delta}} + \delta_{\underset{\sim}{q}\underset{\sim}{\delta}})\Delta\bar{\underset{\sim}{x}} \qquad (4.8b)$$

with

$$\Delta = I \sum_{\underset{\sim}{k}} \langle \hat{b}^{+}_{\underset{\sim}{k}+\underset{\sim}{\delta}\uparrow} \hat{a}_{\underset{\sim}{k}\downarrow} \rangle + \text{H.C.}$$

and the self consistent SDW state is defined by three coupled equations for Δ, $\delta = |\underset{\sim}{Q}-\underset{\sim}{Q}_0|$ and h' the Fermi level of the SDW state as a function of h and n -the density of states of the reservoir compared to $N(E_F)$.

If the spheres are found to differ too greatly in size, the SDW cannot exist, even at T = 0. Rice finds the critical value of the nesting parameter to be $h = 0.753\ \Delta_{00}$, where Δ_{00} is the hypothetical order parameter for the SDW state having $\delta = h = 0$ at T = 0 and reduces to the FM result (4.7a) in the absence of a reservoir. The SDW state which first occurs below this critical value has a wavevector determined by the maximum of the unenhanced paramagnetic susceptibility $\underset{\sim}{\delta} \simeq 1.2\ h/v_F$. As the degree of nesting is increased, at T = 0, the wavevector of the SDW snaps into the commensurate wavevector $\underset{\sim}{Q}_0$ once h is below a critical value determined by the properties of the reservoir. If the reservoir is large, this first order change occurs for h below $0.71\ \Delta_{00}$. In the other limit, $n \to 0$, the commensurate phase is only found at perfect nesting, h = 0.

The temperature variation of the order parameter and wavevector may also be calculated as a function of nesting. The

Fig.4.3 Schematic energy bands for the Rice (1970) unequal sphere model.

Fig.4.4 Magnetic phase diagram for the unequal sphere model as a function of the imperfect nesting parameter h/Δ_o. The solid curve is the Hartree-Fock result (Rice (1970)). The more exact calculation of Hasegawa (1968) is shown by the dashed curve.

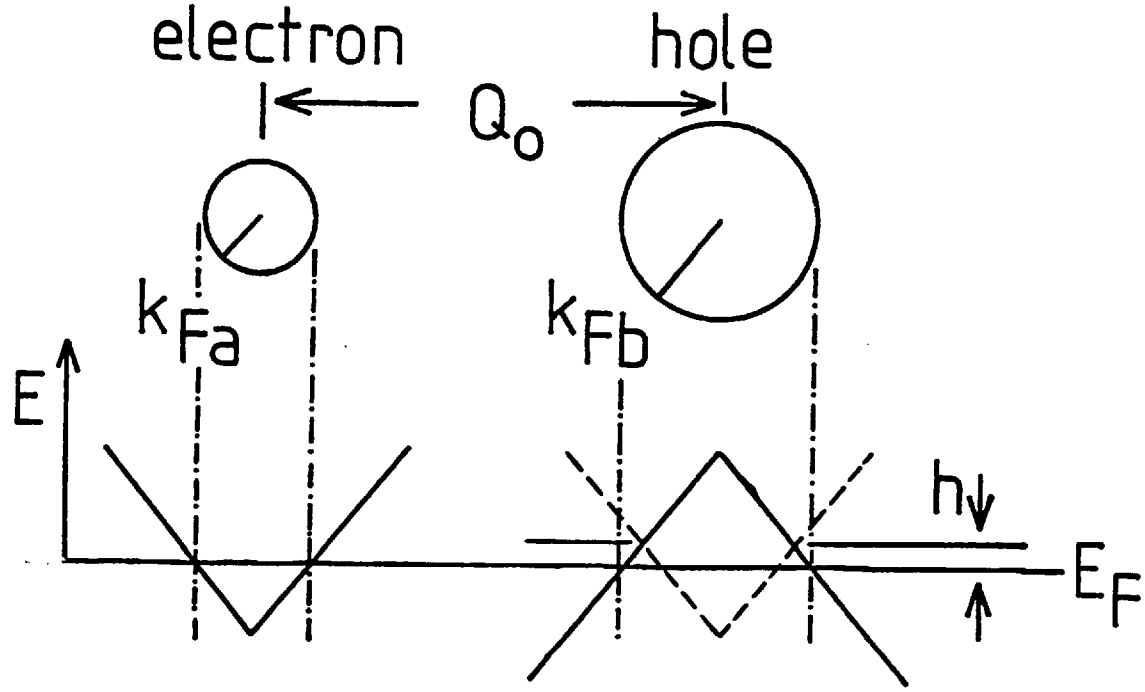

Fig.4.3 $E_a(k)$ $E_b(k)$

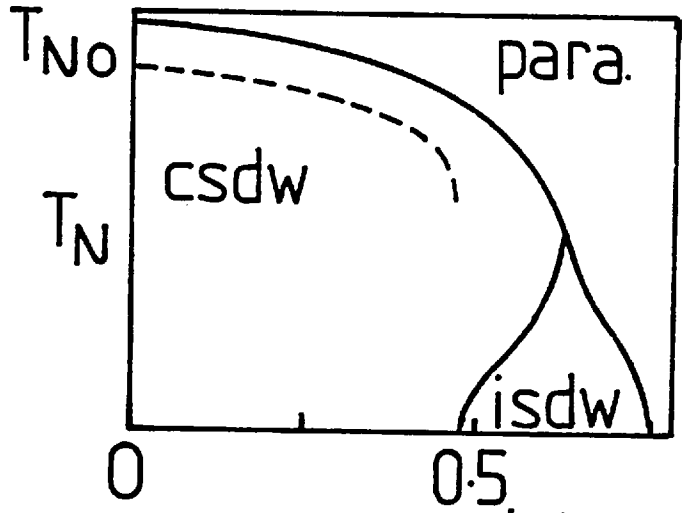

Fig.4.4

resulting phase diagram is shown in Fig. 4.4. A value of n = 1 has been assumed, as the density of states in pure Cr is approximately halved at T_N.

These ideas have been extended by a number of later workers: for example Kotani (1974, 78). The extension to the alloy problem will be discussed in the next section.

4.1.5 Alloying behaviour

The effect of even a small degree of alloying on the magnetic properties of Cr is dramatic. For example, the addition of 1% V is sufficient to lower the Néel temperature by 100 K whereas the addition of 1% Mn raises the Néel temperature by 150 K. To illustrate these rapid changes with alloying, the variation of T_N as a function of excess electron concentration for a number of dilute Cr alloys selected from the enormous number of experimental investigations undertaken in recent years is presented in Fig. 4.5. These data have been extracted from the work of Koehler et al. (1966), Arajs et al. (1973) and Booth et al. (1978). The variation of ordered moment and the wavevector for CrMn, CrRe and Cr(MnV) alloys (Komura, 1967, Lebech and Mikke, 1972) is also presented.

For the 'normal' solutes presented in Fig. 4.5 the variation of T_N, $\bar{\mu}$ and Q depends to a first approximation only on the electron to atom ratio of the alloy. The addition of V, Nb, Ta and Ti which reduce the electron to atom ratio reduce T_N, $\bar{\mu}$ and $\underset{\sim}{Q}$. On the other hand, the addition of Mn, Tc, Re, Ru, Os, Ir and Pt which increase the electron to atom ratio increase the Néel temperature and ordered moment, which reach a maximum of some 700 K and 0.75 μ_B at high concentrations. The wavevector of the SDW also increases with increasing electron to atom ratio until $\underset{\sim}{Q}$ abruptly changes from incommensurate to commensurate in a narrow range of temperature centred about an excess electron concentration of $\sim$ 1%. A simple two sublattice antiferromagnet is then found at higher concentrations. Furthermore, alloying with isoelectronic Mo and W leads to only a relatively small decrease in T_N. The presence of 1% Mo and 1% W

Fig.4.5 Variation of T_N with alloying for 'normal' solutes in Cr. The dotted line is the theoretical variation according to the Sato-Maki model (1973).

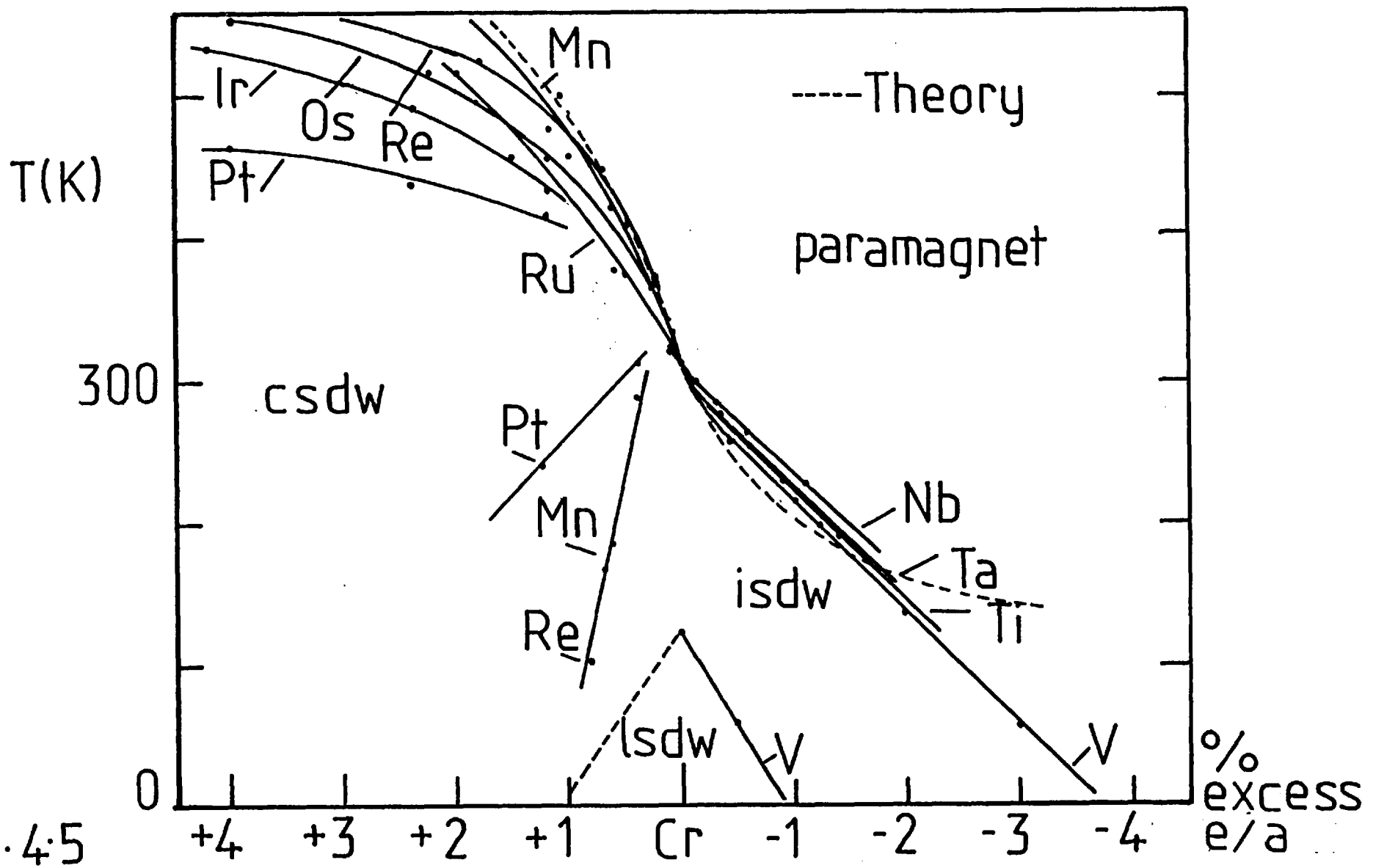
T(K)
300
0
Mn
Ir
Os
Re
Pt
Ru
-----Theory
paramagnet
csdw
Pt
Mn
Re
isdw
Nb
Ta
Ti
lsdw
V
V
%
excess
e/a
+4
+3
+2
+1
Cr
-1
-2
-3
-4

Fig. 4.5

depress T_N by 17 K and 33 K respectively (Arajs et al. 1978), such a small change may be expected as e/a remains constant in this case.

The magnetic behaviour of these Cr alloys may be understood in terms of changes in Fermi surface nesting. If we assume the Rice (1970) unequal sphere model, making the rigid band assumption, the addition of solutes to the left of Cr in the periodic table increase the value of h i.e. the electron sphere becomes smaller and the hole sphere larger than for pure Cr. The nesting between these two pieces of Fermi surface is thus reduced, leading to a decrease in T_N, $\bar{\mu}$ and Q. Alloying with components to the right of Cr on the other hand decrease the value of h, by allowing the electron sphere to increase in size with respect to the hole sphere, giving an increase in T_N, Q and $\bar{\mu}$. A sudden transition to the commensurate structure is also predicted as h becomes less than a critical value.

To go beyond this rigid two band approximation it is necessary to consider how the band structure is altered by the impurity atoms. In the context of the Rice model this possibility can be included by the ad hoc variation of Δ_{00} with concentration. For example, one may expect a small decrease in T_N with isoelectronic alloying with 4d Mo and 5d W due to the reduction in the effective interaction strength I. It is more satisfactory to consider the scattering from the impurity atom explicitly, by the addition of a scattering term $\hat{H}_2$ to the two band Hamiltonian eq. (4.3). Following Zittartz (1967),

$$\hat{H}_2 = \sum_{\underset{\sim}{k}\underset{\sim}{k}'}{}' U(\underset{\sim}{k} - \underset{\sim}{k}')[\hat{a}^{\dagger}_{\underset{\sim}{k}\sigma}\hat{a}_{\underset{\sim}{k}'\sigma} + \hat{b}^{\dagger}_{\underset{\sim}{k}\sigma}b_{\underset{\sim}{k}'\sigma} + \hat{r}^{+}_{\underset{\sim}{k}}\, r_{\underset{\sim}{k}'\sigma}] \qquad (4.9a)$$

takes account of the intraband scattering of electrons in bands a, b and r by impurity atoms situated at lattice sites $\underset{\sim}{R}_i$. Here

$$U(\underset{\sim}{q}) = \sum_i U(\underset{\sim}{R} - \underset{\sim}{R}_i)e^{i\underset{\sim}{q}\cdot\underset{\sim}{R}} \qquad (4.9b)$$

is the Fourier transform of the interaction, which is taken to be spin independent, that is "normal".

Zittartz (1967) investigated this problem by applying the theory of Abrikosov and Gorkov (1960), originally proposed to deal with impurity scattering in superconductivity, to the case of isoelectronic Cr alloys. It was found that the spin independent impurity scattering $\hat{H}_2$, which acts with opposite sign on electron and hole states, is very effective in decorrelating the electron-hole pairs which are responsible for the SDW state. One notes, by contrast, that such normal impurity scattering has no effect on the electron hole pairs in BCS superconductivity. In effect, the normal impurity produces an electric field which breaks the symmetry of the two band order parameter $\langle \hat{b}^{\dagger}_{k\sigma} a_{k-\sigma} \rangle$ in the same way as a magnetic field breaks the symmetry of a Cooper pair $\langle \hat{C}_{k\sigma} \hat{C}_{-k-\sigma} \rangle$. The effect of such pair breaking is to reduce the Néel temperature. In the perfect nesting model considered by Zittartz, where the normal impurity is isoelectronic with Cr, T_N is found to decrease according to the Abrikosov-Gorkov expression,

$$- \ell n \frac{T_N}{T_{NO}} = \psi(\frac{1}{2} + \frac{\alpha}{2\pi T_N}) - \psi(\frac{1}{2}) \tag{4.10a}$$

where T_{NO} is the Néel temperature of the pure material, $\psi(z)$ is the digamma function and α is a pair breaking parameter which depends on the details of the scattering potential but is linear in concentration,

$$\alpha \sim c \int d\Omega |U(\theta)|^2$$

According to (4.10a) the SDW can only exist if the pair breaking parameter is less than a critical value,

$$\alpha_C = \frac{\pi}{2\gamma_e} \quad T_{NO} \tag{4.10b}$$

and hence a critical concentration for SDW order exists. In contrast to the previous two band models it is found that the SDW does not necessarily introduce an energy gap at the Fermi surface. Beyond a critical value of the pair breaking parameter

$$\alpha'_c = 2\alpha_c \exp(- \frac{\pi}{4}) \tag{4.10c}$$

which is 91% of the value which destroys the SDW completely, a gapless region is found to extend from T=0 to T_N. In general, the gapless régime is restricted to a narrow band around T_N (Fig. 4.6), where the broadening in electron energy levels due to scattering is of the same magnitude as the order parameter and the energy gap disappears, even though the system is still in an ordered state.

The combined effects of pair breaking and changes in excess electron concentration were considered by Sato and Maki (1973) using the SMN imperfect nesting band structure. In this case the dominant mechanism for pair breaking was assumed to be electron-phonon scattering, which corresponds to a pair breaking parameter which is proportional to temperature but independent of concentration. For CDSW alloys, T_N was determined by

$$-\ln\frac{T_N}{T_{NO}} = \mathrm{Re}\{\psi(\tfrac{1}{2}+\frac{\alpha}{2\pi T_N}+i\frac{h}{2\pi T_N}) - \psi(\tfrac{1}{2})\} \tag{4.11}$$

where T_{NO} is the hypothetical Néel temperature for $\alpha = h = 0$. The nesting parameter h is defined in the same way as in the Rice model. A more complicated result is found for the ISDW. With a physically reasonable choice of T_{NO} and α the concentration dependence of T_N for dilute CrMn, CrRe and CrMnV alloys could be reproduced quite well (as shown in Fig. 4.5).

Variations on this theme have been proposed by many authors. The most comprehensive treatment is that of Nakanishi and Kasuya (1977) using the SMN imperfect nesting model including an electron reservoir as well as inter and intra band scattering via the term

$$\begin{aligned}\hat{H}_2 = \sum_{\underset{\sim}{R}_i}\sum_{\underset{\sim}{k}\underset{\sim}{k}'}\sum_{\sigma\sigma'} e^{i(\underset{\sim}{k}-\underset{\sim}{k}').\underset{\sim}{R}_i}\big[&(V_{aa})_{\sigma\sigma'}\hat{a}^{\dagger}_{\underset{\sim}{k}'\sigma'}\hat{a}_{\underset{\sim}{k}\sigma} \\ &+ (V_{bb})_{\sigma\sigma'}\hat{b}^{\dagger}_{\underset{\sim}{k}'\sigma'}\hat{b}_{\underset{\sim}{k}\sigma} + (V_{rr})_{\sigma\sigma'}\hat{r}^{\dagger}_{\underset{\sim}{k}'\sigma'}\hat{r}_{\underset{\sim}{k}\sigma} + (V_{ab})_{\sigma\sigma'}\hat{a}^{\dagger}_{\underset{\sim}{k}'\sigma'}b_{\underset{\sim}{k}\sigma} \\ &+ (V_{ar})_{\sigma\sigma'}\hat{a}^{\dagger}_{\underset{\sim}{k}'\sigma}\hat{r}_{\underset{\sim}{k}\sigma} + (V_{br})_{\sigma\sigma'}b_{\underset{\sim}{k}'\sigma'}r_{\underset{\sim}{k}\sigma}\big] + \text{H.C.}\end{aligned} \tag{4.12}$$

Fig.4.6 Depression of T_N by scattering processes for the equal sphere model. (Zittartz (1967)). Here α is the pair breaking parameter. The region of gapless SDW order is shaded.

Fig.4.7 The interband contributions to the generalized non-interacting susceptibility of paramagnetic Cr at 312K. (Windsor (1972)). The weak contribution from the nesting bands Γ-H should be noted.

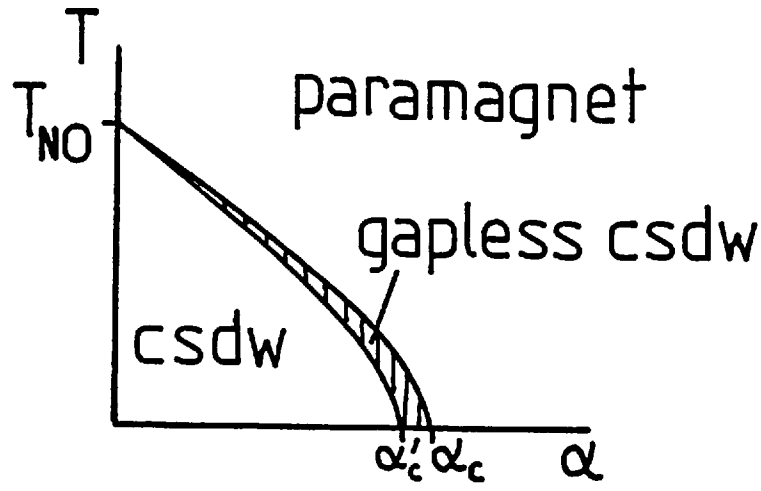
T
T_{NO}
paramagnet
gapless csdw
csdw
α_c'
α_c
α

Fig. 4·6

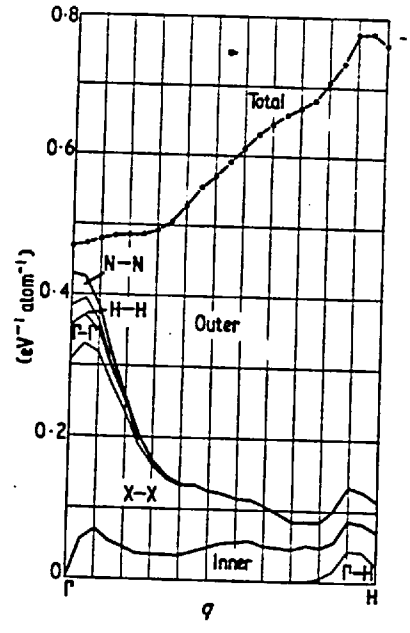
0·8
0·6
0·4
0·2
0
Total
N–N
H–H
Γ–Γ
Outer
X–X
Inner
Γ–H
Γ
H
q
(eV⁻¹ atom⁻¹)

Fig. 4·7

where $(V_{\alpha\beta})_{\sigma\sigma'} = \delta_{\sigma\sigma'} V_{\alpha\beta}$ describes normal scattering from randomly distributed impurities and may also simulate electron-phonon scattering. The stability of the ISDW and CSDW states were investigated as the degree of nesting and scattering strength were varied. The CSDW state was found to be stable below a Néel temperature given by

$$-\ln \frac{T_N}{T_{NO}} = \mathrm{Re}\{\psi(\tfrac{1}{2} + \frac{\alpha_1}{2\pi T_N} + \frac{\alpha_r}{2\pi T_N} + i\,\frac{h}{2\pi T_N}) - \psi(\tfrac{1}{2})\} \qquad (4.13)$$

where $k\alpha_r = 2\pi N(E_F)C(V_{aa}^2 + V_{ab}^2)$ is the normal pair breaking due to bands a and b, and $k\alpha_r = \pi N_r(E_F)C\,V_{ar}^2$ is the normal pair breaking due to the reservoir having a density of states $N_r(E_F)$. These authors also extended the argument to deal with the spin dependent scattering which occurs in those Cr alloys with magnetic impurities e.g. CrCo, CrNi, CrPd and CrFe. These alloys are 'anomalous' in the sense that they do not follow the general trends outlined in this section and CrFe alloys, in particular, are the topic of section 4.2.

4.1.6 Discussion

The itinerant electron nesting model for Cr and its alloys gives a good account of a wide range of behaviour. However this picture is not without its difficulties. Most serious is that the SDW-paramagnetic transition in Cr is first order whereas all the models in section 4.1.4 predict a second order transition. On a formal level, the argument put forward in section 4.1.3, which is based on the susceptibility is valid only for a second order transition.

Young and Sokoloff(1974) propose that a first order transition cannot be explained using a two band Hartree Fock model and demonstrate that a first order transition may be obtained in a three band model provided higher order harmonics of the SDW are taken into account. A second harmonic charge density wave (CDW) and third harmonic SDW were predicted, and subsequently observed experimentally

by Tsunoda et al. (1974) and Pynn et al. (1976). More detailed calculations were performed by Kotani (1974, 1978). A first order transition was found in this case if the electron-phonon coupling was sufficiently large. Since these mechanisms rely on the presence of harmonics of the SDW they cannot operate in a commensurate system. The fact that a first order transition is observed for several CSDW CrFe alloys (Suzuki, 1976) suggests that this explanation is invalid. The order of the transition and the role of higher order harmonics remains an open question. As the observed first order transition is almost indistinguishable from a second order transition this question may only have formal significance.

Let us assume, for arguments sake, that the susceptibility is a useful function in the description of a 'weak' first order transition. According to Windsor's (1972) calculation of the paramagnetic susceptibility of Cr, the major part of the noninteracting susceptibility $\chi^0(q)$ (eq. 4.2) arises from bands more than $\frac{1}{2}$ eV from the Fermi surface. The Γ-H nesting contribution is small and peaks in the vicinity of the nesting wavevector. The overall maximum in the generalized noninteracting susceptibility is determined by the position of this small sharply peaked nesting contribution which sits on top of the much broader maximum arising from the other bands (Fig. 4.7). This result contradicts the basic 'two band' assumption,but may have been anticipated by the need to include an electron reservoir in order to generate a reasonable value of the ordered moment. A more realistic model for Cr must include the broad response of non nesting bands near $\frac{1}{2}\,\underset{\sim}{G}$.

Windsor (1972) and Gupta and Sinha (1971) also point out that the basic nesting argument itself is invalid because the matrix elements $M^{\mu\nu}_{k\ k+q}$ which occur in the Lindhard expression for the susceptibility (eq. 4.2) are strongly q dependent and cannot be treated as slowly varying or constant. Thus the peak in $\chi^0(q)$ cannot be determined solely by satisfying the energy denominator with nesting portions of Fermi surface, the matrix elements must be taken into account. The difference is fortuitously small according

to Windsor's calculation and the peak in the Γ-H contributions is found to lie very close to the nesting wavevector.

The validity of the Hartree Fock approximation for the two band models of Rice and SMN was investigated by Hasegawa (1978). As expected, the effect of spin fluctuations is to depress the tendency toward magnetic order as illustrated in Fig. 4.4.

In view of these difficulties it is worthwhile noting that a theory for the SDW in Cr can be constructed without the nesting requirement. Teraoka and Kanamori (1977), using an extension of the single orbital Anderson model, are able to describe the SDW first and third harmonic, the CDW, the magnetic moment at the incommensurate-commensurate transition and the strain wave with a great deal of success. A first order transition is also found.

4.2 Previous work on CrFe antiferromagnetic alloys

4.2.1 Metallurgy of the CrFe alloy system

The equilibrium phase diagram for Cr-Fe binary alloys is shown schematically in Fig. 4.8. According to Hansen's (1958) diagram a complete range of b.c.c. solid solutions (α) exist from pure Cr to pure Fe, apart from an f.c.c. γ loop for Fe concentrations up to 13% and a σ phase which forms for middiagram alloys below 815°C. Later work summarized by Elliots' diagram (1965) shows the eutectoidal decomposition of the σ phase at 520°C. There is no evidence for atomically ordered compounds Fe_3Cr, FeCr or $FeCr_3$.

A low temperature miscibility gap is also present i.e. the b.c.c. solid solution retained after quenching from high temperature is only metastable at room temperature. Prolonged ageing of quenched alloys will ultimately result in the separation of the alloy into Fe and Cr rich precipitates. At room temperature this transformation is extremely slow. The reaction is faster at 475°C; Fisher, Dulis and Carroll (1953) found fine Cr rich precipitates of some 200 Å in diameter after annealing an 82% Fe alloy at 475°C for 1-3 years. More recent work by Chandra and Schwartz (1971) and de Nys and Gielen (1971) suggests that the decomposition may proceed by nucleation and growth of the second phase for alloys close to pure Fe or pure Cr (as in the previous case) or via the spinodal decomposition of alloys in middiagram which lie within the chemical spinodal sketched in Fig. 4.8. These workers determined the rate of decomposition at 475°C for alloys of 40-80% Fe. Solute redistribution occured even at short annealing times (30h) for alloys lying within the miscibility gap but outside the spinodal. However no change could be seen even after 1050 h for alloys lying within the spinodal.

The b.c.c. solid solution found in equilibrium outside the miscibility gap is not atomically random and there is a strong tendency for Fe atoms to cluster. This has been confirmed by a number of techniques, notably by neutron diffuse scattering (Aldred, Rainford, Kouvel and Hicks, 1976) where such clustering was observed in alloys quenched from high

temperature in the α phase field.

The tendency for Fe segregation to a greater or lesser degree within the CrFe alloy system makes the magnetic properties very sensitive to heat treatment. Thus to ensure a small and reproducible amount of atomic short range order all alloys used in the present work were quenched rapidly from the same temperature (∿ 1100°C). Furthermore all alloys lying within the room temperature miscibility gap were exposed to the smallest possible amount of room temperature ageing, not exceeding ∿ 200 h. This precaution, as shown by the small angle scattering measurements in Ch. 5 was unnecessary because of the sluggish reaction rate at room temperature.

4.2.2 Dilute CrFe alloys (c < 5%)

The magnetic properties of antiferromagnetic CrFe alloys have attracted much theoretical and experimental interest over recent years. Most of this interest has revolved around the behaviour of the more dilute alloys (less than 5% Fe) whose properties are now known in detail.

4.2.2.1 Magnetic transitions in dilute CrFe alloys

The magnetic phase diagram for dilute CrFe alloys is presented in Fig. 4.9. The ordering temperatures have been selected from the neutron diffraction data of Arrott, Werner and Kendrick (1967) and Ishikawa, Hoshino and Endoh (1967), X-ray strain wave and lattice parameter measurements of Mori et al. (1974) and the specific heat data of Suzuki (1976) and Åstrom, Benediktsson and Rao (1978).

The addition of Fe to antiferromagnetic Cr causes a decrease in T_N, contrary to the general trend of raising T_N for solutes to the right of Cr in the periodic table (section 4.1.5). The transverse incommensurate SDW phase of pure Cr gives way to commensurate SDW order as the Fe concentration exceeds some 3%. For concentrations in the vicinity of the triple point a transition between the high temperature TSDW and low temperature CSDW phases occurs. In contrast to the CrMn system the commensurate - incommensurate phase boundary has a positive gradient with respect to impurity concentration. The longitudinal

Fig.4.8 Constitution diagram for Cr Fe alloys. (Hansen (1956)). The miscibility gap and spinodal are also shown.

Fig. 4.9 Magnetic phase diagram for dilute Cr Fe alloys. (Suzuki (1976)).

Fig.4.10 Ordered antiferromagnetic moment at 4.2K for dilute Cr Fe alloys. (O, Ishikawa et al (1967); ●, Arrott et al (1967)).

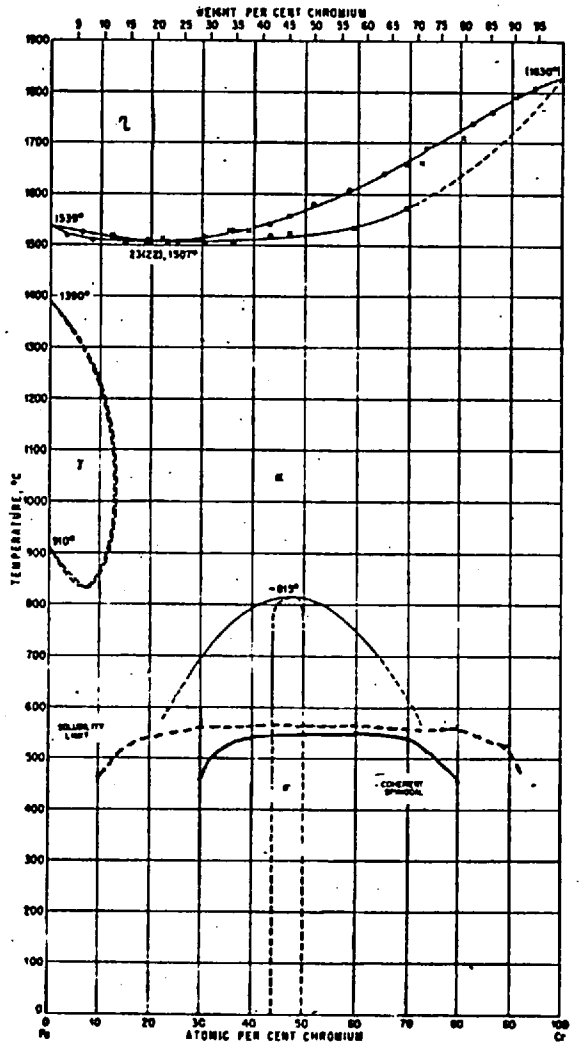

Fig·4·8

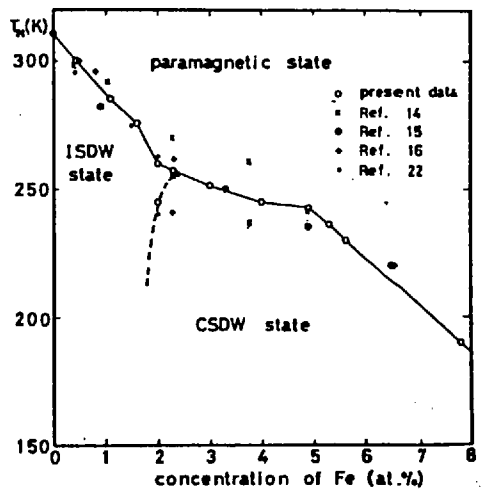

Fig·4·9

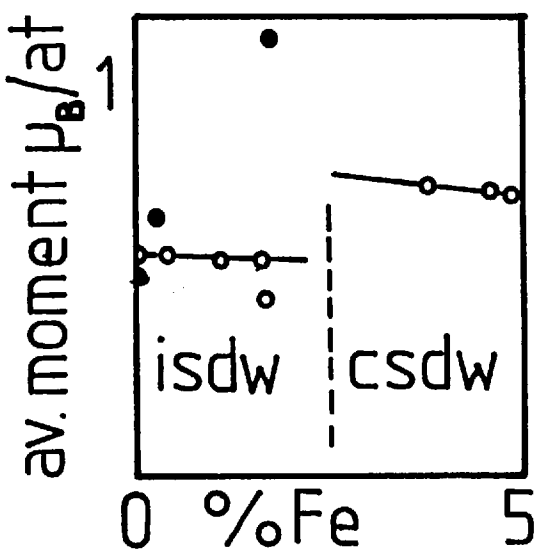

Fig·4·10

incommensurate SDW phase rapidly disappears with the addition of Fe, T_N reaching zero at $\sim$ 1%.

The commensurate - incommensurate (C-I), paramagnetic-incommensurate (P-I) and paramagnetic-commensurate (P-C) transitions are all of first order. Large volume changes accompany the P-C and C-I transitions for alloys between 2-4% Fe. The P-C transition becomes second order in the vicinity of 4.9% Fe (Suzuki, 1976) and this point provides a convenient upper limit to the 'dilute' concentration range.

According to the neutron diffraction measurements of Arrott, Werner and Kendrick (1967) both the wavevector and amplitude of the ISDW are increased by alloying with Fe. Ishikawa, Hoshino and Endoh (1967) find the amplitude of the ISDW to remain more or less constant in this phase. The fact that neither group observes a decrease in the ordered moment whilst T_N is decreased is significant.

The ordered moment ($\bar{\mu}$) increases as the SDW changes from incommensurate to commensurate. Ishikawa et al. (1967) note a change from 0.6 μ_B on the incommensurate side of the phase diagram at 1% Fe to 0.76 μ_B on the commensurate side at 3.75% Fe. The commensurate moment then decreases with increasing Fe concentration. At the highest concentration studied (4.9%) the moment was reduced to 0.73 μ_B. The data of Arrott et al. (1967) confirm these trends although the quantitative agreement is not good. These results are shown in Fig. 4.10.

The lack of agreement between the work of Arrott et al. (1967) and Ishikawa et al. (1967) is due in large part to sample homogeneity and difficulties in correction for extinction. As explained in the previous section, the sensitivity of the magnetic properties to heat treatment is also a major source of discrepancy.

4.2.2.2 The nature of the Fe moment in dilute CrFe alloys

Susceptibility measurements show that the SDW coexists with magnetic moments localized on the Fe sites. Much theoretical and experimental effort has been spent in trying to understand the exact nature of the Fe moment and its interaction with the SDW. Some of this work, particularly the diffuse neutron scattering measurements of

Cywinski and Hicks (1980) and Kazjar, Babic and Parette (1980) as well as the theoretical model of Friedel and Hedman (1978), has occured during the course of the present study and is thus not strictly "previous" work. It is convenient to discuss these concurrent developments along with earlier work in the present section.

Newmann and Stevens (1959) found, in contrast to the essentially temperature independent susceptibility of pure Cr, that the susceptibility of dilute CrFe alloys showed considerable temperature dependence. After subtracting the small contribution due to the Cr matrix the remaining susceptibility (which was identified with the Fe impurity) followed a Curie-Weiss law with a small positive interaction temperature θ above T_N with an effective moment of 2.9 μ_B, which remained constant over the concentration range 1% - 6% Fe studied. This implies that the two extra d electrons contributed by each Fe atom remain localized at the Fe sites. A more extensive study by Ishikawa, Tournier and Filippi (1966) shows that below T_N the impurity susceptibility followed essentially a Curie law. To explain this surprising result it was suggested that below T_N the Fe moments were only weakly coupled to the SDW and were free to rotate paramagnetically.

This interpretation was adopted by a number of subsequent investigations. In a more quantitative attempt to understand the problem Hedgecock, Strom-Olsen and Wilford (1977) fitted the low temperature susceptibility of 3-6% Fe alloys using a simple model due to Lomer (1960). The interaction between the SDW and the local moment was characterised by a coupling constant J. A good fit to the data for a 5% alloy was found with $J \sim 0.35$ meV, indicating very weak coupling between the Fe moment and the SDW. A good fit to the magnetoresistance of these alloys was also obtained. However this model failed to account for the high field magnetization.

Recent measurements of both dilute CrFe 1-3% alloys and ternary CrV Fe and CrSi Fe by Hedman, Rao and Åstrom (1978) and Åstrom, Gudmansson, Hedman and Rao (1977) claim to isolate a temperature independent component to the susceptibility coming from Fe impurities which appears below T_N, as well as the previously observed Curie/Curie-Weiss contributions. In order to make such a separation the

susceptibility of the host (χ_h) must be accurately subtracted. To achieve this, the data is fitted to

$$\chi = (1 - c)\chi_h + A + C_L/(T - \theta_L) \quad T < T_N \tag{4.14a}$$

$$\chi = (1 - c)\chi_h + C_H/(T - \theta_H) \quad T > T_N \tag{4.14b}$$

where $\chi_h = A_0 + B_0T^2$ and the subscripts L and H refer to $T > T_N$ and $T < T_N$ respectively. It is difficult to assess the validity of this procedure. The fact that A_0 and B_0 are nearly constant for all alloys of a given host both above and below T_N suggests that it is correct. Such a fit is motivated by the observation of a sharp change in χ at T_N.

To explain the concentration dependence of these results the authors differentiate between isolated Fe atoms and nearest neighbour pairs. It is inferred that isolated Fe moments give rise to a temperature independent susceptibility below T_N, the size of which increases by two on cooling from the TSDW to the LSDW and decreases by two on cooling from the TSDW to the CSDW state. These isolated moments also contribute a Curie-Weiss term in the TSDW and paramagnetic phases. On the other hand, nearest neighbour Fe pairs give Curie-Weiss paramagnetism in all phases. This complex set of observations has recently been explained by Friedel and Hedman (1978) who propose that isolated Fe moments are strongly coupled to the SDW, whereas nearest neighbour pairs of moments are uncoupled from the SDW and rotate as paramagnetic entities. The postulate of strong coupling to the SDW is in complete contrast to the earlier proposals.

Babic, Kazjar and Parette (1980) have measured the high field magnetization of Cr 1-5% alloys in pulsed fields up to 33T. The magnetization is linear with field at 4.2 K for 1% - 1.5% Fe. This is not consistent with the concept of weakly coupled paramagnetic moments and tends to support the Friedel and Hedman (1978) model having strong coupling. As the Fe concentration is increased to 2.4% a saturating component of the magnetization is developed in addition to the linear response found at lower concentration. This component

is identified with the Curie-Weiss paramagnetism of ferromagnetically coupled nearest neighbour pairs of Fe moments, each moment being $\sim 1.5\ \mu_B$, again in agreement with Friedel and Hedman's model.

There have been many Mossbauer effect measurements on dilute CrFe alloys. The earliest, by Wertheim (1961), revealed only a single unsplit Mossbauer line. This was originally interpreted as evidence for the paramagnetism of Fe impurities below T_N. Later work showed that this line was in fact broadened and Herbert, Clark and Wilson (1972) obtained well resolved seven line spectra for very dilute (0.2%) alloys. Careful analysis of this data demonstrated that the distribution of hyperfine field at the Fe nuclei was bimodal, having one component at zero hyperfine field and a second, temperature dependent, component which tended to a value of $\sim$ 35T at 4.2 K. Strong coupling between the local moment and the SDW was suggested.

The small value of hyperfine field seen in the Mossbauer data of Herbert et al. (1972) and the Curie-Weiss susceptibility were explained in terms of a spin compensated Fe moment of 0.5 μ_B with a Kondo temperature of 60 K. The existence of a resistance minimum at low temperature in CrFe alloys (Katano and Mori (1979)) has also been interpreted along these lines. It should be noted that similar resistance minima are also found in CrSi and CrGe where there is no question of Kondo moment. For comparison, one should note $T_K \sim 300$ mK for Fe in bcc Mo (Amamou et al. (1975)). Katano and Mori (1979) also report a cusplike susceptibility maximum at 2.7 K for a 1.5% alloy, well below the postulated T_K of 60 K. This spin-glass like behaviour is inconsistent with the supposed Kondo instability of the Fe moments in this concentration range. In the absence of any detailed measurements on very dilute alloys (100 ppm) Kondo behaviour of isolated Fe moments in the single impurity limit cannot be ruled out, however in the concentration range above 0.2% such behaviour seems unlikely.

These problems have provoked a number of diffuse neutron scattering experiments, all of which have been performed concurrently with the present investigation. The major difficulty in these experiments is to separate the small magnetic diffuse scattering signal from the larger nuclear incoherent contribution, as discussed in 4.4. Holden and

Fawcett (1978) could not detect any magnetic incoherent scattering to within ± 15 mb $sr^{-1}at^{-1}$ from a 2.8% Fe single crystal. Kazjar, Babic and Parette (1980) used the polarized diffuse technique (usually restricted to the study of ferromagnets) to measure the magnetic-nuclear interference scattering in a number of CrFe CSDW alloys by applying a field of 1.3 T. No magnetic-nuclear difuse scattering could be isolated in 1.5% and 2.4% Fe samples at 4.6 K to within ± 3 mb $sr^{-1}at^{-1}$. A small degree of clustering, corresponding to $\alpha_1 = 0.14$ was detected in the 2.4% sample.

Cywinski and Hicks (1980) claim to have separated the magnetic and nuclear defect scattering from a 6.5% alloy using the polarization-analysis technique. The atomic defect scattering showed a small amount of clustering, $\alpha_1 = 0.14$ in agreement with Kazjar et al. (1980). By fitting the magnetic defect scattering using the formalism of 2.2.3, it was suggested that the ordered moment on Cr sites was reduced almost to zero in the first and second coordination shells surrounding the Fe impurity. Zero moment was found on the Fe sites themselves. This was explained by assuming that the Fe moments fluctuate paramagnetically and do not give a nett time averaged moment. The lack of any paramagnetic scattering from these fluctuating Fe moments within the experimental κ range ($0.35 < \kappa < 2\text{Å}^{-1}$) was explained by the coupling of Fe moments into superparamagnetic assemblies, taking the response beyond the κ range of the measurement. These observations are discussed in more detail and compared to the results of this present work in 4.4.

4.2.2.3 Theory: dilute alloys

Theoretical study of dilute CrFe alloys has tended to follow two distinct themes: the effect of local moment impurities on the SDW and the nature of the Fe moment and its coupling to an unpeturbed SDW. As yet no complete microscopic theory combining these two aspects has emerged.

(a) The effect of local moment impurities on the SDW

The SDW systems in which the impurity possesses a local moment do not follow the general trends for Cr alloys outlined in section 4.1.5. To explain the complicated changes seen in CrFe antiferromagnetic alloys

it is necessary to consider:

(i) the change in electron concentration on alloying with Fe. The fact that an Fe moment of $\sim 1.5\ \mu_B$ is found in SDW Cr suggests that up to 0.5 electrons/Fe are contributed to the rigid band structure. This will tend to expand the electron surface at the expense of the hole surface and improved Fermi surface nesting may result.

(ii) the scattering from Fe impurities (which will include both 'normal' and magnetic terms). This scattering will tend to decorrelate the electron-hole pairs responsible for the SDW and thus lower T_N.

(iii) the polarization of the local moment by the SDW. This may lead to exchange enhancement of the electron-hole pairing which tends to raise T_N.

(iv) the modification of band structure. The band structure itself may be altered, in this case following the large volume changes found at the transition temperature.

Shibatani (1971) applied Abrikosov-Gorkov theory to the problem of scattering from local moment impurities in a one band model. The possibilities (ii) and (iii) above were investigated. The competition between these two effects leads in certain circumstances to a decrease in T_N with $\bar{\mu}$ remaining almost constant, as in CrFe.

This work was extended by Antonoff (1977, 78) to include the possibilities (i), (ii) and (iii) for a two band model with imperfect nesting. The interaction between the conduction electrons which give rise to the SDW and the impurity spin was assumed to be of the form

$$\hat{H}_3 = \frac{1}{2} \sum_{in} J\, \underset{\sim}{S}_n . \sigma_i \qquad (4.15a)$$

where the impurity spin $\underset{\sim}{S}_n$ at a site n is treated classically and σ_i is a conduction electron spin. J is an effective exchange constant. The CSDW was considered and the Neel temperature was given by

$$-\ln \frac{T_N}{T_{NO}} = (1 + \frac{\lambda}{T_N}) \mathrm{Re}\left[\psi(\frac{1}{2} + \frac{\alpha}{2\pi T_N} + \frac{ih}{2\pi T_N}) - \psi(\frac{1}{2})\right] \qquad (4.15b)$$

where the pair breaking parameter α is the sum of the magnetic and non-magnetic pair breaking parameters. The non magnetic terms have been dealt with previously (eq. 4.13). The magnetic pair breaking parameter α_{M1}, although not explicitly written, is given in Abrikosov-Gorkov theory by

$$k_B\alpha_{M1} = 2\pi cN(E_F)\frac{1}{3}\, S(S+1)J^2 \qquad (4.15c)$$

in the limit of small polarization. The factor λ arises from spin polarization and is zero in the limit of small polarization, whereas the pair breaking parameter α and the imperfect nesting parameter h depress T_N, the factor λ tends to increase T_N. The competition between these three effects may lead to a minimum in T_N as a function of concentration, as in CrCo or a monotonic decrease as in CrFe. The behaviour of the ordered moment was not considered.

Nakanishi and Kasuya (1977) studied the effects (i), (ii) and magnetostriction (essentially the change in band structure (iv)) on a two band SDW. The Hamiltonian for this model is given in section 4.1.5 with the scattering term H_2 from eq. (4.12), and may be extended to the case of magnetic scattering by writing the inter and intra band scattering matrix elements for bands α,β = a, b, r as,

$$(V_{\alpha\beta})_{\sigma\sigma'} = \delta_{\sigma\sigma'}V_{\alpha\beta} + J_{\alpha\beta}(\underset{\sim}{S}.\underset{\sim}{\sigma})_{\sigma\sigma'} \qquad (4.16a)$$

No polarization of the local moment was considered and weak coupling $J_{ab} = J_{ba} = 0$ was assumed. For simplicity $J_{aa} = J_{bb}$ and $J_{ac} = J_{bc} = J_{cb} = J_{ca}$. For the CSDW the magnetic scattering contributes a further pair breaking parameter α_{Mr} to the expression (4.15b) in addition to α_{M1} so that in full,

$$\alpha = \alpha_r + \alpha_1 + \alpha_{Mr} + \alpha_{M1} \qquad (4.16b)$$

where α_r, α_1 and α_{M1} are given by (4.15c) and (4.13), whilst

$$k_B\alpha_{Mr} = \pi N_r(E_F)c(S(S+1))J_{ac}^2 \qquad (4.16c)$$

The volume change at T_N is incorporated by allowing a flow of electrons from the local moment to the SDW band structure which forces a change in the nesting parameter. Semiquantitative agreement with the phase diagram could be achieved with a reasonable choice of parameters.

(b) The nature of the Fe moment and coupling to the SDW

The question as to why Fe should have a local moment in Cr has not been explained in any detail. According to the Anderson picture the fact that Fe does sustain a moment in bcc Cr but not in bcc V can, presumably be explained by the narrow band width of Cr compared with V. A similar argument is advanced to account for the relative stability of the Fe moment in bcc Mo compared with bcc Nb. The questions of whether there is a component of the SDW at the Fe site and the coupling between the Fe moment and the neighbouring SDW also have not been examined from first principles.

In the absence of a complete first principles theory, Friedel and Heldman (1978) adopted a phenomenological approach to the problem. A local moment on the Fe sites was assumed to exist. It was argued that, to a first approximation, the Fe moment did not perturb the SDW and simply removed one Cr moment from the otherwise perfect sinusoidal modulation and replaced it with an Fe moment. The coupling between this substituted Fe moment and its surrounding SDW was presumed to be strong, simply on the basis that the substituted moment was large compared with the Cr moment it replaced.

Friedel and Hedman (FH) distinguish between isolated Fe moments in the LSDW, TSDW and CSDW phases:

(1) Isolated moment in the CSDW phase

The impurity moments are aligned along the direction of sublattice magnetization, either up or down depending on the sublattice upon which they are found. The Fe moments, being strongly coupled to the local CSDW, are only weakly susceptible. This results in a rigid Ising spin glass.

(2) Isolated moments in the ISDW phases

The strong coupling between the isolated Fe moment and the ISDW constrains the Fe moment to lie along the polarization direction

of its surrounding ISDW.To optimize the coupling energy the phase of the ISDW slips in such a way that the Fe moment finds itself occupying the position of the maximum SDW amplitude. The ISDW and the Fe moment are thus locked together. FH argue that this composite system may be excited by (one dimensional) spin reversal along the polarization direction of the LSDW and by (two dimensional) rotation about the propagation direction of the TSDW. As such excitations only change the phase of the ISDW they may occur at little energy cost so that they result in a Curie like susceptibility. However, any attempt to pull the Fe moment away from the local SDW polarization as in the CSDW phase results in a weak temperature independent susceptibility. Hence the susceptibility in the ISDW phases is highly anisotropic.

(3) Finite concentration effects, ISDW phases

At a small but finite concentration of isolated impurities the Fe moments will tend to compete for the most favourable phase of the SDW, this leads to a long range distortion of the SDW which inhibits the 2d rotation or spin flip of the Fe-SDW. Thus the Curie like susceptibility $\rightarrow$ Curie-Weiss form with a small negative θ. Below θ the collective motion becomes progressively blocked and the susceptibility tends to a temperature independent value.

(4) Nearest neighbour moments

Nearest neighbour Fe moments are expected to behave in a super-paramagnetic fashion in all phases. In the CSDW the ferromagnetic coupling between two nearest neighbour (nn) Fe moments frustrates any coupling to the two different sublattices on which they are found. This allows the coupled moments to rotate with little or no interaction with the matrix, giving a Curie-Weiss susceptibility. In the ISDW phases such cancellation is incomplete.

At the heart of the FH model is the strong coupling between the SDW and the Fe moment. Such strong coupling had been previously suggested by Herbert et al. (1972) based on Mossbauer data. The magnitude of the coupling may be estimated from the high field magnetization data

of Babic et al. (1980). Using a model by Lomer (1960) the interaction between a local spin $\underset{\sim}{S}$ and the SDW $\underset{\sim}{\sigma}$ is characterized by a coupling constant J,

$$H = - g\mu_B \underset{\sim}{H}.\underset{\sim}{S} - \frac{1}{2} J|\underset{\sim}{\sigma}|\hat{\underset{\sim}{\sigma}}.\underset{\sim}{S} \qquad (4.17a)$$

where $\hat{\underset{\sim}{\sigma}}$ is the local SDW polarization. Lomer calculated the impurity susceptibility for $S = \frac{1}{2}$. The calculation was extended to the case $S = 1$ (appropriate to Fe impurities) by Hedgecock, Strom-Olsen and Wilford (1977) who calculated an impurity susceptibility,

$$\chi = \frac{C(g\mu_B)^2}{J\sigma}\left(\frac{\sinh(\beta J\sigma/2)}{1+2\cosh(\beta J\sigma/2)} + \frac{(2+\cosh(\beta J\sigma/2)}{(1+2\cosh(\beta J\sigma/2))^2}\right) \qquad (4.17b)$$

which tends to constant value

$$\chi = cg^2\mu_B^2/J\sigma \qquad (4.17c)$$

in the limit of large coupling. The high field magnetization data for 1% and 1.5% alloys is linear with field up to 33T and consistent with the limit (4.17c), giving a value $J \sim 200$ K which is of the same order as T_N. As discussed previously the high field magnetization measurements also show evidence for the Curie-Weiss susceptibility of nn pairs of Fe moments.

Thus the phenomenological FH model accounts well for both the low field magnetization data of Hedman et al. (1978) and Åstrom et al. (1977) as well as the high field data of Babic et al. (1980).

4.2.3 Concentrated antiferromagnetic alloys (5% < c < 20%)

In contrast to the dilute alloys, relatively little work has been devoted to the properties of more concentrated antiferromagnetic alloys (5% < c < 20%). In this concentration range the SDW order associated with pure Cr gives way to the ferromagnetic order of pure Fe.

4.2.3.1 The critical concentration for antiferromagnetism

As no neutron Bragg scattering data is available for the concentrated alloys, the concentration dependence of T_N cannot be determined directly but must be inferred from anomalies in the bulk magnetic and transport properties. No information exists for the ordered antiferromagnetic moment.

Magnetic phase diagrams covering this more concentrated region have been compiled by Mitchell and Goff (1972) and Loegel (1975). These diagrams are based on the anomalies in resistivity (Arajs and Dunmyre (1966), Rajan, Waterstrat and Beck (1960), Suzuki (1966) and Newmann and Stevens (1959)), magnetic susceptibility (Ishikawa et al. (1965), Newman and Stevens (1959), Suzuki (1966) and Booth (1966) and thermal expansion (Ishikawa et al. (1967), Suzuki (1966) and Newmann and Stevens (1959)). More recently data from specific heat for $c < 8\%$ (Suzuki (1976)) and Mossbauer effect (Kuwano and Ono (1977)) have become available. The electrical resistivity of CrFe SDW alloys shows a shallow minimum which is identified with T_N whereas the magnetic susceptibility shows a change in Curie constant at T_N. The bulk of this data has been collected for $c < 10\%$ and only resistivity data exists for the higher concentration range. See Fig. 4.11.

These phase diagrams show T_N decreasing monotonically with concentration, reaching zero at $\sim$ 20% Fe. Both phase diagrams show a region of overlap between antiferromagnetism and ferromagnetism.

4.2.3.2 Bulk magnetization

The bulk magnetic properties of the more concentrated antiferromagnetic alloys show characteristics of 'superparamagnetism'. e.g. the data of Ishikawa et al. (1965) shows the develop ment of a nonlinear component of the low temperature magnetization as the concentration increases above $\sim$ 5%. The curvature of the low temperature M-H plots essentially follow a Langevin function with a slow approach to saturation. Hysteresis and time dependent remanence develop as c exceeds 10%.

In its original sense 'superparamagnetism' is a term used to describe the paramagnetic behaviour of a collection of small ferromagnetic

particles: such as precipitates of Co in Cu, see for example Bean and Livingston (1959). This concept has been applied with minor modifications to the description of concentrated CrFe alloys. According to Ishikawa et al. (1965) nn Fe moments couple ferromagnetically at low temperature to form a correlated network of many spins with a nett moment of several hundred μ_B. The nett moment is free to rotate like a giant paramagnetic spin (hence 'super' paramagnetism), giving a Langevin type magnetization. Time dependent remanence and hysteresis may be explained by assuming anisotropy barriers to the free rotation of such particles. (Street and Wooley (1949)). The size of these correlated networks is dictated by the concentration and temperature, they are not distinct metallurgical particles with a large T_C. Typically the superparamagnetic assemblies are destroyed by heating above $\sim$ 100 K.

The data of Ishikawa et al. (1965) has recently been supplemented by Babic et al. (1980). The magnetization could be virtually saturated in a pulsed field of 33T, and a moment of 1.8 μ_B/Fe was derived for 12% and 14% alloys. These workers also carried out polarized diffuse neutron scattering measurements on the same alloys (Kazjar et al., 1979-80) and deduce an average Fe moment of 2.0 μ_B in good agreement with the magnetization measurements. These measurements, which were performed concurrently with the present work are discussed in more detail in section 4.4.

Fig.4.11 Magnetic phase diagram for Cr Fe alloys compiled by Loegel (1975).

Fig.4.12 Neutron powder diffraction scans through the (100) position for Cr Fe 12% alloy above and below T_N.

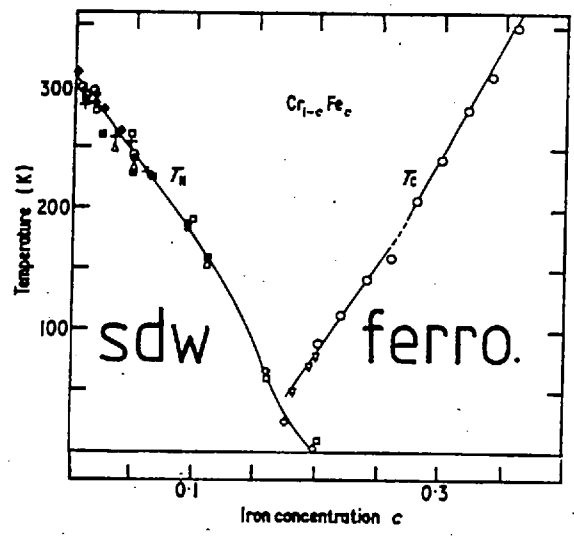

Fig. 4·11

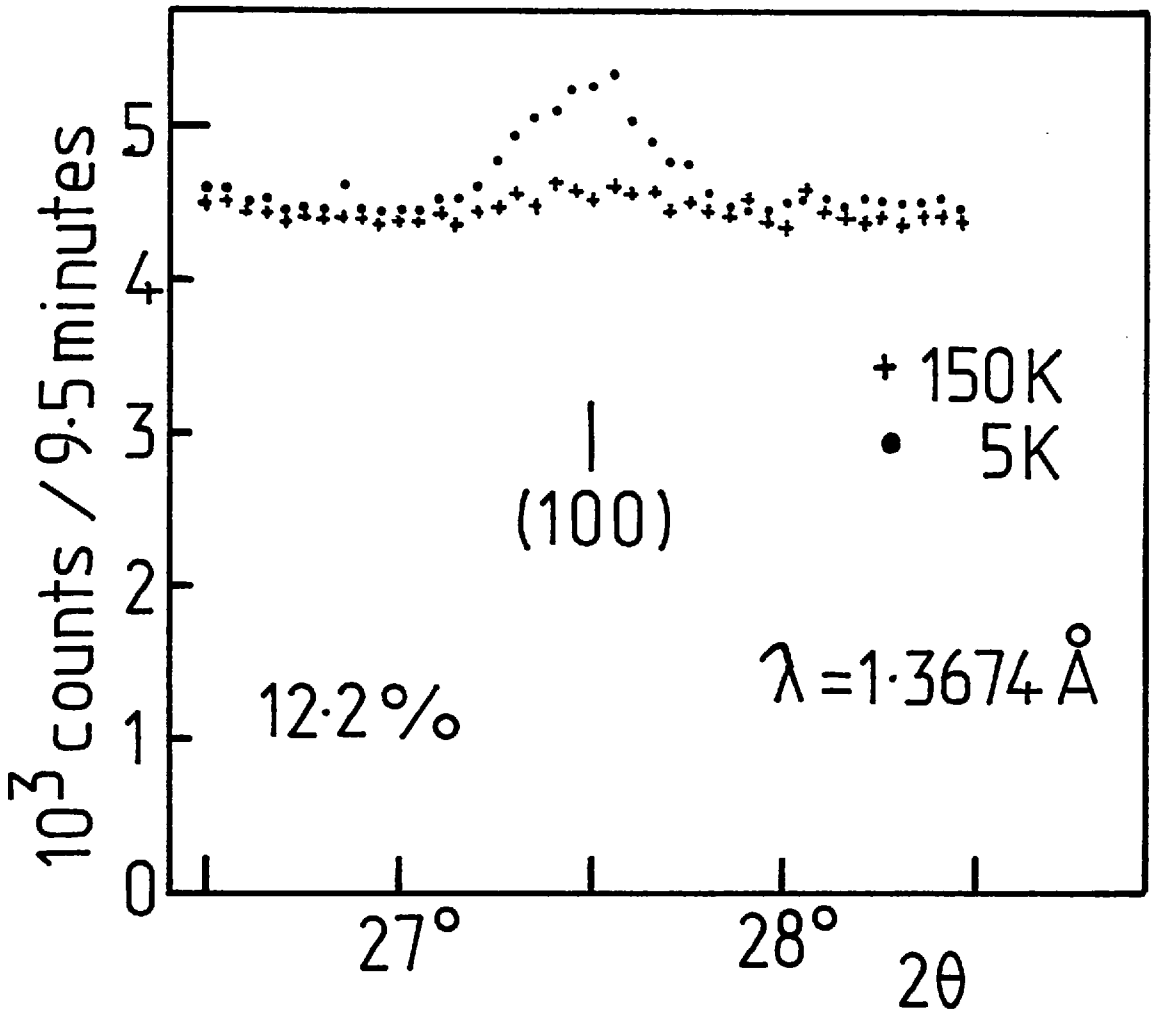

Fig. 4·12

4.3 Determination of the commensurate antiferromagnetic phase boundary

4.3.1 Introduction

Despite the immense amount of work on dilute CrFe alloys there is a lack of detailed information concerning more concentrated alloys. No neutron Bragg diffraction data exist for concentrations above 5%, yet it is precisely between 5 and 20% that SDW order is destroyed. A knowledge of both T_N and the ordered SDW moment ($\bar{\mu}$) as the concentration is increased towards the critical concentration for SDW order is fundamental to the understanding of the 'anomolous' behaviour of the CrFe SDW.

The phase diagrams of Loegel (1975) and Mitchell and Goff (1972) show a region of overlapping ferromagnetism and antiferromagnetism between 15 and 20% Fe. Physically, such an overlap is difficult to understand. As the antiferromagnetic segments of these diagrams above 5% were deduced from resistivity measurements an independent determination of the antiferromagnetic phase boundary was initiated using neutron diffraction. Apart from clarifying the phase diagram problem, such measurements enable the concentration dependence of T_N and $\bar{\mu}$ to be determined.

4.3.2 Results of Bragg scattering measurements

The ordered antiferromagnetic moment at 4.2 K($\bar{\mu}_0$) was determined for a series of CrFe alloys spanning the concentration range 4.5 to 17% Fe. The details of sample preparation are outlined in 3.1. The ordered moment was calculated by normalizing the magnetic (100) intensity to either the (110) or (200) nuclear reflections as discussed in 3.4.1. A typical neutron Bragg scattering pattern is illustrated in Fig. 4.12. The (100) reflection was always observed unsplit, consistent with the samples having the simple two sublattice antiferromagnetic CSDW structure.

The values of $\bar{\mu}_0$ determined in this way are shown as a function

of concentration in Fig. 4.13. The data is in good agreement with the values of Ishikawa et al. (1967) taken on more dilute alloys, $c < 4.7\%$. $\bar{\mu}_0$ for these CSDW alloys decreases as the Fe concentration is increased, reaching zero at a critical concentration of $16.0 \pm 0.5\%$. Values are given in table 4.1.

The temperature variation of $\bar{\mu}$ was followed for the 10.2, 12.2, 13.6, 14.2 and 15.4% alloys as shown in Fig. 4.14. The temperature dependence of the 10.2% and 15.4% samples was followed in detail. For the remaining alloys, only sufficient data was taken to bracket the Néel temperature. T_N deduced from this data is also presented in table 4.1. The concentration dependence of T_N is shown in Fig. 4.15. The Néel temperature decreases rapidly with increasing concentration, extrapolating to zero at the critical concentration $16.0 \pm 0.5\%$ found from the $\bar{\mu}_0$ measurements.

Table 4.1

Ordered moment at 4.2 K($\bar{\mu}_0$) and Néel temperature (T_N) determined by neutron diffraction

Concentration % Fe	$\bar{\mu}_0$ μ_B/at	T_N K
4.5	0.69 ± .01	-
7.0	0.65 ± .01	-
9.2	0.49 ± .01	-
10.2	0.42 ± .01	153 ± 5
11.2	0.41 ± .01	-
12.2	0.37 ± .01	115 ± 10
13.2	0.30 ± .01	-
13.6	0.28 ± .01	90 ± 10
14.2	0.21 ± .01	65 ± 5
15.3	0.16 ± .01	49 ± 3
15.4	0.13 ± .05	-
16.7	0.00 ± .05	-

Fig.4.13 Ordered antiferromagnetic moment for Cr Fe alloys at 5K. For comparison, the moment corresponding to the maximum amplitude of the ISDW is shown. The full curve is a guide to the eye. ●, this work; Δ, Arrott et al (1967) ▲, Ishikawa et al (1967).

Fig.4.14 Temperature dependence of the ordered moment. The full curve is the $B_{\frac{1}{2}}$ function. ▽, 15.4%, ◆, 14.2%; ▲, 13.6%; Δ, 12.2%, ○, 10%.

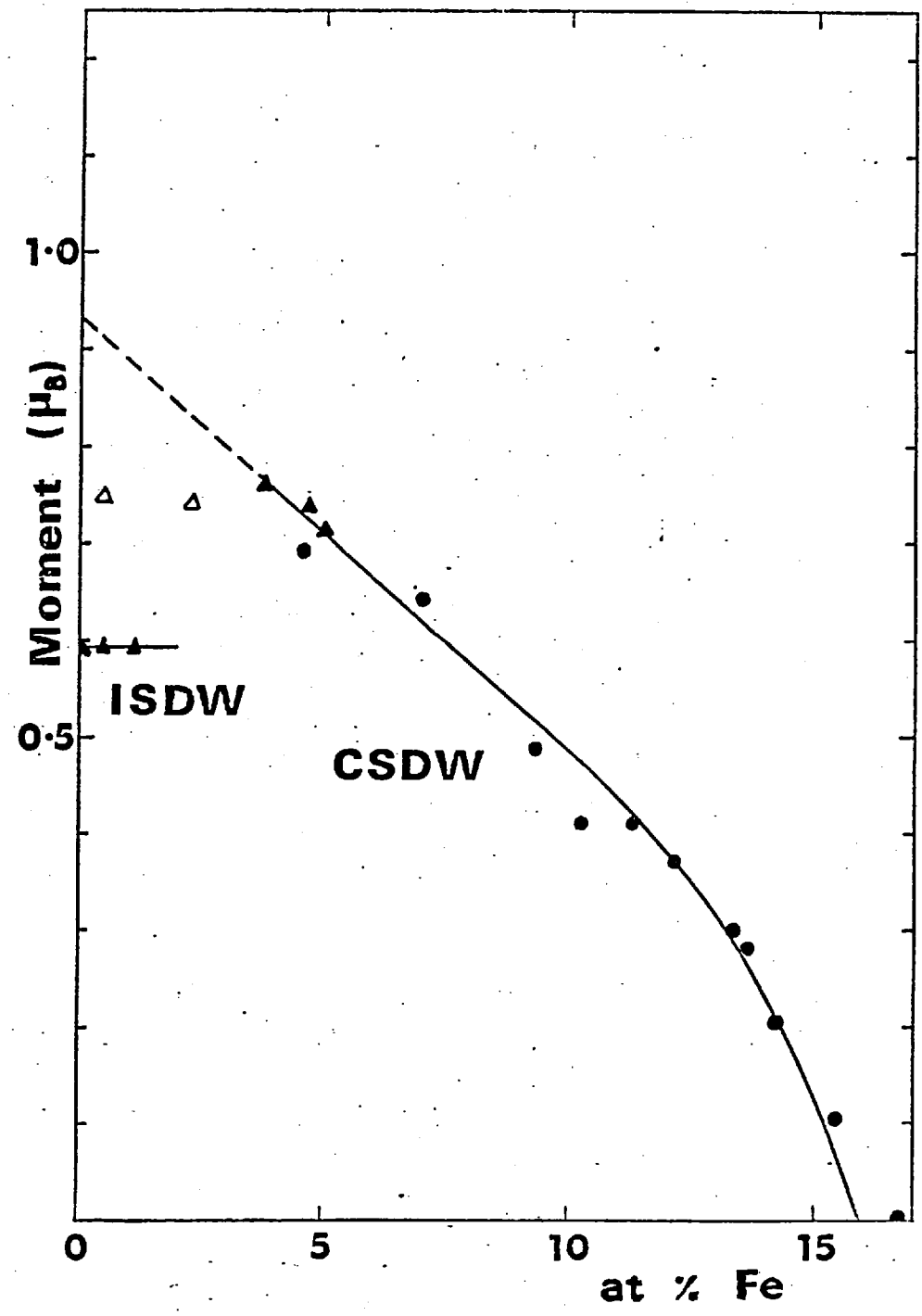

Fig. 4·13

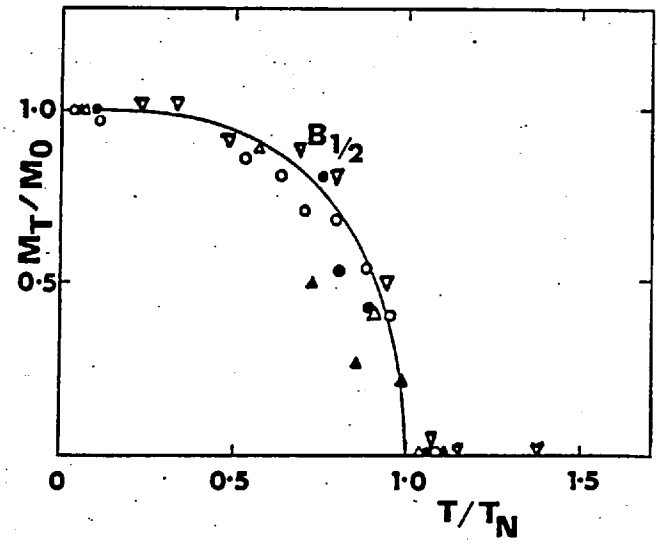

Fig. 4·14

Fig.4.15 Antiferromagnetic phase boundary in binary Cr Fe alloys compiled from various sources. The broken line is the Abrikosov-Gorkov relation (eq.4.19) with $T^* = 300K$. To illustrate the scaling between the ordered moment at 5K and T_N the same curve used in Fig.4.13, scaled by a constant value has been reproduced (full curve). ⊛ , this work; O , neutron diffraction; Δ $(\frac{d\rho}{dT})$ anomaly; ∇, susceptibility.

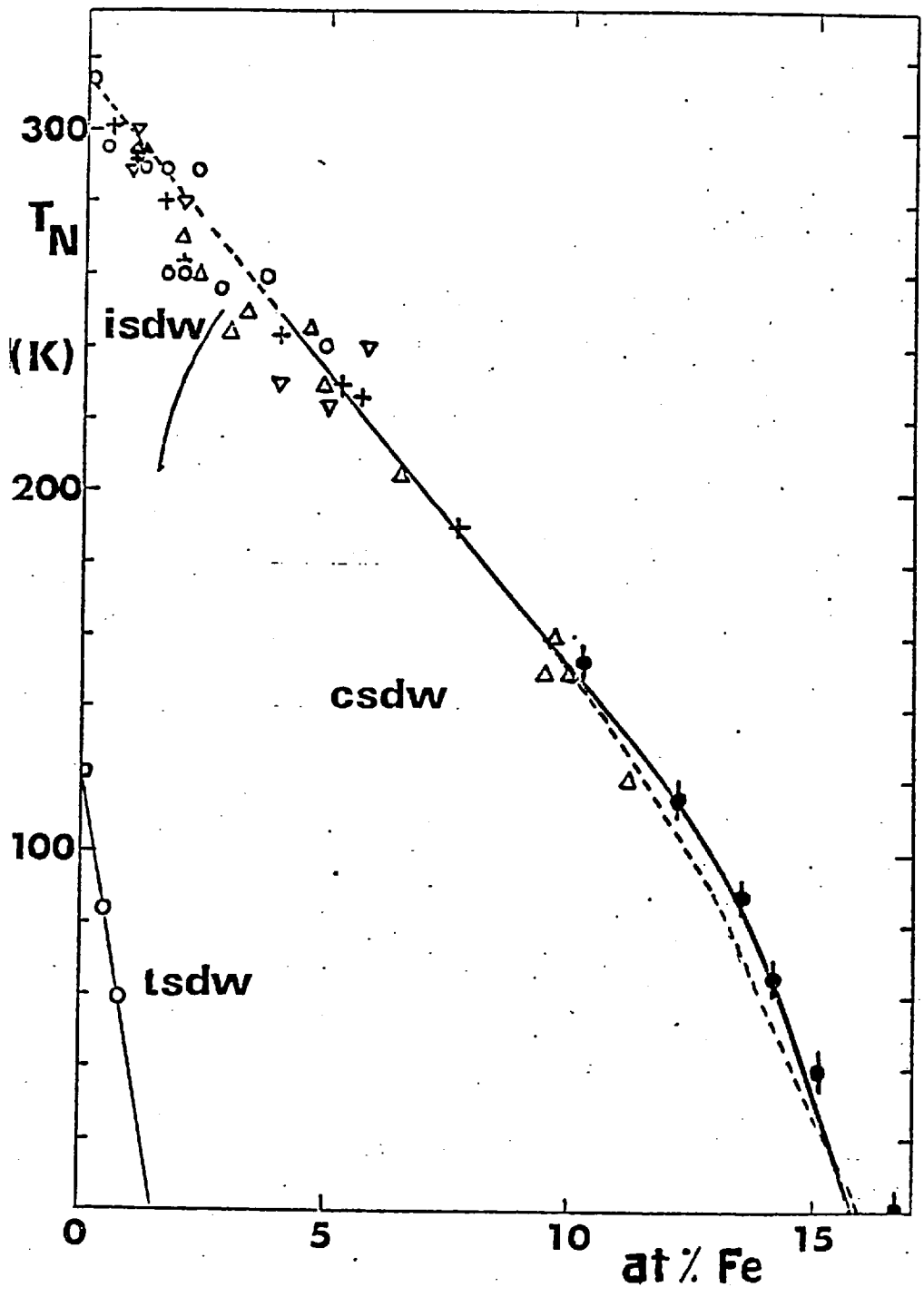

Fig. 4·15

4.3.3 Determination of T_N from resistivity measurements

There is a large discrepancy between the neutron diffraction data above and T_N determined from resistivity measurements (Loegel (1975) Mitchell and Goff (1972)), amounting to almost 30 K in the case of the 10% alloy.

There has been some disagreement in the literature as to which feature of the resistivity marks T_N. For example, Mitchell and Goff (1972) and Loegel (1975) assumed the minimum of resistivity occurs at T_N whereas Trego and Mackintosh (1968), Ausloos (1977) and Åstrom et al. (1977) exphasise that the minimum in the thermal coefficient of resistivity marks T_N.

To our knowledge this point has not been resolved by reference to neutron diffraction, so that a sample suitable for resistance measurements was spark cut from the neutron 10.2% alloy and the resistivity measured using a standard 4 point DC technique. The experimental details are given in 3.9. The results, expressed in terms of $-\frac{d\rho}{dT}$, are shown in Fig. 4.16. It can be seen that T_N found from neutron diffraction lies close to the maximum in $-\frac{d\rho}{dT}$ for this alloy, whilst the resistivity minimum ρ_{min} occurs some 30 K higher. Thus T_N must be identified with $-\frac{d\rho}{dT}$ maximum.

Using this criterion, T_N was deduced from the resistivity data of Arajs and Dunmyre (1966) and Rajan et al. (1960) for a number of CrFe alloys. The results, as shown in Fig. 4.15, are in excellent agreement with T_N determined by neutron diffraction. There is, thus, good agreement with the resistivity data once the correct criterion for identification of T_N is used.

4.3.4 Analysis and discussion

The correct identification of T_N with the maximum of $-\frac{d\rho}{dT}$ brings the critical concentration for antiferromagnetism estimated from resistivity into line with the present value of 16.0 ± 0.5 % from neutron diffraction. By moving the critical concentration to lower Fe concentration these measurements resolve the problem of overlapping

ferromagnetism and antiferromagnetism previously reported by Mitchell and Goff (1972) and Loegel (1975).

The behaviour of T_N and $\bar{\mu}_0$ for these more concentrated alloys is quite different to that reported for the dilute ISDW (4.2.1). Both T_N and $\bar{\mu}_0$ decrease monotonically with increasing Fe content for the CSDW whilst $\bar{\mu}_0$ remains almost constant and T_N decreases for the ISDW. Furthermore a significant increase in $\bar{\mu}_0$ occurs as the SDW becomes commensurate. This is well illustrated by the extrapolated value of 0.94 μ_B for a hypotherical CSDW in pure Cr, compared to the actual value of 0.59 μ_B for ISDW Cr.

The most striking aspect of this data is the scaling between $\bar{\mu}_0$ and T_N. This is illustrated in Fig. 4.17. Additional data for T_N has been taken from the resistivity measurements of Rajan et al. (1960) and Arajs and Dunmyre (1966) using the $-\frac{d\rho}{dT}$ criterion for those alloys where T_N has not been measured by neutron diffraction. T_N and $\bar{\mu}_0$ for a (CrMo 2%) Fe 14% alloy have also been included. This plot shows a constant value of $\bar{\mu}_0/T_N$ amounting to 3.1×10^{-3} μ_B/at/K. To emphasise this scaling the same curve has been drawn through the data of Fig. 4.13 and Fig. 4.15 and has simply been multiplied by the appropriate value. The constancy of $\bar{\mu}_0/T_N$ has been noted for ISDW alloys of Cr with Mo, W and V by Koehler et al. (1966) although with a smaller ratio $\mu_0/T_N = 1.89 \times 10^{-3}$ characteristic of the ISDW. Scaling between T_N and the energy gap 2g has also been reported by Barker and Ditzenberger (1970) from optical absorption measurements on both dilute ISDW and CSDW Cr alloys with V, Mo, Ru, Mn and Fe. According to this data the ratio $2g/T_N$ is approximately doubled for the CSDW compared with the ISDW. Making the reasonable assumption that the energy gap is proportional to the order parameter $\bar{\mu}_0$ for these dilute alloys then such a change in $2g/T_N$ is very close to that observed in the present experiments. Strom-Olsen and Wilford (1980) also report a constant ratio Δ/T_N from analysis of resistivity data for CrMo alloys containing less than 10% Mo.

The constancy of $\bar{\mu}_0/T_N$ implies that there is no fundamental difference between the CSDW found in dilute alloys and the CSDW close to the critical concentration. In particular this suggests that a

Fig.4.16 Temperature derivative of the resistivity close to T_N for Cr Fe 10.2%. The maximum in $\frac{-d\rho}{dT}$ closely coincides with T_N determined by neutron diffraction on the same sample (arrowed). The minimum in resistivity is marked.

Fig.4.17 Scaling between the Neel temperature and ordered moment at 5K for CSDW Cr Fe alloys. Data for a (Cr Mo 2%) Fe 14% alloy have also been included (open circle).

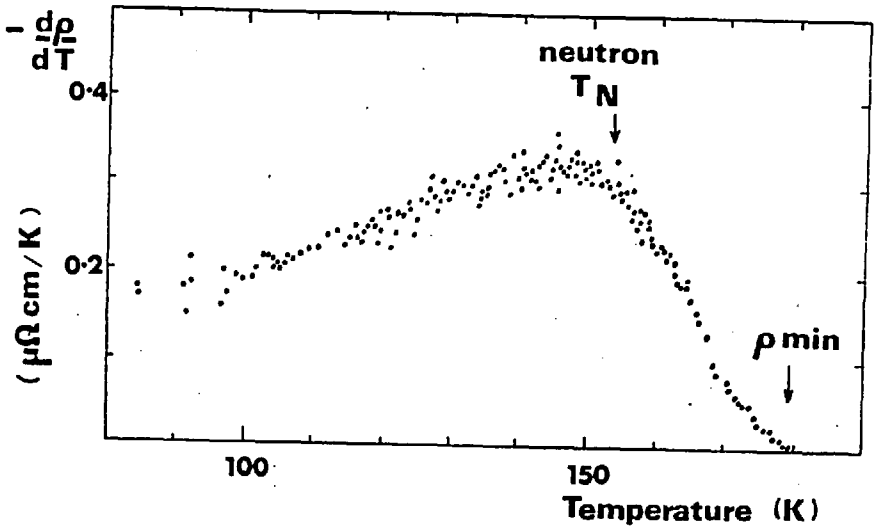

Fig. 4·16

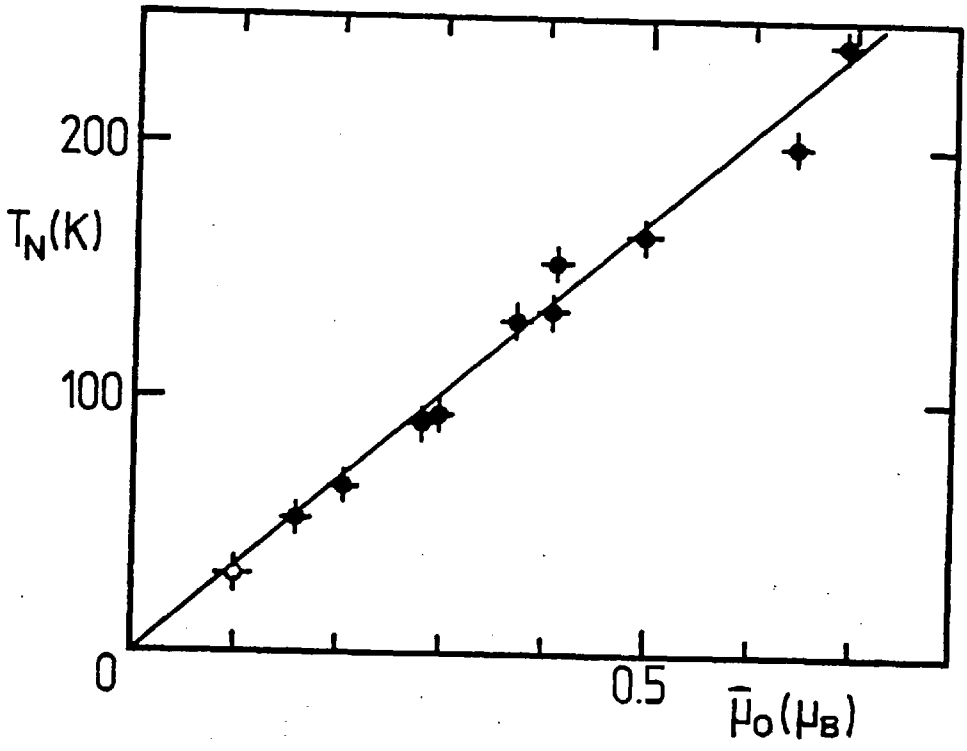

Fig. 4·17

component of the SDW is induced at Fe sites, as $\bar{\mu}_0$ is measured per atom rather than per Cr atom.

Such scaling between T_N and $\bar{\mu}_0$, over at least a limited concentration range, is predicted by the two band models for the SDW discussed in 4.1.4 and 4.1.5. Proportionality between T_N and the order parameter Δ at OK is predicted in the simplest case of perfect nesting in the absence of scattering by the FM model, as shown by eq. 4.7c. This proportionality is retained in the CSDW with imperfect nesting (again in the absence of scattering) for small values of the imperfect nesting parameter h and a small electron reservoir according to the Rice model. This result breaks down in the presence of an electron reservoir. If scattering is present it is important to differentiate between the order parameter Δ, which is proportional to $\bar{\mu}$, and the energy gap 2g. In the CSDW with perfect nesting treated by Zittartz the ratio $\Delta(0)/T_N$ increases with increasing concentration. For small concentrations i.e. T_N linear with C,

$$\frac{\Delta(0)}{T_N} = \frac{\Delta_0(0)}{T_{N0}}\left(1 + \frac{\pi}{4}\left(\frac{\pi-\gamma}{\gamma}\right)\frac{k_B\alpha}{\Delta_0(0)} + \ldots\right) \qquad (4.18)$$

where the subscript 0 indicates the pure system. Thus while $\Delta(0)/T_N = (\pi/\gamma)k_B$ for $\alpha=0$, this value increases by a factor of 2 by the time α is sufficiently large for a gapless CSDW to be retained at T=0, $\alpha_c^1 = 0.913\ \alpha_c$ (c.f. eq. 4.10c). No calculations of $\Delta(0)$ for the more general case of both scattering and imperfect nesting treated by Nakanishi and Kasuya, and Antonoff have been attempted.

The temperature dependence $\bar{\mu}(T)$ is also predicted by the two band models of 4.1.4 and 4.1.5. The FM two band model gives a BCS dependence of $\bar{\mu}$ on T. As shown in Fig. 4.14 this temperature dependence is approximately followed by CrFe CSDW alloys, although the decrease in $\bar{\mu}$ is slower than predicted by the BCS relation (eq. 4.7d) or the $B_{\frac{1}{2}}$ function to which it closely approximates. A deviation of this type is found in the Abrikosov-Gorkov theory of Zittartz for the CSDW. As expected, the deviation from BCS becomes larger for higher impurity concentration.

As previously stated, the decrease in T_N and $\bar{\mu}_0$ with increasing

Fe concentration is contrary to the expectations of the rigid band models which successfully account for the alloying behaviour of 'normal' solutes in Cr. The anomalous behaviour of CrFe alloys is explained by the pair breaking effect of the Fe local moment impurities together with some degree of polarization and electron transfer in the Antonoff model and including magnetostriction in the Nakanishi and Kasuya model.

The concentration dependence of T_N is well described by the Antonoff model. According to eq.(4.15b) and (4.16c) the decrease in T_N simply follows the Abrikosov-Gorkov relation,

$$\ln \frac{T_{NO}}{T_N} = 2\psi\left(\frac{2cT^*}{T_N}\right) - \psi\left(\frac{cT^*}{T_N}\right) + \mathbb{C} \qquad (4.19a)$$

where $\mathbb{C}$ is the Euler constant and α, the pair breaking parameter, is taken to be linear with concentration

$$\alpha = cT^* \qquad (4.19b)$$

with

$$k_B T^* = \frac{1}{3} N(E_F) S(S+1) J^2 \qquad \text{Magnetic only.} \qquad (4.19c)$$

if only magnetic scattering via eq.(4.15c) is taken into account. In writing these expressions it is assumed that there is perfect nesting (h=0) and no change in h with concentration, as well as negligible polarization of the impurity spins. The Néel temperature of (hypothetical) pure CSDW Cr (T_{NO}) is taken to be 311 K, the T_N of pure ISDW Cr. An excellent one parameter fit to the data is obtained with $T^* = 300$ K as shown in Fig. 4.15. The goodness of fit can be judged by the consistency of the initial slope and the critical concentration. From (4.10b) and (4.19a)

$$\frac{dT_N}{dc} = -\frac{\pi^2}{2} cT^* \qquad \text{and} \qquad c_{crit} = \frac{\gamma}{4} \frac{T}{T^*}$$

The measured $\frac{dT_N}{dc} = 1540 \pm 10$ K gives $T^* = 310 \pm 10$ K, whilst

$c_{crit} = 0.16 \pm 0.005$ gives $T^* = 270 \pm 10$ K. The inclusion of polarization and nesting effects will lead to a better fit, also allowing T_{NO} to be modified from the ISDW value.

It is difficult to estimate T^* for purely magnetic scattering from eq. (4.19c) as the interaction strength J is not well known. Using the density of states $N(E_F) = 0.89$ at/eV taken from the band structure calculations of Asano and Yamashita (1967) and S = 1 gives J = 220 meV corresponding to the measured T^* of 300 K. This is an order of magnitude larger than J estimated in 4.2.2.3 from the high field magnetization data of Babic et al. (1980). However this J represents an upper limit,as the measured T^* will also contain normal scattering terms which have not been considered.

The concentration dependence of the ordered moment is not treated by Antonoff. If the Antonoff model is taken in the limit of h = 0 and $\lambda = 0$ it reduces to the Abrikosov-Gorkov model. (This limit was taken, for simplicity, in fitting $T_N(c)$.) The theory in this limit cannot account for $\bar{\mu}_0(c)$ as the model predicts the break down of scaling between $\bar{\mu}_0$ and T_N at high concentration (eq. 4.18). However, in the presence of polarization of the Fe moments this scaling feature may be retained by the Antonoff model. This can be simply demonstrated using eq. 4.18. If polarization effects are present the order parameter $\Delta_0(0)$ for the pure system must be replaced by the order parameter $\Delta_{0c}(0)$ for the system with polarized Fe moments in the absence of scattering. In its simplest form $\Delta_{0c}(0)$ will vary linearly with c,

$$\Delta_{0c}(0) = \Delta_0(0)\left(\frac{(1-c)\mu_{Cr} + c\mu_{Fe}}{\mu_{Cr}}\right)$$

for a fully polarized system. Inclusion of $\Delta_{0c}(0)$ in (4.18) leads to scaling of μ_0/T_N over a wider concentration range. For a more detailed analysis the Antonoff model must be extended to treat $\bar{\mu}_0$.

4.4 The nature of the Fe moment in antiferromagnetic Cr

4.4.1 Introduction

The behaviour of the Fe moment in antiferromagnetic Cr is not well understood. On one hand, the high field magnetization data of Ishikawa et al (1965) and Babic et al (1980) show a localized moment of $1.5\mu_B$ at low temperature and $2\mu_B$ at high temperature, yet the hyperfine field measurements of Herbert et al (1972) are interpreted in terms of a spin compensated moment of $0.5\mu_B$ at low temperatures. The magnetoresistance measurements of Hedgecock et al (1977) suggest extremely weak coupling between the SDW and the local moment whereas Friedel and Hedman (1978) explain the susceptibility of dilute Cr Fe alloys by assuming strong doupling. At higher concentration, the scaling between T_N and $\bar{\mu}_o$ suggests a uniform approach of the CSDW to the critical concentration, however Ishikawa et al (1965) propose the growth of superparamagnetic clusters of ferromagnetically coupled Fe moments in this region.

In an attempt to resolve these conflicting observations a series of neutron scattering measurements was initiated. The dynamical magnetic response of the Fe moments, both above and below the Neél temperature, was determined for a Cr Fe 10% alloy using the neutron TOF technique and is discussed in section 4.4.3. Using the neutron polarization-analysis technique, the average Fe moment and moment disturbance in the vicinity of the Fe atom can be determined, at least in principle. This technique was applied to study the magnetic disturbance in a Cr Fe 5% alloy and is discussed in section 4.4.4. The low field magnetization of several concentrated antiferromagnetic alloys was also measured and is discussed in the following section.

4.4.2 Coexistence of SDW and spin glass states in Chromium alloys containing iron

4.4.2.1 Spin glass behaviour in (Cr Mo 2%) Fe 14% and Cr Fe 14%.

Neutron Bragg scattering, resistivity and low field static susceptibility measurements were performed on two alloys containing 14% Fe dissolved in the SDW hosts Cr and Cr Mo 2%. The neutron diffraction experiments were carried out at AERE Harwell as described in 3.4. The samples were prepared using the procedure outlined in 3.1. The resistivity and susceptibility measurements were made by J. Strom-Olsen and D.F. Wilford using samples spark machined from the neutron diffraction specimens. The resistivity was determined by a four point AC method (Muir and Strom-Olsen (1976)) and the susceptibility data collected in both field cooled (500 Oe) and non-field cooled states using a vibrating sample magnetometer. Further experimental details are given by Strom-Olsen, Wilford, Burke and Rainford (1979). The results of this series of measurements are shown in Fig. 4.18.

The susceptibility data shows clear evidence for 'spin glass' behaviour (5.1). The susceptibility obtained after cooling in zero field shows a peak characteristic of a spin glass at the freezing temperature T_g, while the susceptibility found after cooling in a field of 500 Oe saturates below T_g. The evolution between the field cooled and non field cooled states is governed by the slow time dependence similar to that found by Guy (1977) for Au Fe. This spin glass behaviour is observed below the Neél temperature determined by neutron diffraction. An independent check on the value of T_N is provided by the resistivity data. Excellent agreement with the neutron value results if the $\frac{-d\rho}{dT}$ criterion (4.3.3) is used. The neutron diffraction data show furthermore that the SDW is retained down to lowest temperatures and is not disturbed by the occurrence of spin glass phenomena.

Fig.4.18 Results of neutron Bragg scattering, resistivity and low field susceptibility measurements on (a) Cr Fe 14% (b) (Cr Mo2%) Fe 14% alloys. T_N determined by neutron diffraction and resistivity are arrowed. The spin glass temperature, which occurs below T_N, is also shown by an arrow. The $B_{\frac{1}{2}}$ dependence of the ordered moment is shown by the full curve. Susceptibility data are normalized to the peak values, the open circles represent data taken in a field cooled state and the full circles for zero field cooling.

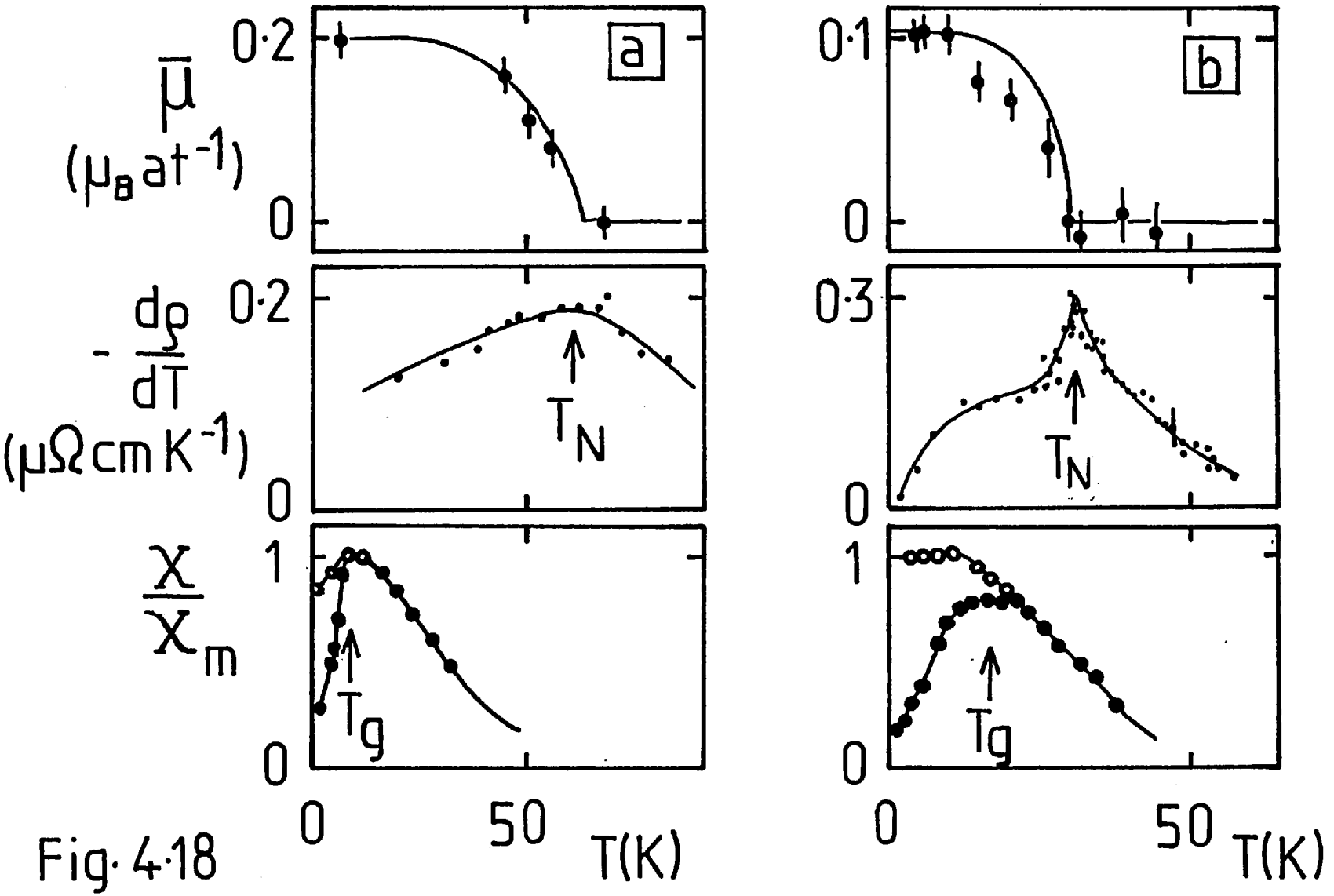
$\bar{\mu}$
$(\mu_B at^{-1})$
0·2
0
a
$-\frac{d\rho}{dT}$
$(\mu\Omega cm\, K^{-1})$
0·2
0
T_N
$\frac{\chi}{\chi_m}$
1
0
T_g
0
50
T(K)
0·1
0
b
0·3
0
T_N
1
0
T_g
0
50
T(K)

Fig. 4·18

4.2.2.2 Results of low field static susceptibility measurements

The static susceptibility of a series of Cr Fe antiferromagnetic alloys was measured below 77K in fields of 20-30 Oe using the vibrating sample magnetometer described in 3.8.2. Needlelike specimens suitable for susceptibility measurements were spark machined from the Cr Fe 10.2%, 13.3% and 15.3% neutron diffraction samples and the 15.5% small angle scattering sample.

The magnetization data were taken in two ways. The non field cooled measurements were made by cooling the sample to the lowest temperature (1.3-4.2K) in zero field. Data were collected with increasing temperature. The magnetization at each temperature was determined 30 sec. after the application of a 20-30 Oe field. The field was then returned to zero and the temperature increased after allowing sufficient time for any remanence to decay. The field cooled data were taken by cooling the sample to the lowest temperature in an applied field of 20-30 Oe. The magnetization was then determined in the same field with increasing temperature, the applied field was not removed.

The field cooled and non field cooled data for the 10.2% and 13.3% samples is shown in Fig. 4.19. The zero field cooled data in both cases show a broad maximum as a function of temperature. This peak is typical of spin glasses, the peak temperature is denoted T_g. The field cooled data follows the zero field cooled data above T_g but shows a tendency to saturate below T_g. The levelling effect seen in the 10.2% sample is an artefact produced by the demagnetizing field of the specimen.

The zero field cooled data for the 15.3% and 15.5% samples are shown in Fig. 4.19. The magnetization is highly temperature dependent, increasing rapidly below 30K and reaching a broad maximum at T_g.

Fig.4.19 Low field magnetization of (a) Cr Fe 10% (b) Cr Fe 13.3% (c) Cr Fe 15.3% (d) Cr Fe 15.5% alloys as a function of temperature. Open circles represent field cooled data and closed circles zero field cooled.

MAGNETIZATION (emu gm-1) ×100
0
10
20
30
T(K)
5
10
15
T(K)
1
2
5
1
2
5
10
a
b
c
d

Fig. 4.19

4.2.2.3 Discussion

The spin glass behaviour is strongly dependent on the amplitude of the SDW. This is well illustrated by the Cr Mo 2%) Fe 14% and Cr Fe 14% data. A summary of the relevent parameters is given in table 4.2, for completeness the data of Amamou et al (1974) for the Mo Fe 14% spin glass is included. As the Fe concentration in these three alloys is constant the increase in T_g on going from Cr to Cr Mo 2% and Mo hosts may be attributed to the decrease in the amplitude of the SDW, at least to a first approximation.

Table 4.2 Ordered antiferromagnetic moment at 4.2K, Neél temperature and spin glass temperature for 14% Fe dissolved in bcc hosts

host	μ_o μ_B/at	T_N K	T_g K
Cr	0.2	65 ± 5	9 ± 0.5
Cr Mo 2%	0.1	30 ± 2	17 ± 0.5
Mo	0	0	30 ± 1

This observation is consistent with the rapid increase in T_g from 14K to 22K for the 15.3% and 15.5% alloys. The neutron diffraction data (section 4.3.2) gives T_N = 43K for the 15.3% sample so in this case T_g lies below T_N. The Neél temperature for Cr Fe 15.5% has not been measured. It is likely that T_N for this sample lies below T_g, i.e. below 22K. (Allowing for a possible error of ± 0.5% in concentration about the nominal value 15.5% leads to T_N between 50K and 0K according to section 3.3.2.) The sudden increase in T_g over this limited concentration range

may thus be attributed to the absence of the SDW at $T = T_g$ for Cr Fe 15.5%.

More weight can be given to this argument if the susceptibility data of 5.4.1 for samples with C > 16% (which do not show antiferromagnetism) are taken into account. As shown in Fig. 5.14, the concentration dependence of T_g shows a sudden rise as the antiferromagnetic phase boundary is crossed and the SDW destroyed.

4.4.3 Spin dynamics in Cr Fe 10%

4.4.3.1 Results

The dynamic magnetic response of an antiferromagnetic Cr Fe 10% alloy was measured at various temperatures above and below T_N using the instrument D7 at ILL, Grenoble. The instrument is described in section 3.5.

The large polycrystalline cylinders, one of pure Cr and the other Cr Fe 10% were prepared according to the method of section 3.1. The overall homogeneity of the Cr Fe 10% alloy was checked by electron microprobe analysis of sections taken from each end of the sample. The concentrations of both sections agreed to within $\pm$ 0.2%. The Neél temperature of the alloy was found by monitoring the (100) magnetic reflection. A value of 175 $\pm$ 5K was obtained, in reasonable agreement with the previous results (section 4.3).

Time of flight spectra were collected for both pure Cr and Cr Fe 10% following the procedure of section 3.5. The pure Cr sample acted as a blank. The magnetic scattering from the Cr Fe 10% alloy was weak, thus the TOF spectra for the 16 low angle banks of detectors were summed to improve the statistics. The resulting TOF spectra are illustrated in Fig. 4.20, for comparison the TOF spectra obtained from the pure Cr standard have been superimposed on the data.

Fig.4.20 Time of flight spectra summed over low angle detectors ($\kappa < 0.5$ Å^{-1}) for Cr Fe 10% alloy at various temperatures and below T_N. The pure Cr spectrum is shown for comparison.

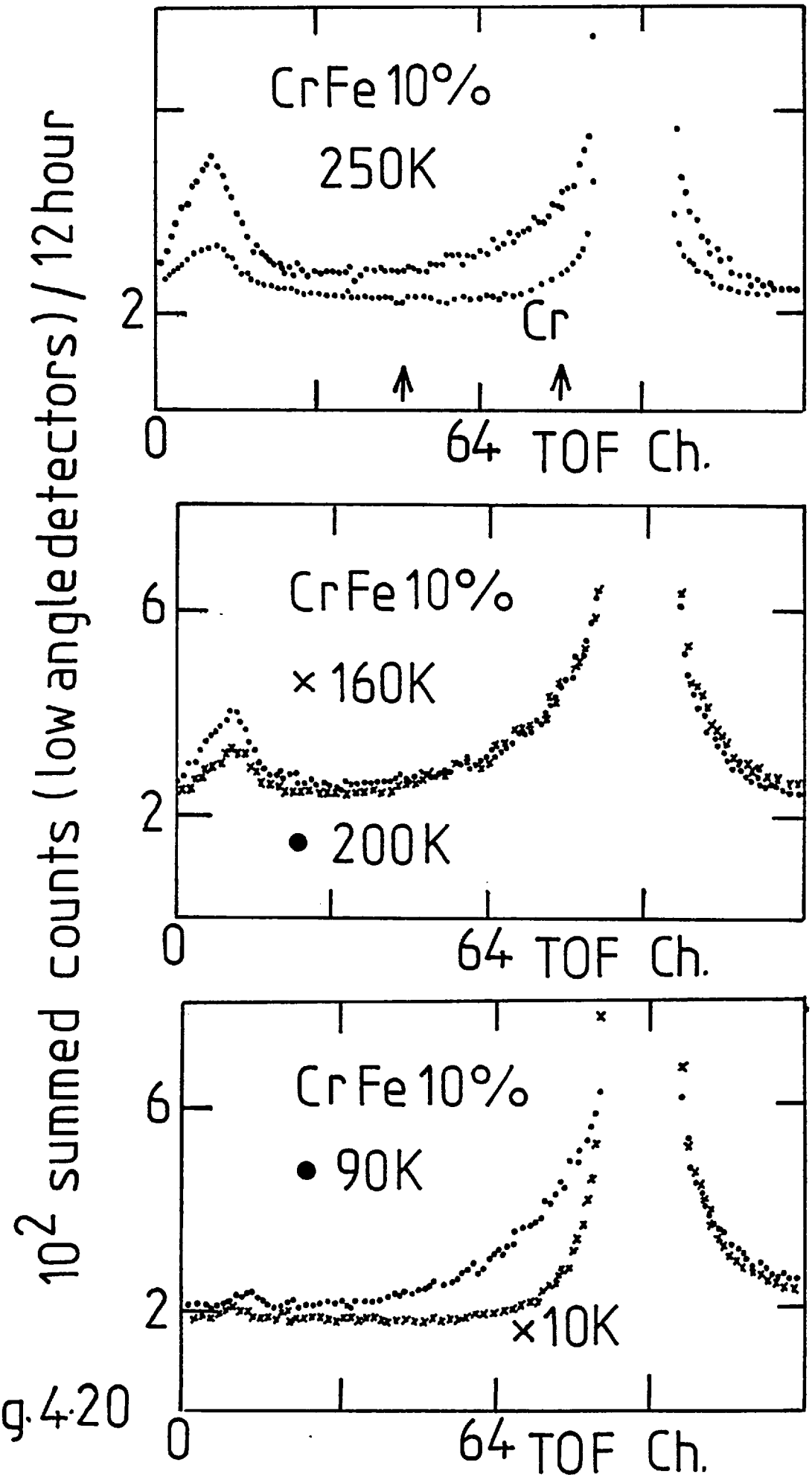
CrFe 10%
250K
Cr
2
0
64 TOF Ch.
CrFe 10%
× 160K
• 200K
6
2
0
64 TOF Ch.
CrFe 10%
• 90K
× 10K
6
2
0
64 TOF Ch.
10^2 summed counts (low angle detectors) / 12 hour

Fig. 4·20

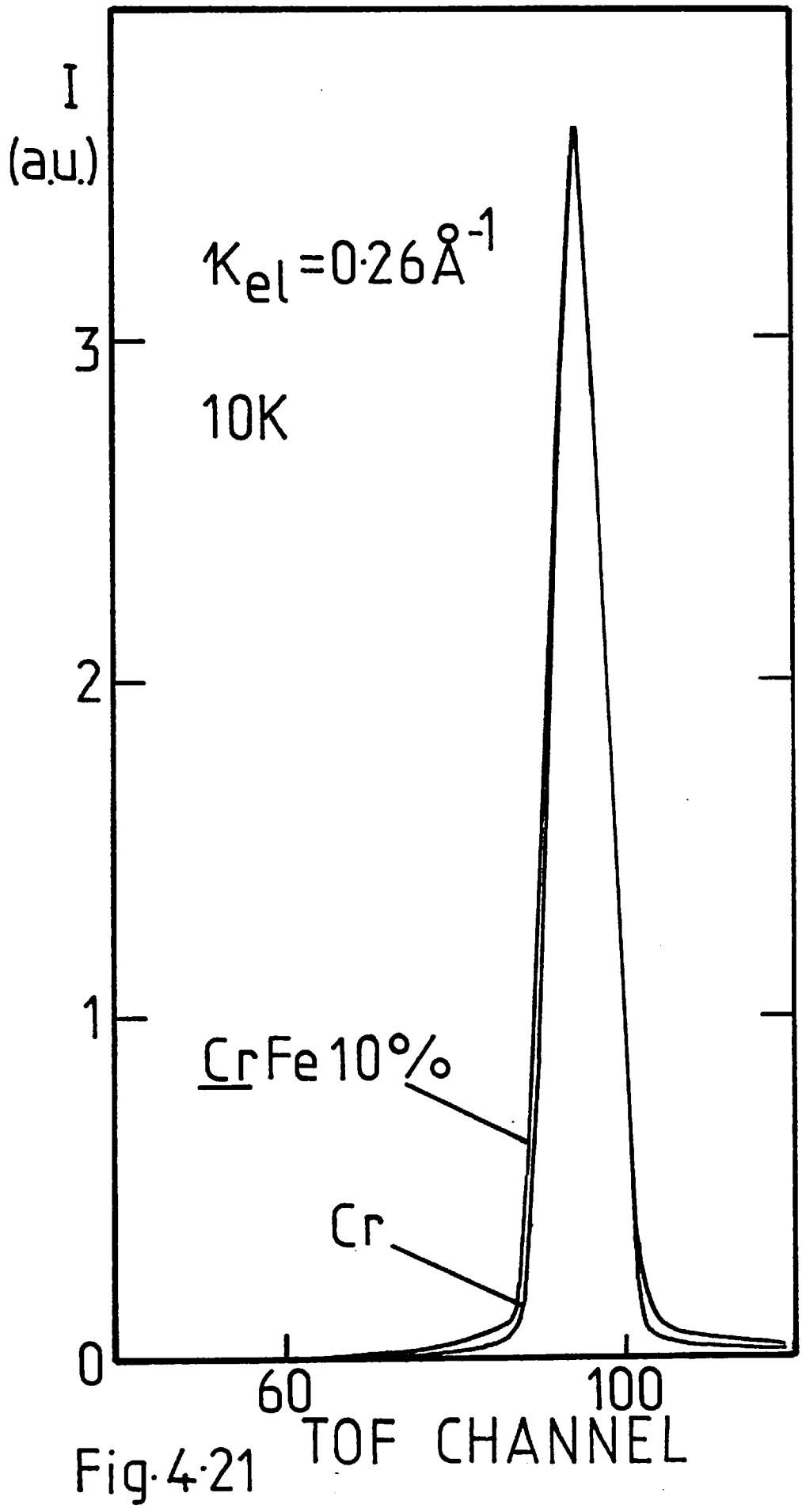

Fig·4·21

Quasielastic scattering from the Cr Fe 10% alloy is observed at all temperatures studied, both above and below T_N. At 10K the quasielastic scattering is almost the same width as the scattering from pure Cr, which is presumed to be elastic. The quasielastic scattering may still be distinguished even at this temperature. This is demonstrated in Fig. 4.21 where the TOF spectra for a single counter have been shown in more detail, the Cr and Cr Fe 10% peak heights have been normalized to each other.

The neutron quasielastic cross section for magnetic scattering has been examined in section 2.2.1 and may be written

$$\frac{d^2\sigma}{d\Omega dE} = \left(\frac{\gamma e^2}{2m_e c^2}\right)^2 \frac{k^1}{k} f^2(\kappa)\, g^2\, \mathcal{S}(\kappa,\omega) \qquad (4.20a)$$

where the spin dynamics are embodied in the function $\mathcal{S}(\kappa,\omega)$. This may be related to the spin relaxation function $F(\kappa,\omega)$ and the isothermal wavevector dependent susceptibility $\chi(\kappa)$ via (eq. 2.12), (eq. 2.14) and (eq. 2.15),

$$\mathcal{S}(\kappa,\omega) \;\alpha\; \frac{\omega}{1 - \exp(-h\omega\beta)}\; \chi(\kappa)\; F(\kappa,\omega) \qquad (4.20b)$$

For simplicity the κ dependence of $F(\omega,\kappa)$ will be neglected and $F(\omega)$ is assumed to have a Lorentzian line shape,

$$F(\omega) = \frac{1}{\pi}\, \frac{\Gamma}{\Gamma^2 + (h\omega)^2} \qquad (4.20c)$$

where Γ is the energy width of the relaxation function and is related to the characteristic time for exponential spin relaxation via $\Gamma = h/\tau$.

The relaxation function $F(\omega)$ was calculated from the experimental (summed) TOF spectra by firstly subtracting the time independent background and empty cell scattering. The resulting intensity was converted to a cross section on an energy rather than

TOF scale using (eq. 3.12), and corrected for the detailed balance factor to yield $F(\omega)$ in arbitrary units. No correction was made for the 3d form factor, which varies only weakly over the κ range of interest. The resulting $F(\omega)$ was fitted to a Lorentzian over the energy range 1.2 - 4.5meV, illustrated by arrows on the TOF spectra in Fig. 4.20. This fitting range lies well outside the wings of the elastic energy resolution function. The fits are shown in Fig. 4.22. With the exception of the 10K data the results are well described by a Lorentzian. As most of the scattering at 10K lies within the elastic resolution a fit at these higher energies is difficult to perform.

The energy widths (Γ) of the relaxation function determined in this way are shown as a function of temperature in Fig. 4.23. The energy width increases with increasing temperature below T_N but shows a decrease as the temperature is raised through T_N. At higher temperatures Γ continues to increase.

To investigate the κ dependence of the scattering the cross sections were put on an absolute scale and corrected for isotropic multiple scattering. The predominantly 'elastic' scattering, obtained by integration between ω = 0.5 meV to ω = -0.5 meV is shown as a function of temperature in Fig. 4.24. The corresponding cross sections for pure Cr are also shown. The scattering from pure Cr is κ independent and in reasonable agreement with the calculated nuclear incoherent cross section, shown arrowed. The cross section varies slightly with temperature indicating some systematic error. The cross section for Cr Fe 10% is peaked in the forward direction but tends to a constant, κ independent value at higher κ. The high κ cross section is larger than the combined calculated nuclear incoherent and Lane cross sections, shown arrowed. Although the forward scattering increases with decreasing temperature, the κ width remains essentially constant. At 250K the half width is 0.45 ± 0.05 Å^{-1} and decreases slightly to 0.35 ± 0.02 Å^{-1} at 10K. The fact that the forward scattering is strongly temperature dependent suggests that it is predominantly magnetic, rather than nuclear in origin.

Fig.4.22 Lorentzian fits to the relaxation function $F(\omega)$ for Cr Fe 10% at various temperatures. Here $F(\omega)^{-1}$ in arbitrary units is plotted as a function of ω^2.

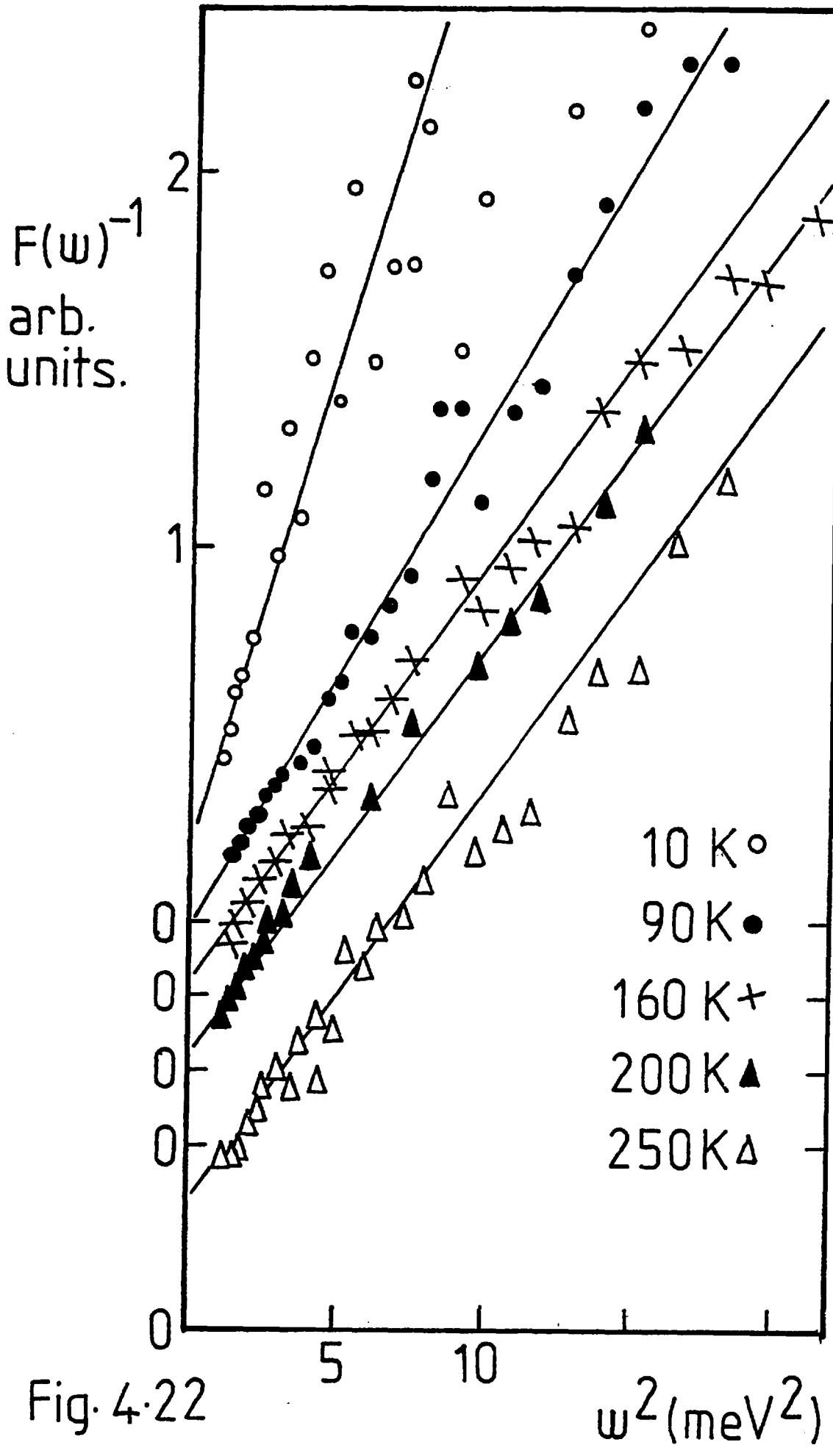

Fig. 4·22

Fig.4.23 Half widths (Γ) as a function of temperature for Cr Fe 10%. The Neél temperature is shown by an arrow. The solid line is a guide to the eye.

Fig.4.24 Integrated scattering cross section within a ±0.5 meV window about the elastic energy transfer for Cr Fe 10% and Cr samples. Calculated nuclear cross sections are shown by an arrow.

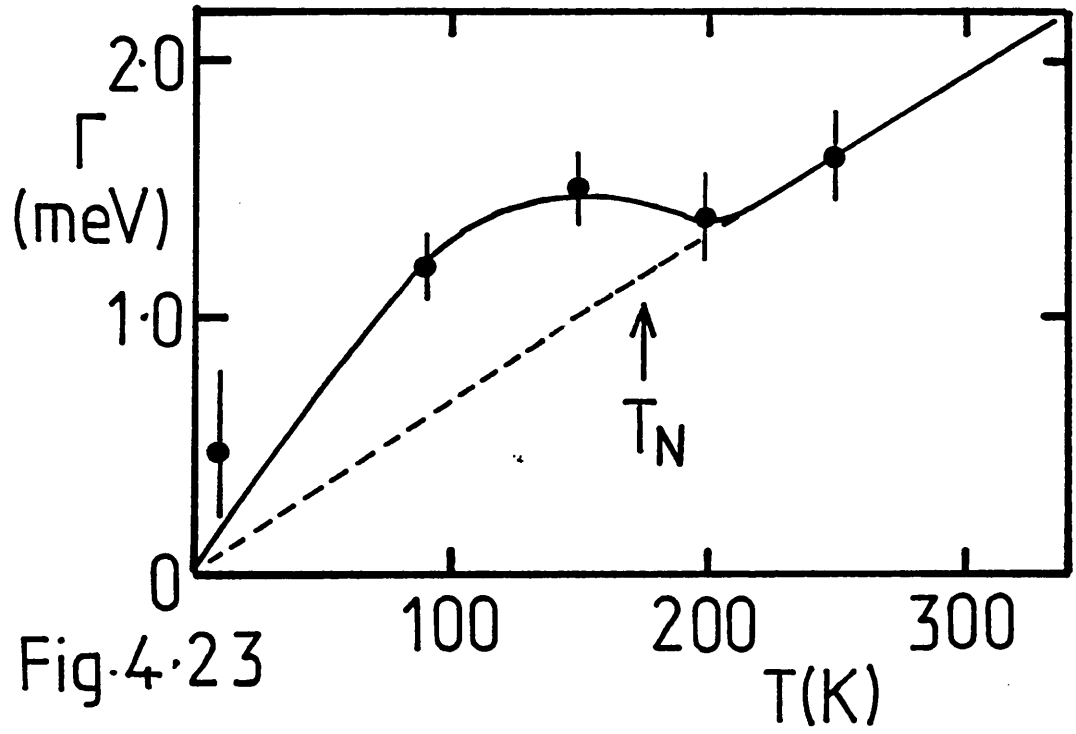

Fig·4·23

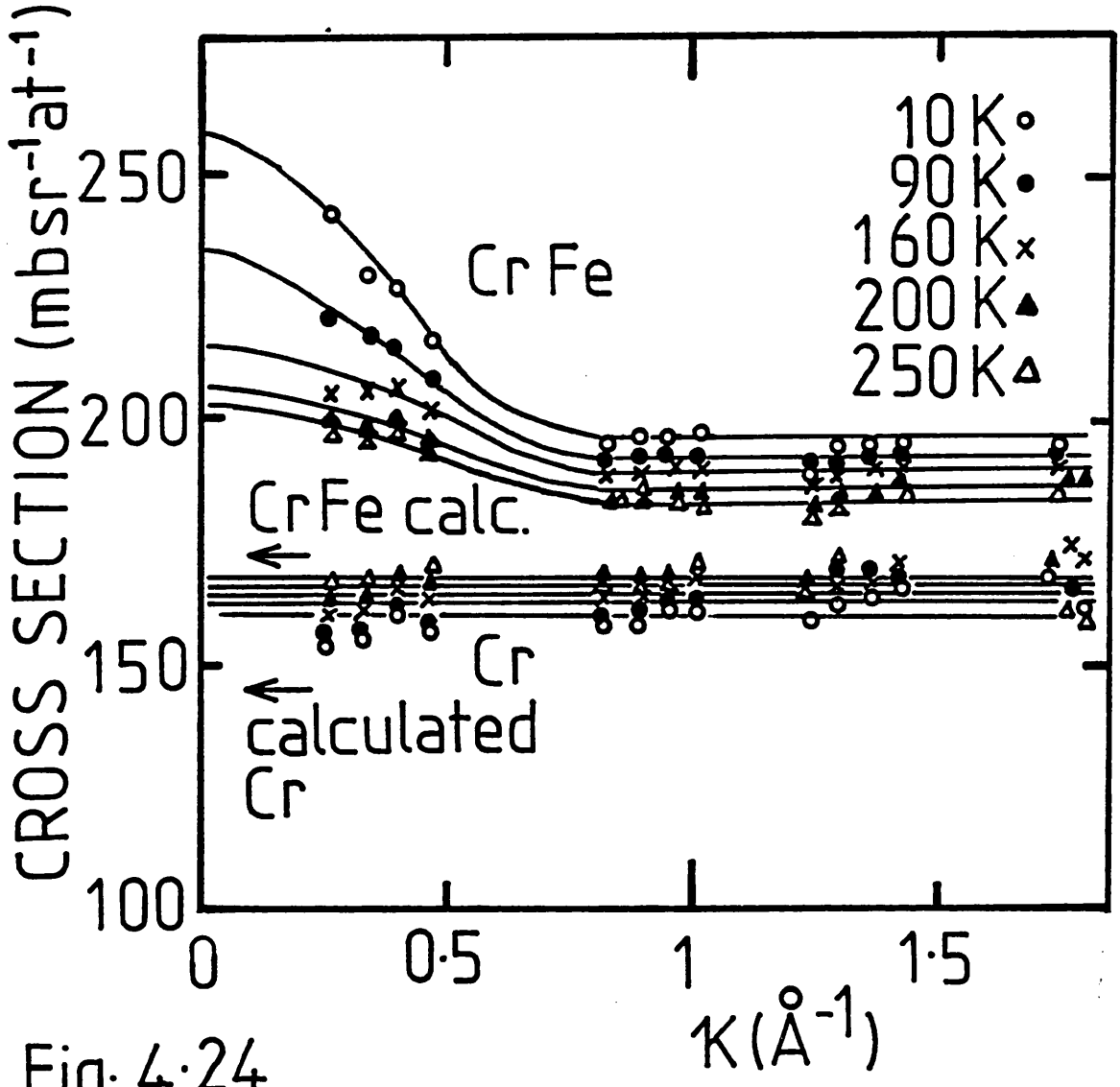

Fig· 4·24

4.4.3.2 Discussion

The quasielastic scattering arises from magnetically correlated clusters of Fe moments rather than the CSDW. This is demonstrated by the temperature dependence of the κ width of the 'elastic' scattering. Above T_N the CSDW does not exist and so the scattering must be associated with local Fe moments. These moments are correlated over a distance of some 5-10 Å at 250K. As the character of the scattering remains essentially unchanged below T_N (in terms of κ width) it is these same Fe moments which contribute to the scattering, even below T_N.

The coexistence of slowly relaxing clusters of Fe moments with the CSDW has been inferred previously from the low field bulk magnetization data (section 4.4.2). The TOF measurements give direct confirmation of this picture.

The dynamical behaviour of the Fe moments is influenced by the CSDW. This is shown by the increase in energy width at T_N, which implies that Fe moments tend to relax more rapidly in the presence of the CSDW. This observation would appear to be consistent with the suppression of the spin glass temperature by the CSDW, at least according to a fine particle model. As outlined in section 5.1.3., the fine particle blocking temperature is determined by the requirement that the experimental observation time (Δt) is equal to the characteristic relaxation time of the particle moment (τ_o). As the Fe moments relax more rapidly in the presence of the CSDW a decrease in T_g would be expected if Δt was held constant.

5.4.4 A polarization-analysis study of Cr Fe 5%

5.4.4.1 Introduction

The magnetic properties of the more concentrated Cr Fe CSDW

alloys are dominated by the large correlated assemblies of Fe moments observed in the preceding TOF measurement. A study of the magnetic disturbance produced on the CSDW by such a large number of interacting moments is intractable. Thus we have chosen to study a more dilute CSDW alloy with a predominance of isolated Fe atoms in an attempt to determine the CSDW moment at the Fe site and the nature of the magnetic disturbance surrounding such an atom.

The addition of Fe to Cr results in an approximately linear reduction in the CSDW average sublattice moment of some $4.6\mu_B$/at. It is important to understand how this reduction in CSDW moment proceeds. In the absence of evidence to the contrary, one must assume that a component of the CSDW exists on both Cr and Fe sites. (The average CSDW Cr moment and Fe moment are denoted $\bar{\mu}_{Cr}$ and $\bar{\mu}_{Fe}$ respectively.)

The decrease in average moment is inconsistent with two concentration independent moments $\bar{\mu}_{Cr}$ and $\bar{\mu}_{Fe}$. If the process were pure dilution ($\bar{\mu}_{Fe} = 0$) such a picture would require $\bar{\mu}_{Cr} = 4.6\mu_B$, independent of concentration. At the other extreme, if each Fe moment entered fully antiparallel into the CSDW with $\bar{\mu}_{Fe} = -2.2\mu_B$ a concentration independent $\bar{\mu}_{Cr} = 2.4\mu_B$ is obtained. These values of $\bar{\mu}_{Cr}$ are unphysically large so that it is apparent that at least $\bar{\mu}_{Cr}$ or $\bar{\mu}_{Fe}$ is concentration dependent.

Allowing for the moments $\bar{\mu}_{Cr}$ and $\bar{\mu}_{Fe}$ to be concentration dependent, the decrease in CSDW moment may proceed in a spatially inhomogeneous or homogeneous way. The inhomogeneity for a dilute alloy would be present only on Cr sites as all Fe atoms have the same local environment. The presence of an Fe moment may perturb the Cr moments in its vicinity, leading to a local reduction in moment. It is also possible to envisage a spatially uniform reduction in moment in which all Cr atoms retain the same moment.

The fact that the ratio of T_N to $\bar{\mu}$ is independent of concentration suggests that the essential nature of the CSDW is is unchanged by the presence of an increasing number of Fe atoms. This is difficult to account for without invoking both a CSDW moment on the Fe sites and a homogeneous distribution of sublattice moment.

The nature of the magnetic defect around an Fe atom and the CSDW moment on both sites may be determined from the magnetic elastic diffuse scattering. By using the polarization-analysis technique, the magnetic diffuse scattering from an antiferromagnet can be separated from the nuclear diffuse and incoherent scattering. The magnetic diffuse scattering is composed of two parts, the elastic defect scattering discussed above and the quasielastic scattering due to dynamical fluctuations in magnetization. The magnetic elastic diffuse scattering cross section has been treated in section 2.2.3 and is given by (eq. 2.29) for a dilute antiferromagnet. The quasielastic scattering has been considered in section 2.2.1. In the present experiment, these two components could not be separated as sufficiently high energy resolution was not available.

It is possible to calculate the magnitude of the magnetic elastic diffuse scattering from the Cr Fe 5% alloy chosen for this study at one special κ value by using the results of section 2.2 in conjunction with the experimentally determined sublattice moments of section 4.3. The elastic magnetic diffuse scattering at the (100) position is then given by,

$$\left(\frac{d\sigma}{d\Omega}\right)_{\text{Mag.El.}} (100) \text{ /mb/sr/at/} = 48.2\ C(1-C)\ f^2(100)\ \left(\frac{d\bar{\mu}}{dc} \text{ /}\mu_B\text{/at/}\right)^2$$

in the absence of nuclear short range order. Using measured values of $\frac{d\bar{\mu}}{dc} = -4.6 \pm 0.2$, $f(100) = 0.68$ and $C = 0.05$ gives

$$\left(\frac{d\sigma}{d\Omega}\right)_{\text{Mag.el.}} (100) = 22 \pm 2 \text{ mb/sr/at}$$

The integrated quasielastic scattering, which will be loosely termed the 'paramagnetic' scattering, may be calculated at $\kappa = 0$, assuming the validity of the quasistatic approximation to give

$$\frac{d\sigma}{d\Omega}_{Para}(0) \quad /mb/sr/at/ = 48.2\ g^2\ \ S(S+1)\ \frac{\chi(0)}{\chi_o}$$

where $\chi(0)$ is the measured bulk susceptibility of the sample and χ_o is the susceptibility of the same sample in the same units assuming that every atom has a spin S, gyromagnetic ratio g and follows a Curie law ($1/3\ g^2\ \ S(S+1)/T$). These latter factors need not have any physical significance and have been artificially introduced to cast the relationship into a form which is independent of the units used to measure the susceptibility. For dilute Cr-Fe alloys, this expression may be more conveniently written as

$$\frac{d\sigma}{d\Omega}_{Para}(0)\ /mb/sr/at/ = 48.2\ C\left(\frac{T}{T-\Theta}\right)\ p^2$$

where $p(\mu_B)$ and $\Theta(K)$ are the effective moment and Curie-Weiss temperature respectively. With the results of Ishikawa et al (1965) for a nominal 5% alloy this gives

$$\frac{d\sigma}{d\Omega}_{Para}(0) = 15 \pm 3 \text{ mb/sr/at (11K), } 13 \pm 1 \text{ mb/sr/at (210K)}$$

and 18 ± 3 mb/sr/at (275K)

which is of the same order as that expected for free paramagnetic Fe moments with S = 1 and g = 2, namely 19 mb/sr/at.

These calculations show that the magnetic elastic diffuse and 'paramagnetic' contributions to the cross section are of

approximately equal magnitude. This magnetic diffuse scattering is small compared to the nuclear contributions which total 160 mb/sr/at. Such a small signal superimposed on the nuclear scattering would be extremely difficult to isolate in an unpolarized beam experiment but can in principle be separated by neutron polarization-analysis.

4.4.4.2 Results and Analysis

The neutron polarization-analysis technique was used to affect an isothermal separation of the magnetic and nuclear defect scattering from an antiferromagnetic Cr Fe 5% alloy. The large polycrystalline sample was prepared according to section 3.1, and the experiment was carried out using the diffractometer D5 at the ILL, Grenoble. Experimental details may be found in section 3.7.

The Neél temperature of this sample was deduced from the temperature variation of the (100) magnetic reflection, giving $T_N = 250 \pm 5$ in good agreement with the results of 4.3. The (100) (111) and (210) magnetic reflections were observed unsplit indicating the CSDW structure.

The spin-flip and non spin-flip scattering cross sections were measured at temperatures of 11K (below T_N), 210K ($T < T_N$) and 275K (above T_N). The results are shown in Fig. 4.25 and Fig. 4.26. The Debye-Waller factor has been removed for convenience using $2W(\kappa) = 3.84 \times 10^{-3} \kappa^2$ (Holden and Fawcett (1978)). This correction is small and amounts to 8% at the largest scattering angle.

The non spin flip cross section will be examined first. As discussed in 2.4.2, the non spin-flip cross section for $\underset{\sim}{\kappa} // \underset{\sim}{P}$ contains only nuclear scattering terms,

$$\frac{d\sigma}{d\Omega}^{11}_{NSF} = \frac{d\sigma}{d\Omega}_{ISO} + \frac{d\sigma}{d\Omega}_{Laue} + {}^{1}/_{3} \frac{d\sigma}{d\Omega}_{nsi} + \text{Nuclear + multiple Bragg}$$

Fig.4.25 Non spin-flip cross sections for Cr Fe 5% at 11K ($T < T_N$), 210K ($T \lesssim T_N$) and 275K ($T > T_N$). Isotopic incoherent, Laue and nuclear spin incoherent levels are shown.

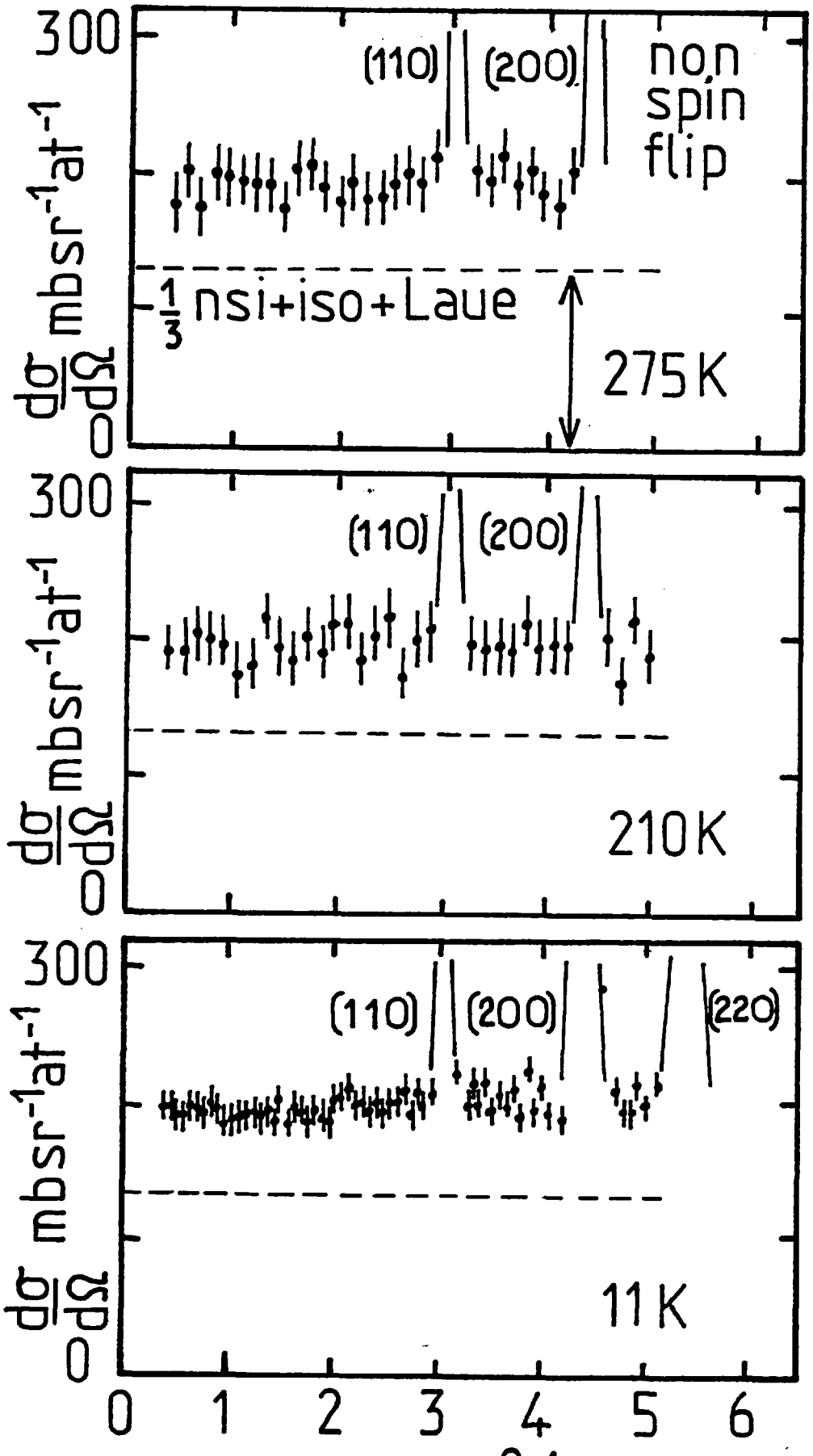
300
(110)
(200)
non
spin
flip
1/3 nsi+iso+Laue
275K
dσ/dΩ mbsr⁻¹at⁻¹
0
300
(110)
(200)
210K
dσ/dΩ mbsr⁻¹at⁻¹
0
300
(110)
(200)
(220)
11K
dσ/dΩ mbsr⁻¹at⁻¹
0
0 1 2 3 4 5 6
K(Å⁻¹)

Fig·4·25

The (110), (200) and (211) nuclear Bragg peaks expected for the bcc structure are present in the data. Between these Bragg peaks the non spin-flip (NSF) cross section is flat, to within experimental error and thus no atomic short range order can be detected. The cross section may be broken down into its constituent parts using the known values of nuclear isotopic and spin incoherent scattering. These cross sections have been measured by Cywinski and Hicks (1978) and Koester, Knopf and Waschkowski (1978) and supercede the older, inaccurate value of BNL 325 (1973). Using the polarization-analysis method, Cywinski and Hicks (1978) find

$$\frac{d\sigma}{d\Omega}_{ISO} = 110 \pm 10 \text{ mb sr}^{-1} \text{ at}^{-1} \quad \text{and} \quad \frac{d\sigma}{d\Omega}_{nsi} = 45 \pm 1 \text{ mb sr}^{-1} \text{ at}^{-1}$$

whereas Koester et al (1978) report

$$\frac{d\sigma}{d\Omega}_{ISO} = 101 \pm 1 \text{ mb sr}^{-1} \text{ at}^{-1} \quad \text{and} \quad \frac{d\sigma}{d\Omega}_{nsi} = 45 \pm 1 \text{ mb sr}^{-1} \text{ at}^{-1}$$

If the more accurate data of Koester et al (1978) are used this gives for Cr Fe 5%

$$\frac{d\sigma}{d\Omega}_{ISO} = 98 \pm 1 \text{ mb sr}^{-1} \text{ at}^{-1} \quad \text{and} \quad \frac{d\sigma}{d\Omega}_{nsi} = 43 \pm 1 \text{ mb sr}^{-1} \text{ at}^{-1}$$

where the nuclear incoherent scattering of Fe is assumed to contribute 1.5 mb sr^{-1} at^{-1} to the isotopic incoherent scattering only (Koester (1977)). This is reasonable as the only isotope with non zero nuclear spin is 2% abundant. These levels are shown in Fig.4.25. The Laue incoherent term given by eq.(2.8a) and (2.28c),

$$\frac{d\sigma}{d\Omega} = c(1-c)\ S(\kappa)\ (b_{Cr}-b_{Fe})^2$$

If the values b_{Fe} = 9.54 fm and b_{Cr} = 3.695 fm are used (Koester(1977)),

this atomic disorder scattering amounts to 17 mb sr^{-1} at^{-1}. This level is also illustrated in Fig. 4.25. The remaining scattering is due to multiple Bragg and multiple diffuse scattering. The multiple diffuse scattering is large because of the small ratio of absorption cross section to scattering cross section at these short wavelengths. The multiple scattering contribution was not estimated. The difference between calculated and measured cross sections indicates a multiple scattering contribution of some 60 mb/sr/at, or 30% of the total.

The spin flip (SF) cross section for $\underset{\sim}{\kappa} // \underset{\sim}{P}$ contains both nuclear and magnetic parts, from eq.(2.49b) and eq.(2.51b)

$$\frac{d\sigma}{d\Omega}^{11}_{SF} = \frac{d\sigma}{d\Omega}_{Mag.Diff.} + 2/3 \frac{d\sigma}{d\Omega}_{nsi} + \text{Magnetic Bragg + multiple.}$$

The (100), (111) and (210) magnetic Bragg reflections allowed for the CSDW structure are seen in the SF data for 11K. At 210K the (100) reflection can be discerned but the weaker (111) and (210) reflections can no longer be distinguished. No magnetic Bragg reflections are seen above T_N at 275K. The magnetic diffuse scattering may be isolated by subtracting the nuclear spin incoherent scattering and the multiple scattering contributions, if they are known to a sufficiently high accuracy. In view of the uncertainty in both these quantities, the magnetic diffuse scattering was estimated by assuming that the cross section above $\kappa = 3.9$ $\mathring{A}^{-1}$ was due entirely to multiple scattering and nuclear spin incoherence. An Fe 3d form factor is 0.4 at this scattering vector so that the magnetic diffuse scattering which depends on f^2 will be negligible in this region.

Following this procedure, the nuclear spin incoherent and multiple scattering contributions to the cross section were found to vary between 29 and 31 mb/sr/at. The calculated nuclear spin incoherent scattering is indicated in Fig.4.26 and is 29 mb/sr/at

Fig.4.26 Spin flip cross sections for Cr Fe 5% at 11K ($T < T_N$), 210K ($T > T_N$) and 275K ($T > T_N$). Calculated forward cross sections and magnetic elastic diffuse cross sections at (100) are shown by an arrow. Dotted curves represent an Fe form factor. The solid line through the 275K data is also an Fe form factor, the remaining solid lines are guides to the eye. The nuclear spin incoherent level is shown by an arrow. P parallel to κ (●) , P perpendicular to κ (○)

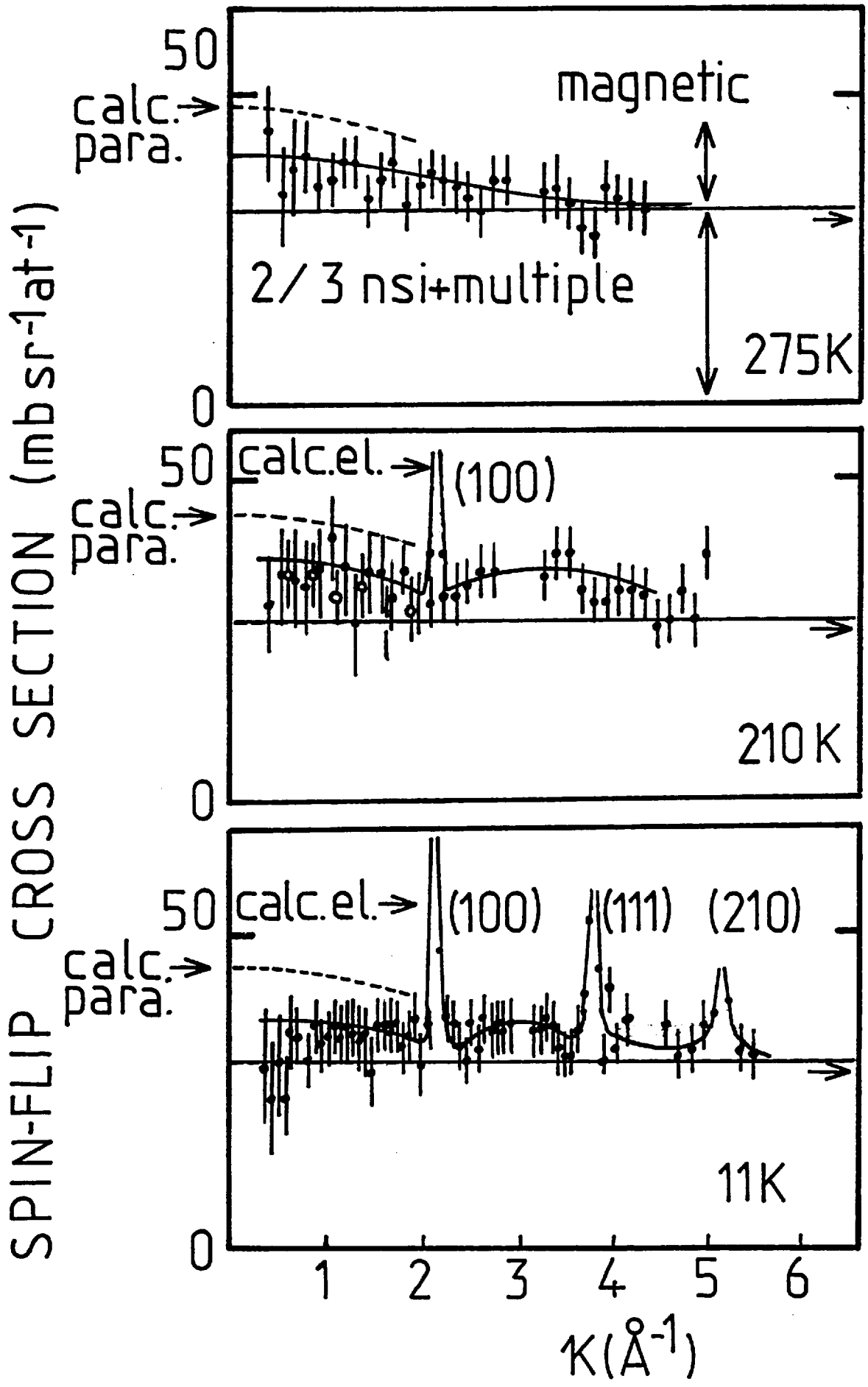
50
calc.
para.
magnetic
2/3 nsi+multiple
275K
0
50
calc.el.
(100)
calc.
para.
210 K
0
50
calc.el.
(100)
(111)
(210)
calc.
para.
11K
0
1
2
3
4
5
6
K(Å-1)
SPIN-FLIP CROSS SECTION (mbsr-1at-1)

Fig. 4·26

according to Koester et al (1978) and 20 mb/sr/at according to Cywinski and Hicks (1978). A check on the validity of the separation procedure was made by carrying out a limited number of scans with $\underset{\sim}{P} \perp \underset{\sim}{\kappa}$. In this configuration the SF scattering is (from eq.(2.51b))

$$\frac{d\sigma}{d\Omega}_{SF} = \tfrac{1}{2}\frac{d\sigma}{d\Omega}_{mag} + \frac{2}{3}\frac{d\sigma}{d\Omega}_{nsi} + \text{Magnetic Bragg} + \text{multiple},$$

having only half the total diffuse magnetic scattering. As shown in Fig. 4.26 the cross sections for $\underset{\sim}{P} \perp \underset{\sim}{\kappa}$ are consistently below those for $\underset{\sim}{P}//\underset{\sim}{\kappa}$. In so far as it can be separated, the diffuse magnetic scattering is approximately halved.

The magnetic diffuse scattering cross sections calculated in this way are small and the overall data quality is poor. Nevertheless, the fact that this cross section of some 10 mb/sr/at could be isolated from a total scattering of over 230 mb/sr/at highlights the power of the polarization-analysis technique. The limiting values of the magnetic elastic diffuse and 'paramagnetic' scattering cross sections calculated in the previous section are shown arrowed in Fig. 4.26. A squared 3d form factor normalized to calculated forward cross section is also shown as a dashed line. No attempt has been made to fit the measured cross sections.

A squared 3d form factor has been drawn through the 275K data, the curves through the 210K and 11K data are suggested guides to the eye.

4.4.4.3 Discussion

A quantitative analysis of the measured magnetic diffuse cross section is not possible. This is due both to the poor data quality and the difficulty in separating the magnetic elastic diffuse

and 'paramagnetic' cross sections. However, some general conclusions may be drawn concerning the nature of the magnetic defect in this alloy.

The most important observation is that the magnetic diffuse scattering on both sides of the (100) reflection is of the order 2 ± 5 mb/sr/at at 11K and 210K. Yet the calculated value of the magnetic elastic diffuse cross section alone is 22 ± 2 mb/sr/at at the (100) position. (It is not possible to measure the diffuse cross section exactly at (100) as it is superimposed on the (100) Bragg reflection.) If the model calculation is correct, the diffuse scattering must increase by an order of magnitude over a κ range of 0.3 $\mathring{A}^{-1}$. This implies a magnetic defect about the Fe atom of at least 14 $\mathring{A}$ in extent. Some structure to the diffuse scattering may be discerned, symmetrically disposed, about the (100) position. This may imply an additional shorter ranged component to the defect. It is not possible to deduce whether a component of the CSDW is induced at Fe sites from this data.

The 'paramagnetic' component of the magnetic diffuse scattering cannot be separated from the elastic component below T_N. Above T_N this problem does not arise and the magnetic diffuse scattering at 275K is consistent with the paramagnetic scattering from weakly coupled Fe moments. The cross section varies approximately as the square of a 3d form factor and the extrapolated forward cross section (10 ± 2mb/sr/at) is in reasonable agreement with the estimate of 18 ± 3mb/sr/at taken from the bulk susceptibility. Below T_N the extrapolated forward scattering at 210K is 8 ± 2mb/sr/at which is in reasonable agreement with the calculated value of 13 ± 3mb/sr/at. The agreement is not as good at 11K where the extrapolated forward scattering, ignoring the first four negative data points, is 6 ± 2 mb/sr/at compared with 15 ± 3 mb/sr/at.

Cywinski and Hicks (1980) reach a different conclusion in their polarization analysis study of a Cr Fe 6.5% alloy at 4.2K. These authors report that the component of the CSDW at the Fe site is zero, that the magnetic disturbance is short ranged and

that a sharp 'superparamagnetic' component of the scattering may be found below $\kappa = 0.3\ \mathring{A}^{-1}$.

The existence of a sharply peaked 'superparamagnetic' component of the scattering at low κ cannot be ruled out. A steeply rising cross-section between $0.4\ \mathring{A}^{-1}$ and $\kappa = 0$ would certainly lead to better agreement with the calculated forward cross sections. The κ width of such a peak must be of the order $0.4\ \mathring{A}^{-1}$ at 11K rising to $1\ \mathring{A}^{-1}$ at 210 and 275K. An alternative explanation for a lack of consistency between an extrapolated and calculated forward cross section may be traced to a failure of the quasistatic approximation, in particular via the requirement that the energy width is small compared to kT.

The conclusion of Cywinski and Hicks that the magnetic disturbance is short ranged and that $\bar{\mu}_{Fe} = 0$ was reached by fitting the magnetic diffuse scattering using a formalism similar to section 2.2.3. The scattering was assumed to be purely elastic. The consistency of this procedure was checked by extrapolation to (100). It is difficult to reconcile this result with the present data which suggests a long ranged component to the magnetic defect. One possible explanation is the restricted κ range of the latter experiments, which did not extend to the (100) position. A sharply peaked magnetic diffuse component in the vicinity of (100) would thus not be detected.

Another source of discrepancy may lie in the microscopic state of the sample. The forward peak in the NSF cross section reported by Cywinski and Hicks (1980) indicates atomic clustering. Such clustering could not be observed in the Cr Fe 5% alloy reported here. This difference may be traced to the use of electrolytic Cr by Cywinski and Hicks and low gas content iodide Cr in the present measurement. The conditions of heat treatment also differ.

It was not possible to decide whether a component of the CSDW exists on the Fe sites in the present experiment. According to Cywinski and Hicks no such component is present, to within experimental error. However, the analysis of Cywinski and Hicks appears to be in error. The error arises in the expression for the average sublattice moment which should be written,

$$C\,G(0) + C\bar{\mu}_{Fe} + (1-C)\mu_{Cr} = \bar{\mu}$$

to be consistent with the definition of μ_{Cr} as the unperturbed moment on Cr sites, as opposed to the average moment on Cr sites (see for example, Marshall and Lovesey (1971) equation 14.77 and 14.78). With a revised analysis, a component of the CSDW at the Fe site is obtained. The analysis gives $\bar{\mu}_{Fe} = 0.41 \pm .08\mu_B$, $\mu_{Cr} = 1.01 \pm .08\mu_B$ or alternatively $\bar{\mu}_{Cr} = 0.63 \pm .09\mu_B$. It is interesting to note that the unperturbed Cr moment is approximately equal to the extrapolated moment of pure CSDW Cr of section 4.1.

CHAPTER 5

THE ONSET OF FERROMAGNETISM IN CrFe ALLOYS

5.1 The evolution of magnetic order in binary alloys

5.1.1 Introduction

A proper description of disorder in physical systems remains one of the most important questions in solid state physics. Magnetically disordered systems have proved to be a very fruitful area for such investigations. This is due in part to the fact that the simple Ising and Heisenberg models for magnetic phenomena are not only mathematically tractable but also provide an accurate description of a large class of real materials. The results of such work also provide a basis for understanding the more complex magnetic behaviour of disordered metallic magnets where the Ising and Heisenberg descriptions are not necessarily valid.

In this section the evolution of magnetic order with concentration from a nonmagnetic system A to a magnetically ordered system B will be discussed for the particular case of cryst alline binary alloys $A_{1-C}\,B_C$. Two types of disorder arise in this context. The first is the positional disorder which comes from the disordered occupation of lattice sites by A and B atoms. This is treated in the limiting case where the magnetic forces are short ranged and concentration independent using percolation theory (section 5.1.2). The second type of disorder comes from disorder in the exchange interactions and leads to a discussion of spin glasses (section 5.1.3). Finally, the application of these concepts to a few systems which show a critical concentration for long range order will be described in (section 5.1.4).

5.1.2 The percolation description

5.1.2.1 Introduction

A critical concentration for long range magnetic order (C_L) is frequently observed for binary crystalline alloys A_{1-C} B_C where the pure material B is magnetically ordered and the pure material A is nonmagnetic. In the most extreme cases there is no sense of evolution of magnetic order with concentration, the alloys for $C < C_L$ show the same nonmagnetic behaviour as pure A and for $C > C_L$ switch immediately to the long range order associated with pure B. This situation is realized in V_{1-C} Cr_C alloys for example, where for $C < C_L$ not only is there no long range order but also no magnetic moment on Cr sites until at $C > C_L$ both a magnetic moment and ordered antiferromagnetic moment are induced by the transition to an exactly scaled version of the ISDW phase of pure Cr. In general , there is a slow evolution of magnetic order with concentration. New magnetic phenomena may occur for $C < C_L$ and the ordered phase which appears at $C > C_L$ may be different to pure B type order. For example, if a local moment can be sustained on some impurity sites for $C < C_L$ a strongly correlated paramagnet (Cu_{1-C} Ni_C), spin glass (Cu_{1-C} Mn_C) or giant moment state (Pd_{1-C} Fe_C) which bears no resemblance to pure Cu or Pd may result. For $C > C_L$ the transition may to be to a state with completely different symmetry, e.g. Pd_{1-C} Mn_C is ferromagnetic for $C \gtrsim C_L$ whereas γMn is antiferromagnetic. The difference may be more subtle, resulting in an ordered phase with different critical exponents to pure B.

The occurence of a critical concentration has been discussed from two divergent points of view. Within the itinerant picture the exchange integral and density of states vary with concentration until at C_L a Stoner criterion $IN(E_F) > 1$ is satisfied at T=0 and long range order results. This type of model has proved very successful in accounting for Cr alloys (section 4.1). At the other extreme the

percolation picture (in which the interactions are assumed to be short ranged and concentration independent) invokes a purely geometrical criterion to locate C_L. This type of model describes well the behaviour of insulating antiferromagnetic alloys (section 5.1.4.1). A more universal description of the onset of long range order must include aspects of both these approaches.

Many features of the percolation description appear to be relevent to the case of $Cr_{1-C}\ Fe_C$ alloys.

5.1.2.2 The pure percolation problem

A brief review of the pure percolation problem will be given here. Further details may be found in the extensive reviews by Shante and Kirkpatrick (1971), Essam (1972) and Stauffer (1979).

The onset of long range order in certain binary alloys may be viewed as a pure site percolation process. The alloy is taken to be a random solid solution with one species (A) nonmagnetic and the other (B) having a well defined local moment which interacts with other moments via nearest neighbour exchange interactions. Consider the effect of increasing the concentration of magnetic species at T=0 in the absence of anisotropy effects. When the concentration is less than C_L, magnetic correlations can only be sustained over finite distances determined by tne nearest neighbour (nn) distribution of magnetic species on the lattice. The three dimensional correlated networks of nn moments (clusters) increase in size as the concentration is increased until such a concentration is reached that one such network penetrates the entire sample. The concentration at which this infinite cluster forms (the percolation limit C_p) is the point at which the range of moment correlations first diverges, signalling the onset of long range order, $C_L=C_p$. For a b.c.c. lattice C_p is 24.3 $\pm$ 1% (Essam (1972)). As the concentration is increased beyond C_p successively more moments are

incorporated into the infinite cluster at the expense of finite clusters. However a sizeable fraction of moments still belong to finite clusters even above C_p. This process is illustrated schematically for a two dimensional square lattice in Fig. 5.1 (K. Mihill, private communication).

The magnetic variant of what is a more general geometrical problem has been given above. It is useful to define the following geometrical quantities (Stauffer (1979)), Essam (1972)). An s-cluster is a group of s occupied lattice sites connected by nn distances. $\bar{n}_s(c)$ is the average number of s clusters (per site) for a given concentration where the average is respect to different configurations. The zeroth, first and second moments of $\bar{n}_s(c)$ are related to the average number of finite clusters (per site),

$$\bar{n}_f(c) = \sum_{s=1}^{f} \bar{n}_s(c) \tag{5.1a}$$

where the summation excludes any infinite cluster; the fraction of occupied sites which belong to finite clusters,

$$\bar{P}_f(c) = \sum_{s}^{f} s\, \bar{n}_s(c) \tag{5.1b}$$

and the average s of finite clusters,

$$\bar{S}(c) = \sum_{s}^{f} s^2\, \bar{n}_s(c) \Big/ \sum_{s}^{f} s\, \bar{n}_s(c) \tag{5.1c}$$

A percolation probability, equal to the fraction of occupied sites belonging to the infinite cluster $\bar{P}_\infty(c)$ is also defined. The variation of $\bar{P}_\infty(c)$ and $\bar{P}_f(c)$ with concentration is shown in Fig.5.2 (Shante and Kirkpatrick (1971)). As expected $P_f(c)$ increases with concentration up to C_p and then decreases as the infinite cluster increases in size. The coexistence of finite and infinite clusters above C_p should be noted.

The average spatial correlation between occupied sites is

Fig.5.1 Percolation on a two dimensional square lattice. Nearest neighbour occupied lattice sites (closed circles) are connected by bonds to form clusters whose size increase with increasing concentration (C = 0.1,0.2,0.3,0.4) until one cluster spans the lattice at the percolation concentration (C = 0.5). Above the percolation concentration, small finite clusters coexist with the spanning or infinite cluster (C = 0.6).

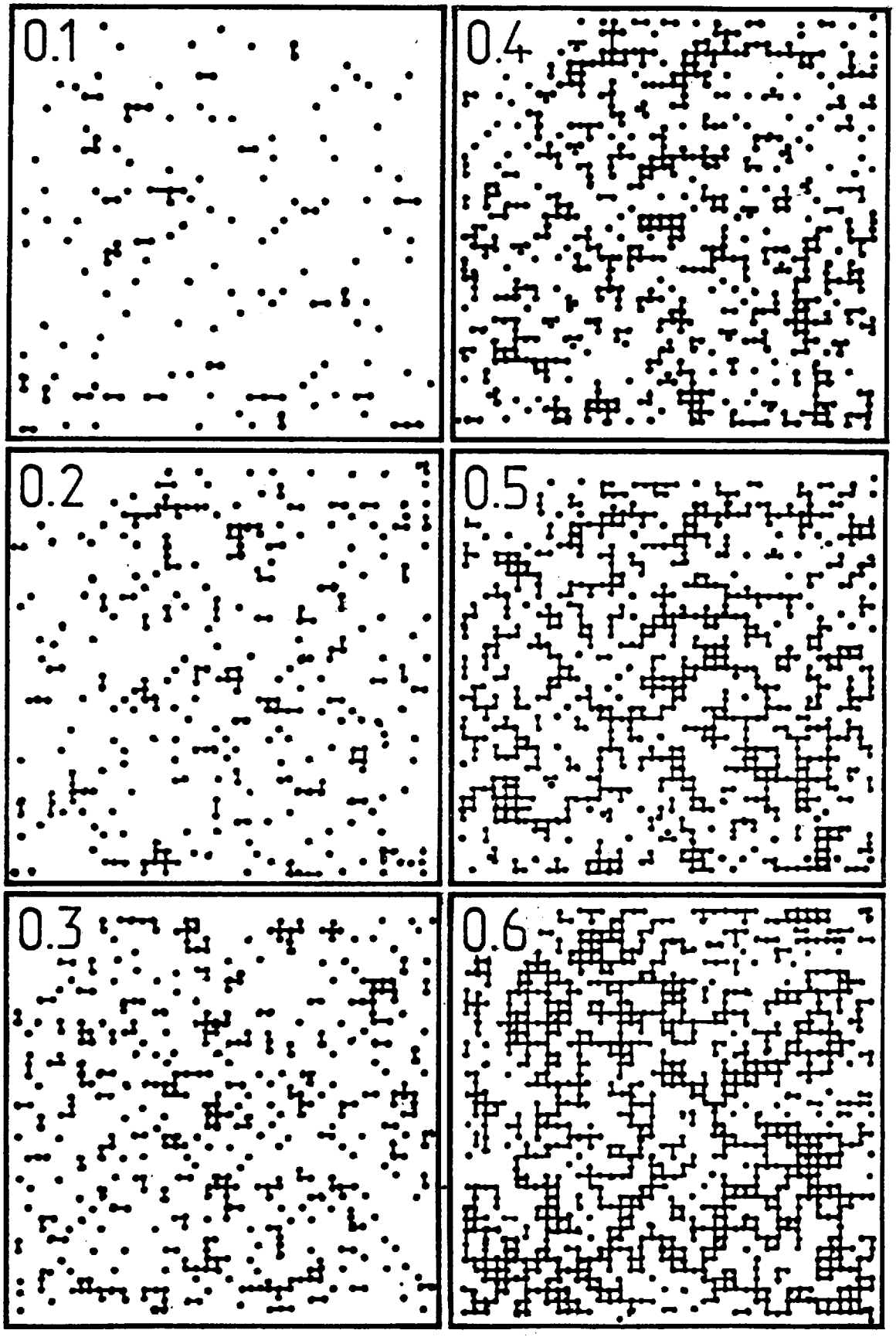

Fig. 5·1

Fig.5.2 Percolation properties of a tree with a coordination number 4 and percolation concentration 1/3: fraction of volume occupied by (a) finite clusters (b) infinite cluster and (c) mean cluster size S(p) are shown as a function of concentration p. (Shante and Kirkpatrick (1971)).

Fig.5.3 Theoretical critical curves for diluted spin $\frac{1}{2}$ Heisenberg (a) and Ising (b) antiferromagnets. Experimental data for $K\,Mn_c\,Mg_{1-c}\,F_3$ and $Cs_3\,Co_c\,Zn_{1-c}\,Cl_5$ are shown. (Stinchcombe (1979b)).

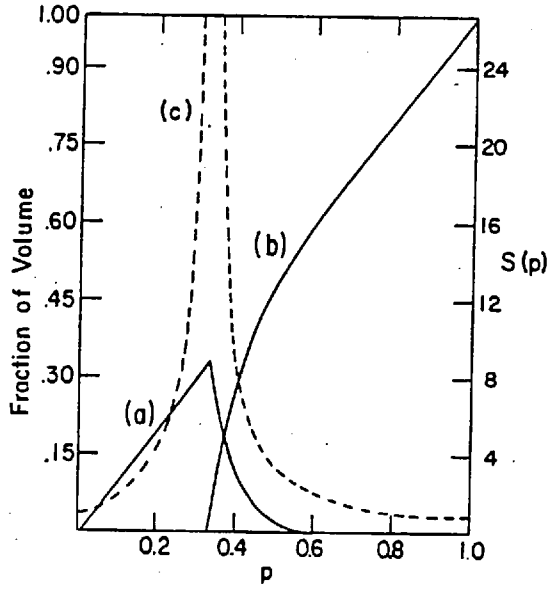

Fig.5.2

a

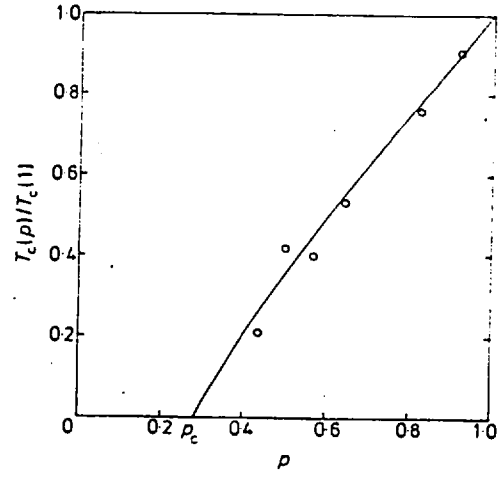

b

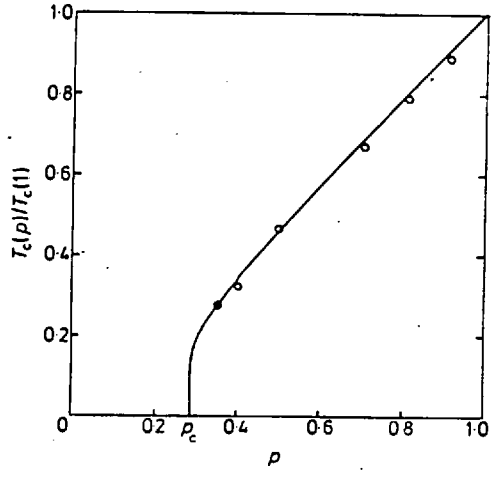

Fig.5.3

described by the pair connectedness $\bar{C}_{ij}(c)$ of sites i and j, where

$$\bar{C}_{ij}(c) = \bar{\gamma}_{ij} - (\bar{P}_{\infty}(c))^2 \tag{5.2a}$$

with $\gamma_{ij} = 1$ if sites i and j are connected by a series of nn bonds and zero otherwise. (With this definition sites belonging to the infinite cluster do not contribute to $\bar{C}_{ij}$). The Fourier transform of the pair connectedness $C_2(\kappa)$ may be expanded to second order in κ^2 after spherical averaging to yield the Guinier law,

$$C_2(\kappa) = C_2(0)\ (1 - 1/3\ \overline{R_G^2}\ \kappa^2 + \ldots\ ) \tag{5.2b}$$

where

$$C_2(0) = \bar{s}(c) \tag{5.2c}$$

by a geometrical fluctuation - dissipation theorem (Birgeneau et al (1980)), and $\overline{R_G^2}$ is the average squared geometrical radius of gyration, which is a measure of the range of geometrical correlations,

$$\overline{R_G^2} = \sum_s^f s^2\, \bar{n}_s(c)\, \overline{R_{Gs}^2} \ \Big/ \ \sum_s^f s^2\, \bar{n}_s(c) \tag{5.2d}$$

This defines an effective geometrical inverse range parameter

$$\kappa_{1G} = \sqrt{3/\overline{R_G^2}} \tag{5.2e}$$

which is equivalent in mean field theory to the true inverse range parameter κ_G dictating the exponential decay of geometrical correlations.

The percolation process has many features common to a second order thermodynamic phase transition. The geometrical system orders at C_p with the spontaneous appearance of the infinite cluster. In the vicinity of C_p the average s of finite clusters and $\overline{R_G^2}$ increase dramatically, tending to diverge at C_p. This conjecture was proved

rigo.rously by Kastelyn and Fortuin (1969). Thus, by analogy with thermodynamic critical behaviour, for $C \sim C_p$ the geometric inverse correlation range tends to zero at C_p,

$$\kappa_{1G} \sim |C-C_p|^{\nu_p} \tag{5.3a}$$

the average s for finite clusters (susceptibility χT) diverges at C_p

$$\bar{s}(c) \sim |C-C_p|^{-\gamma_p} \tag{5.3b}$$

the percolation probability (spontaneous magnetization) first appears

$$\bar{P}_\infty(c) \sim (C-C_p)^{\beta_p} \tag{5.3c}$$

and the Fourier transform of the pair connectedness (χ (κ) T) has the asymptotic form

$$C_2(\kappa) \sim \kappa^{\eta_p - 2} \tag{5.3d}$$

at $C=C_p$. The percolation critical exponents so defined are related by the scaling laws discussed in section 2.2.4. For a three dimensional lattice (Sykes et al (1975))

$$\nu_p = 0.825 \pm 0.02 \quad \gamma_p = 1.66 \pm 0.07 \tag{5.3e}$$

implying $\eta_p \sim -0.01 \pm 0.10$

In common with thermodynamic critical behaviour, scaling laws for geometrical critical phenomena have been proposed. Dunn, Essam and Lovelock (1975) suggest

$$C_2(\kappa) = \kappa^{\eta_p - 2} A(\kappa/\kappa_{1G}) \tag{5.4a}$$

or equivalently

$$C_2(\kappa) = \kappa_{1G}^{\eta_p - 2} \; B(\kappa/\kappa_{1G}) \qquad (5.4b)$$

should hold for $\kappa(c) << 1$, $C \sim C_p$. The Ornstein-Zernicke form of $C_2(\kappa)$ would satisfy such a scaling law as well as the Fisher-Burford modification (eq.2.35a).

Geometric variables which have no obvious thermal analogues have also been investigation (Stauffer (1979)). The 'shape' of percolation clusters is one such example. A number of studies (e.g. Stanley et al (1976)) have revealed that large percolation clusters near C_p are ramified or stringy in shape, rather than compact or droplet like. An effective cluster dimensionality d_p is defined in an attempt to provide a quantitative measure of cluster shape. According to Stanley (1977) such an effective dimensionality relates the average number of occupied sites in finite clusters $\bar{s}(c)$ to the average linear dimensions of finite clusters via,

$$\bar{s}(c) \sim (\kappa_G(c))^{-d_p} \qquad (5.5a)$$

Combining eqs. (5.2c)(5.4b) and (5.5a)

$$d_p = 2 - \eta_p \; . \qquad (5.5b)$$

For a bcc lattice $d_p = 2.01$, significantly smaller than the full three dimensional character of the lattice. Alternative definitions of d_p have been selected by a number of authors and the relative merits of each are discussed by Stauffer (1979). No matter what definition is used, $d_p < d$ in greater than one dimension. For the purposes of this discussion, the definition (eq. 5.5) will be adopted. The infinite cluster for $C \sim C_p$ is also ramified. As one of the large finite clusters for $C < C_p$ develops into the infinite cluster for $C = C_p$ this result is not surprising. The situation changes somewhat for $C >> C_p$; Stauffer (1979) demonstrates that finite clusters tend to

become more droplet like for $C > C_p$.

5.1.2.3 Magnetic percolation at finite temperature

The pure percolation process described above gives a very detailed account of the concentration dependence of magnetic properties in a model binary alloy at T = 0. It remains to generalize these results to finite temperature.

It is convenient to start with the pure system, C = 1. The critical behaviour of pure systems has been subject to exhaustive investigation over recent years and is largely understood. In summary, the inverse correlation range κ_1 tends to zero at the critical temperature $T_c(1)$ with an exponent ν_T

$$\kappa_1 \sim (T-T_c(1))^{\nu_T} \tag{5.6a}$$

the normalized susceptibility $\chi(T)/\chi_o$ diverges at $T_c(1)$,

$$\chi(T)/\chi_o \sim (T-T_c(1))^{-\gamma_T} \tag{5.6b}$$

and at $T_c(1)$ the normalized wave vector dependent susceptibility has the limiting form

$$\chi(\kappa)/\chi_o \sim \kappa^{\eta_T-2} \tag{5.6c}$$

(results which have been discussed in section 2.24). Considerable effort has been spent in calculating the critical exponents ν_T, γ_T etc. for various model systems. A summary of current values is given by Le Guillon and Zinn-Justin (1980) for n vector models (n = 0,1,2 and 3) in 2 and 3 dimensions. Estimates for the 3D Heisenberg model vary but lie within the limits

$$\nu_T = 0.70 \pm 0.02 \quad \gamma_T = 1.40 \pm 0.04 \tag{5.6d}$$

Similarly for the 3D Ising model

$$\nu_T = 0.638 \pm 0.002 \quad \gamma_T = 1.25 \pm 0.005 \tag{5.6e}$$

which should be contrasted with the mean field values

$$\nu_T = \tfrac{1}{2} \quad \gamma_T = 1 \tag{5.6f}$$

The Fourier transform of the spin-spin correlation function $S(\kappa)$ which is proportional to the normalized wavevector dependent susceptibility has the scaling form (Halperin and Hohenberg(1969)) for $T \sim T_c(1)$ and $\kappa >> \bar{d}$,

$$S(\kappa) = \kappa^{\eta_T - 2} \; G(\kappa_1/\kappa) \tag{5.7a}$$

or alternatively

$$S(\kappa) = \kappa_1^{\eta_T - 2} \; F(\kappa/\kappa_1) \tag{5.7b}$$

In the Guinier region $\kappa/\kappa_1 << 1$ (also known as the 'hydrodynamic' region) the function F may be expanded to second order in κ/κ_1 to give the Guinier form

$$S(\kappa) \sim \kappa_1^{-2+\eta_T} \; (1 + b(\kappa/\kappa_1)^2 + \ldots) \tag{5.7c}$$

where to be consistent with the definition of κ_1, $b = -1$. In the opposite limit $\kappa/\kappa_1 >> 1$ (the 'critical' region)

$$S(\kappa) \sim \kappa^{-2+\eta_T} \; (1 + b^1(\kappa_1/\kappa)^2 + \ldots) \tag{5.7d}$$

The forms of critical scattering discussed in section 2.24 are consistent with the scaling law (eq. 5.7). The Ornstein-Zernicke result (eq.2.34a) corresponds to mean field exponents. The more exact result due to Fisher and Burford (1967) (eq.2.35a) satisfies (eq. 5.7) as well as the approximation

$$S(\kappa) \sim [\kappa_1^2 + \kappa^2(1-\eta/2)^{-1}]^{-1+\eta/2} \tag{5.7e}$$

valid for $a\kappa << 1$. Fisher and Burford (1967) draw the distinction

between the true inverse correlation range which governs the exponential decay of correlations at large R and the effective value κ_1 deduced from measurements in the Guinier region. The distinction between these two quantities need only be made for T significantly different to $T_c(1)$ and for $T \sim T_c(1)$ both inverse correlation ranges diverge with the same exponent.

Consider then the effect of a small decrease in concentration from C = 1. The disordered system which results will have a spontaneous magnetization proportional to $\bar{P}_\infty(c)$ at T = 0 but it is not obvious whether a sharp transition to a paramagnetic state will occur as the temperature is increased. According to an argument by Harris (1974) and elaborated by a number of later workers (summarized by Lubensky (1979)) a sharp phase transition will occur if the exponent of the specific heat for the pure system $\alpha_T < 0$. The phase transition at $T_c(c)$ will be unaffected by a small amount of site disorder, the critical exponents remain the same as for the pure system. If $\alpha_T > 0$ the transition remains sharp, at least for a small degree of site disorder but the character of the system is changed and new critical exponents are found. The case $\alpha_T = 0$ (as for the 2D Ising model) is marginal. The generalization of these results to $C \sim C_p$ where disorder is so strong as to destroy the spontaneous magnetization does not appear to be clear cut (Kirkpatrick, 1979). Application of the Harris criterion would predict a sharp transition with 'pure' critical exponents if $\alpha_T > 0$ and either a smeared transition or a sharp transition with different critical exponents for $\alpha_T < 0$. Model calculations for the 2D Ising ($\alpha_T = 0$) (Jayaprakash, Riedel and Wortis (1978)), 2D Heisenberg ($\alpha_T < 0$), 3D Heisenberg ($\alpha_T < 0$) and 3D Ising ($\alpha_T > 0$) (Stinchcombe (1979a)(1979b)) systems reveal sharp transitions near C_p.

Given that a sharp transition exists for $C_p < C < 1$ the removal of sites from the pure system leads to a monotonic decrease in the ordering temperature $T_c(c)$ until long range order is destroyed at C_p, $T_c(C_p) = 0$. The form of critical curve $T_c(c)$ is not

universal and depends upon the details of the model in question. The application of renormalization group techniques has resulted in the accurate calculation of $T_c(c)$ for diluted nn Ising and Heisenberg systems. Stinchcombe (1979b) has calculated the critical curves for the diluted spin $\frac{1}{2}$ models on a simple cubic 3D lattice and the results are shown in Fig. 5.3. In the vicinity of C_p,

$$T_c(c) \sim \ln(C-C_p)^{-1} \quad \text{Ising}$$

$$T_c(c) \sim (C-C_p)^{\phi} \quad \text{Heisenberg} \tag{5.8}$$

where Stinchcombe finds $\phi \simeq 1.0$.

The percolation concentration C_p is a singular point for both thermal and geometrical critical phenomena. The coupled geometrical and thermal behaviour in the vicinity of this generalized critical point were first described by Stauffer (1975) for the Ising model and subsequently generalized by Lubensky (1976) and Stanley, Birgeneau, Reynolds and Nicoll (1976). These theories are based on the assumption that the variables in the vicinity of (C_p, T = 0) can be expressed as 'scaling functions' of the concentration difference $\Delta C = C_p - C$ and a generalized temperature g. (Lubensky (1979)). For example, Stanley et al (1976) argue that the Fourier transform of the fluctuating part of the instantaneous spin-spin correlation function, $S(g,\Delta C,\kappa)$ is a generalized homogeneous function (GHF) of g, ΔC and κ

$$S(g, \Delta C, \kappa) = \lambda^{-(1+db_r)} S(\lambda^{b_w} g, \lambda^{b_i} C, \lambda^{-b_r} \kappa) \tag{5.9a}$$

where λ is an arbitrary constant, b_w, b_r and b_i are undetermined exponents and d is the dimensionality of the lattice. The inverse correlation range is a GHF of ΔC and g,

$$\kappa_1(g,\Delta C) = \lambda^{b_r} \kappa_1(\lambda^{b_w} g, \lambda^{b_i} \Delta C) \tag{5.9b}$$

A wealth of information may be deduced from these scaling forms.

To start with, let us consider these scaling forms in the limit $g \to 0$ in order to regain the pure percolation problem. Let $\lambda^{-b_i} = \Delta C$ in (eq. 5.9a) in the special case $\kappa = 0$, this gives

$$S(g,\Delta C,\kappa = 0) = (\Delta C)^{(1+db_r)/b_i} \; H(g/(\Delta C)^{b_w/b_i}) \qquad (5.10a)$$

and similarly

$$\kappa_1(g,\Delta C) = (\Delta C)^{-b_r/b_i} \; F(g/(\Delta C)^{b_w/b_i}) \qquad (5.10b)$$

In the limit $g \to 0$ these forms must go over to the pure percolation relations given by (eq.5.5). For consistency $-b_r/b_i = \nu_p$, $(1+db_r)/b_i = -\gamma_p$ and $H(0)$, $L(0)$ are constants related to the geometry.

Consider now the behaviour at $C = C_p$ as the temperature is increased. Let $\lambda = g^{-1/b_w}$ in (eq. 5.9a) to give for $\kappa = 0$,

$$S(g,\Delta C,\ \kappa = 0) = g^{(1+db_r)/b_w} \; N(\Delta C/g^{b_i/b_w}) \qquad (5.10c)$$

and similarly

$$\kappa_1(g,\Delta C) = g^{-b_r/b_w} \; M(\Delta C/g^{b_i/b_w}) \qquad (5.10d)$$

At $C = C_p$, $\Delta C = 0$ and $N(0)$, $M(0)$ are constants. The normalized susceptibility $S(g,\Delta C = 0,\kappa = 0)$ and inverse range parameter $\kappa_1(g,\Delta C = 0)$ show singular behaviour as the temperature approaches zero, $g \to 0$. The unknown exponents $-(1+db_r)/b_w$ and $-b_r/b_w$ govern the purely thermal critical behaviour and for convenience are denoted as γ and ν. It must be stressed that these thermal critical exponents are in general not equal to those of the pure system but are directly related to the pure percolation exponents via

$$\nu\emptyset = \nu_p \text{ and } \gamma\emptyset = \gamma_p \qquad (5.10e)$$

where the exponent $\phi = b_w/b_i$ is termed the crossover exponent. Two different sets of critical exponents are defined at C_p depending on whether C_p is approached along the concentration axis (ν_p, γ_p etc.) or along the temperature axis (ν,γ etc.). As the percolation exponents are known quantities, a knowledge of the crossover exponent ϕ is sufficient to describe the combined geometrical and thermal critical phenomena at the percolation multicritical point.

The κ dependence of $S(\kappa)$ may be derived by letting $\lambda = \kappa_1^{1/b_r}$ so that

$$S(g,\Delta C,\kappa) = \kappa_1^{\lambda(1+db_r)/b_r} \; P(g/\Delta C^{\phi},\ \kappa/\kappa_1) \qquad (5.10f)$$

which reproduces the scaling relations (eq. 5.4b) and (eq.5.7b) in the appropriate limits ($g \to 0$ and $\Delta C \to 0$). For consistency then $(1+db_r)/b_r = 2-\eta_p = 2-\eta$ so $\eta = \eta_p$.

So far only the critical phenomena encountered by moving along the concentration axis or temperature axis at $\Delta C = 0$ has been considered. The results may be extended somewhat by noting that the scaling forms depend on the effective temperature and concentration only in the combination $g/\Delta C^{\phi}$. It is plausible that geometric critical behaviour will be observed if $g/\Delta C^{\phi} << 1$ and thermal critical behaviour will prevail if $g/\Delta C^{\phi} >> 1$. The line $g = \Delta C^{\phi}$ serves to delineate the two regions.

It is argued by Stauffer (1975), Birgeneau et al (1976) and Lubensky (1976) that the temperature like variable g is the inverse correlation length of the one dimensional version of the pure system , $\kappa_{1D}(T)$. So, for Ising and Heisenberg systems, g is the inverse correlation length of the pure Ising and Heisenberg chains,

$$g = \kappa_{1D}(T) \sim 2\exp(-2J/kT) \quad kT << J(\text{Ising}) \qquad (5.11)$$

$$g = \kappa_{1D}(T) \sim kT/J \quad kT << J(\text{Heisenberg}).$$

If the system has uniaxial anisotropy the longitudinal inverse correlation length of the anisotropic chain, $\kappa_{1D}^{11}(T)$, becomes the appropriate temperature variable (Stinchcombe (1980)).

The physical explanation behind such a choice is outlined by Birgeneau et al (1976) for $C < C_p$ and Lubensky (1976) for $C > C_p$ and relies on the observation (section 5.1.2.2) that large percolation clusters are ramified or stringy in shape. If the system is viewed on a sufficiently small length scale (ι), it will appear as a collection of one dimensional chains of occupied nn lattice sites. The extent to which the moments along the chain are correlated with each other depends on the ratio of the thermodynamic inverse correlation length of moments in a one dimensional chain ($\xi_{1D}(T)$) to the geometrical length of the chain itself (ι). Here ι is a measure of the number of steps traced in a zig-zag path along the backbone of a finite cluster or between the nodes of the infinite cluster. Thus Lubensky writes

$$S(\xi_{1D}(T),\ \Delta C,\kappa) = \kappa^{-2+\eta}\ f^{\pm}\ (\frac{\kappa}{\kappa_G},\ \frac{\iota}{\xi_{1D}(T)}) \tag{5.12a}$$

and

$$\kappa_1(\xi_{1D}(T),\Delta C) = \Delta C^{\nu_p}\ \ h^{\pm}\ (\iota/\xi_{1D}(T)) \tag{5.12b}$$

so that the susceptibility and inverse correlation length depend upon the extent to which the one dimensional links are perturbed by thermal agitation via $\iota/\xi_{1D}(T)$ and on whether one is looking within a cluster or at many clusters via the ratio κ/κ_G. By comparing (eq. 5.12b) and (eq.5.10b) one may associate g with $\kappa_{1D}(T)$ and ι with $\Delta C^{-\phi}$, providing a physical interpretation of the scaling forms (eq.5.10) which depend on the ratio $g/\Delta C^{\phi}$. Furthermore the condition $\xi_{1D}(T) = \iota$ implies ordering of the infinite cluster for $C > C_p$ at a temperature $T_c(c)$ which varies as

$$\kappa_{1D}(T_c) = \Delta C^{\phi} \tag{5.13}$$

This result is verified by the results of Stinchcombe (1979b) presented in Fig.5.3 and (eq.5.8). For $C < C_p$ this condition defines a temperature $T^*(c)$ at which finite clusters become fully correlated. The lines $T_c(c)$ and $T^*(c)$ separate regions in which geometric and thermal critical behaviour are observed.

Much theoretical work has been spent in estimating the crossover exponent ϕ for various model systems. As a result of this work it is concluded that $\phi = 1$ for Ising systems in all dimensions (Stinchcombe (1979b), Stephen and Grest (1977), Wallace and Young (1978)). The situation is not so clear for the Heisenberg case. In d = 1 the exact solution of Thorpe (1975) for the classical Heisenberg chain gives $\phi = 1$. Stinchcombe's analysis of the classical Heisenberg system suggests $\phi = 1$ in all d. (Stinchcombe (1979a)) although slightly larger values are found in the analysis of the spin $\frac{1}{2}$ Heisenberg model in d = 2, d = 3 (Stinchcombe (1979b)). A substantially larger value ($\phi = 1.7$ d = 2, $\phi = 1.58$ d = 3) is predicted by Stanley et al (1976) by assuming that magnetic correlations spread along paths which are self-avoiding walks.

So far only the general form of physical quantities near C_p have been described. Exact analytical results have been obtained in one specific case, that of a classical diluted Heisenberg chain (Thorpe (1975)). The percolation concentration for a chain is $C_p = 1$ and the pure system orders in the limit $T \to 0$. Thorpe deduces

$$S(U,C,\kappa) = C(1-(CU)^2)/[1 + (CU)^2 - 2(CU)\ \mathrm{Cos}\kappa a] \qquad (5.14a)$$

where a is the lattice parameter, and $U = \coth \beta J - (\beta J)^{-1}$ is a measure of the temperature. For $\kappa a \ll 1$ this may be expanded in the Guinier form

$$S(U,C,\kappa) = S(U,\ C,\kappa = 0)\ (1-\kappa^2/\kappa_1^{\ 2} + \ldots) \qquad (5.14b)$$

where the inverse correlation range is given by

$$\kappa_1^{\ 2} = (1 - CU)^2/a^2(CU)^2 \qquad (5.14c)$$

The geometrical properties of the diluted chain may be deduced in the limit $T \to 0$ or $U \to 1$.

$$S(1, \Delta C, \kappa = 0) = (1 - \Delta C)(2 - \Delta C)/\Delta C^2 \qquad (5.15a)$$

and

$$\kappa_{1G}^2(1,\Delta C) = \Delta C^2/(1-\Delta C)a^2 \qquad (5.15b)$$

where the argument C has been replaced by ΔC to emphasise the critical behaviour as $\Delta C \to 0$. The percolation critical exponents are thus $\gamma_p = 2$, $\nu_p = 1$.

The thermal critical behaviour at $C = C_p$ is found by setting $\Delta C = 0$ and expressing the temperature in terms of the inverse correlation length of the pure chain, $g = \kappa_{1D}(T)$. Thus κ_1 and $S(\kappa)$ show temperature driven critical behaviour at $\Delta C = 0$ according to,

$$S(g, 0, \kappa = 0) \sim g^2 \quad \text{and} \quad \kappa_1(g,0) = g^1 \qquad (5.15c)$$

giving thermal critical exponents $\gamma = 2$, $\nu = 1$. The crossover exponent is $\phi = 1$.

The combined geometrical and thermal critical behaviour may be deduced by expanding (eq.5.14a) in the vicinity of $\Delta C = 0$. This results in an Ornstein-Zernicke form $\kappa a \ll 1$.

$$S(g, \Delta C, \kappa) = A/(\kappa_1^2 + (\kappa a)^2) \qquad (5.16a)$$

where (Birgeneau et al (1980))

$$A \simeq \kappa_1(0,\Delta C) \doteq \kappa_1(g,0) + O(\Delta C^2, g^2) \qquad (5.16b)$$

and

$$\kappa_1(g,\Delta C) \doteq \kappa_1(0,\Delta C) + \kappa_1(g,0) + O(\Delta C^2, g^2) \qquad (5.16c)$$

which gives the intriguing result that the inverse correlation range is the sum of the purely thermal and purely geometrical inverse correlation ranges. Whether this result is valid in general remains an open question. It is at least consistent with the recent scaling forms for $\kappa_1'(g,\Delta C)$ in anisotropic dilute systems (Stinchcombe (1980)).

5.1.3 Spin Glasses and Superparamagnets

5.1.3.1 Introduction

At present there is no consensus, experimentally or theoretically, on the fundamental nature of spin glasses. It is therefore not surprising that no widely held definition of the spin glass state exists. For the purposes of this summary we shall take a spin glass to be a system which does not support long range order but which shows a peak in the low field susceptibility at some characteristic temperature T_g. This behaviour is thought to arise from the freezing of individual moments in random directions to produce a state with no long range order ($\overline{\langle S_i \rangle \langle S_j \rangle} = 0$ $R_{ij} \to \infty$) but with a non zero time averaged moment at each impurity site ($q = \overline{\langle S_i(0)\, S_i(t) \rangle} \neq 0$ $t \to \infty$), hence the term 'spin glass'.

This behaviour has been observed in a wide range of materials, from amorphous insulating glasses $Al_2\ Mn_3\ Si_3\ O_{12}$ (Nägele, Blanckenhagen, Knorr and Suck (1979)) and dilute rare earth semiconductors (Sr Eu)S (Malletta and Felsch (1980)) to dilute transition metal solid solutions such as Au Fe (Guy (1977)). Of these materials the dilute solid solutions Cu Mn, Au Fe have been most extensively studied. Some of the properties of Au Fe alloys will be discussed in section 5.1.4.2. For illustrative purposes, it is sufficient to summarize the experimental situation for Cu Mn alloys. Further details may be found in a review by Beck (1979).

Cu Mn alloys are spin glasses at all but the lowest concentrations of Mn (less than 10ppm) up to the critical concentration for antiferromagnetism (about 75% Mn). In the dilute alloys (C < 2%) the Mn moments occupy well separated random sites and interact via long range oscillatory RKKY forces. The magnetic properties follow universal laws which depend only on the reduced variables H/C, T/C. This fact is interpreted as evidence of the $1/r^3$ dependence of the RKKY interaction (Tholence and Tournier (1974)). At higher concentrations an increasingly larger fraction of Mn moments are found as near neighbours and the presence of tenacious nn magnetic interactions and strong atomic short range order tends to complicate matters (David, Burke and Rainford (1980)). These more concentrated spin glass alloys are termed 'mictomagnetic' or 'cluster spin glasses' to distinguish them from the dilute alloys which obey the H/C, T/C scaling laws. For convenience, the dilute alloys will be considered.

A sharp cusplike peak in the AC susceptibility as a function of temperature is found for these dilute alloys (Cannella (1973)). The peak temperature (T_g) is frequency independent to within experimental error in the range 10Hz to 10kHz (Mulder, Duyneveldt and Mydosh (1980)). This suggests a cooperative phase transition of some sort. This view is supported by the Mossbauer and muon depolarization data. However, no anomaly is seen in the magnetic specific heat which remains smoothly varying in the vicinity of T_g (Wenger and Keesom (1976)). Anomalies are observed in the ESR line width some 60% above T_g and in the thermal coefficient of resistivity some 50% below T_g. (Beck (1979)).

Souletie and Tournier (1969) demonstrated that whilst the static susceptibility exhibits a sharp peak at T_g similar to the AC susceptibility if the spin glass is cooled in zero applied field to below T_g, no such peak is present if the spin glass is cooled in a small magnetic field. This thermomagnetic treatment results in an almost temperature independent magnetization below T_g. Under these conditions a remanent magnetization (termed the thermoremanent

magnetization, TRM) is developed below T_g. This remanence is not stable and decays logarithmically with time. A remanent magnetization could also be created by application of a field at constant temperature below T_g (the isothermal remanent magnetization, IRM). The IRM increases logarithmically with the time during which the field is applied. Tholence and Tournier (1974) argue that the static susceptibility is composed of a reversible part (zero field cooled) which is measured by the AC technique and an irreversible part (TRM) which cannot be switched during the time scale of an AC experiment. This dependence of observed properties on time scale is particularly important in the understanding of spin glasses.

The importance of observation time is well illustrated by neutron quasielastic scattering experiments. In this case the temperature at which magnetic 'elastic' scattering first appears (that is magnetic scattering which lies within the spectrometer energy resolution, ΔE) depends strongly on ΔE and is always found at higher temperature than T_g determined by AC methods. (Murani (1980)). This implies a very broad spectrum of magnetic response times, extending from 10^{-12} sec to 10^{-2} sec at least. These conclusions are vividly illustrated by the neutron spin echo determination of the magnetic intermediate scattering law $S(\kappa, t)$ for a Cu Mn 5% alloy (Mezei and Murani (1980)) shown in Fig. 5.4. One may interpret the temperature at which $S(\kappa, t) \to 0$ for a given time t as the spin glass freezing temperature for a measurement with time constant t. So $T_g \simeq 100K$ would be determined by a measurement which is sensitive only to processes faster than 10^{-11} sec whereas $T_g \simeq 36K$ would be found if the time constant were 10^{-9} sec. An AC susceptibility measurement ($t \sim 10^{-2}$ sec) returns a value $T_g \simeq 28K$. A phase transition would be indicated if for some temperature $S(\kappa, t) \neq 0$ $t \to \infty$ and would appear to be an open question.

5.1.3.2 Theory

In the dilute Cu Mn spin glass the magnetic moments interact

Fig.5.4 Measured time dependent spin correlation function for a Cu-5% Mn spin glass at various temperatures. (Mezei and Murani (1979)).

Fig.5.5 Magnetic phase diagram for quenched Au Fe alloys (Coles et al (1978)). Here sg, f, p and cg refer to spin glass, ferromagnetic, paramagnetic and cluster glass regimes.

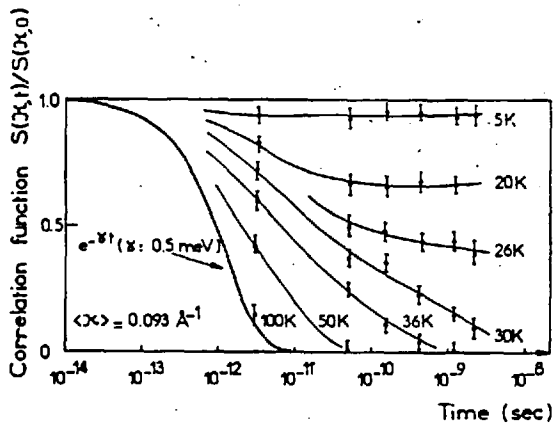
Correlation function S(χ,t)/S(χ,0)
1.0
0.5
0
e^{-γt} (γ: 0.5 meV)
<χ> = 0.093 Å^-1
.5K
20K
26K
30K
100K
50K
36K
10^-14
10^-13
10^-12
10^-11
10^-10
10^-9
10^-8
Time (sec)

Fig. 5·4

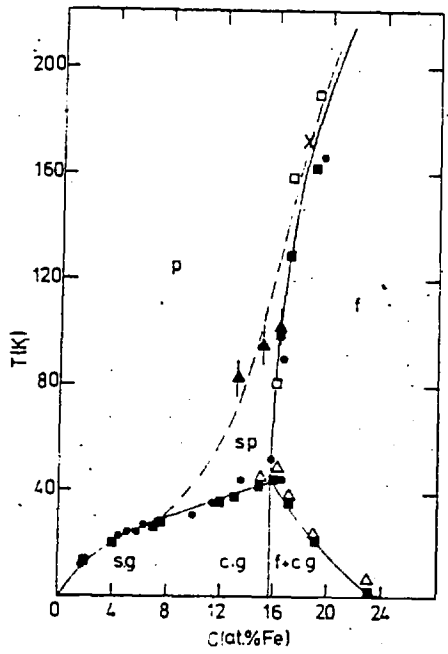
200
160
120
80
40
T(K)
p
f
sp
s.g
c.g
f+c g
0
4
8
12
16
20
24
C(at.%Fe)

Fig·5·5

by exchange forces which alternate in sign. As a result, any given moment is subject to contradictory orientation requirements which cannot be simultaneously satisfied. This rather special type of spatial disorder in the exchange interactions has been termed 'frustration' and has become the essential ingredient in theoretical studies of model spin glass systems. An extensive review of these theoretical developments is given by Anderson (1979). A brief outline of some of this work will be given in this section.

For the most part, theoretical attention has been directed toward the properties of a pure Ising or Heisenberg system with randomly distributed positive and negative nn exchange interactions. At first glance, such models would appear to have little in common with a dilute Cu Mn alloy which has both site disorder and long ranged interactions, however the essential competition between exchange forces is present in both cases.

The mean field treatment of the classical Heisenberg system with randomly distributed (Gaussian) ferromagnetic and antiferromagnetic nn interactions by Edwards and Anderson (1975) is the seminal work in this field. A phase transition to a state in which individual moments are frozen in random directions below a critical temperature T_g was found in this model. The new phase has no long range order and is described by a single site order parameter

$$q = \overline{\langle \underset{\sim}{S}_i(0) . \underset{\sim}{S}_i(t) \rangle} \quad t \to \infty \tag{5.17a}$$

which is zero above T_g and approaches unity at T = 0. The susceptibility

$$\chi = C/T\ (1-q) \tag{5.17b}$$

has a sharp peak at T_g in agreement with experiment but the model fails to reproduce the monotonic increase in specific heat in the region of T_g .

It has subsequently been found out that the mathematical details

of the Edwards and Anderson (1975) (EA) mean field calculation are in error for $T << T_g$. This mathematical problem has been discussed by many authors in the context of the spherical model for an Ising spin glass. Improved mathematical methods reproduce the susceptibility peak but reveal critical phenomena at all temperatures below T_g. The significance of this result and a discussion of the mathematics may be found in the review by Anderson (1979).

The validity of mean field theory for the EA spin glass has also been closely scrutinized. Mean field theory is correct in $d \geq 6$ but fails for lower dimensions. The work of Bray and Moore (1979, 1980) suggests that the phase transition observed in the mean field treatment of the EA model is an artifact of mean field theory for $d \leq 4$, i.e. the lower critical dimensionality (LCD) of the EA spin glass is four. Other treatments conclude that the LCD is two or three. This conflict has not been resolved (Stauffer and Binder (1980)). Anderson (1979) is led to conjecture that critical behaviour in a spin glass is of a fundamentally different nature to that in conventional systems and that the application of orthodox phase transition theory to the problem may well be irrelevent.

There are a number of unanswered questions in regard to spin glass theory. One, the existence of a phase transition would appear to be open. Another would be to reconcile the successful phenomenological fine particle model (discussed in the following section) with more complete microscopic theory.

5.1.3.3 Ferromagnetic fine particles

For the most part, first principles microscopic theory has not been used in the analysis of experimental spin glass data. Rather, the bulk of experimental work has been analysed using a phenomenology based on the well-established theory of ferromagnetic fine particles or rock magnetism (Wohlfarth (1977), Tholence and Tournier (1974)).

A brief outline of this description will be given here. Further details may be found in the extensive reviews by Neél (1955), Jacobs and Bean (1963) and Kneller (1969).

The model relies on the postulate of non interacting assemblies of coupled moments fluctuating against anisotropy barriers. The magnetic assemblies have been identified with magnetization 'clouds', composed of randomly oriented and randomly distributed moments, each cloud having a nett moment proportional to the square root of the number of moments present for spin glasses in the scaling regime. (Tholence and Tournier (1974)). In more concentrated alloys, the 'clouds' may be derived from a nucleus of near neighbour moment clusters. The nature of anisotropy barriers remains unclear. Dipolar forces have been suggested (De Rozario and Smith (1977), Tholence and Tournier (1977)) and more recently spin orbit coupling (Fert and Levy (1980)). This description is incomplete in many respects. In particular, the discovery of rapid magnetization reversal (Monod and Prejean (1978)) and cooperative remanent effects (Alloul (1979)) suggest that the postulate of independent clusters must be modified.

For argument's sake, we shall assume that the magnetic assemblies are distinct non interacting ferromagnetic particles embedded in a non magnetic matrix. The distribution of magnetization within such particles depends on their shape and size. Large particles will be made up of a number of ferromagnetic domains, the number of domains decreasing with particle size until a single domain particle results below a critical radius ($\sim$150 Å for Fe). The magnetization within a single domain particle is in general non uniform. We shall restrict our discussion to the case of single domain ellipsoidal particles which have a uniform magnetization and which retain this uniform magnetization in the presence of an external field. The particle may be characterized by Curie temperature T_c and saturation magnetization M_s.

In the absence of anisotropy forces, the individual moment within a single domain may freely rotate in unison to follow the direction of an applied field. The resulting magnetization may be calculated using Boltzmann statistics to give

$$\bar{M} = nm \left[\coth \left(\frac{mH}{kT}\right) - \frac{kT}{mH}\right] \tag{5.18}$$

for a collection of n identical particles per unit volume, having each a total magnetic moment $m = VM_s$ where V is the particle volume. This result is the same as a classical Langevin paramagnet except with a paramagnetic moment m, which may be several hundred Bohr magneton. Hence the term 'superparamagnetism' applied to this case by Bean and Livingston (1959).

This free rotation is impeded by the presence of anisotropy forces which act to constrain the direction of the nett particle moment to lie along certain preferred orientations. The anisotropy forces are a result of particle shape, crystal structure and applied stress. The particle 'shape anisotropy' arises from the basic magnetostatic requirement that the nett moment lies along a direction of minimum demagnetizing field. So for an ellipsoid of revolution the magnetostatic energy is minimized if the total moment is oriented along the major axis. The change in magnetostatic energy involved in rotating the nett moment by an angle ϕ from this easy direction is (Neél (1955))

$$E = KV \sin^2 \phi \tag{5.19a}$$

where the anisotropy constant

$$K = \tfrac{1}{2}(D_{\perp} - D_{//})\, M_s^2 \tag{5.19b}$$

depends on the difference between the demagnetizing factors perpendicular ($\perp$) and parallel (//) to the particle long axis. The two stable

magnetization directions are separated by energy barrier KV. Magnetocrystalline anisotropy, magnetostriction, surface effects, etc. also may contribute to such barriers. For convenience all such contributions will be assumed to produce a uniaxial anisotropy of the type given by (eq.5.19a) with a modified K value.

Anisotropy barriers have a profound effect on the response of the particle moment to an applied field. This may be demonstrated by considering a collection of identical, non interacting, uniaxial single domain particles with the anisotropy axes oriented along the field direction. Suppose at T = 0 the particle moments are equally distributed among the two stable magnetization directions. A magnetization can only be created by moment reversal across the anisotropy barrier KV and at T = 0 this is not possible until the field reaches a threshold value $H_K = 2K/M_s$ and the magnetization jumps from zero to nm. The resulting hysteresis loop is square with a coercive force $H_C = H_K$. In the more general case where both anisotropy axes and nett moments are randomly distributed in space the hysteresis loqp is rounded with $H_C = 0.479\ H_K$, saturation magnetization 0.500 mn ($H \to \infty$) and initial susceptibility $\chi = 0.333\ nm^2/K$. (Stoner and Wohlfarth (1948)).

At T > 0 the magnetization process may be assisted by thermal activation over the anisotropy barriers. For $H < H_K$ the magnetization increases slowly with time and reaches the thermal equilibrium value after a time Δt which is large compared with the transition time τ for thermally activated flipping of the moment across the anisotropy barrier. The system will also require a finite time to relax back to an unmagnetized state after a saturating field has been removed. The remanent magnetization decays exponentially,

$$\bar{M}_r(t) = nm \exp(-t/\tau_o) \tag{5.20a}$$

with a time constant τ_o given by (Kneller (1969))

$$\tau_o^{-1} = 2f_o \exp(-KV/kT) \tag{5.20b}$$

where f_o varies weakly with temperature and field, and is given to within an order of magnitude by the expression

$$f_o(\text{Hz}) \sim 3 \times 10^6 \, H_K \, (\text{Oe}) \qquad (5.20c)$$

For fine Fe particles $H_K \sim H_C = 1000$ Oe and $f_o \sim 10^9$ Hz. The result of any experiment depends on the ratio of experimental measuring time Δt to the relaxation time τ_o. If $\Delta t >> \tau_o$ the equilibrium thermodynamic magnetization is measured and the system appears superparamagnetic, there is no remanence or hysteresis. In the opposite limit $\Delta t << \tau_o$ the system appears static and will display the frozen hysteretic behaviour discussed at T = 0. In the intermediate case $\Delta t \sim \tau_o$ time dependent magnetization and remanence will be observed as the system creeps toward thermal equilibrium.

As τ_o depends exponentially on T there will be a sharp demarkation between superparamagnetic and frozen ferromagnetic behaviour at a 'blocking temperature ' T_B which depends on the time scale of the experiment,

$$kT_B = KV/\log\,(2\Delta t\, f_o) \qquad (5.21a)$$

or using the Ansatz $H_K \sim H_C(T = 0)$

$$kT_B \sim VM_s \, H_C(0)/\ln(6 \times 10^6 \, H_C(0)\,[\text{Oe}]\;\Delta t\,[\text{s}]) \qquad (5.21b)$$

As the temperature is decreased toward T_B the superparamagnetic susceptibility increases monotonically according to a Curie law, in small fields (mH << kT)

$$\chi = nm^2/j\,kT \qquad T > T_B \qquad (5.22a)$$

with j = 1 if KV >> kT and j = 3 if KV << kT, but drops steeply below T_B to a small value given in the simplest case by Wohlfarth (1977),

$$\chi = nm^2/3K(T) \qquad T < T_B \qquad (5.22b)$$

This decrease is of the order $\log (2\Delta t\ f_o) \sim 25$ for Fe particles with $\Delta t \sim 10^{-2}$ sec, giving a very sharp, asymmetric peak in the susceptibility at T_B. Remanent magnetization first appears on the time scale of the measurement below T_B. If the system is cooled in a field through T_B, a TRM will be found. In the simple case under consideration here the TRM results from the freezing of the magnetization present at T_B, and so $TRM(T) = \chi(T_B)H$ for $T < T_B$. The TRM will decay exponentially with time according to (eq.5.20a). The IRM may be treated in a similar manner.

The concepts may be readily generalized to include a distribution of particle sizes, interparticle interactions and the temperature dependence of M_s and K. (Kneller (1969)). The effect of particle size distribution on the sharpness of the susceptibility peak has been considered by Wohlfarth (1979). It was shown that a sharp peak could be retained if the distribution of particle sizes (blocking temperatures)satisfied certain general conditions. A distribution of blocking temperatures modifies the exponential decay of remanence to a logarithmic decay

$$M_r(t) = \text{const} - S \ln t \tag{5.23}$$

a result first derived by Street and Woolley (1949). Relationships between the IRM and TRM which first appear below T_B are described by Guy (1977).

5.1.4 Some systems with a critical concentration

5.1.4.1 Dilute insulating antiferromagnets

Much of the theoretical work outlined in section 5.1.2.3 has been stimulated by experimental study of insulating antiferromagnets and these experiments have provided strong confirmation of the picture

of C_p as a multicritical point with $g = \kappa_{1D}(T)$. The systems chosen for investigation have the attractive properties of both site randomness as well as magnetic interactions which closely approximate the nn Ising and Heisenberg models in d = 2 and d = 3. Notable among such systems are: $Rb_2\ Mn_c\ Mg_{1-c}\ F_4$ (2D Heisenberg), $Rb_2\ Co_c\ Mg_{1-c}\ F4$ (2D Ising), $Mn_c\ Zn_{1-c}\ F_2$, $K\ Mn_c\ Zn_{1-c}\ F_3$, $K\ Mn_c\ Zn_{1-c}\ F_3$ (3D Heisenberg) and $Cs_3\ Co_c\ Zn_{1-c}\ Cl_5$ (3D Ising).

The first test of the percolation model for such systems is the location of the critical concentration. In so far as the critical concentration can be bracketted, it is in good agreement with the calculated percolation concentration for the appropriate 2D and 3D lattices (Birgeneau et al (1980), Cowley et al (1980), Cowley et al (1977), Stinchcombe (1979b)). A more stingent test is the critical curve $T_c(C)$ which was calculated by Stinchcombe (1979b) in a parameter free model and found to be in excellent agreement with the data for the 3D Ising system $Cs_3\ Co_c\ Zn_{1-c}\ Cl_5$ and the 3D Heisenberg system $K\ Mn_c\ Mg_{1-c}\ F_3$ (shown in Fig. 5.3).

The direct observation of spin correlations in the vicinity of C_p by neutron scattering have played a seminal role in the description of the percolation multicritical point. The first measurements (Birgeneau et al (1976)) examined the dilute 2D Heisenberg like system $Rb_2\ Mn_c\ Mg_{1-c}\ F_4$ at concentrations $C < C_p$, leading to the suggestion $g = \kappa_{1D}(T)$. A detailed analysis of these experiments (Birgeneau et al (1980)) was carried out assuming a scattering law,

$$S(g, \Delta C, \kappa) = A\ \kappa_1^{\eta} / (\kappa^2 + \kappa_1^2) \tag{5.24a}$$

consistent with the experimental Ornstein-Zernicke form of the scattering and an inverse correlation length,

$$\kappa_1\ (g, \Delta C) = \kappa_1(g, 0) + \kappa_1(0, \Delta C) \tag{5.24b}$$

following the result (eq. 5.16c) for the one dimensional chain.

These two expressions are consistent with the scaling forms (eq.5.9). The temperature like variable g was taken as the inverse correlation length of the pure Heisenberg chain including the effect of a small uniaxial anisotropy. The simple addition of thermal and geometrical inverse correlation ranges (eq.5.24b) was verified by experiment. The thermal inverse correlation length tended to zero with an exponent $\nu = 0.9 \pm 0.05$ whilst the geometrical inverse correlation range was not inconsistent with the percolation value $\nu_p = 1.35$. This implies a cross over exponent $\phi = \nu_p/\nu = 1.5 \pm 0.08$ which favours the value 1.7 proposed by Stanley et al (1976). The susceptibility exponent γ proved more difficult to extract. It was estimated using the postulated form of the scattering law as $\kappa \to 0$, $S(g,\Delta C,\kappa = 0) \sim \kappa_1^{2-\eta}$ in conjunction with measured value of ν using the relation $(2-\eta)\nu = \gamma$. A value $\gamma = 1.50 \pm 0.15$ was deduced in this way. Taken together with the calculated percolation exponent $\gamma_p = 2.43$, this gives $\phi = \gamma_p/\gamma = 1.9 \pm 0.2$ in good agreement with the value determined from the correlation range exponents.

The spin correlations in the vicinity of C_p for the 2D Ising $Rb_2 Co_c Mg_{1-c} F_4$ have also been extensively studied (Cowley et al (1980)). In this case, too, the inverse correlation range for all alloys studied with $C < C_p$ was well described by the sum of geometrical and thermal parts. The thermal part tended to zero with an exponent $\nu = 1.32 \pm 0.04$ which is identical to the pure percolation exponent (within error). The cross over exponent is thus consistent with the theoretical estimate $\phi = 1$. Furthermore, the geometrical inverse correlation range is well described by the calculated percolation exponent. The exponent γ was calculated in a number of ways. Using the method given above, γ was found to depend weakly on concentration and was extrapolated to C_p giving $\gamma = 2.4 \pm 0.1$ consistent with $\phi = 1$. The difficulty in obtaining a good estimate of γ lies in the uncertainty of the exact functional form of $S(g, \Delta C, \kappa)$.

The correlations for $C > C_p$ have also been well studied but are not understood in such great detail as for $C < C_p$. The two dimensional systems undergo a smeared transition to the ordered state with exponents γ_T, ν_T which are close to those expected. In contrast, the transition to an ordered state for the 3D Heisenberg like system $Mn_c\ Zn_{1-c}\ F_2$ (Cowley et al (1977)) occurs without divergence of the correlation range at T_N. This puzzling feature has yet to be fully understood.

5.1.4.2 Au Fe

The magnetic phase diagram for quenched f.c.c. Au Fe alloys deduced from a variety of techniques is presented in Fig. 5.5. (Coles, Sarkissian and Taylor (1978)). The state of magnetic order changes from a scaling spin glass regime dominated by indirect RKKY interactions at low concentration ($C \lesssim 1\%$) (Tholence and Tournier (1974)) to a cluster spin glass regime at higher concentrations as progressively more Fe moments are coupled into nn clusters via ferromagnetic direct exchange interactions (Murani (1974)). The spin glass gives way to ferromagnetism at $15.5 \pm 0.5\%$ Fe, somewhat lower than the pure percolation limit of 19.8% Fe expected for an fcc lattice.

The spin glass behaviour in the scaling region is similar to Cu Mn (section 5.1.3.1). The cluster spin glass which occurs at higher concentration deserves further comment. These alloys show the susceptibility peak, time dependence and thermomagnetic effects characteristic of spin glasses and have been analysed by Guy (1977) using the phenomenological fine particle model discussed in section 5.1.3.3. Early work (Crangle and Scott (1974)) claimed such alloys to be ferromagnetic. This contradiction was resolved by low field magnetization measurements (Murani (1974)) which showed superparamagnetic behaviour resulting from the formation of large ferromagnetically coupled clusters of Fe moments at low temperatures.

Subsequent neutron small angle scattering experiments (Murani et al (1976)) confirmed this inference and furthermore ruled out any possibility of ferromagnetism by the lack of a critical scattering peak. The method of Arrott plots (section 5.2.1) used by earlier workers to determine T_c from high field magnetization data is invalid in the presence of such an inhomogeneous magnetization distribution (Edwards, Mathon and Wohlfarth (1975)) and it was argued by Murani (1974) that T_c determined in this way could be linked with an effective T_c for formation of superparamagnetic clusters (shown as dashed line in Fig. 5.5). The observation of such clusters gives some credence to the fine particle description used by Guy (1977).

A gradual increase in the small angle scattering intensity was observed as cluster spin glass alloys were cooled to low temperature (Murani et al (1976)) suggesting a gradual increase in cluster moment with decreasing temperature. On extending these data to lower κ the small angle scattering intensity went through a well defined maximum as a function of temperature in the vicinity of T_g (Murani (1976)). The peak temperature itself varied smoothly with κ tending to T_g (AC susceptibility) as $\kappa \to 0$. Murani (1976) suggested that this peak was a result of competition between elastic and quasielastic components of the scattering, implying a non unique freezing temperature for the system. The data was reinterpreted by Soukoulis, Grest and Levin (1978) as a unique freezing process. An adequate explanation for this phenomenon is still lacking.

The ferromagnetic phase boundary itself was deduced from the temperature dependence of neutron critical scattering peaks together with resonance and spectroscopic techniques summarized by Coles et al (1978). It has been suggested that ferromagnetic alloys close to C_L revert to a cluster spin glass state at low temperature (Verbeek and Mydosh (1978)). The temperature at which this ferromagnet-spin glass transition is currently unclear. The recent work of Sarkissian

(1980) emphasises the care which must be taken to avoid artefacts produced by demagnetizing fields. In addition, the neutron Bragg scattering measurements of Murani (1980) reveal that although the magnetic peak intensity tends to decrease at the 'transition', the integrated intensity in fact increases. The broadening of the magnetic Bragg peak coincides with a rapid increase in small angle scattering, suggesting a change in the magnetic 'mosaic' structure rather than a transition to a spin glass.

5.2 Previous work

5.2.1 Pure Fe

To put the more complex magnetic behaviour of Cr Fe alloys close to C_F into persepctive some of the properties of pure ferromagnetic iron will be briefly recalled.

The ferromagnetism of Fe is still not wholly understood. The conventional itinerant electron theory which proved so successful for Chromium and its alloys (section 4.1) can only partially account for the ferromagnetic properties of Fe. An improved itinerant model must account for the low Curie temperature and the occurrence of local moments and spin waves above T_c. This problem is at present a very active area of theoretical interest. (Edwards (1980)). An improved model which synthesises aspects of both the itinerant and local pictures has been suggested by Hubbard (1979 a,b). The most significant result of Hubbard's treatment is the observation of a Heisenberg like dependence of the energy required to rotate a single spin about the ferromagnetic direction at T = 0 (Hubbard (1979a)). On extending the theory to finite temperature (Hubbard (1979b)) it was found that the decrease in spontaneous magnetization with increasing temperature was due to disorder in spin direction rather than a change in their magnitude. A Curie-Weiss susceptibility with an effective moment $2.7\mu_B$ was found above T_c.

Experimentally, Fe shows a number of Heisenberg-like properties. The critical exponents: $\beta = 0.379 \pm 0.004$ (Suter and Hohenemser (1979)), $\gamma = 1.333 \pm 0.015$ (Noakes, Arrott and Thornberg (1966) and $\nu = 0.69 \pm 0.02$ (Als Nielsen (1976)) agree well with theoretical estimates (section 5.1.2.3). The dynamical critical behaviour is also consistent with theoretical predictions for a Heisenberg ferromagnet. (Boronkay and Collins (1973), Collins, Minkiewicz, Nathans, Passell and Shirane (1969)). The low lying excitations are simple spin waves with a stiffness consistent with T_c if a Heisenberg analysis is used. The moment itself is weakly temperature dependent. Thus, as a first approximation, it may be reasonable to treat the ground state properties of iron, the ordered moment for example,

as given by itinerant electron theory but to treat the low lying excitations as having Heisenberg-like degrees of freedom.

The host of 'technical' magnetic properties of Fe which arise in one way or another from ferromagnetic domains demonstrate that Fe is not purely a Heisenberg ferromagnet. As an example, the magnetization and low field permeability ($\mu = 1 + M/H$) for polycrystalline Fe between 77 and 1100K is shown in Fig. 5.6 (Bozorth (1951)). The most striking reature of these data is the appearance of a peak in the low field magnetization in the vicinity of T_c, which shifts to lower temperatures as the field is increased from 0.2 to 3 Oe. This peak, which does not occur at T_c, is the result of the competition between increasing spontaneous magnetization on one hand and increasing magnetocrystalline anisotropy on the other. This 'Hopkinson' peak (Hopkinson (1885)) is one of a number of complicated phenomena observed in the low field static and alternating susceptibility of Fe near the critical point as a result of dipole-dipole interactions, magnetocrystalline anisotropy and domain formation. It has been suggested by Arrott, Heinrich and Noakes (1972) that dipolar forces may even play a significant role in the critical phenomena,moving the exponents more toward mean field values.

The data in Fig. 5.6 illustrate the difficulty in determining T_c from magnetization measurements. It is clearly incorrect to associate T_c with the maximum in the low field static or alternating susceptibility. Rather, it has been proposed that T_c lies closer to the maximum in $\frac{d\chi}{dT}$ or the temperature at which the magnetization first reaches the demagnetizing limit. High field magnetization data also suffer from similar difficulties. Various extrapolation schemes have been used to define T_c by identification of the temperature at which a spontaneous magnetization first appears. In its simplest form this entails extrapolation of the high field M vs H curve to H = 0. This method was used for the data in Fig. 5.6 and the Curie temperature (Θ) is indicated. An improved extrapolation procedure based on a

Fig.5.6 Magnetism of Fe close to T_c.

(a) Low and high field magnetization of pure Fe close to T_c (arrowed). (Bozorth (1951)).

(b) Neutron critical scattering from pure Fe. Intensity at a given scattering angle θ as a function of temperature. (Villain (1964)).

(c) Neutron critical scattering from pure Fe. Reciprocal scattering intensity versus scattering vector squared. (Popovici (1971)).

a

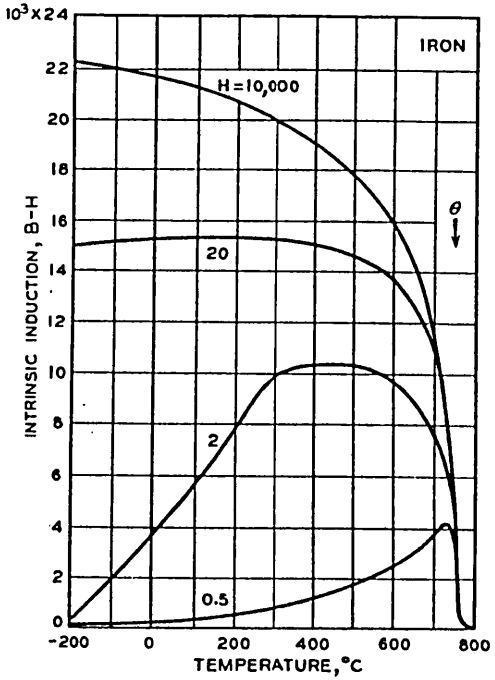
IRON
H=10,000
20
2
0.5
θ
INTRINSIC INDUCTION, B-H
TEMPERATURE, °C

b

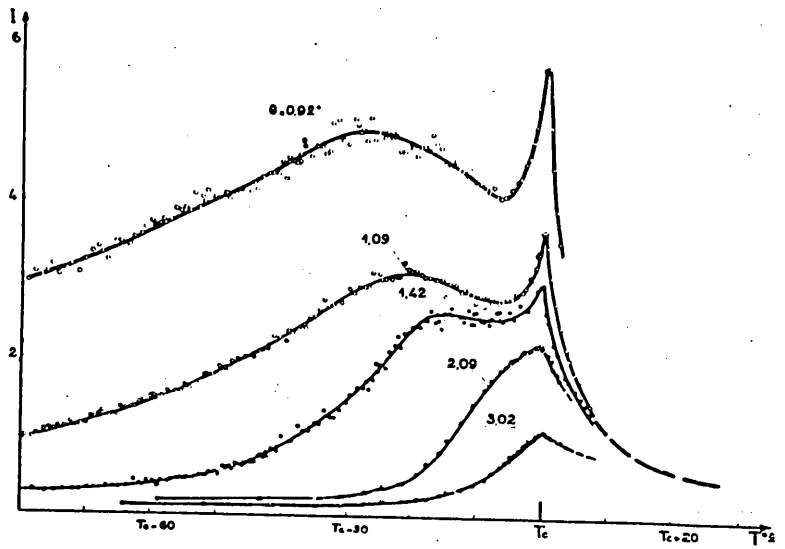
θ=0.92°
1.09
1.42
2.09
3.02
Tc-60
Tc-30
Tc
Tc+20

c

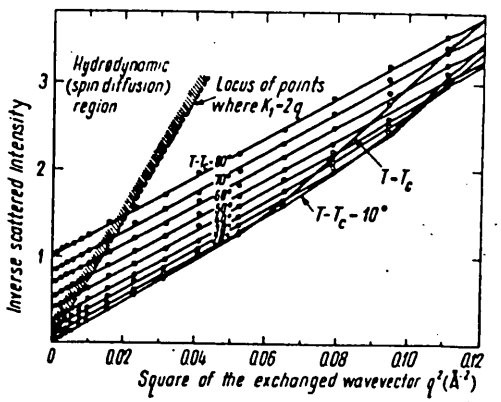
Hydrodynamic (spin diffusion) region
Locus of points where $K_1=2q$
$T-T_c$
$T-T_c-10°$
Inverse scattered intensity
Square of the exchanged wavevector $q^2(Å^{-2})$

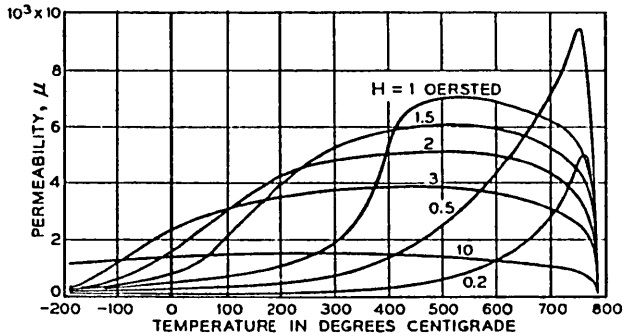
H = 1 OERSTED
1.5
2
3
0.5
10
0.2
PERMEABILITY, μ
TEMPERATURE IN DEGREES CENTIGRADE

Fig. 5.6

phenomenological equation of state has been outlined by Arrott (1957). In this case the magnetization is plotted in the form M^2 vs H/M for a given temperature and extrapoled to H = 0. T_c is given by the temperature for which such an extrapolation first passes through the origin. The alternative methods which use the Curie-Weiss constant or the disappearance of remanence are unreliable.

T_c may be determined unambiguously in zero field by neutron critical scattering. The results of Villain (1964) are shown in Fig. 5.6. The sharp peak in the critical scattering is located at T_c in the limit $\kappa \to 0$. For completeness, the κ dependence of the crit ical scattering taken from the work of Popovici (1971) is also illustrated (Fig. 5.6). The deviations from Lorentzian line shape below T_c should be noted.

5.2.2 Cr Fe ferromagnetic alloys

Ferromagnetism occurs in Fe rich Cr Fe b.c.c. solid solutions over a wide range of concentration. The addition of Cr to ferromagnetic Fe results in an initial increase in Curie temperature, followed by a slow decrease in both the average moment (μ) and Curie temperature (Fallot (1936)). Ferromagnetism is retained above a critical concentration (C_F) of some 10% to 20% Fe. T_c as a function of concentration taken from the high field magnetization measurements of Fallot (1936), Nevitt and Aldred (1963) and Read and Temple (1974) is shown in Fig. 4.11. T_c decreases linearly between 60% and 20% Fe, extrapolating to zero at $C_F \sim 15\%$ Fe.

The early work of Fallot (1936), supplemented by Nevitt and Aldred (1963), suggest a linear decrease in mean moment as the Fe concentration is decreased, consistent with the Slater-Pauling curve. This decrease is not entirely a simple dilution effect as may be judged by the value $\frac{d\mu}{dc} = 2.36\ \mu_B$ which is larger than the moment of pure Fe ($2.22\mu_B$). This suggests a negative induced moment on Cr sites. More accurate bulk magnetization data taken by Aldred (1976) reveal

small but significant deviations from linearity.

The individual Cr and Fe average moments can be determined by neutron diffuse scattering. The data of Aldred et al (1976) (together with that of Shull and Wilkinson (1955) and Lander and Heaton (1971)) reveal that the average Fe moment initially increases with decreasing Fe concentration, peaking at $\sim$ 80%., and then slowly decreases. The mean Cr moment is oppositely directed to the Fe moment and decreases rapidly with Fe concentration. These two trends combine to give the approximately linear decrease in mean moment for the alloys with decreasing Fe content. For our purposes the most significant finding of this work is the very weak concentration dependence of Fe moment below 50% Fe. In fact, the mean Fe moment remains essentially constant between 30% Fe and the 12% Fe alloy studied by Babic et al (1980). The induced Cr moment on the other hand is zero, to within experimental error, below 50% Fe.

The g factors and magnetocrystalline anisotropy constant K_1 have been determined by David and Heath (1971). The g factor is concentration and temperature independent. The anisotropy constant at $T \to 0$ decreases with decreasing Fe concentration tending to a constant value of 2×10^5 erg/cm^3 between 7 0% and 3 0% Fe.

The spin wave stiffness shows a monotonic decrease with decreasing Fe concentration and is linear in c below 70% Fe. (Aldred (1976)). The linear portion extrapolates to zero at 18.0 $\pm$ 0.2% Fe, close to C_F estimated from high field susceptibility.

The low temperature specific heat of bcc Cr Fe alloys shows a celebrated anomaly in the vicinity of C_F. In particular the coefficient of specific heat which is linear in T has a large peak as function of concentration at 19% Fe (Cheng, Wei and Beck (1960)). Originally thought to be the result of the peak in d electron density of states this anomaly is now thought to reflect the presence of large magnetic clusters. (Ishikawa et al (1965)). A similar effect is seen Au Fe alloys close to C_F (Dawes and Coles (1979)). A large linear component

in the magnetic specific heat is typical of spin glasses (Alderson, Halperin and Varma (1972)).

There is thus considerable disagreement in the precise location of C_F. Extrapolation of the mean moment determined by high field magnetization results in $C_F \sim 10\%$ Fe whereas extrapolation of the high field $T_c(C)$ data gives $C_F \sim 16\%$ Fe. Somewhat higher values are suggested from the extrapolation of the spin wave stiffness ($C_F \sim 18\%$ Fe) and the peak in the coefficient of specifid heat ($C_F \sim 19\%$ Fe). Higher still is the estimate of Shull and Beck (1975) from low field susceptibility data ($C_F \sim 23\%$ Fe).

In spite of the disagreement in C_F there is universal agreement that the ferromagnetism of Cr Fe alloys changes character below 30% Fe. Whereas for higher concentrations the magnetization could be well saturated in a field of 0.4T and the low temperature magnetization well described by spin wave theory, the magnetization of alloys containing less than ~35% Fe is strongly field dependent and the spin wave fit breaks down (Aldred (1976)). Arrott plots develop pronounced curvature (Loegel (1975)) and the low field magnetization shows field cooling effects in this region (Shull and Beck (1975)). The temperature dependence of the resistivity crosses over from a T^2 regime to a $T^{3/2}$ regime below 30% Fe (Loegel (1975)) and the Mossbauer hyperfine field measurements result in a T_c well below those determined by bulk magnetization. (Loegel, Friedt and Poinsot (1975)). The effective Curie constant also shows a rapid increase as the concentration is lowered below 30% Fe (Aldred and Kouvel (1977)).

This change coincides with the development of forward peaking in the magnetic moment disturbance $M(\kappa) = T(\kappa)/S(\kappa)$ (section 2.2.3) in the neutron diffuse scattering measurements of Aldred et al (1976), indicating a tendency toward long range spatial inhomogeneity in the magnetization distribution. Such spatial inhomogeneity may be expected to develop as C_F is approached and it would appear that the change in character of ferromagnetism in Cr Fe alloys below 30% Fe is the result of such a process.

Explanations along these lines have been put forward by a number of groups. Loegel (1975) suggested that a breakdown into inhomogeneous ferromagnetic order occurred below ∿29%. Aldred and Kouvel (1977) invoke the presence of giant moment clusters below 30% Fe to account for the unusually large critical exponent γ in this concentration range. Shull and Beck (1975) attribute the micto-magnetic or cluster spin glass phenomena in alloys with less than 23% Fe to superparamagnetic clusters. The presence of supermagnetic clusters is also well established in SDW alloys ($C \lesssim 15\%$) (section 4.2) and may be expected to persist to higher concentrations. Shull and Beck (1975) conclude that the change to ferromagnetism was gradual but alloys above 25% Fe were essentially 'good' homogeneous ferro-magnets.

5.3 Determination of the ferromagnetic phase boundary

5.3.1 Introduction

The present program of experiments was initiated to clarify the nature of magnetic inhomogeneity in Cr Fe alloys close to C_F and to provide a more accurate estimate of the ferromagnetic phase boundary $T_c(C)$ and the critical concentration for ferromagnetism.

The determination of the ferromagnetic phase boundary by neutron small angle scattering in conjunction with low field static and AC susceptibility techniques is presented in the present section. The results of susceptibility measurements on alloys which lie between the critical concentration for antiferromagnetism and the critical concentration for ferromagnetism are presented in section 5.4. A quantitative account of the spin correlations in the vicinity of C_F is given in section 5.5. Finally the effect an applied field has on the spin correlations is discussed in section 5.6.

5.3.2 Results of neutron small angle scattering measurements

5.3.2.1 Zero applied field: D17

Neutron small angle scattering (SAS) measurements were carried out initially on a series of alloys with concentrations between 16.7% Fe and 25% Fe (essentially spanning the range of critical concentrations discussed in section 5.2.2) using the D17 spectrometer at ILL Grenoble. The samples were prepared following the procedure of section 3.1. The spectrometer was set up according to the procedure given in section 3.3.3. A sample to detector distance of 2.82 m and incident wavelength of 11.7Å gave a range of useful momentum transfer between 0.010 and 0.060 $Å^{-1}$. The data were collected following the method outlined in section 3.3.3 and the results were analysed to give radial averages of the scattering collected by the D17 area

detector (section 3.3.4). The scattering intensity $I(\kappa)$ for three selected values of κ are shown in Fig. 5.7.

The SAS exhibits two distinct features. All samples studied display a dramatic increase in scattering as the temperature is lowered. For alloys with concentrations of 19.9% Fe or greater the SAS also rises to a maximum at a finite temperature. This maximum is well defined for the Cr Fe 25% sample but falls away to a weak shoulder for Cr Fe 19.9%. These maxima are attributed to ferromagnetic critical scattering which peaks at T_C. The absence of a critical scattering peak in the 16.7% alloy indicates that long range ferromagnetic order does not exist at this concentration. These observations bracket C_F between 16.7% Fe and 19.9% Fe.

5.3.2.2 Zero applied field: D11 (5m)

A further series of SAS experiments were performed on a second set of alloys which filled the gap between 16.7% and 19.9% Fe left by the D17 measurements. Alloys of concentrations 19.5%, 18.5%, 17.5% and 15.5% Fe were prepared, allowing the critical concentration to be bracketted within $\pm$ 0.5% Fe. These measurements were carried out using the D11 spectrometer at ILL, Grenoble. Data were collected with an incident wavelength of 7.0Å at the sample to detector distance of 5m, covering a momentum transfer between 0.008 to 0.050 Å^{-1} which overlaps with the previous D17 scattering range. The experimental details, data analysis and sample preparation are covered in sections 3.1, 3.3.2 and 3.3.4. The radially averaged intensity $I(\kappa)$ obtained from these alloys is shown as a function of temperature in Fig. 5.8. For ease of comparison with the previous D17 data (Fig. 5.7) the same three κ values have been used and the intensities have been normalized to each other.

These data show an increase in SAS with decreasing temperature for all alloys studied, as seen previously. A weak shoulder superimposed on this increase may be discerned for the Cr Fe 19.5% Fe sample and represents the ferromagnetic critical scattering occuring at $T_c = 45 \pm 5$K. No trace of this shoulder remains at a concentration

Fig.5.7 Temperature variation of small angle scattering for Cr Fe alloys from D17 experiments. Radially averaged intensity as a function of temperature is shown for constant κ value of 0.019Å^{-1} (upper curves), 0.032Å^{-1} (middle curves) and 0.040Å^{-1} (lower curves).

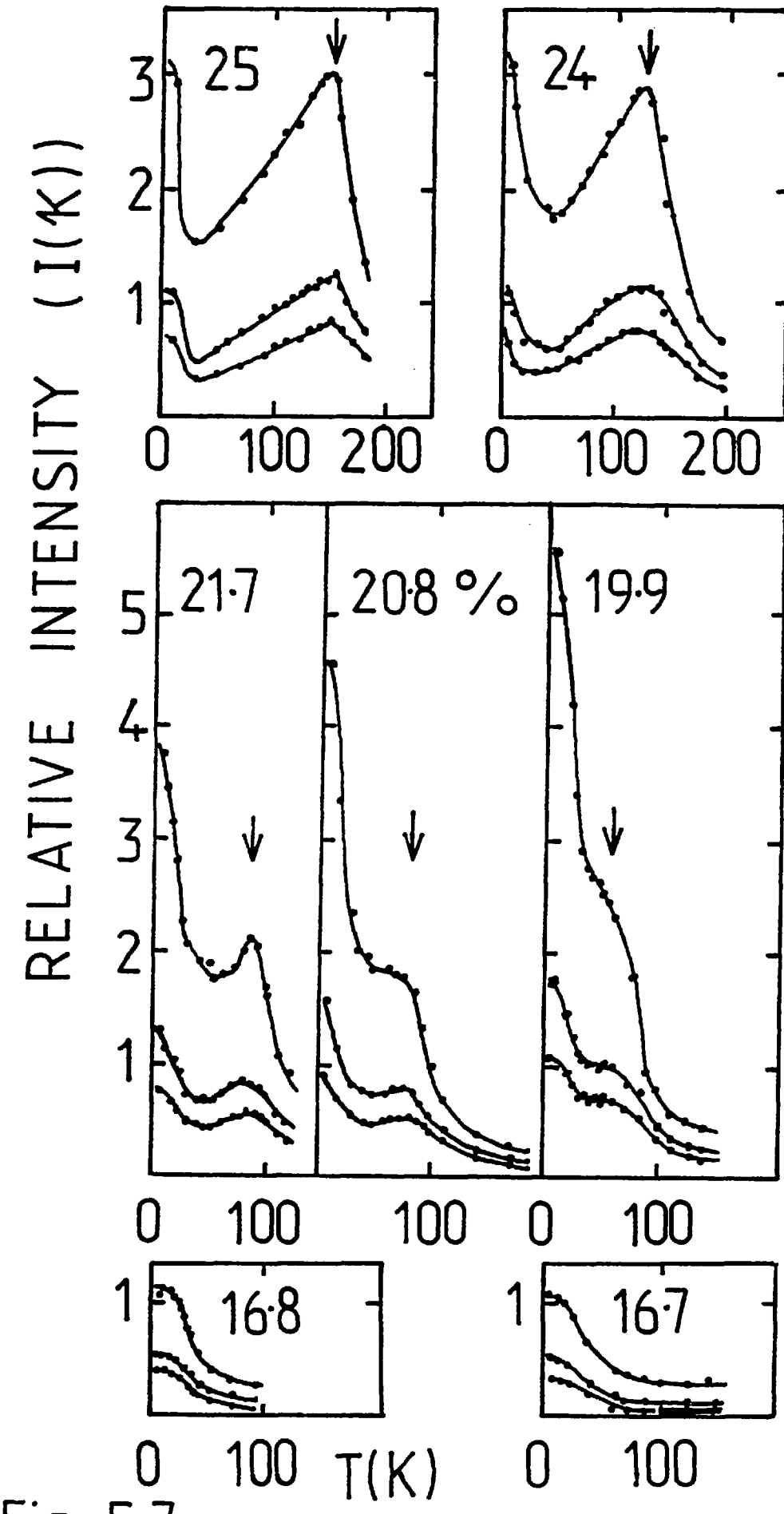

Fig. 5·7

Fig.5.8 Temperature variation of small angle scattering for Cr Fe alloys from D11 (5m) experiments. Radially averaged intensity as a function of temperature is shown for constant κ values of 0.019 $\mathring{A}^{-1}$ (upper curves) 0.032 $\mathring{A}^{-1}$ (middle curves) and 0.040 $\mathring{A}^{-1}$ (lower curves).

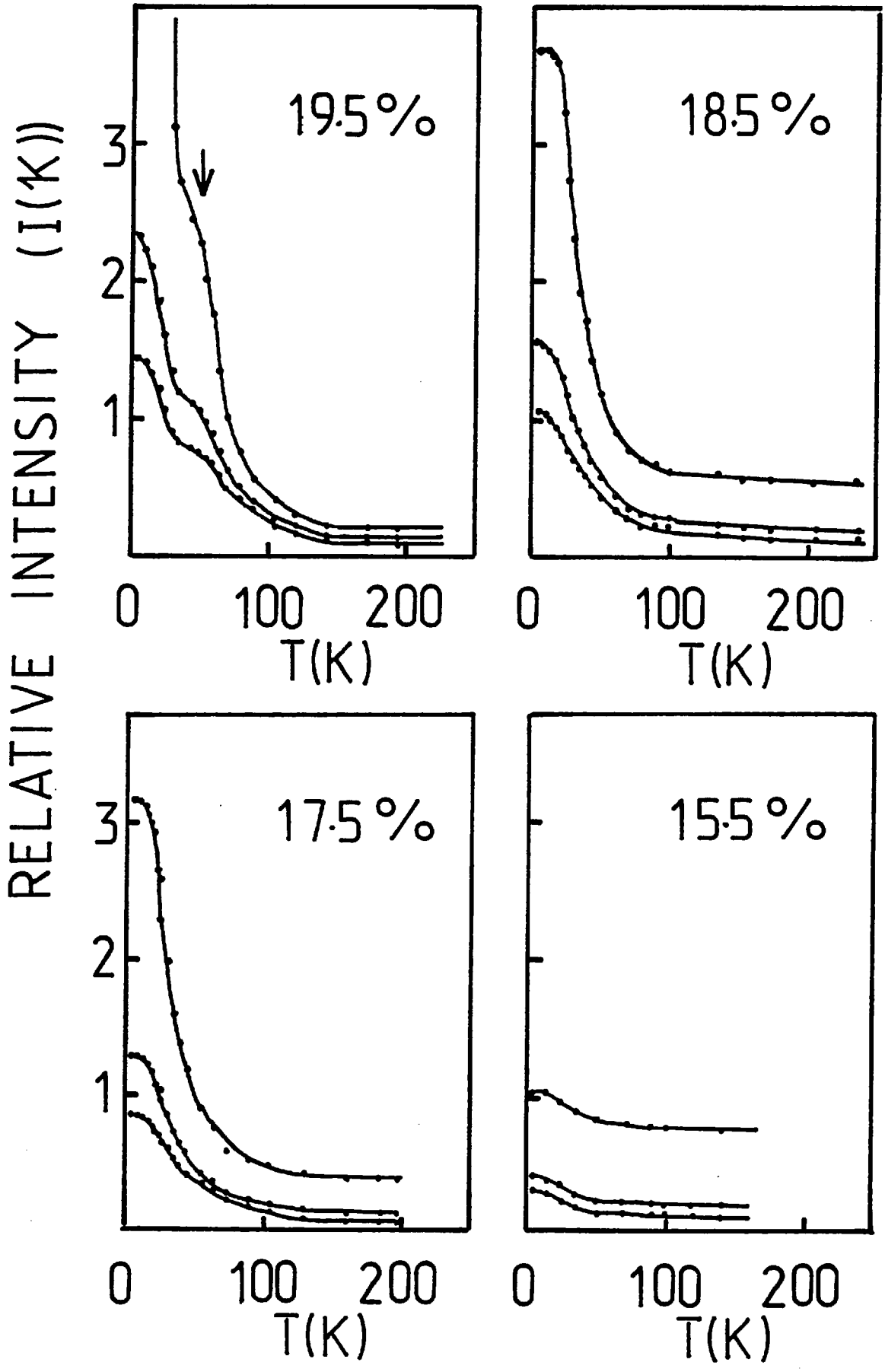

Fig. 5·8

of 18.5%. This information, together with the concentration dependence of T_c places the critical concentration for ferromagnetism at $C_F = 19.0 \pm 0.5\%$ Fe.

5.3.3 Low field susceptibility measurements

The magnetization of several ferromagnetic alloys was measured in very low fields (2.5-10 Oe) using the vibrating sample magnetometer described in section 3.8.2. Thin disc shaped samples suitable for magnetization measurements were spark machined from the Cr Fe 19.9%, 20.8% and 25% samples used in the SAS experiments. To minimize demagnetization effects, the field was applied parallel to the disc axis. The results are shown in Fig. 5.9.

The magnetization increases rapidly with decreasing temperature until the demagnetizing limit is reached at the 'kink point' temperature. The magnetization remains at the demagnetizing limit as the temperature is further decreased and at low temperatures drops rapidly. The 'kink point' temperature is commonly used to estimate T_c (section 5.2.1) and T_c determined in this way lies some 5K below the T_c determined from neutron SAS on the same alloys. In view of the uncertainty in estimating T_c from bulk magnetization data this discrepancy may be regarded as negligible.

AC susceptibility measurements were also made on two alloys, one on either side of the critical concentration. These samples, Cr Fe 17.5% and Cr Fe 19.5%, were spark machined from the neutron SAS specimens and had the form of long thin needles ($c/a \sim 20$) in an attempt to reduce the demagnetizing field below that of the disc-like samples used in the static susceptibility measurements. The AC susceptibility was determined between 4.2K and 77K using the AC bridge described in section 3.8.3. An alternating field of 80 Hz and 300 mOe was employed. The results are shown in Fig. 5.10.

The susceptibilities of these two samples are remarkably similar, both showing a sharp asymmetric peak at 30K. On the basis of these

Fig.5.9 Low field magnetization of several ferromagnetic Cr Fe alloys as a function of temperature. T_c determined from neutron SAS is shown by an arrow.

Fig.5.10 AC susceptibility for Cr Fe 17.5% ($C < C_F$) and Cr Fe 19.5% ($C > C_F$) as a function of temperature. T_c determined by neutron SAS for the 19.5% alloy is shown by an arrow.

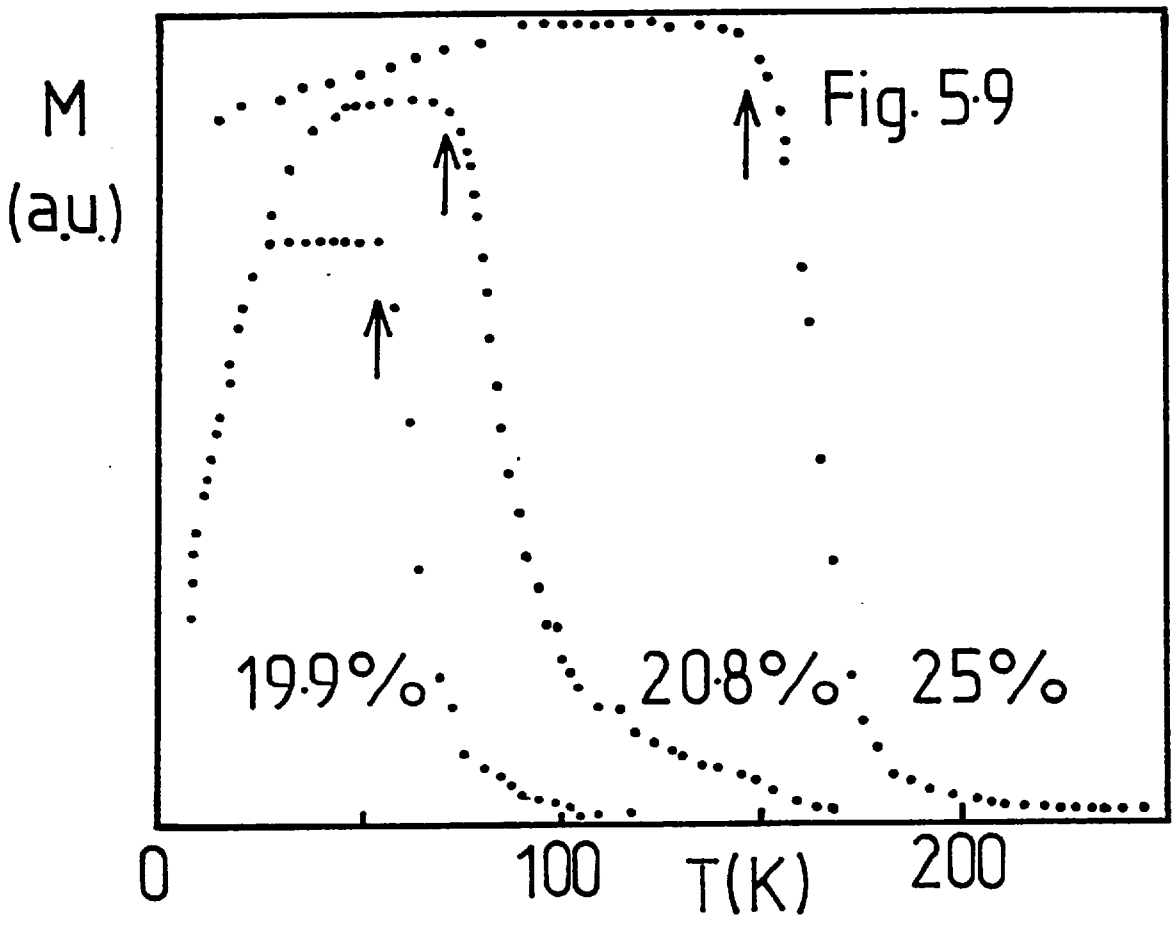

Fig. 5.9

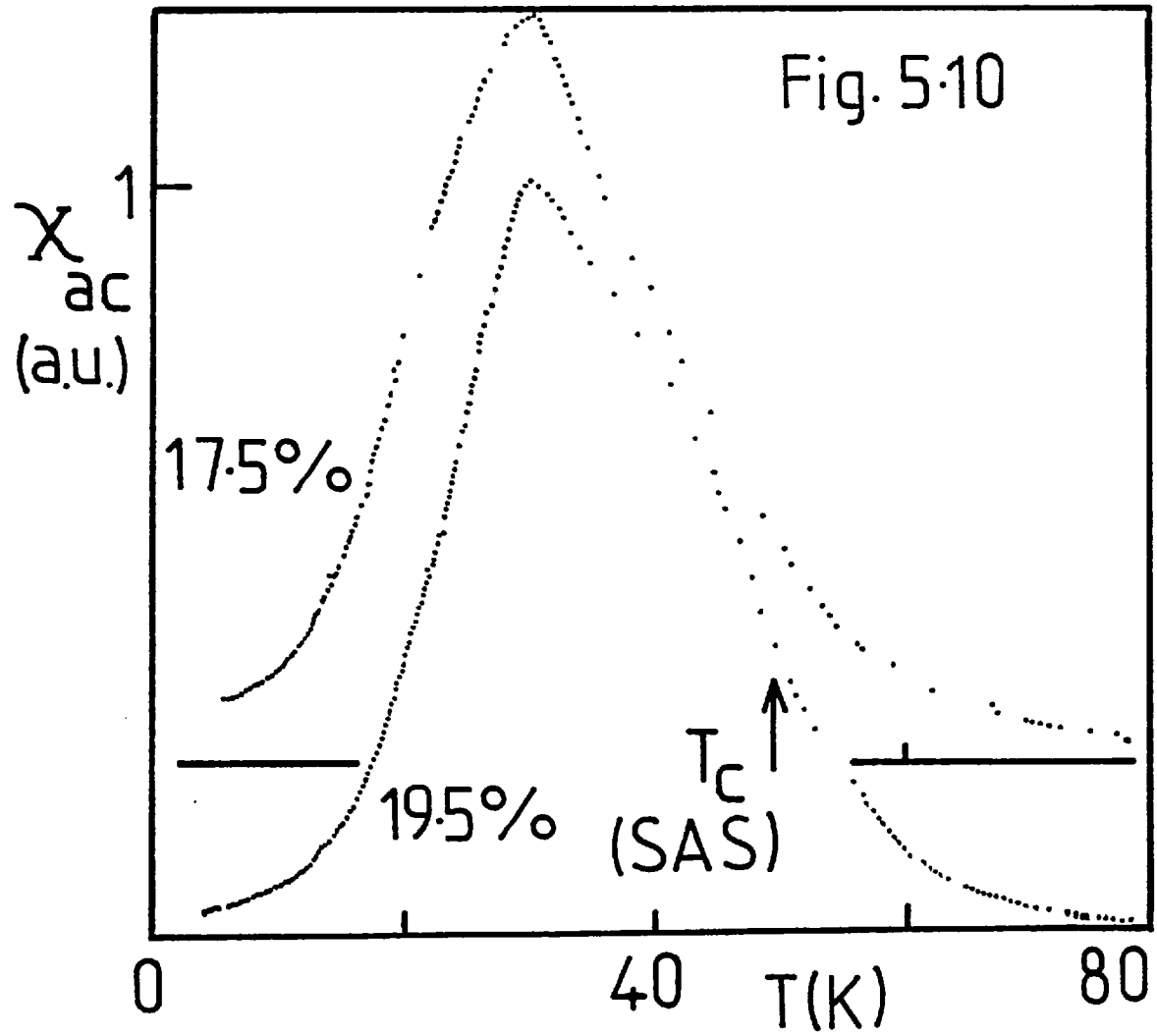

Fig. 5.10

data it is difficult to discern any difference between the ferromagnetic Cr Fe 19.5% alloy and the paramagnetic Cr Fe 17.5% alloy. Closer examination of the 19.5% Fe data reveals a slight shoulder between 40K and 60K which is absent in the 17.5% Fe data. This shoulder gives a weak maximum in $\frac{d\chi}{dT}$, commonly identified with T_c (section 5.2.1) at 44K. This estimate is in excellent agreement with the neutron SAS value of 45K. The absence of a shoulder and the cusplike maximum in the susceptibility of the 17.5% alloy suggest that it is not ferromagnetic, in line with the neutron SAS result.

The values of T_c determined by these methods is given in Table 5.1

Table 5.1

Curie temperatures (T_c) for Cr Fe alloys determined by neutron critical scattering and low field magnetization

Concentration (atomic percent Fe)	T_c (Critical scattering) (K)	T_c (Magnetization) (K)
25	148	145 ± 3
24	122	-
21.7	84	-
20.8	72	70 ± 3
19.9	55 ± 5	55 ± 5
19.5	45 ± 5	44 ± 3

5.3.4 Discussion

The critical concentration of 19.0 ± 0.5% Fe is considerably larger than

the reported values of 15.5% Fe estimated from high field $T_c(c)$ data and 10% Fe estimated from the high field $\mu(c)$ data but lies close to the value of 18% Fe estimated from spin wave stiffness and 19% Fe estimated from the specific heat (section 5.2.2).

The discrepancy is due to systematic overestimation of T_c for near critical alloys by the high field magnetization technique, even to the extent of assigning a Curie temperature to an alloy which does not show long range order (Nevitt and Aldred (1963)). This difficulty arises from spatial inhomogeneity within the alloy which tends to produce highly curved Arrott plots (Loegel (1975)) which cannot be easily extrapolated to H = 0 in order to determine T_c. A similar conclusion has been drawn for Au Fe alloys close to C_F (Murani (1974) and section 5.1.4.2.). A related difficulty arises in the high field determination of the spontaneous magnetization. In this case, the saturation of highly susceptible superparamagnetic clusters on both sides of the critical concentration results in a misleadingly high value of the spontaneous magnetization.

Shull and Beck (1975) suggest a critical concentration above 23% Fe on the basis of low field magnetization measurements. If the data of these authors is re-examined in the light of the present measurements it is apparent that the 23% Fe alloy which was considered mictomagnetic is in fact ferromagnetic. This brings the value of the critical concentration to $\sim$ 19% in excellent agreement with the present value.

The critical concentration is lower than the calculated nn percolation limit for a bcc lattice (24.3%) but higher than the calculated next nn percolation limit (17.8%) (Essam (1972)). It should be noted that the tendency toward atomic clustering in these alloys would lead to a critical concentration below that calculated for purely random nn percolation.

One of the most striking features of the SAS is the rapid increase in scattering below T_c for ferromagnetic alloys. This

increase has been observed in a number of SAS studies of binary alloys close to C_F (Murani et al (1975), Cywinski, Booth and Rainford (1977), Malletta and Felsch (1980)) and has been termed 'subcritical scattering' by Goman'kov, Mokhov and Nogin (1980). It has been suggested by a number of groups (Malletta et al (1980), Goman'kov et al (1980), Nieuwenhuys et al (1979)) that this subcritical scattering is associated with a ferromagnet - spin glass phase transition in the vicinity of the temperature for which the magnetization first decreases below the demagnetizing limit. This transition being responsible for the low temperature drop in magnetization seen for example in Fig. 5.9. However, the data of Fig. 5.10, in which the demagnetizing field has been made very small, show that this decrease is part of a Hopkinson peak (similar to that observed for pure Fe (section 5.2.1))and may be understood without invoking a ferromagnet - spin glass transition. Such a peak is explained by the competition between increasing magnetic anisotropy and increasing spontaneous magnetization. It is unlikely that the mechanism of magnetic anisotropy in this case is the same as in pure Fe. By noting the similarity between the low field susceptibility of the 17.5% and 19.5% Fe alloys (Fig. 5.10) one may conclude that the anisotropy mechanism operating in spin glass alloys is still present in ferromagnets close to C_F. Magnetostatic shape anisotropy is a possible candidate.

It is suggested in section 5.5 that the subcritical scattering reflects the presence of finite magnetic clusters. This is the limiting case of a more general argument which attributes the subcritical scattering to the mosaic broadening of the magnetic (000) Bragg peak by microdomains. It is perhaps a matter of semantics whether the subdivision of an inhomogeneous ferromagnet into microdomains may be regarded as ferromagnet - spin glass transition.

5.4 Magnetization between the critical concentrations

5.4.1 Results

The low field static magnetization of Cr Fe 17.5% and 18.5% samples was determined by use of the low field vibrating sample magnetometer described in section 3.8.2. Needle shaped specimens with a low demagnetization factor were spark machined from the ingots used for neutron SAS experiments. These alloys do not support long range antiferromagnetic order or long range ferromagnetic order as they lie between the critical concentrations C_A = 16% and C_F = 19% respectively.

The Cr Fe 17.5% specimen was studied in detail. The magnetization in an applied field of 35Oe was determined in both zero field cooled (ZFC) and field cooled (FC) conditions. The results are depicted in Fig. 5.11. The ZFC magnetization shows a peak at 24K, somewhat rounded compared to the AC susceptibility peak found for the same alloy (section 5.3.3) and occurs at a lower temperature. A similar discrepancy between static and AC susceptibility for Cr Fe alloys was noted by Shull and Beck (1975). The magnetic response below the peak temperature is time dependent. The magnetization increases slowly in time with constant applied field, this is shown inset in Fig. 5.11 for a field of 35 Oe at 4.2K. The time dependence is closer to logarithmic than exponential. The IRM which remains after the field has been removed also decays slowly with time.

The FC magnetization shown in Fig.5.11 follows the ZFC data above the peak temperature but tends to a constant value below the peak. This magnetization did not appear to be time dependent over the period of 30 m during which a field was applied at 4.2K. The magnetization which remained after the field was removed (TRM) decayed slowly with time. The temperature dependence of the TRM measured 10s after the removal of the cooling field is shown in Fig.5.11. The approximate addition of the TRM and ZFC magnetization to produce the FC magnetization should be noted as well as the disappearance of remanence above the peak temperature.

Fig.5.11 Low field magnetization for Cr Fe 17.5% (35.) Oe) Zero field cooled magnetization (ZFC), field cooled (35 Oe) magnetization (FC) and thermoremanent magnetiation (TRM) are shown. Increase in ZFC magnetization at 4.2K with time is shown inset.

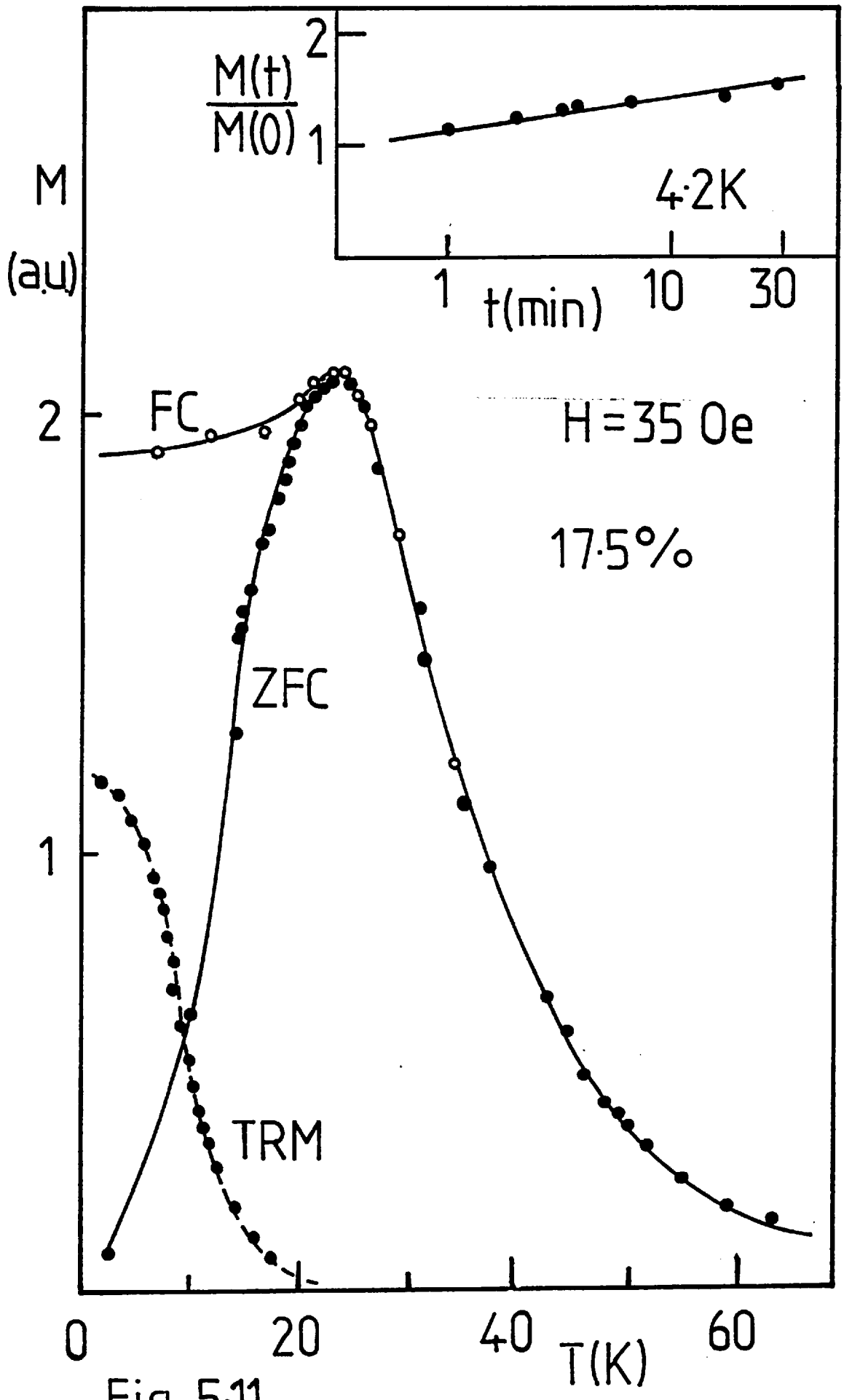

Fig. 5·11

Hysteresis loops were taken at 4.2K in ZFC and FC states. The loop obtained after field cooling is of similar shape to that measured in after cooling in zero field but is displaced along the magnetization axis by an amount approximately equal to the TRM at 4.2K (Fig. 5.12). This is consistent with the appearance of remanent magnetization which cannot be switched over the time period of the experiment. It is interesting to note that the AC susceptibility, which is in reality an effective susceptibility found by traversing a very small hysteresis loop, is virtually unchanged for FC and ZFC states.

A hysteresis loop was also taken at 4.2K in the ZFC state in large fields. In contrast to the symmetrical loop found in the previous low field determination, the high field loop is markedly asymmetric. The magnetization does not approach saturation in applied fields up to 5000 Oe. This data is shown in Fig. 5.12 and compared to the hysteresis loop for a ferromagnetic 25% Fe alloy which does show saturation. (P. Mitchell, Private communication).

The Cr Fe 18.5% sample shows similar behaviour. The ZFC magnetization and IRM obtained after application of a field of 3 Oe for 30S are shown in Fig. 5.13.

5.4.2 Discussion

The magnetic behaviour of these alloys between the two critical concentrations is very similar to that of Au Fe alloys close to C_F for which the term 'cluster spin glass' has been used. (Section 5.1.4.2). The term 'spin glass' alludes to peak in the susceptibility which is seen in these more concentrated alloys as a result of the freezing of large correlated clusters of spins into random anisotropy directions. It must be stressed that although these alloys satisfy the operational definition of the spin glass state given in section 5.1.3.1, there is no obvious element of

Fig.5.12 Hysteresis loops for (a) Cr Fe 17.5% in ZFC and FC states at 4.2K. (b) Cr Fe 17.5% zero field cooled and measured in high fields at 4.2K (c) Cr Fe 17.5% ferromagnet measured in high fields at 4.2K.

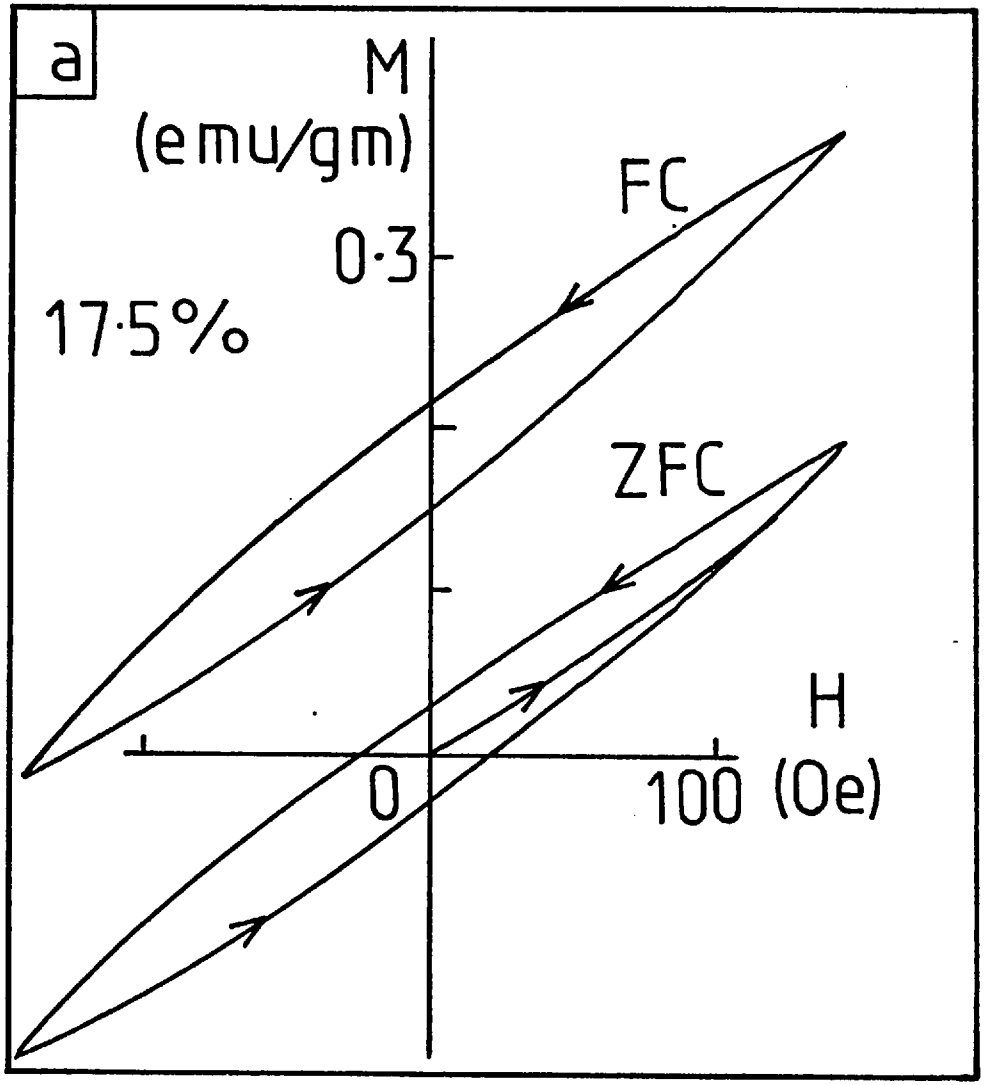

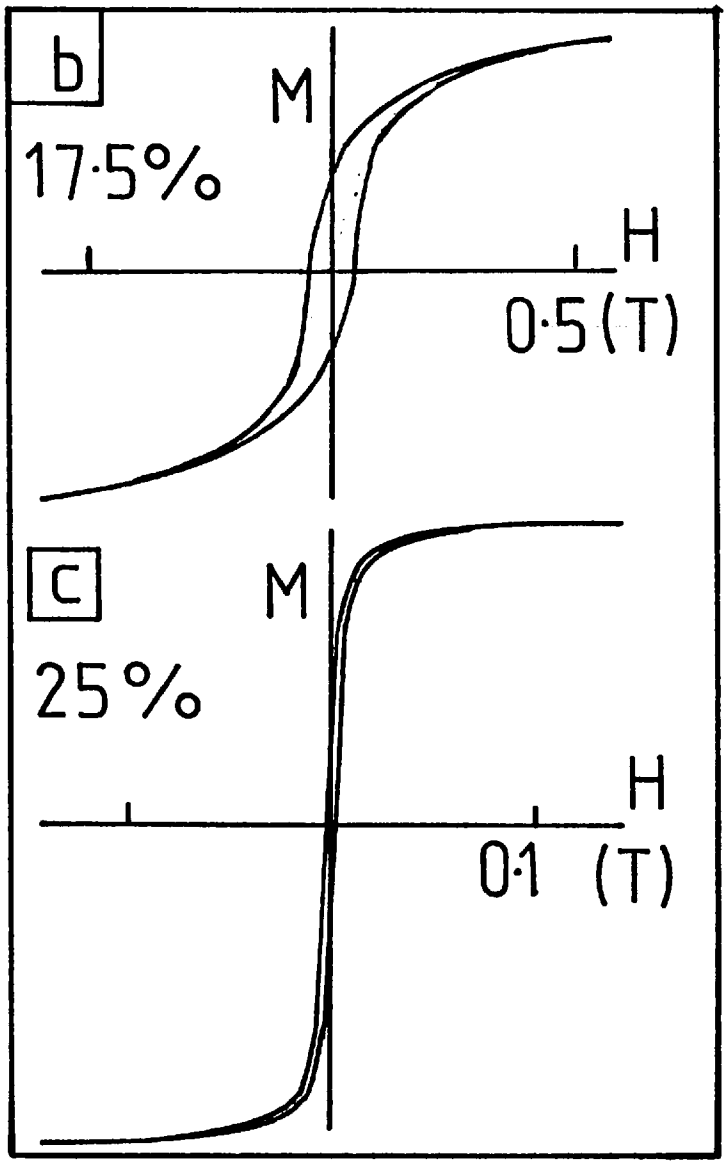

Fig. 5·12

Fig.5.13 Low field magnetization for Cr Fe 18.5% Zero field cooled magnetization and IRM remaining after the application of a 3.0 Oe field for 30 sec.

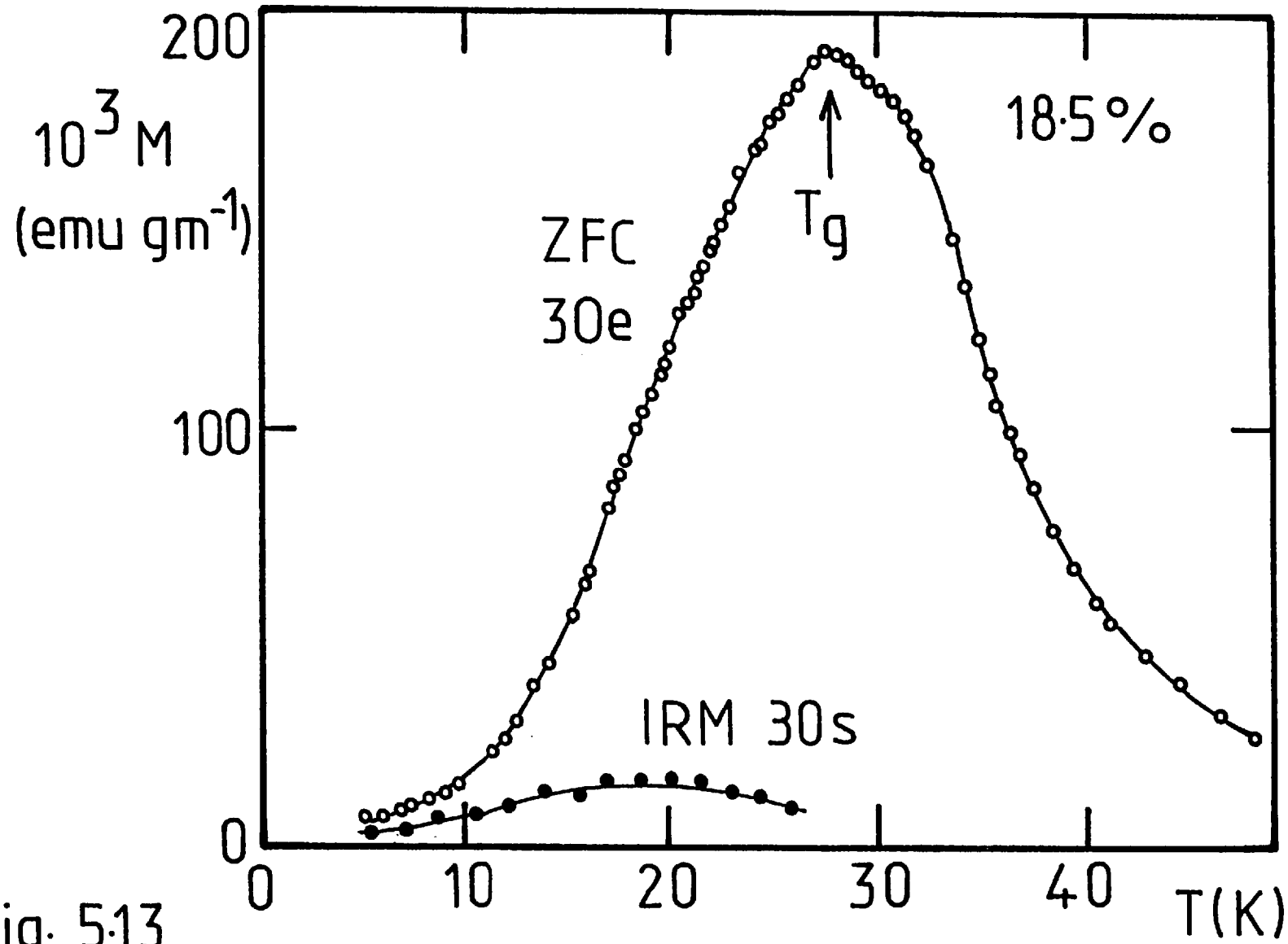

Fig. 5·13

'frustration' present in these alloys (section 5.1.3.2). It is possible to account for the behaviour of the Cr Fe cluster spin glasses using the phenomenological ferromagnetic fine particle model described in section 5.1.3.3 without invoking frustrated exchange interactions.

According to the fine particle phenomenology the peak in the susceptibility, time dependence and remanence can be analysed by postulating the existence of magnetically correlated clusters whose total moment fluctuates thermally against the cluster anisotropy barriers. It is clear that large ferromagnetically coupled clusters of Fe moments are present in Cr Fe alloys from the nature of the neutron SAS. However, in contrast to the simple fine particle theory these clusters are not well defined metallurgical precipitates but appear to be more akin to nn percolation clusters. Furthermore, these clusters do not become fully correlated until a low temperature is reached. The analysis of section 5.5 shows the correlation range of these clusters to be increasing down to a temperature of the order of the susceptibility peak temperature T_g. This effect leads to a sharper susceptibility maximum than expected for clusters which are well correlated above T_g. The second ingredient of the fine particle model, the anisotropy barriers, are more difficult to identify. Magnetostatic shape anisotropy, as will be demonstrated, appears to be a major influence. The simplest version of the fine particle description forms a useful basis for discussion as long as these comments are borne in mind.

On a qualitative level the observed magnetic properties of Cr Fe cluster spin glasses follow well the behaviour described in section 5.1.3.3. To proceed beyond a qualitative acount is difficult in view of the many approximations inherent in the model. It is possible to perform some approximate order of magnitude calculations to test the validity of the fine particle description.

The blocking temperature may be calculated using (eq.5.21b)

with $H_c(0)$ = 300 Oe taken from the hysteresis loop in Fig. 5.12 for the Cr Fe 17.5% specimen, M_s = 1400 gauss (the saturation magnetization of a cluster of Fe atoms with moment $1.8\mu_B$) and time constant Δt = 30 sec corresponding to a 'static' magnetization measurement. An estimate of the particle volume is also required. The SAS measurements on the Cr Fe 17.5% specimen indicate $R_G \sim 100\text{Å}$; assuming a spherical particle shape this gives a calculated blocking temperature of 50K. This is of the same order of magnitude as that observed (24K).

The fact that the AC susceptibility peak is observed at a higher temperature than the peak in the static susceptibility for the 17.5% Fe alloy is also consistent with the fine particle model. The AC measurement, having a smaller time constant than the 'static' measurement, would find a superparamagnetic particle to be blocked at a correspondingly higher temperature. Repeating the order of magnitude calculation with Δt = 0.013 sec results in a blocking temperature of 70K. The increase in blocking temperature of 20K is of the same order of magnitude as that observed (6K).

More detailed calculations which take into account the distribution of anisotropy barriers and temperature dependence of Ms are required to describe adequately the peak shape. As a first approximation the overall peak height $\chi(T_g)/\chi(4.2K)$ may be estimated according to the simple model of Wohlfarth (1979) in which the decrease in susceptibility is of the order $\log(2\Delta t\, f_o)$. Using the approximations $f_o \sim 3 \times 10^6 H_K$ (eq.5.20c) and $H_K \sim H_c$ this leads to $\chi(T_g)/\chi(4.2) = 17$ for the AC susceptibility and 25 for the 'static' susceptibility; values which are in remarkably good agreement with those deduced from Fig. 5.10 and Fig. 5.11, being 13 and 30 respectively.

It is important to verify that the magnitude of the anisotropy constant K used in these calculations is physically reasonable. The value of $K \sim M_s H_c(0) = 3 \times 10^{-3}$ Kelvin/Å^3 may be compared with that

expected for magnetocrystalline anisotropy and that of shape anisotropy. The anisotropy constant for shape anisotropy calculated from (eq. 5.19b) with Ms = 1400 gauss is $K = 9 \times 10^{-2} (D_\perp - D_{//})$ Kelvin/Å^3 and for magnetocrystalline anisotropy is $K = 1.2 \times 10^{-4}$ Kelvin/Å^3 (taken from the data of David and Heath (1971)). The magnetostatic shape anisotropy will thus dominate if $D_\perp - D_{//} > 0.001$, or if the cluster c/a > 1.001. Hence the value of K calculated for magnetostatic shape anisotropy will be of the same order of magnitude as that used in the previous calculations if $D_\perp - D_{//} > 0.03$. Such a difference in demagnetization factors would correspond to c/a ratio of 1.03 which is physically reasonable.

5.4.3 The magnetic phase diagram

The magnetic phase diagram for Cr Fe alloys compiled from the data of section 4.3 for the antiferromagnets, section 5.3 for the ferromagnets and section 5.4.1 is presented in Fig. 5.14. The spin glass alloys have been characterized by the peak temperature (T_g) deduced from static susceptibility measurements. The T_g data for antiferromagnetic alloys (section 4.4.2) have been included.

In contrast to earlier phase diagrams (Loegel (1975), Mitchell and Goff (1972)) there is no region of overlapping ferromagnetism and antiferromagnetism. SDW order is maintained up to a concentration of 16 ± 0.5% Fe and ferromagnetism is found above 19%. Spin glass behaviour occurs in the narrow concentration range between 16% and 19% Fe where long range order cannot be supported. The concentration dependence of the Neél temperature has been analysed quantitatively using the pair breaking model in section 4.3. It is not possible to account for the concentration dependence of T_g and T_c in such quantitative terms, however the overall features may be understood on a qualitative basis. According to simple fine particle theory $T_g(c)$ will depend on concentration via (eq. 5.21a)

$$kT_g(c) = \tfrac{1}{2}(D_\perp - D_{//})\, M_s^2\, V(C) \,/\, \log\,(6 \times 10^6\, \Delta t\, (D_\perp - D_{//})M_s) \quad (5.25)$$

Fig.5.14 Magnetic phase diagram for Cr Fe alloys deduced from this work. The spin glass alloys have been characterized by the peak temperature of the low field magnetization. For comparison, transition temperatures taken from previous work are included. ●, this work. Ferromagnetic boundary: ○, Loegel (1975); △, Shull and Beck (1975) ▽, Aldred and Kouvel (1977). Antiferromagnetic boundary: ○, Ishikawa et al (1967); △, Arrott et al (1967); ▽, Mori et al (1974); ▼, Arajs and Dunmyre (1966); ▲, Rajan et al (1960); ×, Suzuki (1976).

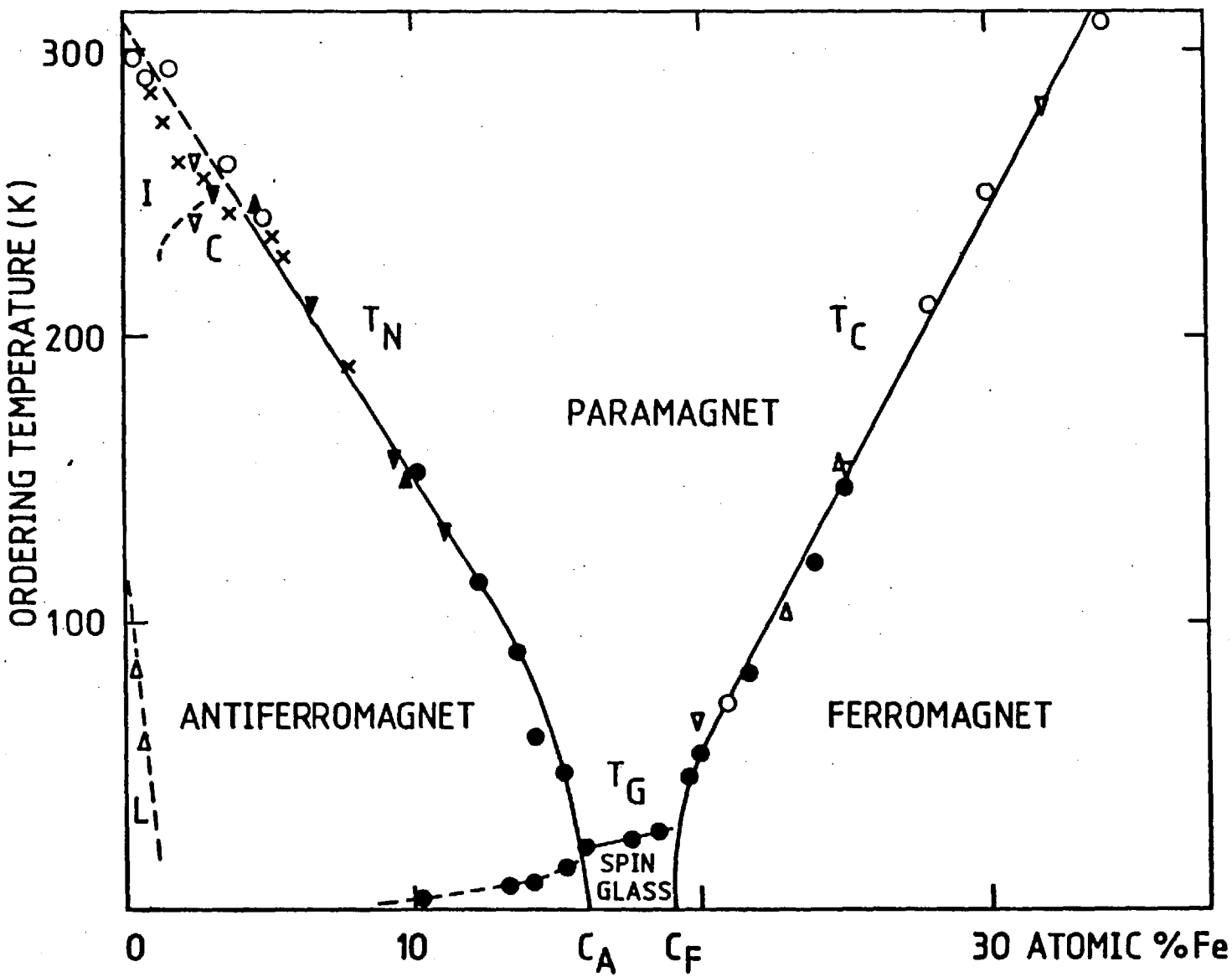
300
200
100
ORDERING TEMPERATURE (K)
I
C
L
T_N
T_C
PARAMAGNET
ANTIFERROMAGNET
FERROMAGNET
T_G
SPIN
GLASS
0
10
C_A
C_F
30 ATOMIC %Fe

Fig.5.14

assuming magnetostatic shape anisotropy dominates. This will give a monotonic increase of T_g with concentration as cluster volume V(c) increases. The suppression of T_g by the SDW is discussed in section 4.4.1. The Curie temperature increases precipitously in the vicinity of 19% Fe but tends to a linear increase at higher concentration. This form of $T_c(c)$ would be predicted by assuming an anisotropy induced crossover from Heisenberg like behaviour to Ising like behvaiour (Stinchcombe, 1980) as T_c is reduced.

5.5 Spin correlations in the vicinity of the critical concentration

5.5.1 Introduction: General trends

The neutron SAS data not only allow the determination of $T_c(c)$ but reveal the evolution of long range magnetic correlations with concentration and temperature in the vicinity of the critical concentration for ferromagnetism. The very observation of SAS close to C_F implies that the onset of magnetic order in this system is not uniform but spatially inhomogeneous. The same conclusion has been drawn from the bulk magnetic properties (section 5.2.2 and 5.4.1). The purpose of the present section is to analyse the spatial correlation between Fe moments as a function of temperature and concentration in an attempt to understand the nature of magnetic inhomogeneity in Cr Fe alloys close to C_F.

The interpretation of this data is simplified in two major ways. Firstly, the observed SAS is almost entirely magnetic in origin and is not associated with gross atomic heterogeneity. This is demonstrated by the suppression of SAS in an applied field (section 5.6) and the weak, quasi-isotropic temperature independent scattering at elevated temperatures. Secondly, as the Cr moment is zero and the Fe moment concentration independent in the range of concentrations studied (section 5.2.2) it is only the correlation between Fe moments which is observed.

The neutron SAS exhibit two main features. For ferromagnetic alloys the critical scattering peak weakens as C_F is approached whereas the SAS at temperatures well below T_C increases rapidly as C approaches C_F. This behaviour is mirrored for $C < C_F$ where the low temperature SAS increases with increasing concentration, reaching a maximum at C_F. This is shown in Fig. 5.15 by plotting the intensity at 4.2K as a function of concentration and the estimated critical scattering intensity at $T = T_c$ for a scattering vector $\kappa = 0.02\ \text{Å}^{-1}$.

Fig.5.15 Concentration dependence of various features of the small angle scattering (a) Intensity at 4.2K, I(4.2)
(b) Estimated peak value of the ferromagnetic critical scattering, (I (T_c)). Radially averaged magnetic scattering at κ = 0.019 $\AA^{-1}$ are displayed.

Fig.5.16 Neutron SAS spectra at high temperature (250K) and low temperature (22K) for Cr Fe 17.5%.

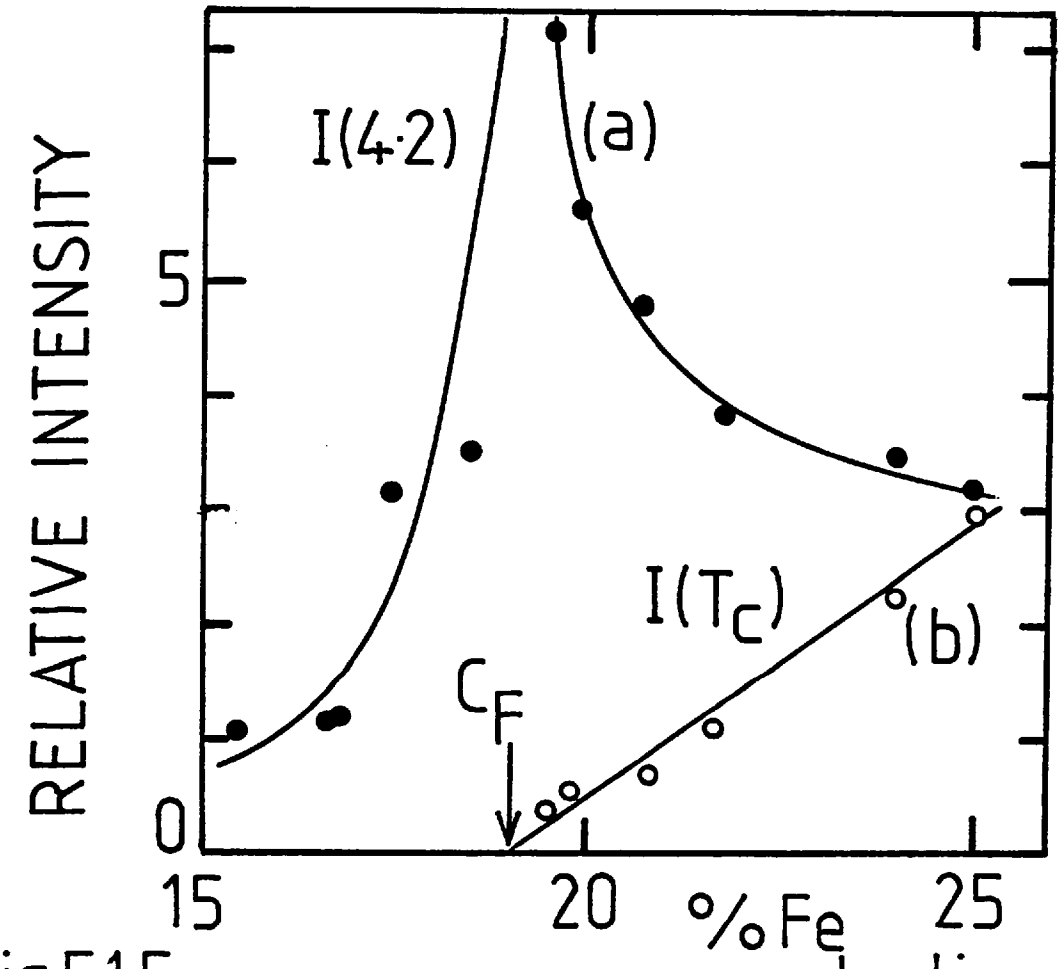

Fig·5·15

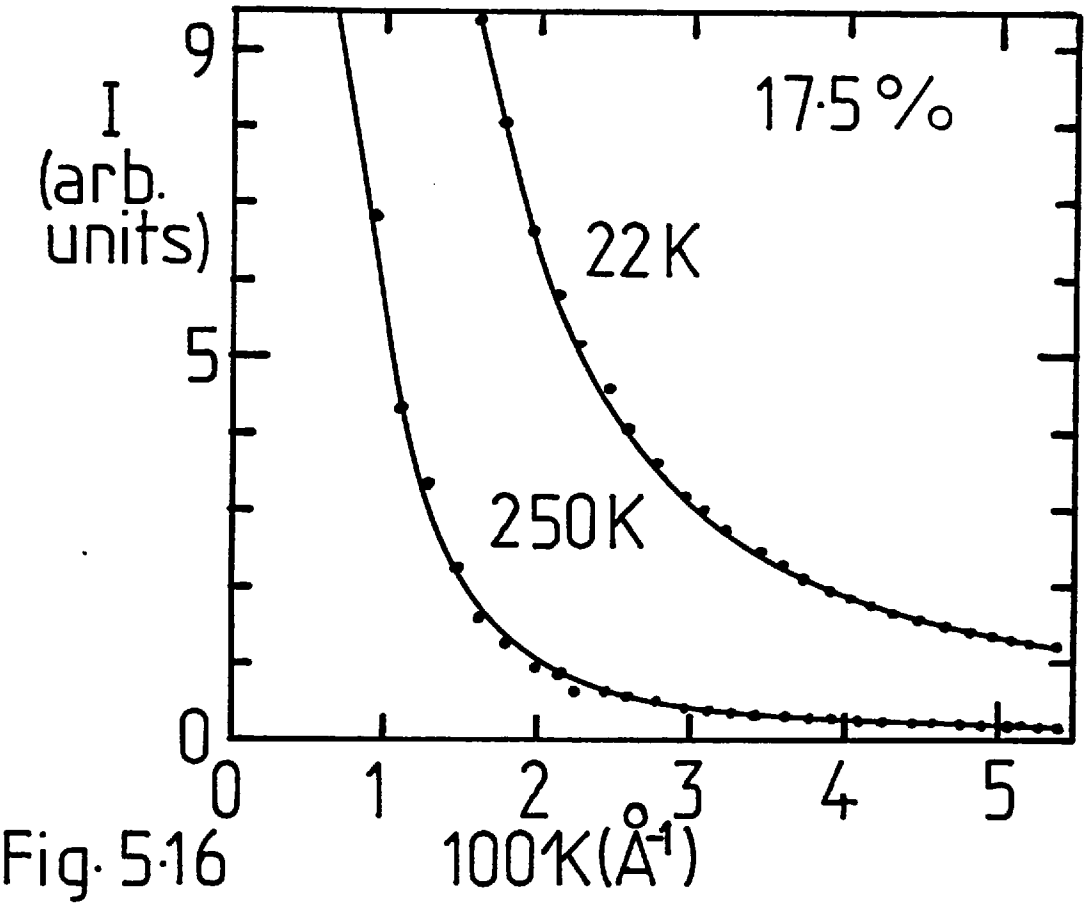

Fig· 5·16

If the magnitude of the Fe-Fe exchange interaction remains essentially constant over this concentration range, the decrease in the size of the ferromagnetic critical scattering peak suggests that the number of Fe moments involved in the ferromagnetic ordering process decreases as $C \to C_F$. In terms of percolation theory, this reflects the concentration dependence of the volume of the ferromagnetic infinite cluster.

The peaking of the low temperature SAS at C_F implies that the system is spatially most inhomogeneous at this concentration, i.e. the fluctuations $\overline{\langle S_i S_j \rangle - \langle S \rangle^2}$ are maximum at $C = C_F$. As C_F is the concentration at which long range order first appears such a conclusion is reasonable. According to percolation theory the infinite cluster simply contributes a delta function at $\kappa = 0$ for low temperatures and the finite clusters dominate the low temperature SAS. The peaking of the low temperature SAS at $C = C_F$ would thus reflect the fact that the average size of finite clusters peaks at $C = C_F$.

It is difficult to justify the application of percolation concepts to Cr Fe alloys as the magnitude, range and concentration dependence of exchange interactions are not known. Some justification may be drawn from the constant magnitude of the Fe moment in this concentration range and the persistance of strong Fe-Fe coupling into the SDW regime. The critical concentration itself is not far removed from the calculated percolation limit, which suggests that nn exchange interactions are dominant. The bulk magnetic properties discussed previously strongly suggest that some geometrical element is necessary in the description of Cr Fe alloys. For example, the division of ferromagnetic alloys into finite and infinite clusters provides a natural explanation for the occurrence of subcritical scattering and cluster spin glass type behaviour in alloys close to C_F. Clusters of some description are also required for the fine particle description of alloys with $C < C_F$.

A description based on percolation theory provides a good first approximation on which to discuss the evolution of long range ferromagnetic order in Cr Fe alloys. The validity of this assumption may be tested by a quantitative analysis of the neutron SAS data.

5.5.2 The small angle scattering law

5.5.2.1 The κ dependence of the small angle scattering

The connection between the neutron magnetic SAS cross section and long range spin correlations has been outlined in sections 2.3 and 2.5. To discuss the κ dependence of the SAS it is convenient to deal with a 'small angle scattering law' $S(\kappa)$ rather than the full cross section. At small κ, in the quasistatic approximation $S(\kappa)$ may be defined by (eq. 2.3)b)

$$\frac{d\sigma}{d\Omega} = \left(\frac{\gamma e^2}{2m_e c^2}\right)^2 g^2 f^2(\underset{\sim}{\kappa} \to 0) \quad e^{-2W(\underset{\sim}{\kappa} \to 0)} \quad S(\underset{\sim}{\kappa}) \tag{5.26a}$$

where the κ dependence of the cross section is contained in $S(\kappa)$,

$$S(\underset{\sim}{\kappa}) = \sum_{\delta\beta} (\delta\alpha\beta - \bar{K}\alpha\ \bar{K}\beta) \sum_{i,j} \exp\ (i\underset{\sim}{\kappa}.\underset{\sim}{R}_{ij}) \overline{< S_i^{\alpha}(0)\ S_j^{\beta}(0)>} \tag{5.26b}$$

When dealing with polycrystalline samples, it is necessary to average $S(\kappa)$ over all orientations. The resulting form of $S(\kappa)$ is given by (eq. 2.39) in the general case, and reduces to the expression

$$S(\kappa) = 2/3 \sum_{i,n} \overline{<\underset{\sim}{S}_i.\underset{\sim}{S}_j>} \quad \frac{\sin \kappa r_n}{\kappa r_n} \tag{5.26c}$$

if the correlations are isotropic. At very small κ, $S(\kappa)$ takes the model independent Guinier quadratic form discussed in sections 2.5 and 5.1.2 but at higher κ shows system dependent deviations from the Guinier law, reflecting the detailed nature of correlations.

The form of $S(\kappa)$ for a model percolating system close to C_F has been discussed by referring to scaling laws (section 5.1.2). Unfortunately, these scaling laws do not say anything about the explicit functional form of $S(\kappa)$. Thus the analysis of the κ dependence of the SAS must be performed without any firm theoretical predictions. To a certain extent one may be guided by the exact one dimensional result of Thorpe (1975) as adopted by Birgeneau et al (1980) (section 5.1.4.1) and by the explicit results for pure thermal and pure percolative critical phenomena in the form of the Ornstein-Zernicke and Fisher-Burford results (sections 2.3 and 5.1.2).

It is worthwhile drawing attention to certain explicit results which arise in the study of SAS from polymers. As the relevance of this approach to Cr Fe alloys close to C_F is uncertain and lies outside the main arguments of this thesis this theme is briefly explored in Appendix B.

5.5.2.2 Results and Analysis

The purely magnetic SAS cross section was obtained from the D17 and D11 data of section 5.3.2 by subtracting the purely nuclear SAS cross section using the high temperature data. The high temperature data in each case was taken at the highest temperature of measurement, in the regime where the SAS remained temperature independent. The SAS at high temperatures is only weakly dependent and contains temperature independent contributions from nuclear incoherent, nuclear defect, grain boundary and surface scattering. A typical spectrum is shown in Fig. 5.16. The weak κ dependence and absence of inter-particle interference peaks rules out any gross atomic heterogeneity in these alloys. The effect of the subtraction was negligible for low temperature spectra, but tended to become more important at high temperature.

The resulting intensities are illustrated in the form of 'Debye plots', $1/I$ vs. κ^2 in Figs. 5.17-5.20 for three alloys with

Fig.5.17 Reciprocal intensity versus κ^2 (Debye) plot for Cr Fe 16.7% ($C < C_F$) at a number of temperatures.

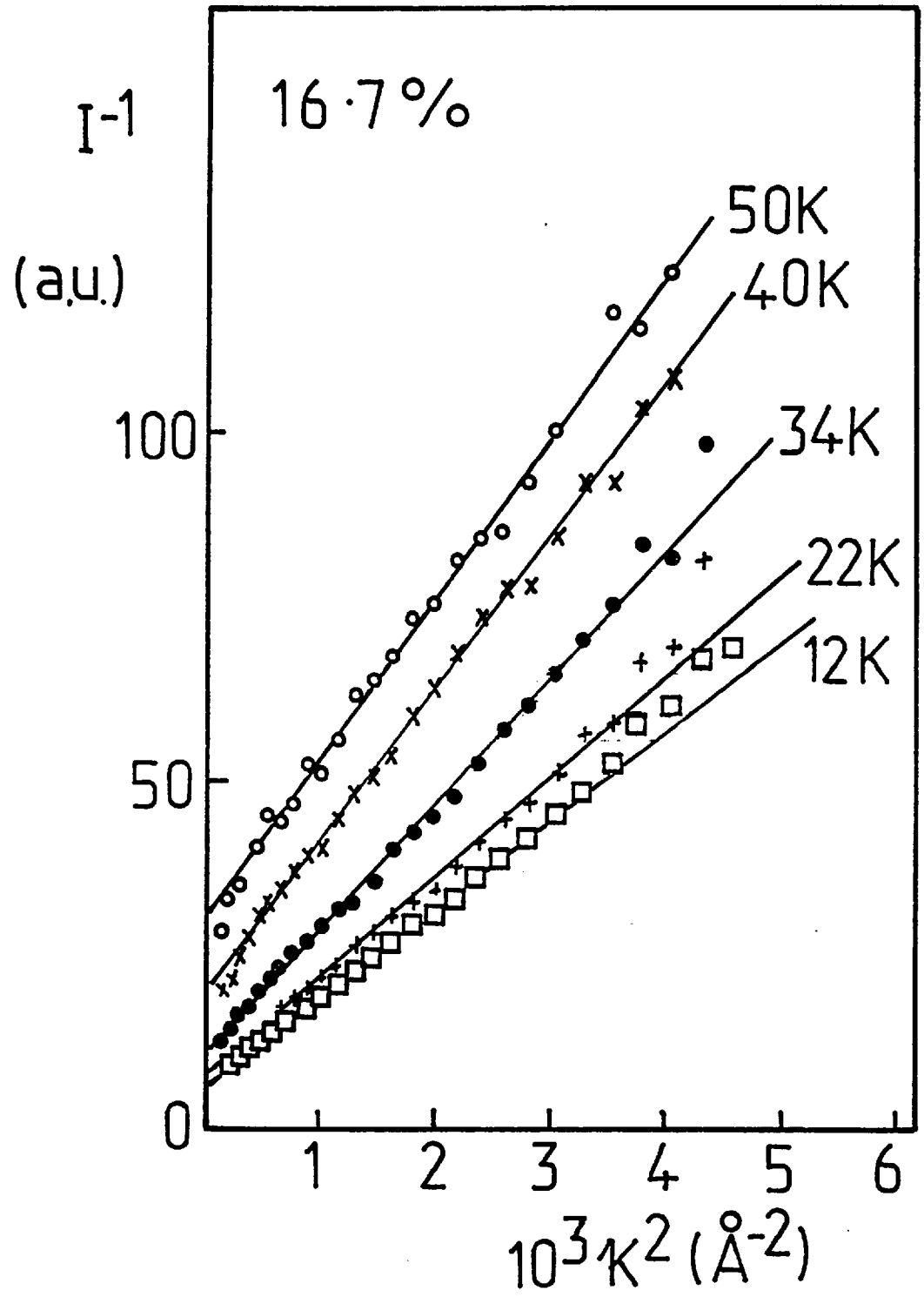

Fig. 5.17

Fig.5.18 Reciprocal intensity versus κ^2 (Debye) plot for Cr Fe 20.8% ($C \gtrsim C_F$) at a number of temperatures.

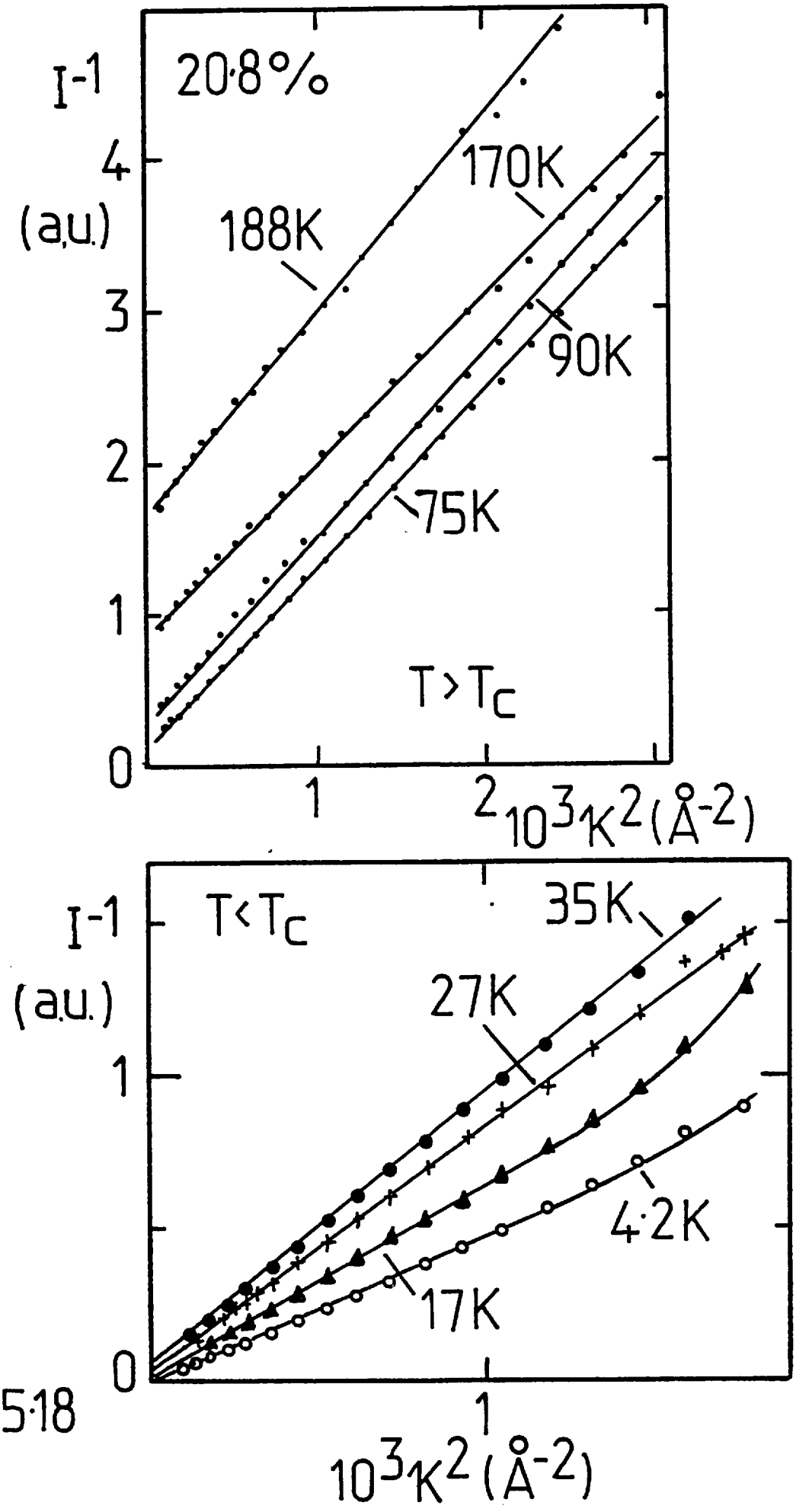
I-1
(a.u.)
20·8%
188K
170K
90K
75K
T>Tc
0
1
2
3
4
1
2
10³K²(Å⁻²)
I-1
(a.u.)
T<Tc
35K
27K
17K
4·2K
0
1
1
10³K²(Å⁻²)

Fig· 5·18

Fig.5.19 Reciprocal intensity versus κ^2 (Debye) plot for Cr Fe 24% ($C > C_F$) at various temperatures above T_c.

Fig.5.20 Reciprocal intensity versus κ^2 (Debye) plot for Cr Fe 24% ($C > C_F$) at various temperatures below T_c.

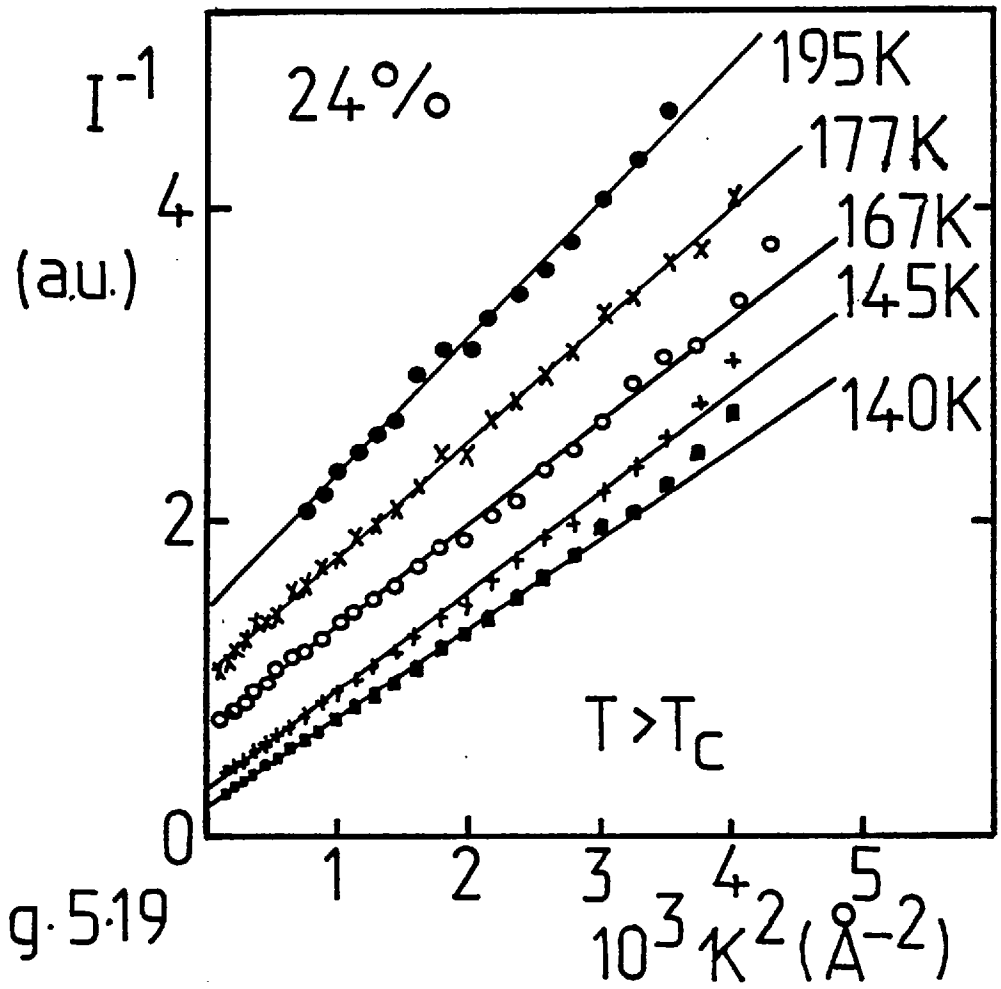

Fig. 5.19

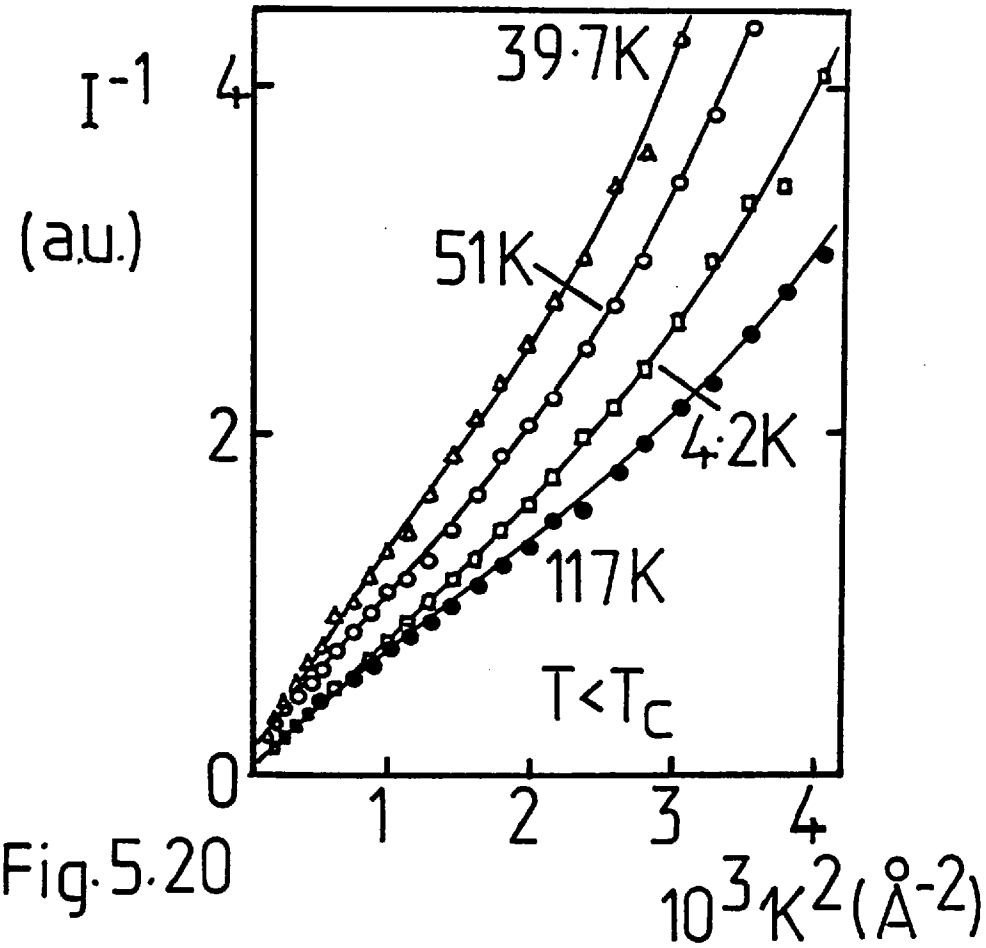

Fig. 5.20

concentrations $C > C_F$, $C \sim C_F$ and $C < C_F$ respectively, at various temperatures. The data follow good straight lines over almost all of the κ range when plotted in this way for $C < C_F$ and $C > C_F$, $T > T_C$, implying a Lorentzian or Ornstein-Zernicke form of $S(\kappa)$. The inverse correlation range κ_1 may be readily estimated by extrapolating the Debye plots to $1/I = 0$.

Lorentzian behaviour is also observed for $C > C_F$, $T < T_C$ at small κ but pronounced deviations occur at higher κ. It is difficult to estimate the inverse correlation range in this case as κ_1 approaches zero. These deviations are seen in all ferromagnetic alloys studied, and also in pure Fe (Fig. 5.6).

These deviations from Lorentzian behaviour are present in all alloys at sufficiently high κ. It is only by virtue of the small κ_1 for ferromagnetic alloys below T_C that the deviations become marked over a significant fraction of the experimental κ range. The value of κ/κ_1 below which Lorentzian behaviour is observed may be estimated by plotting the κ value (κ^*) at which $S(\kappa)$ first deviates from Lorentzian against κ_1. The results for ferromagnetic 25%, 24%, 21.7% and 20.9% Fe alloys are shown in Fig. 5.21. There is considerable scatter in the data due to the difficulty in estimating κ_1, but it appears that the Lorentzian breaks down for κ greater than 3-6 κ_1.

The behaviour of the scattering law at very small κ was also investigated in an attempt to collect data within the Guinier region ($\kappa << \kappa_1$). A series of measurements were carried out using the instrument D11 at the 20m position, allowing data to be collected over the κ range 0.0015-0.010 Å^{-1}. The resultant magnetic scattering at 5 K for three alloys with concentrations $C > C_F$, $C \sim C_F$ and $C < C_F$ is shown in Fig. 5.22. (For comparison, the scattering found at higher κ in the D17 measurements is also shown.) The scattering from these three alloys is Lorentzian over the κ range of the D17 experiments, apart from the large κ upturn discussed above. However, considerable deviation from this Lorentzian behaviour is

Fig.5.21 High κ deviations from Lorentzian scattering law. The estimated κ value at which the scattering law deviates from Lorentzian (κ^X) is plotted as a function of the inverse range parameter (κ_1).

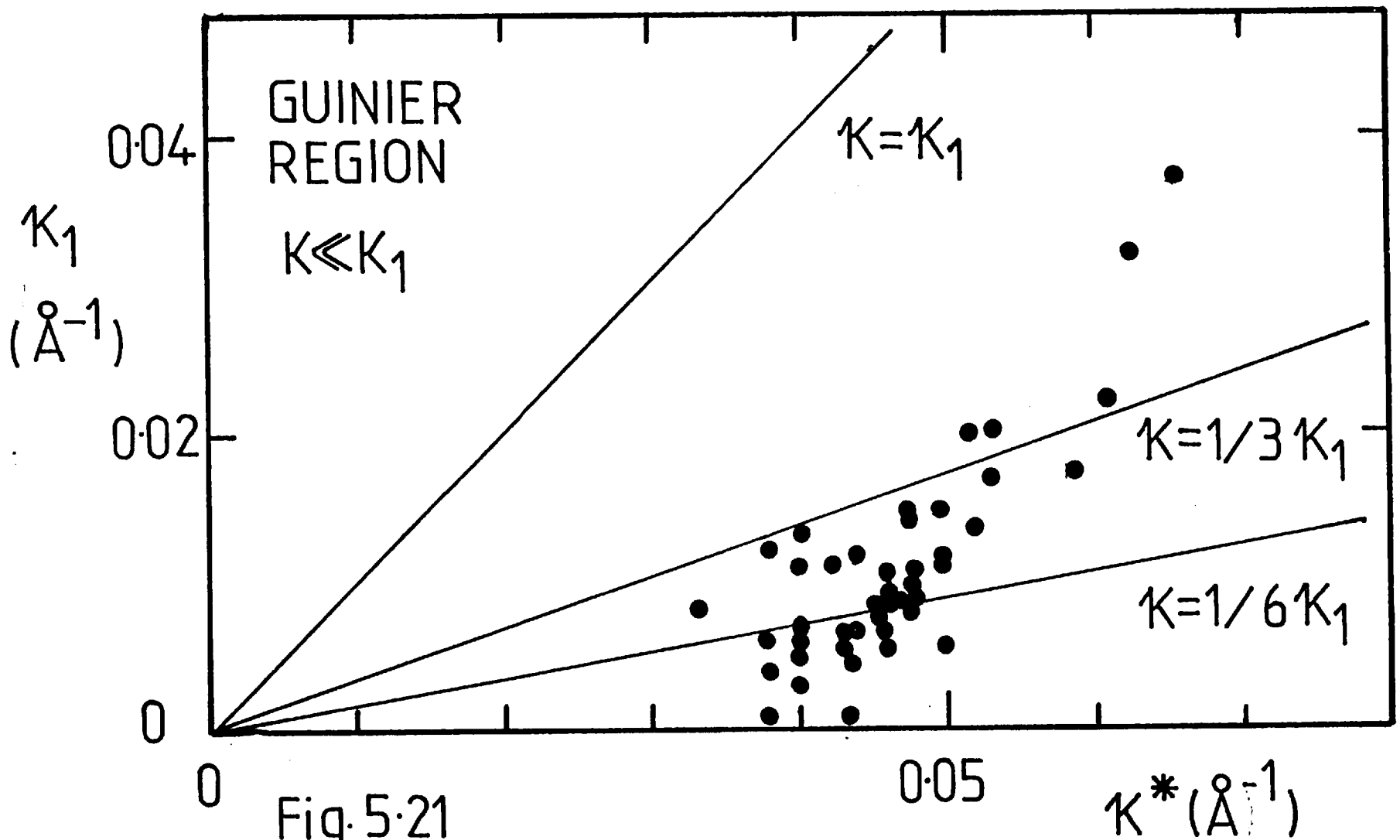

Fig. 5·21

Fig.5.22 Debye plots of the magnetic SAS at very small κ for three alloys, 16.7% ($C < C_F$), 20.8% ($C \gtrsim C_F$) and 24% Fe ($C > C_F$), at 4.2K. The larger κ variation is also shown.

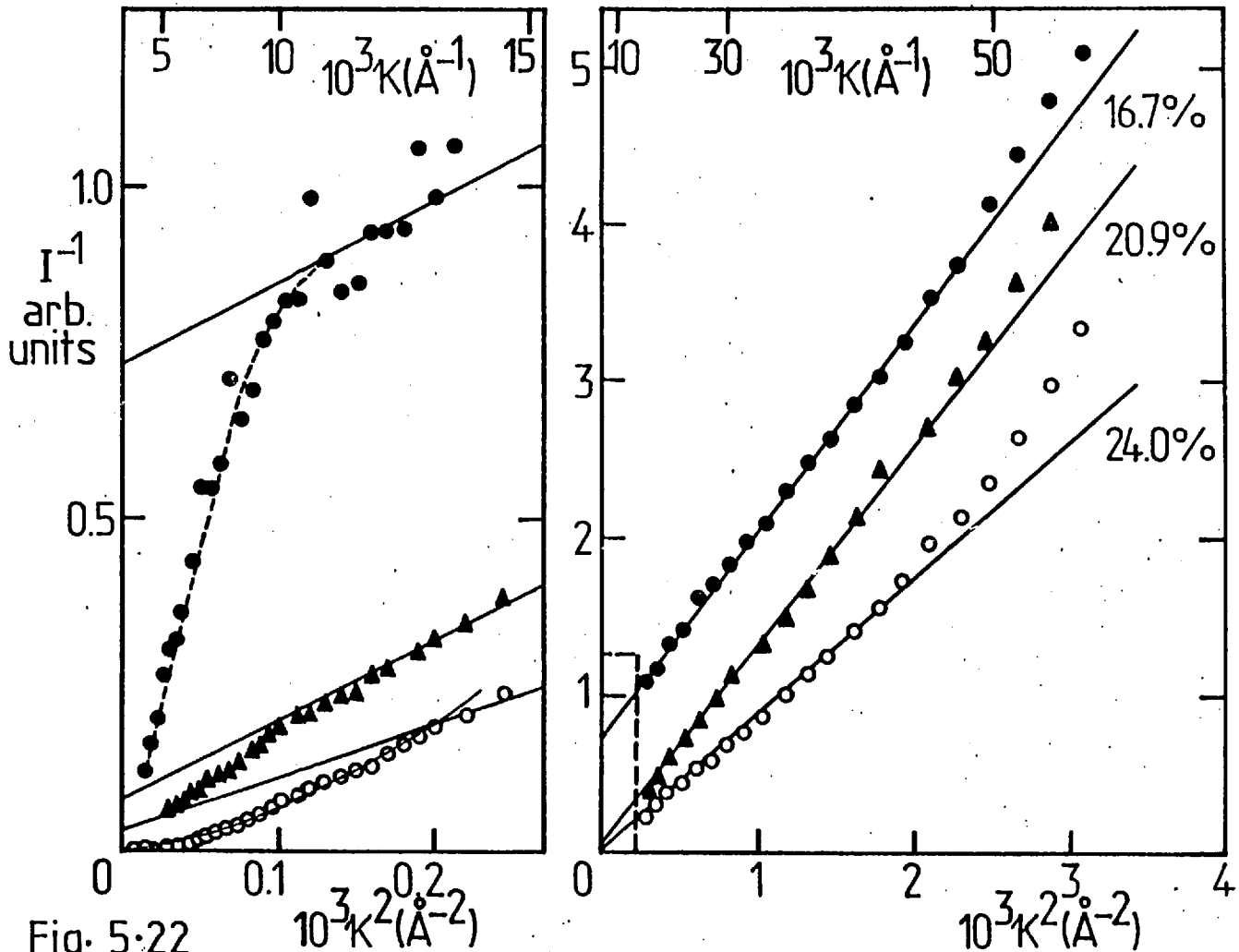
5
10
10^3K(Å^{-1})
15
1.0
I^{-1}
arb.
units
0.5
0
0.1
0.2
10^3K^2(Å^{-2})
10
30
10^3K(Å^{-1})
50
5
4
3
2
1
0
1
2
3
4
10^3K^2(Å^{-2})
16.7%
20.9%
24.0%

Fig. 5·22

Fig.5.23 Guinier plot of the magnetic scattering from Cr Fe 19.9% at 4.2K for incident wavelengths of 9 Å and 14 Å. No well defined Guinier region exists.

Fig.5.24 Debye plots at very low κ, Cr Fe 21.7%

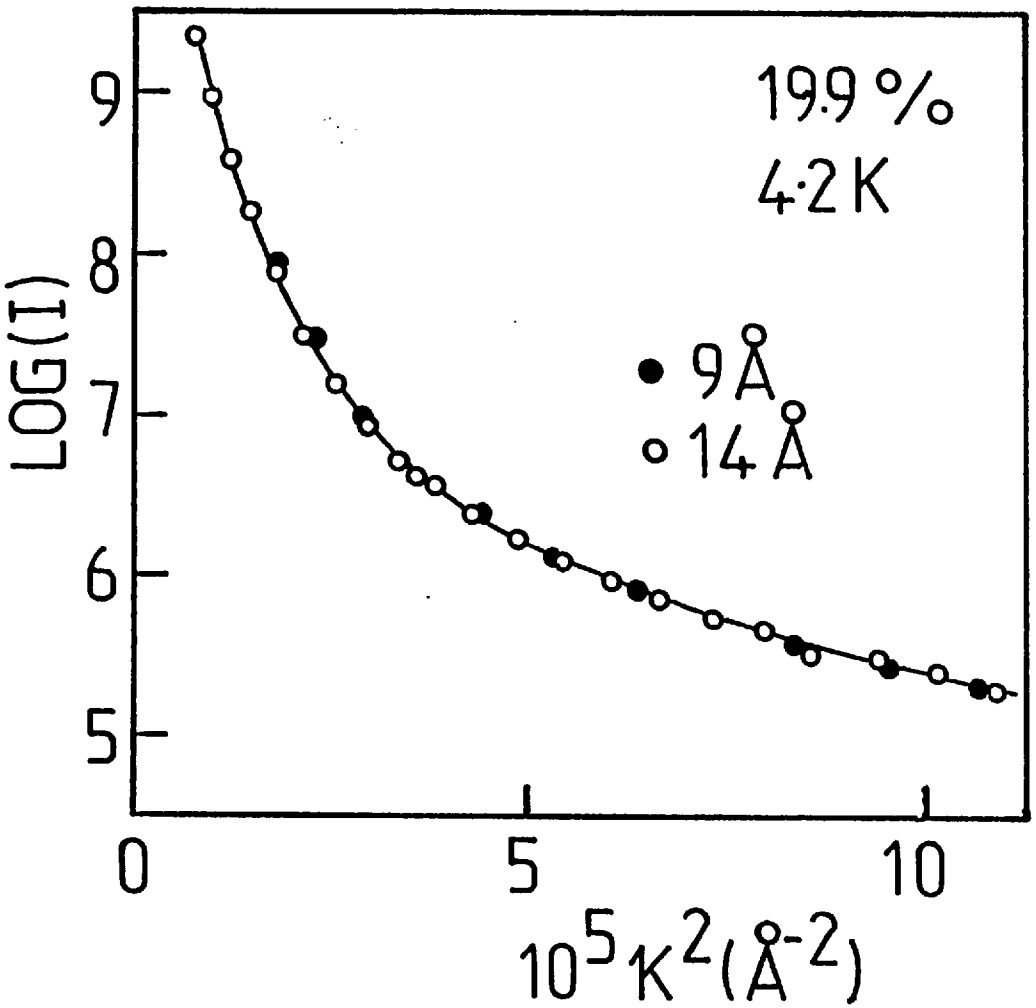

Fig. 5.23

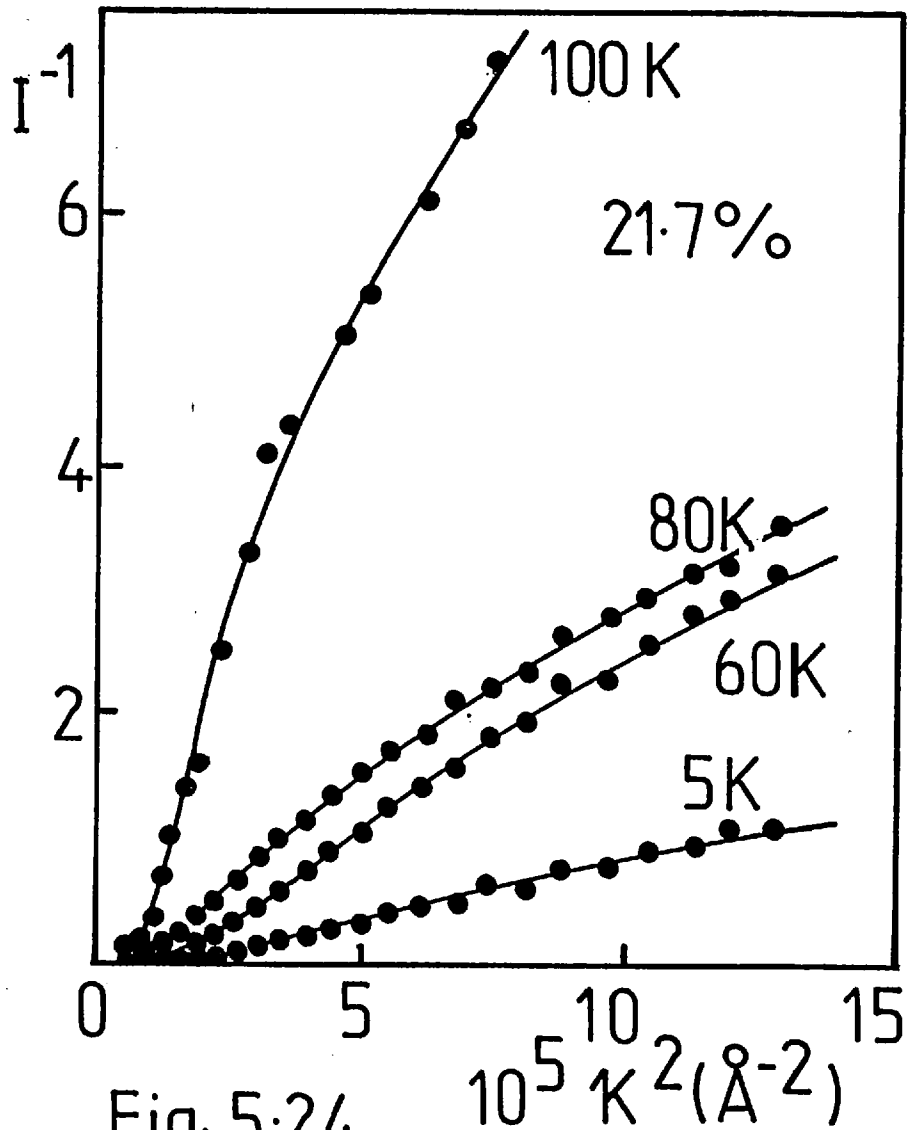

Fig. 5.24

Fig.5.25 Temperature dependence of the SAS at very low κ . Radially averaged intensity is shown for constant κ values of 13.7×10^{-3} $\mathring{A}^{-1}$, 8×10^{-3} $\mathring{A}^{-1}$, $4 \times 10^{-3}\mathring{A}^{-1}$ and $3.5 \times 10^{-3}\mathring{A}^{-1}$. The Curie temperature is shown by an arrow.

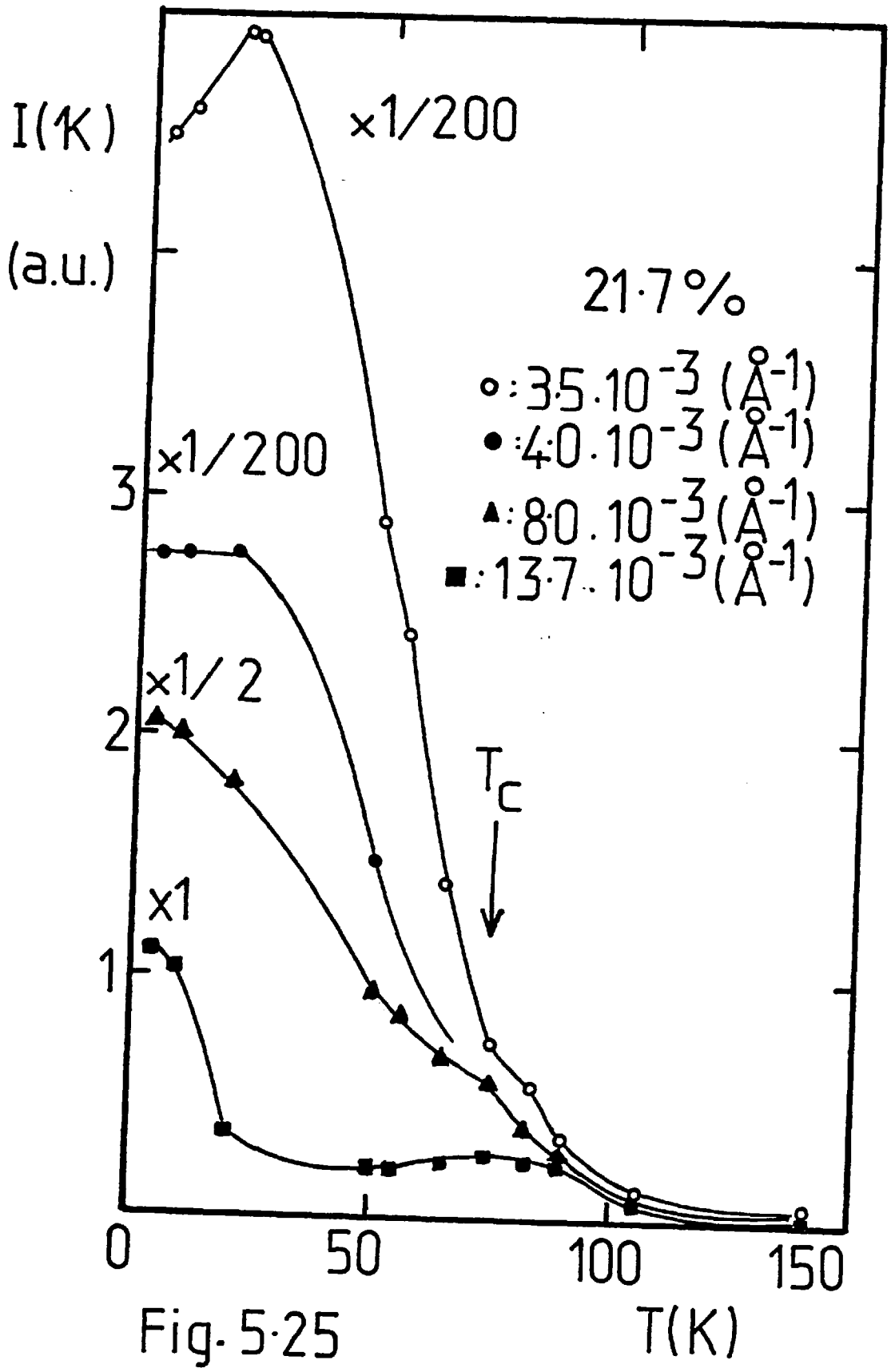
I(K)
(a.u.)
×1/200
21·7%
○ : 3·5 . 10⁻³ (Å⁻¹)
● : 4·0 . 10⁻³ (Å⁻¹)
▲ : 8·0 . 10⁻³ (Å⁻¹)
■ : 13·7 . 10⁻³ (Å⁻¹)
×1/200
×1/2
×1
T_C
3
2
1
0
50
100
150
T(K)

Fig. 5·25

apparent at the very small κ values obtained using D11 (20m). The scattering from the 24% Fe ferromagnetic alloy ($C > C_F$) appears to vary as κ^{-4} in this region, shown by the fitted curve through the data. Small deviations are also seen in the 16.7% Fe alloy ($C < C_F$) and the 20.9% alloy ($C \sim C_F$). No well defined Guinier region can be established in these alloys at very low κ. This is illustrated by the Guinier plot (lnI vs κ^2) for a 19.9% Fe alloy at 4.2K which is curved over the entire κ range. (Fig. 5.23).

The temperature dependence of the SAS at very small κ was followed in detail for the ferromagnetic 21.7% Fe alloy. Debye plots of the SAS at several temperatures are shown in Fig. 5.24. Deviations from Lorentzian behaviour are apparent even above T_C and become larger as the temperature is reduced. The temperature dependence of the SAS intensity at a given κ is very sensitive to the value of κ in this κ range. At "large" κ (0.014Å^{-1}) the temperature dependence of $I(\kappa)$ is similar to that seen in the D17 measurements; a fairly broad critical scattering peak at T_c and the development of 'subcritical' scattering as the temperature is reduced below T_c. However, as κ is successively reduced, the subcritical SAS increases dramatically, swamping the ferromagnetic critical scattering. Moreover, a well defined peak in the subcritical develops in the vicinity of 20K. These observations are shown in Fig. 5.25.

The possibility that the deviations at very low κ were due to the broadening of the incident beam by multiple refraction was examined by performing measurements at two different wavelengths. (The refractive index depends on λ^2 and thus any multiple refraction would be more pronounced at longer wavelengths). The results of measurements at very low κ for a 19.9% Fe alloy at 4.2K using an incident wavelength of 9.0Å and 14Å are shown in Fig.5.23. As the results are identical to within experimental error, multiple refraction can be ruled out. This result also dismisses the possibility of large multiple SAS. (The multiple scattering depends on the ratio of the scattering to absorption cross sections and the absorption cross

section varies approximately as $1/\lambda$ in this region. As no change in the SAS is observed on changing the absorption cross section, any multiple SAS must be negligible.)

5.5.2.3 Discussion

No obvious analytical form for the scattering law capable of describing the SAS over the entire experimental κ range is suggested by the present data. The scattering from Cr Fe alloys is Lorentzian over almost a decade of κ but shows significant deviations both at very low κ ($\kappa < 0.01\text{Å}^{-1}$) and high κ ($\kappa \gtrsim 3\kappa_1 - 6\kappa_1$).

The deviation from a Lorentzian scattering law for $\kappa \gtrsim 3\kappa_1 - 6\kappa_1$ has been noted in many small angle scattering studies of binary alloys and is also seen in pure Fe (section 5.2.1). This deviation has been attributed to higher order terms normally neglected in the series expansion used to derive the Lorentzian scattering law. At high κ terms in κ^4, κ^6 etc. become increasingly important leading to a deviation from Lorentzian line shape. Inclusion of a term in κ^4 leads to an improved fit at high κ (shown in Fig. 5.26 for Cr Fe 24% at 4.2K). An alternative explanation for the high κ deviation may be that the Fisher-Burford form of the cross section (eq. 5.7e) is followed. To test this hypothesis the scattering law for Cr Fe 24% at various temperatures has been plotted against $\kappa^2 + \kappa_1^2$ (with κ_1 derived from the initial Lorentzian part of the cross section) on a log-log scale in Fig. 5.27. A good fit to the data at all temperatures is found with $\eta = -.22 \pm 0.02$ below T_c and $\eta = 0.00 \pm .02$ above T_c. The negative value for η is somewhat surprising but is also encountered in the analysis of section 5.5.3. This analysis of section 5.5.3 returns $\eta = 0.00 \pm 0.05$ for the 24% alloy below T_c in disagreement with the above value. This lack of consistency suggests that the former explanation is more likely.

A number of alternative forms for the scattering law in this κ range have been proposed. Cywinski et al (1977) suggest that a squared Lorentzian should be used for the SAS in ferromagnetic

alloys below T_c whereas Gray (1978) proposes an exponential dependence exp $(-A\kappa)$. Power laws of the form κ^a where a is an undetermined constant have also been considered (Boucher et al (1979)). None of these expressions lead to a significantly better fit to the experimental data (shown in Fig. 5.26). The latter two expressions are unphysical as $\kappa \to 0$ in that they do not reduce to a Guinier quadratic form. The squared Lorentzian fits the data well at high κ but fails at smaller κ. As the squared Lorentzian includes a term in κ^4 the improvement at larger κ is to be expected.

The deviation from Lorentzian behaviour at very low κ is an interesting and unexpected result. A similar observation has been reported by Murani (1976) for Au Fe alloys. It is possible that this effect is due to dipole-dipole interactions. Some support for this speculation may be drawn from the theoretical work of Maleev (1974) and Aharony and Fisher (1973). Maleev (1974) has examined the effect of dipole-dipole interactions on the critical dynamics of pure ferromagnets above T_c. For wavevectors greater than $q_o = 1/a\ (T_D/T_c)^{\frac{1}{2}}$ where $kT_D = 4\pi g\ \mu_B\ M_{sat}$ is the characteristic energy of dipole-dipole interactions the correlation functions reduce to the conventional forms obtained if dipole forces are neglected. However at low κ, $\kappa << q_o$ the presence of long range dipolar forces changes the form of the correlation functions and new phenomena are found. In this régime Aharony and Fisher (1973) find deviations from Lorentzian cross-sections. Arrott, Heinrich and Noakes (1972) have also speculated that dipolar interactions tend to enhance $S(\kappa)$ at low κ.

A full analysis of the concentration and temperature dependence of these effects will not be attempted. It is interesting to note that the conjectured dipolar contribution increases with increasing Fe concentration as may be expected and, that substituting typical values of T_c and M_{sat} for ferromagnetic Cr Fe alloys yields $q_o \sim 10^{-2}$ $Å^{-1}$ giving order of magnitude agreement with the κ values for which deviations are observed.

Fig.5.26 Magnetic scattering from Cr Fe 24% at 4.2K. The data are plotted in a number of ways to illustrate possible (a) Lorentzian with additional κ^4 terms (b) squared Lorentzian (c) Power law and (d) exponential forms of the scattering law.

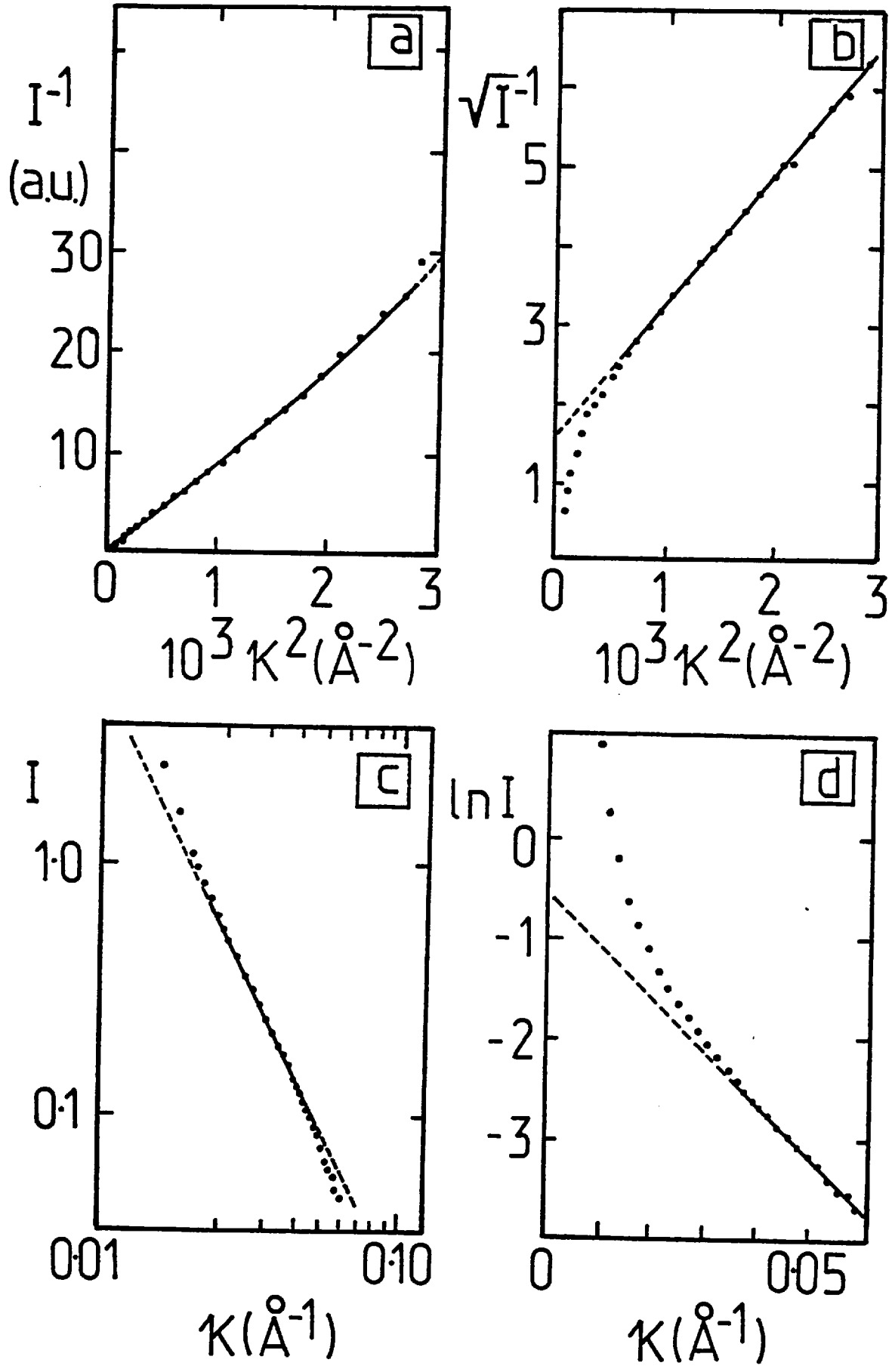
a
I^{-1}
(a.u.)
30
20
10
0
1
2
3
$10^3 K^2 (Å^{-2})$
b
$\sqrt{I}^{-1}$
5
3
1
0
1
2
3
$10^3 K^2 (Å^{-2})$
c
I
1·0
0·1
0·01
0·10
$K (Å^{-1})$
d
ln I
0
-1
-2
-3
0
0·05
$K (Å^{-1})$

Fig. 5·26

Fig.5.27 Magnetic scattering from Cr Fe 24% at various temperatures above and below T_c. Data are plotted according to the Fisher and Burford form of the cross section (eq.5.7e) with κ_1 determined from a Lorentzian fit.

Fig.5.28 Typical time of flight spectrum for Cr Fe 17.5%. The elastic energy resolution is indicated. Inset: A possible broad quasielastic signal which would be difficult to detect in these measurements is shown schematically.

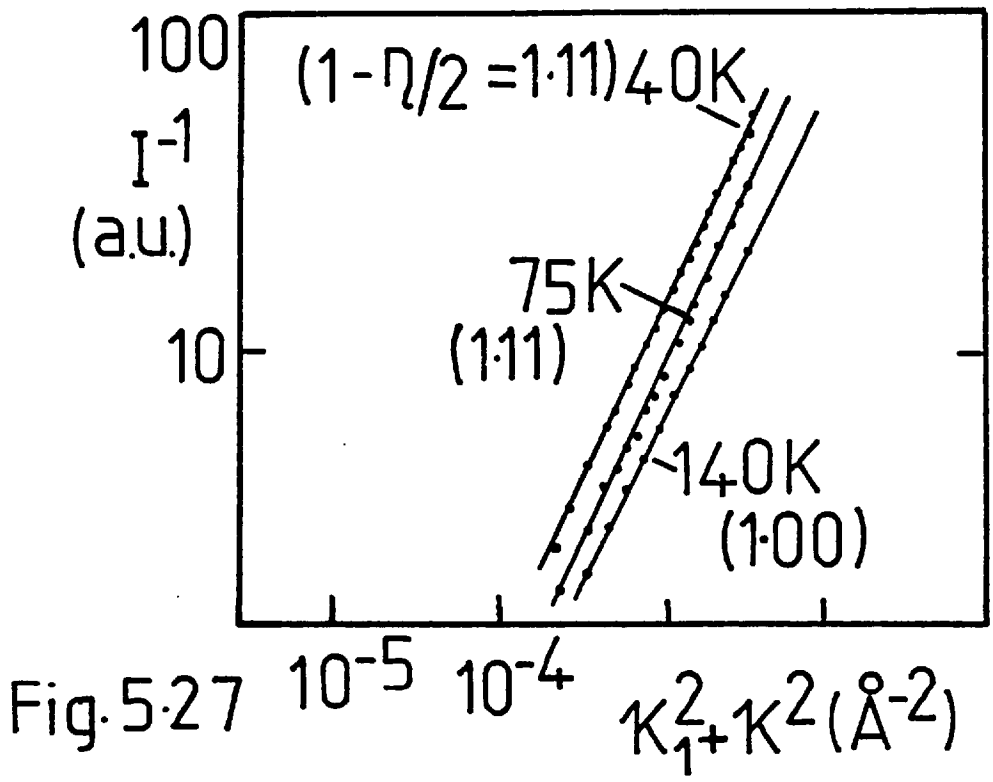

Fig. 5·27

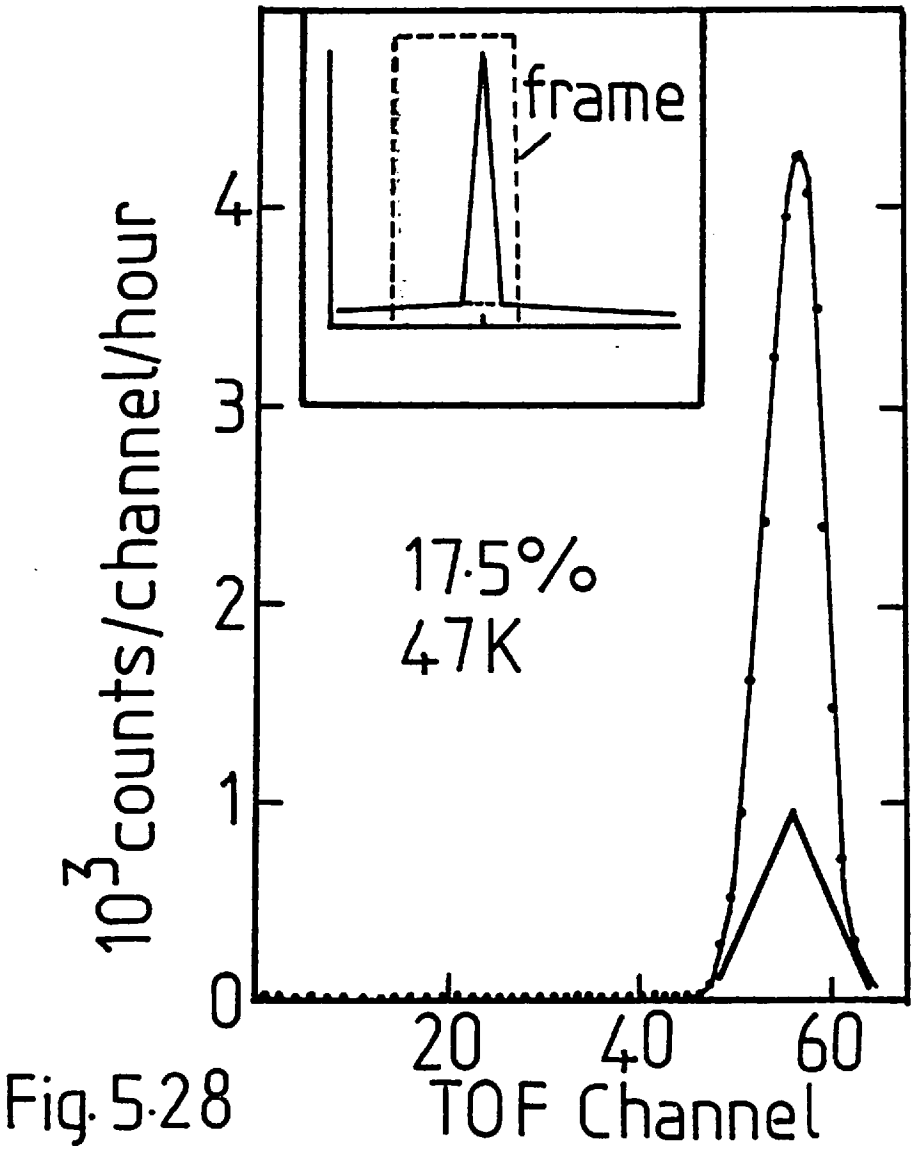

Fig. 5·28

Deviations aside, the fact that the scattering is Lorentzian over almost a decade in κ is in itself a significant result, considering the lack of theoretical predictions in this area.

5.5.3 Test of the quasistatic approximation

5.5.3.1 Results

The validity of the quasistatic approximation which relates the integrated quasielastic scattering cross section to the isothermal wavevector dependent susceptibility (section 2.2.4) was tested by performing a series of small angle time-of-flight experiments using the instrument D17 at ILL, Grenoble. The experimental details and measurement procedure are described in section 3.3.3.4.

TOF spectra were collected at several temperatures between 2K and 120K for two alloys, 17.5% ($C < C_F$) and 19.5% Fe ($C > C_F$). (The total scattering from these alloys had been measured previously using D11 (5m)). No quasielastic component to the scattering could be detected, i.e. the scattering from both alloys at all temperatures lay within the instrumental resolution of 80 μeV FWHM. A typical spectrum is shown in Fig. 5.28.

To test whether this scattering was superimposed on a much broader quasielastic signal which would be difficult to detect in the present measurements (shown schematically in Fig. 5.28), the integrated intensity within an $\pm$ 80 μeV window centred on the elastic time of flight channel was compared with the total scattering intensity observed without TOF in the previous measurements on these alloys. The results of this comparison are shown in Table 5.2 for three different κ values.

Table 5.2

Comparison of total scattering intensity from D11 (5m) experiments and integrated intensity within a ± 80μeV window from D17 TOF experiments

17.5% alloy

T (K)	κ = 0.024 Å^{-1}			κ = 0.032 Å^{-1}			κ = 0.040 Å^{-1}		
	D17	D11	Ratio	D17	D11	Ratio	D17	D11	Ratio
2	240	554	0.43	169	336	0.50	110	225	0.49
8	235	554	0.42	163	330	0.49	104	223	0.47
16	221	521	0.42	151	307	0.49	98	207	0.48
22	206	457	0.45	142	272	0.52	89	186	0.48
47	86	195	0.44	66	130	0.51	46	98	0.47
100	49	83	0.59	31	52	0.60	21	41	0.52

19.5% alloy

T (K)	κ = 0.024 Å^{-1}			κ = 0.032 Å^{-1}			κ = 0.040 Å^{-1}		
	D17	D11	Ratio	D17	D11	Ratio	D17	D11	Ratio
10	505	1011	0.50	341	599	0.57	179	352	0.51
42	221	450	0.49	160	285	0.56	104	200	0.52
50	204	415	0.49	143	266	0.54	97	189	0.51
60	157	331	0.47	118	226	0.52	84	167	0.50
75	84	181	0.56	53	98	0.54	45	82	0.55
90	69	123	0.56	53	98	0.54	45	82	0.55
120	31	57	0.54	23	49	0.47	19	44	0.44

The scaling between the total scattering and the scattering which lay within the TOF elastic energy resolution indicates that any such broad component to the scattering is insignificant.

The κ dependence of the SAS which lay within a ± 80 μeV window

centred on the elastic time of flight was investigated for the 17.5% alloy. The κ dependence is Lorentzian, shown in Fig. 5.29. The forward scattering and inverse range parameters were determined at various temperatures and are compared with the fits to the D11 total scattering measurements in Table 5.3.

Table 5.3

Comparison of forward scattering and inverse range parameters for D11 total scattering measurements and D17 TOF measurements

17.5% alloy

T(K)	I(0)			κ_1 ($\AA^{-1}$)	
	D17	D11	Ratio	D11	D17
2	810	2015	0.40±0.13	0.013	0.025
8	910	2124	0.42±0.12	0.013	0.023
16	1020	2278	0.44±0.10	0.012	0.020
22	1220	1767	0.69±0.10	0.013	0.017
47	145	270	0.54±0.06	0.029	0.037
100	32	61	0.52±0.06	0.054	0.047

The forward scattering in both cases scale with each other to within experimental error but there is some inconsistency in the κ_1 values. This may be due to the difference in κ resolution and residual nuclear scattering which was not subtracted from the TOF data.

These measurements demonstrate that the small angle magnetic scattering has an energy width less than 80 μeV at temperatures between 2K and 120K in the κ range 0.01-0.06 $\AA^{-1}$. To satisfy the quasistatic approximation, two requirements must be met. Firstly, the inelasticity of the scattering must be small with respect to the incident energy so that a total scattering measurement effectively

Fig.5.29 Debye plots of the scattering lying within the elastic window for Cr Fe 17.5% at various temperatures.

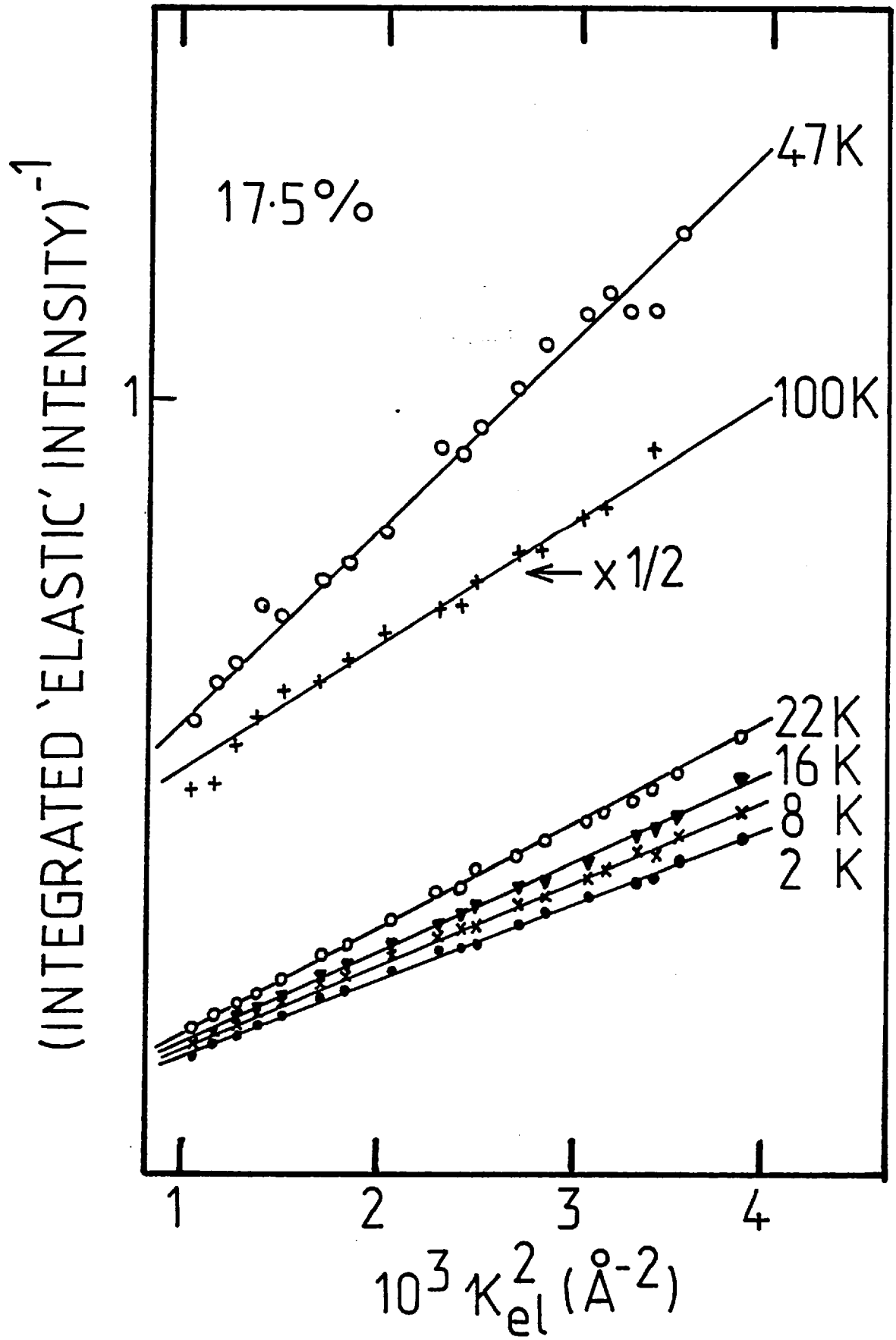
(INTEGRATED 'ELASTIC' INTENSITY)$^{-1}$
17·5%
47K
100K
x 1/2
22K
16K
8 K
2 K
1
1
2
3
4
$10^3 K_{el}^2$ (Å^{-2})

Fig·5·29

integrates over all energies of interest, This criterion is satisfied both by the D17 and D11 experiments, having incident energies of 620 μeV and 1730 μeV respectively. The second requirement is that the inelasticity of the scattering is small compared to the temperature, so that the detailed balance factor is effectively unity. This criterion is also satisfied over the temperature range of these measurements 2K - 250K (200 μeV - 20μeV). It should be stressed that the inelasticity of 80 μeV is an upper limit and may be expected to decrease with temperature. Thus the quasistatic approximation would appear to be valid for the present series of experiments.

Independent confirmation of this assertion may be drawn from the data of Fig. 5.23. The magnetic scattering cross section is unchanged on decreasing the incident energy by a factor of two, from 9Å (1meV) to 14 Å (420 μeV).

5.5.3.2 Comparison with bulk susceptibility

If the quasistatic approximation is valid, the total magnetic SAS cross section is proportional to the Fourier transform of the instantaneous spin-spin correlation function. As discussed in section 2.2.4, this correlation function is made up of average and fluctuating parts. The average part gives elastic scattering and the fluctuating part is related to the susceptibility $\chi(\kappa)$. Making this separation, the SAS intensity as $\kappa \to 0$ may be written,

$$I(\kappa \to 0) = I_{el}(0) + \text{const } T\ \chi(0) \qquad (5.27)$$

where $\chi(0)$ is the bulk susceptibility, T the absolute temperature and $I_{el}(0)$ an elastic scattering contribution. Thus in the absence of elastic scattering the neutron forward cross section is proportional to $T\ \chi(0)$.

$\chi(0)$ was estimated from the neutron SAS data for two alloys (17.5% and 19.5%) by extrapolation of the Lorentzian SAS cross section to $\kappa = 0$. The forward scattering obtained in this way was divided by the absolute temperature and normalized to the experimentally determined bulk susceptibility at one temperature (T = 35K). This normalization was necessary as absolute cross sections were not measured. The resulting $\chi(0)$ is compared to the bulk susceptibility for the same samples (section 5.3 and 5.4) in Fig. 5.30.

The agreement between the susceptibilities determined from the neutron SAS and the bulk AC and low field 'DC' measurements for the 17.5% 'cluster spin glass' alloy above the susceptibility peak temperature is excellent. Poorer agreement is found for the ferromagnetic 19.5% alloy in this temperature range. At lower temperatures a large discrepancy between the two techniques is apparent: the neutron derived $\chi(0)$ continues to increase rapidly whilst the bulk $\chi(0)$ shows a sharp decrease.

5.5.3.3. Discussion

The agreement between the neutron SAS derived susceptibility and the bulk values above T $\sim$ 25K is a valuable check on the measurement techniques and the validity of the quasistatic approximation. The two orders of magnitude discrepancy between the neutron scattering and bulk susceptibility data at low temperature indicates a fundamental failure in one of the methods of susceptibility determination in this regime.

One explanation for this discrepancy is to postulate the development of elastic scattering below 25K. According to (eq.5.27) such an elastic component would lead to an overestimate of the susceptibility. This view has been put forward by Murani (1976). An alternative explanation is to assume that no elastic scattering is present and that the discrepancy lies on the side of the bulk measurements; the bulk susceptibility being artificially reduced by measuring time considerations along the lines of fine particle theory (section 5.1.3.3). As it is not possible to separate any elastic

Fig.5.30 Comparison between the bulk AC susceptibility, low field susceptibility (DC) and susceptibility derived from the small angle scattering measurements using the quasistatic approximation (SAS) for Cr Fe 17.5% and Cr Fe 19.5% alloys. T_c is shown by an arrow.

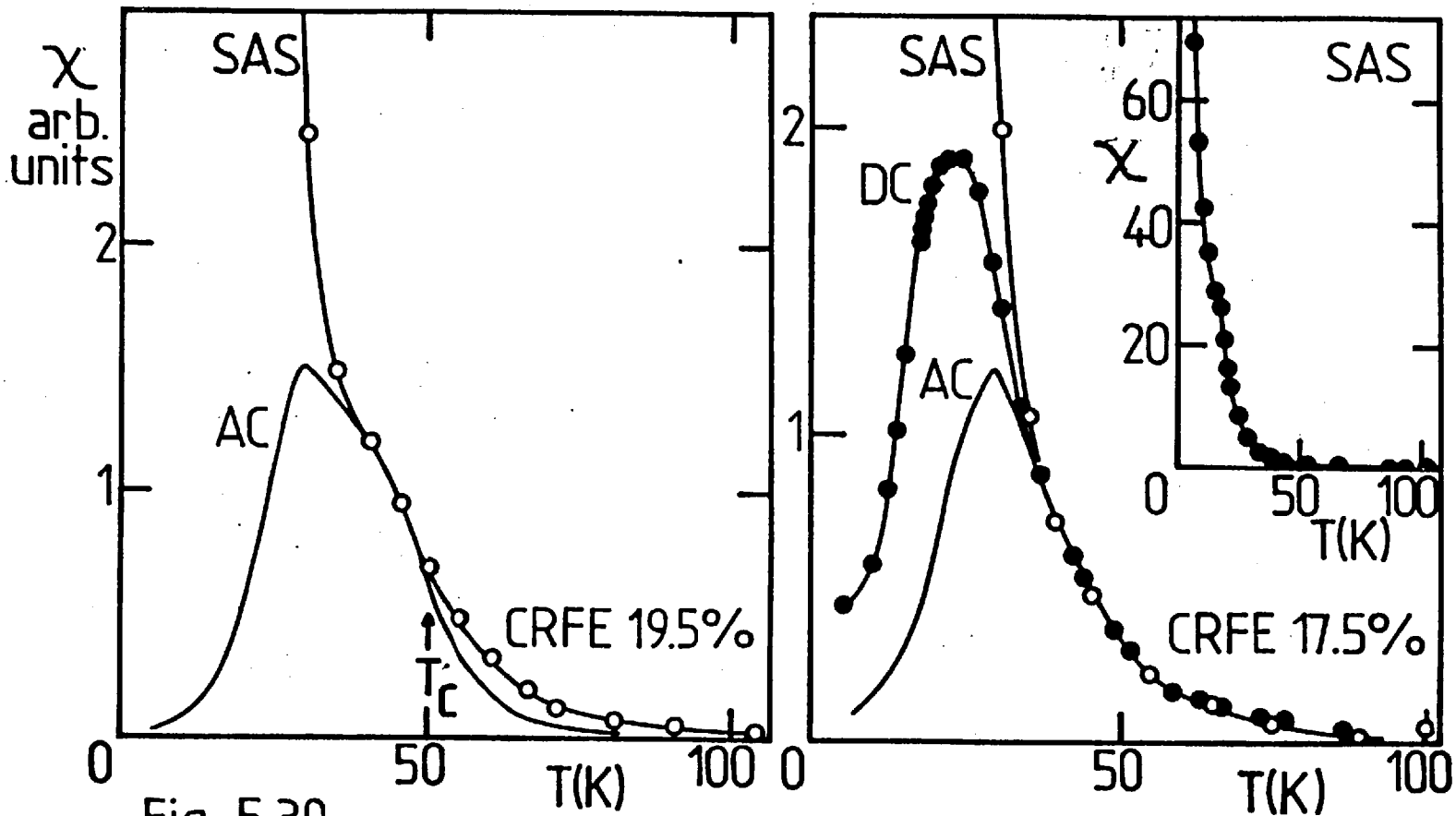
χ
arb.
units
SAS
AC
CRFE 19.5%
T_C
0
50
100
T(K)
2
1
SAS
DC
AC
CRFE 17.5%
SAS
χ
60
40
20
0
50
100
T(K)

Fig. 5·30

component of the SAS experimentally, it is very difficult to distinguish between these two possible explanations.

It should be noted that at low temperatures the deviations from Lorentzian cross-section at very low κ become increasingly more important, leading to higher I(0) than expected from a Lorentzian extrapolation. A larger difference between bulk and neutron derived χ would occur if the very low κ data were extrapolated. It should also be stressed that the lack of consistency between the two techniques at low temperature does not imply a breakdown of the quasistatic approximation. The SAS cross section remains proportional to the Fourier transform of the instantaneous spin-spin correlation function. The difficulty arises in the break down of the correlation function into its constituent parts.

5.5.4 Magnetic correlations below C_F

5.5.4.1 Introduction

Having established the validity of the quasistatic approximation the magnetic SAS may be analysed to yield the strength and range of magnetic correlations as a function of concentration and temperature in the vicinity of C_F. To do this, the D11 (5m) and D17 SAS data are fitted to a Lorentzian scattering law of the form

$$I(\kappa) = A/(\kappa_1^2 + \kappa^2)$$

allowing the inverse correlation range κ_1 and the 'scattering amplitude' A to be extracted. The deviations from a Lorentzian $I(\kappa)$ at very small κ are insignificant over the κ range of these particular measurements, although the fact that the cross section deviates from Lorentzian between the lowest κ of these measurements and $\kappa = 0$ should be borne in mind. Alloys with concentrations less than C_F will be considered first.

5.5.4.2. Results

The inverse range parameters obtained from least squares fits to the magnetic SAS for five alloys with concentrations less than C_F (15.5%, 16.7%, 16.8%, 17.5% and 18.5% Fe respectively) are shown as a function of temperature in Fig. 5.31. The parameters are expressed in dimensionless units $\kappa_1 a_{nn}$ where a_{nn} is the nearest neighbour distance (2.48 Å). The inverse range parameters for these alloys appear to follow essentially the same curve which is offset along the κ_1 axis by various amounts depending on the concentration. The approximate superposition of these five curves is demonstrated in Fig. 5.32.

This superposition implies that $\kappa_1(C, T)$ may be expressed as the sum of a purely concentration dependent part, $\kappa_G(C)$, and a purely temperature dependent part $\kappa_T(T)$,

$$\kappa_1(C,T) = \kappa_G(C) + \kappa_T(T) \qquad (5.28)$$

The concentration dependent part, $\kappa_G(C)$, for each alloy was chosen to be the minimum value of $\kappa_1(C,T)$. The concentration dependence of κ_G is shown in Fig. 5.33. κ_G decreases monotonically with increasing concentration and tends to zero at C_F = 19%. The temperature dependent part $\kappa_T(T)$ is approximately linear in temperature above $\sim$ 20K but shows a shallow minimum at low temperature.

The Lorentzian scattering amplitude A obtained from least squares fits to the magnetic SAS is shown in Fig. 5.34 for the same alloys as a function of temperature. This quantity is expressed in arbitrary units which differ only by a constant multiplicative factor from the absolute units mb/sr/at/Å^{-2}. The curves have been offset for clarity. A decreases smoothly as the temperature is increased and shows no anomalous behaviour in the vicinity of the minimum in κ_1.

Fig.5.31 Inverse range parameters ($\kappa_1 a_{nn}$) as a function of temperature for alloys below the critical concentration. The data have been offset from each other for clarity. Solid lines are a guide to the eye.

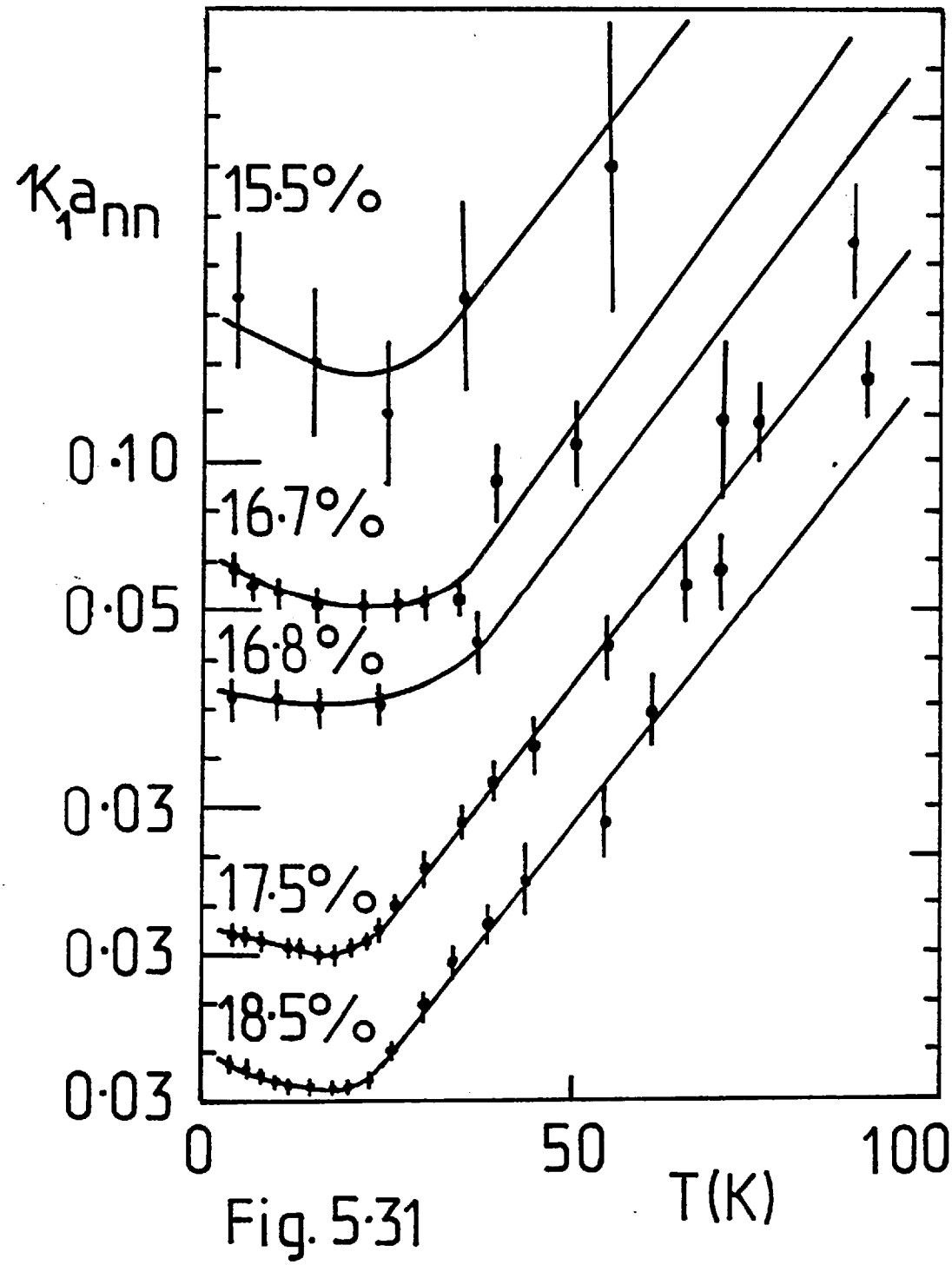

Fig. 5·31

Fig.5.32 Superposition of the inverse correlation range - temperature characteristic for alloys below C_F.

Fig.5.33 Concentration dependence of the geometrical inverse correlation range.

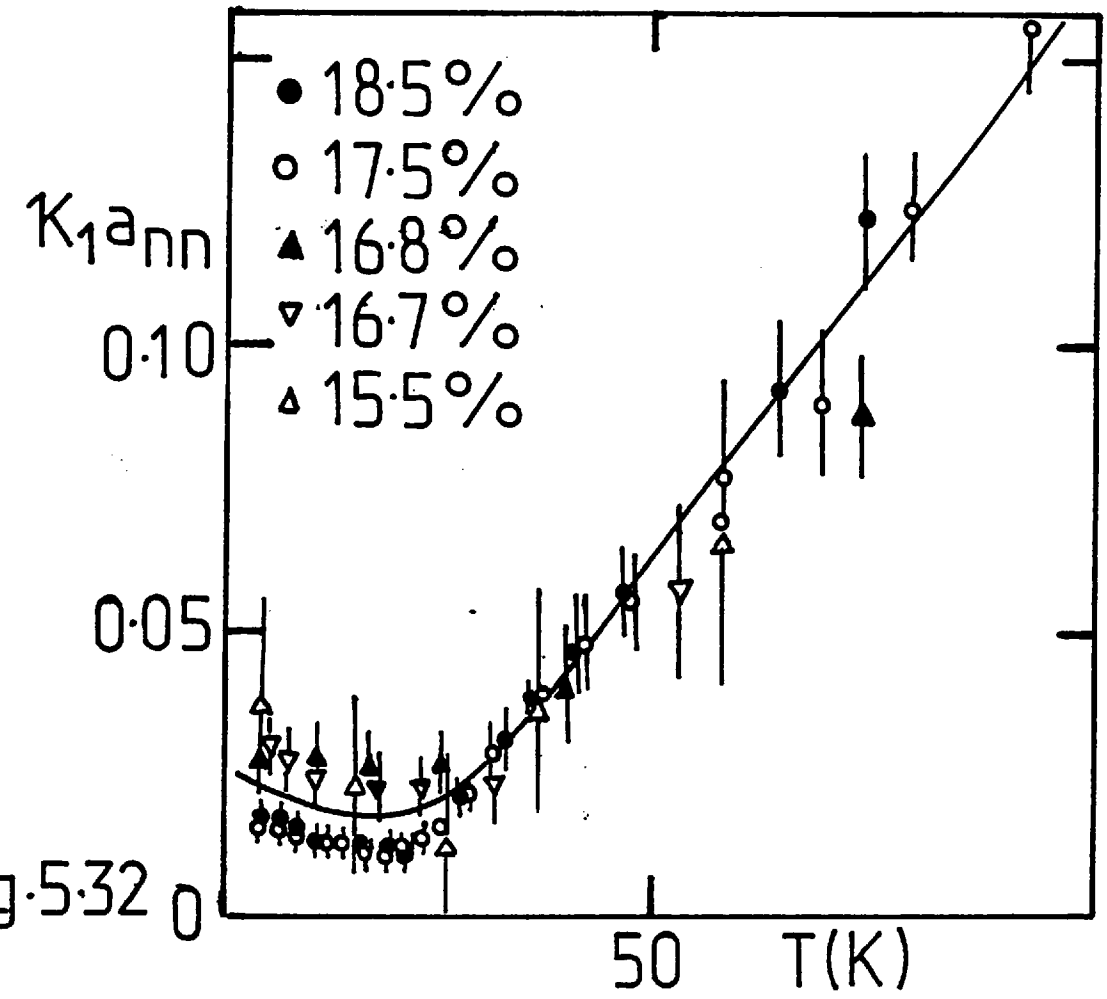

Fig·5·32

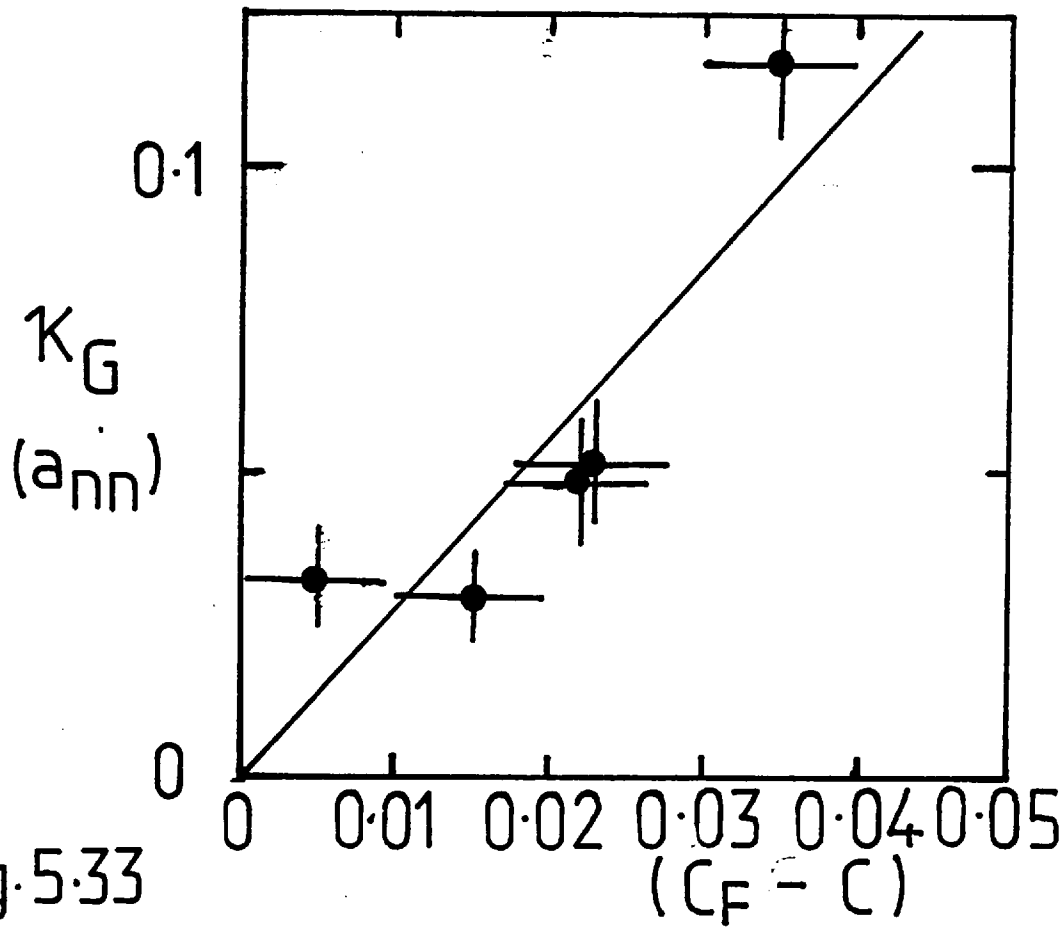

Fig·5·33

Fig.5.34 Temperature dependence of the Lorentzian scattering amplitude (A) for $C < C_F$. The curves have been offset for clarity. The dotted lines through the data for the 18.5% and 17.5% alloys are best fits according to (eq.5.31).

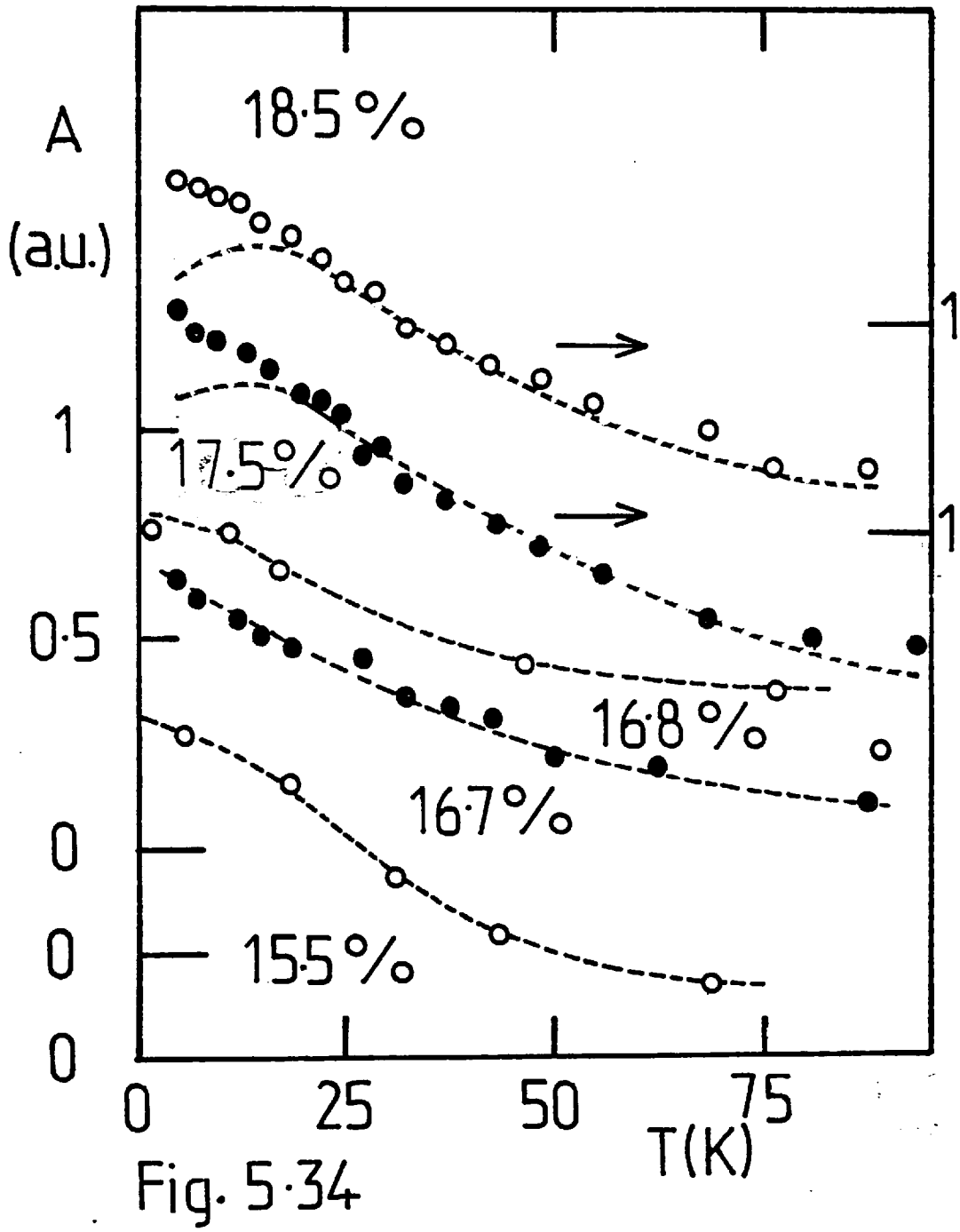

Fig. 5·34

Fig.5.35 Extrapolated forward scattering as a function of temperature for $C < C_F$. Data have been offset from each other in the interests of clarity.

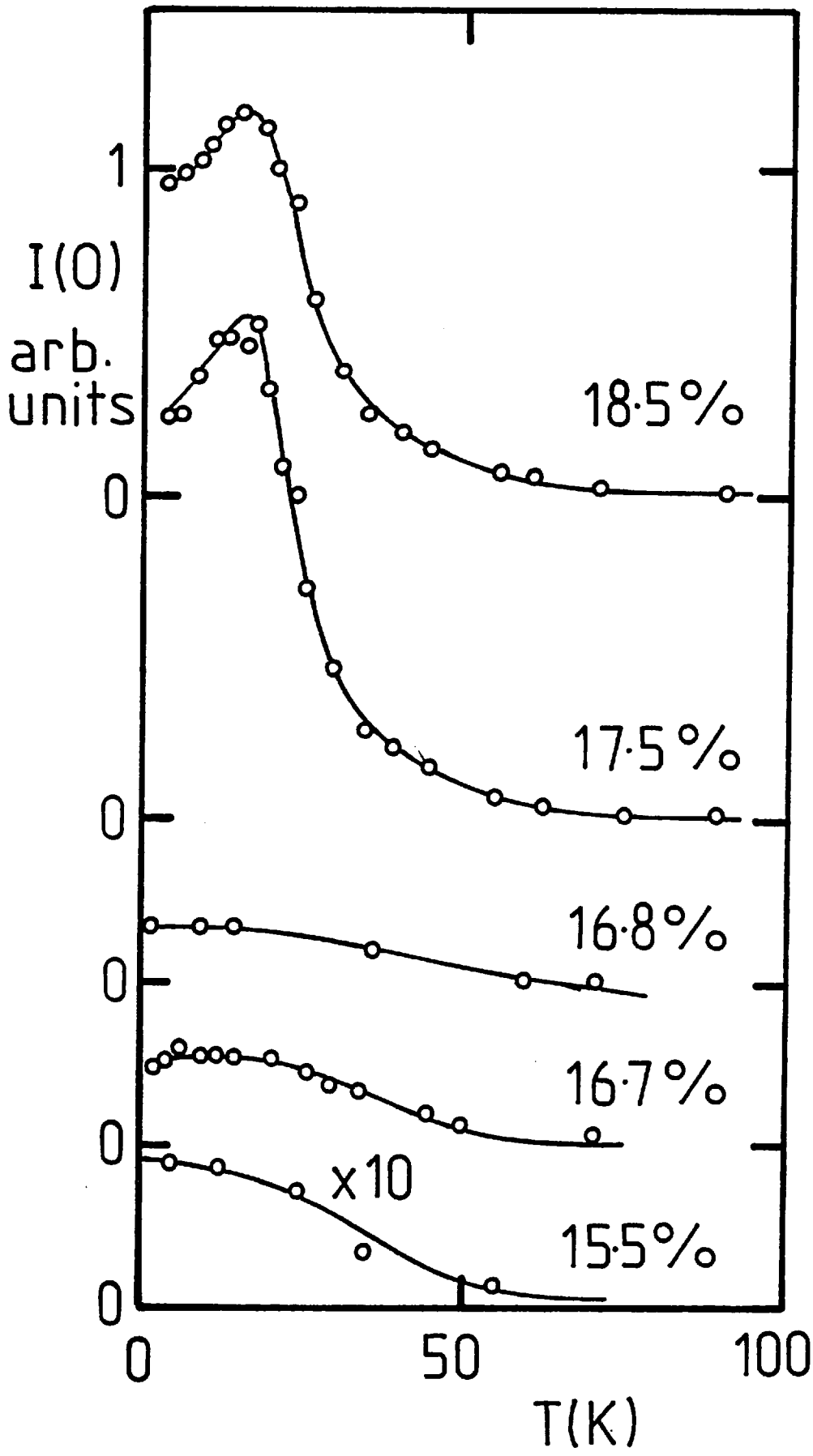

Fig. 5.35

The forward scattering I(0) has also been calculated and is shown as a function of temperature in Fig. 5.35. The curves have been offset for clarity. I(0) calculated in this way displays a well defined maximum for all alloys in the vicinity of 15K.

5.5.4.3 Analysis and Discussion

These results show many features in common with the percolative insulating antiferromagnets discussed in section 5.1.4.1 and suggest that the evolution of magnetic order in Cr Fe alloys may be analysed along the lines adopted by Birgeneau et al (1980) for systems close to a percolation multicritical point. This analysis can, at most, be semiquantitative as the exact form of the temperature variable g(T) appropriate for Cr Fe alloys is unknown.

The superposition of the inverse correlation range - temperature characteristics for percolating systems has been discussed in section 5.1.2.3 and 5.1.4.1. The fact that such a superposition is observed for Cr Fe alloys below C_F is an important result and strongly suggests that geometrical factors are involved in the evolution toward long range order. This is well illustrated by the concentration dependence of the 'geometrical' inverse correlation length, $\kappa_G(C)$, which tends to zero at the critical concentration of 19%: consistent with the growth of geometrical clusters of Fe atoms with increasing concentration until an infinite cluster is formed at C_F. It is worthwhile pointing out that the extrapolation of $\kappa_G(C)$ to zero at 19% provides an independent check on C_F, which was initially placed at 19% by measurements along the ferromagnetic phase boundary.

According to percolation theory κ_G should tend to zero at C_F with an exponent $\nu_p = 0.825 \pm 0.02$ (eq. 5.3e). The present data is not of sufficiently high quality to allow this relationship to be tested. An adequate description of the results is obtained by the straight line

$$\kappa_G \, a_{nn} = (2.5 \pm 0.5) \, (C_F - C) \qquad (5.29)$$

which implies an exponent of order 1. The choice of $\kappa_G a_{nn}$ as the minimum value of $\kappa_1 a_{nn}$ for a particular alloy is not exact. A more strict identification of κ_G requires a knowledge of g(T) and thus cannot be attempted. As κ_G so chosen tends to zero at C_F the error introduced by this procedure is small. It is important to emphasise that the geometrical clusters described by (eq. 5.29) are unlikely to be random percolation clusters in view of the tendency for atomic clustering in Cr Fe alloys.

The 'thermal' inverse correlation range is more difficult to analyse. Following the discussion of pure Fe (section 5.2.1) one may expect Cr Fe alloys to display essentially Heisenberg like properties. Indeed, the linear temperature dependence of κ_T above 20K indicates Heisenberg like correlations. However, the tendency of κ_T to saturate below 20K suggests a cross-over to Ising like behaviour at this temperature. This cross-over is probably induced by dipolar anisotropy. The minimum in κ_T as a function of temperature is also linked with anisotropy. To analyse these phenomena in the framework of percolative multicritical behaviour, the exact form of the pure one dimensional inverse correlation range g(T) is required. Unfortunately, it is not possible to calculate g(T) exactly, even assuming a Heisenberg-Ising description, as both the appropriate exchange and anisotropy constants are unknown..

As a first approximation g(T) will be assumed to follow the asymptotic forms proposed by Stinchcombe (1980) for an anisotropy induced cross-over from Heisenberg to Ising behaviour in a linear chain. Only the data above 20K will be considered. In this regime the distinction between transverse and longitudinal inverse correlation ranges is unimportant and following Stinchcombe (1980) g(T) may be written

$$g(T) = a(b + T) \quad T > 20K \tag{5.30a}$$

where a and b are undetermined parameters related to the exchange and anisotropy constants. With b chosen as 20.0K so that the κ_T - g(T) characteristic passes through the origin, a linear dependence of κ_T on g(T) is obtained for all alloys studied, illustrated in Fig. 5.36. These data are well described by the relation

$$\kappa_T \, a_{nn} = (1.75 \pm 0.10) \times 10^{-3} \, (20.0 + T) \qquad (5.30b)$$

which would suggest a thermal inverse correlation length exponent $\nu \sim 1$. In view of the uncertainty in this analysis, a more precise determination of ν was not attempted.

The work of Birgeneau et al (1980) suggests that the constant of proportionality between $\kappa_T \, a_{nn}$ and $g(T)^{\nu}$ is unity. If this is the case, the parameter a derived from the fits of Fig. 5.36 should be of the order 1/J predicted for the pure one dimensional Heisenberg chain (see (eq.5.11)), giving $J \sim 600K$. The value of J for nn Fe interactions in Cr Fe alloys is not known but may be expected to be of the same order of magnitude as that in pure Fe, $J \sim T_c = 1000K$, which is consistent with J derived from the correlation range analysis.

The minimum in κ_T as a function of temperature may arise in two ways. Firstly, it is well known that the transverse component of κ_T for a one dimensional anisotropic chain shows a weak minimum at low temperature whilst the longitudinal part tends to zero (see for example Stinchcombe (1980)). A similar effect is seen in three dimensional anisotropic systems (Cowley et al (1979)). As the SAS measurements do not distinguish between the longitudinal and transverse components of κ_T, the minimum in κ_T simply reflects this fact. Secondly, as outlined in Appendix A , a minimum in $\kappa_1 = \kappa_T + \kappa_G$ itself may arise in an artificial way if the motion of the total cluster moment is correlated with the shape of the cluster by shape anisotropy. For a needle-like cluster, which may resemble one arm of a ramified percolation

Fig.5.36 Thermal inverse correlation ranges for $C < C_F$ as a function of the one dimensional inverse correlation length g(T). g(T) is assumed to be linear in temperature and is expressed in Kelvin.

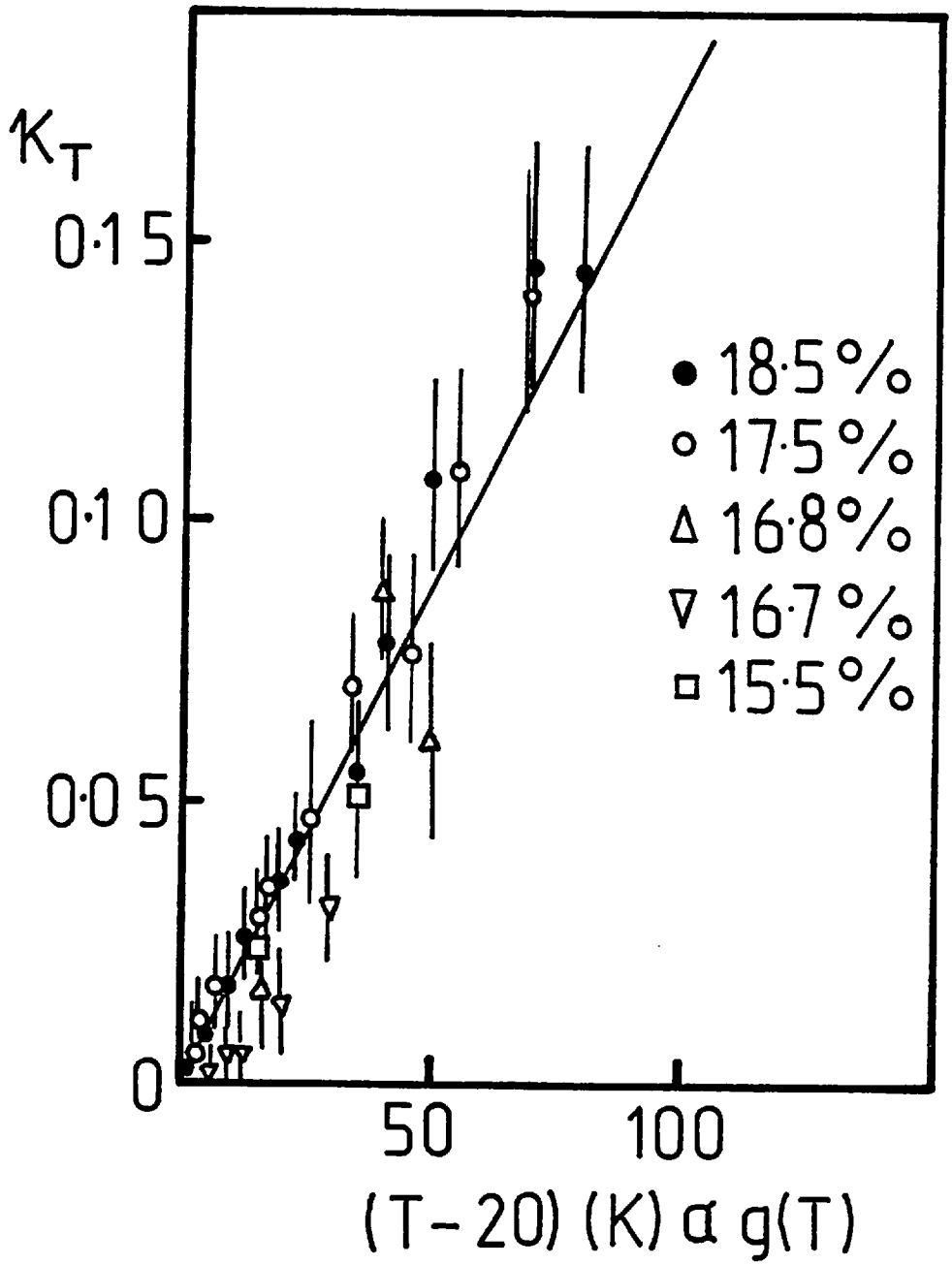

Fig. 5·36

cluster the ratio of the minimum κ_1 to the value at T = 0 is given by (eq. A.2),

$$\kappa_1(T = 0)/\kappa_1(\text{min}) = \sqrt{5/3} \sim 1.29$$

An experimental value of 1.20 ± 0.05 for this ratio may be estimated from the data of Fig. 5.31, in good agreement with that predicted.

There has been little theoretical discussion of the Lorentzian scattering amplitude A. Birgeneau et al (1980) (section 5.1.4.1) have proposed that the scattering amplitude is related to the exponent η via

$$A = B\,\kappa_1^{\eta} \qquad (5.31)$$

As A decreases with increasing κ_1 for the Cr Fe alloys studied this yields $\eta < 0$ in contrast to the results of Birgeneau et al (1980) and Cowley et al (1980) which show A to increase with increasing κ_1 implying $\eta > 0$. Fits to the data using the relation above are shown as dashed lines in Fig. 5.34 for the 18.5% and 17.5% alloys. An excellent fit to the data is found above 20K for both alloys with $\eta = -0.40 \pm 0.10$ (17.5%), and $\eta = -0.41 \pm 0.05$ (18.5%), but fails below 20K. The failure at low temperature may be due to the artificial increase in κ_1 due to shape anisotropy, discussed previously.

A negative value of η_p is slightly favoured for the pure percolation process in three dimensions, although the error limits are large. Stanley (1977) gives $\eta_p = -0.01 \pm 0.10$ (eq. 5.3e). η_p becomes increasing negative for $d > 3$. Scaling theory for the percolation multicritical point gives $\eta = \eta_p$. The η value derived above is much larger in magnitude than that estimated theoretically. This may be due to the presence of atomic clustering in Cr Fe alloys. This value of η implies that the correlations vary asymptotically as $1/R^{0.6}$ rather than 1/R expected for random percolation, indicating that the geometrical correlations are longer

ranged than for a purely random system. This may be expected for a clustering type alloy.

If the percolation model is strictly followed this value of $\eta = \eta_p$ allows the effective cluster dimensionality to be calculated, giving from (eq. 5.5b) $d_p = 2.40 \pm 0.01$. The exponent γ may also be estimated using the scaling relation $\gamma = \nu(2 - \eta)$ with $\nu \sim 1$ and $\eta \sim -0.40$ resulting in $\gamma \sim 2.4$. The crossover exponent ϕ can be calculated using the pure percolation exponents $\gamma_p = 1.66$ and $\nu_p = 0.825$ to give $\phi = \nu/\nu_p \sim 1.2$ or equally $\phi = \gamma/\gamma_p \sim 1.4$. These estimates should be treated with caution as the pure percolation exponents are not strictly applicable in the presence of atomic clustering and the value of ν has been deduced without an exact knowledge of g(T).

The forward scattering I(0) according to the previous analysis varies as $\kappa_1^{-2.4}$ above 20K and reaches a well defined maximum at lower temperature. This maximum is associated with the minimum in κ_1 via $I(0) = A/\kappa_1^2$ as A is slowly varying in this region. Thus the peak may be explained by the same arguments used to account for the minimum in κ_1. If the shape anisotropy contribution is dominant this peak would appear to be an artifact of the neutron SAS technique. The temperature of this maximum (15K) is concentration independent and unrelated to the peak in the low field bulk susceptibility, which varies from 22K to 28K over this concentration range.

In conclusion, an analysis of the SAS data for Cr Fe alloys for $C < C_F$ is in semiquantitative agreement with models of the percolation multicritical point. The magnetic correlations evolve toward long range order by spreading along geometrical pathways whose size becomes progressively larger as C_F is approached. The correlations are Heisenberg like at high temperature but tend to become Ising like at low temperature as a result of anisotropy forces. Thermal critical exponents $\gamma \sim 2.4$, $\nu \sim 1$ and $\eta \sim -0.4$ have been estimated from these data above 20K. A link with the

observed cluster spin glass behaviour is provided by the presence of a minimum in κ_1 at low temperatures which was ascribed to the magnetostatic shape anisotropy of well correlated clusters of spins. This anisotropy mechanism was used in section 5.4.2 to account for the bulk magnetic properties using fine particle theory.

5.5.5 Magnetic correlations above C_F

5.5.5.1 Results

The results of Lorentzian fits to the magnetic SAS from the ferromagnetic 19.5%, 19.9%, 20.8%, 21.7%, 24% and 25% Fe alloys studied using D17 and D11(5m) are shown in Fig. 5.37 and Fig. 5.38. The inverse range parameters displayed in Fig. 5.37 have been offset from each other by a constant amount for the sake of clarity, as also are the Lorentzian amplitudes in Fig. 5.38.

The temperature variation of $\kappa_1 a_{nn}$ changes as the concentration is decreased to C_F. For all alloys studied κ_1 decreases linearly as the temperature is decreased to T_c. For concentrations greater than 20.8% Fe the inverse correlation range reaches a local minimum at T_c but for lower concentrations κ_1 decreases monotonically through T_c, which is marked by a weak shoulder rather than a minimum. κ_1 remains non zero at T_c for all alloys.

The Lorentzian scattering amplitude A, shown as a function of temperature in Fig. 5.38 also shows qualitative changes as the concentration is decreased to C_F. For the more concentrated ferromagnetic alloys ($c \geq 21.7\%$) the amplitude increases gradually as the temperature is lowered and becomes constant in the vicinity of T_c. As the temperature is lowered further the amplitude decreases, reaching a shallow minimum at $T \sim 30K$ and then proceeds to increase rapidly as T tends to zero. For alloys closer to C_F ($c \leq 20.8\%$) no such low temperature minimum is observed.

The forward scattering I(0) calculated from these Lorentzian

Fig.5.37 Inverse correlation range ($\kappa_1 a_{nn}$) for ferromagnetic Cr Fe alloys as a function of temperature. The curves have been offset from each other for clarity. Solid curves are guides to the eye.

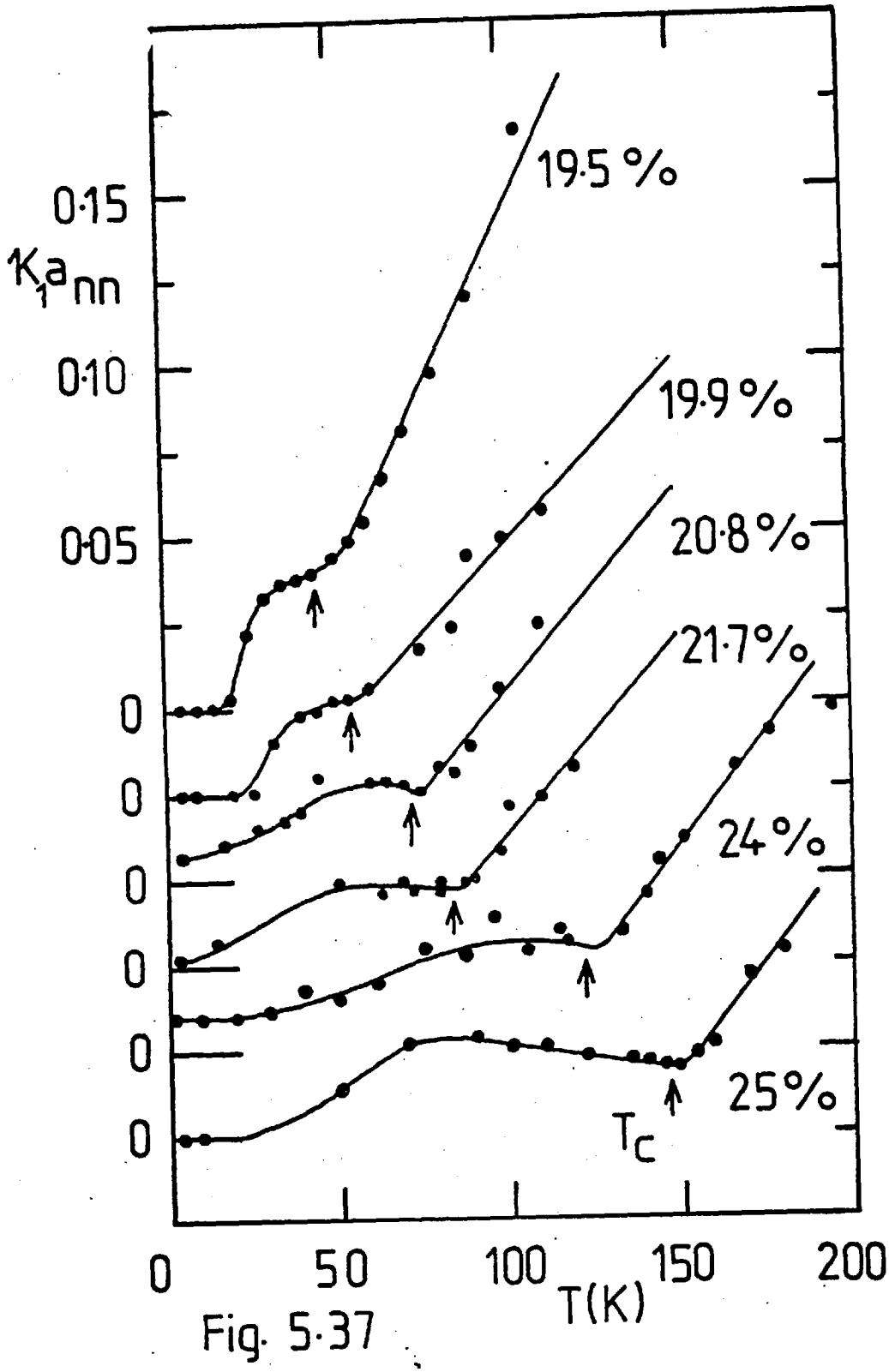
0·15
$K_1 a_{nn}$
0·10
0·05
0
0
0
0
0
0
19·5 %
19·9 %
20·8 %
21·7 %
24 %
25 %
T_C
0
50
100
150
200
T(K)

Fig. 5·37

Fig.5.38 Lorentzian amplitude (A) for ferromagnetic Cr Fe alloys as a function of temperature. The data are offset for clarity. Solid curves are guides to the eye.

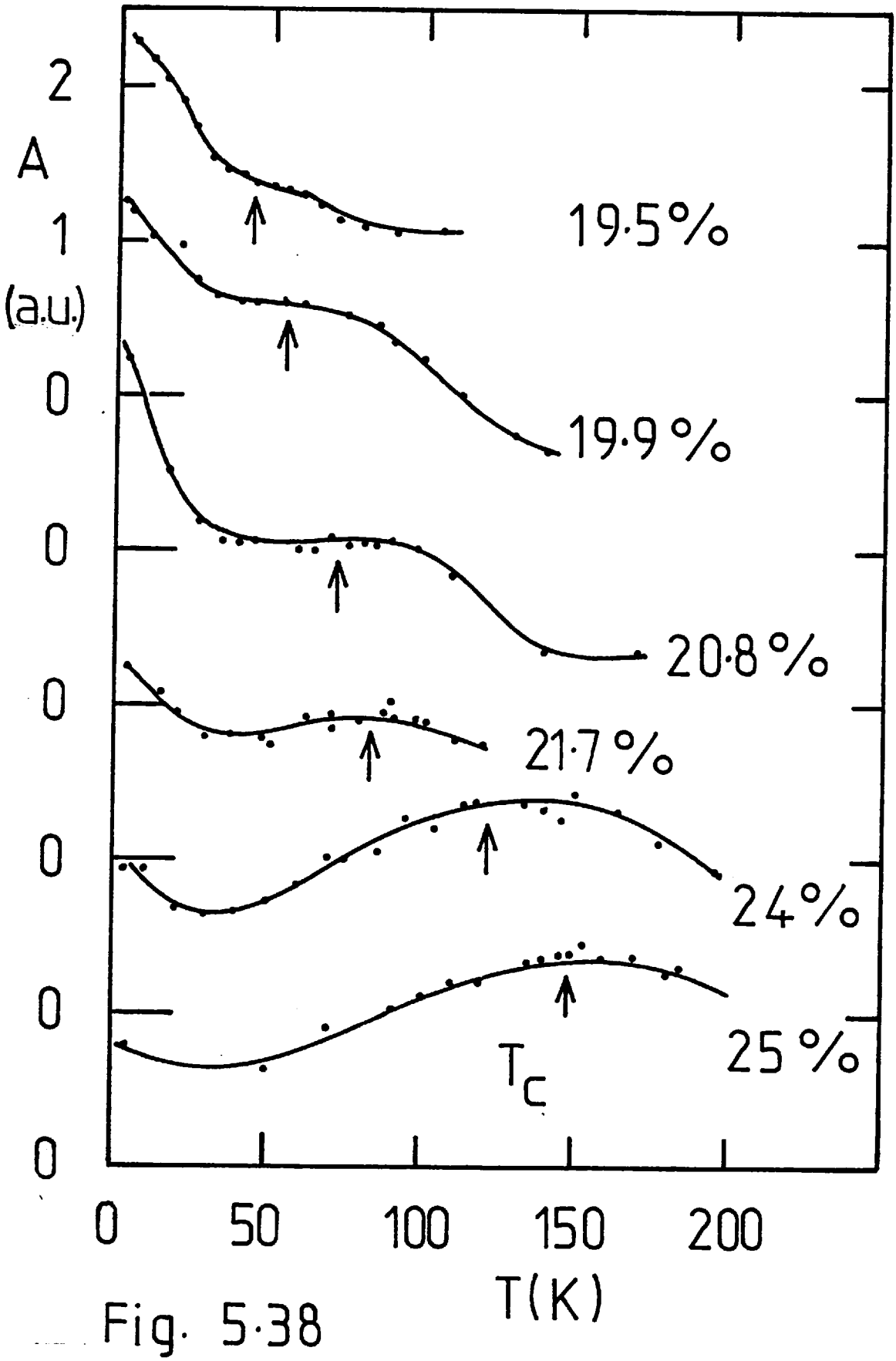

Fig. 5·38

fits is shown in Fig. 5.39. The temperature variation of I(0) is composed of two components: a critical scattering peak at T_c combined with the low temperature 'sub critical' scattering discussed in section 5.3.2. These two components are well separated for higher concentrations but tend to merge as C approaches C_F, reducing the critical scattering contribution to a weak shoulder.

5.5.5.2 Analysis and Discussion

The concentration and temperature dependence of the magnetic correlations in these ferromagnetic alloys is more complex than that observed for alloys which do not support long range order.

The fact that κ_1 reaches a local minimum at T_c and tends to zero at lower temperatures is difficult to understand. Ideally κ_1 should reach zero at T_c. (A non zero κ_1 at the ordering temperature has been reported for many systems close to a critical concentration (see for example Cowley et al (1979)). This may be due to chemical inhomogeneity which tends to smear the ferromagnetic transition. Alternatively, the contribution from finite clusters co-existing with the infinite cluster may dominate the scattering, tending to obscure the contribution from the infinite cluster. Small concentration fluctuations of the order $\pm$ 1% have been revealed in these alloys by electron microprobe analysis (section 3.1) so that chemical smearing of the transition is undoubtedly present. However, the overall behaviour of the SAS is consistent with the subdivision of the ferromagnetic alloys into an infinite cluster and finite clusters, as discussed in section 5.5.1.

The dependence of κ_1, A and I(0) on these two components is evident from Figs. 5.37, 5.38 and 5.39. The finite and infinite cluster contributions appear well separated in temperature for high concentrations, the infinite cluster contribution giving a V shaped minimum in κ_1 at T_c and the finite cluster contribution giving a monotonic decrease in κ_1 as the temperature is lowered

Fig.5.39 Extrapolated forward intensity for ferromagnetic Cr Fe alloys. Data are offset for clarity. Solid curves are guides to the eye.

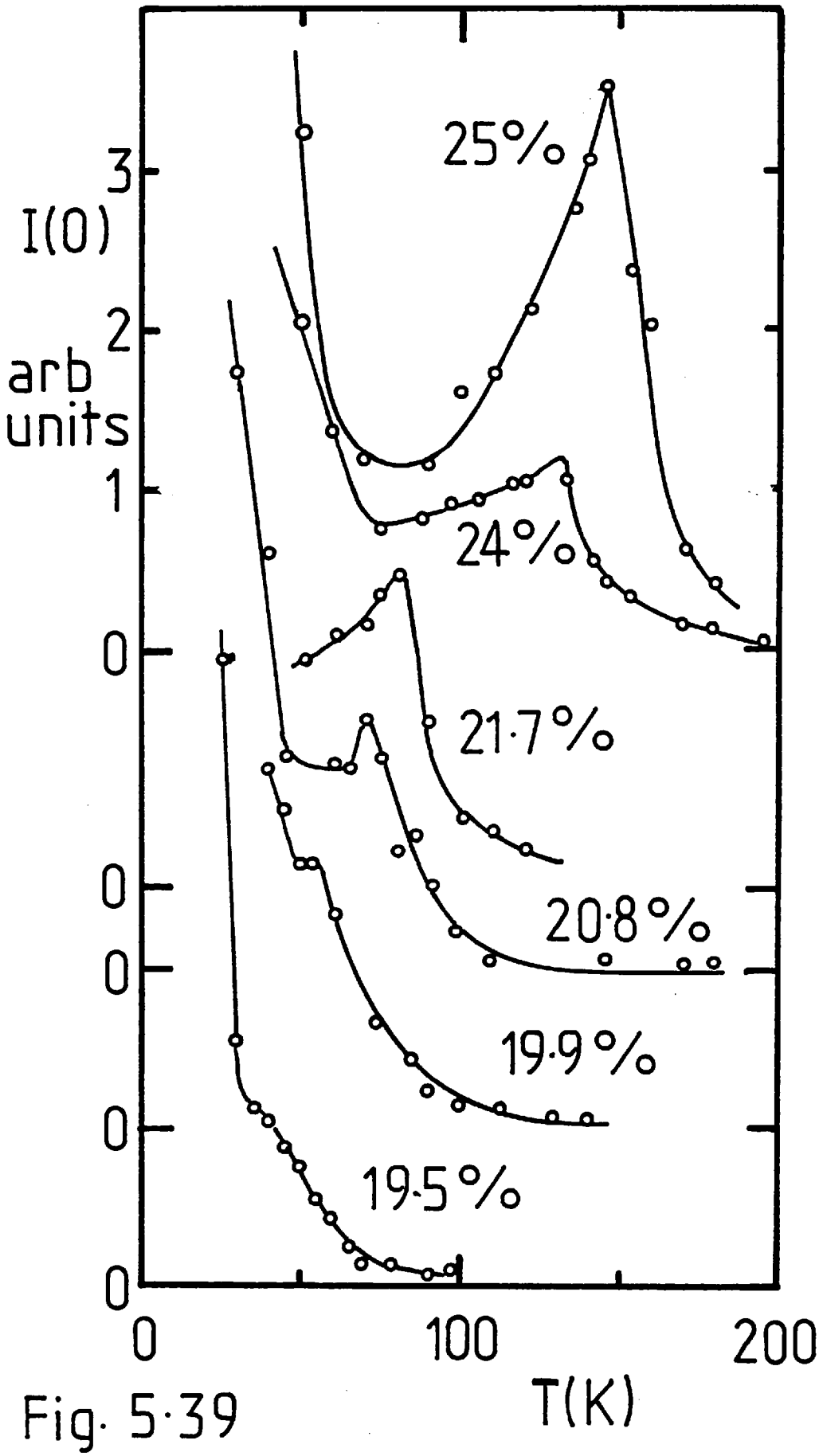

Fig. 5·39

toward T = 0. As the concentration is decreased toward C_F the finite cluster contribution increases and the infinite cluster contribution decreases. Similar comments may be made for the Lorentzian amplitude.

The temperature dependence of κ_1 above T_c has been analysed by fitting the data to two relations,

$$\kappa_1 a_{nn} = F \left(\frac{T-T_c}{T_c}\right)^{\nu(1)} \qquad T > T_c \tag{5.32a}$$

and

$$\kappa_1 a_{nn} = G \left(\frac{T-T_c}{T_c}\right)^{\nu(2)} + \kappa_R \tag{5.32b}$$

The first relation constrains $\kappa_1 \to 0$ at $T = T_c$ and so may be expected to hold away from T_c. This constraint is removed in the second fit, allowing κ_1 to reach a finite value at T_c. The results of these fits are given in Table 5.4, and the log-log plots are shown in Fig. 5.40.

Table 5.4

Results of fits to data using equations (5.32a) and (5.32b)

C	$\nu(1)$	F	$\nu(2)$	G	κ_R
0.25	0.62 ± 0.1	0.13 ± .06	1.3 ± 0.2	0.28 ± .05	0.019
0.24	0.52 ± 0.05	0.11 ± .02	1.3 ± 0.1	0.21 ± .03	0.028
0.217	0.54 ± 0.05	0.085 ± .005	1.26 ± 0.05	0.11 ± .02	0.021
0.209	0.51 ± 0.05	0.072 ± .005	1.18 ± 0.05	0.069 ± .01	0.024
0.199	0.51 ± 0.1	0.063 ± .005	1.22 ± 0.1	0.052 ± .005	0.026
0.195	-	-	1.5 ± 0.1	0.066 ± .006	0.040

The results again should be treated with caution considering the small number of data points used and the lack of data very close to T_c.

Fig.5.40 Power law fits to the temperature dependence of the inverse correlation range above T_c. (a) according to (eq.5.32a) (b) according to (eq.5.32b).

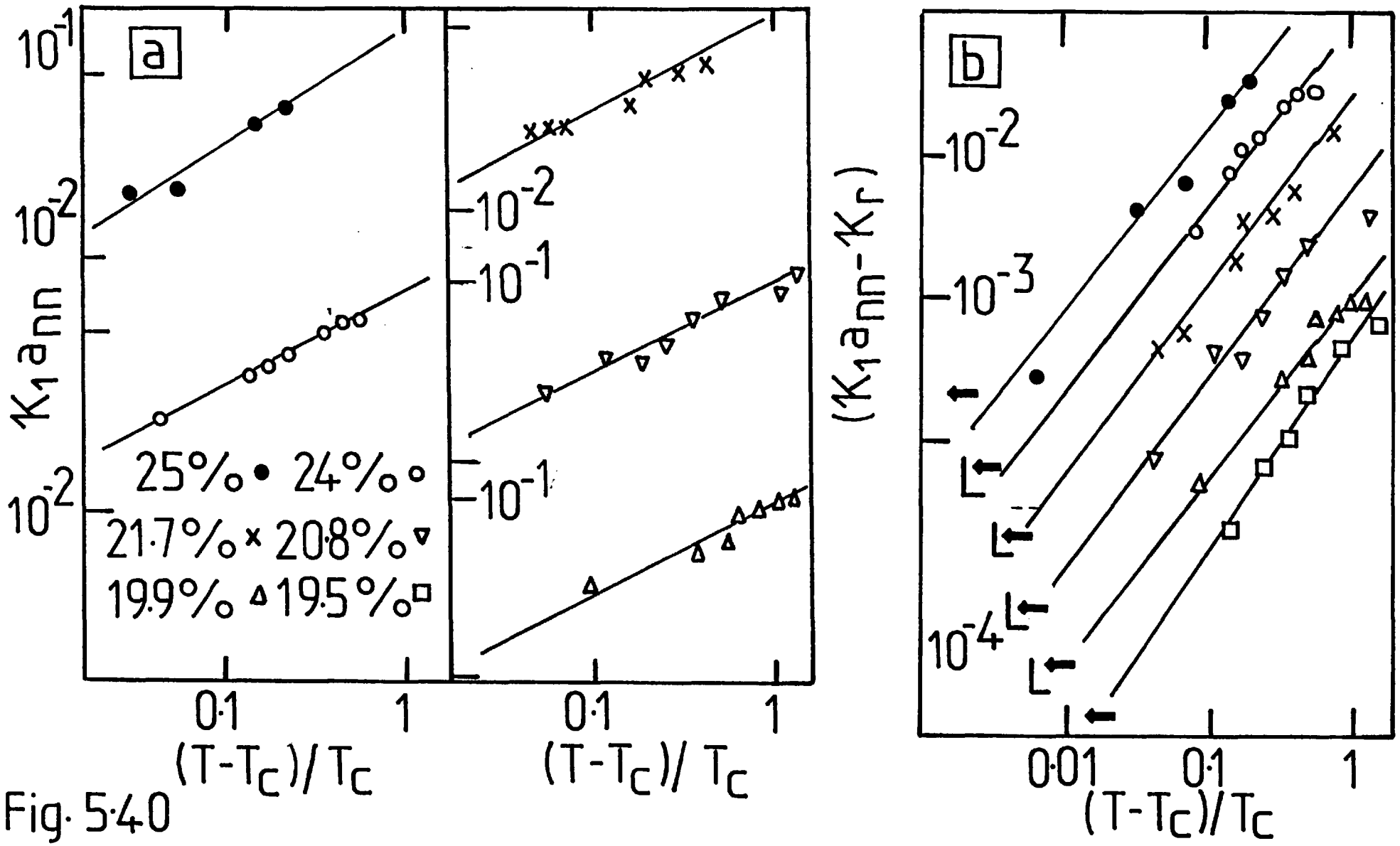
a
b
10^{-1}
10^{-2}
10^{-2}
10^{-1}
10^{-1}
10^{-2}
10^{-3}
10^{-4}
$K_1 a_{nn}$
$(K_1 a_{nn} - K_r)$
25% • 24% ○
21·7% × 20·8% ▽
19·9% △ 19·5% □
0·1
1
0·01
0·1
1
$(T-T_C)/T_C$
$(T-T_C)/T_C$
$(T-T_C)/T_C$

Fig. 5·40

However, a few general conclusions may be drawn. Firstly, the exponents $\nu(1)$ and $\nu(2)$ are, to within experimental error, concentration independent and bracket the theoretical estimate $\nu = 0{,}70 \pm 0.02$ (eq.5.6d) for a 3d Heisenberg ferromagnet. Secondly, the prefactors F, G are not concentration independent but show large deviations from each other.

In fact, these prefactors vary systematically with concentration as shown in Fig. 5.41 and are well described by the relations

$$F = (0.60 \pm .05)\ (C - C_F)^{\frac{1}{2}} \qquad (5.33a)$$

$$G = (4.7 \pm 0.3)\ \ (C - C_F) \qquad (5.33b)$$

It is not clear which of the fits is to be preferred. If the experimentally determined relations are extrapolated to C = 1 (pure Fe), (eq. 5.33a) gives $F = 0.54 \pm .04$ whilst (eq. 5.33b) gives $G = 3.8 \pm 0.2$ assuming $\kappa_R = 0$. The experimental result for pure Fe is F = G = 3.1 (Als Nielsen (1976)) which favours the fit (eq. 5.32b). Furthermore, the large value of $\nu(2) = 1.2 \pm 0.1$ derived from this fit is consistent with the anomalous, large exponent γ found in the bulk measurements of Aldred and Kouvel (1977) on Cr Fe alloys between 25% Fe and 20% Fe. Using the scaling relation $\gamma = \nu(2 - \eta)$ with η assumed zero allows ν to be estimated from the data of Aldred and Kouvel, giving $\nu = 1.06 \pm 0.01$ in reasonable agreement with $\nu(2)$.

Irrespective of which fit is the more valid the observation,

$$\kappa_1\ a_{nn} \sim (C - C_F)^{\alpha}\ \ \left(\frac{T-T_c}{T_c}\right)^{\beta}$$

for ferromagnetic alloys close to C_F is an interesting and unexpected result. A result of this form is consistent with the scaling laws proposed by Stinchcombe (1980) for dilute anisotropic magnets.

Fig.5.41 Concentration dependence of the inverse correlation range prefactors F and G.

(a) F as a function of $(C - C_F)^{\frac{1}{2}}$

(b) G as a function of $(C - C_F)$

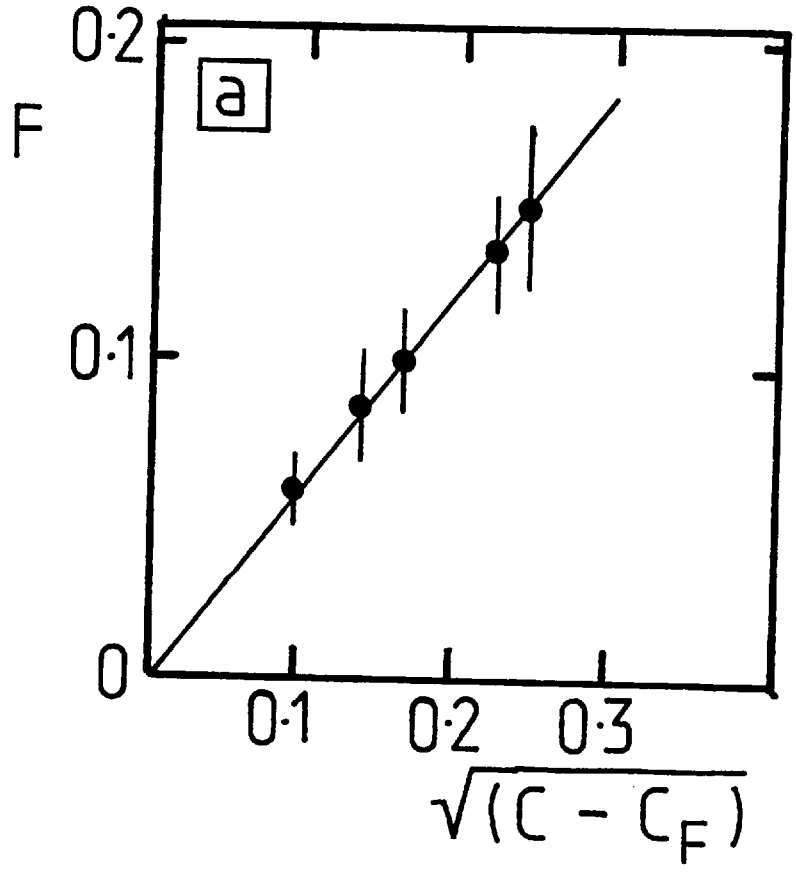

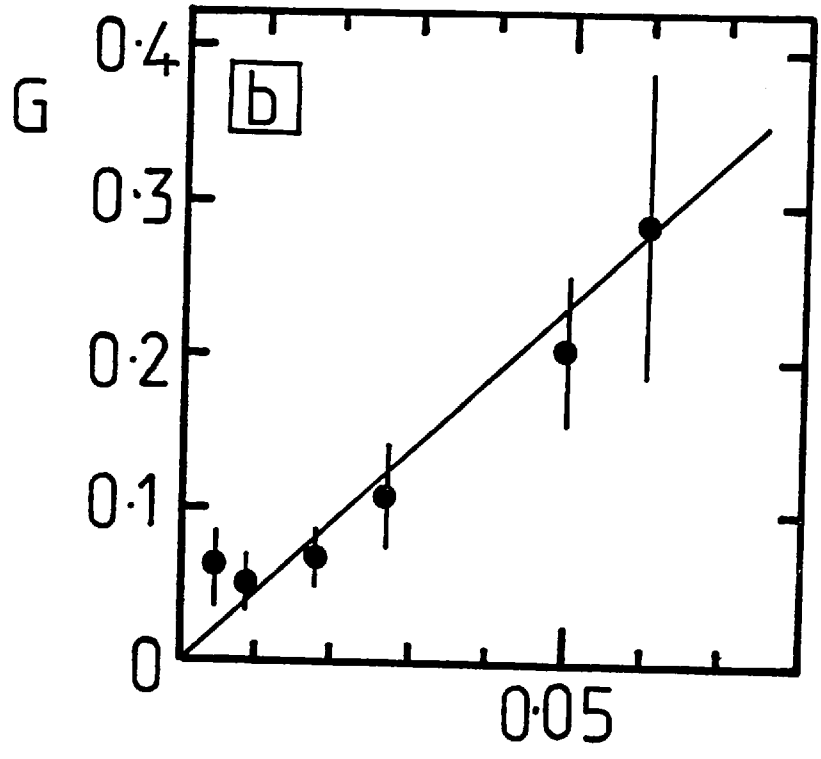

Fig. 5.41

According to Stinchcombe the exponents α and β are not related in a straightforward way to the usual percolative or thermal exponents defined in section 5.1.3.3. The occurrence of a multiplicative factor $(C - C_F)^{\alpha}$ itself demonstrates that, in a sense, the ferromagnetic alloys are 'aware' of the singularity at $C = C_F$.

5.6 Small angle scattering in an applied field

5.6.1 Results

SAS data were collected for several alloys spanning the critical concentration for ferromagnetism in applied fields of up to 0.3T and at temperatures between 1.5K and 4.2K using the instrument D17. The experimental procedure has been outlined in section 3.3.3. Application of a magnetic field resulted in anisotropic SAS which was least squares fitted to the function

$$I(\kappa,\alpha) = A(\kappa) + B(\kappa) \cos^2\alpha$$

where α is the angle between the applied field direction and the scattering vector in the plane of the detector. $A(\kappa)$ will be referred to as the isotropic part of the scattering and $B(\kappa)$ the anisotropic part.

The application of a magnetic field at low temperature has the same effect on all alloys studied, ferromagnetic or otherwise. Typical results are shown in Fig. 5.42 for the Cr Fe 25% alloy at 2.2K, where contours of constant scattering intensity in the plane of the detector are plotted as a function of field. The dotted contour represents the same intensity level in each case. In zero field the contours are circular. As the field is applied the contrours become elongated along the field direction and collapse into the centre of the detector. The scattering is suppressed by the field. At the highest field of 0.4T the scattering is weak and tends to be elongated perpendicular to the field direction.

The isotropic part of the scattering $A(\kappa)$ showed a Lorentzian dependence on κ in all fields. $B(\kappa)$, the anisotropic part, could also be fitted to a Lorentzian but the poor data quality in the case of very small anisotropy only allowed a meaningful analysis over the field range 200 Oe - 3600 Oe in the best cases. Typical Debye plots of $A(\kappa)$ and $B(\kappa)$ for the 25% alloy are shown in Fig. 5.43 and Fig. 5.44. The forward intensity, Lorentzian amplitude and inverse correlation range derived from least squares fits to $A(\kappa)$ and $B(\kappa)$ are shown in Fig. 5.45 for all alloys studied. (It should

Fig.5.42 Equal intensity contours in the plane of the detector for 25% Fe at 2.2K as a function of increasing magnetic field. The field direction is shown by an arrow. Dotted contours represent the same intensity level.

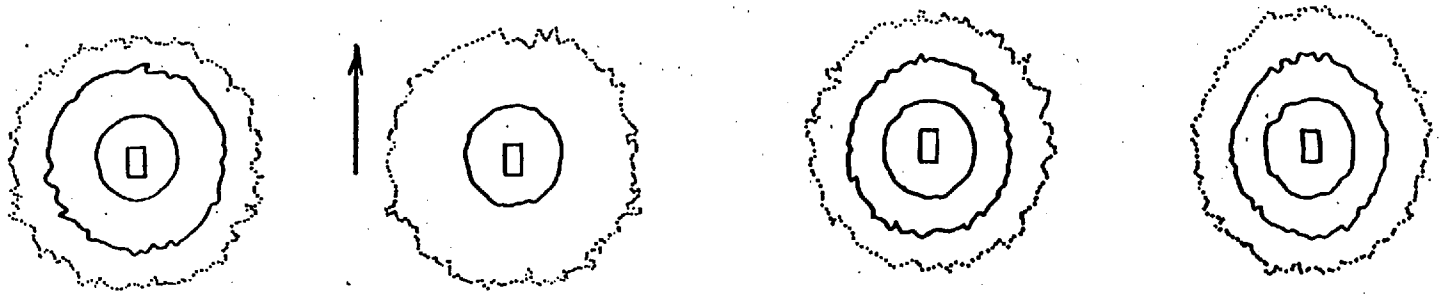

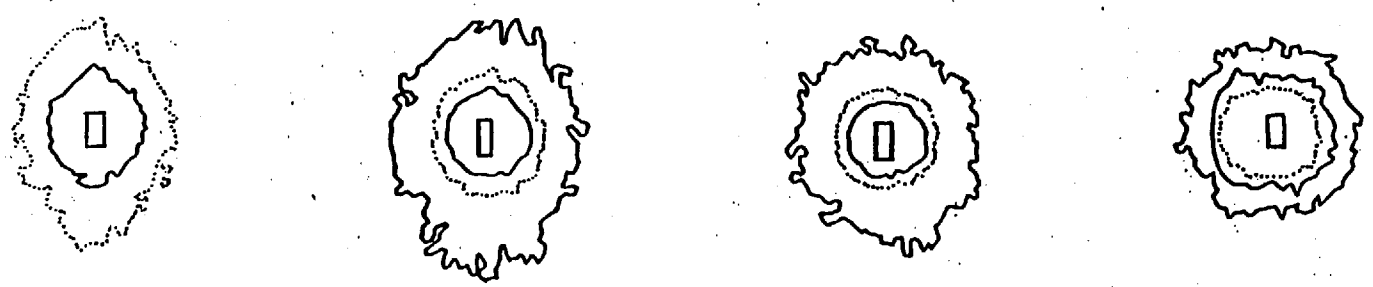

Fig·5·42

Fig.5.43 Debye plots of the isotropic part of the SAS ($A(\kappa)$) for Cr Fe 25% at 4.2K for several values of applied field.

Fig.5.44 Debye plots of the anisotropic part of the SAS ($B(\kappa)$) for Cr Fe 25% at 4.2K for several values of applied field.

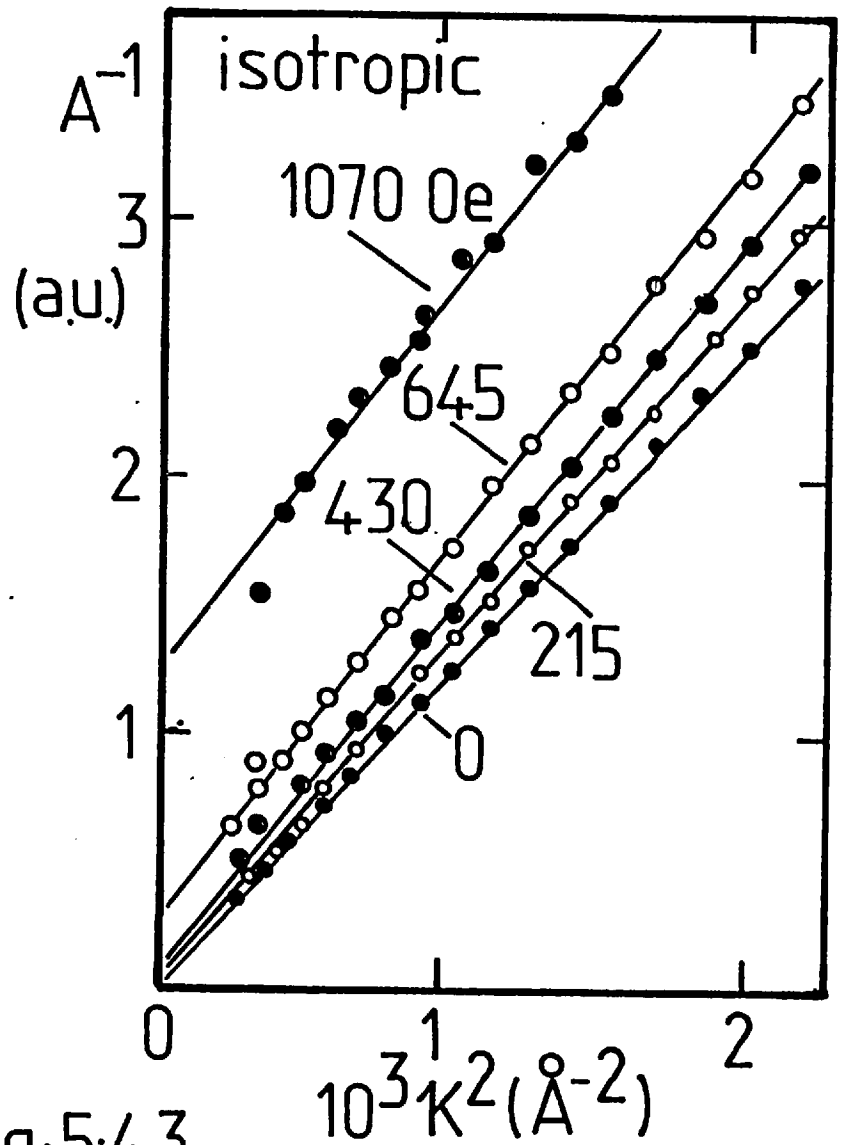

Fig·5·43

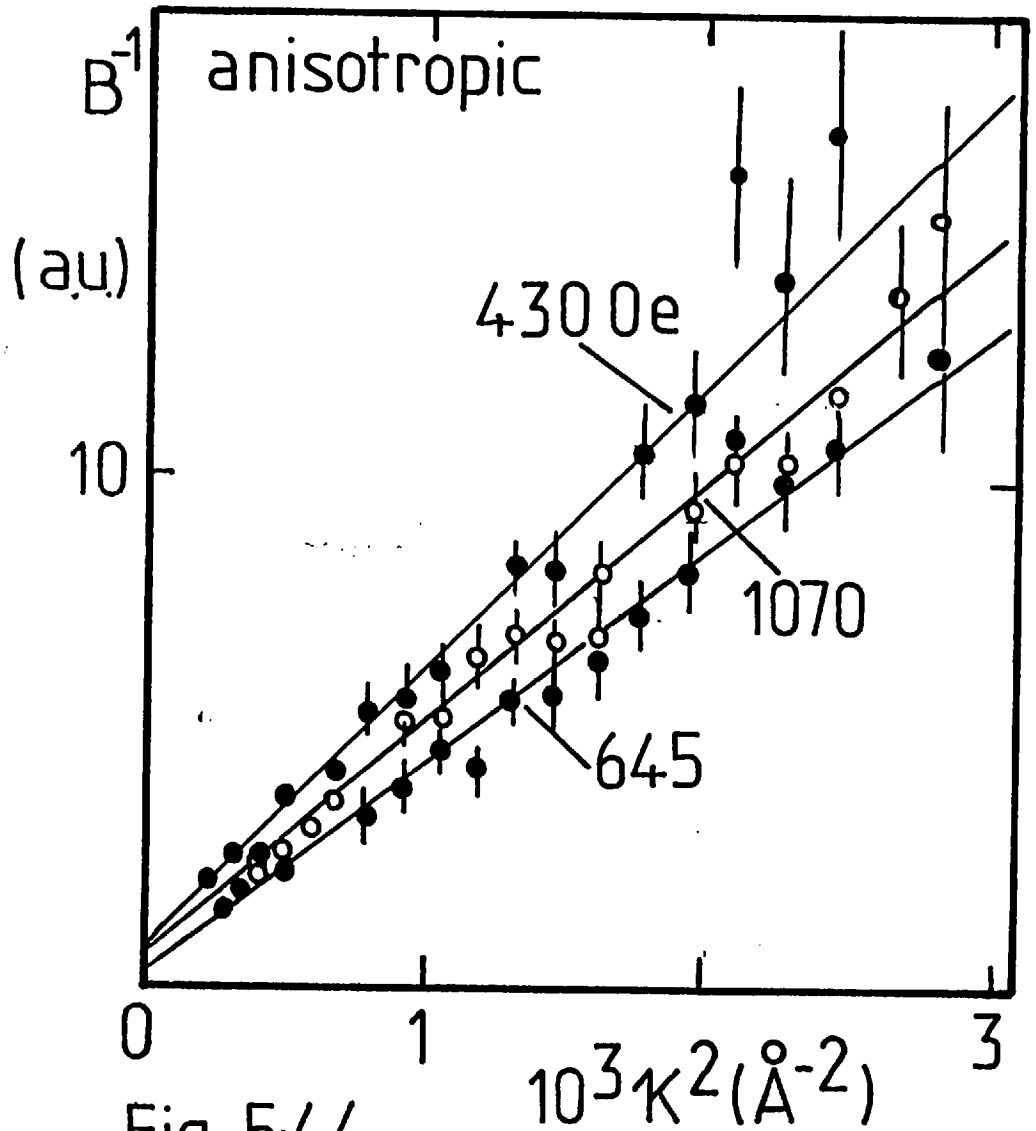

Fig·5·44

Fig.5.45 Field dependence of the inverse range parameters ($\kappa_A(H)$,$\kappa_B(H)$), Lorentzian Amplitudes (LA(H), LB(H)) and extrapolated forward intensity (A(H),B(H)) for the isotropic and anisotropic parts of the SAS. Dashed curves are best fits using (eq.5.34) for S values indicated. The extrapolated forward intensities have been normalized by A(O), the estimated forward scattering in zero field.

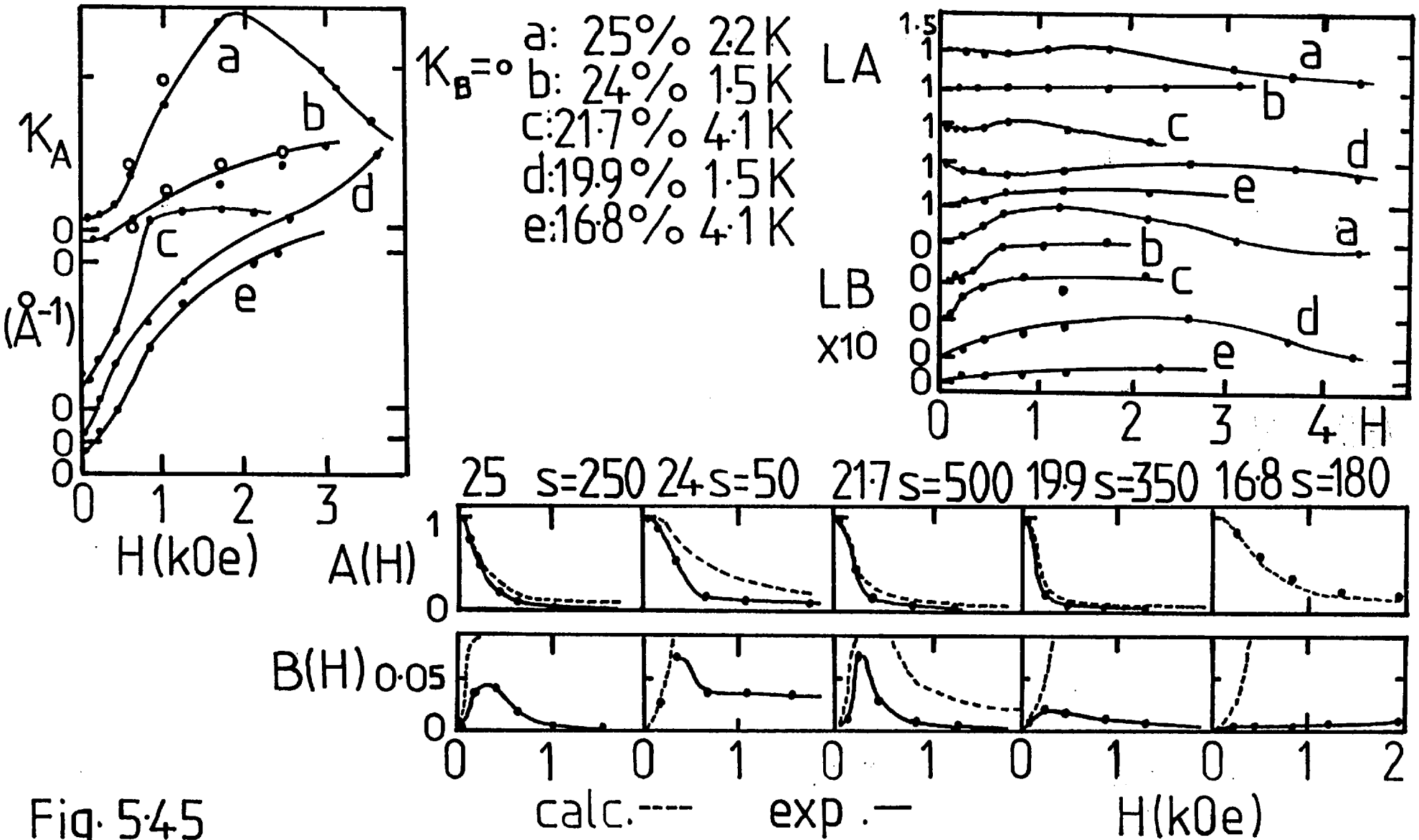
K_A
(Å^{-1})
a
b
c
d
e
H(kOe)
A(H)
K_B=o
a: 25% 2.2K
b: 24% 1.5K
c:21.7% 4.1K
d:19.9% 1.5K
e:16.8% 4.1K
LA
LB
x10
H
25 s=250 24 s=50 21.7 s=500 19.9 s=350 16.8 s=180
B(H)
calc.---- exp .—
H(kOe)

Fig. 5.45

be noted that a simplified analysis was used to calculate the anisotropic parameters for C < 24%. This was based on the assumption that inverse correlation ranges of the anisotropic and isotropic parts were equal, a result found for the 24% and 25% alloys. Consequently, the anisotropic $\kappa_1 a_{nn}$ is not shown for these alloys).

The same overall behaviour was found for all alloys studied, both above and below C_F. The isotropic part of the forward scattering is rapidly suppressed by an applied field whereas the anisotropic part peaks at a finite field. The isotropic Lorentzian amplitude is only weakly field dependent in low fields in contrast to the anisotropic Lorentzian amplitude which tends to increase with increasing field. The inverse correlation ranges for the isotropic and anisotropic parts are equal to within experimental error for the two cases investigated and both increase with increasing field. For the remaining alloys, the isotropic inverse correlation range was found to increase with field, in some cases reaches a broad maximum at higher fields.

5.6.2 Analysis and Discussion

The effect of an applied field on the low temperature SAS from alloys with $C < C_F$ and $C > C_F$ is remarkably similar. In particular the field induced anisotropy $B(\kappa)$ is always positive below 0.3T. A negative anisotropy is only found at very large fields in the more concentrated alloys and constitutes a negligible contribution to the SAS.

This observation rules out ferromagnetic elastic diffuse scattering as a cause of the low temperature SAS in these alloys. The elastic diffuse scattering from a ferromagnet always occurs with an orientation factor $(1 - \cos^2\alpha)$ (section 2.2.3) which implies a negative value of $B(\kappa)$. A positive $B(\kappa)$ is consistent with the presence of superparamagnetic clusters at low temperatures, both

for $C < C_F$ and $C > C_F$. For $C \lesssim C_F$ such clusters may be identified with the geometrical entities described in section 5.5.4 and invoked in the fine particle description of the cluster glass behaviour in section 5.4.2. For $C > C_F$ such clusters may represent finite clusters coexisting with the infinite cluster.

It is possible to give a semiquantitative account of the field dependence of the SAS by considering the scattering from an assembly of superparamagnetic particles in an applied field. This calculation has been performed by Cywinski et al (1977) by drawing an analogy with the scattering from a perfect paramagnet. According to this calculation the forward scattering is given by

$$I(0) = A(H) + B(H) \cos^2 \alpha \qquad (5.34)$$

where

$$A(H) = \tfrac{1}{2} S(S+1) + \tfrac{1}{2}\langle (S^Z)^2 \rangle - \langle S^Z \rangle^2$$

$$B(H) = \tfrac{1}{2} S(S+1) - {}^3/_2 \langle (S^Z)^2 \rangle + \langle S^Z \rangle^2$$

and

$$\langle S^Z \rangle = \tfrac{1}{2} \left((2S+1) \coth \left(\tfrac{1}{2} u(2S+1) \right) - \coth u/2 \right)$$

$$\langle (S^Z)^2 \rangle = S(S+1) - \langle S^Z \rangle \coth u/2$$

with $u = \hat{g}\mu_B \bar{H}/kT$

The results of this calculation for various values of the total superparamagnetic spin S as a function of $g\mu_B H/kT$ taken from the work of Cywinski et al (1977) are reproduced in Fig. 5.46. The variation of A(H) and B(H) with H/T is in qualitative agreement with the present data.

Fig.5.46 Theoretical variation of the isotropic and anisotropic parts of the forward scattering (A(H) and B(H) respectively) for a superparamagnetic system as a function of $g \mu_B H/kT$ for various values of the cluster spin S. Cywinski et al (1977).

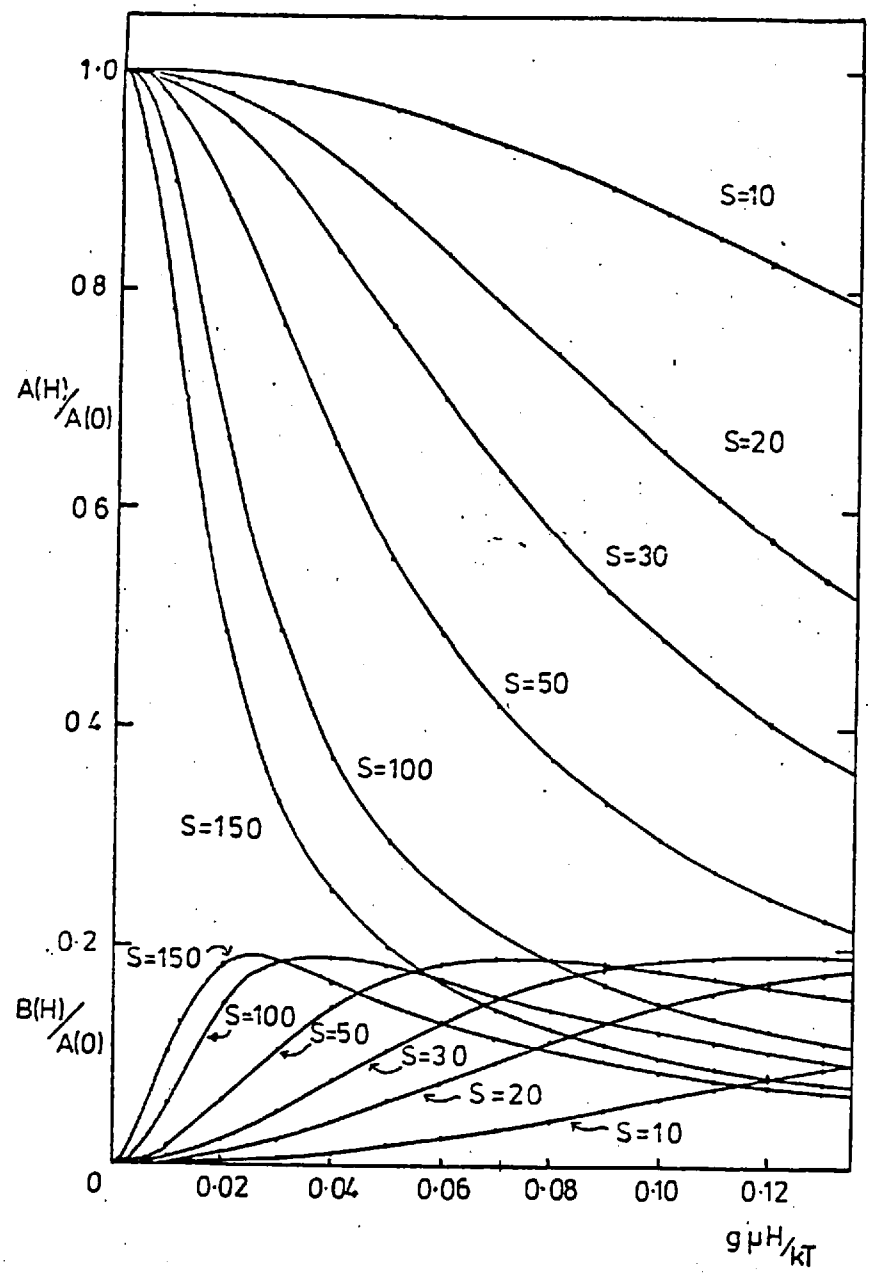
1·0
0·8
0·6
0·4
0·2
0
A(H)/A(0)
B(H)/A(0)
S=10
S=20
S=30
S=50
S=100
S=150
S=150
S=100
S=50
S=30
S=20
S=10
0·02
0·04
0·06
0·08
0·10
0·12
gμH/kT

Fig. 5·46

An attempt to fit the data of Fig.5.45 using (eq.5.34) with a unique value of S proved successful for $C < C_F$ but failed to account for the high field behaviour for $C > C_F$. Fits to the data are illustrated in Fig. 5.45.

To go beyond this simple model the effects of anisotropy, cluster size distribution and possible inter cluster interactions need to be considered. A more sophisticated model is required to account for the increase in κ_1 with field.

CHAPTER 6

MAGNETIZATION DENSITY IN Pt_3Cr

6.1 Introduction

In common with many of the 3d transition metals, Cr forms an ordered Cu_3Au compound with Pt. Pt_3Cr is reported to show ferrimagnetic order; the Pt moment is opposite in direction to that of the 3d moment. (Pickart and Nathans (1962)(1963)). This is in contrast to the other ordered Pt_3 - 3d compounds (3d = Mn, Co, Fe) which are antiferromagnetic or ferromagnetic. The atomic moments reported by Pickart and Nathans combine to give a total magnetization which is substantially lower than the accepted value (Besnus and Meyer (1973a)(1973b), Goto (1977), Williams and Lewis (1979)). The present polarized neutron study was initiated to determine the magnetization density in Pt_3Cr. This provides complementary data to the measurements of magnetization density in ferromagnetic Pt_3Mn and Pt_3Co (Menzinger and Paoletti (1966), Antonini, Lucari, Menzinger and Paoletti (1969)).

6.2 Previous work

6.2.1 Metallurgy of the Pt-Cr system

The Pt-Cr constitution diagram has been recently studied by Waterstrat (1973) and is reproduced in Fig. 6.1. In addition to the γ f.c.c. and α b.c.c. terminal solid solutions, an intermediate β phase which possesses the complex A15 structure is found.

The f.c.c. solid solution alloys are atomically disordered in the γ phase region which extends to 71% Cr at 1530°C, but undergo a transition to an ordered γ^1 phase at lower temperatures. The equilibrium ordering temperatures are shown in Fig. 6.1. The kinetics of the order-disorder transition are rapid and appear to go to completion so that, for example, at the stoichiometric concentration Pt_3Cr the disordered f.c.c. solid solution transforms to a fully ordered Cu_3Au ($L1_2$) structure below 1100°C. This ordered structure is shown in Fig. 6.2. The Cr atoms occupy the cube corners of the f.c.c. unit cell whilst the Pt atoms occupy the sites on cube faces. The ordered structure varies continuously with concentration until Cu Au ($L1_0$) order is reached in the vicinity of 50% Cr.

6.2.2 Magnetic Properties of Pt_3Cr

Atomically ordered Pt_3Cr orders magnetically below 490-480K (Besnus and Meyer (1973a)(1973b), Williams and Lewis (1979)). The ordered structure is thought to be ferrimagnetic. (Pickart and Nathans (1962)(1963)). Atomically disordered Pt_3Cr does not order magnetically. (Besnus and Meyer (1973b)).

The Cr and Pt moments deduced by Pickart and Nathans (1963) at room temperature, Cr = $2.33\mu_B$ and Pt = $-0.27\mu_B$ are not in agreement with the bulk magnetization of fully ordered Pt_3Cr. The average moment of $0.38\mu_B$/at obtained from these values is considerably lower than the currently accepted room temperature

Fig.6.1 Constitution diagram for Pt-Cr alloys. The order-disorder transition from γ to γ^1 is shown as a dotted line (Waterstrat (1973)).

Fig.6.2 Atomic order in Pt_3Cr.

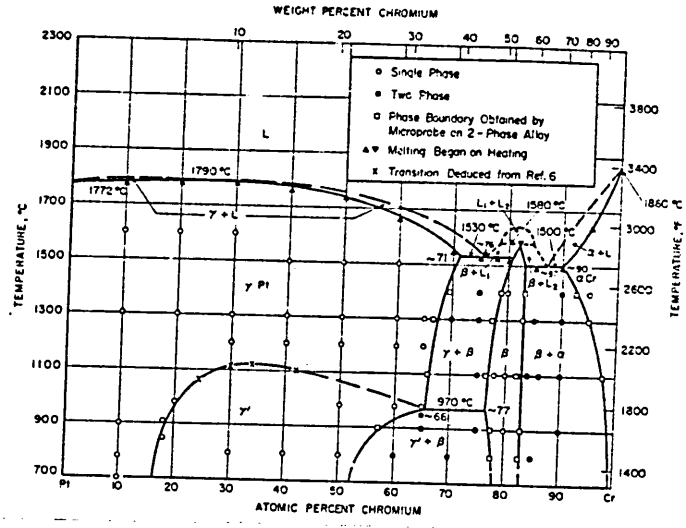
WEIGHT PERCENT CHROMIUM
ATOMIC PERCENT CHROMIUM
TEMPERATURE, °C
TEMPERATURE, °F
Single Phase
Two Phase
Phase Boundary Obtained by Microprobe on 2-Phase Alloy
Melting Began on Heating
Transition Deduced from Ref. 6
L
1790 °C
1772 °C
1530 °C
1580 °C
1500 °C
970 °C
~71
~77
~66
γ + L
γ Pt
γ + β
β
β + σ
β + L
σ Cr
Pt
Cr

Fig·6·1

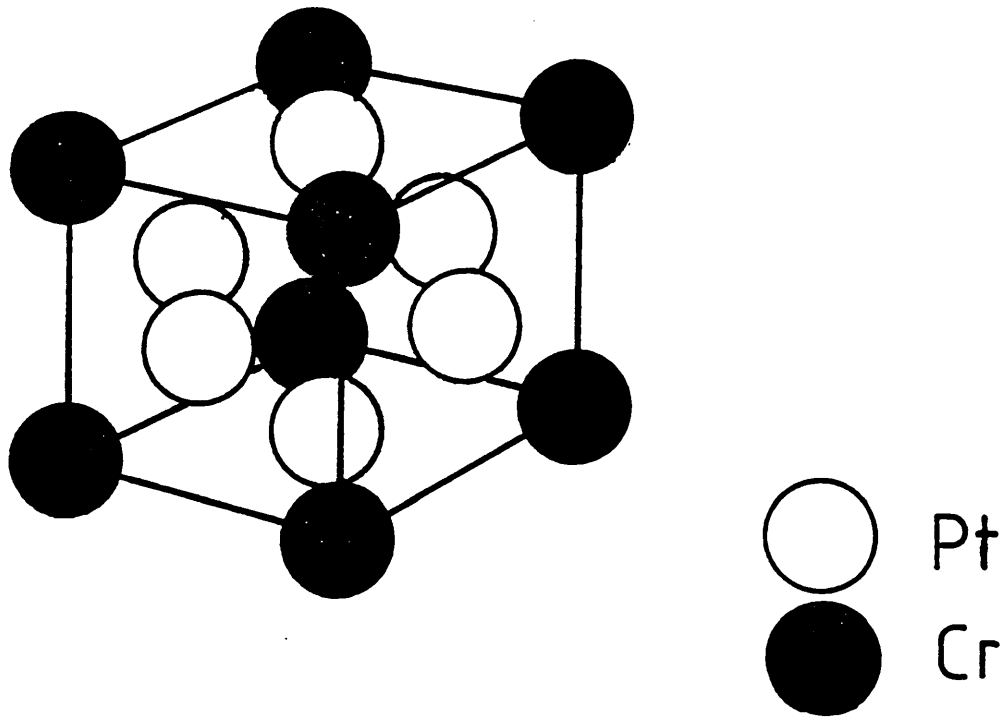
Pt
Cr

Fig. 6·2

value of $0.56\mu_B$/at (Besnus and Meyer (1973)). This may suggest some atomic disorder in the sample used by Pickart and Nathans. The existence of a moment on the Pt site has recently been put in doubt by the Pt Mossbauer effect measurements of Vincze, Wagner, Baggio-Saitovitch and Koch (1976).

Ordered Pt rich Pt-Cr alloys between 15% and 50% Cr also order magnetically. The saturation magnetization of these alloys increases from near zero at 15% Cr to a maximum of $0.63\mu_B$/at at the stoichiometric composition of 25% Cr and subsequently decreases to zero at 50% Cr. The Curie (or Neél) temperature, on the other hand, increases continuously over this concentration range and reaches a maximum of 1200K at 50% Cr. (Besnus and Meyer (1973a)). The magnetic order appears to evolve gradually from ferrimagnetism at 25% Cr to antiferromagnetism at 50% Cr (Pickart and Nathans (1963)). These systematic trends have been interpreted by Besnus and Meyer (1973) in terms of antiferromagnetic coupling between Cr nearest neighbours.

6.2.3 Magnetic properties of related Pt_3-3d compounds

Several 3d metals form magnetically and atomically ordered compounds of the form Pt_3-3d with Pt. Of these; Pt_3Fe, Pt_3Co, and Pt_3Mn have the same crystal structure as Pt_3Cr. Pt_3V is known to order atomically into the Cu_3Au structure but also exists in a tetragonal $TiAl_3$ form. Magnetic order has been established for the latter form of Pt_3V (Bieber, Chakari and Kuentzler (1980)). There is some evidence that the Cu_3Au crystal modification of Pt_3V may also order magnetically (Kawakami and Goto (1979)).

Ordered Pt_3Co and Pt_3Mn are ferromagnetic (Pickart and Nathans (1962), whilst Pt_3Fe is antiferromagnetic (Bacon and Crangle (1963)). The magnetization density in ordered Pt_3Mn and Pt_3Co has been studied by Antonini et al (1969), Menzinger et

al (1972) and Menzinger and Paoletti (1966).

A small, asymmetric Pt moment which follows well a Pt^{2+} form factor was found to be aligned parallel to the 3d moment in these two compounds. The magnetic moments deduced for the series of compounds Pt_3V, Pt_3Cr, Pt_3Mn, Pt_3Fe and Pt_3Co are summarized below in Table 6.1. The moments in Pt_3V have been extrapolated from the moments in $(Pt\text{-}Ir)_3V$ (Kawakami and Goto (1979)).

Table 6.1

Magnetic moments for ordered Pt_3-3d compounds with Cu_3Au structure

3d metal	V	Cr	Mn	Fe	Co
3d moment (μ_B)	1.0	2.33	3.64	3.3	1.64
Pt moment (μ_B)	-0.3	-0.27	0.26	$\sim$0	0.26
Reference	1	2	3	4	5

Reference : (1) Kawakami and Goto (1979)
(2) Pickart and Nathans (1963)
(3) Antonini et al (1969)
(4) Bacon and Crangle (1963)
(5) Menzinger and Paoletti (1966)

6.3 Magnetization density in Pt_3Cr

6.3.1 Introduction

The Pt_3Cr crystal was grown by Dr. D. Hukin. The crystal was in the form of a regular parallelipiped with dimensions $1 \times 1 \times 10$ mm^3. The crystallographic $\langle 1\bar{1}0 \rangle$ direction lay some 10° from the sample long axis.

The crystal was annealed for 6 hours at 950°C in the γ' phase field and slow cooled to allow the development of long range atomic order. The Curie temperature, measured after this heat treatment, was 494 $\pm$ 1K (D.E.G. Williams, private communication). This is in excellent agreement with the reported values of 480-490K for fully ordered, stoichiometric Pt_3Cr.

In order to deduce the spin density from a polarized neutron measurement the nuclear structure factors must be known. Thus, an unpolarized neutron diffraction experiment was performed to determine the degree of long range order in the crystal.

6.3.2 Nuclear structure factor determination.

Two sets of Bragg reflection occur for Cu_3Au crystal structures. The first is the fundamental set of reflections for an f.c.c. lattice,

$$F_N \text{ (Fundamental)} = b_B + 3b_A \qquad (6.1a)$$

and are observed for h,k,l all even or all odd.

Here b_B and b_A are the average scattering lengths for the sites on cube edges (B sites) and face centres (A sites). In fully ordered Pt_3Cr the A site is occupied by Pt and the B site by Cr. The second set of reflections are due to atomic ordering on

the four simple cubic sublattices which make up a f.c.c. lattice. These superlattice reflections have a structure factor

$$F_N \text{ (Superlattice)} = b_B - b_A \qquad (6.1b)$$

and are observed for mixed even and odd values of h,k, and 1.

The scattering lengths b_B and b_A depend on the degree of long range atomic order and the concentration. It is useful to define the long range order parameter, S, via (Cowley (1950))

$$S = \frac{3}{4}\ \frac{(r_A - C_A)}{1 - C_A} + \frac{1}{4}\ \frac{(r_B - C_B)}{1 - C_B} \qquad (6.2)$$

where r_A and r_B are the fraction of A and B sites which are correctly occupied by A (Pt) and B(Cr) atoms, C_A and C_B are the concentrations. With this definition S = 1 for a fully ordered structure. Using this definition,

$$F_N \text{ (Fundamental)} = 4(C\ b_{Cr} + (1-C)\ b_{Pt}) \qquad (6.3a)$$

$$F_N \text{ (Superlattice)} = (b_{Cr} - b_{Pt})(16/3\ C(1-C)\ S) \qquad (6.3b)$$

where b_{Cr} and b_{Pt} are the nuclear scattering lengths for Cr and Pt. Thus, if the concentration is known, S may be determined by comparing the integrated intensity of the fundamental and superlattice reflections at sufficiently high $\sin\theta/\lambda$ for the magnetic scattering to be negligible.

An unpolarized neutron diffraction experiment was carried out using the Mark VI diffractometer at AERE, Harwell. Instrumental details and experimental procedure are given in section 3.6.3. The crystal was mounted with the <ITO> axis vertical and the integrated intensity for all reflections in the zeroth layer out to $\sin\theta/\lambda = 0.7\ \text{Å}^{-1}$ was found by ω rocks through the peaks. The measurements were performed at 77K. The structure factors

deduced from these measurements were averaged over equivalents and the results are given in Table 6.2, and shown as a function of $\sin\theta/\lambda$ in Fig. 6.3.

Table 6.2

Measured structure factors of Pt_3Cr at 77K

Superlattice Reflections		Fundamental Reflections	
(hkl)	F(hkl) (arb.units)	(hkl)	F(hkl) (arb.units)
(100)	7.16 ± 0.2	(111)	23.9 ± 0.5
(011)	6.86 ± 0.2	(200)	24.0 ± 0.6
(211)	6.26 ± 0.1	(022)	25.9 ± 1.2
(300)	6.06 ± 0.1	(311)	26.7 ± 0.2
(322)	5.96 ± 0.3	(222)	26.9 ± 0.3
(033)	5.79 ± 0.2	(004)	27.1 ± 0.5
(411)	5.92 ± 0.2	(133)	26.8 ± 0.7
(233)	5.84 ± 0.6	(422)	26.9 ± 0.8
(055)	5.73 ± 0.1	(511)	26.7 ± 1.1
		(333)	26.6 ± 0.8

As these measurements have been made below T_c there are both nuclear and magnetic contributions to the scattering and hence to the observed structure factors. The magnetic structure factors for fundamental and superlattice reflections have the same form as the nuclear structure factors,

$$F_M \text{ (Fundamental)} = 4(C\,\mu_B\,f_B + (1-C)\mu_A\,f_A) \qquad (6.4a)$$

$$F_M \text{ (Superlattice)} = (\mu_B\,f_B - \mu_A\,f_A)(16/3\;C(1-C)\;S) \qquad (6.4b)$$

Fig.6.3 Fundamental and superlattice structure factors for Pt_3Cr determined by unpolarized neutron diffraction at 77K.

Fig.6.4 Flipping ratio R as a function of λ^2 and $\lambda^3/\sin\theta$ for low angle fundamental reflections at 4.2K

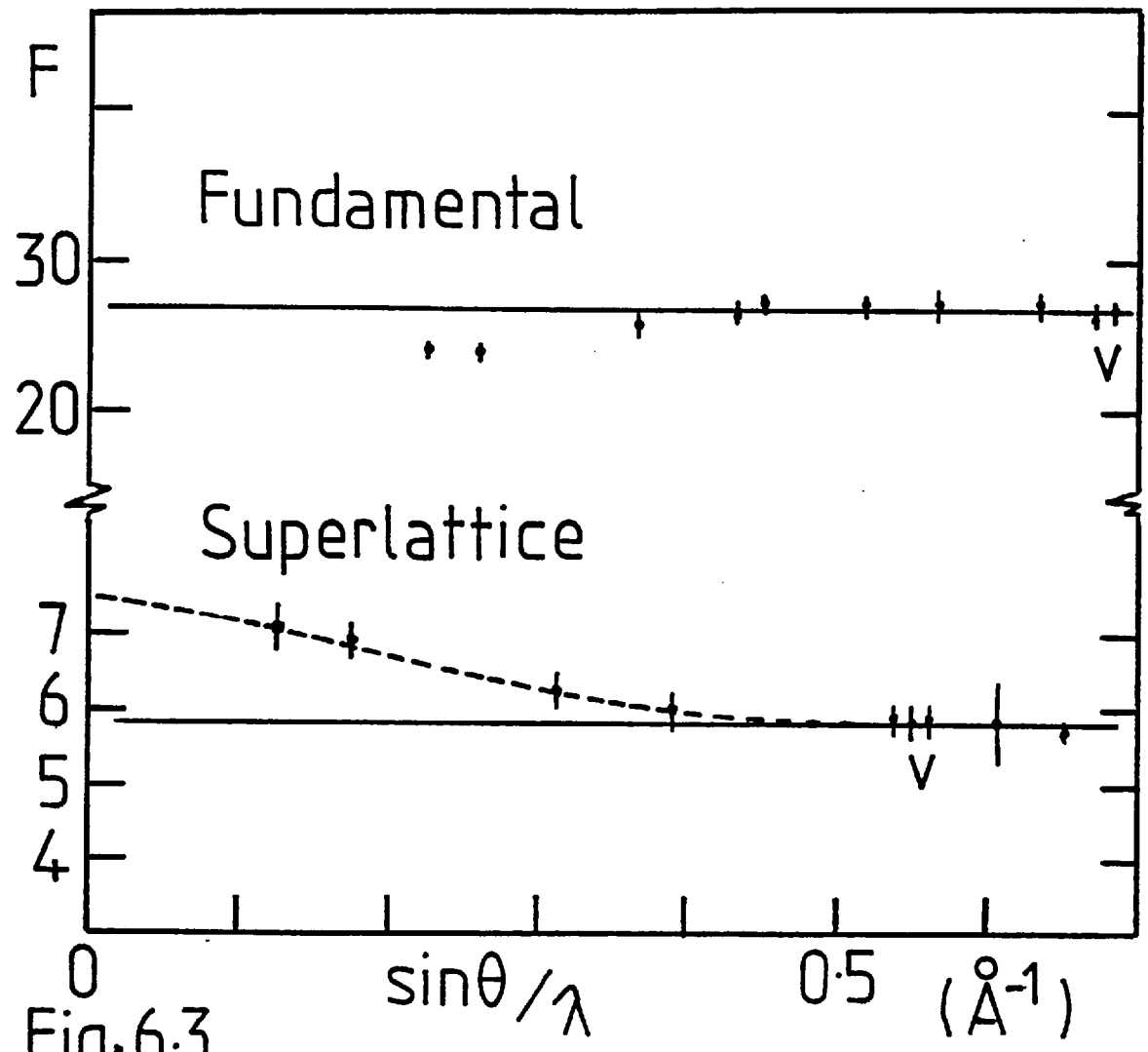
F
Fundamental
30
20
V
Superlattice
7
6
5
4
V
0
sinθ/λ
0·5
(Å-1)

Fig. 6.3

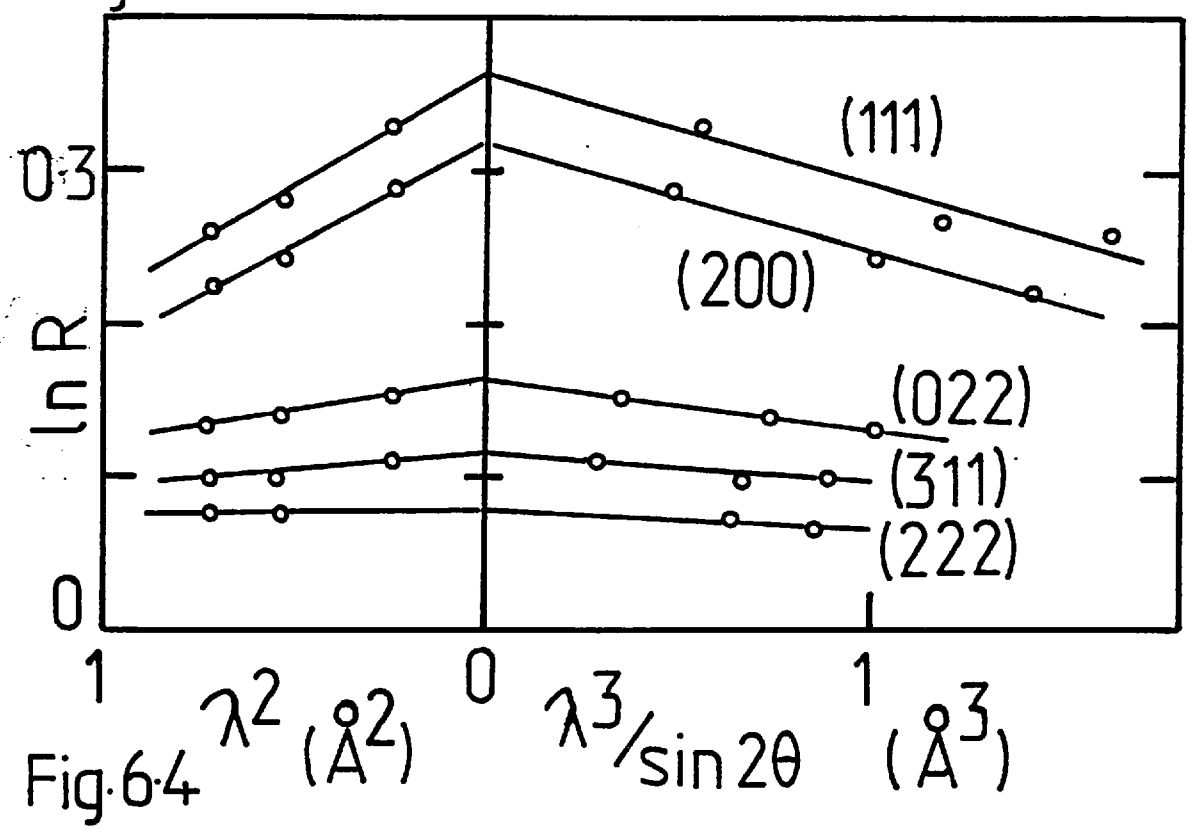
0·3
ln R
0
(111)
(200)
(022)
(311)
(222)
1
λ2 (Å2)
0
λ3/sin 2θ
1
(Å3)

Fig. 6.4

where μ_A, μ_B and f_A, f_B are the magnetic moments and magnetic form factors for A and B sites. The measured structure factor is then,

$$F(hkl) = (F_N^2 + 2/3\ F_M^2)^{\frac{1}{2}} \qquad (6.5)$$

The magnetic contribution to F(hkl) may be estimated from the moments of Pickart and Nathans (1963) together with theoretical Cr and Pt form factors (Watson and Freeman (1961), Watson-Yang, Freeman and Koelling (1977)). The magnetic contribution to the fundamental reflections is negligible in all cases (less than 0.3%) and cannot be distinguished to within experimental error (2%). The magnetic contribution to the superlattice reflections is significant at small $\sin\theta/\lambda$, amounting to 30% of F(100), but decreases rapidly for the higher angle reflections. The magnetic contribution is insignificant (less than 0.1%) beyond the (322) reflection.

The first three fundamental structure factors are considerably lower than the higher angle values and are probably affected by extinction. The variation of the Debye-Waller factor over the measured range of $\sin\theta/\lambda$ is too small to be distinguished within experimental error. Apart from the first three reflections, the fundamental structure factors are constant,

$$F_N \text{ (fundamental)} = 26.8 \pm 0.5 \text{ (arb. units)}$$

The magnetic contribution to the superlattice reflections is clearly seen in Fig. 6.3. The nuclear structure may be estimated by averaging the four highest angle reflections, for which the magnetic component is negligible, to give

$$F_N \text{ (superlattice)} = 5.85 \pm 0.10 \text{ (arb. units)}$$

The long range order parameter may be calculated from (eq6.3) using these values if the concentration and scattering lengths of Cr and Pt are known. The good agreement between T_c for this

sample, and the accepted value of T_c for stoichiometric Pt_3Cr suggests that the concentration of the crystal is close to the nominal value of 25.0% Cr. The measured lattice parameter $a = 3.88 \pm 0.02$ Å is also close to the accepted value for Pt_3Cr $a = 3.877$ Å (Lewis and Williams (1976)) but is not known to a sufficiently high accuracy to provide a sensitive check. Assuming $C = 0.25$ and $b_{Cr} = 3.532 \pm 0.01$ fm and $b_{Pt} = 9.5 \pm 0.3$ fm (Koester (1977)), a long range order parameter of

$$S = 1.08 \pm 0.05$$

is obtained. As S must always be smaller than 1.0, which corresponds to a fully ordered state, this result indicates that either some systematic error is present (perhaps due to extinction, unknown temperature factors or residual magnetic scattering) or the concentration is slightly higher than 25%. A value of $S = 1.0$ will be assumed.

With this assumption, the magnetic moments on Cr and Pt atoms may be estimated by extrapolation of the superlattice structure factor data to $\sin\theta/\lambda = 0$ (shown in Fig. 6.3). This gives

$$\mu_{Cr} - \mu_{Pt} = 2.50 \pm 0.1\mu_B$$

which, together with the bulk magnetization (Besnus and Meyer (1973))

$$C\mu_{Cr} + (1-C)\mu_{Pt} = 0.630\ \mu_B$$

gives $\mu_{Cr} = 2.5 \pm 0.1\ \mu_B$ and $\mu_{Pt} = 0.005 \pm 0.02\ \mu_B$

A more accurate measurement of the Cr and Pt moments was made with the polarized neutron technique described in the following section.

6.3.3 Measurement of magnetization density

6.3.3.1 Introduction

The principles of polarized beam diffraction in the determination of accurate magnetic structure factor data have been discussed in section 2.3. In summary: the sample is placed in a saturating magnetic field, a measurement of the scattered intensity for a particular reflection with the incident polarization parallel (I^+) and antiparallel (I^-) to the magnetization direction allows the ratio of magnetic to nuclear structure factors of the reflection to be determined with a high degree of accuracy. The ratio of I^+ to I^-, termed the flipping ratio, R, is related to the structure factors via

$$R = \frac{(1 + \varepsilon\gamma)^2}{(1 - \varepsilon\gamma)^2}$$

where ε is a contrast factor which depends on the scattering geometry and, with units explicit,

$$\gamma = 2.69\ F_M(\mu_B)/F_N(\text{fm})$$

So if F_N is known, it is possible to deduce both the magnitude and sign of F_M. The real space collinear (z) component of the magnetization density may be then found by Fourier inversion.

6.3.3.2 Results

Flipping ratios were collected using the D3 polarized neutron diffractometer at ILL, Grenoble. Measurements were performed at 4.2K in a saturating magnetic field of 1.7T. The incident polarization was 97% and flipping efficienty 97%. All accessible reflections in the $[1\bar{1}0]$ zone out to $\sin\theta/\lambda = 0.92\ \text{Å}^{-1}$ were

collected. This covered 59 independent reflections. At least three equivalent reflections were measured for each independent (hkl). The instrument and measuring procedure are described in section 3.6.2.

The γ values determined from experimental flipping ratios were corrected for imperfect polarization and flipping efficiency, scattering geometry and instrumental dead time. The corrected γ's were averaged over all equivalents.

As it was apparent from the unpolarized measurements that some of the more intense fundamental reflections suffered from extinction, the (111), (200), (222) and (311) reflections were measured again at wavelengths of 0.84 Å, 0.72 Å and 0.50 Å using the instrument D5. The instrument and experimental procedure are described in section 3.7.2. The extinction corrections were estimated using the procedure of Radhakrishna, Brown and Kaxjar (1977). The observed flipping ratios were plotted as a function of $\bar{\lambda}^2$ (primary extinction) and also as a function of $\lambda^3/\sin 2\theta$ (secondary extinction). The results are shown in Fig. 6.4.

No attempt was made to model the extinction and these plots served simply as a basis for extrapolation to $\lambda = 0$ to give the extinction free flipping ratio. The same extrapolated values were obtained, to within error, irrespective of the plotting procedure. The corrections determined in this way were important for the (111) and (200) reflections, amounting to an increase in γ of about 20%. The corrections became smaller for the higher angle reflections and amounted to 5% for the highest angle reflection investigated, (311). Reflections lying beyond (311) were assumed to be extinction free.

A series of azimuthal scans (i.e. rotation of the crystal about the scattering vector) were performed to assess the importance of simultaneous reflections (Moon and Shull (1964)). The (100) (110) (111) (200) (220) (222) and (311) sets of reflections

were studied. Multiple reflections were absent for all but the (100) and (110) reflections where a 20% variation in flipping ratio was noted. The (100) and (110) reflections have large flipping ratios, making them inherently more sensitive to multiple reflections. No attempt was made to correct for this effect. The unpolarized neutron data for (100) and (110) was used to calculate γ and the polarized neutron data discarded.

The corrected γ values are given in Table 6.3. The factor 2.69 fm/μ_B which appears in (eq.6.4b) has been incorporated into F_M so that both F_N and F_M are in units fm.

6.3.3.3 Analysis

Magnetic structure factors were calculated from the corrected γ values using the known scattering lengths of Pt and Cr and with the assumption C = 25% and S = 1.0 (section 6.3.2). The results are shown in Fig. 6.5 and Fig. 6.6. The differences in structure factor for the same (hkl) indicates an aspherical component to the magnetization density.

The real space magnetization density was obtained by Fourier transforming the magnetic structure factor data using the Cambridge Crystallography Subroutine Library (CCSL) (Brown and Mathewson (1978)). The magnetization density in the (100) plane was calculated by averaging over a cube of volume 0.2 x 0.2 x 0.2 a^3 and is shown in Fig. 6.7. A negative density, shown by dotted contours, is found at the Pt site. The magnetization density about the Cr site is spherical, whereas the distribtuion of magnetization about the Pt site shows some asphericity. A fairly constant negative magnetization is found between the sites.

The variation of magnetization density (M(r)) as a function of distance from the Cr and Pt sites along the <100> and <110> directions is shown in more detail in Fig. 6.8. M(r) decays smoothly with increasing distance from the Cr site and shows no

Table 6.3

Corrected γ values for Pt_3Cr at 4.2K

Superlattice			Fundamental		
hkl	γ	error in last digit	hkl	γ	error in last digit
100	-0.860*	60	111	0.0880	10
110	-0.750*	50	200	0.0770	10
210	-0.409	6	220	0.0440	10
211	-0.341	4	311	0.0290	10
(300	-0.235	3	222	0.0195	5
(221	-0.217	2	400	0.0179	2
310	-0.212	3	331	0.0075	3
320	-0.140	2	420	0.0082	3
321	-0.125	1	422	0.0033	2
(410	-0.111	2	(511	0.0065	6
(322	-0.076	1	(333	-0.0005	3
(411	-0.079	1	440	0.0001	6
(330	-0.053	2	531	0.0000	10
421	-0.045	1	(600	0.0051	5
332	-0.024	2	(442	-0.0017	8
(500	-0.046	2	620	0.0012	7
(430	-0.030	4	533	-0.0031	7
(510	-0.051	3	622	-0.0002	8
(43	-0.026	3	711	0.0028	6
(520	-0.029	3	551	0.0031	7
(432	-0.008	3			
521	-0.022	6			
(522	-0.009	5			
(441	-0.011	3			
(530	-0.006	3			
(433	0.010	3			
610	-0.032	5			
(611	-0.021	5			
(532	0.014	4			
(443	0.014	6			
(540	0.003	6			
(621	-0.015	3			
541	0.006	7			
542	-0.004	8			
631	0.013	8			
550	0.029	6			
(700	-0.013	10			
(632	0.009	8			
710	-0.010	7			

* Taken from unpolarized data

Fig.6.5 Magnetic structure factors for fundamental reflections at 4.2K; solid line is Fit 4 as described in the text.

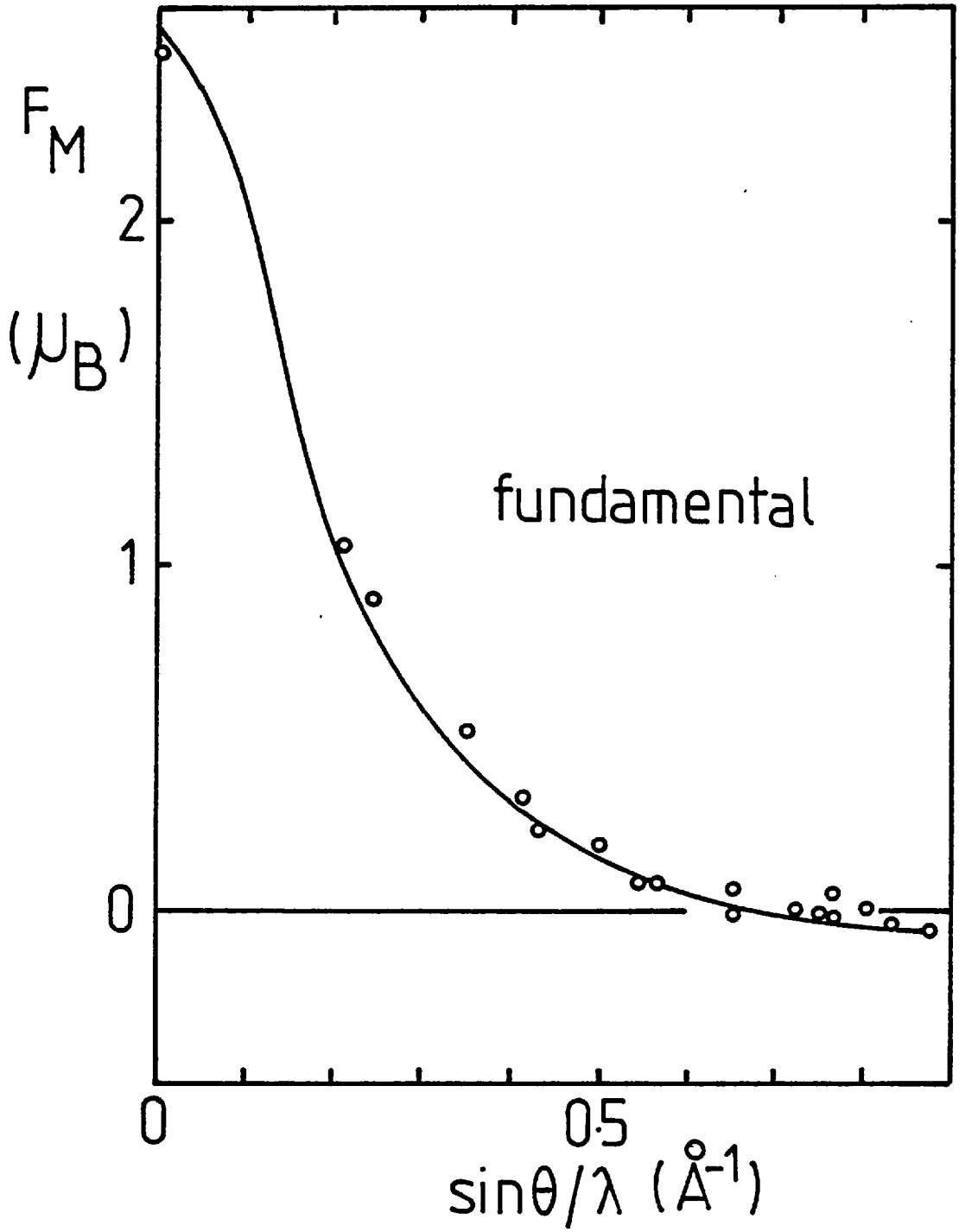

Fig·6·5

Fig.6.6 Magnetic structure factors (F_M) in μ_B for superlattice reflections at 4.2K. Full circles are results of unpolarized measurements. Solid line is Fit 4 as described in text.

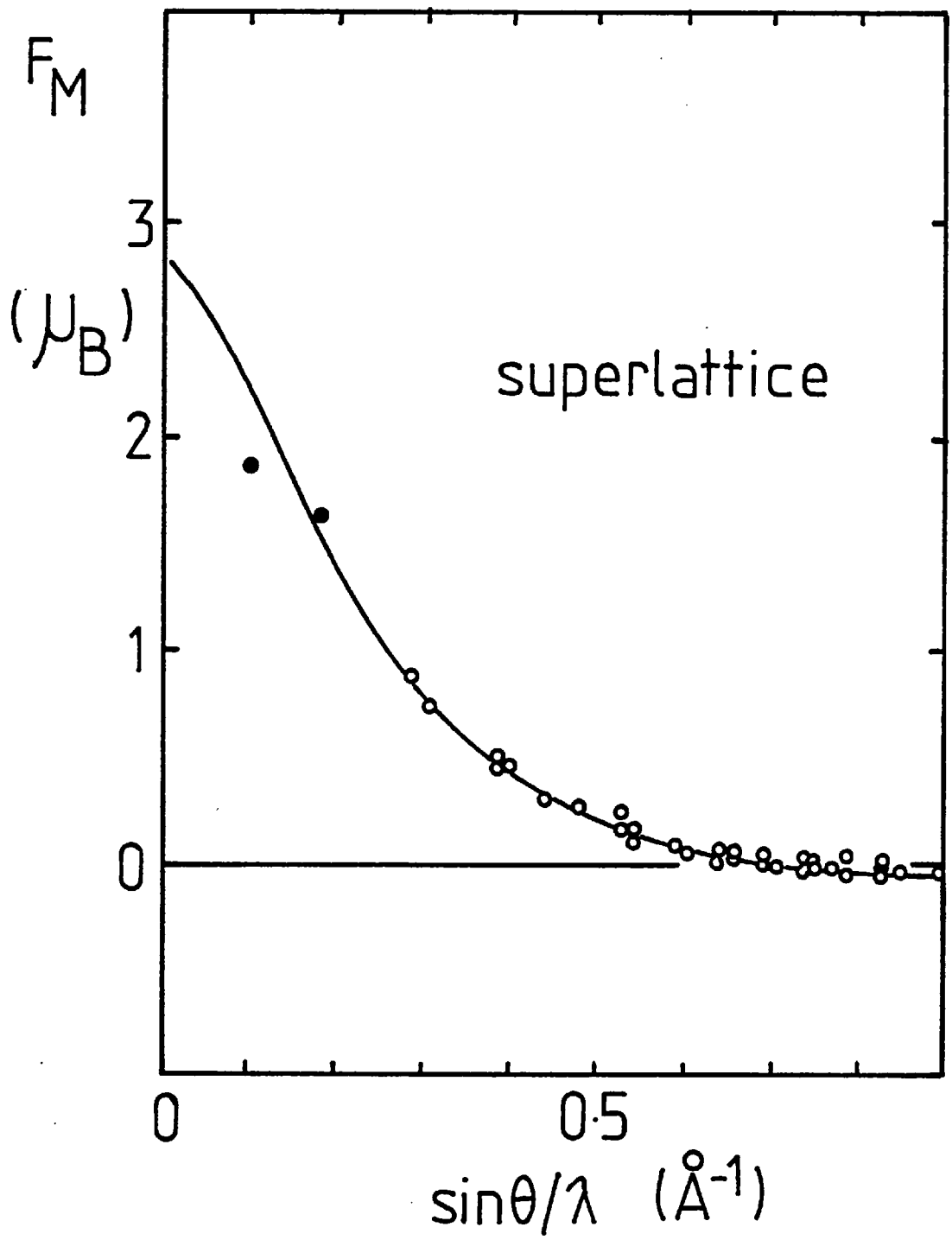

Fig. 6·6

Fig.6.7 The magnetization density in the (100) plane for Pt_3Cr. Contour levels are in units $\mu_B/\mathring{A}^3$ and negative contours are shown dashed.

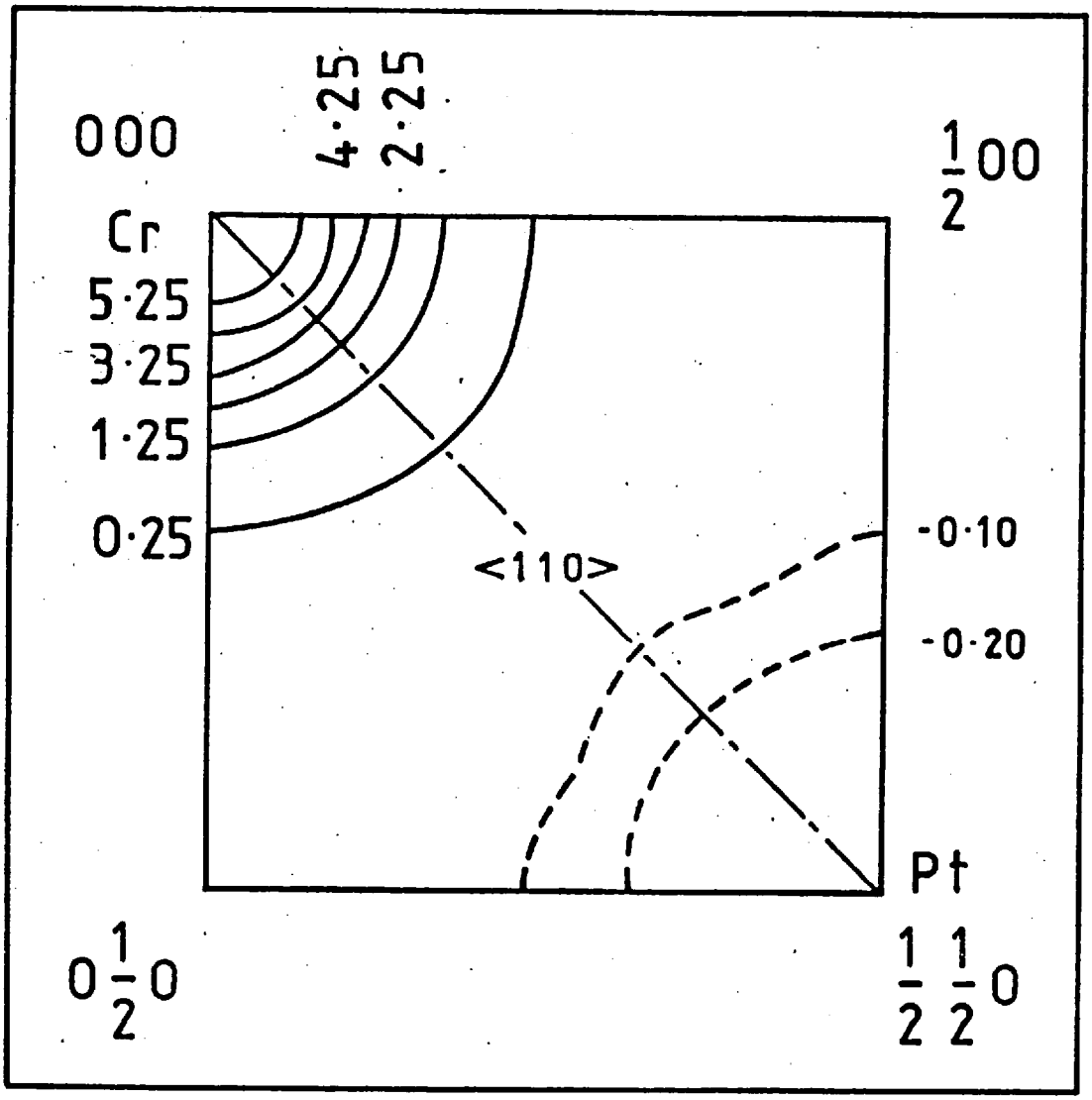

Fig. 6·7

Fig.6.8 Distribution of magnetization density about Pt and Cr sites along the <100> and <110> directions

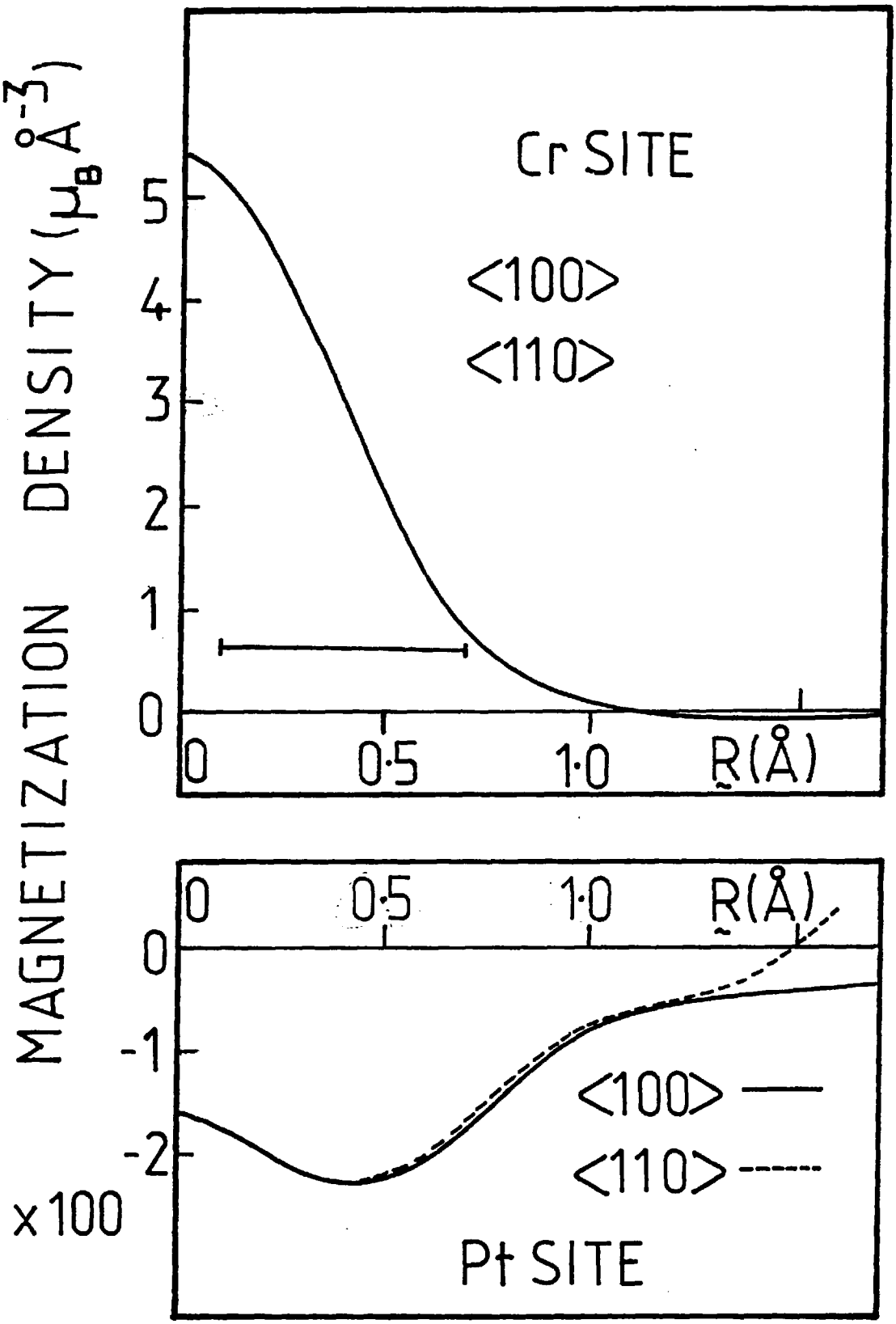
MAGNETIZATION DENSITY (μ_B Å^{-3})
Cr SITE
<100>
<110>
5
4
3
2
1
0
0
0·5
1·0
R(Å)
0
0·5
1·0
R(Å)
0
-1
-2
x100
<100>
<110>
Pt SITE

Fig. 6·8

asphericity. The variation of M(r) around the Pt site is quite different; M(r) does not reach a minimum value at the Pt site itself but shows a local minimum at a radius of $\sim$0.5 Å. As M(r) must decrease monotonically with distance from a Pt atom (Watson-Yang et al (1977)), this implies that both Cr and Pt moments, coupled antiparallel, are present on the Pt sites. This indicates that the alloy is either not fully ordered or deviates from the stoichiometric Pt_3Cr composition.

The disposition of Pt and Cr moments at the Pt site is not immediately obvious. The Pt moment may be antiparallel and the Cr moment parallel to the moment on Cr sites, as for ferrimagnetic Pt_3Cr. Alternatively, the Pt moment may be parallel and the Cr moment antiparallel to the moment on Cr sites, indicating a ferromagnetic structure for fully ordered, stoichiometric Pt_3Cr. Whatever the case, this observation implies a non zero moment on Pt atoms in Pt_3Cr.

The individual moment values were estimated by least squares fitting the magnetic structure factor data using spin only theoretical spherical form factors. No attempt was made to analyse the anisotropic part of the form factors, partly due to the fact that the anisotropic temperature factors were not known. The Cr form factor was taken from the Hartree-Fock calculations of Watson and Freeman (1961) for atomic Cr and the Pt form factor from the relativistic calculation of Watson-Yang, Freeman and Koelling (1977), only the $\langle j_o \rangle$ part was used. The fits were carried out using the CCSL least squares fitting routine.

A number of fits were attempted:

Fit 1: Cr moment on Cr site, zero moment on Pt site.

Fit 2: Cr moment on Cr site, Pt moment on Pt site.

Fit 3: Cr moment on Cr site, Cr moment on Pt site.

Fit 4: Cr moment on Cr site and both Cr moment and Pt moment on Pt site.

Two different weighting schemes were used. In the first scheme, all structure factors were given unit weight (W = 1) and in the second, statistical weighting ($W = 1/\text{error}^2$) was used. The bulk magnetization taken from Besnus and Meyer (1973) was entered as a structure factor for the (000) fundamental reflection but was not used as a constraint for the fits.

The results of these fits are given in Table 6.4. Here CRS, PTS and CRPS are respectively the moment on Cr sites, the Pt moment on Pt sites and the Cr moment on Pt sites. RW is a measure of the goodness of fit,

$$RW = \frac{\Sigma W \left| F_{obs} - F_{calc} \right|^2}{\Sigma W \left| F_{obs} \right|^2}$$

Table 6.4

Results of least squares fits to magnetic structure factor data using theoretical form factors

FIT	UNIT WEIGHTS				STATISTICAL WEIGHTS			
	CRS (μ_B)	PTS (μ_B)	CRPS (μ_B)	RW	CRS (μ_B)	PTS (μ_B)	CRPS (μ_B)	RW
1	2.776	ZERO	ZERO	2.09	2.734	ZERO	ZERO	1.39
2	2.935	-0.124	ZERO	1.36	2.869	-0.114	ZERO	0.69
3	2.935	ZERO	-0.124	1.32	2.877	ZERO	-0.118	0.66
4	2.944	-0.008	-0.118	1.32	2.886	0.318	-0.439	0.62

The moments on Pt and Cr sites are relatively insensitive to the nature of the fit, as long as a moment is allowed on the

Pt site. The Cr moment varies between 2.87 μ_B and 2.94 μ_B and the moment at the Pt site varies from -0.11μ_B to -0.12 μ_B. In both weighting schemes, Fit 3 is marginally preferred to Fit 2, the moment distribution at the Pt sites is better described by a single Cr form factor rather than a single Pt form factor. This tendency is born out more clearly in the best fit, Fit 4, where the major part of the negative moment is described by a Cr form factor. If statistical weighting is used, a positive Pt moment and a negative Cr moment on Pt sites is obtained. This latter fit is shown in Figs. 6.5 and 6.6.

Better fits could be obtained using more parameters. In particular the $\langle j_2 \rangle$ term which occurs in the orbital part of the form factor and the $\langle j_4 \rangle$term which appears in the aspherical part of the form factor could be included. A better knowledge of the site disorder is required before such a scheme can be completed.

In summary, the present data give a moment on Cr sites of 2.88 $\pm$ 0.06 μ_B and a moment on Pt sites of -0.12 $\pm$ 0.01μ_B, where the error has been estimated from the variations according to fitting routine. The moment at the Pt sites is best described by a ferromagnetic Pt moment and an antiferromagnetic Cr moment.

6.3.4 Discussion

A moment of 2.9μ_B is large for Cr. By comparison, Pickart and Nathans (1963) obtained 2.33 μ_B. Some support for this larger value may be derived from susceptibility measurements above T_c for which P_{eff} = 3.6 μ_B is obtained (Goto (1977)). It is interesting to note that large 3d moments are observed in other Pt_3 - 3d compounds (Table 6.1).

A positive Pt moment implies a ferromagnetic, rather than ferrimagnetic structure for Pt_3Cr, in contradiction with the

results of Pickart and Nathans (1962)(1963). The present result is not solely dependent on fits to the magnetic structure factor data. The fact that the Fourier maps reveal a two component structure at the Pt sites, together with the assumption of antiferromagnetic nn Cr-Cr interactions used in phenomenological descriptions of Pt-Cr alloys, also implies a positive Pt moment.

A larger Cr moment and a positive Pt contribution is more consistent with the Pt Mossbauer data of Vincze et al (1976).

APPENDIX A

EFFECT OF SHAPE ANISOTROPY ON SMALL ANGLE SCATTERING

Consider an ensemble of rodlike particles with random orientations. Each atomic spin within the cluster ($\underset{\sim}{S}_i$) is strongly coupled via ferromagnetic interactions to every other spin to form the total moment $\underset{\sim}{S}_{tot}$. The total moment tends to be aligned along the rod axis to minimize the dipolar magnetostatic energy of the rod, this tendency toward alignment is described by the Hamiltonian,

$$\mathcal{H} = - KV\cos^2\psi \tag{A.1}$$

where ψ is the angle between the rod axis and the total spin. This tendency toward alignment along the rod axis is known as "shape anisotropy".

For convenience let us assume that there is no correlation between the total spins on distinct particles and that the rods are one dimensional with a (nuclear) radius of gyration R_G which is the same for each particle. The small angle scattering from such a system is described by the Guinier formula (2.52a) with the κ^2 term dependent on the function $\overline{R^2}$ given by (2.52b). It has been shown by Blech and Averbech (1964) and section 2.2.5, that the coefficients a_n and b_n can be related to the angles ψ and ψ' shown in Fig. 2.1. In our case ψ is the angle made between the rod axis (identical to $\underset{\sim}{r}_n$) and the total spin $\underset{\sim}{S}_{tot}$. As the atomic spins at $\underset{\sim}{R}_i$ and $\underset{\sim}{R}_{i+n}$ are rigidly correlated, $\psi' = \psi$, equations (2.39) become

$$a_n = \overline{\langle S^2 p_i p_{i+n} \sin^2\psi \rangle}$$

$$b_n = \overline{\langle S^2 p_i p_{i+n} (2\cos^2\psi - \sin^2\psi) \rangle}$$

Substituting these results in (2.52b) one finds

$$\overline{R^2} = \left(\frac{1}{2}\frac{\sum_n \overline{p_i p_{i+n}}\, r_n^2}{\sum_n \overline{p_i p_{i+n}}}\right) \frac{\langle\sin^2\psi\rangle + \frac{1}{5}\langle 2\cos^2\psi - \sin^2\psi\rangle}{\langle\sin^2\psi\rangle + \frac{1}{3}\langle 2\cos^2\psi - \sin^2\psi\rangle}$$

which is easily simplified to give

$$\overline{R^2} = R_G^2\left(\frac{3}{5}\langle 1 + \sin^2\psi\rangle\right) \qquad (A.2)$$

At high temperatures $\langle\sin^2\psi\rangle = \frac{2}{3}$ as the total moment is free to rotate over all orientations with equal probability and $\overline{R^2} = R_G^2$ as expected. However, at low temperatures the total spin is constrained to lie along the rod axis and $\langle\sin^2\psi\rangle = 0$ which gives a lower value of $\overline{R^2}$, $\overline{R^2} = \frac{3}{5} R_G^2$. This is a direct consequence of the vector form of the neutron-magnetic moment interaction and does not reflect a physical decrease in correlation length which remains constant at R_G.

The behaviour between these two limits can be calculated by using the Hamiltonian A.1,

$$\langle\sin^2\psi\rangle = \frac{\int_0^\pi \sin^2\psi \exp(\beta KV \cos^2\psi)\sin\psi d\psi}{\int_0^\pi \exp(\beta KV \cos^2\psi)\sin\psi d\psi}$$

which can be alternatively written

$$\langle\sin^2\psi\rangle = 1 - \frac{d}{dx}\ln\int_0^1 e^{xu^2}\, du$$

where $X = KV/kT$. The integral is simply the hypergeometric function ${}_1F_1(\frac{1}{2}; \frac{3}{2}; X)$ which has the derivative $\frac{1}{3}\,{}_1F_1(\frac{3}{2}; \frac{5}{2}; X)$ and so

$$\langle\sin^2\psi\rangle = 1 - \frac{1}{3}\frac{{}_1F_1(\frac{3}{2}; \frac{5}{2}; X)}{{}_1F_1(\frac{3}{2}; \frac{3}{2}; X)} \qquad (A.3)$$

The confluent hypergeometric functions are tabulated and substitution of the appropriate values gives the variation of R with KV/KT shown in Fig. A.1.

Fig.A.1 Variation of the apparent radius of gyration (R) with KV/kT for a one dimensional particle with radius of gyration R_G and shape anisotropy KV.

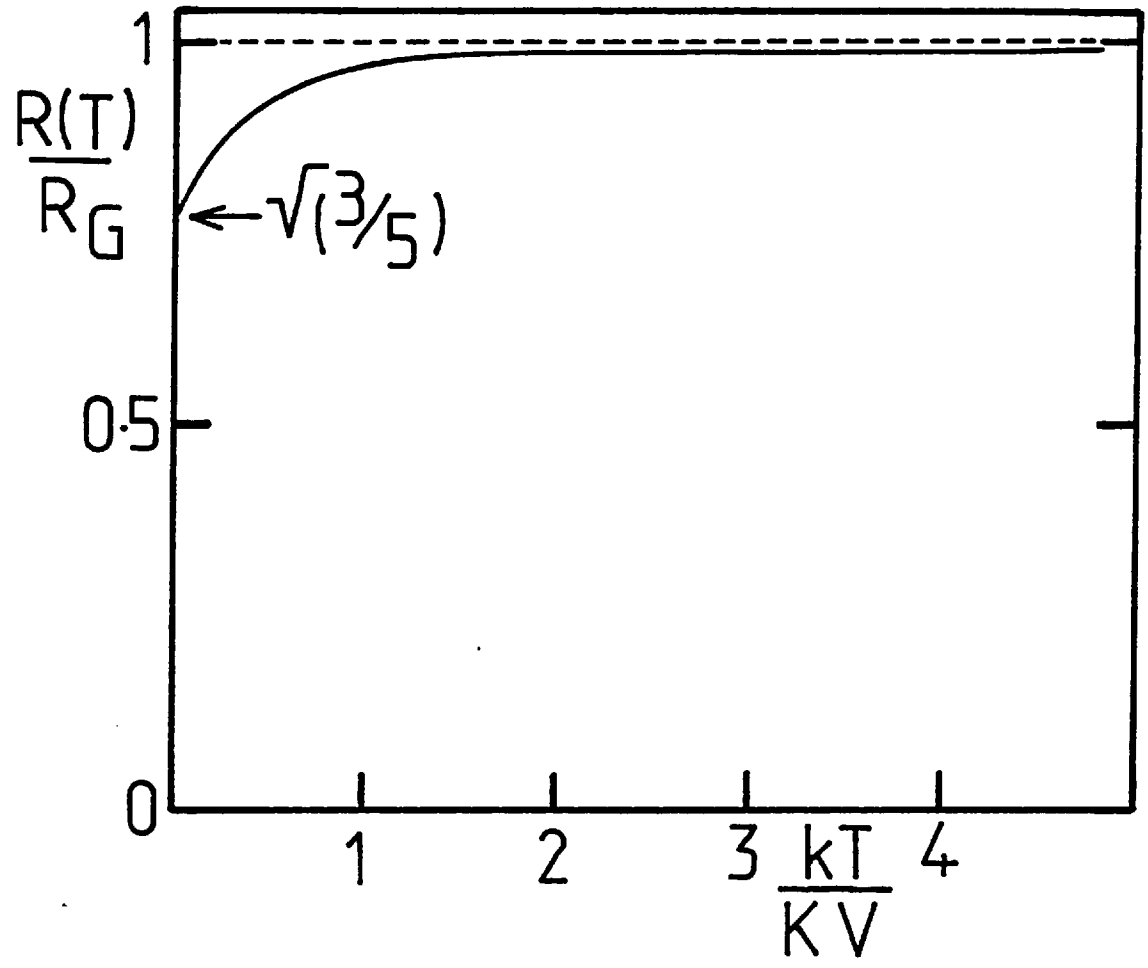

Fig. A·1

APPENDIX B

A polymer model for the small angle scattering law

In this appendix an analogy is drawn between the scattering law for polymers in solution and magnetic correlations close to C_F. This idea was developed in collaboration with M. Warner of Imperial College (Burke, Rainford and Warner (1980)). Whilst it is not expected that magnetic correlations in Cr Fe alloys should behave like a polymer, the random walk statistics of a polymer chain provide an interesting class of geometrical correlations which are worth exploring: especially in view of the lack of closed forms for the small angle scattering law. The model is simple enough to allow magnetostatic shape anisotropy to be treated.

The small angle magnetic scattering law may be written,

$$S(\kappa) \sim N^{-2} \sum_{ij} \overline{\langle \underset{\sim}{S}_i \cdot \underset{\sim}{S}_j \exp\left(i \underset{\sim}{\kappa} \cdot (\underset{\sim}{R}_i - \underset{\sim}{R}_j)\right) \rangle} \qquad (B.1)$$

In the spirit of percolation theory, we consider the scattering to be due to large but finite clusters of ferromagnetically coupled spins. Intercluster interactions will be neglected and the infinite cluster, if present, contributes a delta function response at $\kappa = 0$ and need not be considered.

In order to calculate $S(\kappa)$ we represent a finite cluster by a chain of N spins connected in a random walk. All clusters are assumed to contain the same number of spins. The clusters so described correspond to a Gaussian polymer chain. This description may bear some relation to the actual 3 dimensional clusters near C_F in that percolation clusters tend to be ramified or stringy in shape. Furthermore, predominantly one dimensional clusters will dominate the average in (eq. B.1).

In calculating $S(\kappa)$ we consider two possibilities,

(a) Exchange only

In this case, the temperature is sufficiently low that all spins within the cluster are well correlated with each other and are oriented along a common, fixed magnetic axis (Fig. B.1). Then,

$$S(\kappa) \sim 2/3\ S^2\ N^{-2} \sum_{ij}^{N} \langle\langle \exp(i\underset{\sim}{\kappa}\ (\underset{\sim}{R}_i - \underset{\sim}{R}_j)) \rangle\rangle \qquad (B.2)$$

where $\langle\langle\ \rangle\rangle$ is the configurational average over Gaussian walks. Following a standard argument in polymer physics (Flory (1969)), we have

$$\sum_{ij} \langle\langle \exp\ (i\underset{\sim}{\kappa}.(\underset{\sim}{R}_i-\underset{\sim}{R}_j)) \rangle\rangle \ = \sum_{ij} \exp(-\kappa^2\ a^2 C\ |i-j|\ /6) \quad (B.3)$$

where the mean square distance between spins number i and j is proportional to $|i-j|$, the number of steps separating them along the chain. Here a is the nearest neighbour distance and C, the 'characteristic ratio' is a measure of chain stiffness. C = 1 for a freely jointed chain.

The double summation in (eq.B.3) may be evaluated to give

$$\sum_{ij} \exp(-\ |i-j|\ m) \ = \ (1-x)^{-2}\ (2N(1-x)-2x(1-x^N)-N(1-x)^2) \quad (B.4)$$

where $m = \kappa^2\ a^2\ C/6$ and $x = \exp(-m)$. In the limit of small m but finite Nm this expression leads to the Debye scattering law,

$$S_D(V) \sim 2V^{-2}\ (V + \exp(-V) - 1) \qquad (B.5)$$

where $V = Nm = \kappa^2\ R^2$ and R is the average radius of gyration of

Fig.B.1 The spin configuration (a) due to ferromagnetic exchange only has a large magnetostatic energy due to dipolar fields. This energy may be lowered by allowing the spins to follow the local chain axis as in configuration (b), resulting in spin correlations over a characteristic length λ.

Fig.B.2 Plot of reciprocal scattering law $S(V)^{-1}$ versus V for values of r^2/R^2 of 0, 0.01 and 0.04. The dashed line represents the Lorentzian approximation to the scattering at low V.

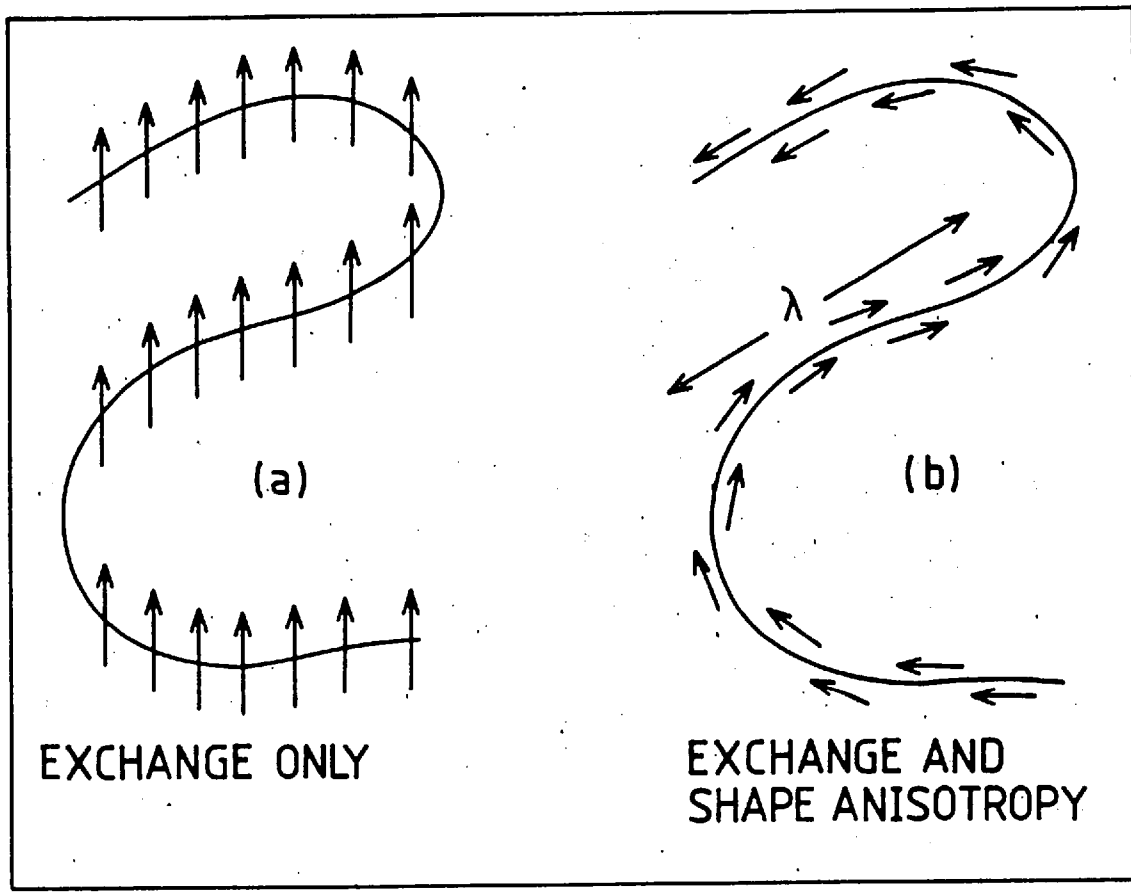
(a)
EXCHANGE ONLY
λ
(b)
EXCHANGE AND
SHAPE ANISOTROPY

Fig.B.1

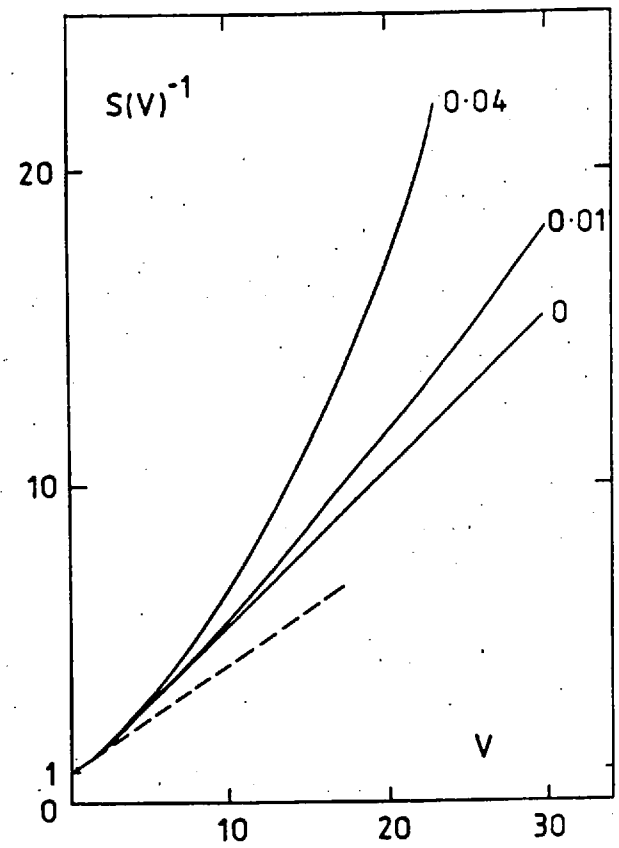
S(V)⁻¹
0·04
0·01
0
20
10
1
0
10
20
30
V

Fig.B.2

the chain. This expression closely resembles a Lorentzian for $V \lesssim 3$ and reduces to the familiar Guinier limit for $V \ll 1$. For large V, further terms must be taken into account leading to

$$S(V) \sim S_D(V) + r^2 R^{-2} (2V^{-1}(1 - \exp(-V) - \tfrac{1}{2}V)) \qquad (B.6)$$

where $r^2 = Ca^2/6$. A plot of $1/S(V)$ VS V for various values of r^2/R^2 is shown in Fig. B.2. It is interesting to note that a deviation from Lorentzian behaviour similar to that observed in section 5.5.2 is seen at large V, $V \gtrsim 3$.

(b) Exchange and magnetostatic shape anisotropy

The magnetostatic energy of the cluster will tend to be minimized if the spins are aligned along the local 'chain' axis. The final spin configuration will be determined by the competition between this shape anisotropy and the exchange interaction (Fig.B.1). Firstly, without exchange, the correlations can only persist over a distance typical of the correlation in direction of the tangent of the 'chain' trajectory. The correlations will be enhanced by the presence of exchange interactions. Denoting the correlation length along the chain by λ the spin correlations along the chain are given by

$$\langle \underset{\sim}{S}_i . \underset{\sim}{S}_j \rangle \sim \exp(- |i-j| \, a/\lambda) \qquad (B.7)$$

Using this expression, $S(\kappa)$ may be calculated by replacing m in (eq.B.4) with $(\kappa^2 Ca^2/6 + a/\lambda)$. For $\kappa a \ll 1$ and $\lambda \gg a$ with Na/λ and $\kappa^2 R^2$ finite (eq.B.5) may be used to yield,

$$S(\kappa) \sim 2 (\kappa^2 R^2 + L/\lambda)^{-2} (\kappa^2 R^2 + L/\lambda - 1 + e^{-L/\lambda} e^{-\kappa^2 R^2})$$

which reduces to a Guinier law with a squared radius of gyration

$$R_G^2 = R^2 \ (1 - L/2\lambda) \qquad (B.8)$$

if $L/\lambda, \kappa^2 R_G^2 << 1$. Here L is the total length of the chain. The presence of shape anisotropy reduces the range of magnetic correlations. (It should be noted that the interplay between cluster shape and moment direction discussed in Appendix A has not been considered here.)

REFERENCES

Abrikosov A.A. and Gorkov L.P., 1961
Sov. Phys. JEPT 12 1243-54.

Aharony A. and Fisher M.E. 1973
Phys. Rev. B8 3323-3341

Aldred A.T. 1976
Phys. Rev. B14 219-227

Aldred A.T., Rainford, B.D., Kouvel J.S. and Hicks T.J. 1976
Phys. Rev. B14 228-234

Aldred A.T. and Kouvel J.S. 1977
Physica 86-88B 329-30

Alloul H. 1979
Phys. Rev. Lett. 42 603-6

Als-Nielsen J.1976
Phase Transitions and Critical Phenomena Vol.5A,
ed. C. Domb and M.S. Green (Academic Press: London) 87-164

Amamou A., Caudron R., Costa P., Freidt J.M., Gautier F. and Loegel B.
1976 J. Phys. F: Metal Physics 6 2371-88

Anderson P.W. 1979
Ill Condensed Matter - Les Houches 1978
ed. R. Balion, R. Maynard and G. Toulouse (North Holland-Amsterdam)
Course 3

Anderson P.W., Halperin B.I. and Varma C.M. 1972
Phil. Mag. 25 1-9

Antonini B., Lucari F., Menzinger F. and Paoletti A. 1969
Phys. Rev. 187 611-618

Antonoff M.M. 1977
Physica 91B 193-8

Antonoff M.M. 1978
Inst. Phys. Conf. Ser. No. 39: Chapter 7 613-616

Arajs S. and Dunmyre G.R. 1966
J. Appl. Phys. 37 1017-18

Arajs S., Rao K.V., Åström H.V. and de Young F.T. 1973
Phys. Scripta 8 109-112

Arrott A. 1957
Phys. Rev. 108 1394-1396

Arrott A, 1966
Magnetism Vol.2B ed. G.T. Rado and H. Suhl
(Academic Press: New York.) 295-416

Arrott A., Werner S.A. and Kendrick H. 1967
Phys. Rev. 153 624-31

Arrott A.S., Heinrich B. and Noakes J.E., 1972
AIP Conf. Proc. No. 10 822-26

Asano S. and Yamashita J. 1967
J. Phys. Soc. Japan 23 714-736

Åström H.V., Gudmundsson H., Hedman L. and Rao K.V. 1977
Physica 86-88B 332-4

Åström H.V., Benediktsson G. and Rao K.V. 1978
J. Phys. Colloq. 39 C6

Ausloos M. 1977
J. Magn. Magn. Mater. 5 156-60

Babic B., Kazjar F. and Parette G. 1980
J. Physique to be published.

Bacon G.E. 1962
Neutron Diffraction (Clarendon Press: London) second edition p.96 ff

Bacon G.E. and Crangle G. 1963
Proc. Roy. Soc. (London) 272 387-405

Barber A. 1974
Thesis, University of London, unpublished.

Barker A.S. and Ditzenberger J.A. 1970
Phys. Rev. B1 4378-4400

Baston A.H. 1972
Internal Report AERE Harwell, AERE-M 2570

Bean C.P. and Livingston J.D. 1959
J. Appl. Phys. 30 Suppl. 1205-1295

Beck P.A. 1979
Prog. Mater. Sci. 23 1-49

Besnus M.J. and Meyer A.J.P. 1973a
Phys. Stat. Sol. (b) 55 521-525

Besnus M.J. and Meyer A.J.P. 1973b
Phys. Stat. Sol.(b) 58 533-543

Bieber A., Chakari A. and Kuentzler R. 1980
J. Mag. Mag. Mater. 15-18 1161-2

Birgeneau R.J., Cowley R.A., Shirane G. and Guggenheim H.J.
Phys. Rev. Lett. 37 940-943

Birgeneau R.J., Cowley R.A., Shirane G., Tarvin J.A. and Guggenheim H.J.
1980 Phys. Rev. B21 317-22

Bleck I.A. and Averbech B.L. 1964
Physics 1 31-44

BNL 325 1973
Neutron Cross Sections

Booth J.G. 1966
J. Phys. Chem. Solids 27 1639-1645

Booth J.G., Ziebeck K.R.A. and Chagnon R. 1978
J. Phys. F.: Metal Phys. 8 1303-8

Boronkay S. and Collins M.F. 1973
Int. J. Magn. 4 205-212

Boucher B., Lienard A., Rebouillat J.P. and Schweizer J. 1979
J. Phys. F: Metal Phys. 9 1433-1440

Bozorth R.M. 1951
Ferromagnetism (Van Nostrand: New Jersey) p714.

Bray A.J. and Moore M.A. 1979
J.Phys. C: Sol. State 12 79-104

Bray A.J. , Moore M.A. and Reed P. 1980
J. Magn. Magn. Mater. 15-18 102

Brown P.J. and Forsyth B. 1964
Brit. J. Appl. Physics 15 1529

Brown P.J. Wilkinson C., Forsyth J.B. and Nathans R. 1965
Proc. Phys. Soc. 85 1185-89

Brown P.J. and Mathewson J.C. 1978
"Cambridge Crystallography Subroutine Library Users' Guide"
Rutherford Laboratory RL 78 010/C

Burke S.K., Rainford B.D. and Warner M. 1980
J. Mag. Mag. Mater. 15-18 259-261

Canella V. 1973
Amorphous Magnetism ed. Hooper and Graaf (Plenum Press: New York) 195-206

Chandra D. and Schwartz L.H. 1971
Met. Trans. 2 511-519

Cheng C.H., Wei C.T. and Beck P.A. 1960
Phys. Rev. 120 426-36

Coles B.R. Sarkissian B.V.B. and Taylor, R.H. 1978
Phil. Mag. 37 489-98

Collins M.F., Minkjewicz V.J., Nathans R, Passell L. and Shirane G.1969
Phys. Rev. 179 417-430

Corliss L., Hastings J., and Weiss R. 1959
Phys. Rev. Letts. 3 211

Cowley J.M. 1950
J.Appl.Phys. 21 24-30

Cowley R.A., Shirane G, Birgeneau R.J. and Svensson E.C. 1977
Phys. Rev. Lett. 39 894-897

Cowley R.A., Birgeneau R.J. and Shirane G. 1979
Lecture notes on 'Ordering in Strongly Fluctuating Condensed Matter Systems'
NATO Advanced Study Institute, Geilo (Norway) (New York: Plenum)

Cowley R.A., Birgeneau R.J., Shirane G., Guggenheim H.J. and Ikeda H. 1980 Phys. Rev. B21 4038-48

Crangle J. and Scott W.R. 1964
Phys. Rev. Lett. 12 126-8

Cywinski R., Booth J.G. and Rainford B.D. 1977
J.Phys. F.: Metal Physics 7 2567-2581

Cywinski R. and Hicks T.J. 1978
J. Phys. C: Sol. State 11 L899-901

Cywinski R. and Hicks T.J. 1980
J.Phys.F: Metal Physics 10 693-707

David P. and Heath M. 1971
J.Physique.Colloq. C1 112-113

Davis J.R. and Hicks T.J. 1977
J.Phys.F: Metal Physics 7 2153-2161

Davis J.R. and Hicks T.J. 1979
J.Phys.F: Metal Physics 9 753-761

Davis J.R., Burke S.K. and Rainford B.D. 1980
J.Magn.Magn.Mater. 15-18 151-152

Dawes D.G. and Coles B.R. 1979
J.Phys.F: Metal Phys. 11 L215-20

de Nys T. and Gielen P.M. 1971
Met. Trans. 2 1423-28

De Rozario F.A. and Smith D.A. 1977
Physica 86-88B 873-4

Dilg W. 1974
Nucl.Instr.Meths. 122 343-6

Dunn A.G, Essam J.W. and Lovelock J.M. 1975
J.Phys.C: Sol.State 5 743-750

Edwards D.M. 1980
J.Magn.Magn.Mater. 15-18 262-8

Edwards D.M. Mathon J. and Wohlfarth E.P. 1975
J.Phys.F: Metal Phys. 5 1619-1624

Edwards S.F. and Anderson P.W. 1975
J.Phys.F: Metal Physics 5 965-74

Elliot R.P. 1965
Constitution of binary alloys, first supplement (McGraw Hill: New York)

Essam J.W. 1972
Phase Transitions and Critical Phenomena Vol. 2,eds. C.Domb and M.S. Green. (Academic Press: London) 197-270

Fallot M 1936
Ann. Physique (Paris) 6 305-325

Fedders P.A. and Martin P.C. 1966
Phys.Rev.143 245-259

Fisher M.E. and Burford R.J. 1967
Phys. Rev. 156 583-622

Fisher R.M., Dulis E.J. and Carroll K.R. 1953
Trans. AIME. 197 690-700

Flory P.J. 1969
Statistical Mechanics of Chain Molecules (Wiley:New York) 340 ff.

Freeman F.F., Meardon B.H. and Williams W.G. 1978
J.Appl.Cryst. 11 80-86

Friedel J. and Hedman L.E. 1978
J. Physique 39 1225-32

Ghosh R. 1978
Internal Report I.L.L. Grenoble 78GH247T

Gorman'kov V.I., Mokhov B.N. and Nogin N.I. 1980
Sov. Phys. JEPT 50 317-322

Goto T. 1977
J.Phys.Soc. Japan 43 1848-53

Gray E. 1978
Ph.D. thesis. Monash University (unpublished)

Guinier A. and Fournet G. 1955
Small Angle Scattering of X-Rays (Wiley: New York)

Gunnarsson O. 1976
J.Phys.F: Metal Physics 6 587-606

Gupta R.P. and Sinha S.K. 1971
Phys.Rev. B3 2404-11

Guy C.N. 1976
J.Phys.F: Sci.Inst.9 790-1

Guy C.N. 1977
J.Phys.F: Metal Physics 7 1505-19

Haas J. 1978
Primary Beam Intensity on D11 and D17, Report, unpublished

Hance N.J. 1973
Internal Report, AERE Harwell, AERE M-2583

Hansen M. 1956
Constitution of binary alloys, second edition
(McGraw-Hill: New York)

Harris A.B. 1974
J.Phys.C: Sol. State 7 1671-92

Hasegawa H. 1978
J.Low Temp. Phys . 22 475-496

Hedgecock F.T. Strom Olsen J.O. and Wilford D.F. 1977
J.Phys.F: Metal Physics 7 855-868

Hedman L.E., Rao K.V. and Åström H.V. 1978
J. Physique Colloq. 39 C6-7

Herbert I.R. Clark P.E. and Wilson G.V.H. 1972
J.Chem. Phys. Solids 33 979-991

Holden T.M. and Fawcett E 1978
J.Phys.F: Metal Physics 8 2609-14

Hopkinson J. 1885
Phil.Trans. Royal Soc. A180 433-451

Howarth W. 1978
Thesis, University of London, unpublished.

Hubbard J. 1979a
Phys.Rev B19 2626-2636

Hubbard J. 1979b
Phys.Rev. B19 4584-4595

Ibel K. 1976
J.Appl.Cryst. 9 296-309

Ishikawa Y, Tournier R. and Filippi J. 1965
J.Phys.Chem.Solids 26 1727-45

Ishikawa Y, Hoshino S. and Endoh Y. 1967
J.Phys.Soc.Japan 22 1221-32

Jacobs I. and Bean C.P. 1963
Magnetism Vol.3 ed. F.T. Rado and H.Suhl
(Academic Press: London) 296-350

Jayaprakash C., Riedel E.K. and Wortis M. 1978
Phys. Rev. B18 2244-2255

Just W. 1978
Internal Report, I.L.L. Grenoble 78 JU363T

Kastelyn P.W. and Fortuin C.M. 1969
J.Phys.Soc.Japan 26 11-14

Katano S. and Mori N. 1979
J.Phys.Soc.Japan 46 1265-72

Kawakami M. and Goto T. 1979
J.Phys.Soc.Japan 46 1492-1495

Kawano H. and Ono K. 1977
J.Phys.Soc.Japan 42 72-75

Kazjar F., Parette G. and Babic B. 1979
J. Appl.Phys. 50 7519-21

Kazjar F., Parette G. and Babic B. 1980
J.Physique to be published

Kessler J. 1976
Polarized electrons (Springer-Verlag: Berlin)

Kirkpatrick S. 1979
Ill Condensed Matter - Les Houches 1978
ed. R. Balian, R. Maynard and G. Toulouse (North Holland-Amsterdam/
Course 5)

Kneller E. 1969
Magnetism and Metallurgy Vol.1 eds. A.E. Berkowitz and E. Kneller
(Academic Press: London) p365-471

Köehler W.H., Trego A.L. and Mackintosh A.R. 1966
Phys. Rev. 151 495-506

Koester L. 1977
Springer Tracts in Modern Physics 80
ed. G. Höhler (Springer Verlag Berlin) p1-56

Koester L., Knopf K. and Waschkowski W. 1978
Z.Physik A281 61-69

Komura S. 1967
JAERI Report 1137

Kotani A 1975
J.Phys.Soc.Japan 39 851-9

Kotani A. 1978
J.Phys.Soc.Japan 44 1455-1464

Lander G.H. and Heaton L. 1971
J.Phys.Chem.Solids 32 427-435

Lebech B. and Mikke K. 1972
J.Phys.Chem.Solids 33 1651-1663

Le Guillon J.C. and Zinn-Justin J. 1980
Phys.Rev. B21 3976-3998

Lewis B.G. and Williams D.E.G. 1976
J.Less. Comm.Metals 44 337-9

Loegel B. 1975
J.Phys.F: Metal Phys. 5 497-505

Loegel B., Friedt J.M. and Poinsot R. 1975
J.Phys.F: Metal Phys. 5 L54-57

Lomer W.M. 1960
Australian J.Phys. 13 451-3

Lomer W.M. 1962
Proc. Phys.Soc. 80 489-496

Lomer W.M. 1964
Proc.Phys.Soc. 84 327-330

Loucks T.L. 1965
Phys. Rev. 139 A1181

Low G.G. 1969
Adv. Phys. 18 371-400

Lubensky T.C. 1976
Phys.Rev. B15 311-314

Lubensky T.C. 1979
Ill Condensed Matter - Les Houches 1978
ed. R. Balian, R. Maynard and G. Toulouse (North Holland: Amsterdam) Course 6

Maier B. 1977
Neutron beam facilities at the HFR available for users, Office of the Scientific Secretary, I.L.L. Grenoble

Maleev S.V. 1974
Sov.Phys. JEPT 39 889-895

Malletta H. and Felsch W. 1980
Z. Phys. B. 37 55-64

Marshall W. and Lowde R.D. 1968
Rep. Prog. Phys. 31 705-775

Marshall W. and Lovesey S.W. 1971
Theory of thermal neutron scattering (Oxford University Press:London)

Menzinger F. and Paoletti A. 1966
Phys.Rev. 143 365-372

Menzinger F., Sachetti F., and Romanzzo M. 1972
Phys. Rev. B5 3778-3782

Mezei F. and Murani A.P. 1980
J. Magn. Magn. Mater. 14 211-13

Mitchell M.A. and Goff J.F. 1972
Phys. Rev. B5 1163-70

Monod P. and Prejean J.J. 1978
J. Physique Colloque C6 910-11

Moon R.M. and Shull C.G. 1964
Acta Cryst. 17 805-812

Moon R.M., Koehler W.C. and Trego A.L. 1966
J.Appl.Phys. 37 1036-7

Moon R.M. Riste T. and Koehler W.C. 1969
Phys. Rev. 181 920-932

Moon R.M. 1971
Int.J. Magn. 1 219-231

Mori M., Tsunoda Y. and Kunitomi N. 1974
Sol.State. Comm. 18 1103-1105

Muir W.B. and Strom-Olsen J.O. 1976
J.Phys.E: Sci. Inst. 9 163-4

Mulder C.A.M., Duyneveldt A.J. and Mydosh J.A. 1980
J.Magn.Magn.Mater 15-18 141

Murani A.P. 1974
J.Phys.F: Metal Phys. 4 757-766

Murani A.P. 1976
Phys. Rev. Lett. 37 450-3

Murani A.P. 1980
Sol. Stat. Comm. 34 705-708

Murani A.P., Roth S., Radhakrishna P., Rainford B.D., Coles B.R.,
Ibel K., Goeltz G. and Mezei F. 1976
J.Phys. F: Metal Phys. 6 425-432

Nägele W., Knorr K, Prandl W, Convert P. and Buevoz J.L. 1978
J.Phys.C: Solid State Phys. 11 3295-3305

Nägele W., Blankenhagen P., Knorr K. and Suck J.B. 1979
Z.Phys. B 33 251-4

Nakanishi K. and Kasuya T. 1977
J.Phys.Soc.Japan 42 833-844

Neél L. 1932
Ann. Phys. (Paris) 10 64-74

Neél L. 1955
Ad. Phys. 4 191-243

Nevitt M.V. and Aldred A.T. 1963
J.Appl. Phys. 34 463-68

Newmann M.M. and Stevens W.H. 1959
Proc. Phys. Soc. Lond. 74 290-6

Nieuwenhuys G., Verbeek B.H. and Mydosh J.A. 1979
J.Appl. Phys. 50 1685-92

Noakes J.E., Arrott A. and Tornberg N.E. 1966
J.Appl. Phys. 37 1264-5

Overhauser A.W. 1959
Phys. Rev. Lett. 3 414

Overhauser A.W. 1962
Phys. Rev. 128 1437-1452

Pickart S.J. and Nathans R. 1962
J.Appl. Phys. 33S 1366-8

Pickart S.J. and Nathans R.1963
J. Appl. Phys. 34 1203-4

Poncet P. 1977
Internal Report I.L.L. Grenoble 77 P0139S

Popovici M. 1971
Phys.Lett. 34A 319-20

Pynn R., Press W., Shapiro S.M. and Werner S.A. 1976
Phys.Rev. B13 295-298

Radhakrisha P, Brown P.J. and Kajzar F. 1977
J.Phys.F: Metal Phys. 7 2583-2591

Rajan N.S., Waterstrat R.M. and Beck P.A. 1960
J.Appl. Phys. 31 731-2

Rath J. and Callaway 1973
Phys. Rev. B12 5398-5403

Read D.A. and Temple B.K. 1974
(unpublished)

Rice T.M. 1970
Phys. Rev. B2 3619-3630

Sarkissian B.V.B. 1980
J. Magn.Magn.Mater. 15-18 225-6

Sato H. and Maki K. 1973
Int. J. Magn. 4 163-172

Schmatz W., Springer T., Schelten J. and Ibel K. 1974
J.Appl. Cryst. 7 96-116

Sears V.F. 1975
Adv. Phys. 24 1-45

Shante V.K.S. and Kirkpatrick S. 1971
Adv. Phys. 20 325-357

Sharif B., 1979
M.Phil. Dissertation, University of London, unpublished.

Shibatani A., Motizuki K. and Nagamiya T. 1969
Phys. Rev. 177 984-1000

Shibatani A, 1971
J.Phys.Soc. Japan 31 1642-49

Shirane G. and Takei W.J. 1962
J.Phys.Soc. Japan 17 Suppl.B3 35-7

Shull C.G. and Wilkinson M.K. 1955
Phys. Rev. 97 304-310

Shull R.D. and Beck P.A. 1975
Magnetism and Magnetic Materials, San Francisco 1974:
AIP Conf. Proc. 24 95-6

Soukoulis C.M., Grest G.S. and Levin K. 1978
Phys. Rev. Lett. 41 568-571

Souletie J. and Tournier R. 1969
J.Low Temp. Phys. 1 59-68

Stanley H.E. 1967
Phys.Rev. 158 543-544

Stanley H.E. 1977
J.Phys.C: Sol.State 11 L211-20

Stanley H.E., Birgeneau R.J., Reynolds P.J. and Nicholl J.F. 1976
J.Phys.C: Sol.State 9 L553-60

Stassis C., Kline G.R. and Sinha S.K. 1975
Phys.Rev. B 2171-76

Stauffer D. 1975
Z.Phys.B 22 161-171

Stauffer D. 1979
Phys. Reports 54. 1-74

Stauffer D. and Binder K. 1980
J.Magn.Magn, Mater. 15-18 113-4

Stephen M.J. and Grest G.S. 1977
Phys. Rev. Lett. 38 567-70

Stinchcombe R.B. 1979a
J.Phys. C: Sol.State 12 2625-36

Stinchcombe R.B. 1979b
J.Phys. C: Sol.State 12 4533-4552

Stinchcombe R.B. 1980
J.Phys. C: Sol.State 13 (to be published)

Stoner E.C. and Wohlfarth E.P. 1948
Phil. Trans. Roy. Soc. A240 599-605

Street R.A. and Woolley J.C. 1949
Proc. Phys. Soc. A62 562-572

Strom-Olsen J.O., Wilford D.F., Burke S.K. and Rainford B.D. 1979
J.Phys.F: Metal Physics 9 L 95-98

Strom-Olsen J.O. and Wilford D.F. 1980
J.Phys.F: Metal Phys. 10 1467-73

Suter R.M. and Hohenemser C. 1979
J.Appl. Phys. 50 1814-16

Suzuki T. 1966
J.Phys.Soc. Japan 21 443-450

Suzuki T. 1976
J.Phys.Soc.Japan 41 1187-1194

Sykes M.F., Gaunt D.S. and Glen M. 1976
J.Phys. A: Math. Gen. 9 1705-12

Teraoka Y. and Kanamori J. 1977
Physica 91B 199-204

Tholence J.L. and Tournier R. 1974
J.Physique 35 C4 229-35

Thorpe M.F. 1975
J.Physique 12 1177-1181

Trego A.L. and Mackintosh A.R. 1968
Phys. Rev. 166 495-506

Tsunoda Y, Mori M., Kunitomi N., Teraoka Y. and Kanamori J. 1974
Sol. Stat. Comm. 14 287-9

Van Hove L. 1954a
Phys.Rev. 95 249-262

Van Hove L. 1954b
Phys. Rev. 95 1374-1384

Verbeek B.H. and Mydosh J.A. 1978
J.Phys.F: Metal Phys. 8 L 109-11

Villain J. 1964
J.Physique 25 618-26

Vincze I., Wagner F.E., Baggio-Saitovitch E. and Koch W. 1976
J. Physique 37 C6 423-5

Wallace D.J. and Young A.P. 1978
Phys. Rev. B17 2384-7

Waterstrat R.M. 1973
Met.Trans. 4 1585-1592

Watson R.E. and Freeman A.J. 1961
Acta Cryst. 14 27-37

Watson-Yang T.J., Freeman A.J. and Koelling D.D. 1977
J. Mag. Mag. Mater, 5 277-286

Wenger L. and Keeson P. 1976
Phys. Rev. B13 4053-59

Wertheim G.K. 1961
J.Applied Phys. 32 1105-1115

Wilkinson M.K. Wollan E.O. Koehler W.C. and Cable J.W. 1962
Phys. Rev. 127 2080-83

Williams D.E.G. and Lewis B.G. 1979
Z. Metallk 70 441-8

Williams I.S., Gopal, E.S.R. and Street R. 1979
J.Phys.F: Metal Physics 9 431-445

Windsor C.G. 1972
J.Phys.F: Metal Physics 2 742-8

Wohlfarth E.P. 1977
Physica 86-88B 852-3

Wohlfarth E.P. 1979
Phys.Lett. 70A 489-491

Young C.Y.and Sokoloff J.B. 1974
J.Phys.F.: Metal Phys. 4 1304-1319

Zittartz J. 1967
Phys.Rev. 164 575-582

ppl. Cryst. (1978). **11**, 644–648

Superparamagnetism and the Character of Magnetic Order in Binary Cr–Fe Alloys near the Critical Concentration*

S. K. BURKE, R. CYWINSKI† and B. D. RAINFORD, *Physics Department, Imperial College, London SW7, England*

(*Received* 3 *November* 1977; *accepted* 30 *May* 1978)

Although the magnetic properties of Cr–Fe alloys have been widely studied, there are different interpretations of existing data in the literature, especially for alloys in the concentration range 10 to 25% Fe. The onset of ferromagnetism occurs somewhere in this concentration range, but there is little direct evidence of the precise critical concentration. Detailed small-angle scattering measurements have been carried out on alloys containing 16·7, 19·9, 20·9, 21·7, 24 and 25% Fe over a wide range of temperatures and magnetic fields. Small-angle scattering peaked in the forward direction develops at low temperatures, corresponding to the growth of magnetic correlations over distances of the order of 400 Å. The response of the scattering to the application of a magnetic field suggests that the scattering at low temperatures arises from superparamagnetic clusters. Curie temperatures were deduced from the critical scattering, and the variation of T_c with composition suggests that the critical concentration is close to 19% Fe.

Introduction

A series of b.c.c. solutions exists from pure iron across to pure chromium. The addition of Cr to Fe lowers the Curie

Work carried out at Laue–Langevin, Grenoble, France.

Present address: Physics Department, Monash University, Clayton, Victoria 3168, Australia.

temperature gradually so that alloys with iron concentrations greater than about 30% are good ferromagnets, whereas the addition of Fe to antiferromagnetic chromium lowers the Néel temperature fairly rapidly. There is, however, considerable uncertainty at present about the extent of the antiferromagnetic and ferromagnetic phases. Alloys in the composition range between 8 and 25% Fe have complex behaviour of both magnetic and transport properties. Some of these complexities have been attributed to the persistence of antiferromagnetism to concentrations as high as 18% Fe (Rajan, Waterstrat & Beck, 1966). Other workers report that the alloys in this regime have superparamagnetic or mictomagnetic behaviour, characterized by strongly field-dependent magnetization, remanence and broad maxima in the low-field magnetization as a function of temperature (Shull & Beck, 1975; Ishikawa, Tournier & Filippi, 1965).

The precise critical concentration for the onset of ferromagnetism, c_F, is somewhat uncertain: the Curie temperatures reported by different workers vary considerably for alloys with the same nominal composition (Loegel, 1975). This is due, in part, to the different techniques used to determine T_C and in part due to the different heat treatments applied to the alloys. It has been noted that aging affects the magnetic properties of Cr-rich alloys (Ishikawa *et al.*, 1965). This is related to clustering of Fe atoms. The clustering occurs, as is clearly seen by diffuse neutron scattering, (Aldred, Rainford, Kouvel & Hicks, 1976), even in alloys quenched from high temperatures.

Diffuse neutron scattering measurements, combined with magnetization measurements, have allowed the atomic moments of Fe and Cr to be determined in the ferromagnetic regime, *viz.* for iron concentrations greater than 30% (Aldred *et al.*, 1976). These show that whereas the Fe moment falls slowly from $2{\cdot}2\mu_B$ at pure Fe to $1{\cdot}8\mu_B$ in a 73% Cr alloy, the Cr moment decreases more rapidly from $-1{\cdot}2\mu_B$ in the dilute limit (2% Cr) to almost zero at 73% Cr. Thus in the concentration range where the onset of ferromagnetism occurs, it appears that the Fe atoms carry a good local moment, whilst the Cr atoms are essentially non-magnetic. In order to investigate the onset of ferromagnetism and to clarify the nature of the magnetism in the vicinity of the critical concentration we have carried out small-angle neutron measurements on a series of alloys with Fe concentrations between 16 and 25%. Low-field magnetization measurements have also been made on most of these alloys.

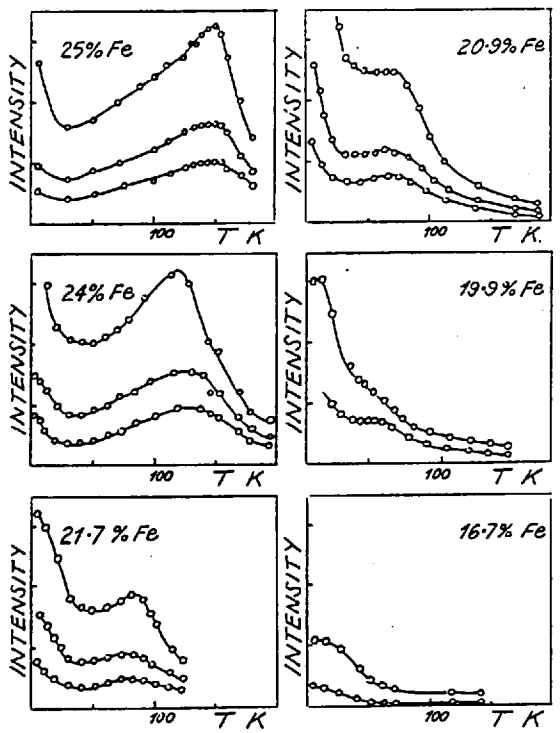

Fig. 1. Temperature variation of small-angle scattering for Cr–Fe alloys. Radially averaged intensity as a function of temperature for constant Q values of 0·017 Å^{-1} (upper curves), 0·026 Å^{-1} (middle curves) and 0·034 Å^{-1} (lower curves). For the 19·9 and 16·7% Fe the middle curves (0·026 Å^{-1}) are omitted.

Experimental procedure

The alloys were prepared by arc melting appropriate weights of pure constituent metals (4*N*5) under an argon atmosphere. Weight losses were small, of the order of 0·3%. The resulting ingots, containing 16·7, 19·9, 20·9, 21·7, 24 and 25% Fe, were spark machined to give discs 15 mm diameter and 8 mm thick. The alloys were sealed in quartz ampoules and given a homogenizing anneal at 1100°C for six days followed by 24 h at 850°C and water quenched. Microprobe analysis showed a homogeneous distribution of iron; some samples were found to contain non-metallic inclusions.

Small-angle neutron scattering measurements were made using the D17 diffractometer at the ILL Grenoble. Neutrons of wavelength 11·7 Å and a counter–detector distance of 2·82 m gave a range of useful momentum transfer from 0·007 to 0·065 Å^{-1}. The sample temperature could be varied in the range from 1·2 to 300 K. Superconducting Helmholtz coils allowed a vertical magnetic field of up to 5 KOe to be applied to the specimens.

Zero-field data were processed to give radial averages of the scattering collected by the D17 two-dimensional multidetector. When magnetic fields were applied, the resulting anisotropic scattering on the detector was least-squares fitted to the function (Cywinski, Booth & Rainford, 1977*b*)

$$I(Q,\alpha) = A(Q) + B(Q)\cos^2\alpha,$$

where Q is the magnitude of the scattering vector and α the angle between the direction of the applied magnetic field in the plane of the detector and the scattering vector. $A(Q)$ is the isotropic part of the scattering and $B(Q)$ is the anisotropic part of the scattering.

Low-field magnetization measurements were performed with a vibrating-sample magnetometer in fields as low as 2 Oe.

Results

The small-angle scattering observed in zero field exhibits two distinctive features. All samples studied display a dramatic increase in the small-angle scattering, peaked in the forward direction, as the temperature is lowered. For the alloys with iron concentration of 19·9% and above the forward scattering also rises to a maximum at a finite temperature (Fig. 1).

These maxima are attributed to ferromagnetic critical scattering occurring in the vicinity of the Curie temperature for the alloy. The temperatures at which the maxima occur agree well with those determined by low-field magnetization measurements performed on the same samples. However, these maxima are broader than those usually encountered in this kind of system, suggesting a distribution of Curie

temperature associated with microscopic concentration fluctuations within the alloy. Such an explanation is supported by Mössbauer spectroscopy (Loegel, Friedt & Poinsot, 1975). The absence of a critical scattering peak in the 16·7% Fe alloy indicates that long-range ferromagnetic order does not exist at this composition. This fact, together with the variation of Curie temperature with composition places the critical concentration for ferromagnetism (c_F) in Cr–Fe alloys at close to 19% Fe.

The increase in scattering at low temperatures is attributed to the growth of magnetically correlated clusters of spins. A similar effect has been observed in Au–Fe alloys (Murani *et al.*, 1976) and in Co–Ga alloys (Cywinski *et al.*, 1977*a*, *b*) close to the critical composition. The extent of these magnetic clusters and the range of magnetic correlations can be determined from the form of the scattering $S(Q)$ as discussed in the next section.

The application of a magnetic field provides further information as to the character of the magnetic correlations. Typical results are shown in Fig. 2, where contours of constant scattering intensity in the plane of the detector are plotted. These measurements were made on the 25% Fe sample at 2·2 K in vertical magnetic fields up to 3·6 k Oe. The dotted contour represents the same intensity level in each case. As the field is applied, the contours become prolate (elongated) with respect to the field direction and the contours collapse into the centre of the detector indicating that the scattering is reduced by the field. This behaviour will be shown to be consistent with the effect of a magnetic field on the scattering from superparamagnetic clusters.

Discussion

The onset of ferromagnetism in certain binary alloys may be discussed in terms of a percolation process (see for example, Essam, 1972). The alloy is taken to be a random solid solution, one species being essentially non-magnetic, whilst the other has a well defined local moment which interacts with other moments according to a nearest-neighbour ferromagnetic coupling. Consider the effect of increasing the concentration of magnetic species at $T=0$. When the concentration of magnetic atoms is less than the critical composition for ferromagnetism (c_F), magnetic correlations can be sustained only over finite distances determined by the nearest-neighbour distribution of magnetic species on the lattice. The three-dimensional correlated networks of nearest-neighbour moments ('clusters') increase in size as the concentration of magnetic atoms is increased until such a concentration is reached that one such network penetrates the entire sample. The concentration at which this infinite cluster forms (the percolation limit) is the point at which the range of spin correlations first diverges, signalling the onset of long-range ferromagnetic order. As the concentration is increased beyond this critical composition the Curie temperature and spontaneous magnetization increase, as the number of magnetic atoms belonging to the infinite cluster increases. However, a sizable fraction of magnetic atoms may still belong to finite clusters. At low temperatures, although the magnetic moments within the finite clusters are highly correlated, the cluster moment is free to rotate as a whole, giving rise to superparamagnetic behaviour.

This picture is probably oversimplified in the case of Cr–Fe alloys, since it ignores the possible role played by magnetic coupling between finite clusters or between the finite and infinite clusters. There is no information available at present on the range of the magnetic interactions in Fe–Cr alloys. The inevitable atomic short-range order, always present in these alloys, also provides a perturbation on calculations based on random alloys. Nonetheless, this simplified picture forms a basis for discussion. In all cases the data for small $Q(Q \leq 0{\cdot}02\ \text{Å}^{-1})$ have been corrected for the presence of

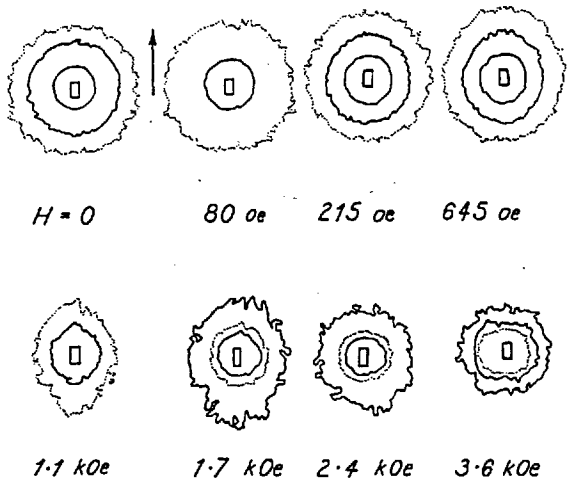

Fig. 2. Intensity contour plots for 25% Fe alloy at 2·2 K as a function of increasing magnetic field. The field is vertical (arrow) and dotted contours represent the same intensity level.

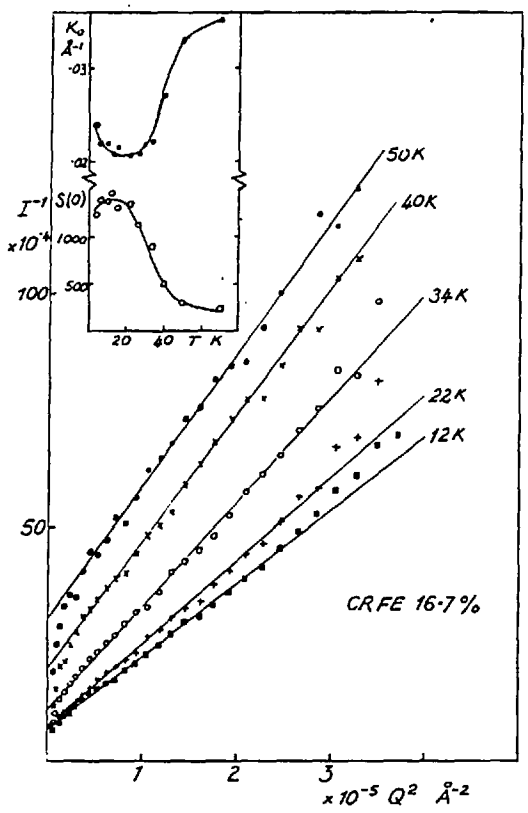

Fig. 3. Reciprocal intensity *vs* Q^2 plot for 16·7% Fe alloy at a number of temperatures. Inset: Temperature variation of $S(0)$ and the inverse range parameter K.

a small extra temperature-independent nuclear defect scattering. This was estimated by using a straight-line extrapolation of the I^{-1} *versus* Q^2 plots for the highest-temperature data, where the magnetic contribution is the smallest. The validity of this procedure is supported by the good straight lines obtained at all other temperatures.

First, consider the 16·7% alloy, where the iron concentration is less than c_F. The variation of scattered intensity in zero field with wavevector **Q** is shown by plotting inverse intensity *versus* Q^2, as in Fig. 3. These plots yield good straight lines out to large Q, and the scattering is therefore well represented by a Lorentzian function

$$S(Q)=S(0)/(1+Q^2/K^2),$$

implying that the magnetic correlations have the Ornstein–Zernike form with K as an inverse range parameter

$$\langle \mathbf{M}(0).\mathbf{M}(r)\rangle \sim (1/r)\exp(-Kr).$$

The temperature dependences of $S(0)$ and K are shown inset in Fig. 3. Firstly, as expected for an alloy below the percolation limit the range of magnetic correlations increases (K decreases) with decreasing temperature, reaching a finite value at low temperatures. Secondly, the value of $S(0)$ shows a shallow maximum at low temperatures. This is consistent with the temperature dependence of low-field magnetization in these alloys, for iron concentrations less than c_F. As long as the quasi-static approximation is valid, the neutron cross section is proportional to $\chi(Q)$, the wavevector-dependent susceptibility. Thus one would expect the forward cross section $S(0)$ to follow the behaviour of the static susceptibility $\chi(0)$. The maximum in $\chi(0)$ with temperature is usually attributed to the freezing of clusters due either to the growth of shape anisotropy or to residual magnetic interactions. The observed minimum in the inverse range parameter at a temperature corresponding to the maximum in $S(0)$ is not understood at present.

If we now turn to a discussion of the ferromagnetic 24% Fe alloy, reciprocal intensity *versus* Q^2 plots for this alloy at temperatures above the Curie temperature are shown in Fig. 4. This is typical of the data for alloys with iron concentrations greater than c_F. Excellent linear plots are obtained out to large values of Q^2. The variation of the inverse correlation range, K, with temperature is shown inset. As expected for magnetic correlations in the vicinity of the Curie temperature, the correlation range tends to diverge at T_C, *i.e.* K tends to zero.

Below T_C, there is a rather different behaviour as illustrated in Fig. 5. The I^{-1} *versus* Q^2 plots are linear only over a limited Q^2 range and show marked upward curvature at large Q. The values of the inverse range parameter K, derived from the initial linear portion of the plots, are shown inset in Fig. 4. One may relate these values to the root-mean-square radius of gyration for clusters using the relation

$$\langle R_G^2\rangle^{1/2}=\sqrt{3}/K.$$

At low temperatures $\langle R_G^2\rangle^{1/2}$ is of the order of 400 Å. This estimate is of course independent of the shape of the cluster. Once long-range magnetic correlations are established within a cluster, the scattering is given by the Fourier transform of the spatial distribution of the iron atoms in it. Models for percolation on lattices show that the clusters are ramified in form, with many one-dimensional links (Stanley, Birgeneau,

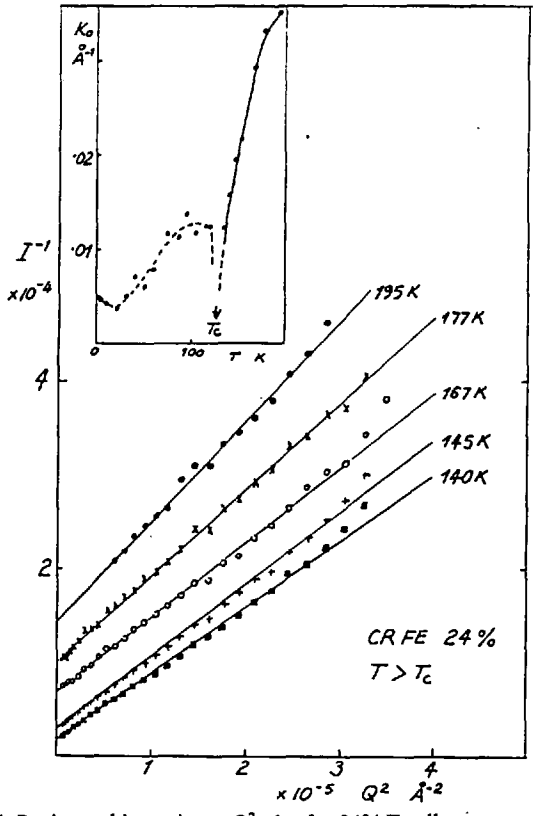

Fig. 4. Reciprocal intensity *vs* Q^2 plot for 24% Fe alloy at temperatures above the Curie temperature. Inset: Temperature variation of the inverse range parameter K.

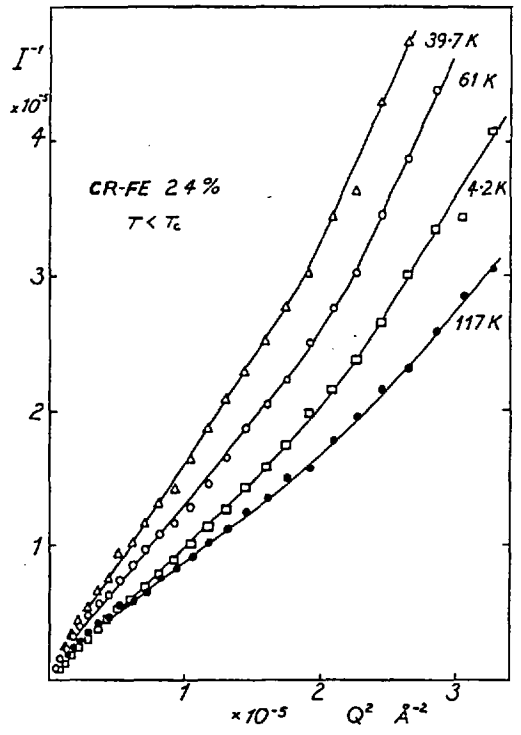

Fig. 5. Reciprocal intensity *vs* Q^2 plot for 24% Fe alloy at temperatures below the Curie temperature.

Reynolds & Nicoll, 1976). The form of scattering in Fig. 5 is characteristic of the structure of clusters of this type. No detailed calculations have been carried out at present, though it may be noted that scattering from a branched polymer has a similar form (Kratochvil, 1972). If the clusters are approximated to Gaussian coils the radius of gyration corresponds to a mean end-to-end distance of 1000 Å.

The striking field dependence of the scattering observed for all alloys studied may be accounted for if the finite clusters behave as superparamagnetic entities at low temperatures. In zero magnetic field the average fluctuations of the spin components about their mean values of zero are equal and the small-angle scattering is isotropic. If a magnetic field is applied in the z direction, the fluctuation in the z component of spin must be reduced because of the partial alignment in that direction. This leads to anisotropic scattering. The diffuse scattering cross section in this case may be written in the form (Cywinski, Booth & Rainford, 1977*b*)

$$\frac{d\sigma}{d\Omega} \sim F^2(Q)\{[\langle S_x^2\rangle + \langle S_z^2\rangle - \langle S_z\rangle^2] + \cos^2\alpha[\langle S_x^2\rangle - \langle S_z^2\rangle + \langle S_z\rangle^2]\},$$

where S_x, S_z are spin components of the total *cluster* spin in the x and z directions, α is the angle between the scattering vector and the field direction, and $F(Q)$ is the *cluster* form factor. It can be shown that the coefficient of $\cos^2\alpha$ is positive for all values of the field, so that the anisotropic scattering may be written in the form

$$I(Q,\alpha) = A(Q) + B(Q)\cos^2\alpha,$$
$$B(Q) \geq 0,$$

generating a series of prolate ellipses. Furthermore, $A(Q)$ is found to be a decreasing function of H/T where $B(Q)$ increases with H/T to a shallow maximum and then decreases. This predicted behaviour with increasing field strength is seen in the contours given in Fig. 2, confirming the superparamagnetic behaviour of the clusters. A quantitative analysis of the scattering as a function of field will be presented elsewhere.

This behaviour should be contrasted with the diffuse scattering due to fluctuations in ferromagnetic long-range order, which is proportional to $(1-\cos^2\alpha)$ (Marshall & Lovesey, 1971). While these alloys are ferromagnetic, the volume fraction occupied by the infinite cluster is relatively small and much of the magnetic response is dominated by finite clusters which behave as superparamagnetic entities.

We would like to thank M. Roth for his invaluable experimental assistance, and A. P. Murani for his support and collaboration in some preliminary experiments. This work was supported by the Neutron Beam Research Committee of the SRC. One of us (SKB) acknowledges receipt of the Rutherford Scholarship of the Royal Society.

References

ALDRED, A. T., RAINFORD, B. D., KOUVEL, J. S. & HICKS, T. J. (1976). *Phys. Rev.* B**14**, 228–234.

CYWINSKI, R., BOOTH, J. G. & RAINFORD, B. D. (1977*a*). *Physica*, **86–88B**, 404–406.

CYWINSKI, R., BOOTH, J. G. & RAINFORD, B. D. (1977*b*). *J. Phys. F*, **7**, 2567–2581.

ESSAM, J. W. (1972). *Percolation and Cluster Size*, in *Phase Transitions and Critical Phenomena*, Vol. 2, edited by C. DOMB & M. S. GREEN. New York: Academic Press.

ISHIKAWA, Y., TOURNIER, R. & FILIPPI, J. (1965). *J. Phys. Chem. Solids*, **26**, 1727–1745.

KRATOCHVIL, P. (1972). *Particle Scattering Functions*, in *Light Scattering from Polymer Solutions*, edited by M. B. HUGLIN. New York: Academic Press.

LOEGEL, B. (1975). *J. Phys. F*, **5**, 497–505.

LOEGEL, B., FRIEDT, J. & POINSOT, T. (1977). *J. Phys. F*, **7**, L54–57.

MARSHALL, W. & LOVESEY, S. (1971). *Theory of Thermal Neutron Scattering*, p. 505ff. Oxford Univ. Press.

MURANI, A. P., ROTH, S., RADHAKRISHNA, P., RAINFORD, B. D., COLES, B. R., IBEL, K., GOELTZ, G. & MEZEI, F. (1976). *J. Phys. F*, **6**, 425–432.

RAJAN, N. S., WATERSTRAT, R. M. & BECK, P. A. (1966). *J. Appl. Phys.* **31**, 731–732.

SHULL, R. D. & BECK, P. A. (1975). *AIP Conf. Proc.* **24**, 95–96.

STANLEY, H. E., BIRGENEAU, R. J., REYNOLDS, P. J. & NICOLL, J. F. (1976). *J. Phys. C*, **9**, L553–560.

J. Phys. F: Metal Phys., Vol. 8, No. 10, 1978. Printed in Great Britain

LETTER TO THE EDITOR

Determination of the antiferromagnetic phase boundary in Cr–Fe alloys

S K Burke and B D Rainford

Imperial College, The Blackett Laboratory, Prince Consort Road, London SW7 2BZ

Received 15 August 1978

Abstract. The antiferromagnetic phase boundary in the Cr–Fe system has been determined by neutron diffraction. Antiferromagnetism disappears at a concentration of 16·0 ± 0·5 at% Fe. Resistivity measurements indicate that T_N is marked by the maximum in the temperature coefficient of resistivity rather than the minimum in the resistivity. On the basis of these measurements it is apparent that no long-range order exists in Cr–Fe alloys between 16 and 19 at% Fe.

A large amount of experimental and theoretical work has been devoted to the Cr–Fe system. The dilute alloys (less than 5 at% Fe) have been most extensively investigated, in this composition region the antiferromagnetic order changes from an incommensurate to commensurate spin density wave (Ishikawa *et al* 1967, Suzuki 1976). However, comparatively little is known about the evolution of magnetic order from commensurate spin density wave (CSDW) to ferromagnet at higher Fe concentrations (15–25 at% Fe). There is conflicting evidence for antiferromagnetism and ferromagnetism in this composition range. The magnetic phase diagrams compiled by Loegel (1975) and Mitchell and Goff (1972) show overlapping antiferromagnetic and ferromagnetic phase boundaries. The antiferromagnetic phase boundary, determined from resistivity measurements, was reported to extend to 20 at% Fe. On the other hand, the use of Arrott plots derived from high-field magnetisation measurements (Nevitt and Aldred 1963) show the existence of ferromagnetism at Fe concentrations greater than 16 at%. Small-angle neutron scattering measurements (Burke *et al* 1978) which avoid the difficulties of Arrott plots in magnetically inhomogeneous systems placed the critical composition for ferromagnetism at 19 at% Fe. A series of neutron diffraction measurements were consequently undertaken to determine the extent of antiferromagnetism in Cr–Fe alloys.

Polycrystalline samples containing 4·5, 7·0, 9·2, 10·2, 11·2, 12·2, 13·3, 13·6, 14·2, 15·4 and 16·7 at% Fe were prepared by arc melting appropriate weights of 4N5 Fe and 4N5 Cr (Johnson Matthey 'Specpure') under an argon atmosphere. After a number of melting cycles the alloys were cast to produce roughly cylindrical ingots. Weight losses were small and attributed to the evaporation of Cr. The alloys were sealed in evacuated quartz ampoules, homogenised for six days at 1050 °C and water-quenched.

Neutron Bragg scattering experiments were carried out on the two-axis diffractometers PANDA and CURRAN at AERE Harwell. Incident wavelengths of 1·55 Å

0305-4608/78/0010-9239 $01.00

M.P.(F). 8/10—3

(PANDA) and 1·37 Å (CURRAN) were selected for high intensity and low second-order contamination. Samples were mounted in a variable-temperature He cryostat and were continuously rotated to minimise the effects of preferred orientation. Scans were made through the (100) magnetic and either the (110) or (200) nuclear reflections at each temperature. The ordered moment could then be calculated in the usual way, normalising the magnetic to the nuclear reflections after taking into account the $\lambda/2$ contamination which was measured separately.

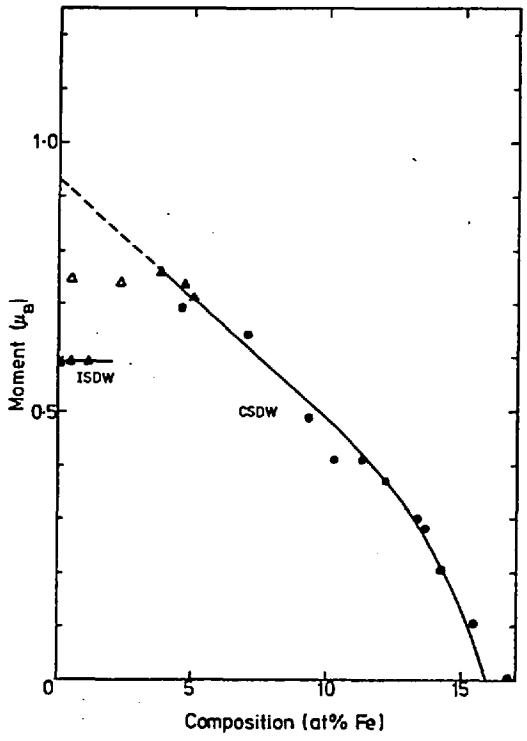

Figure 1. The variation of ordered moment with composition for Cr–Fe alloys at 4·2 K. For comparison the moment corresponding to the maximum amplitude of the incommensurate spin density wave (ISDW) is shown in addition to the moments determined for commensurate spin density wave (CSDW) ordering. The full curve is a guide to the eye. ●, this work; △, Arrott *et al* (1967); ▲, Ishikawa *et al* (1967).

The ordered antiferromagnetic moment determined in this way is shown as a function of composition in figure 1, for a temperature of 4·2 K. The data is in good agreement with the measurements of Ishikawa *et al* (1967) which extended to a composition of 4·7 at% Fe. The moment increases as the order changes from incommensurate at low concentrations to commensurate at higher concentrations. (An extrapolation of the data leads to a moment of 0·94 μ_B for a hypothetical CSDW in pure Cr.) The order remains commensurate and the moment decreases with increasing Fe concentration, reaching zero at the critical concentration of 16 at% Fe.

Néel temperatures were determined for the 10·2, 12·2, 13·6 and 14·2 at% alloys. The results are shown in the composite phase diagram (figure 2). The temperature dependence of the 10·2 at% Fe alloy was followed in detail. This was found to fit the $B_{1/2}$ function well, which approximates the BCS relation expected for Cr alloys. In the case of the other alloys only sufficient data were taken to bracket the Néel temperature (figure 3). It is apparent that there is a large discrepancy between the present data and Néel temperatures reported from resistivity measurements. There has been some disagreement in the literature as to which feature of the resistivity

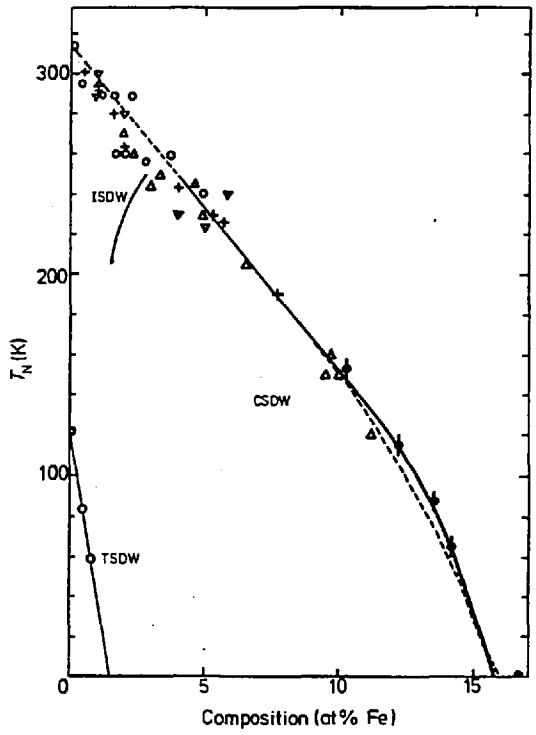

Figure 2. Antiferromagnetic phase boundaries in the Cr–Fe system, compiled from various sources: Mitchell and Goff (1972), Suzuki (1976) and Loegel (1975). The broken curve is the Abrikosov–Gorkov relation with $T^* = 300$ K (equation (1)). To illustrate the scaling between ordered moment at 4·2 K and Néel temperature the same curve used in figure 1 scaled by a constant value has been reproduced (full curve). ●, this work; ○, neutron diffraction; △, $(d\rho/dT)_{max}$; ▽, magnetic susceptibility.

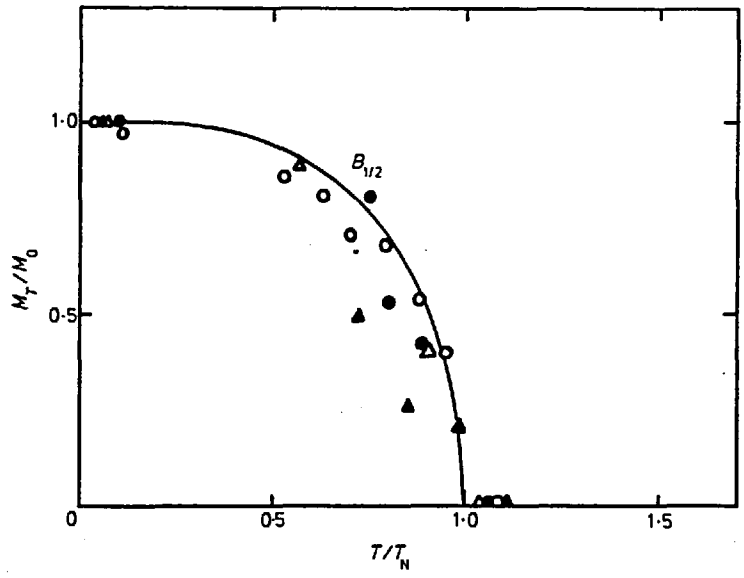

Figure 3. Temperature dependence of the ordered moment. The full curve is the Brillouin function for spin ½, which closely approximates the BCS relation. ●, 14·2 at% Fe; ▲, 13·6 at% Fe; △, 12·2 at% Fe; ○, 10·2 at% Fe.

marks the Néel temperature. For example Mitchell and Goff (1972) and Loegel (1975) assume that the minimum of the resistivity occurs at T_N, whereas Trego and Mackintosh (1968), Ausloos (1977) and Åstrom *et al* (1977) emphasise that the maximum in the thermal coefficient of resistivity marks T_N. To our knowledge this point has not been resolved by reference to neutron diffraction, so that a sample suitable for resistivity measurements was spark-cut from the neutron 10·2 at% Fe alloy. The resistivity was measured by a standard four-terminal DC technique. The results are shown in figure 4, expressed in terms of $d\rho/dT$ for convenience. It can be seen that

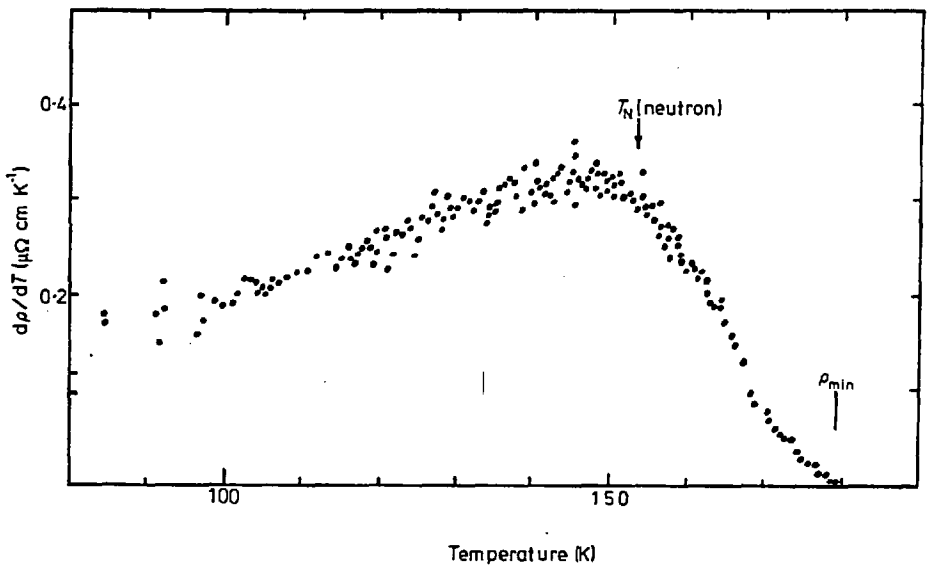

Figure 4. Temperature derivative of the resistivity close to T_N for Cr–Fe 10·2 at%. The maximum in $(d\rho/dT)$ closely coincides with T_N determined by neutron diffraction measurements on the same alloy. The minimum in resistivity ρ_{min} is marked.

the Néel temperature lies close to the maximum in $d\rho/dT$ for the CSDW state. Furthermore, Néel temperatures determined from $d\rho/dT$ using the data of Arajs and Dunmyre (1966) and Rajan *et al* (1960) are in good agreement with the Néel temperatures found by this work, as shown in figure 2. This brings the critical composition for antiferromagnetism deduced from resistivity measurements close to the present value.

It is clear that Fe is not a normal solute in chromium. The decrease in T_N with increasing Fe concentration is contrary to the expectations of the rigid-band models which have successfully accounted for the properties of many Cr alloys (for example Trego and Mackintosh 1968). The destruction of the SDW in Cr–Fe alloys has been attributed to the depairing of the correlated electron–hole pairs responsible for the SDW state by scattering from localised Fe moments and the impurity Coulomb field. This mechanism may be modified by exchange enhancement of the electron–hole pairing due to polarisation of impurity moments via interaction with the SDW. In Cr–Fe alloys this effect is probably small as the interaction between local moment and SDW is known to be weak; certainly no extra contribution to the ordered moment due to ordering of the Fe moment is seen above 4·2 K. In addition, as the Fe moment is $\simeq 1{\cdot}6\,\mu_B$ in Cr there is the possibility that 0·4 electrons per Fe atom are contributed to the conduction band, with a consequent change in Fermi surface nesting. The

effect of local moment impurities on the second-order paramagnetic–CSDW transition has been treated by Antonoff (1977) in the framework of the two-band model with imperfect nesting. Under the assumptions of perfect nesting and negligible polarisation of the impurity moments the dependence of T_N with impurity concentration c reduces to the Abrikosov–Gorkov relation

$$\ln(T_N/T_0) = \psi(\tfrac{1}{2}) - \psi[\tfrac{1}{2} + (cT^*/T_N)] \tag{1}$$

where T_N is the Néel temperature of Cr, T^* is an effective interaction temperature and ψ is the digamma function. If magnetic scattering only is considered, T^* is given by

$$T^* = \frac{\hbar}{12k_B} S(S+1) \frac{I_{eff}^2}{E_F} \tag{2}$$

where, for reasonable values of the parameters, T^* lies between 200 and 1000 K. A reasonable fit to the present data is found for $T^* = 300$ K, shown in figure 2 as a broken curve.

The ordered moment at 4·2 K scales with the Néel temperature for the CSDW state, giving a constant value of $\mu/T_N = (3{\cdot}1 \pm 0{\cdot}1) \times 10^{-3}\ \mu_B\,K^{-1}$. This relationship has been observed for ISDW alloys by Koehler *et al* (1966) and is to be expected if T_N is linearly related to the zero-temperature energy gap.

The determination of the critical composition for antiferromagnetism at 16 at% Fe implies a concentration range of some 3 at%, which does not support long-range magnetic order. Spin glass behaviour has been observed in this region. A detailed account of this work is to be published.

This work is supported by the Neutron Beam Research Committee of the SRC. S K Burke acknowledges receipt of the Rutherford Scholarship of the Royal Society.

References

Antonoff M-M 1977 *Physica* **91B** 193–8
Arajs S and Dunmyre G R 1966 *J. Appl. Phys.* **37** 1017–8
Arrott A, Werner S A and Kendrick H 1967 *Phys. Rev.* **153** 624–31
Åstrom H U, Gudmundsson H, Hedman L and Rao K V 1977 *Physica* **86–88B** 332–4
Ausloos M 1977 *J. Magn. Magn. Mater.* **5** 156–60
Burke S K, Cywinski R and Rainford B D 1978 *J. Appl. Crystallogr.* to be published
Ishikawa Y, Hoshino S and Endoh Y 1967 *J. Phys. Soc. Japan.* **22** 1221–32
Koehler W C, Moon R M, Trego A L and Mackintosh A R 1966 *Phys. Rev.* **151** 405–13
Loegel B 1975 *J. Phys. F: Metal Phys.* **5** 497–505
Mitchell M A and Goff J F 1972 *Phys. Rev.* **B5** 1163–70
Nevitt M V and Aldred A T 1963 *J. Appl. Phys.* **34** 463–8
Rajan N S, Waterstrat R M and Beck P A 1960 *J. Appl. Phys.* **31** 731–2
Suzuki T 1976 *J. Phys. Soc. Japan* **41** 1187–94
Trego A L and Mackintosh A R 1968 *Phys. Rev.* **166** 495–506

J. Phys. F: Metal Phys., Vol. 9, No. 5, 1979. Printed in Great Britain

LETTER TO THE EDITOR

The coexistence of spin density wave ordering and spin glass ordering in chromium alloys containing iron

J O Strom-Olsen†, D F Wilford†, S K Burke‡ and B D Rainford‡
† Rutherford Physics Building, McGill University, 3600 University Street, Montreal, Quebec, Canada H3A 2TB
‡ Blackett Laboratory, Imperial College, Prince Consort Road, London SW7 2BZ

Received 22 December 1978

Abstract. Neutron scattering, transport and magnetic measurements are presented on two spin density wave hosts, Cr and Cr–Mo 2%, each containing 14% Fe. The results show that in both systems antiferromagnetism and spin glass ordering coexist at low temperatures.

CrFe is an alloy system which has attracted a great deal of interest in the past two decades, interest stimulated partly by chromium having an unusual spin density wave (SDW) antiferromagnetism and partly by iron being one of the few solutes in chromium to sustain a local moment. The addition of Fe to antiferromagnetic Cr reduces the Néel temperature gradually, the SDW disappearing at a concentration of some 16%Fe (Burke and Rainford 1978). The onset of ferromagnetism occurs at approximately 19%Fe (Burke *et al* 1978), no long-range order can be sustained in the narrow region between 16% and 19% and spin glass type behaviour is observed (Shull and Beck 1975, S K Burke and B D Rainford 1979 unpublished).

There is evidence that the iron moment acts largely independently of the SDW: the susceptibility of dilute samples is Curie-like below T_N down to all but the lowest temperatures (Ishikawa *et al* 1965) and the magnetoresistance is characteristic of scattering from free magnetic impurities (Hedgcock *et al* 1977). Recent work by Friedel and Hedman (1979) interprets this behaviour in terms of a strong coupling between isolated Fe moments and the SDW, but with clusters of iron moments remaining largely uncoupled to the SDW. This raises the intriguing possibility that, in more concentrated samples, the state of magnetic order of the iron moments may be determined solely by iron–iron interactions, independent of the SDW. The spin glass type of behaviour of the iron moments may, in fact, extend into the antiferromagnetic regime.

Preliminary measurements indicated that this may be so. Neutron small-angle scattering measurements performed on a Cr–Fe15·5% alloy showed ferromagnetic Fe–Fe correlations extending over a range of some 40 Å at 4·2 K (Burke *et al* 1978). High-field magnetisation measurements (Ishikawa *et al* 1965) were interpreted in terms of superparamagnetic behaviour of the iron moments. In a recent publication, Hedgcock *et al* (1978) presented results of susceptibility and resistivity measurements on a sample containing 14% Fe† dissolved in the SDW host Cr-Mo 2%. The

† This corrects the reported concentration of 10% Fe.

0305-4608/79/050095 + 04$01.00

susceptibility indicated spin glass behaviour, and although no direct evidence was presented for the alloy undergoing a transition to an SDW state, the resistivity measurements indicated that this may have taken place.

In order to establish whether the spin glass type of order could coexist with an SDW, neutron Bragg scattering, resistivity and magnetisation measurements were performed on two alloys containing 14% Fe dissolved in the SDW hosts Cr and Cr–Mo2%.

Samples were prepared from 4N5 or 5N starting materials (Johnson–Matthey 'Spec-pure') by melting in an argon atmosphere and homogenised by annealing under vacuum at 1000 °C for five days. Resistance and susceptibility samples were spark-cut from the samples used for neutron diffraction. The neutron diffraction experiments were carried out at AERE Harwell as described by Burke and Rainford (1978). Resistance was measured using a four-terminal AC technique (Muir and Strom-Olsen 1976). Magnetisation measurements were obtained using a vibrating sample magnetometer; both field-cooled and non-field-cooled measurements were made. The non-field-cooled

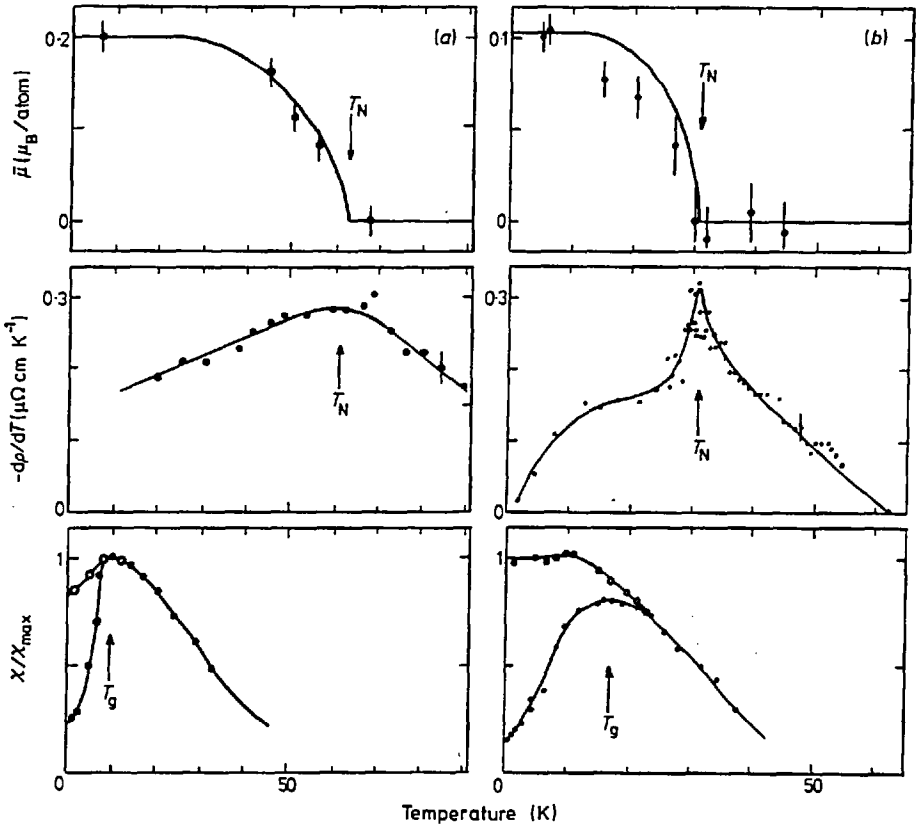

Figure 1. Results of neutron Bragg scattering, resistivity and susceptibility measurements on: (*a*), Cr–Fe14%; (*b*), Cr–Mo2%–Fe14%. The Néel temperatures determined by neutron diffraction and resistivity are arrowed. The spin glass transition temperature, which occurs below T_N, is also arrowed. The $B_{\frac{1}{2}}$ temperature dependence expected for the ordered antiferromagnetic moment $\bar{\mu}$ determined by neutron diffraction is represented by the solid curve. For the susceptibility data, normalised to the peak susceptibility χ_{max}, the open circles represent data taken in a field-cooled state and full circles represent zero-field cooling.

Table 1. Ordered antiferromagnetic moment, Néel temperature and spin glass temperature.

	T_N (K)	$M(0)$ (μ_B/atom)	T_G (K)
Cr–Fe14%	65 ± 5	0·20	9 ± 0·5
Cr–Mo2%–Fe14%	30 ± 2	0·10	17 ± 0·5
Mo–Fe14%	0	0	30 ± 1

results were obtained by cooling in zero field to 1·2 K and sweeping the field by ±10 Oe at progressively higher temperatures to obtain the low-field susceptibility. The field-cooled results were obtained by cooling the sample in a field of 500 Oe; the measured magnetisation divided by the field then gave the susceptibility.

The results of this series of measurements are presented in figure 1. The resistivity data are expressed in terms of $-d\rho/dT$†, as it is the maximum in this quantity rather than the minimum in the resistivity which marks T_N (Burke and Rainford 1978). Comparison of T_N determined in this way with the results of neutron diffraction determination of the ordered antiferromagnetic moment as a function of temperature shows the two values to be in excellent agreement. Furthermore, the neutron data show the SDW state to be maintained down to the lowest temperatures. The susceptibility shows clear evidence for spin glass ordering below T_N. The susceptibility obtained by cooling the samples in zero field shows a peak characteristic of a spin glass at the freezing temperature T_g (rounded somewhat in comparison to AC results), while the susceptibility obtained after field cooling saturates below T_g. The evolution between the field-cooled and zero-field-cooled states is governed by a slow time dependence similar to that found by Guy (1977) on AuFe.

A summary of the relevant parameters is given in table 1. Both systems exhibit transitions to both SDW states and spin glass states. However, although the two types of magnetic order coexist at low temperatures, the two ordering temperatures are not independent: a higher T_N gives a lower T_g. For completeness, data on the Mo–Fe14% spin glass is included (Amamou *et al* 1976).

Now T_g is controlled by: (i), direct Fe–Fe coupling; (ii), indirect Fe–Fe coupling via the conduction electrons; and possibly (iii), a small residual direct interaction with the SDW. Since the percentage occupancy of the BCC matrix is the same in the two systems, the direct Fe–Fe couplings may be assumed to be the same. The conduction electron coupling, however, may be different. The sample with the lower T_N will have more electron-hole pairs excited over the SDW energy gap, and these carriers may be expected to have a strong influence on the Fe–Fe interactions because of their predominantly d character. Thus one would expect the sample with lower T_N to have a higher T_g, as observed. Mo–Fe14% also fits in with this trend, but as the lattice parameter in this alloy is significantly larger than in the CrFe and CrMoFe samples the direct Fe–Fe interactions may have been modified. The same trend will also be given by the direct SDW coupling, although presumably the functional dependences would be different. At present, there is little information to say which, if either, of these mechanisms is important.

Finally, it should be noted that although the SDW is destroyed in CrFe before long-range ferromagnetic order appears it might be possible to have the two states coexisting in an alloy such as CrReFe. According to percolation models the onset

† This corrects the omission of a negative sign.

of ferromagnetism will be determined by the Fe occupancy of the BCC lattice, and so may be expected to remain at ~19% Fe. On the other hand, the addition of 1% Re raises T_N of Cr by ~150 K (Trego and Mackintosh 1968); thus, all other factors being the same, the SDW state should not be destroyed until well beyond the percolation limit for ferromagnetism. We are currently investigating this interesting situation.

This work was supported by the Neutron Beam Research Committee of the SRC and by NRC grant A 5948. S K Burke acknowledges receipt of the Rutherford Scholarship of the Royal Society. J Strom-Olsen would like to thank Professor B R Coles and the Metal Physics Group at Imperial College for their hospitality during his leave of absence. We wish to thank Dr C N Guy for his help with preliminary measurements and for helpful discussion. S K Burke and B D Rainford wish to thank the University Support Group at Harwell for their assistance with the neutron measurements.

References

Amamou A, Caudron R, Costa P, Friedt J M, Gautier F and Loegel B 1976 *J. Phys. F: Metal Phys.* **6** 2371–88

Burke S K, Cywinski R and Rainford B D 1978 *J. Appl. Crystallogr.* **11** 644–48

Burke S K and Rainford B D 1978 *J. Phys. F: Metal Phys.* **8** L239–43

Friedel J and Hedman L E 1979 to be published

Guy C N 1977 *J. Phys. F: Metal Phys.* **7** 1505–19

Hedgcock F T, Strom-Olsen J O and Wilford D F 1977 *J. Phys. F: Metal Phys.* **7** 855–68

——1978 *J. Physique* C6 790–1

Ishikawa Y, Tournier R and Filippi J 1965 *J. Phys Chem. Solids* **26** 1727–45

Muir W B and Strom-Olsen J O 1976 *J. Phys. E: Sci. Instrum.* **9** 163–4

Shull R D and Beck P A 1975 *Magnetism and Magnetic Materials, San Francisco 1974: AIP Conf. Proc.* no. **24** 95–6

Trego A L and Mackintosh A R 1968 *Phys. Rev.* **166** 495–506

SPIN CORRELATIONS CLOSE TO THE CRITICAL CONCENTRATION IN Cr–Fe ALLOYS

S. K. BURKE, B. D. RAINFORD and M. WARNER*
Blackett Laboratory, Imperial College, London SW7 2B, UK

A model is presented to account for the small angle neutron scattering from Cr–Fe alloys close to the critical concentration for ferromagnetism. The spin–spin correlations are treated as a random walk and are considered in a similar way to a polymer chain. The effect of magnetostatic shape anisotropy in determining the resultant correlations is discussed.

The development of long range spin correlations a function of temperature and composition in vicinity of the critical concentration for ferromagnetism in Cr–Fe alloys has been studied by small angle neutron scattering [1]. A marked nge in the q dependence of the scattering is rved for ferromagnetic alloys as the tempera- is lowered below T_c. Close to T_c the scattering orentzian implying that the instantaneous spin elations have the classical Ornstein–Zernike n. However, at temperatures below T_c the ming increasingly deviates from this Lorent- form as shown in fig 1a. In ref. [1] it was posed that this small angle scattering reflected geometry of clusters of correlated iron mo- s. This idea is developed by using a polymer logy.

The neutron scattering cross section is proportional to the Fourier transform of the spin–spin relation function,

$$S(q) \sim \frac{1}{N^2} \sum_{i,j} \langle\langle S_i \cdot S_j \, e^{iq\cdot(R_i - R_j)} \rangle\rangle, \qquad (1)$$

where $\langle\langle\ \rangle\rangle$ is both a thermal and configurational average. In the spirit of percolation theory we consider the small angle scattering (SAS) to be due to large but finite clusters of ferromagnetically coupled nearest neighbour spins. The response of the infinite cluster at low temperatures will be a delta function at $q = 0$ and may be neglected. It is assumed that there is no intercluster correlation.

In order to evaluate $S(q)$, we assert that the average over finite clusters is dominated by those clusters with one-dimensional character. Some justification for this assertion can be drawn from computer simulations of percolation clusters which show a large degree of "ramification" or stringiness [2]. Thus we represent a finite cluster by a chain of N spins connected in a random walk and replace the ensemble average by an average over random walks.

(*a*) *Exchange only*. In the case when a cluster has a common fixed magnetic axis, $S(q)$ is

$$S(q) \sim \tfrac{2}{3}\varepsilon S^2 \frac{1}{N^2} \sum_{i,j=0}^{N-1} \langle e^{iq\cdot(R_i - R_j)} \rangle, \qquad (2)$$

where $\langle\ \rangle$ is the configurational average for a Gaussian walk and ε measures the degree of spin correlation within the cluster ("chain").

Consider the case when $\varepsilon = 1$. This corresponds to complete ferromagnetic alignment between all spins in the chain as shown in fig 2a. Following a standard argument [3], we have for a Gaussian chain,

$$\sum_{i,j} \langle e^{iq\cdot(R_i - R_j)} \rangle = \sum_{i,j} e^{-q^2 C l^2 |i-j|/6}, \qquad (3)$$

where the mean square distance between spins i and j is assumed to be proportional to the number of steps separating them along the chain. Here l is the nearest neighbour distance and C, the "characteristic ratio," is a measure of chain stiffness and is unity for a freely jointed chain. Replacing the double summation by a sum over $|i - j|$ one finds after a straightforward calculation,

$$\sum_{i,j} e^{-|i-j|\gamma} = \frac{1}{(1-x)^2}\left[2N(1-x) - 2x(1-x^N) - N(1-x)^2\right], \qquad (4)$$

where $\gamma = q^2 C l^2/6$ and $x = \exp(-\gamma)$. In the limit of small γ but finite $N\gamma$ this result reduces to the Debye expression,

$$S_D(V) \sim (2/V^2)\left[V + e^{-V} - 1\right], \qquad (5)$$

with $V = N\gamma = q^2 R^2$ where R is the radius of

* K33-281, IBM Research Labs, San Jose, CA 95114, USA.

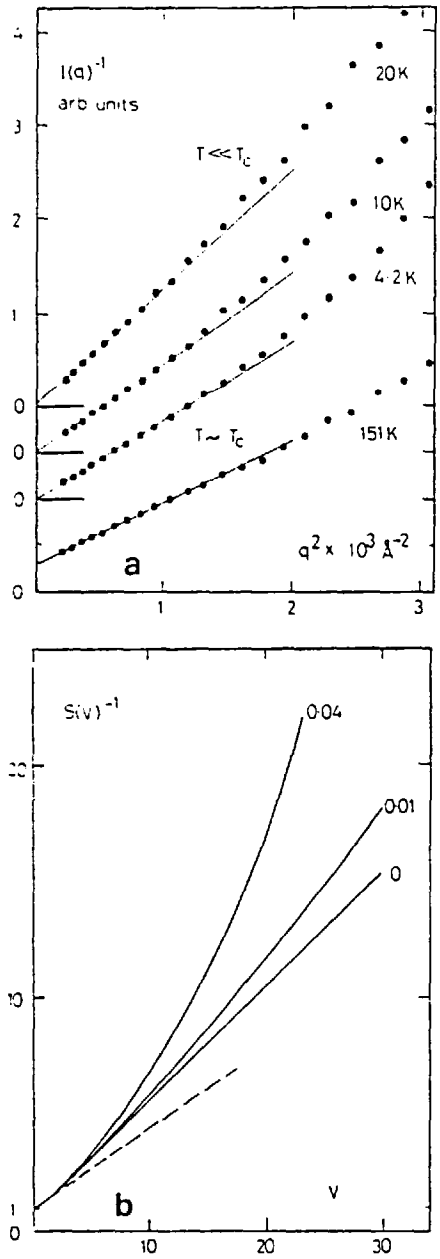

Fig. 1. (a) Plot of reciprocal intensity versus q^2 for a ferromagnetic Cr–Fe 24% alloy. The q dependence of the small angle scattering close to T_c is Lorentzian, lower curve. The scattering deviates from Lorentzian at temperatures below T_c, upper curves. (b) Plot of reciprocal scattering function versus $V = q^2R^2$ for values of r^2/R^2 of 0, 0.01 and 0.04. The dashed line represents the Lorentzian approximation to the scattering at low V.

gyration of the chain. The Debye form closely

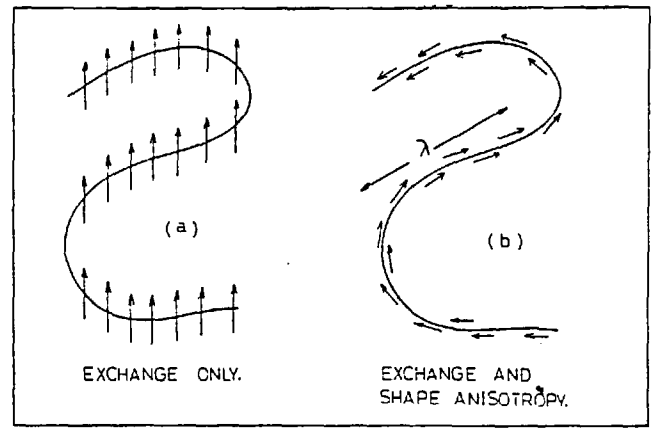

Fig. 2. The spin configuration (a) corresponding to $\epsilon = 1$ has a large magnetostatic energy due to dipolar fields. This energy may be lowered by allowing the spins to follow the local chain axis as in configuration (b), resulting in spin correlations over a characteristic length λ.

approximates a Lorentzian for $V \lesssim 3$. For large $N\gamma$ further terms must be taken into account leading to

$$S(V) \sim S_D(V) + \frac{r^2}{R^2}\left[\frac{2}{V}\left(1 - e^{-V} - \tfrac{1}{2}V\right)\right], \quad (6)$$

where $r^2 = Cl^2/6$. A plot of $1/S(q)$ against q^2 is shown in fig 1b, a Lorentzian is linear on this scale. This is in qualitative agreement with the SAS data at low temperature (fig 1a), displaying an upturn in $1/S(q)$ as the scattering deviates from Lorentzian at higher q.

An estimate of the radius of gyration for these clusters may be obtained from the initial linear portion of the graph $1/I(q)$ vs. q^2 using eq. (6). The resultant R is of the order of 250 Å. Such a large ramified aggregate of spins possesses considerable magnetostatic energy and leads us to the consideration of another possibility.

(*b*) *Exchange and magnetostatic anisotropy*. The magnetostatic energy of the cluster will tend to be minimized if the spins are aligned along the local "chain" axis. The final spin configuration will be determined by the competition between this shape anisotropy and the exchange interaction (fig 2b). Firstly, without exchange, the correlations can only persist over a distance typical of the correlation in direction in the tangent of the "chain" trajectory. With the additional competition of exchange forces of (a) the correlation is further spatially enhanced.

If the correlation along the chain is characterised by the length λ (measured along the chain) the vector ε is now given by

$$\varepsilon_{ij} = \langle S_i \cdot S_j \rangle S^2 / \sim e^{-|i-j|Ct/\lambda}.$$

Using this relation $S(q)$ may be calculated by replacing γ in eq. (4) by $Cl(q^2/6 + 1/\lambda)$. The existence of a second characteristic length λ may lead to a variety of interesting phenomena, in particular one may expect a crossover in behaviour to be detected in the SAS in the range $1/R \leqslant q \leqslant 1/l$

The SAS experiments were performed at ILL, Grenoble. S.K.B. acknowledges receipt of the Rutherford Scholarship of the Royal Society.

References

[1] S. K. Burke, R. Cywinski and B. D. Rainford, J. Appl. Cryst. 11 (1978) 644.
[2] H. E. Stanley, R. J. Birgeneau, P. J. Reynolds and J. F. Nicoll, J. Phys. C 9 (1976) L553.
[3] P. J. Flory, Statistical Mechanics of Chain Molecules (Wiley, New York, 1969) p. 340.
[4] B. Farnoux, M. Daoud, J. P. Cotton, G. Jannink, M. Nierlich and F. Boue, J. Appl. Cryst. 11 (1978) 511.

MAGNETIZATION DENSITY IN FERRIMAGNETIC Pt_3Cr

S. K. BURKE, B. D. RAINFORD, D. E. G. WILLIAMS*, P. J. BROWN† and D. A. HUKIN‡
Blackett Laboratory, Imperial College, London SW7 2BZ, UK

The magnetization density in ordered Pt_3Cr has been measured by polarized neutron diffraction. The induced Pt moment is small ($0.26\mu_B$) and oppositely directed to the large Cr moment of $3.37\mu_B$. The magnetization has a delocalized component of $-0.07\mu_B$.

In common with many of the 3d transition metals, Cr forms an ordered Cu_3Au phase with Pt. Pt_3Cr shows ferrimagnetic order; the induced Pt moment is opposite in direction to that of the 3d moment. This is in contrast to the other ordered alloys (table 1). The existence of ferrimagnetic order in Pt_3Cr polycrystals was reported by Pickart and Nathans in 1962 [1, 2]. However, the atomic moments in that study combine to give a total magnetization which is substantially lower than the accepted value [3–5]. The present polarized neutron study was initiated to determine the magnetization distribution in ferrimagnetic Pt_3Cr. This provides complementary data to the measurements of spin density in ferromagnetic Pt_3Mn and Pt_3Co [6, 7].

Electron microprobe analysis showed the crystal to be within ± 1% of stoichiometry. The crystal was annealed for 6 h at 950°C and slow cooled to allow the development of atomic order. The magnetic moment per unit cell was found to be $2.48\mu_B$, the Curie temperature 494 K and the lattice parameter 3.877 Å in good agreement with values reported for fully ordered Pt_3Cr [3–5, 9].

The degree of long range order was determined by unpolarized neutron diffraction at AERE, Harwell. The long range order parameter S was found to be $S = 1.1$. As S must always be less than 1.0 it is assumed that $S = 1$ in the calculation of the nuclear structure factors.

The polarized neutron experiments were performed at $T = 4$ K using the instrument D3 at ILL. Flipping ratios were collected for all reflections in the [1$\bar{1}$0] zone out to a value of $\sin\theta/\lambda$ of 0.92 $Å^{-1}$. The flipping ratios were corrected for extinction by measurements at three wavelengths using the diffractometer D5. The fundamental reflections showed extinction decreasing from 8% at (111) to below 1% for the (222) reflections. No correction was applied beyond the first five fundamental reflections. The (100) and (110) superlattice reflections had large flipping ratios which were sensitive to correction and were omitted from the analysis. The magnetic structure factors could then be extracted from the corrected flipping ratios using the nuclear structure factors.

A Fourier inversion of the data resulted in the magnetization density shown in fig. 1. The negative magnetization at the Pt sites shows that the alloy is ferrimagnetic. It is also apparent that the distribution of Cr moment is spherical whereas the distribution of Pt moment is rather aspherical. A small constant negative spin density is found between the sites. The maximum negative density does not occur at the Pt site, indicating the presence of some atomic disorder.

The magnetic moments associated with each site were determined by least squares fits to the experimental magnetic structure factors using the Freeman and Watson atomic Cr spin only form factor

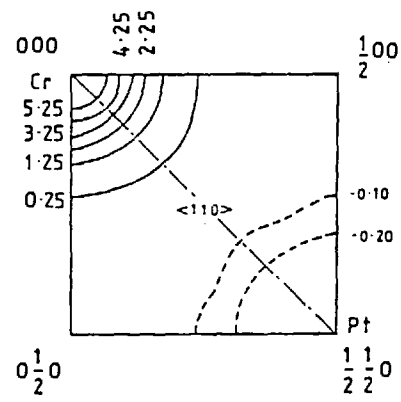

Fig. 1. The magnetization density in the (100) plane for Pt_3Cr. Contour levels are in units $\mu_B/Å^3$.

*Physics Department, LUT, Loughborough, LE11 3TU, Leics., UK.
†Institut Laue-Langevin, BP156X, Centre de Tri, Grenoble, France.
‡Clarendon Laboratory, Oxford, UK.

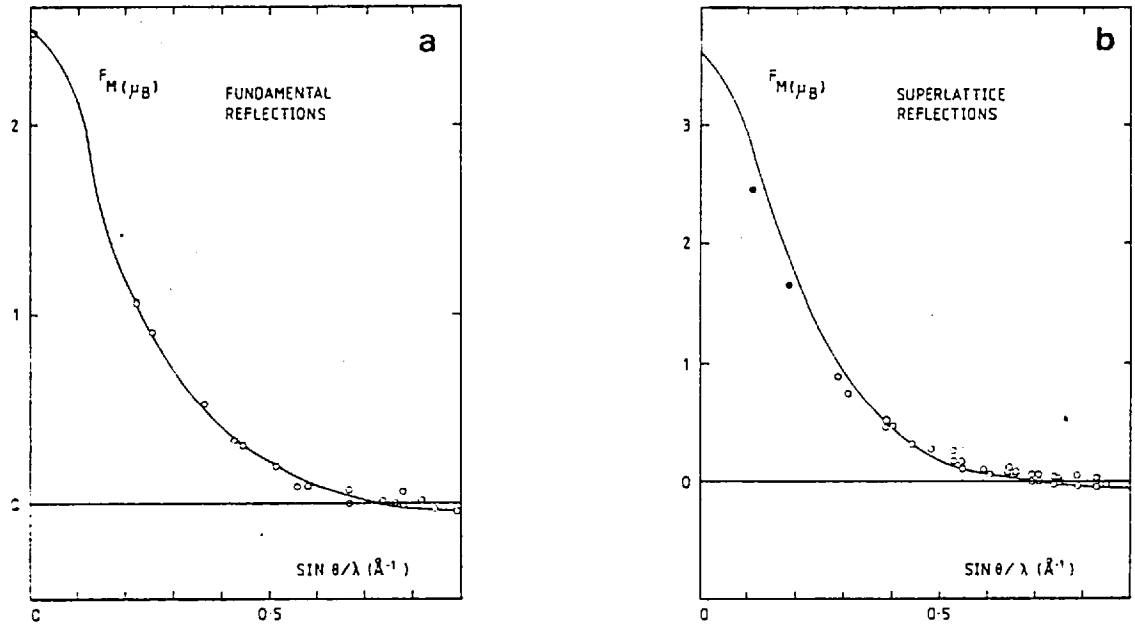

Fig. 2. Experimental magnetic structure factors in μ_B for (a) fundamental and (b) superlattice reflections. The full curve represents the structure factor calculated by assigning $3.37\mu_B$ to a Cr site and $-0.26\mu_B$ to the Pt site with a delocalized moment of $-0.07\mu_B$. The open circles are the results of the polarized neutron measurements, closed circles are from unpolarized measurements.

TABLE 1

Comparison of magnetic moments for the series of ordered Pt_3–3d transition metal alloys with Cu_3Au structure. Pt_3Fe is antiferromagnetic, Pt_3Mn and Pt_3Co are ferromagnetic and Pt_3Cr is ferrimagnetic

	Pt_3Cr	Pt_3Mn	Pt_3Fe	Pt_3Co
3d moment (μ_B)	3.37	3.64	3.3	1.64
Pt moment (μ_B)	−0.26	0.26	≈0	0.26
Reference	this work	[7]	[8]	[6]

for the Cr sites and a relativistic Hartree–Fock Pt^{2+} spin only form factor for the Pt sites [10, 11]. According to this procedure $\mu_{Cr} = 3.37\mu_B$, $\mu_{Pt} = -0.26\mu_B$ and a delocalized negative density of $-0.07\mu_B$. As shown in fig. 2 the fit is good for the fundamental reflections but overestimates the superlattice structure factors below 0.3 $Å^{-1}$. The value of the bulk magnetization was used in the fit but was not a constraint.

A moment of $3.37\mu_B$ is large for Cr. By comparison Pickart and Nathans, using a delta function form factor for Pt derived $\mu_{Cr} = 2.33\mu_B$ and $\mu_{Pt} = -0.27\mu_B$. However, support for this large value may be derived from susceptibility measurements above T_c for which $p_{eff} = 3.6\mu_B$ [4]. The bulk magnetization cannot be reconciled with ferrimagnetism without a large Cr moment. It is also interesting to note that large 3d moments are also observed in Pt_3Mn, Pt_3Co and Pt_3Fe (table 1). A more detailed analysis including the effects of disorder, orbital contributions to the moment and asymmetry is proceeding.

This work was supported by the Neutron Beam Research Committee of the SRC. SKB acknowledges receipt of the Rutherford Scholarship of the Royal Society.

References

[1] S. J. Pickart and J. Nathans, J. Appl. Phys 33 (1962) 1336.
[2] S. J. Pickart and J. Nathans, J. Appl. Phys 34 (1963) 1203.
[3] M. J. Besnus and A. J. P. Meyer, Phys. Stat. Sol (b) 55 (1973) 537.
[4] T. Goto, J. Phys. Soc. Japan 43 (1977) 1848.
[5] D. E. G. Williams and B. G. Lewis, Z. Metall. 70 (1979) 441.
[6] F. Menzinger and A. Paoletti, Phys. Rev. 143 (1966) 365.
[7] B. Antonini, F. Lucari, F. Menzinger and A. Paoletti, Phys. Rev. 187 (1969) 611.
[8] G. E. Bacon and J. Crangle, Proc. Phys. Soc. A273 (1963) 387.
[9] B. G. Lewis and D. E. G. Williams, J. Less Common Metals 44 (1976) 337.
[10] A. J. Freeman and R. E. Watson, Acta Cryst. 14 (1961) 27.
[11] T. J. Watson-Yang, A. J. Freeman and D. D. Koelling, J. Magn. Magn. Mat. 5 (1977) 277.